Theses and Dissertations   Thesis Collection

2005-09

Fluid-structure interaction effects resulting from hull appendage coupling

Avcu, Mehmet

Monterey California. Naval Postgraduate School

http://hdl.handle.net/10945/2019

NAVAL POSTGRADUATE SCHOOL

MONTEREY, CALIFORNIA

THESIS

**FLUID-STRUCTURE INTERACTION EFFECTS
RESULTING FROM HULL APPENDAGE COUPLING**

by

Mehmet Avcu

September 2005

Thesis Advisor: Young S. Shin
Co-Advisor: Jarema M. Didoszak

Approved for public release; distribution is unlimited

THIS PAGE INTENTIONALLY LEFT BLANK

REPORT DOCUMENTATION PAGE			*Form Approved OMB No. 0704-0188*
Public reporting burden for this collection of information is estimated to average 1 hour per response, including the time for reviewing instruction, searching existing data sources, gathering and maintaining the data needed, and completing and reviewing the collection of information. Send comments regarding this burden estimate or any other aspect of this collection of information, including suggestions for reducing this burden, to Washington headquarters Services, Directorate for Information Operations and Reports, 1215 Jefferson Davis Highway, Suite 1204, Arlington, VA 22202-4302, and to the Office of Management and Budget, Paperwork Reduction Project (0704-0188) Washington DC 20503.			
1. AGENCY USE ONLY *(Leave blank)*	**2. REPORT DATE** September 2005	**3. REPORT TYPE AND DATES COVERED** Master's Thesis	
4. TITLE AND SUBTITLE: Fluid-Structure Interaction Effects Resulting From Hull Appendage Coupling			**5. FUNDING NUMBERS**
6. AUTHOR(S) Mehmet Avcu			
7. PERFORMING ORGANIZATION NAME(S) AND ADDRESS(ES) Naval Postgraduate School Monterey, CA 93943-5000			**8. PERFORMING ORGANIZATION REPORT NUMBER**
9. SPONSORING /MONITORING AGENCY NAME(S) AND ADDRESS(ES) N/A			**10. SPONSORING/MONITORING AGENCY REPORT NUMBER**
11. SUPPLEMENTARY NOTES The views expressed in this thesis are those of the author and do not reflect the official policy or position of the Department of Defense or the U.S. Government.			
12a. DISTRIBUTION / AVAILABILITY STATEMENT Approved for public release; distribution is unlimited			**12b. DISTRIBUTION CODE**
13. ABSTRACT (maximum 200 words) 　　In previous work conducted in the modeling and simulation of ships subjected to underwater explosions, there has been some debate over the influence that hull appendages have upon the dynamic response of a multi-degree-of-freedom structural model surround by a fluid mesh. This thesis investigates the effects on the dynamic response of a structural model resulting from the inclusion of hull appendages such as rudders, shafts and keel boards. Moreover, it examines the differences resulting from these appendages having been modeled as coupled or uncoupled structures with respect to the surrounding fluid in the finite element analysis. In this case, a Meko-like box model, based on the actual dimensions of a typical Meko-class ship, was investigated using the underwater shock modeling and simulation methodology developed at the Naval Postgraduate School's Shock and Vibration Computational Laboratory. Presented herein is a detailed study on the validity of including hull appendages, the proposed coupling scheme for these appendages, and the resulting effects on the vertical and athwartship velocity response motions.			
14. SUBJECT TERMS Underwater Explosion, Shock and Vibration, Modeling and Simulation, UNDEX, Shock Response, Ship Shock, Meko			**15. NUMBER OF PAGES** 426
			16. PRICE CODE
17. SECURITY CLASSIFICATION OF REPORT Unclassified	**18. SECURITY CLASSIFICATION OF THIS PAGE** Unclassified	**19. SECURITY CLASSIFICATION OF ABSTRACT** Unclassified	**20. LIMITATION OF ABSTRACT** UL

THIS PAGE INTENTIONALLY LEFT BLANK

FLUID-STRUCTURE INTERACTION EFFECTS RESULTING FROM HULL APPENDAGE COUPLING

Mehmet Avcu
Lieutenant Junior Grade, Turkish Navy
B.S. ME, Turkish Naval Academy, 1999

Submitted in partial fulfillment of the
requirements for the degree of

MASTER OF SCIENCE IN MECHANICAL ENGINEERING

from the

NAVAL POSTGRADUATE SCHOOL
September 2005

Author: Mehmet Avcu

Approved by: Young S. Shin
                 Thesis Advisor

                 Jarema M. Didoszak
                 Co-Advisor

                 Anthony J. Healey
                 Chairman, Department of Mechanical and Astronautical
                 Engineering

iii

THIS PAGE INTENTIONALLY LEFT BLANK

ABSTRACT

In previous work conducted in the modeling and simulation of ships subjected to underwater explosions, there has been some debate over the influence that hull appendages have upon the dynamic response of a multi-degree-of-freedom structural model surrounded by a fluid mesh. This thesis investigates the effects on the dynamic response of a structural model resulting from the inclusion of hull appendages such as rudders, shafts and keel boards. Moreover, it examines the differences resulting from these appendages having been modeled as coupled or uncoupled structures with respect to the surrounding fluid in the finite element analysis. In this case, a Meko-like box model, based on the actual dimensions of a typical Meko-class ship, was investigated using the underwater shock modeling and simulation methodology developed at the Naval Postgraduate School's Shock and Vibration Computational Laboratory. Presented herein is a detailed study on the validity of including hull appendages, the proposed coupling scheme for these appendages, and the resulting effects on the vertical and athwartship velocity response motions.

THIS PAGE INTENTIONALLY LEFT BLANK

TABLE OF CONTENTS

THIS PAGE INTENTIONALLY LEFT BLANK

LIST OF FIGURES

xvii

THIS PAGE INTENTIONALLY LEFT BLANK

LIST OF TABLES

ACKNOWLEDGMENTS

THIS PAGE INTENTIONALLY LEFT BLANK

I. INTRODUCTION

A. BACKGROUND

As early as the mid-1800's, the application of underwater explosions (UNDEX) in Undersea Warfare was recognized to be a real threat to surface ships. During World War I, the war at sea revealed the influence of the torpedo, as well as floating and anchored mines, and indicated the necessity for better defense against these weapons. Even though some efforts were being pursued at the turn of the century, it was not until the late 1930's that an intensive attempt was made to develop the experimental program in the U.S. Navy. Personnel at the Norfolk Naval Shipyard were assigned by the Bureau of Ships to conduct testing of underwater explosion effects on small structural models of recently designed naval vessels. This initial group designed the Underwater Explosions Barge (UEB - 1), and then manufactured it in the early 1940's. This barge design was extremely instrumental in broadening the experimental testing capabilities of the program in which many tests were executed to learn ways of advancing the strength of ship's hulls to resist the destructive effects of underwater explosions [Ref. 1].

World War II was the war which introduced more complex weapons than ever before. Ships increasingly were disabled by non-contact UNDEX, that is, a direct strike was not required to eliminate a ship from naval combat. Since the U.S. Navy experienced the destructive effects of near proximity UNDEX from mines and torpedoes during wartime, naval leaders noticed that a new destructive phenomenon was occurring, and it was responsible for sending many ships to the bottom of the sea with no direct hit from a mine or torpedo. Ships sank due to the explosives detonating under their keels, breaking the ship's back as the ships were raised up and then banged down into the water into the void left by the explosion. With the capability to deliver increasing charge sizes efficiently, it became obvious that hitting the hull of the ship was no longer as significant as once had been the case. For an UNDEX to be effective in damaging the ship, a direct hit delivered to a weapons magazine or fuel storage tanks that would make possible the occurrence of internal explosions and final catastrophic loss due to fire, which would be both convenient and desirable. On the other hand, when an insightful analysis of the wartime losses is made, it is noted that most ship losses experienced throughout the first

1

half of the 20th century were due to the incident shock wave and gas bubble pulse forces resulting from UNDEX events. The incident shock wave and gas bubble pulse forces can be considered as main initiators of structural damage, material failure and final loss in the sinking of many ships [Ref. 2].

Consequently, investigation on the effects of underwater explosions was intensified in the U.S. Navy, and in 1946, the Underwater Explosions Research Department (UERD) was founded as a division of the Norfolk Naval Shipyard in Portsmouth, Virginia [Ref. 1]. UERD embarked on experimental plans to examine techniques for developing the resistance of ships and submarines to underwater weapons, to establish methods to evaluate the effects of underwater explosions on ships and to supply guidance for the development of U.S. weapons' efficiency. From the time when it was established, UERD has worked with many other Navy and Department of Defense activities, conducting full scale surface ship and submarine shock trials, test section and weapons effects trials, equipment shock hardening and shock qualification tests, precision experiments with scale-model targets, free field phenomena experiments, and exercise torpedo impact [Ref. 1].

During the last 50 years, a large amount of knowledge has been amassed in the UNDEX area, resulting in a better understanding of the UNDEX shock phenomena. As a result, the need for ships that were resilient in UNDEX situations has been realized, and thus, guidelines and specifications were developed for the design and shock testing requirements of all naval surface combatants and hardening of shipboard equipment and systems. The Department of the Navy set forth guidance for shock hardening of surface ships in OPNAVINST 9072.2 [Ref. 3], with additional requirements defined in NAVSEA 0908-LP-000-3010A [Ref. 4] and MIL-S-901D [Ref. 5]. Completed in the summer of 2001, the DDG-81 Ship Shock Trials are the most recent set of Live Fire Testing & Evaluations (LFT&E) to be conducted in completion of these requirements.

The shock trials, a series of underwater explosions, created by the detonation of charges placed at varying distances from the ship, attempt to test the ship at "near combat conditions" [Ref. 3]. The effects of the shock trials to ship systems are observed and the response of the ship, weapons systems, specific equipment and the crew are measured

and recorded to assess their performance in a shock atmosphere for each shot. The lead ship of each class, or a ship significantly deviating from other ships of the same class due to the major design changes during construction, is required to experience these shock trials in order to analyze and make recommendations for the modification of existing ships or for a change in the design of following ships to be constructed within the same ship class.

While the shock trials supply accurate evidence about how the systems of the ship respond in a real UNDEX case and are beneficial in training the crew, they are very expensive and extremely dangerous. In addition, such events need years of preparation, planning and coordination and are potentially destructive to the ship structure, weapons systems and electronics. Although these shock trials provide useful information about the ship's potential reaction in a shock environment, they do not permit testing up to the ships' design limits or even the true naval combat shock environment due to the safety concerns. Therefore, they are limited to test only as much as two-thirds of the ships' design limits. LFT&E program limitations cause some concerns about the validity of these shock trials and their costs as in the situation of the USS JOHN PAUL JONES (DDG-53) ship shock trials conducted in 1994 [Ref. 6]. The ship shock trial costs could vary as high as 5% of the delivery cost of the ships. Consequently, in the Aegis Destroyer program alone, tens of millions of dollars were expended for the ship shock trials conducted on USS JOHN PAUL JONES (DDG-53) in 1994 and once more for the ship shock trials conducted on USS WINSTON S. CHURCHILL (DDG 81) in 2001.

Exceptional advances in computer modeling and simulation in the last few decades have provided the possibility of moderating some costs related to the LFT&E activities during the use of virtual shock environment analysis [Ref. 7]. These advances have allowed not only many events to be tested in a virtual shock environment, but also have allowed for more rapid improvements in design. The use of finite element method ship models makes it possible to couple the fluid mesh to the ship structural model and accurately predict the dynamic response of the whole ship system to an UNDEX event. Creating a virtual UNDEX environment for the entire ship system can provide many real-life benefits. One of these, as stated before, is the extensive cost saving over traditional at-sea shock testing. Another benefit is that it allows for a greater diversity in explosive

3

shot scenario geometries. Removing potential risk to the crew, ship structure and equipment as well as mitigating operational demands on commissioned ships used in testing can be considered one of the other benefits. Moreover, there will be no negative environmental impact which can occur due to the ship shock trials. Consequently, the virtual UNDEX testing of ship systems presents an extremely useful design tool and an attractive to the future ship shock trials.

In order to provide accurate results by using a computer simulation, the detailed structural finite element model must be utilized and the surrounding acoustic fluid must be coupled with the wetted surface of the structural model entirely. It is obvious that the UNDEX environment is very complicated, i.e. there exists an initial kick-off due to the incident shock wave and then the effects of the cavitation, bubble pulse and structural whipping. While the computational time step should be small, on the order of microseconds, to perform the dynamic response of ship systems accurately, the actual response in an UNDEX event ends in a matter of seconds.

Even though virtual UNDEX testing is not considered sufficiently reliable at this time to replace the LFT&E process entirely, it is used in conjunction with LFT&E and supposed to be a predictive design tool. In other words, while computer modeling and simulation provides good results in the prediction of the ship system dynamic response, it is proposed as a design tool to be used in combination with LFT&E events and other shock testing methods to confirm the shock survivability of a new class of ship. For instance, because they represent virtual UNDEX testing, shock simulations can be conducted at or beyond the design limits, offering more useful design facts than those which are provided by conducting ship shock trials. In addition, by validating the dynamic response predictions made by using a virtual UNDEX testing, it can be used to improve and accelerate the combatant ship system design and, if further advancements in computer processing technology happen in the future, these virtual tests may reduce or eliminate the need for wide scope shots and encourage concentrated investigation of UNDEX events with the use of scaled charges located at particular locations related to the points of concern discovered in previous shock simulations. Furthermore, the future achievement of computer modeling and simulation instead of the entire ship shock trial testing will be determined by LFT&E reserves in an attempt to allow the specific testing

and further investigation of ship systems response in more realistic threat scenarios like near field explosions.

B.   SCOPE OF RESEARCH

Utilizing the data resulting from the shock simulations conducted on the meko-like box model, this thesis serves as a virtual shock environment analysis based on the modeling and simulation methodology established by the Shock and Vibration Computational Laboratory at the Naval Postgraduate School (NPS). In previous efforts performed in the modeling and simulation of ships subjected to UNDEX, there have been some arguments over the influence that hull appendages have upon the dynamic response of a multi-degree-of-freedom structural model surrounded by a fluid mesh. Using the NPS shock modeling and simulation process, this thesis investigates the effects on the dynamic response of the meko-like box model owing to the inclusion of hull appendages such as rudders, shafts and keel boards and the differences resulting from these appendages having been modeled as coupled or uncoupled structures with regard to the surrounding fluid in the finite element analysis. This thesis presents a detailed examination on the validity of including hull appendages, the projected coupling method for these appendages, and consequential effects on the vertical and athwartship velocity responses by comparing the data obtained from all of the shock simulations conducted. The findings of these comparisons will also be presented herein.

THIS PAGE INTENTIONALLY LEFT BLANK

II.   UNDERWATER EXPLOSIONS

Since the underwater shock phenomena are complex, to comprehend the destructive effects of shock, it is necessary to begin with some background information about these phenomena. The most important features will be studied to be able to understand the underwater shock phenomena with its many complex stages related to the system response.

A.   UNDERWATER SHOCK PHENOMENA

First, it is necessary to understand that the pressure wave, in fact, happens to be the nature of the explosion. The pressure wave starts in one part of the explosive, and as long as it propagates through the explosive, it begins the chemical reaction which, in turn, emits more pressure waves. Hence, the wave pressure is inclined to propagate by itself throughout the explosive once the explosion is started. There are actually two different phenomena which are usually described as explosives such as combustion (deflagration) and detonation. Combustion or deflagration can be thought as a burning process. A chemical reaction occurs slowly in this process. Since the fuel releases energy by combustion which is described as a relatively slow process, there will be enough time for the energy to be transported to the surroundings via heat conduction, radiation and non-destructive mechanical process [Ref. 9]. Therefore, the amount of the energy release is more than that of the detonation process. Whenever the combustion process is unconfined, i.e., the discharge of the gaseous yield is allowed, there will generally be a small pressure rise behind the combustion front. However, if the room is not unconfined, the pressure increase behind the combustion front will be much more than the pressure rise in the first situation. It is obvious that, as the pressure increases, the speed of the combustion or deflagration increases as well. Furthermore, as the pressure increases, the wave velocity increases until it exceeds the speed of sound of the explosive. Then, with the pressure wave velocity exceeding the acoustic velocity of the explosive material by anywhere from three to fives times, the shock wave is formed which has a constant velocity through the explosive. The extremely high pressure, which is behind the shock wave front, with the temperature change starts the explosive reaction. Therefore, the

detonation can be considered a self exerted progression that maintains a steady rate. The shock wave propagates outward from the nucleus of the charge at a velocity of approximately 25,000 ft/sec [Ref. 9]. The detonation process converts the original explosive material from its original form (solid, liquid, or gas) into a gas at a very high temperature and pressure which approaches 3000° Celsius and 50000 atmospheres [Ref. 10], respectively. HBX-1, TNT, PENTOLITE, TETRYL or RDX can be considered as these explosives. The starting process takes just nanoseconds to occur in many high explosives [Ref. 11]. Hence, in a very short time, the shock wave is released into the surrounding fluid.

In most scientific applications, water is considered a homogeneous and incompressible fluid which is always incapable of supporting shear stress. On the other hand, for UNDEX purposes, the extremely high pressurized shock wave actually causes the water surrounding the explosive charge to compress. This compression generates a high-pressure shock wave in the water which, in turn, propagates outward from the charge location. While the shock wave, in the beginning, passes through much faster than the speed of sound, as it expands outward, it rapidly slows to the speed of sound [Ref. 9]. The speed of sound is generally assumed as 5000 ft/sec. However, because the factors such as temperature, hydrostatic pressure, and salinity have an effect on the actual speed of sound, for the simulation purposes, 5078 ft/s is used in all cases in this study.

After it is generated by the detonation process, the pressure wave has an extremely large quantity of force exerting outward from the charge center. If a 300 lb. TNT charge is investigated as an example, the pressure wave has the value on the order of $2 \times 10^6 \, \text{lb/in}^2$. As seen in Figure 1, the pressure profile of TNT implies that the initial shock wave illustrates a discontinuous pattern of exponential decay as it radiates outward [Ref. 9]. In general manner, the pressure profile is proportional to the inverse of the standoff distance of the charge, which is considered as the distance from the charge to the submerged structure, and so decreases in magnitude, and expands as it travels outward in a spherical wave pattern.

34,000 lb./in.²

3,400 lb./in.²

2,200 lb./in.²

340 lb./in.²

160 lb./in.²

RADIUS

0   5   40   45   50   400   495   500   FEET
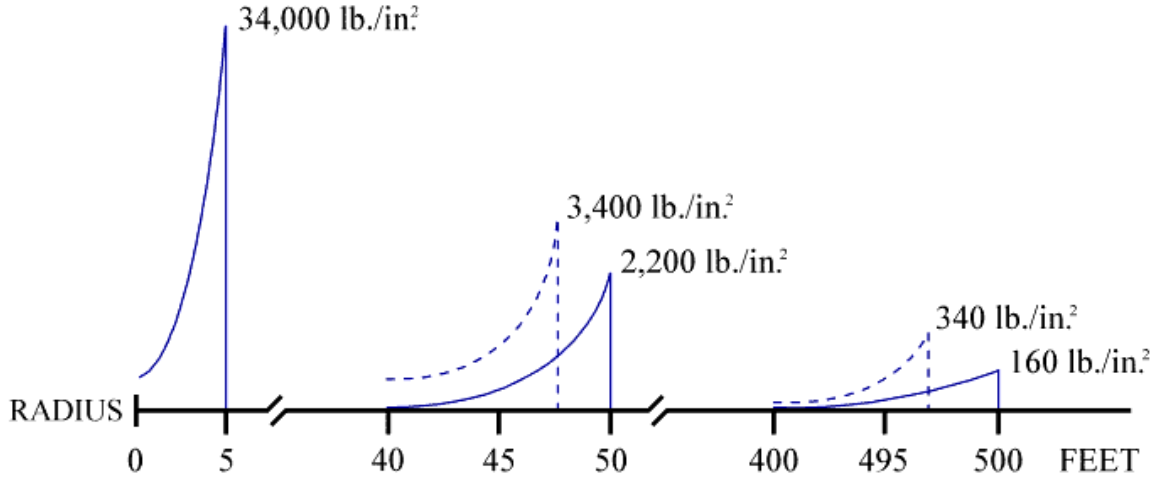
Figure 1.   Shock Wave Pressure Profiles for 300 lb TNT Charge [from Ref. 9]

The following empirical equations were derived to be able to describe the pressure profile of the shock wave. These empirical equations are valid for distances from 10 to 100 charge radii and for the duration of one time decay constant [Ref. 9]. Equations (2.1) – (2.5), are used to calculate the pressure P(t), the peak pressure (P_{max}), and the decay constant (θ) in the shock front, respectively, the maximum bubble radius (A_{max}), and the time of the first pulse of the bubble (T).

$$P(t)=P_{max}e^{-\frac{t-t_1}{\theta}} \quad \text{(psi)} \qquad\qquad (2.1)$$

$$P_{max}=K_1\left(\frac{W^{\frac{1}{3}}}{R}\right)^{A_1} \quad \text{(psi)} \qquad\qquad (2.2)$$

$$\theta=K_2 W^{\frac{1}{3}}\left(\frac{W^{\frac{1}{3}}}{R}\right)^{A_2} \quad \text{(msec)} \qquad\qquad (2.3)$$

$$A_{max}=K_6\frac{W^{\frac{1}{3}}}{(D+33)^{\frac{1}{3}}} \quad \text{(ft)} \qquad\qquad (2.4)$$

9

$$T = K_5 \frac{W^{\frac{1}{3}}}{(D+33)^{\frac{5}{6}}} \qquad \text{(sec)} \qquad\qquad (2.5)$$

where the variables can be defined as follows.

        W = weight of the explosive (lb)

        R = standoff distance of the charge (ft)

        D = charge depth (ft)

        t_1 = arrival time of the shock wave (msec)

        t = time of interest (msec)

        $K_1, K_2, K_5, K_6, A_1, A_2$ = constants which depend on explosive type

Table 1 provides a list of shock wave parameters of some explosives used for UNDEX purposes.

Table 1.   **List of Shock Wave Parameters [from Ref. 9]**

	CONSTANTS	HBX-1	TNT	PENTOLITE	NUKE
P_{max}	K_1	22347.6	22505	24589	4380000
	A_1	1.144	1.18	1.194	1.18
DECAY CONSTANT	K_2	0.056	0.058	0.052	2.274
	A_2	-0.247	-0.185	-0.257	-0.22
BUBBLE PERIOD	K_5	4.761	4.268	4.339	515
BUBBLE RADIUS	K_6	14.14	12.67	12.88	1500

The following pressure waves known as bubble pulses are generated by the oscillation of the gas bubble created by the UNDEX. The peak pressure of the first bubble pulse is about 10-20% of the shock wave. The first high pressure in the gas sphere is significantly reduced after the primary part of the shock wave has been emitted. It can be said that about half of the energy of the explosion is emitted in the shock wave.

10

However, the pressure has still much higher value than the pressure which is required to provide equilibrium with the hydrostatic and atmospheric pressures. The closest water region of the gas sphere is known as a bubble. The water has a large velocity, and so the diameter of the bubble becomes larger quickly. The expansion of this gas bubble is maintained for a long time. In the meantime, the internal pressure of the gas bubble reduces gradually. However, the movement of the water perseveres due to the inertia of the water which is flowing outward. The gas pressure, at some moment in the motion, reaches the equilibrium point which is equal to the hydrostatic pressure. In fact, the gas pressure of the bubble drops until the dynamic equilibrium is achieved. The dynamic equilibrium has a somewhat lower value than that of the surrounding hydrostatic pressure of the water because, while the pressure of the gas bubble reaches the equilibrium point with the hydrostatic pressure, the outward flow of the water continues radially, and so the gas pressure starts to fall below the hydrostatic pressure. When the dynamic equilibrium is accomplished, the gas bubble reaches the maximum radius given by Equation (2.4) above. At this point, the internal energy of the gas in the bubble is very small and, in actual fact, is negligible. The radius of the gas bubble at the equilibrium point is less than half of the actual maximum radius which is ultimately reached. Furthermore, after the generation of the maximum bubble radius, the hydrostatic pressure reverses the radial flow, i.e., causes the outward water flow to stop and then flow reversely. Therefore, the radius of the gas bubble gets smaller, i.e., the gas bubble collapses by creating a pressure pulse [Ref. 9]. The elastic properties of the gas in the bubble and the inertia of the water obtain the required conditions for the oscillation of the gas bubble. The gas bubble, in reality, experiences recurring cycles of the expansion and contraction. The cycle or the number of the oscillation depends on the loss of the energy of the gas bubble due to the radiation and turbulence. Hence, it can be said that the oscillation process repeats until the total bubble energy is dissipated, or the gas bubble is vented to the air above the free surface. The effect of the gravity usually makes the gas bubble migrate upward while the oscillation process is occurring. Since the gas bubble contains about half of the explosive energy, it can cause damages as great as the shock wave can cause. Due to the migration and buoyancy effects, the gas bubble can collapse close to or on the ship's hull. Figure 2 shows this oscillation process along with the migration pathway.

11
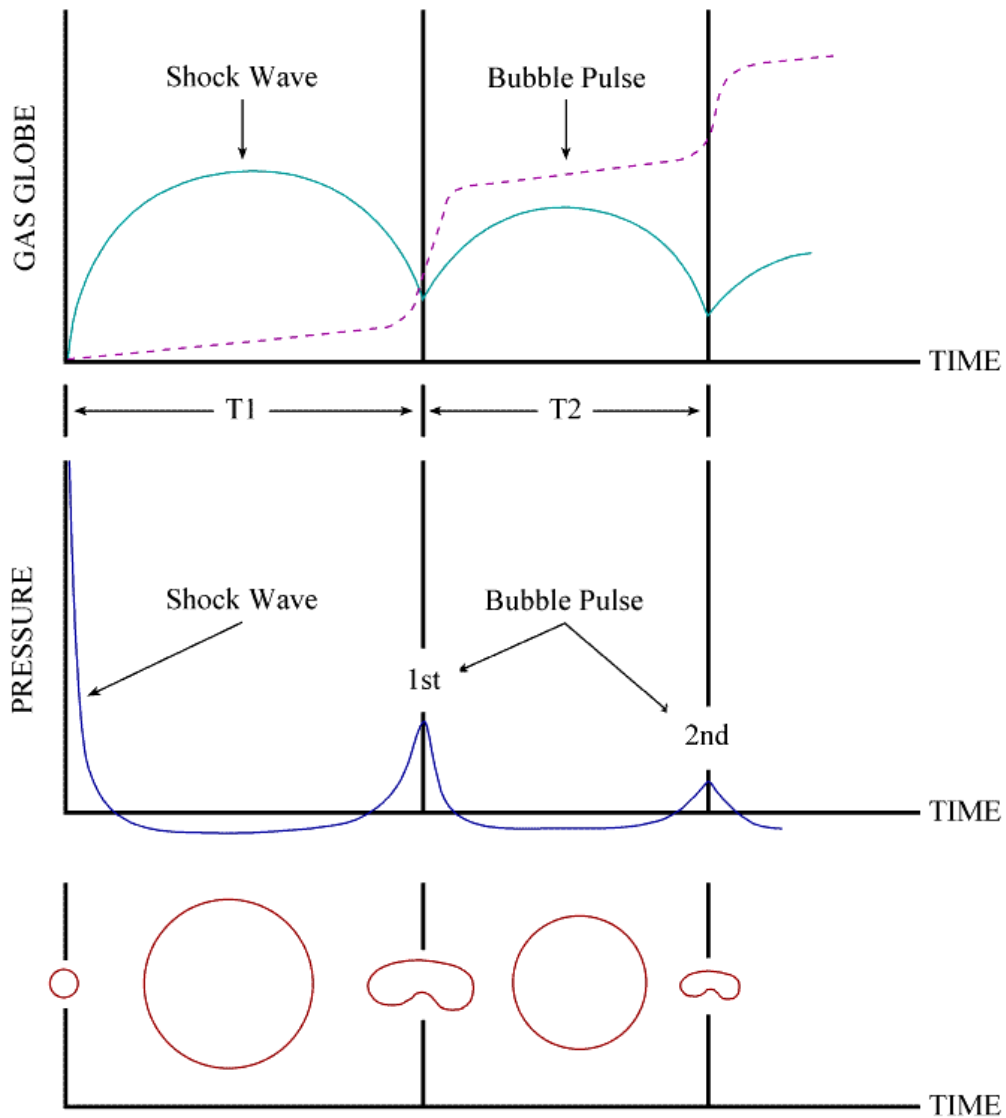
Figure 2.   Migration Pathway, Pressure Pulse and Gas Bubble Oscillation [from Ref. 9]

B.   BULK/LOCAL CAVITATION

Cavitation is a phenomenon which occurs when there is a region of negative absolute pressure present in the water. Since this negative pressure causes the tensile force in the water, and therefore, the water cannot sustain this force, cavitation or separation is formed. During an UNDEX event, there are two types of cavitations present in the water "bulk cavitation" and "local cavitation". Bulk cavitation can be considered a large region of low pressure at the free surface while local cavitation is a small region of

low pressure usually occurring at the fluid-structure interface. When cavitation occurs in water, it has a large effect on the overall response of the ship during an UNDEX event. Therefore, this phenomenon must be considered a significant factor, and thus is included in the simulation process for a more accurate prediction [Ref. 11].

1.   Bulk Cavitation

The shock wave propagates in a spherical enlarging circle from the charge detonation point in an UNDEX event. As seen in Figure 3, the incident shock wave, which is compressive, reflects from the free surface and results in a tensile reflected (rarefaction) wave. Since the water is unable to sustain a significant amount of tension, due to the reflected wave, the fluid pressure is reduced and bulk cavitation occurs when the absolute pressure drops to zero or below in the water. As a matter of fact, water can support a small quantity of tension (approximately a negative pressure of 3 to 4 psi), but zero psi is normally used for design and calculation purposes [Ref. 12]. In the guidance of cavitation, the water and the surrounding pressures rise to the vapor pressure of water, which is about 0.3 psi. As shown in Figure 4, the reflected wave arrives at the image charge after the incident shock wave. The incident wave pressure has decayed, and then, the arrival of the rarefaction wave causes a sharp drop or so-called "cut-off" in the pressure. Notice that, as mentioned previously, cavitation occurs at cut-off when the absolute pressure in the water drops below the cavitation pressure, which is about a negative pressure of 3 to 4 psi [Ref. 12].

Although it is not shown in the figures below, a bottom reflection wave may be present due to the reflection of the shock wave from the sea ground as well. Nevertheless, because the bottom reflection wave mostly depends on the properties of the sea ground and its closeness to the ship, for an UNDEX event, this type of pressure wave is less important [Ref. 9].
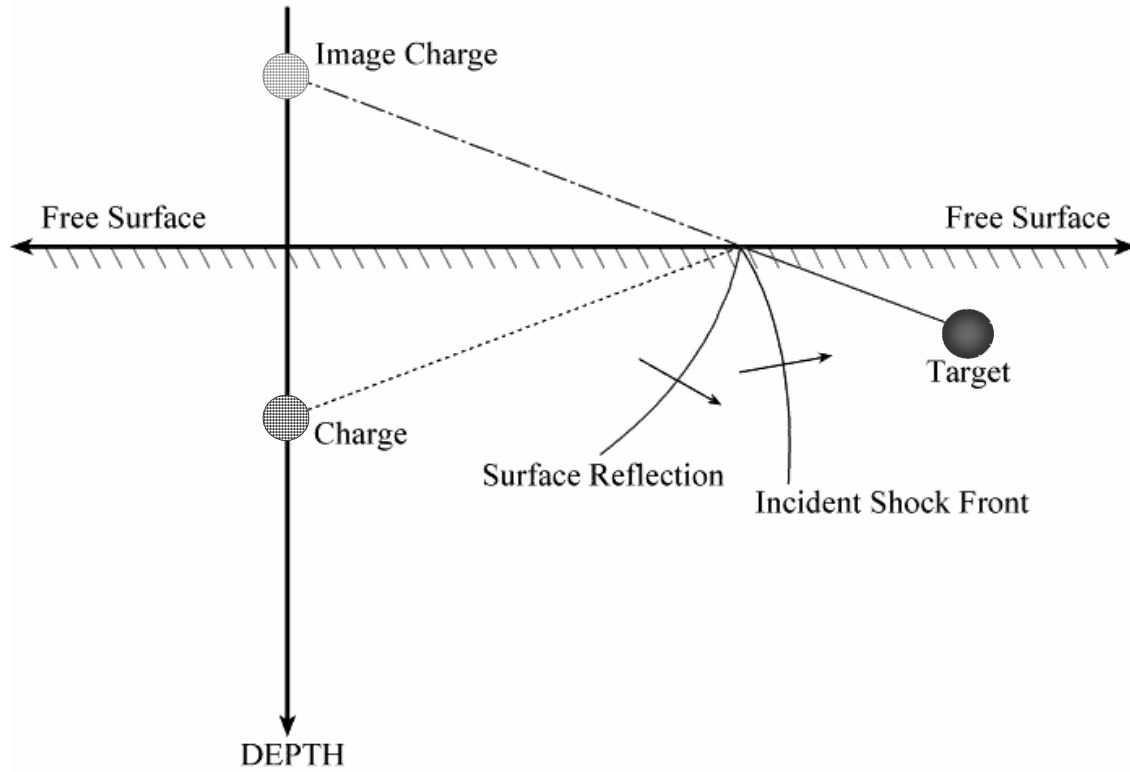
Figure 3. **Underwater Explosion Geometry [from Ref. 9]**
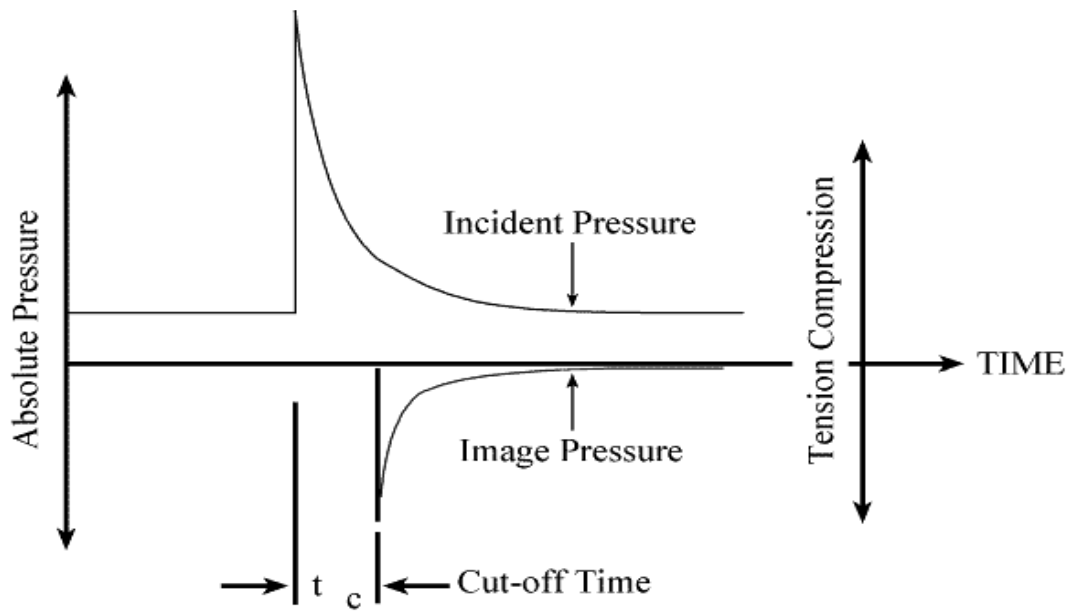
Figure 4. **Shock Wave Pressure Profile with Cut-off Time [from Ref. 9]**

The bulk cavitation region is described by an upper and a lower boundary. These boundaries are a function of the size, type and depth of the charge that is detonated in an

UNDEX event [Ref. 9]. By varying the weights and the depths of TNT charge, this dependency can be shown in Figures 5 and 6. The MATLAB® code used to generate these figures appears in Appendix A.
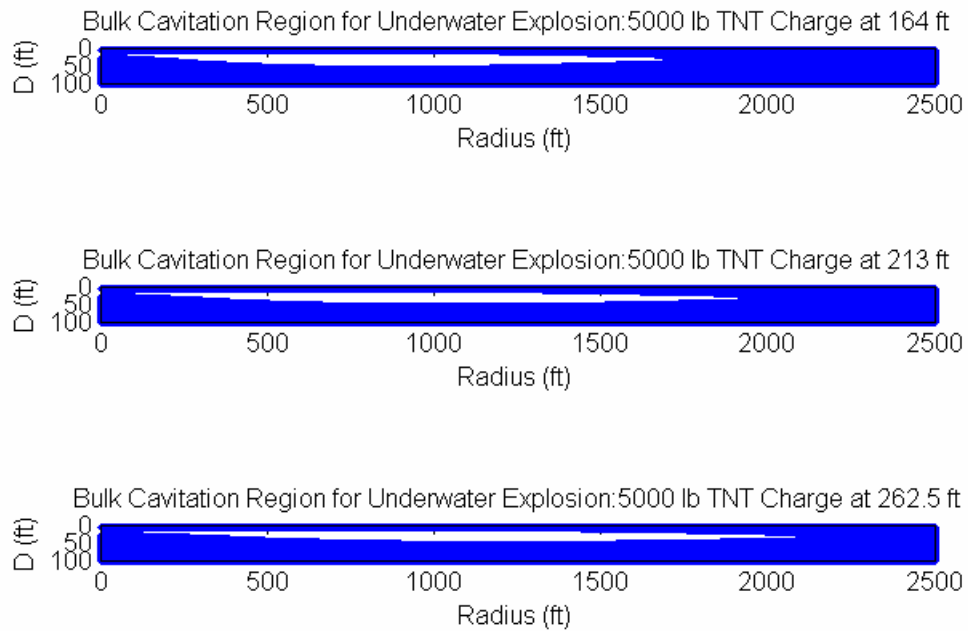
Figure 5.   Bulk Cavitation Region for 5000 lb TNT Charge Detonated at Varying Depths

If Figure 5 and 6 are compared in terms of the charge depths, it is obvious that, as the depth increases, the horizontal distance of the bulk cavitation region increases as if the bulk cavitation area is being stretched and the vertical distance of the bulk cavitation area decreases. As the charge weight increases, the bulk cavitation area increases as well. If two cases are combined, whenever the charge depth and weight increase, the vertical and horizontal distances will change (negative contribution from the charge depth change and positive contribution from the charge weight change for the vertical distance) and the bulk cavitation region will vary with respect to the contributions resulting from the charge depth and weight changes.

Bulk Cavitation Region for Underwater Explosion:10000 lb TNT Charge at 164 ft

Radius (ft)

Bulk Cavitation Region for Underwater Explosion:10000 lb TNT Charge at 213 ft

Radius (ft)

Bulk Cavitation Region for Underwater Explosion:10000 lb TNT Charge at 262.5 ft

Radius (ft)
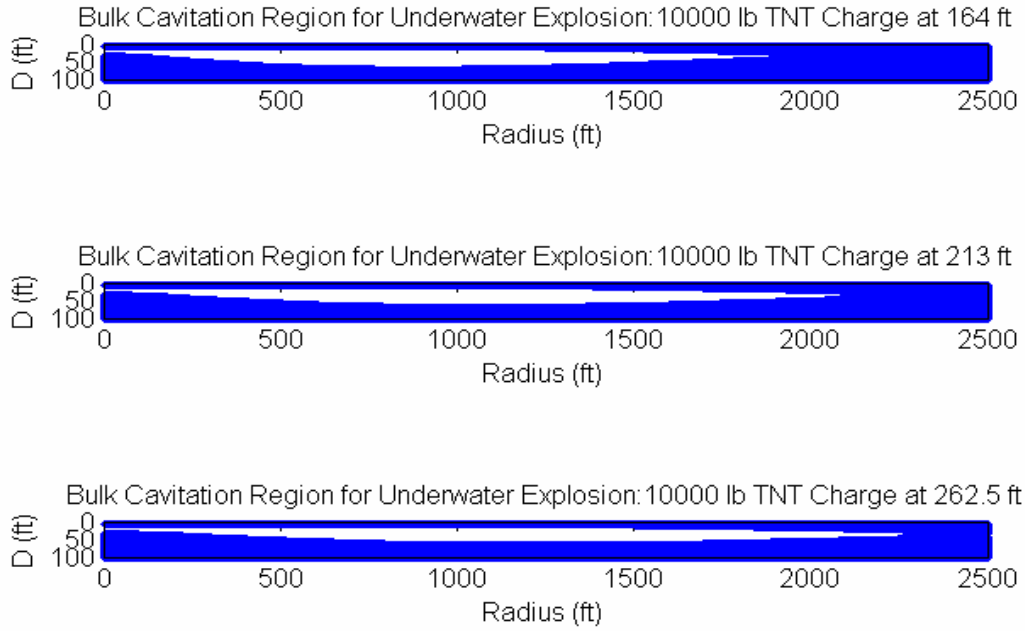
Figure 6.   Bulk Cavitation Region for 10000 lb TNT Charge Detonated at Varying Depths

Upper cavitation boundary is defined as the locus of points at which the absolute pressure falls to the cavitation pressure upon arrival of the reflected wave [Ref. 12]. As long as the absolute pressure does not go higher than the vapor pressure of water, the bulk cavitation area will remain cavitated. Since vapor and cavitation pressures are small enough, they can be taken as zero. To be able to determine the upper cavitation boundary, the total pressure must be considered. The upper cavitation boundary, which is defined as the region in which the total pressure is equal to zero in, is calculated by using Equation (2.6) along with Equations (2.7) and (2.8) [Ref. 9].

$$F(x,y) = K_1\left(\frac{W^{\frac{1}{3}}}{r_1}\right)^{A_1} e^{-\frac{(r_2-r_1)}{C\theta}} + P_A + \gamma y - K_1\left(\frac{W^{\frac{1}{3}}}{r_2}\right)^{A_1} = 0 \qquad (2.6)$$

$$r_1 = \sqrt{(D-y)^2 + x^2} \quad \text{and} \quad r_2 = \sqrt{(D+y)^2 + x^2} \qquad (2.7)\text{and }(2.8)$$

16

x, y = the horizontal range and the vertical depth of the point

r_1 = standoff distance from the charge to the point

r_2 = standoff distance from the image charge to the point

C = acoustic velocity in the water

D = charge depth

θ = decay constant (Equation (3))

P_A = atmospheric pressure

γ = weight density of water

W = charge weight

K_1, A_1 = shock wave parameters (depends on charge type, Table 1)

If the breaking pressure is defined as the rarefaction or reflected pressure that reduces the absolute pressure at the position to the cavitation pressure, the lower cavitation boundary is computed by making the decay rates of the absolute pressure and breaking pressure equal. The equation for this calculation is demonstrated in Equation (2.9) which makes use of the same variables as in Equations (2.6), (2.7), (2.8) [Ref. 9].

$$G(x,y) = -\frac{P_i}{C\theta}\left\{1 + \left[\frac{r_2 - 2D\left(\frac{D+y}{r_2}\right)}{r_1}\right]\left[\frac{A_2 r_2}{r_1} - A_2 - 1\right]\right\}$$

$$-\frac{A_1 P_i}{r_1^2}\left[r_2 - 2D\left(\frac{D+y}{r_2}\right)\right] + \gamma\left(\frac{D+y}{r_2}\right) + \frac{A_1}{r_2}(P_i + P_A + \gamma y) = 0 \qquad (2.9)$$

where P_i, the incident pressure at cut-off time, is provided by the following expression,

$$P_i = P_{max} e^{-\left[\frac{(r_2 - r_1)}{C\theta}\right]} \qquad (2.10)$$

Figure 7 shows a cross-section view which represents the bulk cavitation region generated by a 5000 lb TNT charge exploded 164 ft. below the free surface. It must be noted that the bulk cavitation region in Figure 7 is actually three-dimensional, and normally symmetric about an imaginary vertical axis passing through the charge. The water particles behind the shock wave front have velocities depending on their position

relative to the charge location and the free surface at the time of cavitation. For instance, water particles near the free surface will have a primarily vertical velocity at cavitation. As the reflected wave passes, the particles will be acted upon by gravity and atmospheric pressure.
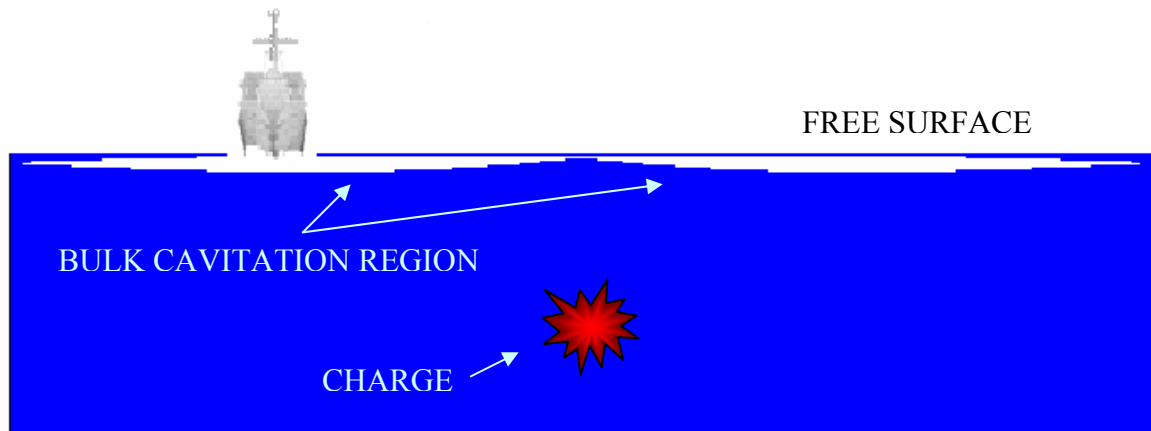
Figure 7.   Bulk Cavitation Region in an Underwater Explosion Event

2.   Local Cavitation

The shock pressure pulses which are created by an underwater explosion impinging on a ship agitate the structure which causes dynamic responses. As long as the pressure pulses impinge the flexible surface of the structure, a fluid-structure interaction takes place. When this fluid-structure interaction occurs, the total pressure throughout the ship's hull turns out to be negative. Since the water can not sustain tension, the water pressure decreases the vapor pressure, and then local cavitation occurs. For the simplest fluid-structure interaction situation, the Taylor flat plate theory will be used to be able to illustrate how the local cavitation occurs. Figure 8 shows a Taylor flat plate subjected to a plane wave.
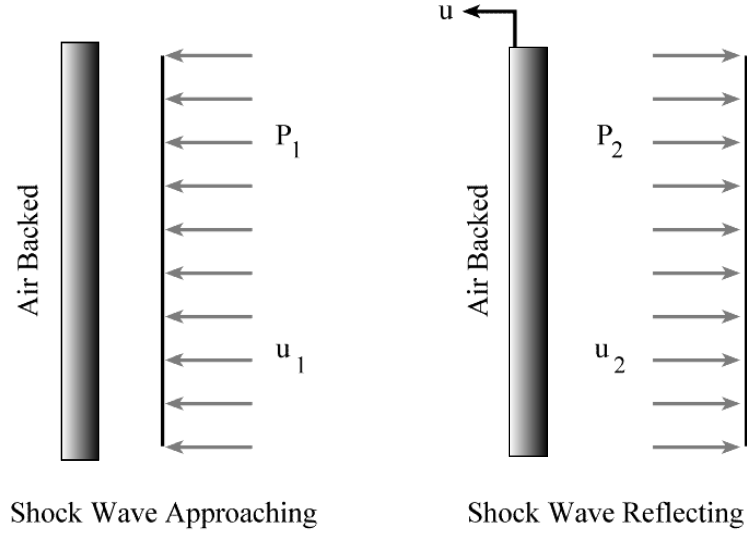
Figure 8.   Taylor Plate Subjected to a Plane Wave [from Ref. 9]

An infinite and air backed plate of mass is subjected to the incident plane shock wave of pressure $P_1(t)$. When the incident plane shock wave interacts with the plate, the reflection wave of pressure $P_2(t)$ will be reflected off the plate. If the velocity of the plate is defined as $u(t)$, the equation of motion of the plate utilizing Newton's 2nd law can be written as

$$m\frac{du(t)}{dt} = P_1(t) + P_2(t) \qquad (2.11)$$

where m is the mass of the plate per unit area.

The fluid particle velocities behind the incident and reflected shock waves are defined as $u_1(t)$ and $u_2(t)$, respectively. The interface between the surface of the plate and the fluid is expressed as

$$u(t) = u_1(t) - u_2(t). \qquad (2.12)$$

For a one-dimensional wave, the incident and reflected shock wave pressures can be shown as follows:

$$P_1(t) = \rho C u_1(t) \qquad (2.13)$$

19

$$P_2(t) = \rho C u_2(t) \tag{2.14}$$

where ρ and C are the fluid density and acoustic velocity, respectively. Substituting Equations (2.13) and (2.14) into Equation (2.12) results in the next equation for the velocity of the fluid particle along the fluid-structure interface,

$$u(t) = u_1(t) - u_2(t) = \frac{P_1(t) - P_2(t)}{\rho C} \tag{2.15}$$

Once more, substituting Equation into (2.15) and solving for $P_2(t)$, the reflected pressure wave equation is defined as

$$P_2(t) = P_{max} e^{-\left(\frac{t - t_1}{\theta}\right)} - \rho C u(t) \tag{2.16}$$

and then, the equation of motion, Equation (2.11) can be rewritten as

$$m\left(\frac{du}{dt}\right) + \rho C u(t) = 2 P_{max} e^{-\left(\frac{t - t_1}{\theta}\right)} \tag{2.17}$$

If the first order linear differential equation, Equation (2.17) is solved, it results in the following relationship for the plate velocity.

$$u(t) = \frac{2 P_{max} \theta}{m(1 - \beta)} \left\{ e^{-\left[\frac{\beta(t - t_1)}{\theta}\right]} - e^{-\left[\frac{(t - t_1)}{\theta}\right]} \right\} \tag{2.18}$$

where $\beta = \dfrac{\rho C \theta}{m}$ and $t > 0$. Finally $P_2(t)$ and the total net pressure at the plate can then be expressed as

$$P_2(t) = \frac{P_{max}}{1 - \beta} \left[(1 + \beta) e^{-\left(\frac{t - t_1}{\theta}\right)} - 2\beta e^{-\left[\frac{\beta(t - t_1)}{\theta}\right]} \right] \tag{2.19}$$

$$P_1 + P_2 = P_{max} \left\{ \frac{2}{1-\beta} e^{-\left[\frac{(t-t_1)}{\theta}\right]} - \frac{2\beta}{1-\beta} e^{-\left[\frac{\beta(t-t_1)}{\theta}\right]} \right\} \qquad (2.20)$$

Equation (2.20) illustrates that, as β becomes large, which corresponds to a light weight plate, the total net pressure turns out to be negative at a very early time. Therefore, local cavitation occurs as the vapor pressure of water is reached. This local cavitation essentially separates the plate from the water [Ref. 9]. Furthermore, because the pressure in front of the plate occurs at cut-off time, the plate reaches its maximum velocity. The time when the maximum plate velocity occurs can be calculated by setting $P_1 + P_2$ equal to zero and solve for t. By using Equation (2.20), t_0, the time for the maximum plate velocity is expressed as

$$t_0 = \frac{\ln \beta}{\beta - 1} \theta \qquad (2.21)$$

then substituting t_0 into Equation (2.18), the maximum plate velocity results in the following equation.

$$u_{max} = \frac{2P_{max}\theta}{m(1-\beta)} \left[e^{-\left(\frac{\beta t_0}{\theta}\right)} - e^{-\left(\frac{t_0}{\theta}\right)} \right] \qquad (2.22)$$

It can be noticed that the equations used in the Taylor plate theory are valid only up to the time when the cavitation starts. After that, this problem turns into nonlinear and possibly nonconservative. Since the momentum of the plate equals to no more than a fraction of the impulse in the shock wave for the light plate weights, a second loading which increases the plate velocity will arise. This second loading can be more damaging than the first.

C. FLUID-STRUCTURE INTERACTION

As a consequence of an underwater explosion, the fluid-structure interaction between the surrounding water and the ship's hull mainly occurs in the vertical direction. The fluid-structure interaction should be considered as a significant phenomenon because

21

the impinging shock wave, which is transmitted through the water surrounding the ship can excite the dynamic responses on the ship structure. The generalized differential equations will be studied in this part to examine the fluid-structure interaction. Equation (2.23) used to describe the structural motion is considered as the discretized differential equation.

$$[M_s]\{\ddot{x}\} + [C]\{\dot{x}\} + [K]\{x\} = \{f\}$$
(2.23)

where $\{x\}$ is the structural displacement vector, $[M_s]$, $[C]$ and $[K]$ are the symmetric linear structural mass, damping and stiffness matrices, respectively, $\{f\}$ is the external force vector and a dot indicates a temporal derivative.

Equation (2.23) shows the balance of all of the forces acting upon the ship structure. These forces contain inertial forces, damping forces and acoustic fluid pressure forces [Ref. 13].

For a submerged structure excited by an acoustic wave, the external forcing function is,

$$\{f\} = -[G][A_f](\{p_I\} + \{p_S\}) + \{f_D\}$$
(2.24)

where $\{p_S\}$ and $\{p_I\}$ are the nodal pressure vectors for the wetted surface fluid mesh pertaining to the (unknown) scattering wave and the (known) incident wave, respectively. Moreover, $\{f_D\}$ is the dry-structure applied force vector, $[G]$ is the transformation matrix that relates the structural and fluid nodal surface forces and $[A_f]$ is the diagonal area matrix associated with the elements in the fluid mesh [Ref. 14].

The Doubly Asymptotic Approximation (DAA) is utilized to solve the fluid-structure interaction problem. This approach is called DAA because it approaches exactness in both the high-frequency (early time) and low-frequency (late time) limits [Ref. 17]. The DAA represents the surrounding fluid of the structure throughout the interaction of state variables pertaining only to the wetted surface of the structure [Ref. 18]. The First Order Doubly Asymptotic, (DAA₁) is used for the long cylindrical shell

structures such as surface ships or submarines. This approach is exact only when the shell structure is spherical. The DAA$_1$ is expressed as,

$$[M_f]\{\dot{p}_S\} + \rho c[A_f]\{p_S\} = \rho c[M_f]\{\dot{u}_S\}$$ (2.25)

where $\{u_s\}$ is the scattered wave fluid particle velocities vector normal to the structure's wetted surface, $[M_f]$ is the symmetric fluid mass matrix for wetted surface fluid mesh, ρ is the fluid mass density, and c is the acoustic velocity of the fluid [Ref. 16]. A boundary-element treatment of Laplace's equation is used to generate $[M_f]$ for the irrotational flow created in an infinite, inviscid and incompressible fluid by the motion of the wetted surface of the structure.

For the high-frequency (early time) motions, because the approximation, $|\dot{p}_S| \gg |p_S|$ can be made, Equation (2.25) reduces to $p_S = \rho c u_S$ which implies a plane wave approximation. However, for the low-frequency (late time) motions, the assumption, $|\dot{p}_S| \ll |p_S|$ is considered, and thus, Equation (2.25) reduces to $A_f p_S = M_f \dot{u}_S$ which implies a virtual mass approximation [Ref. 17].

Since this process takes into account the solution of the fluid-structure interaction just in terms of a wetted surface response, the excitation of the wetted surface structure by an incident shock wave, $\{f\}$ is provided by Equation (2.26) [Ref. 19].

$$\{f\} = -[G][A_f](\{p_I\} + \{p_S\})$$ (2.26)

The following equation is the compatibility relation on the wetted surface of the structure. It expresses that the restriction of the normal fluid particle velocities match the normal structural velocities on the wetted surface of the structure.

$$[G]^T \{\dot{x}\} = \{u_I\} + \{u_S\}$$ (2.27)

where T implies matrix transpose.

Substituting Equation (2.26) into Equation (2.23) and Equation (2.27) into Equation (2.25), DAA Interaction Equations are provided as

$$[M_s]\{\ddot{x}\} + [C]\{\dot{x}\} + [K]\{x\} = -[G][A_f](\{p_I\} + \{p_S\}) \tag{2.28}$$

$$[M_f]\{\dot{p}_S\} + \rho c[A_f]\{p_S\} = \rho c[M_f]([G]^T\{\ddot{x}\} - \{\dot{u}_I\}) \tag{2.29}$$

Equations (2.28) and (2.29) which have two unknown quantities, x and p_S, can be solved by using a staggered solution scheme [Ref. 15].

III. MODELING

A. MEKO-LIKE BOX MODEL

1. Structural Model

The finite element model of the meko-like box, which is considered a rectangular barge, was constructed by using the finite element mesh generation program TrueGrid [Ref. 20]. The construction of the structural model using TrueGrid is explained in detail in Appendix B. This model, which is basically consistent with the actual dimensions of a typical meko-class ship, was utilized to simulate the general structure of that type of ship. The meko-like box model is 4800-in long, 600-in wide and 400-in deep. Figure 9 illustrates a model picture of one of the meko-class ships in use in today's Navy of various countries in the world. Table 2 shows the similarity of the meko-like box model and meko-class ships [Ref. 21].

Figure 9.   MEKO A-200 Class Ship

Table 2.   **Comparison of the meko-like box model and meko-class ships**

MEKO-LIKE BOX MODEL		TCG YAVUZ TURKISH NAVY MEKO A-200 TRACK I		TCG BARBAROS TURKISH NAVY MEKO A-200 TRACK II	
Length	4800 in (121.92 m)	Length Overall	115.5 m	Length Overall	118 m
Beam	600 in (15.24 m)	Maximum Beam	14.20 m	Maximum Beam	14.80 m
Draft	160 in (4.06 m)	Draft	4.10 m	Draft	4.30 m

The meko-like box model contains 16 athwartship bulkheads and 3 decks including the top one. The first deck was located at the waterline (160 in) while the second and top decks were placed at 280 in and 400 in, respectively. In order to simulate the small volume of spaces located at the bow and stern sides of a meko-class ship, the first two athwartship bulkheads on each side were spaced at a distance of 160 in although the distance of 320 in was used to locate the rest of them. Although the dimensions of the model are similar to a typical meko-class ship, the meko-like box model has more underwater volume than the draft used. Thus, the displacement of the box model turns out to be more than the actual displacement of a meko-class ship due to its simplified underwater hull form, which is essentially a rectangular box. When the value of 1.025 $MTON/m^3$ is used for the seawater weight density, the displacement value of 7945 MTON, which is about twice as much as the actual displacement value of a classic meko ship, is reached for the box model. Using the seawater mass density of 9.345E-05 $lbf\text{-}sec^2/in^4$, the total lumped mass of 43061.760 $lbf\text{-}sec^2/in$ is consistent with the displacement value based on the underwater volume of the box model.

To make the box model more realistic, 136 lumped masses were distributed through the center two nodes between every two athwartship bulkheads on each deck of the structure. Furthermore, to ensure the center of gravity remained on the centerline, the lumped mass value of 179.424 $lbf\text{-}sec^2/in$ was used for each center node of the regions that cover the first two athwartship bulkheads of the bow and stern sides of the box model, while the value of 358.848 $lbf\text{-}sec^2/in$ was assigned to the rest of the center

nodes. The shell plating was constructed of 0.3937-in steel base on the shell thickness value of 1 cm. which has a mass density of 7.350E-04 lbf-sec^2 / in^4 , a Young's Modulus of 3.000E+07 psi and a Poisson's ratio of 0.3. The shell elements were modeled by one of the LS-DYNA elastic material types: Belytschko-Tsay. The shell elements size decided upon was a square element having a length of 40 in. Structural beam (stiffener) elements were constructed of the same material as the shell elements. The Belytschko-Schiwer beam element, a purely elastic material type in LS-DYNA, was used to build the rectangular cross-section beam elements. These structural beam (stiffener) elements were distributed to increase the plating rigidity of the structure and to reflect the actual structural boundary conditions of a meko ship. Each of them is 5.905-in by 0.295-in wide high based on the height and width values of 15 cm and 0.75 cm, respectively. The overall finite element mesh of the structural model consists of 11202 nodes, 12300 quadrilateral (4-noded) shell elements, 13870 beam elements and 136 lumped masses. Table 3, Figures 10 and 11 summarize specifics of the structural model by slicing the model. Moreover, Figures 12, 13 and 14 show the overall finite element structural model, the beam cross-section, and the beam elements, respectively, on it.

Table 3.   Meko-Like Box Model Specifications

Length	4800 in
Beam	600 in
Depth	400 in
Draft (Design Waterline)	160 in
Shell Plating/Beam Element Material	Steel
Shell Plating Thickness	0.3937 in (1 cm)
Beam Element Dimensions (Height x Width)	5.905x0.295 in^2 (15x0.75 cm^2)
Number of Nodes	11202
Number of Lumped Masses	136
Number of Belytschko-Tsay Shell Elements	12300
Number of Belytschko-Schiwer Beam Elements	13870

BOW

STERN

Top Deck at 400 in

Second Deck at 280 in

First Deck at 160 in

Keel at Bottom

16 Athwarthship Bulkheads
throughout the model
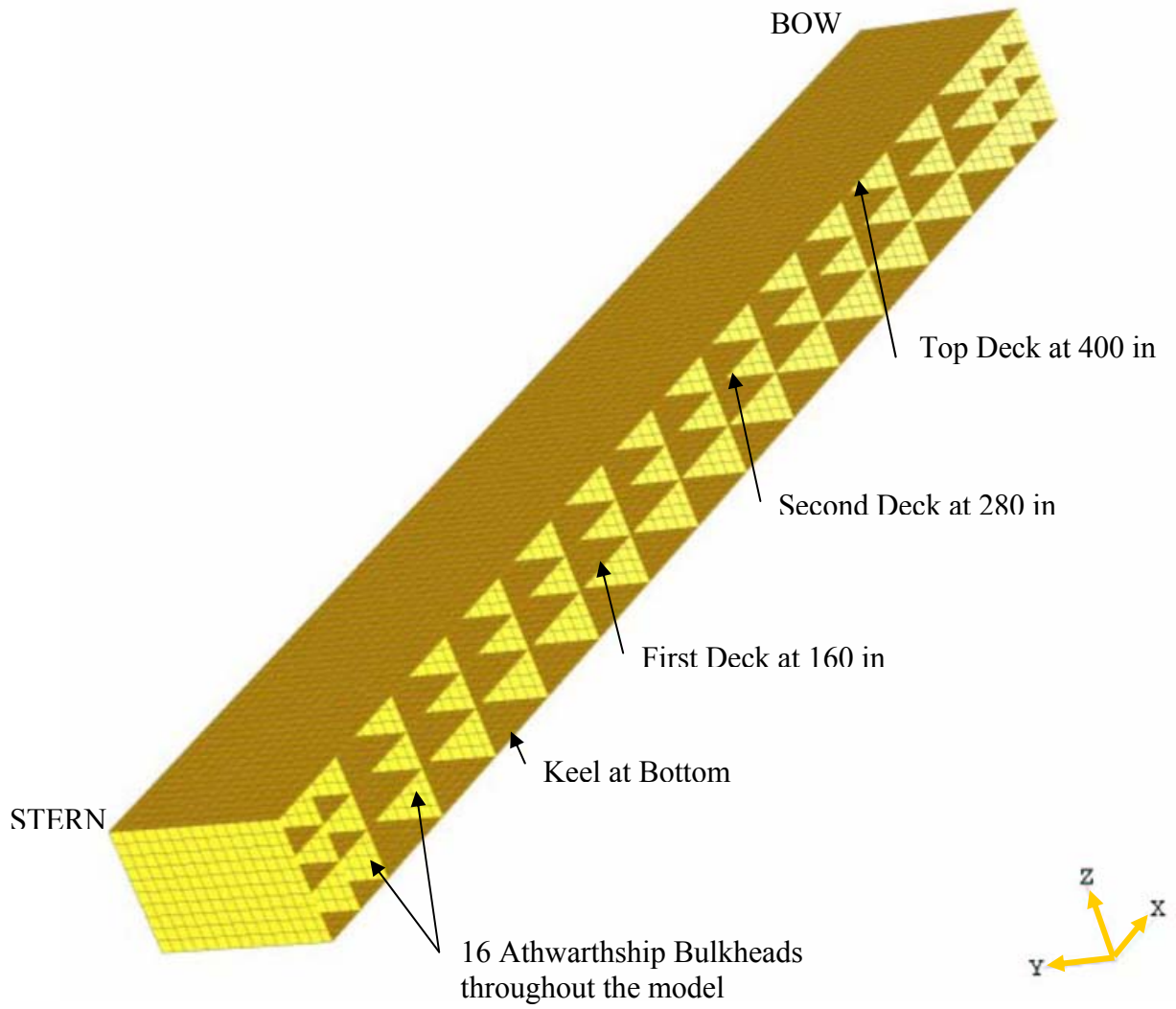
Figure 10.   Profile Cut-Away View of Meko-Like Box Model

136 lumped masses are distributed all the way through the model
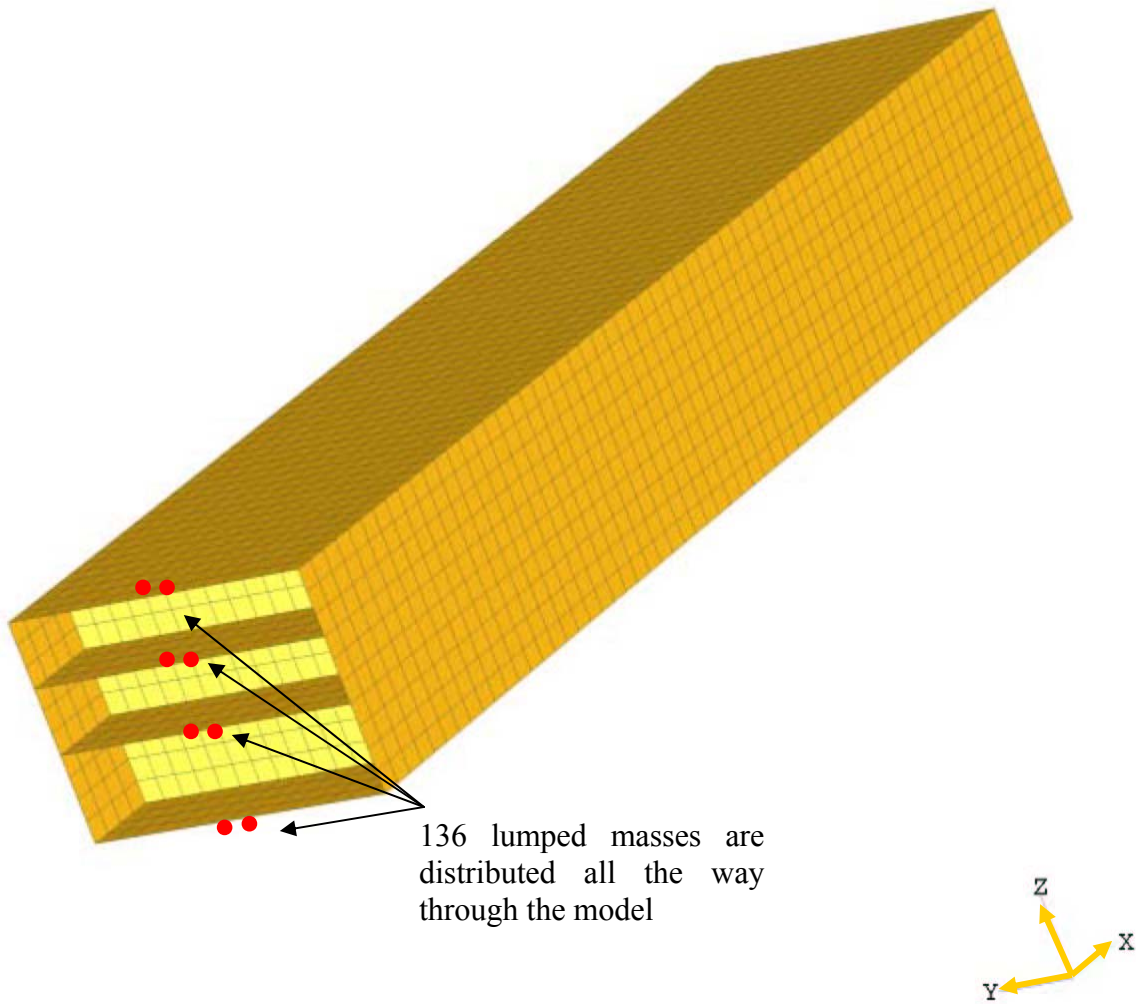
Figure 11.   Stern View of Meko-Like Box Model (Half Model)
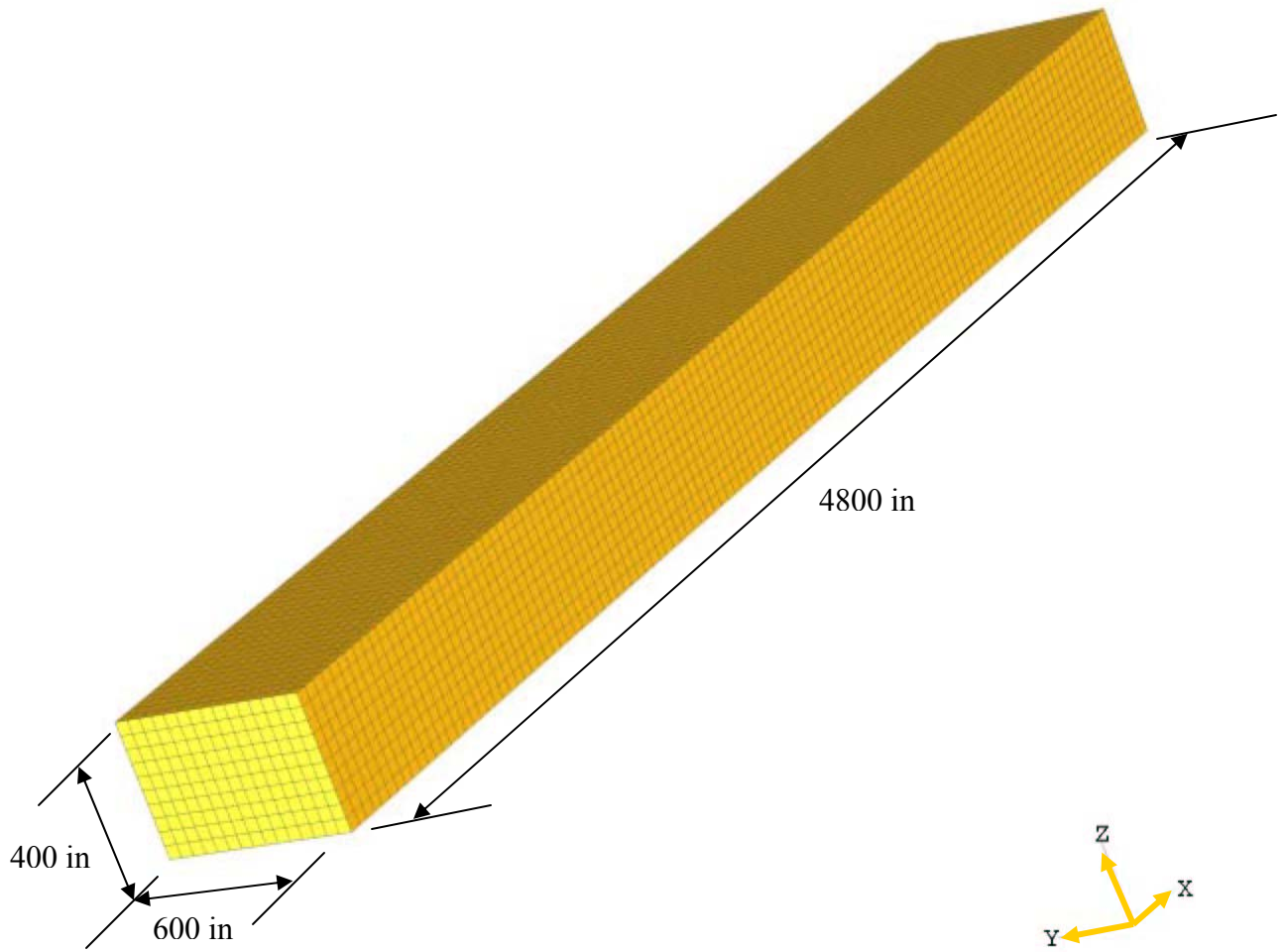
Figure 12. **Dimensions of Complete Meko-Like Box Model**

0.295 in (0.75 cm)

|←→|

5.905 in (15 cm)
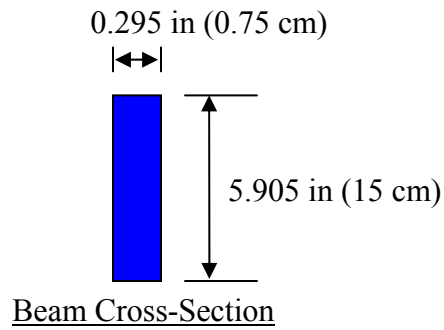
Beam Cross-Section

Figure 13.   Beam Cross-Section of Beam Elements

X

Z

Y
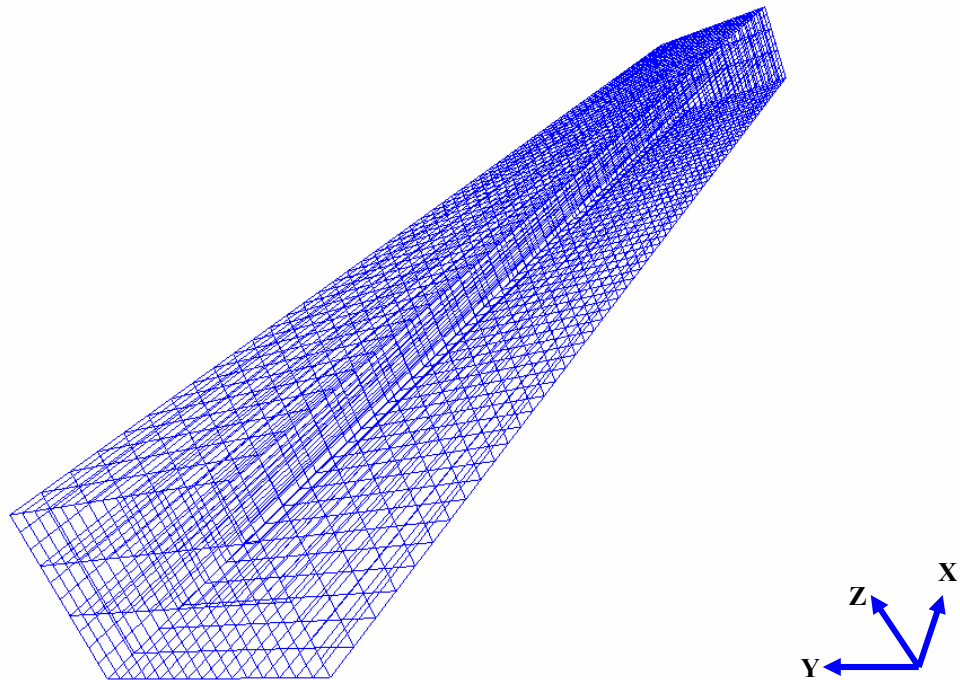
Figure 14.   Beam Elements of Meko-Like Box Model

The meko-like box model has been essentially used to see what happens when any kind of hull appendage is added to the structure in both cases in which these hull appendages are not only coupled but also are uncoupled with the fluid surrounding the structure. To be able to simulate different kinds of hull appendages on an actual meko-class ship, the structural model was modified in accordance with the type of appendage that would be attached to the hull accounting for the part dimensions that would be used for it. It should be stated that, while they were being constructed, varying dimensions of

the adjacent fluid mesh elements were used for the appendage elements as well. No modifications were made in terms of the lumped masses, i.e., no lumped mass was added due to the hull appendage attached.

The first modification applied to the structure was the addition of a keel board to the hull of the box model. The keel board was constructed first by hexahedral solid elements, and then by shell elements to make two separate appendage analyses. Hence, from this point, the solid keel board and shell keel board will imply that they have been built by solid and shell elements, respectively. The same material properties of the structure were used for the construction of the shell and solid keel board while 14 point integration quadratic 8-node brick element, an elastic material element type in LS-DYNA, was used for solid element of the solid keel board. However, to do the analysis of different weight percentages of the solid keel board, the mass density of the brick elements were changed, but that did not affect the way of the construction of the keel board. The thickness of the shell elements of the shell keel board is the same as that of the shell elements of the structure. Both solid and shell keel board were modeled as 20.5 % of the underwater surface area of the structural model. Table 4 and Figure 15 show specifics of the solid and shell keel boards built on the meko-like box model.

Table 4.   Solid and Shell Keel Board Specifications

Solid Keel Board		Shell Keel Board	
Length	2400 in	Length	2400 in
Width	40 in	Width	40 in
Depth	110 in	Depth	110 in
Solid Element Material	Steel	Shell Element Material	Steel
Varying Solid Element Dimensions (Height x Width x Length)	7x40x40 in^3 16x40x40 in^3 20x40x40 in^3 24x40x40 in^3 36x40x40 in^3	Varying Shell Element Dimensions (Height x Length)	7x40 in^2 16x40 in^2 20x40 in^2 24x40 in^2 36x40 in^2
Number of Nodes	854	Number of Nodes	854
Number of 14 Point Integration Quadratic 8-node Solid Elements	360	Number of Belytschko-Tsay Shell Elements	852
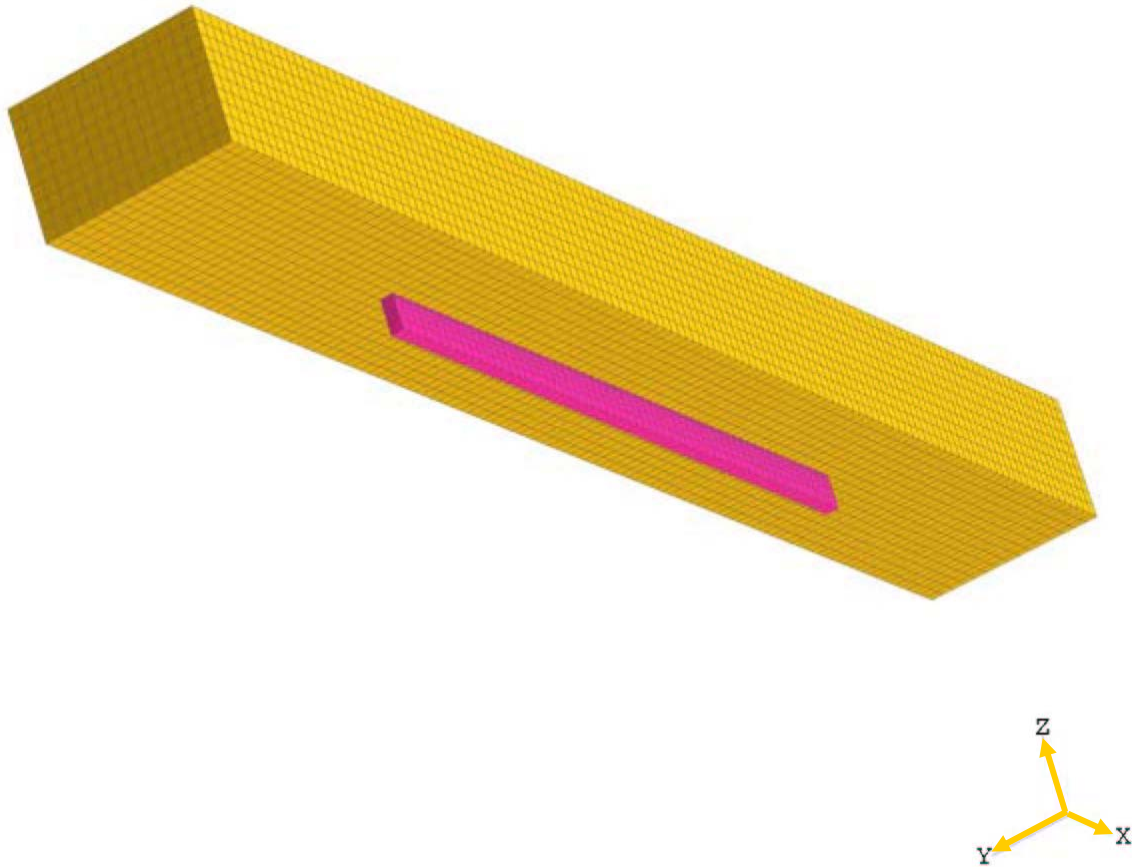
Figure 15.   Meko-Like Box Model with Keel Board (Solid and Shell) on The Hull

Another modification was made for the construction of the open keel board. The open keel board that was built by using the same solid elements and material properties of the solid keel board was created to simulate the two shafts of a meko-class ship. Regarding the total surface area of both shafts exposed to the UNDEX, the rectangular cross-section area of the brick element was assumed to simulate the circular cross-section area of an actual shaft. The open keel board was modeled as 9.4 % of the underwater surface area of the structural model. The open keel board can be thought of as the solid keel board with a big hole where the material has been removed, as illustrated in Figure 16. The length, the width and the depth of the open keel board are the same as those of the solid keel board. Therefore, the dimensions of solid elements of the open keel board have exactly the same values as the outer solid elements of the solid keel board. The open keel board consists of 70 solid elements.
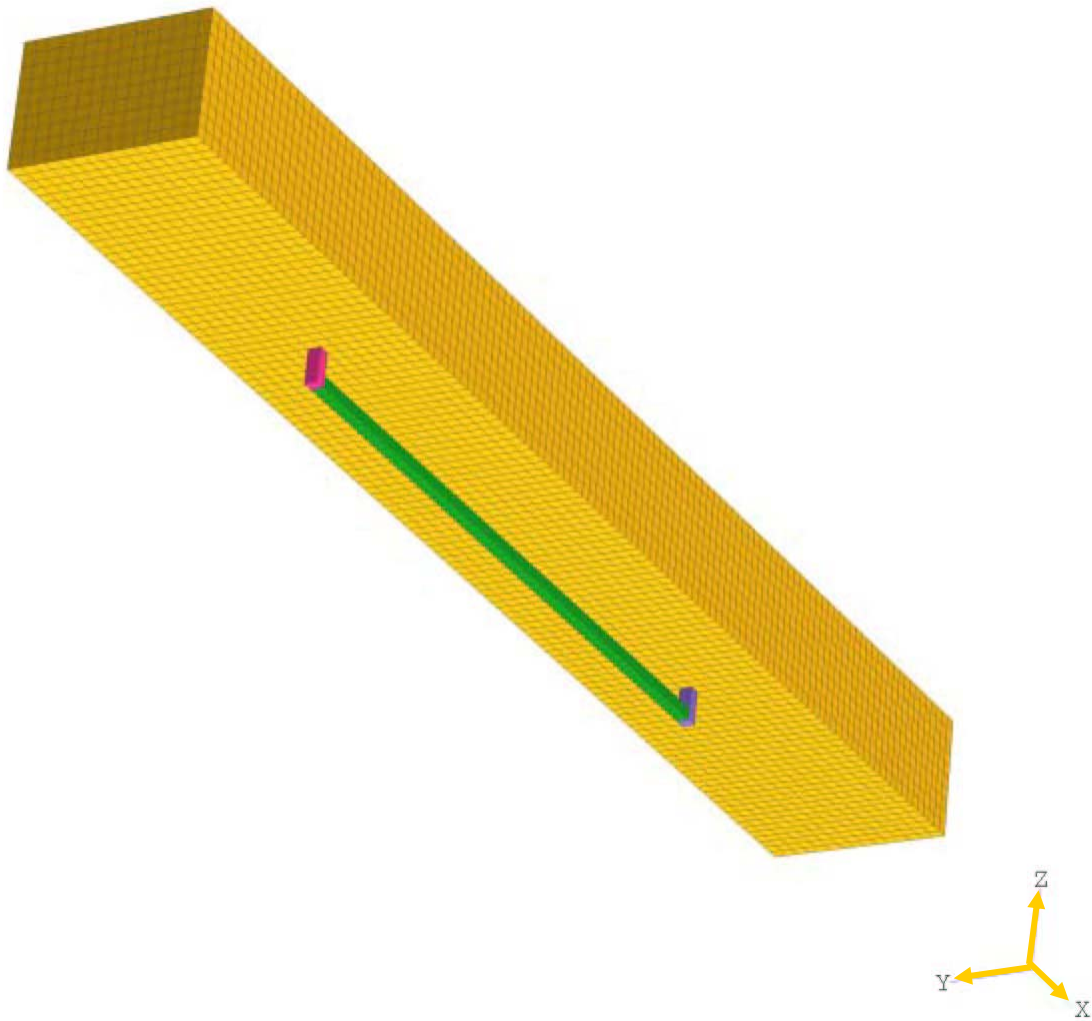
Figure 16.   Meko-Like Box Model with Open Keel Board (Solid) on The Hull

The final modification applied to the meko-like box model was the addition of two rudders. Once again, the Belytschko-Tsay shell elements were used for the shell elements of the structure just as in the shell keel board model. Since the rudders were created by the same kind of shell elements, the material properties of these elements were unchanged for them. The overall dimensions and the location of the rudders were determined by inspecting the different classes of meko ships [Ref. 21].

The shell element dimensions of both rudders change relative to the varying fluid element dimensions as has been done for the shell keel board and the other hull appendages. In order to determine what occurs when the surface area exposed to the UNDEX changes, the overall surface area of both rudders has been examined. Three

35

cases were studied in all. The first case used the actual size of the rudders. The second used rudders modeled with a surface area of 53 % of the actual one. In the final case, the size of the surface area was modified so it would be 180 % of the actual surface area. These cases are referred to henceforth as actual, half and twice the sizes, respectively, for the surface area of the rudders. The half, actual, and double surface areas of the rudders created correspond to approximately 1 %, 1.9 %, and 3.3 %, respectively, of the underwater surface area of the structural model. Table 5 shows the overall dimensions and number of nodes and elements of rudders for all three cases discussed above. The corresponding material properties and dimensions of elements can be seen in Tables 3 and 4, as they are the same as those previously used. Figure 17 shows the meko-like box model with the rudders having actual sizes of surface area.

Table 5.   Rudder Specifications

Rudder with Actual Size of Surface Area		Rudder with Half Rudder Surface Area		Rudder with Double Rudder Surface Area	
Length	120 in	Length	80 in	Length	160 in
Width	40 in	Width	40 in	Width	40 in
Depth	74 in	Depth	50 in	Depth	110 in
Number of Nodes	96	Number of Nodes	60	Number of Nodes	140
Number of Belytschko-Tsay Shell Elements	92	Number of Belytschko-Tsay Shell Elements	56	Number of Belytschko-Tsay Shell Elements	136
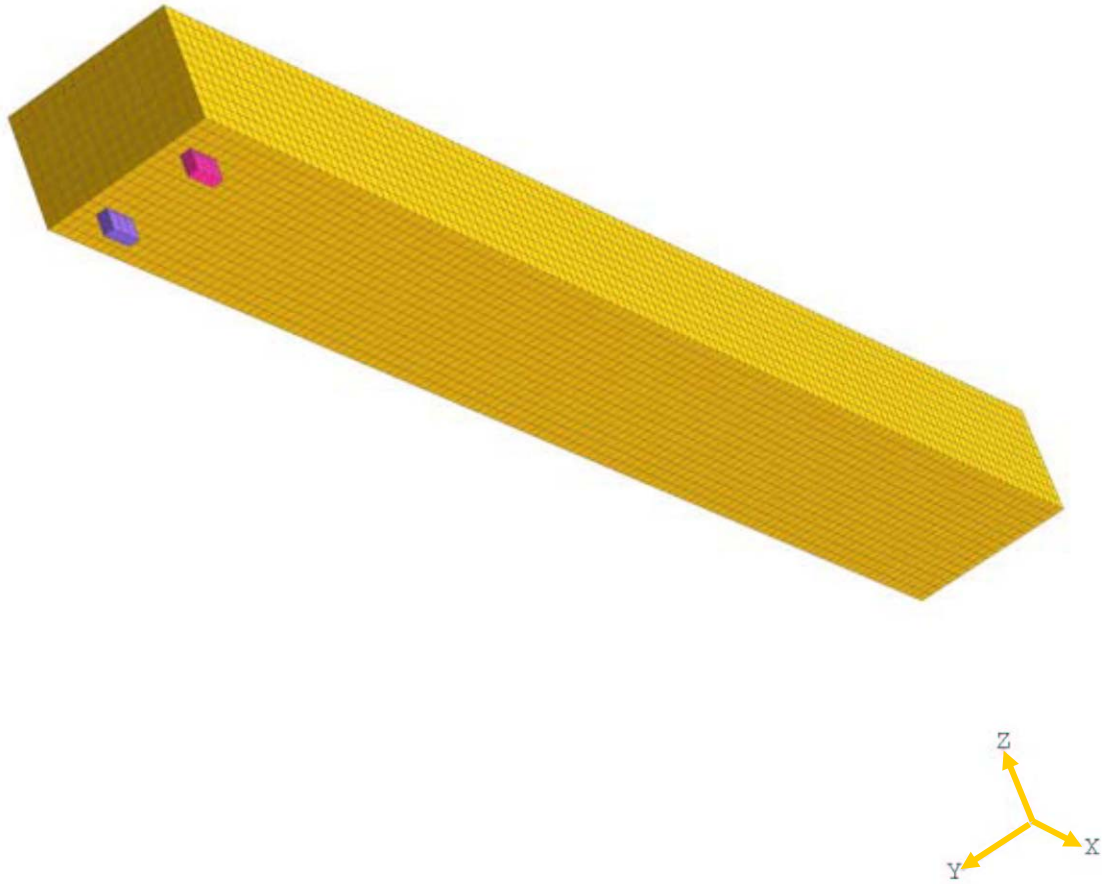
Figure 17.   Meko-Like Box Model with Rudders (Shell) Having Actual Sizes of Surface Area on The Hull

2.   Fluid Mesh Modeling

The next step in the meko-like box model construction was to generate the fluid mesh (fluid volume finite element model). The element extrusion feature in TrueGrid was utilized to build the fluid mesh. The method of building fluid mesh including the extrusion feature in TrueGrid and all the difficulties overcome while using TrueGrid is described in detail in Appendix B. The meko-like box model has been used in investigating what happens when any kind of hull appendage is added to the structure, and specifically in the case in which these hull appendages are not only coupled but also uncoupled with the fluid surrounding the structure. Therefore, the extrusion procedure of the fluid finite element mesh was used to build the fluid model as it is coupled or uncoupled with the hull appendages created. The elements of the fluid mesh consist of

hexahedral solid elements for which LS-DYNA's Material Type 90 (acoustic pressure element) is used to model the pressure wave transmission properties of seawater [Ref. 22]. The mass density and the acoustic speed of these solid elements have the values of 9.345E-05 $\text{lbf-sec}^2/\text{in}^4$ and 60945 in/sec, respectively. Figures 18, 19, 20 and 21 illustrate different views of the fluid mesh designed for the meko-like box model.
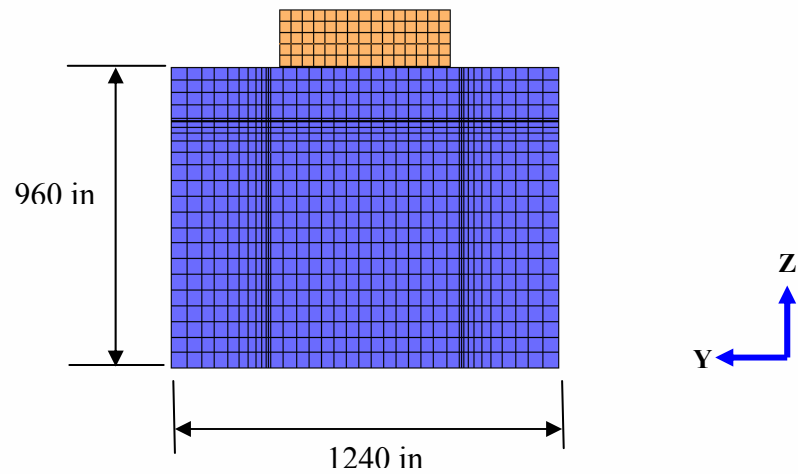
Figure 18.   Stern View of Meko-Like Box Model with Fluid Mesh
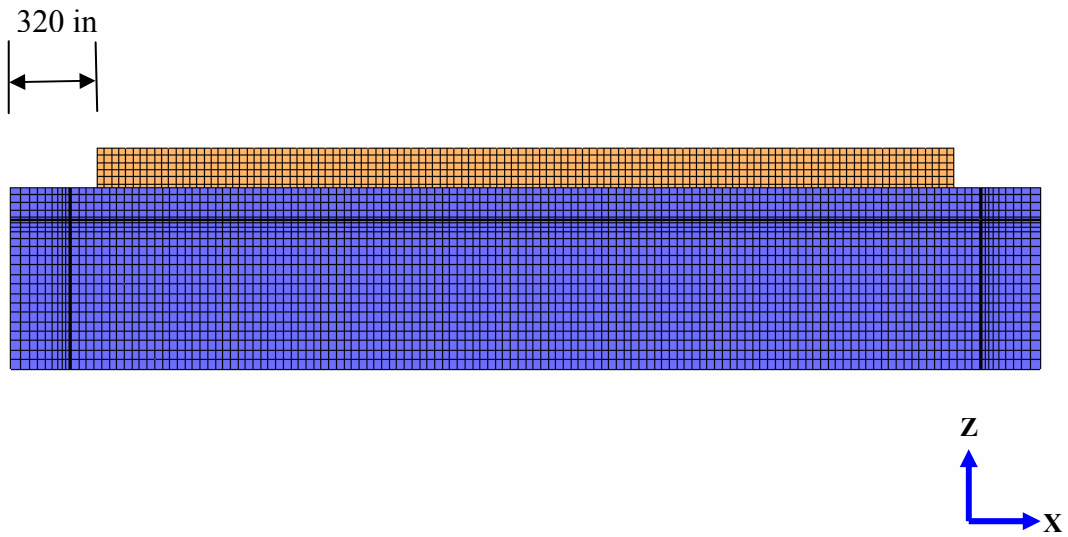
Figure 19.   Profile View of Meko-Like Box Model with Fluid Mesh
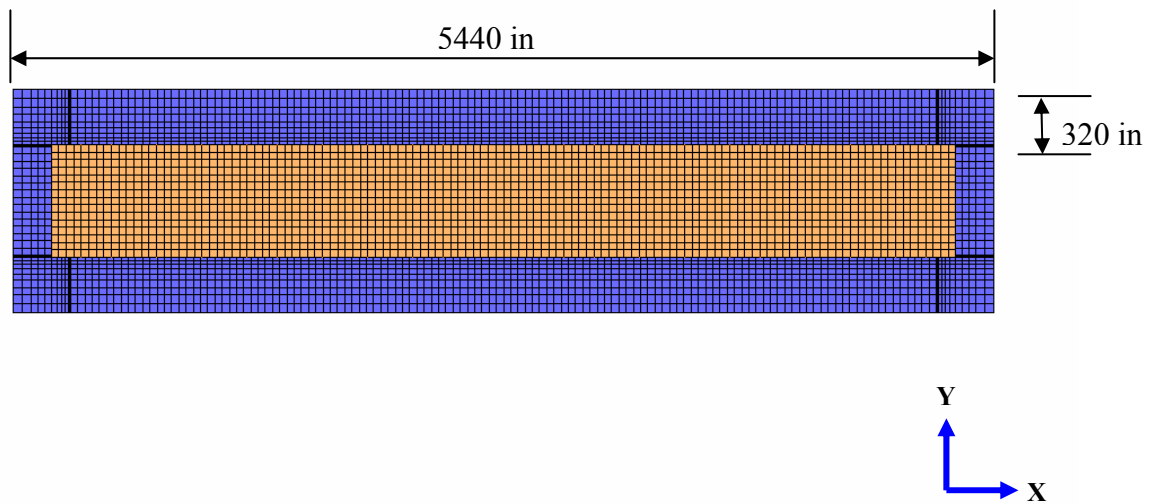
Figure 20.   Top View of Meko-Like Box Model with Fluid Mesh

The fluid mesh in the x and y directions was set to the value of 320 in while the depth of the fluid mesh in the z direction was set to the value of 800 in (from the bottom of the structure) which is greater than the depth of the computed bulk cavitation zone, 57 ft (684 in) to capture the effects of the bulk and local cavitation (to be discussed later). Table 6 lists the number of nodes and hexahedral solid elements created for the fluid mesh of separate meko-like box models constructed. It can be noted that, since the fluid mesh built for the structures is generally very large and complex, extensive computational power is a must to run a shock simulation of these kinds of models (meko-like model or an actual ship model) involving a fluid mesh. Accordingly, for 0.5 sec of data, the computational time of each simulation for the hull appendage analysis of the meko-like box model took approximately two to three days on average by using the computers which have double and single processors, respectively.

Table 6.   Fluid Mesh Specifications (N/A = not applicable)

Coupled with Fluid		Uncoupled with Fluid	
Meko-Like Box Model with	Number of fluid elements	Meko-Like Box Model with	Number of fluid elements
No Appendage	118896	No Appendage	N/A
Solid Keel Board	118536	Solid Keel Board	118896
Shell Keel Board	118536	Shell Keel Board	118896
Open Keel Board	118826	Open Keel Board	118896
Original Rudders	118866	Original Rudders	118896
Half The Rudders	118880	Half The Rudders	118896
Twice The Rudders	118848	Twice The Rudders	118896

The nodal spacing adjacent to the structural model is important for the stability of the USA analysis. The nodal distance normal to the structural mesh limits the size of the first layer of fluid elements [Ref. 17]. This critical fluid element size is determined by the following equation:

$$\frac{2\rho D}{\rho_s t_s} \leq 5 \qquad (3.1)$$

where ρ is the mass density of seawater, D is the thickness of the fluid element in the direction normal to the wetted surface of the structure, ρ_S is the mass density of the submerged structure, and t_S is the thickness of the submerged structure. It can be shown

for the meko-like box model that the critical fluid element thickness D is 7.741 in. The first two layers of the fluid mesh for all separate meko-like models were set to 7 in. Then, to generate a consistent mesh quality at a given distance from the structure, the fluid elements gradually increased in size until the thickness reached 50 in x, y and z directions.

Fluid elements sizes gradually increase up to 50 in

Free Surface (All other sides are part of DAA_1 boundary)

First two fluid elements sizes normal to the structure are 7 in
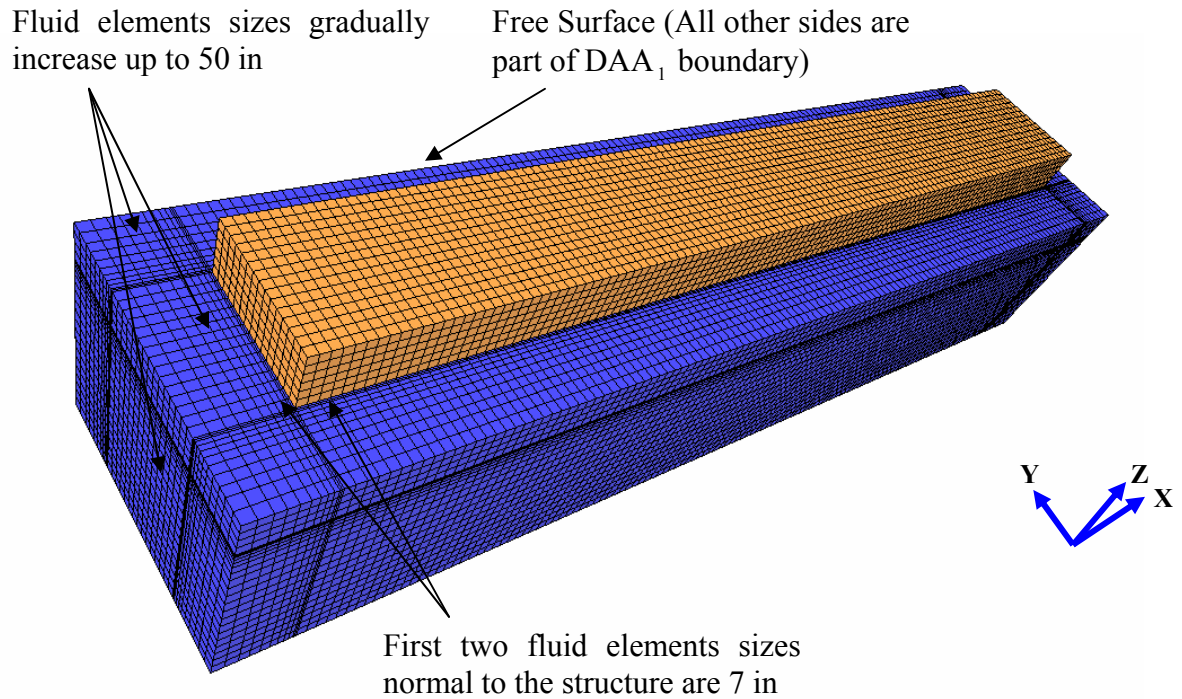
Figure 21.   3-D View of Meko-Like Box Model with Fluid Mesh

THIS PAGE INTENTIONALLY LEFT BLANK

IV. SIMULATION

A. MODEL GENERATION, PRE-PROCESSING AND CONVERSION

The modeling and simulation process involves model generation, pre-processing and simulation processing as well as post-processing, data extraction, data processing and comparison resulting from the simulation processing. The following flow chart of the procedure was utilized for the meko-like box model in this thesis.
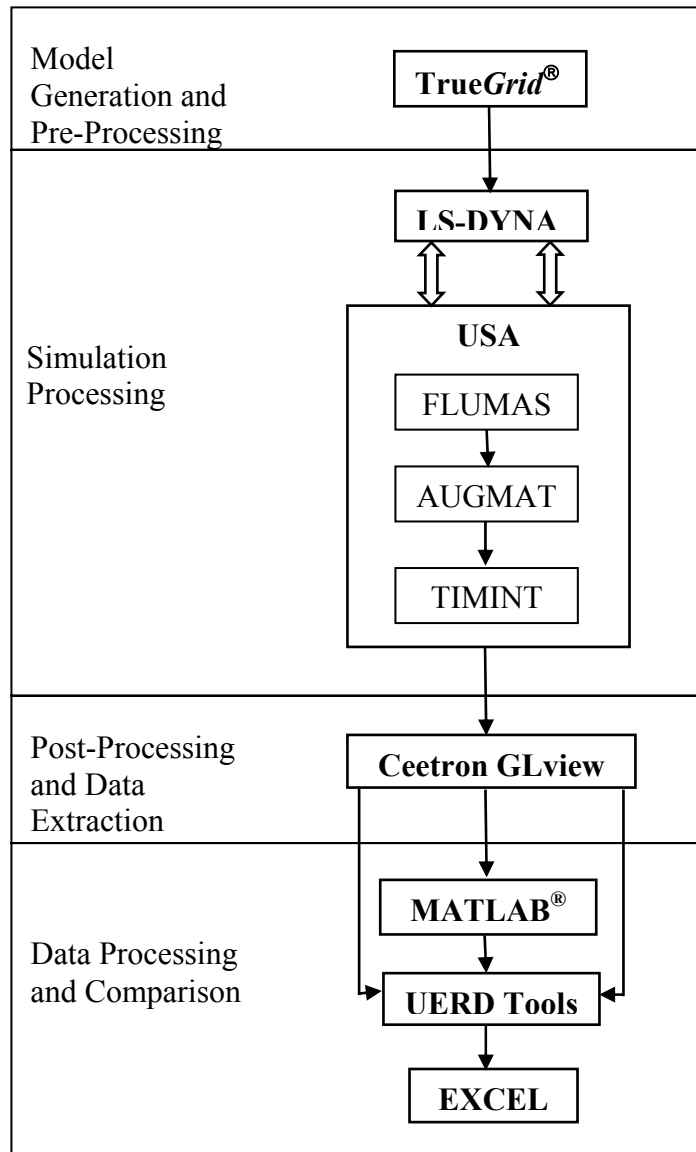
Figure 22.   Modeling and Simulation Flow Chart

B.   SIMULATION PROCESSING

1.   LS-DYNA

After generating the finite element model, it must be translated into LS-DYNA keyword format. LS-DYNA, which was chosen as a primary means to perform the simulations, is an explicit finite element program used for the analysis of the non-linear dynamic response of three dimensional structures [Ref. 22]. Although LS-DYNA is a very popular computational tool in the automotive industry where it is commonly used to simulate such events as automobile crashes and airbag deployment, it can be also used for large structures, including structures coupled to fluids by the introduction of arbitrary Lagrange-Eulerian and Euler solution techniques. LS-DYNA is used as a non-linear three-dimensional analysis code that performs the time integration for the structure.

2.   Underwater Shock Analysis Code

The underwater shock analysis code (USA) [Ref. 11] was used to calculate the transient response of a totally or partially submerged structure to acoustic shock waves of arbitrary pressure-profile and source location. It counts on a structural analysis code for modeling of the structure. LS-DYNA is one of those structural analysis codes coupled with USA with that purpose. USA is a boundary element code that solves the fluid-structure interaction equations using the Doubly Asymptotic Approximation (DAA) used in Equation (2.25). In fact, USA has a cavitating fluid volume element modeling capability. However, at this time it mainly relies on boundary element implementations of Doubly Asymptotic Approximations (DAA) for the treatment of the fluid- structure interaction. Several different DAA formulations, of increasing complexity and accuracy, are available like second-order mode-derived DAA (DAA_{2M}) and second-order curvature-corrected DAA (DAA_{2C}) as well as first-order DAA (DAA_1) which was illustrated in Equation (25) and used for the analyses in this thesis [Ref. 11]. As stated before, the DAA approach models the response in terms of the wet-surface variables only. This allows the problem to be solved without requiring a large fluid volume. This method has been shown to work well for submerged structures such as submarines, but has some difficulties exist in describing the ship shock phenomena accurately near the

free surface due to the bulk cavitation associated with the UNDEX event of the surface ships. However, cavitation (bulk and local) has a major effect on the response of a surface ship subjected to an underwater shock, particularly in the late time response. Therefore, to overcome this problem, a finite element model of the surrounding fluid elements was created an adequate distance from the structure as in the meko-like box model to account for the occurrence of both bulk and local cavitations appropriately inside the UNDEX environment so that the calculations could be executed. In the recent work completed by Hart [Ref. 24], it was concluded that the surrounding fluid mesh must be extended radially outward from the hull to a radius equal to the maximum depth of the lower cavitation boundary. This fluid volume model (fluid mesh) should be extruded from the wetted surface of the structure, matching the structural element faces and nodes as perfectly as possible [Ref. 25]. The DAA boundary is then truncated to the outer surface of the fluid mesh [Ref. 6].

The USA code is present in two forms: a standalone form and a closely coupled form. While USA in the case of the standalone form performs the time-integration of both the fluid and structural systems of equations, in it's closely coupled form, the USA time-integration processor is linked to the structural analysis code and is simply responsible for the solution of the fluid equations [Ref. 11]. Since the structural analysis code is responsible for the entire structural solution, it accommodates the geometric and material non-linearity. The structural analysis code and the USA code exchange their information at each time step of the solution. LS-DYNA/USA is an example of the closely coupled form. The time integration process utilized in LS-DYNA/USA for the analyses in this thesis will be explained in the section on the time integration processor.

The USA code consists of three components: Fluid Mass Processor (FLUMAS), Augmented Matrix Processor (AUGMAT), and Time Integration Processor (TIMINT) [Ref. 11].

a.   FLUMAS
The FLUMAS processor, which is the first USA module to be run, generates the fluid mass matrix for a structure submerged in an infinite, inviscid and

incompressible fluid by utilizing the boundary-element treatment of Laplace's equation [Ref. 11]. In addition, it creates fluid mesh data and a set of transformation coefficients that relate the structural and fluid degrees of freedom on the wet surface. The user-defined inputs contain fluid mesh and element definitions, location of the free surface, fluid properties like mass density and acoustic speed of sound and atmospheric properties such as pressure and acceleration due to gravity [Refs. 13 and 19]. The FLUMAS processor also generates the directional cosines for the normal pressure force and the nodal weights for the fluid element pressure forces [Refs. 17 and 26]. The fluid area matrix is diagonal while the fluid mass matrix is symmetric. Lastly, it has the capability to solve the fluid eigenvalue problem and automatically computes added mass coefficients of the rigid body [Refs. 11 and 26].

To be able to provide details for the processing of the FLUMAS processor, schematic representation is demonstrated in Figure 23 [Ref. 11]. First, the structural analysis code is in charge for the initial preprocessing step for the generation of the structural mass matrix M_s and the storage of the structural coordinate information, the equation table and potentially the wet-surface connectivity. Then, these data are passed to the USA code on the database STRNUM. As previously stated, the FLUMAS processor performs the calculations for the fluid mass matrix M_f, the diagonal area matrix A_f and the fluid-structure transformation information G. If the wet-surface connectivity exists on STRNAM, the FLUMAS processor will use it. If not, the wet-surface connectivity should be defined at this point. Eventually, the fluid boundary geometry data is stored on the GEONAM and the fluid mass matrix is stored in the FLUNAM database [Ref. 11].
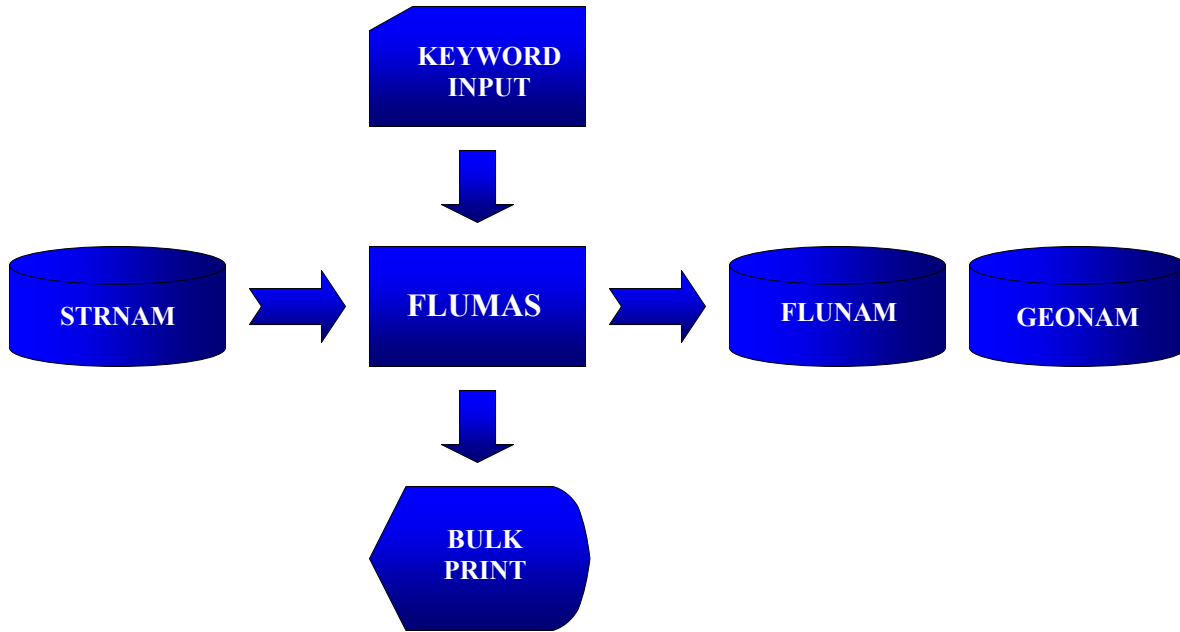
Figure 23.   Flow of Information in The Typical FLUMAS Execution [from Ref. 11]

b.   *AUGMAT*

The AUGMAT processor of the USA code accepts data from the FLUMAS processor and the structural analyzer LS-DYNA to construct the specific constants and arrays which are used in the staggered solution procedure, i.e., in the TIMINT processor, for the transient response analysis of submerged structures [Ref. 13]. By combining the matrices generated in the FLUMAS and the LS-DYNA into one file, AUGMAT creates a more efficient way for TIMINT to access the data.

The USA executable AUGMAT combines the structural model data on STRNAM, the fluid boundary geometric data on GEONAM and the fluid mass matrix on FLUNAM to assemble the Doubly Asymptotic Approximation (DAA) coefficient matrices [Ref. 11]. The particular DAA formulation is asked for in this step. For DAA_1, the AUGMAT processor assembles and stores the matrices $\rho c M_s^{-1}$, D_s and $(D_s + D_{f1})$ in PRENAM database where

$$
\begin{aligned}
D_{f1} &= \rho c A_f M_f^{-1} A_f \\
D_s &= \rho c A_f G^T M_s^{-1} G A_f
\end{aligned}
\tag{4.1}
$$

47

Figure 24 summarizes the flow of information in the typical AUGMAT execution.
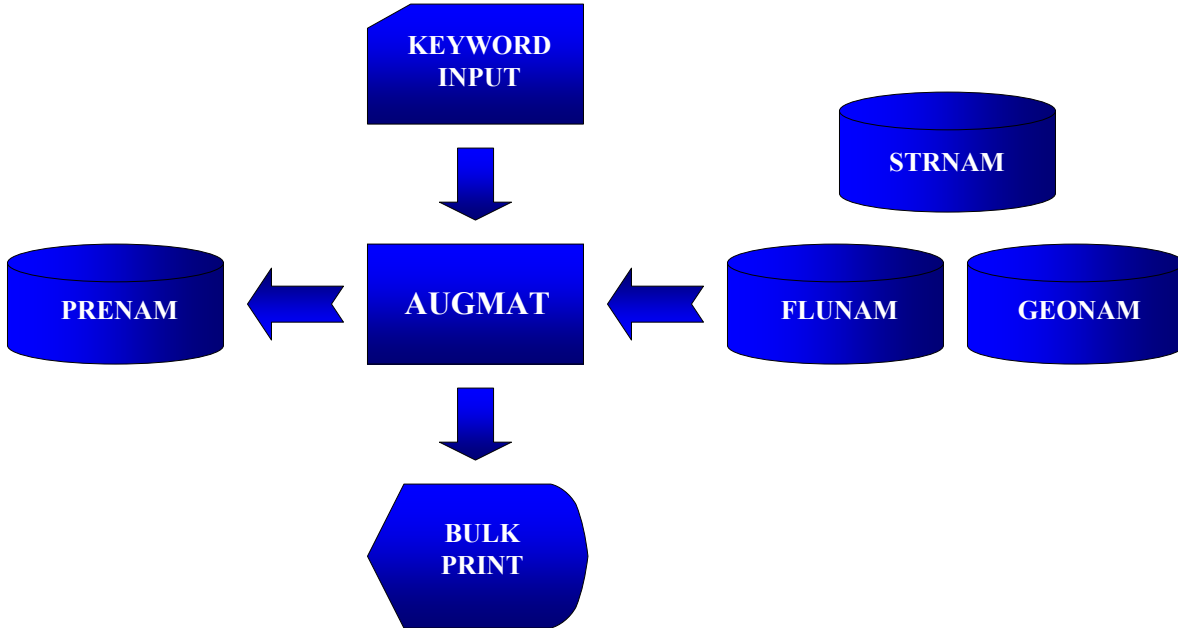
Figure 24. **Flow of Information in The Typical AUGMAT Execution [from Ref. 11]**

c. *TIMINT*

The TIMINT processor gathers information from the AUGMAT processor and uses these data to conduct a step-by-step direct numerical time integration of the structural equation, Equation (2.28) and the fluid equation, Equation (2.29) of submerged structures exposed to spherical shock waves of arbitrary pressure profile and source location [Ref. 11]. This is the most time consuming step of the USA code. The TIMINT processor solves the fluid equations whereas the LS-DYNA solves the structural equations. The staggered solution procedure is utilized where the structural response equations and the fluid response equations are solved separately at each time step through the extrapolation of the terms that couple the two systems [Ref. 11].

By receiving the PRENAM database containing the DAA coefficient matrices as an input, the USA processor TIMINT calculates the incident loads and integrates the equation of motion for the DAA fluid [Ref. 11]. Depending on user

selections, the TIMINT processor optionally writes several databases. For example, HISNAM contains only selective displacement, velocity and pressure time-history data. The TIMINT processor output data is saved as a binary histories file (D3THDT) and as an ASCII file (NODOUT). Therefore, a time history of displacement, velocity and wetted surface pressure is recorded for those nodes previously designated in the LS-DYNA keyword input file. Since TIMINT is the most time intensive in the entire simulation process, response data information is only retained for those nodes that have been chosen based on the user selection [Ref. 11]. Also, outputs from this component are the plot files (D3PLOT) required to perform the animation of the simulation.
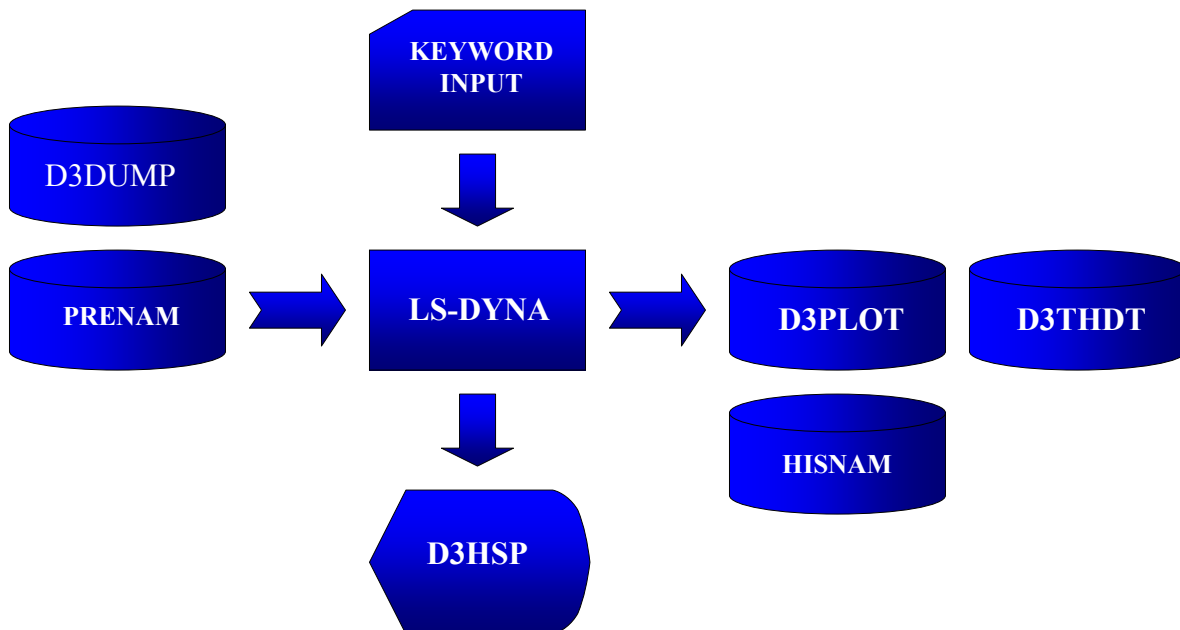
Figure 25.   Flow of Information in The Typical Closely-Coupled (LS-DYNA) TIMINT Execution [from Ref. 11]

Appendix C provides input decks for each of the three USA modules for both the meko-like box model, as well as several parts of LS-DYNA KEYWORD input decks.

C.   POST-PROCESSING AND DATA EXTRACTION

The results obtained from the LS-DYNA and USA codes are then transported into a graphical post-processing software package for further conversion of the data into a

visual representation of shock simulation response data of the meko-like box model. This transformation was achieved by utilizing Ceetron's GLview Pro Suite.

1. GLview

Ceetron's GLview Pro Suite is a commercial application that provides a very powerful 3D visualization and interactive animation of simulations run for large and complex Finite Element Models [Ref. 27]. GLview has the capability to import binary and ASCII type output data files generated by the LS-DYNA/USA processors. It is able to create time-dependent data plots as well as 3D model visualization. GLview Pro's animation software is also capable of displaying time-dependent results in both scalar and vector formats for the stresses, strains, displacements, velocities and accelerations in the fluid-structure model [Ref. 28]. In addition, Glview is used to extract the ASCII history file for each selected node from the LS-DYNA NODOUT file, export them as separate ASCII history files, and import these files into the UERD Tools data analysis and plotting program.

D. DATA PROCESSING AND COMPARISON

The GLview output is exported to the UERD Tools software where velocity time history response plots are created for a comparison of different simulation data performed. In addition, for analysis purposes, MATLAB® and Excel were used to make a comparison of maximum velocity time history responses throughout the structural models by exporting and plotting the GLview output.

1. UERD Tools

Underwater Explosions Research Department (UERD), the history of which has been stated in the introduction section, is a RTD&E organization in the Naval Surface Warfare Center, Carderock Division. The data analysis and plotting program, UERD Tools was particularly designed for the analysis of ship shock trial data. Since it is capable of importing ASCII history files exported from GLview, UERD Tools is also used to compare results generated by the LS-DYNA/USA processors by performing the

data analysis and making plots. Through a host of capabilities such as interpolation, filtering, error analysis, curve integration and derivation of shock spectra, the UERD Tools program allows users to create high quality plots of shock simulation and ship shock trial data. It also allows direct import of ship shock trial data for initial manipulation, such as drift compensation and filtering. After sets of data have been imported, the program allows the time set of all plots to be interpolated to the same time step. This is a necessity not only when conducting error analysis/correlation between the LS-DYNA/USA simulation data and the actual shock trial data but also when conducting error analysis/correlation between separate LS-DYNA/USA simulation data.

THIS PAGE INTENTIONALLY LEFT BLANK

V. DATA COLLECTION AND ANALYSIS

The methods described in this section were utilized in the data processing and error correlation of all of the shock simulations considered in the series of studies presented in this thesis.

A. SHOCK RESPONSE DATA PROCESSING

The existence of high frequency "noise" in shock simulation and shock trial data presents difficulties to be solved. In addition, the existence of low frequency "drift" in shock trial data also brings challenging issues to overcome. Since all the analysis in this thesis was based on the shock simulation data comparison, the "noise" problem was resolved only for the shock simulation data as follows while the "drift" problem in shock trial data was not considered.

1. High Frequency "Noise"

The nodes utilized in the analysis of shock simulation data not only calculate the desired frequency response but also compute the unwanted high frequency "noise". This high frequency response, which is well beyond the interest range for UNDEX events, is likely to clutter the shock simulation data. The unfiltered data, which is shown in red in Figure 26, has a less clear frequency curve if it is compared to the low-pass filtered data, which is shown in blue in Figure 26, for the same node. The time history plot in Figure 26 was taken for node 3883 located on the keel. By using the low-pass filtering technique in UERD Tools, all of the frequencies greater than 250 Hz were removed by leaving a much cleaner plot.

There have been some debates over the validity of applying the same low-pass filter to the shock simulation data while applying this low-pass filter to the shock trial data has been widely accepted. To show the validity of applying a low-pass filter to the shock simulation data, a statistical study based on 233 accelerometer measurements indicated that the shock simulation data, when it was low-pass filtered at 250 Hz, correlated much better with the low-pass filtered raw data for the same sensor [Refs. 8

and 29]. The results of this study showed that an unfiltered shock simulation data mean value was much higher than the measured values and had an excessively large variation value. However, the filtered shock simulation data not only displayed a more accurate mean value but also displayed a more reasonable variation value. As this study recommended, all of the shock simulation responses analyzed in this thesis were low-pass filtered at 250 Hz. Table 7 shows a summary of the statistical results of this study.
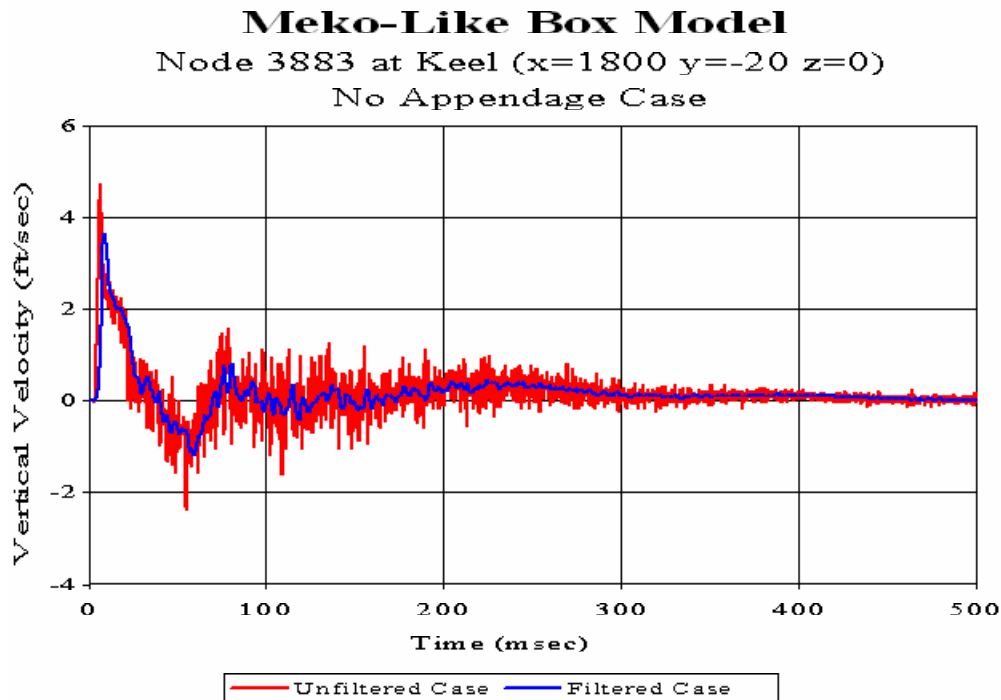
Figure 26.   Comparison of Unfiltered and Low-Pass Filtered Node Data

Table 7.   Summary of The Statistical Study of Unfiltered and Low-Pass Filtered Shock Simulation Data [from Ref. 8]

	Shock Trial Data (Filtered)	Simulation Data (Unfiltered)	Simulation Data (Filtered)
Mean	26.225	82.985	34.297
Variance	520.229	5775.711	606.426
Standard Deviation	22.809	75.998	24.626

54

B.   DATA ANALYSIS AND COMPARISON

1.   Node Location

Three different sets of nodes, two of which consist of 22 nodes and one of which consists of 20 nodes, were selected for the hull appendage analysis of the meko-like box model. Selected nodes slightly differ for the meko-like box model with hull appendages such as (solid and shell) keel board, open keel board and rudders while the same nodes were used for solid and shell keel boards. The nodes to be investigated were determined by selecting them along the interface between the hull and the hull appendage to be used and the decks above the interface. As a result, this selection gave different sets of nodes located on the keel, sides and exterior bulkheads of the meko-like box model. The selected nodes were designated in the LS-DYNA input deck as nodes for which to retain time history response data for comparison. Typically, the vertical and the athwartship velocity responses were analyzed for each shock simulation. Table 8 shows a list of all of these selected nodes and their locations on the structural model along with their ID numbers. Furthermore, Figures 27 and 28 illustrate the node locations depicted in top and profile views, respectively.

Table 8.   Vertical and Athwartship Velocity Response Node Locations (N/A = not analyzed)

| NODE | X (in) | Y (in) | Z (in) | Location | Meko-Like Box Model with | | | |
					Solid Keel Board	Shell Keel Board	Open Keel Board	Rudders
15	0	-20	0	Bulkhead	X	X	X	X
74	120	-140	0	Keel	N/A	N/A	N/A	X
81	120	140	0	Keel	N/A	N/A	N/A	X
148	0	-20	160	Bulkhead	X	X	X	X
214	120	-140	160	First Deck	N/A	N/A	N/A	X
221	120	140	160	First Deck	N/A	N/A	N/A	X
268	0	-20	280	Bulkhead	X	X	X	X
334	120	-140	280	Second Deck	N/A	N/A	N/A	X
341	120	140	280	Second Deck	N/A	N/A	N/A	X
388	0	-20	400	Bulkhead	X	X	X	X
434	120	-140	400	Top Deck	N/A	N/A	N/A	X
441	120	140	400	Top Deck	N/A	N/A	N/A	X
2454	1200	-20	0	Keel	X	X	X	X
2648	1200	-20	160	First Deck	X	X	X	N/A
2820	1200	-20	280	Second Deck	X	X	X	N/A
2970	1200	-20	400	Top Deck	X	X	X	N/A

NODE	X (in)	Y (in)	Z (in)	Location	Meko-Like Box Model with			
					Solid Keel Board	Shell Keel Board	Open Keel Board	Rudders
3883	1800	-20	0	Keel	X	X	X	X
5251	2400	-300	0	Keel	X	X	X	X
5308	2400	-180	0	Keel	X	X	X	X
5310	2400	-100	0	Keel	X	X	X	X
5312	2400	-20	0	Keel	X	X	N/A	N/A
5313	2400	20	0	Keel	X	X	N/A	N/A
5315	2400	100	0	Keel	X	X	X	X
5317	2400	180	0	Keel	X	X	X	X
5320	2400	300	0	Keel	X	X	X	X
6741	3000	-20	0	Keel	X	X	X	X
8170	3600	-20	0	Keel	X	X	X	X
8364	3600	-20	160	First Deck	X	X	X	N/A
8536	3600	-20	280	Second Deck	X	X	X	N/A
8686	3600	-20	400	Top Deck	X	X	X	N/A

MEKO-LIKE BOX MODEL
Vertical and Athwartship Velocity Node Locations
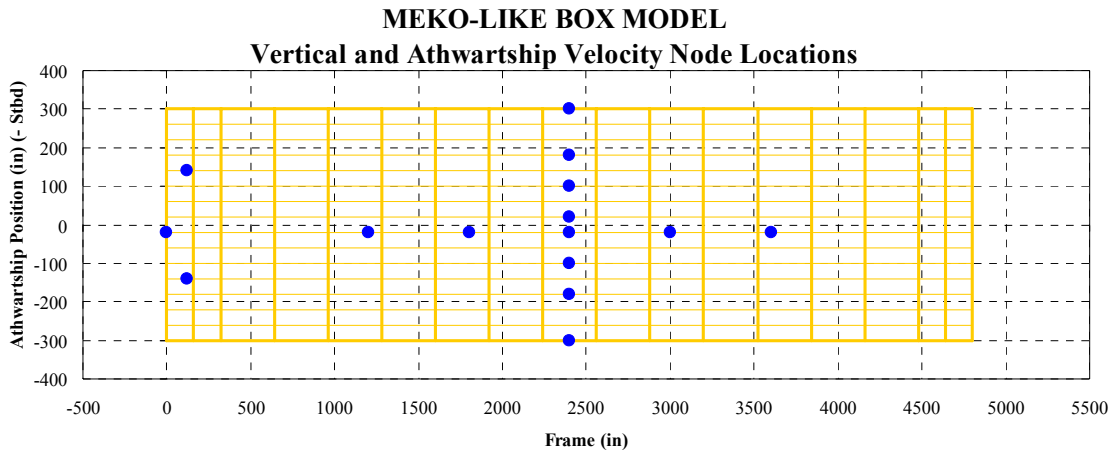
Figure 27.   Node Locations Depicted in Top View of Meko-Like Box Model

MEKO-LIKE BOX MODEL
Vertical and Athwartship Velocity Node Locations
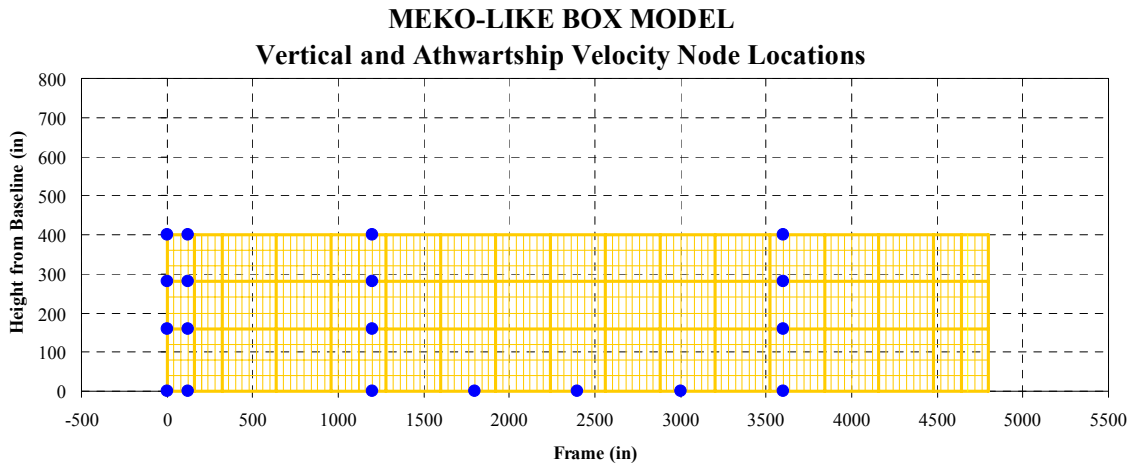
Figure 28.   Node Locations Depicted in Profile View of Meko-Like Box Model

56

### 2.	Error Measurements

Quantifying how well a calculated transient response from shock simulations compares to a measured response from shock trials is very subjective. Using an impartial error measurement such as Russell's error factor is one way to eliminate any bias from the comparison. In previous studies, the use of Russell's error factor as a measurement criterion between the simulated data and the measured data has been well-documented as a valid means of comparison [Refs. 8, 29, 31 and 32]. Furthermore, it provides an unbiased measurement of the error between the two data curves. In this thesis, only the simulated data is available for the comparison. Based on the successful use of Russell's error factor in comparing two data curves, one against the other regardless of the type of the data, this error measurement will thus be utilized for the comparisons in this thesis as well. Russell's error factor evaluates the magnitude and phase errors separately, then combines the two to form a single comprehensive error factor [Ref. 30].

In order to calculate the Russell's error, first, two variables are defined as,

$$A = \sum_{i=1}^{N} f_1(i)^2 \tag{5.1}$$

and

$$B = \sum_{i=1}^{N} f_2(i)^2 \tag{5.2}$$

where $f_1(i)$ and $f_2(i)$ are the two shock simulation response magnitudes to be compared at each time step, which is denoted as i. The variables A and B can then be used to calculate the relative magnitude error of the correlation.

$$m = \frac{(A - B)}{\sqrt{AB}} \tag{5.3}$$

The phase correlation is found as follows,

$$p = \hat{\phi}_1 \bullet \hat{\phi}_2 \tag{5.4}$$

57

where $\hat{\phi}$ is the normalized unit vector of the transient response. Since the unit vectors are normalized, the values of p can range from -1.0 to 1.0 where -1.0 indicates that the two responses are completely out of phase, while 1.0 indicates that they are completely in phase. A measure of the phasing between two transient response vectors in terms of correlation can be found by defining a new term,

$$C = \sum_{i=1}^{N} f_1(i)f_2(i) \qquad (5.5)$$

The phase correlation between the two shock simulation responses can then be computed by,

$$p = \frac{C}{\sqrt{AB}} \qquad (5.6)$$

It is important to note that p represents the phasing correlation between the two responses; it is not a measure of phase error. To calculate the phase error, the following equation is used.

$$RP = \frac{\cos^{-1}(p)}{\pi} \qquad (5.7)$$

The phase error factor has an error range of 0.0 to 1.0 where 0.0 indicates both responses are completely in phase while 1.0 indicates they are completely out of phase.

Although the phase error factor has a maximum value of 1.0, the relative magnitude error factor is unbounded. Since the two are combined to form the comprehensive error, it is easy to see that the magnitude error could easily dominate the comprehensive error, presenting an undesirable bias. To apply a similar bound to the magnitude error factor, the following magnitude error factor is defined.

$$RM = sign(m)\log_{10}(1+|m|) \qquad (5.8)$$

58

This maintains the sign unbiased nature of m while efficiently artificially bounding the magnitude error factor since a RM value of 1.0 represents an order of magnitude error between the two responses. The comprehensive error factor can now be determined utilizing Equation (5.7) and (5.8).

$$RC = \sqrt{\frac{\pi}{4}(RM^2 + RP^2)} \qquad (5.9)$$

where the $\frac{\pi}{4}$ term is a scale factor found by calculating the area of a square with a width of length RM and height of length RP. A circle with a corresponding area has a radius equal to $\frac{\pi}{4}$ times the diagonal of the square [Ref. 30]. The comprehensive error factor is not bounded, but errors in excess of 1.0 indicate substantial error between data sets and virtually no correlation.

Russell's error factor which has been defined in terms of a comprehensive error factor allows an unbiased error value to be assigned to the correlation between the two shock simulation transient responses to be compared. Now, it is time to set a range of Russell's comprehensive error factor to define what will be deemed an acceptable span of error values. Even though there is no definitive number which characterizes a satisfactory correlation between the data sets, Russell's comprehensive error factor values listed in Table 9 have been used as the acceptance criteria in both the earlier DDG-53 and DDG-81 ship shock trial simulation theses [Refs. 29 and 33]. As has been the case in previous studies, the acceptance criteria shown in Table 9, which has been used to correlate between the simulated data and the measured data, will also be used as a criterion to correlate the two sets of simulated data in this thesis.

Table 9. **Russell's Comprehensive Error Factor Acceptance Criteria**

RC < 0.15	EXCELLENT
0.15 ≤ RC ≤ 0.28	ACCEPTABLE
RC > 0.28	POOR

Figure 29 is a plot of the data set that was used in determining the criteria presented in Table 9. Note that in some cases a comparison with a RC = 0.25 or 0.26 was considered poor while, conversely, some plots having correlations as high as 0.33 or 0.34 were given an acceptable rating.
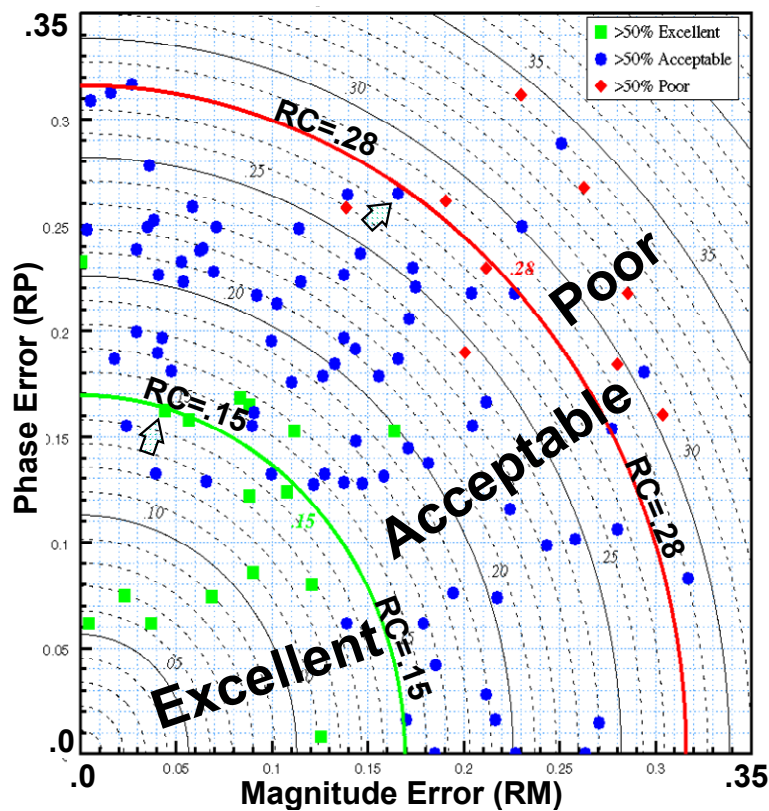
Figure 29. **Russell's Error Criteria Determination Data [from Ref. 29]**

The acceptance criteria found in Table 9 were suggested to be a valid measure of acceptance criteria of 500 msec processed velocity response data comparisons [Ref. 8]. As previously described, the data used in these comparisons was subjected to drift

compensated to remove gauge drift for the shock trial data and low-pass filtering at 250 Hz for the shock trial data and the shock simulation data, which has been the case on which this thesis was based on. Since they have been determined to be valid for only the aforementioned data processing method, the acceptance criteria from Table 9 are not necessarily valid for data, which has been processed using other techniques [Ref. 31].

3. Shock Spectra Analysis

The shock spectra analysis is also used for the data comparison between shock simulations and shock trials or between two distinct shock simulations. This thesis utilized the shock spectra analysis to compare the shock simulations to each other. The shock spectra analysis allows for various aspects of shock simulations to be compared, which are not easily recognizable in the time domain, i.e., in the time history plots. Therefore, as another method of comparing shock simulations to each other, or to shock trials, it can be said that the shock spectra analysis is as practical as the time history analysis.

The shock spectra are defined as the maximum absolute response of an undamped single degree of freedom system generated by a shock loading [Ref. 9]. If one were to compute the response of a system at a certain frequency, a curve would be generated for that particular frequency. Using iterative programming, the response of a system can be described by a series of curves. Each curve represents the response for a particular frequency. Instead of analyzing many different curves, it is more convenient to view the maximum absolute value of the response from each frequency. These maximum values plotted on one curve form the shock spectra. Time history plots can be used to generate shock spectra plots with a simple algorithm. UERD Tools has a very practical shock spectra generating function that enables the fast production of desired spectra plots in various formats.

The following figure is an example of a shock spectra plot and its corresponding time history plot (vertical velocity) including curves from the hull appendage analysis of meko-like box model when the coupled case was compared to the uncoupled case.

61

Meko-Like Box Model with Shell Keel Board

Node 15 at Bulkhead (x=0 y=-20 z=0)
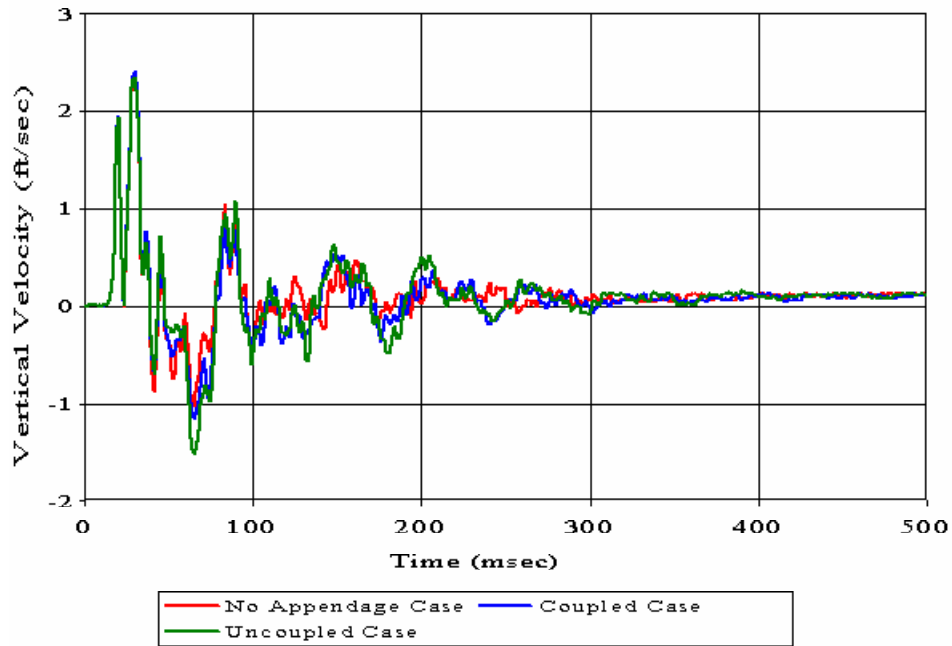
Meko-Like Box Model with Shell Keel Board

Node 15 at Bulkhead (x=0 y=-20 z=0)
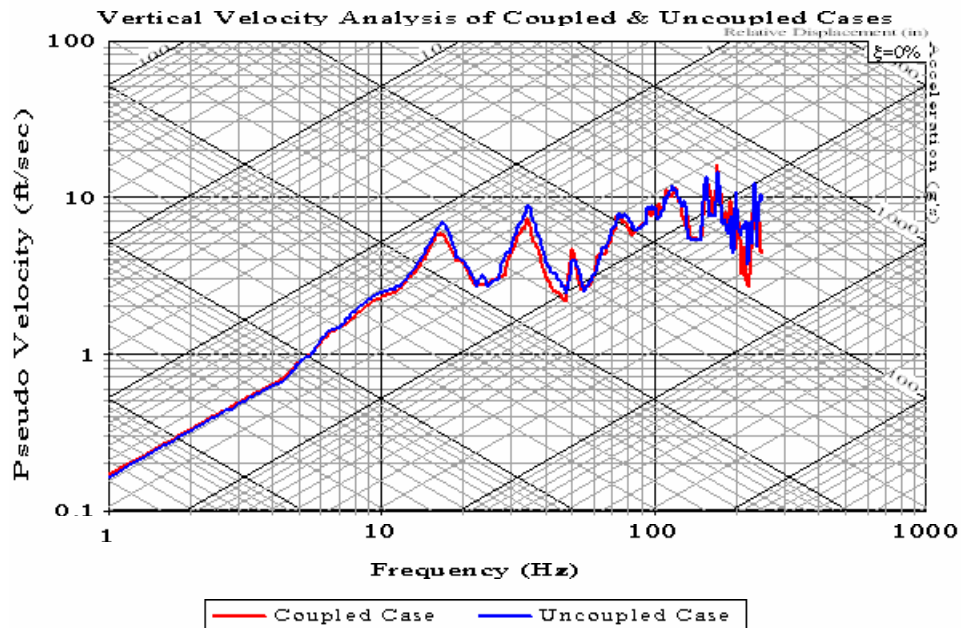
Figure 30.   Sample Time History Plot and Corresponding Shock Spectra Plot

Analyzing or quantifying the data presented in this shock spectra plot may be a little bit overwhelming at first, but essentially, it is very straightforward to recognize the situation. It should be noticed that both axes in the plot are both in logarithmic scale. The axis, which is called vertical velocity, actually implies "Pseudo Velocity" due to the fact that the peak response occurs after the UNDEX event. Being in the frequency domain vice the time domain, it is easy to compare the response at specific frequencies, most importantly at lower natural frequencies of the structure. The diagonal and off-diagonal axes provide the values of the absolute relative displacement and acceleration. For instance, to read the absolute relative acceleration response at a certain frequency, first it is necessary to identify the point at which the curve intersects that particular frequency, and then follow the diagonal axis down and to the right of the plot. Similarly, to read the absolute relative displacement response at a certain frequency, again it is necessary to start at the intersection of the curve at that particular frequency, and then follow the off-diagonal axis up and to the right of the plot. The top and right sides of the plot include values for the relative displacement and the acceleration in logarithmic scale.

THIS PAGE INTENTIONALLY LEFT BLANK

VI. SHOCK SIMULATION ANALYSIS

A. TEST DESCRIPTION

The attack (shot) geometry in Figure 31 was utilized in the shock simulations run during this study. This test geometry was determined with respect to the size of the meko-like box model to be investigated. A charge consisting of 5000 lb TNT was used for all the runs of meko-like box model. In the shot geometry, the charge was located offset from the center (2400 in) of the length of the structural model. The offset distance and the charge depth was set to 3950 in (~ 100 m) and 1960 in (~ 50 m), respectively. In addition, the value of 4069.7 in (~103.4 m) was used for the standoff distance of the charge. Table 10 summarizes the UNDEX parameters of the explosion. As stated before, the bulk cavitation region, which occurs in 684-in depth at most, was computed using the MATLAB program in Appendix A. The bulk cavitation region, which was calculated from this program by using the UNDEX parameters in Table 10 and the shot geometry in Figure 31, are illustrated in Figure 32.
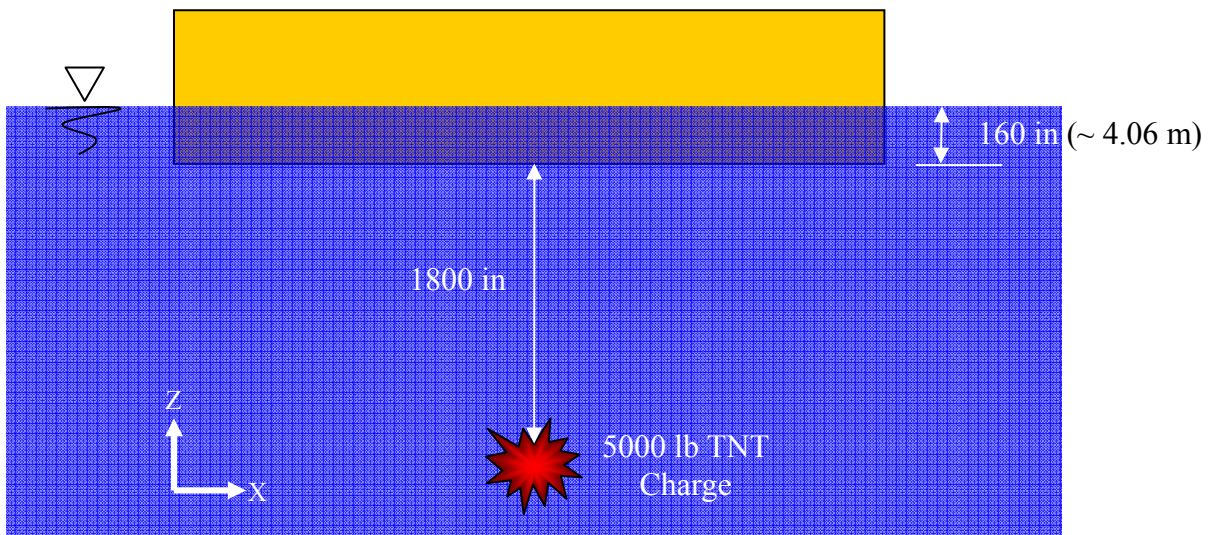
a. Profile View
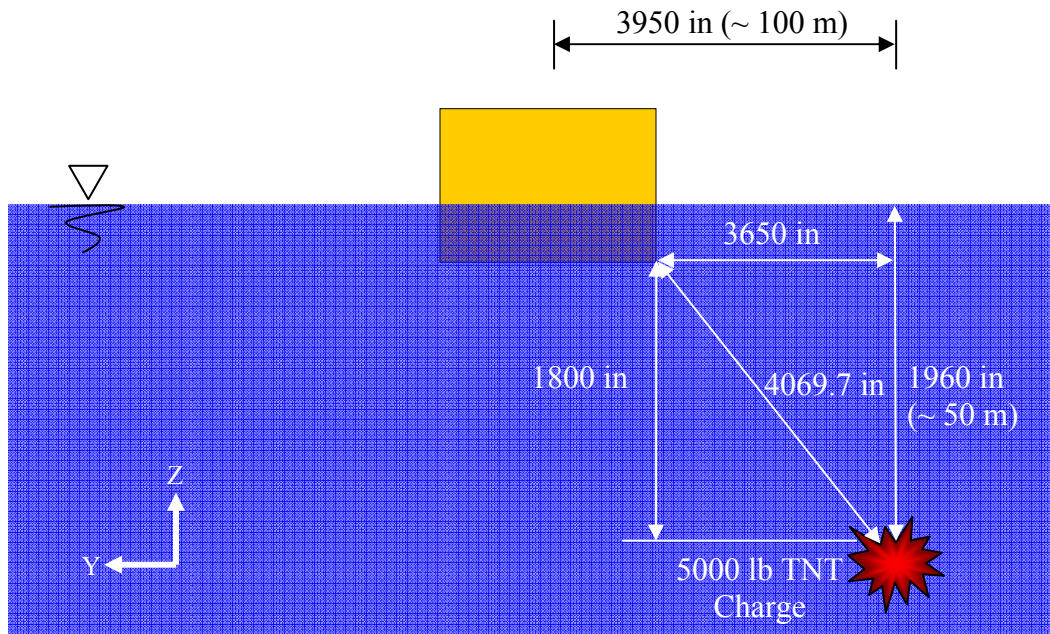
b. Stern View

Figure 31.   Meko-Like Box Model Shot Geometry

Table 10.   UNDEX Parameters for Meko-Like Box Model Simulations

P_{max}	663.32 psi
θ	0.001723 msec
T	0.5 sec
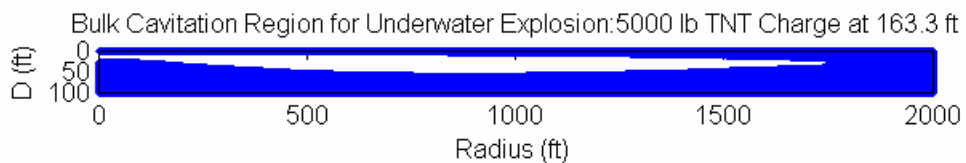
Figure 32.   Bulk Cavitation Region for 5000 lb TNT Charge Detonated at 163.3 ft (1960 in)

B.   DAMPING COEFFICIENTS

Most of the damping within a structure occurs due to the frictional energy dissipation at physical connection positions such as bolted or riveted mechanical joints. Nevertheless, the great majority of joints in ship structure systems are welded rather than mechanically connected, thus reducing the energy dissipation through the welds. Much

66

energy dissipation in a ship, however, occurs due to long cable trays, hangers, snubbers and the surrounding fluid coupled with the hull [Ref. 34].

Rayleigh damping, a particular form of proportional damping, defines the damping matrix, $[C]$, as

$$[C] = \alpha[M] + \beta[K] \tag{6.1}$$

in the general expression for the structural equation of motion.

$$[M]\{\ddot{x}\} + [C]\{\dot{x}\} + [K]\{x\} = \{F\} \tag{6.2}$$

The damping coefficients α and β are constants. Equation (6.1) can be normalized using mass normalization.

$$[\phi]^T[C][\phi] = [2\zeta_r\omega_r]_{diag} = \alpha[I] + \beta[\omega_r^2]_{diag} \tag{6.3}$$

To determine these damping coefficients for a simple system having only two modes with two modal frequencies of interest is simple enough. However, determining the damping coefficients in complex systems such as ships having more than two modes of interest presents a much bigger challenge. In this case, the system is over determined, and so Equation (6.3) has more equations than unknowns. These damping coefficients can be found by using the measured data and a least squares curve fitting method.

For each mode of the ship response, the modal damping ratio is calculated using the Equation (6.4).

$$\zeta_i = \frac{1}{2}\left(\frac{\alpha}{\omega_i} + \beta\omega_i\right) \tag{6.4}$$

A new set of damping coefficient values was determined by performing an extensive study at NPS using the measured data taken from the DDG-53 ship shock trials for 2000 msec [Ref. 34]. The ship was divided into 67 area groups for the damping coefficient analysis including data from 773 sensors. Measured modal response over the

frequency spectrum of interest, 0 to 250 Hz, was recorded for both the vertical and athwartship responses. A least squares curve fit, as illustrated in Figure 33, was then applied to each area group. Next, weighted averages were given to the area groups based on the number of modes used in the least squares curve fitting process required to determine α and β, which are presented in Tables 11 and 12.

Table 11.   **Weighted Mean of α [from Ref. 34]**

Athwartship Direction	Vertical Direction
18.4	19.2

Table 12.   **Weighted Mean of β [from Ref. 34]**

Athwartship Direction	Vertical Direction
2.82E-06	2.09E-06
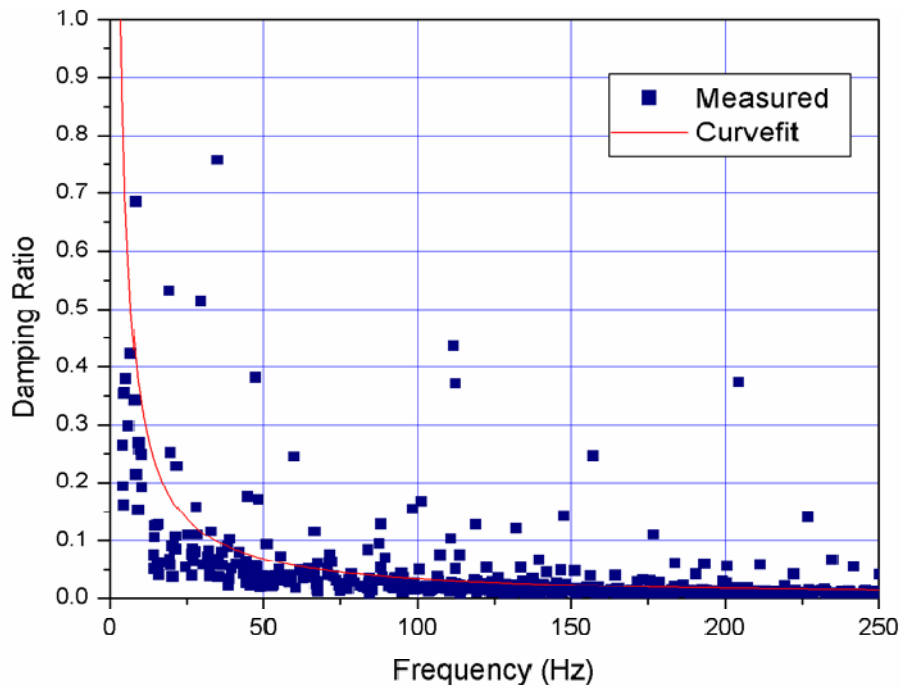
Figure 33.   **Modal Damping Ratio for Single Area Group, Vertical Direction [from Ref. 34]**

Consequently, the damping coefficient values (NPS Damping values) for DDG-53 were defined as $\alpha = 19.2$ and $\beta = 2.09\text{E-6}$ in the vertical direction while they were defined as $\alpha = 18.4$ and $\beta = 2.82\text{E-6}$ in the athwartship direction. The great difference in the two damping coefficients (α and β) implies that the damping within the system is mass-driven. Regarding the similarity of DDG-53 and DDG-81, the resulting damping coefficient values, which were the values in the vertical direction, were used for both since the vertical response is much larger in magnitude than the athwartship response [Refs. 8 and 34]. Since the application of these damping coefficient values to both ships gave very accurate response results close to ship shock trials [Refs. 8 and 29], they were utilized for shock simulations of the meko-like box model as well. The same damping coefficient values calculated for the vertical direction were assigned to all the structural solid, shell and beam elements in the meko-like box model.

C.   HULL APPENDAGE ANALYSIS OF MEKO-LIKE BOX MODEL

In previous efforts conducted in the modeling and simulation of ships subjected to UNDEX, some arguments have arisen concerning the influence that hull appendages have upon the dynamic response of a multi-degree-of-freedom structural model surrounded by a fluid mesh. This analysis investigated the effects on the dynamic response of the meko-like box model, based on the actual dimensions of a typical Meko-class ship, resulting from the addition of hull appendages such as rudders, shafts and keel boards. Moreover, the differences resulting from these hull appendages having been modeled as coupled and uncoupled structures with respect to the surrounding fluid in the finite element analysis were examined. This investigation was accomplished using the underwater shock modeling and simulation methodology. The process, explained in previous chapters, was developed at NPS. A detailed study will be presented on the validity of including hull appendages, the proposed coupling scheme for these appendages, and the resulting effects on the vertical and athwartship velocity responses.

1. Meko-Like Box Model with Solid Keel Board

The solid keel board, which is one of the hull appendages to be investigated, was constructed using 8-node brick (solid) elements along with varying brick element mass densities, which influence the weight percentage of the solid keel board within the structure. The construction process is described in Chapter III. As was previously stated, the solid keel board was modeled as both coupled and uncoupled structures with respect to the surrounding fluid. First, the effects on the dynamic response of the meko-like box model resulting from the inclusion and varying mass densities of the solid keel board will be investigated by utilizing the absolute maximum vertical velocity distribution plots and time history plots of the vertical and athwartship velocity response comparisons. Subsequently, to see the projected coupling scheme for the solid keel board, a comprehensive study will be presented based on the time history and shock spectra plots of the vertical and athwartship velocity response comparisons and Russell's error factor analysis. Table 13 lists the 22 chosen nodes, which were determined by selecting them during the interface between the hull and the solid keel board as well as the decks above this interface, and their positions on the structural model along with their ID numbers to be evaluated in this series of comparisons and analysis.

Table 13.   Vertical and Athwartship Velocity Response Node Locations
(Meko-Like Box Model with Solid Keel Board)

NODE	X (in)	Y (in)	Z (in)	Location
15	0	-20	0	Bulkhead
148	0	-20	160	Bulkhead
268	0	-20	280	Bulkhead
388	0	-20	400	Bulkhead
2454	1200	-20	0	Keel
2648	1200	-20	160	First Deck
2820	1200	-20	280	Second Deck
2970	1200	-20	400	Top Deck
3883	1800	-20	0	Keel
5251	2400	-300	0	Keel
5308	2400	-180	0	Keel
5310	2400	-100	0	Keel
5312	2400	-20	0	Keel
5313	2400	20	0	Keel
5315	2400	100	0	Keel
5317	2400	180	0	Keel
5320	2400	300	0	Keel

NODE	X (in)	Y (in)	Z (in)	Location
6741	3000	-20	0	Keel
8170	3600	-20	0	Keel
8364	3600	-20	160	First Deck
8536	3600	-20	280	Second Deck
8686	3600	-20	400	Top Deck

It should be noted that in this investigation of the applicability of modeling hull appendages the interface nodes corresponding to the attachment points of the hull appendage have not been compared. Although these have the same coordinate locations, the loading applied in the no appendage case and the hull appendage cases is distinctly different. In the no appendage case, these nodes are located at the exterior surface of the structure, whereas in the hull appendage cases the corresponding nodes are interior to the structure and are constrained due to the inclusion of the hull appendage. However, comparison of these nodes is presented in all other cases.
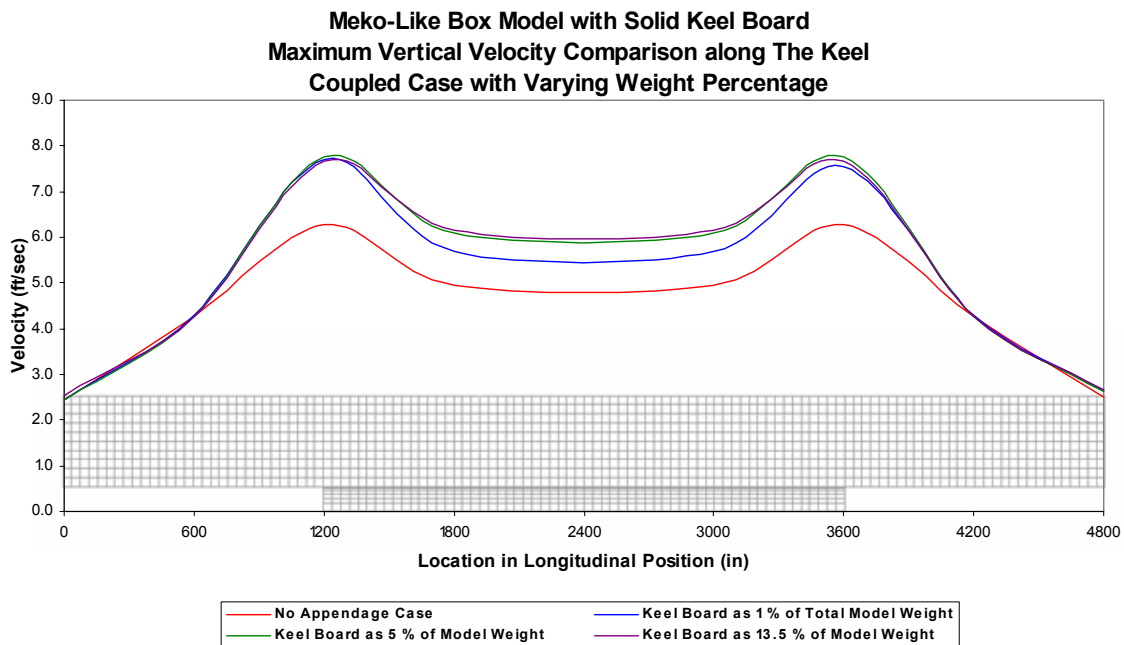
a. *Velocity Plots*

Figure 34.   **Absolute Maximum Vertical Velocity as a Function of Position (Keel)**

Meko-Like Box Model with Solid Keel Board
Maximum Vertical Velocity Comparison along The Second Deck
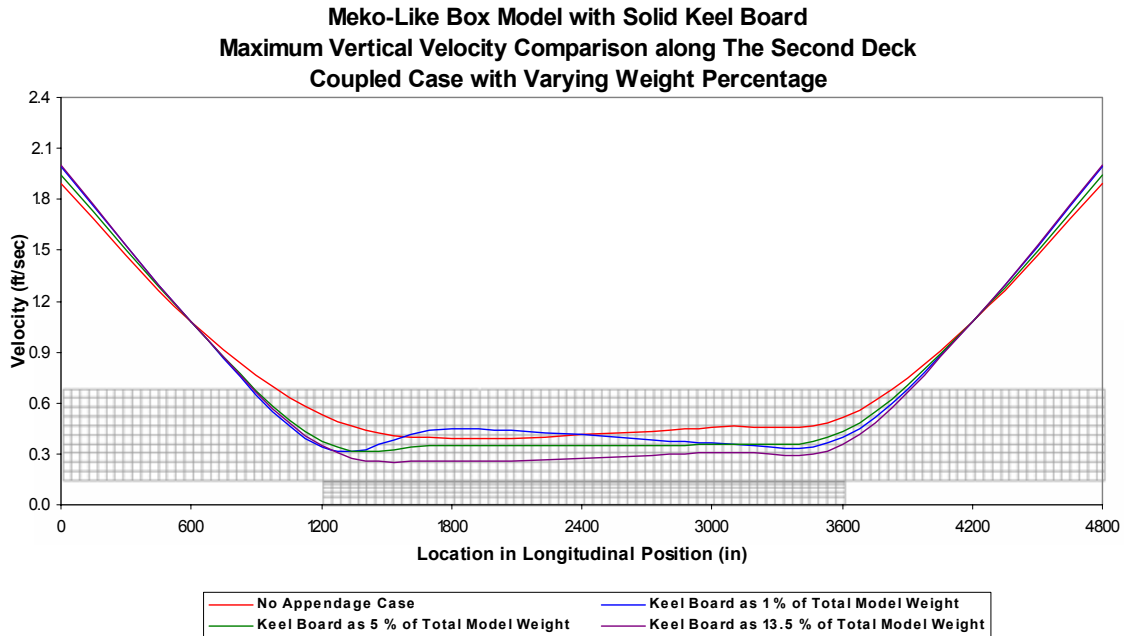**Coupled Case with Varying Weight Percentage**

Figure 35.   Absolute Maximum Vertical Velocity as a Function of Position
(Second Deck)

To show the consequences of the inclusion and changing mass densities of the solid keel board on the dynamic response of the meko-like box model, first, the absolute values of maximum vertical velocity responses of nodes located along the keel and second deck of the structural model will be compared for both the coupled and uncoupled cases. While the solid keel board was being constructed on the hull of the structural model, its mass density was altered so that its weight percentages could be set to 1 %, 2.5 %, 5 % and 10 %. For the simplicity, the weight percentages of 1 % and 5 % as well as the actual weight percentage became the cases to be investigated for the analysis of solid keel board eliminating the weight percentages of 2.5 % and 10 %. The weight percentage of 13.5 % implies the actual weight percentage of the solid keel board based on the actual mass density of the material (steel) of the solid elements. Figures 34, 35, 36 and 37 illustrate the discrepancy when the meko-like box model with the solid keel board having different weight percentages has been compared to the meko-like box model with no appendage. If these figures are investigated carefully, note that the maximum vertical velocity response of the meko-like box model excluding the solid keel board significantly differs from that of the meko-like box model including it.

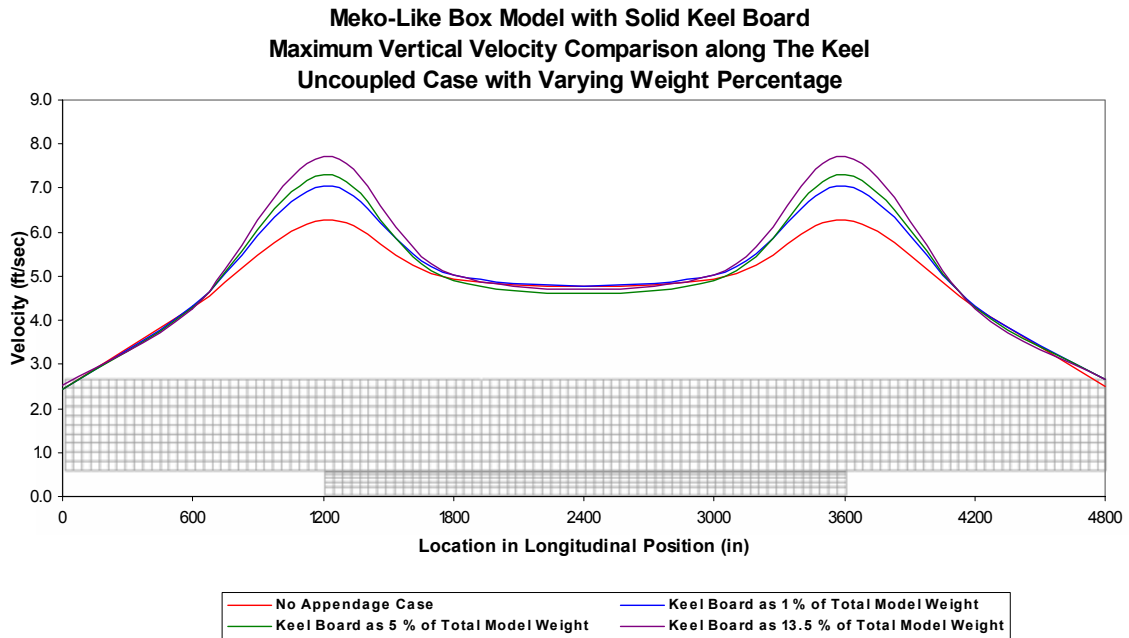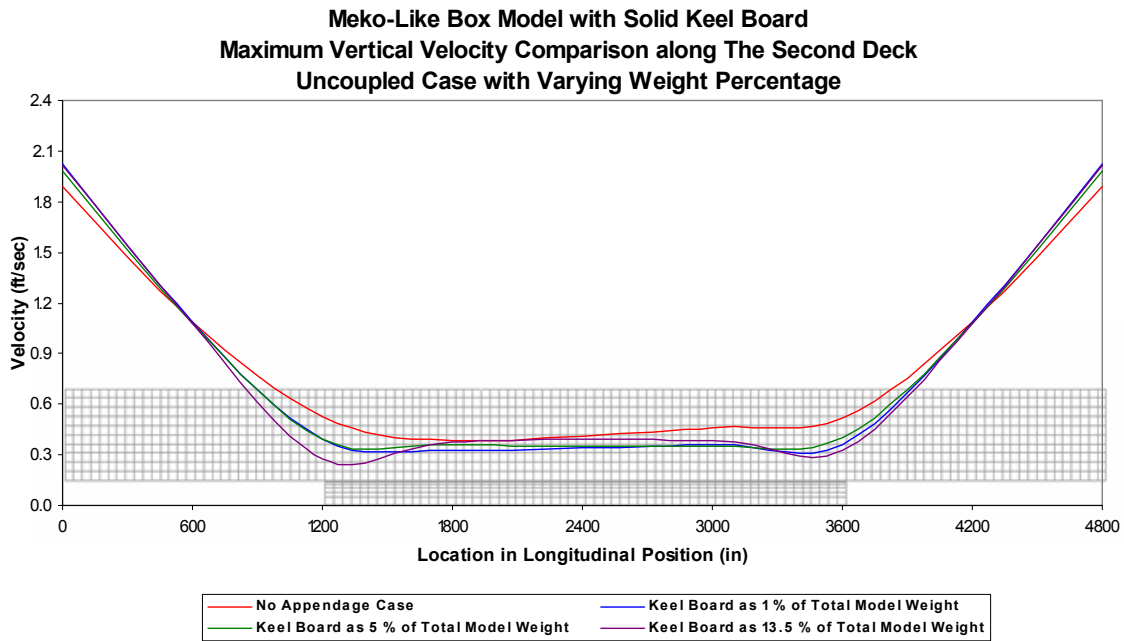**Figure 36.** **Absolute Maximum Vertical Velocity as a Function of Position (Keel)**

Figure 37. **Absolute Maximum Vertical Velocity as a Function of Position (Second Deck)**

The differences of maximum vertical velocity responses among the structural models including the solid keel board having different weight percentages, however, are not as much as the first situation as the curves are very close to each other.

73

This means that the inclusion of the solid keel board considerably affects the dynamic response of the structure for the keel region while different weight percentages of the solid keel board cause small disparities on the dynamic response of the structure. However, for both the coupled and uncoupled cases, there is no large difference in the second deck as there is in the difference for the keel between the meko-like box model with and without solid keel board. A similar situation was witnessed for the first and top decks of the meko-like box model, and their plots presented in Appendix D. Nevertheless, one should investigate the time history plots to determine how much both the inclusion and varying weight percentages of the solid keel board affect the dynamic response of the meko-like box model. The comparison of the time history plots will be conducted herein as the second study. From all the plots of the maximum vertical velocity response comparison including the figures in Appendix D, the meko-like box model without solid keel board gives the largest absolute maximum vertical velocity value of 6.27 ft/sec, while this value for the meko-like box model with solid keel board having different weight percentages is 7.66 ft/sec, and 7.71 ft/sec for coupled and uncoupled cases, respectively. Furthermore, it is observed that, as one moves to the upper decks, the maximum velocity response values almost gradually decrease with respect to those of the keel for all circumstances.
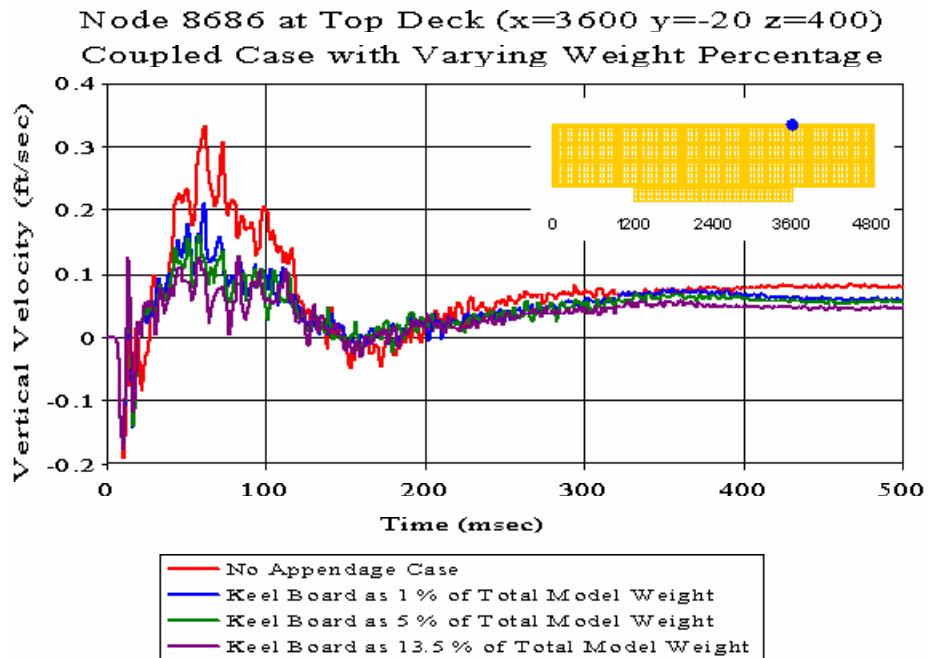
Figure 38.   Coupled Case with Varying Weight Percentage: Top Deck Node 8686

The time history plots are representative of the results obtained from the vertical and athwartship velocity analyses of the meko-like box model with solid keel board, which has different weight percentages of total model weight. These are provided as samples of the total set of time history plots found in Appendices D and E, respectively. These time history plots of both coupled and uncoupled cases were chosen to show large and small differences found between the no appendage case and the case of solid keel board having different weight percentages in the absolute maximum vertical velocity distribution plots discussed previously. Figure 38 with node 8686, where relatively large differences occur, shows that the peak responses of the no appendage case are larger than the other cases. As the weight percentage of the solid keel board increases, the peak responses become smaller. The athwartship velocity response of the same node represents a relatively matched situation between the data sets particularly in the early time response. The inclusion and the varying weight percentage of the solid keel board do not influence the athwartship velocity response as much as the vertical velocity response.
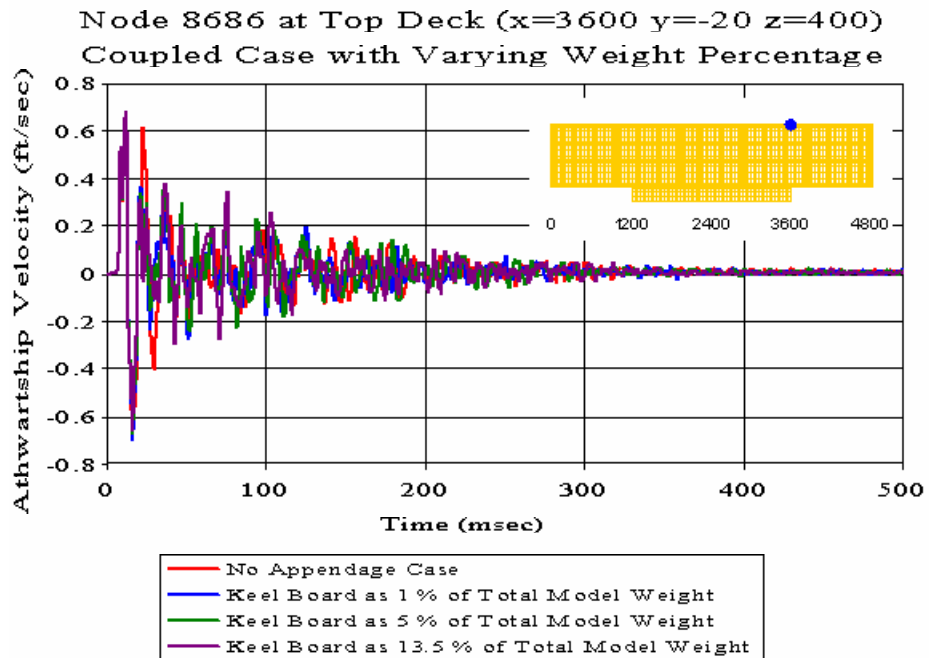
75

Figure 39.   **Coupled Case with Varying Weight Percentage: Top Deck Node 8686**

Node 388 is representative of one of the minimum differences occurring between the data sets obtained from all of the cases. While there are tiny phase differences between the no appendage case and the other cases in the early time response, all of the cases of solid keel board produce a well-behaved match among their data sets. The same kind of relationship is valid for the athwartship velocity response of the same node as seen in Figures 40 and 41 as well.
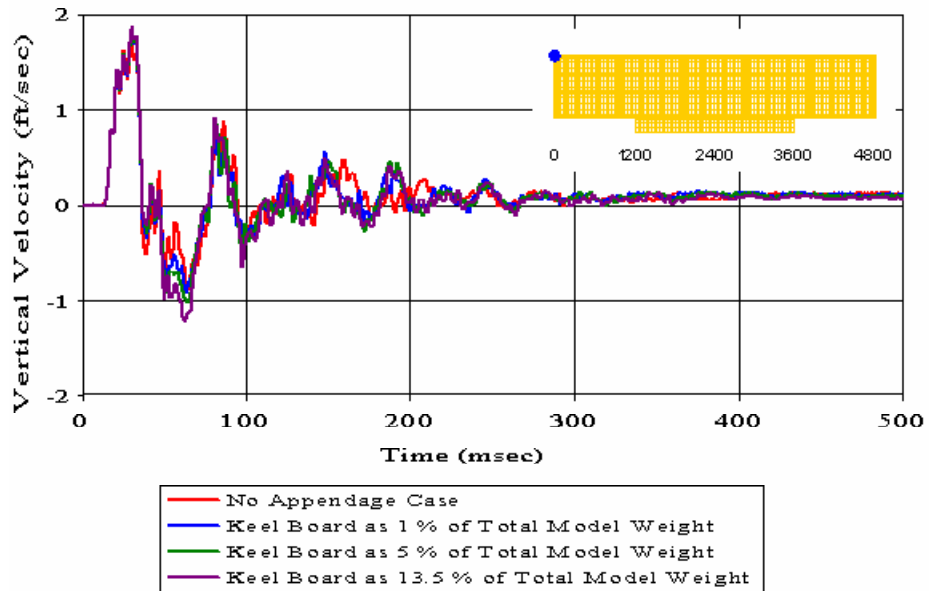
Figure 40. **Coupled Case with Varying Weight Percentage: Bulkhead Node 388**

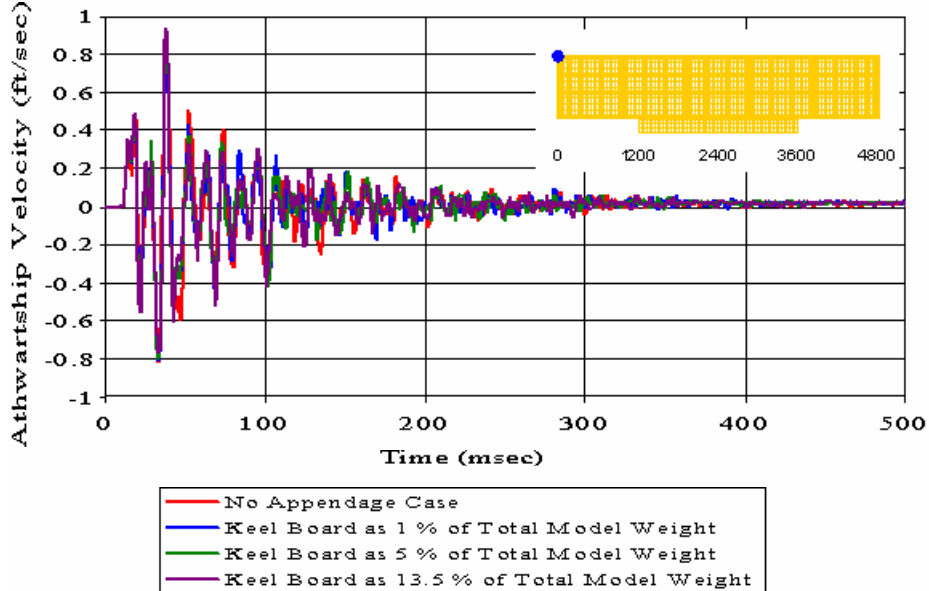**Figure 41.** **Coupled Case with Varying Weight Percentage: Bulkhead Node 388**

77

Node 2820 is located upper side of one of the extremities of the solid keel board. It generates almost the same correlation, as node 8686, among all of the data sets developed from the shock simulations of the uncoupled case. Especially the nodes located close to the solid keel board or its extremities are more affected relative to the other node locations on the structure. Figures 42, 43, 44 and 45 also represent the vertical and athwartship velocity responses observed in the appendage analysis of the solid keel board.
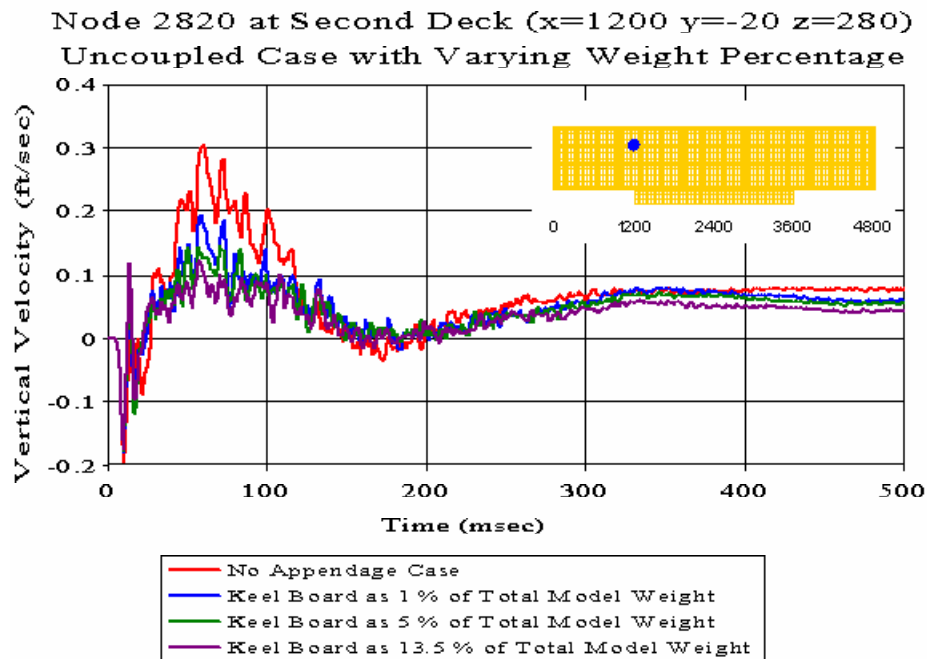
Figure 42.   Uncoupled Case with Varying Weight Percentage: Second Deck Node 2820
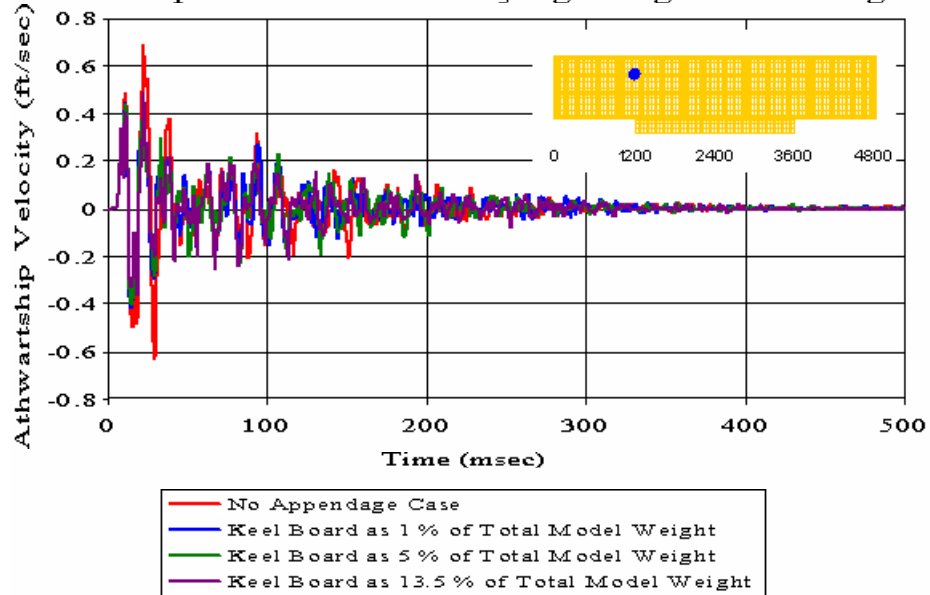
Figure 43. **Uncoupled Case with Varying Weight Percentage: Second Deck Node 2820**
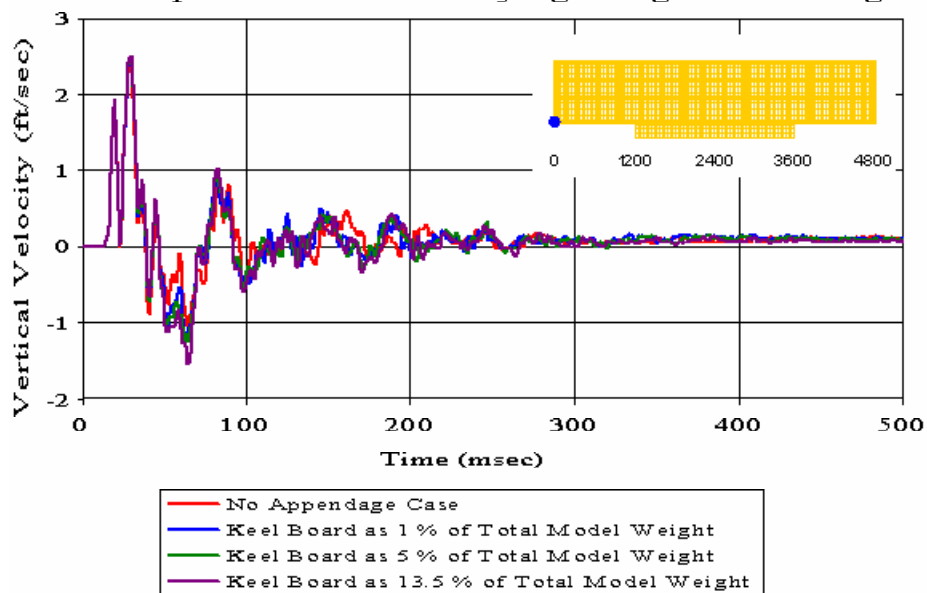
Figure 44. **Uncoupled Case with Varying Weight Percentage: Bulkhead Node 15**

Figure 45.   Uncoupled Case with Varying Weight Percentage: Bulkhead Node 15

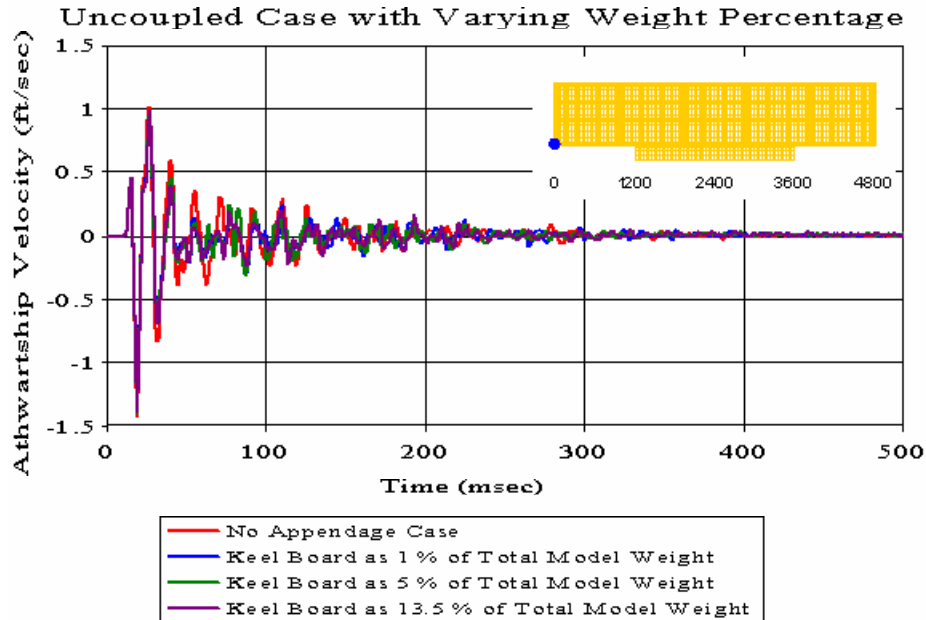Looking into the overall results, it can be said that the inclusion of the solid keel board, which has a relatively large surface area percentage, 20.5 % with respect to the underwater surface area of the structural box model, exposed to UNDEX, noticeably affects the dynamic response of the whole system especially in the vertical direction. However, as the weight percentage of the solid keel board changes, the dynamic response of the structural model varies but not as much as the changes due to the inclusion of the solid keel board to the meko-like box model. Therefore, it can be concluded that the addition of any hull appendage, like solid keel board, containing a large surface area is a more important driving factor affecting the dynamic response than the varying weight percentages of this hull appendage constructed on the structure mostly in the vertical direction. Furthermore, regarding all of the plots of both coupled and uncoupled cases, the responses of the nodes located close to the solid keel board are affected more by the inclusion of the solid keel board having varying weight percentages relative to the locations far away from the solid keel board.

b. *Error Comparison*

The differences resulting from the solid keel board having been modeled as coupled and uncoupled structures with respect to the surrounding fluid in the finite element analysis will be examined next. Vertical and athwartship velocity comparisons between the coupled and uncoupled cases were made for all of the three different weight percentages of the solid keel board. Russell's error factor was conducted as an unbiased error value to correlate the two shock simulation data, based on 500 msec time history plots of the vertical and athwartship velocity responses for both coupled and uncoupled cases.

While the true magnitudes of the simulation data comparison included both positive and negative values, indicating the responses of uncoupled case that were both smaller and larger than the response magnitudes of the coupled case, which, in fact, implies the actual situation in an UNDEX event, all magnitudes of errors were plotted as their absolute values for the simplicity of plotting. The truly computed error magnitudes are found in the corresponding data tables for each set of plots. Figures 46 and 47 are the plots of the complete Russell's error factor comparison consisting of all of the three different weight percentages of the solid keel board for vertical and athwartship velocity analyses, respectively. Separate plots of Russell's error comparison for each weight percentage of the solid keel board can also be found in Appendix G for both vertical and athwartship velocity responses.

If Figure 46 is examined, in all but a few exceptions, the vertical velocity response values fall into the excellent range. Since all error values fall into the excellent and acceptable range, they essentially constitute a desirable correlation between the coupled and uncoupled cases by satisfying Russell's error factor criteria developed in Table 9. The magnitude error is consistently low throughout the data set, while it is the relationship of the phase error that unavoidably drives the overall Russell's Comprehensive error factor higher in some cases. It is obvious to notice that the meko-like box model with the solid keel board having the actual weight percentage of 13.5 % creates the best correlation between the coupled and uncoupled cases with respect to the mean correlation if three different situations are compared to each other.
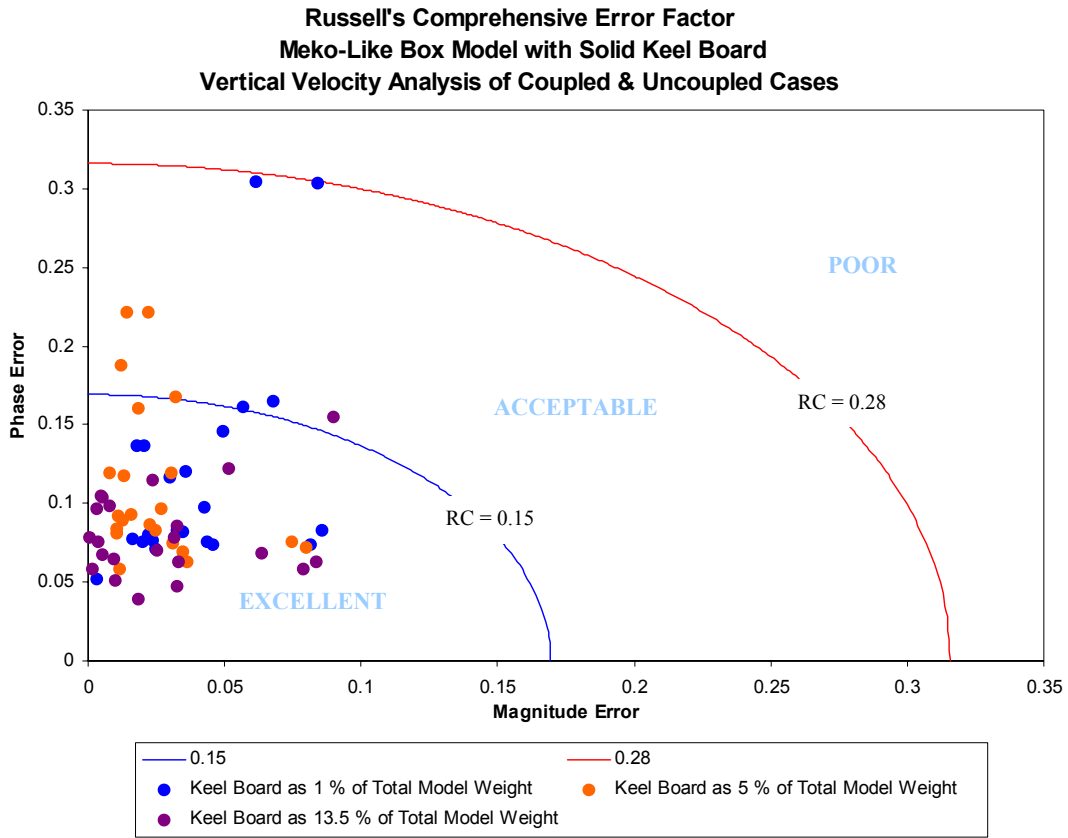
Figure 46. **Complete Russell's Error Factor Comparison for Meko-Like Box Model with Solid Keel Board (Vertical Velocity)**

The Russell's error factor comparison for the athwartship velocity analysis produces relatively worse correlation between the coupled and uncoupled cases. As seen in Figure 47, most of the error values fall into the excellent and acceptable range. Eleven points out of 66 are found in the poor region, which corresponds to the region having greater error values than the 0.28 cut-off value. Most of those falling outside the acceptable region are just barely greater than the 0.28 cut-off value, and therefore, do not necessarily constitute an undesirable correlation. As has been the case in the vertical velocity analysis, the magnitude error is consistently low throughout the data set, while the phase error inevitably drives the overall Russell's comprehensive error higher in most cases. It can be noted that the meko-like box model with the solid keel board having the actual weight percentage of 13.5 % creates the best correlation between the coupled and uncoupled cases with respect to the mean correlation in the athwartship direction as well.
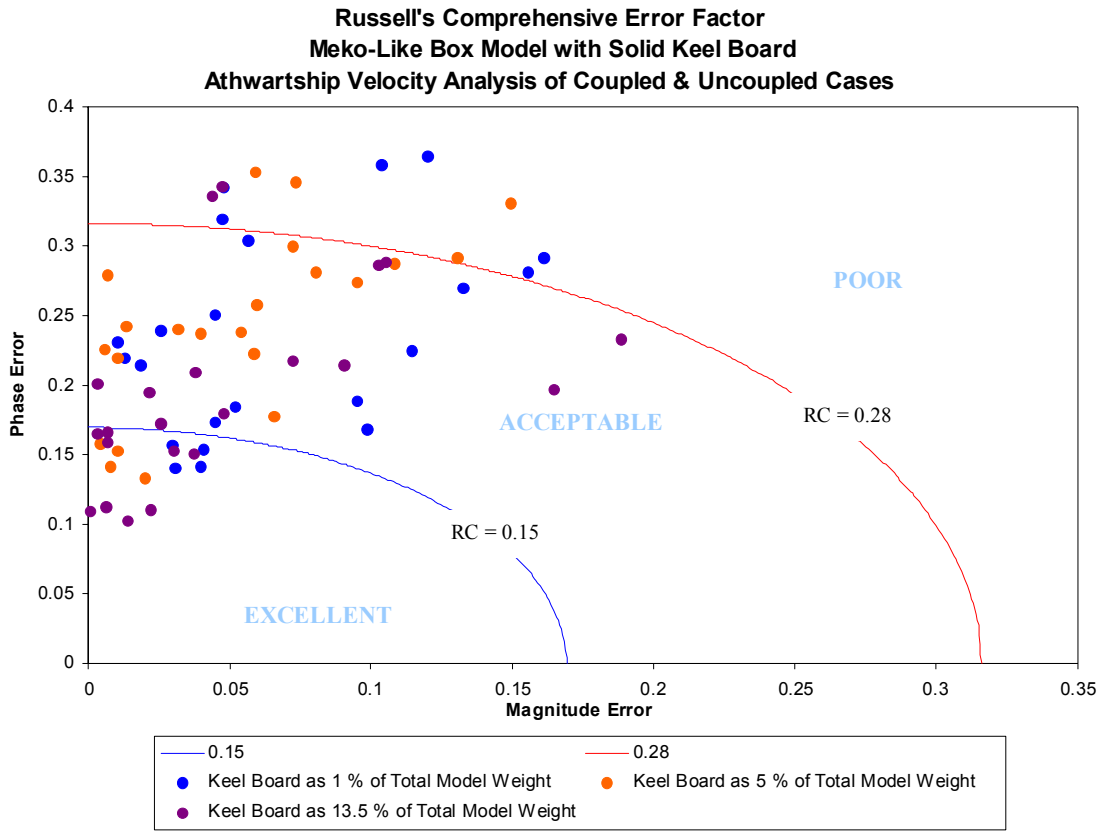
82

Figure 47.   Complete Russell's Error Factor Comparison for Meko-Like Box Model with Solid Keel Board (Athwartship Velocity)

Using the actual weight percentage of 13.5 % for the solid keel board created on the hull of meko-like box model, the average Russell's Comprehensive error factors were found to be 0.0786 and 0.1817 for the vertical and athwartship velocity responses, respectively. In comparison, the mean values, when the weight percentages of the solid keel board are 1 % and 5 %, were 0.1122 and 0.1027 for the vertical velocity response and 0.2207 and 0.2234 for the athwartship velocity response, respectively. The mean values resulting from the vertical velocity analysis anticipate the improved correlation between the coupled and uncoupled cases if compared to the mean values of the athwartship velocity analysis. Table 14 shows the truly computed error magnitudes along with the mean and standard deviation values as supporting data when the solid keel board is modeled as 13.5 % of the total model weight. The other corresponding data tables for each set of Russell's error factor comparison plots can be found in Appendix G.

Table 14. **Russell's Error Factors for Meko-Like Box Model with Solid Keel Board as 13.5 % of Total Model Weight**

Simulation runtime = 500 msec					Meko-Like Box Model with Solid Keel Board as 13.5 % of Total Model Weight					
					Vertical Velocity Comparison			Athwartship Velocity Comparison		
NODE	X (in)	Y (in)	Z (in)	Location	COUPLED & UNCOUPLED CASES			COUPLED & UNCOUPLED CASES		
					LS-DYNA/USA DATA (<250HZ)			LS-DYNA/USA DATA (<250HZ)		
					RM	RP	RC	RM	RP	RC
15	0	-20	0	Bulkhead	0.0253	0.0705	0.0664	-0.0221	0.1100	0.0994
148	0	-20	160	Bulkhead	0.0326	0.0477	0.0512	-0.0143	0.1022	0.0914
268	0	-20	280	Bulkhead	0.0333	0.0625	0.0628	0.0009	0.1085	0.0961
388	0	-20	400	Bulkhead	0.0314	0.0786	0.0750	-0.0067	0.1120	0.0994
2454	1200	-20	0	Keel	0.0032	0.0969	0.0859	0.0477	0.3422	0.3062
2648	1200	-20	160	First Deck	0.0094	0.0645	0.0577	-0.0727	0.2169	0.2027
2820	1200	-20	280	Second Deck	-0.0038	0.0754	0.0669	-0.0379	0.2085	0.1878
2970	1200	-20	400	Top Deck	-0.0003	0.0783	0.0694	-0.0217	0.1939	0.1729
3883	1800	-20	0	Keel	0.0049	0.1050	0.0931	-0.1031	0.2857	0.2691
5251	2400	-300	0	Keel	-0.0237	0.1149	0.1040	-0.0258	0.1715	0.1537
5308	2400	-180	0	Keel	-0.0184	0.0396	0.0387	0.0036	0.1647	0.1460
5310	2400	-100	0	Keel	-0.0634	0.0688	0.0829	0.0069	0.1588	0.1409
5312	2400	-20	0	Keel	-0.0517	0.1220	0.1174	-0.1650	0.1960	0.2271
5313	2400	20	0	Keel	-0.0900	0.1552	0.1590	-0.1888	0.2327	0.2656
5315	2400	100	0	Keel	0.0790	0.0584	0.0871	0.0072	0.1657	0.1470
5317	2400	180	0	Keel	0.0834	0.0631	0.0927	0.0375	0.1502	0.1372
5320	2400	300	0	Keel	0.0324	0.0854	0.0809	0.0306	0.1525	0.1379
6741	3000	-20	0	Keel	0.0051	0.1035	0.0918	-0.1053	0.2881	0.2719
8170	3600	-20	0	Keel	0.0081	0.0981	0.0872	0.0441	0.3348	0.2993
8364	3600	-20	160	First Deck	0.0102	0.0513	0.0464	-0.0908	0.2134	0.2055
8536	3600	-20	280	Second Deck	0.0016	0.0585	0.0519	0.0038	0.2001	0.1774
8686	3600	-20	400	Top Deck	0.0054	0.0675	0.0600	-0.0480	0.1785	0.1638
Russell Error Correlation			Sum(E(X))		0.1140	1.7657	1.7284	-0.7199	4.2869	3.9983
> 0.28	Poor		Sum(E(X^2))		0.0341	0.1578	0.1507	0.1104	0.9338	0.8202
< 0.15	Excellent		**Mean**		**0.0052**	**0.0803**	**0.0786**	**-0.0327**	**0.1949**	**0.1817**
		Standard Deviation			0.0399	0.0277	0.0267	0.0643	0.0685	0.0667

In addition, to predict how well the correlation between the coupled and uncoupled cases was created, statistical data analysis was performed for each Russell's Comprehensive error factor resulting from the three different weight percentages of the solid keel board. Table 15 shows this statistical study performed for the solid keel board having a 13.5 weight percentage while the rest of the statistical analyses is in Appendix G. As seen in Table 15, it is obvious that the correlation of the vertical velocity response

is much better than that of the athwartship velocity response based on the mean correlations and the percentages of the nodes.

Table 15.   **Statistical Data for Meko-Like Box Model with Solid Keel Board as 13.5 % of Total Model Weight (Coupled and Uncoupled Cases)**

Russell's Comprehensive Error Factor	Vertical Velocity Comparison	Athwartship Velocity Comparison
RC < 0.30	100 %	95 %
RC < 0.28	100 %	91 %
RC < 0.25	100 %	77 %
RC < 0.20	100 %	64 %
RC < 0.18	100 %	59 %
RC < 0.15	95 %	41 %
Mean RC	0.0786	0.1817
Standard Deviation	0.0267	0.0667
Mean + Standard Deviation	0.1053	0.2484
Data within One Standard Deviation	91 %	77 %

Table 16 represents the complete statistical data analysis including all the three different weight percentages to see the whole picture of the correlation process in case of the solid keel board. Overall the correlation results in the athwartship direction were found to be slightly worse than those in the vertical direction. This would indicate that the vertical velocity response developed from the shock simulation of the uncoupled case in fact more accurately captured the range of the motion of the coupled case. The phase error dominates the error correlation more in the athwartship direction than in the vertical direction. One of the other possible contributors to the slightly less correlation in the athwartship direction can be because of the inherently smaller magnitudes found in the velocity response if compared to those in the vertical direction. The mean correlation in the vertical direction was determined to be RC = 0.0978; well within the RC = 0.15 excellent limit. Moreover, the mean correlation in the athwartship direction was determined to be RC = 0.2086; well within the RC = 0.28 acceptable limit. The mean correlation in the athwartship direction represents the worst case in the hull appendage analysis of the meko-like box model. The data within one standard deviation was found to be in 86 % and 82 % of the nodes for the vertical and athwartship velocity comparisons, respectively, meaning the percentages are very close to each other. Although the overall results in the athwartship direction seem to generate a slightly weaker correlation than those in the vertical direction, based on the mean correlation

value and the percentages of the nodes in conjunction with Russell's Comprehensive error factors and the data within one standard deviation in the athwartship direction, the athwartship velocity response also constitutes a desirable correlation between the coupled and uncoupled cases.

Table 16. Complete Statistical Data for Meko-Like Box Model with Solid Keel Board (Coupled and Uncoupled Cases)

Russell's Comprehensive Error Factor	Vertical Velocity Comparison	Athwartship Velocity Comparison
RC < 0.30	100 %	89 %
RC < 0.28	100 %	82 %
RC < 0.25	97 %	68 %
RC < 0.20	97 %	47 %
RC < 0.18	94 %	38 %
RC < 0.15	86 %	26 %
Mean RC	0.0978	0.2086
Standard Deviation	0.0467	0.0668
Mean + Standard Deviation	0.1445	0.2754
Data within One Standard Deviation	86 %	82 %

c. Detailed Velocity Plots

The following velocity comparison plots were conducted to make the comparisons between the no appendage case and the case of solid keel board, which was modeled as coupled and uncoupled structures with respect to the surrounding fluid. These time history plots of the vertical and athwartship velocity responses also help envision Russell's error factor correlations discussed previously. The rest of the complete set of the plots can be found in Appendices D and E. Figure 48 with node 8170 illustrates the time history response of the bow point of the solid keel board on the keel, implying the worst correlation at RC = 0.2790 in the vertical velocity analysis of Russell's error factor comparison. This worst correlation occurs between the coupled and uncoupled cases when the solid keel board was modeled as 1 % of the total structural model weight. As seen in Figure 46, the overall correlation of the vertical velocity analysis is affected by the relatively poor correlations of the solid keel board; node 8170 corresponds to one of these nodes while node 2454 corresponds to the other. Although this is the worst correlation in the vertical direction, the uncoupled case predicts the response of the coupled case sufficiently enough based on the similar phases and the Russell's

Comprehensive error factor found in the acceptable region. Figure 49 with node 5308, which is located at the center to the right side of the structural model on the keel, illustrates how similar the time history response of the solid keel board with the actual weight percentage (13.5 %) between the coupled and uncoupled cases are created based on the best correlation at RC = 0.0387. The phases and the magnitudes of the responses of the coupled and uncoupled cases match perfectly in this case while the response obtained from the uncoupled case produces more oscillation, especially in the early time response. It can be concluded that the responses of node 5308 produce an exceptional correlation between the coupled and uncoupled cases because this node is far from the extremities of the solid keel board. Since, in general, the uncoupled case predicts very well based on the Russell's error factor comparison, the complete set of the time history plots of the vertical velocity response represents that the uncoupled case produces well-behaved time histories, validating this high-quality correlation found in the vertical velocity analysis.

Meko–Like Box Model with Solid Keel Board
Node 8170 at Keel (x=3600 y=-20 z=0)
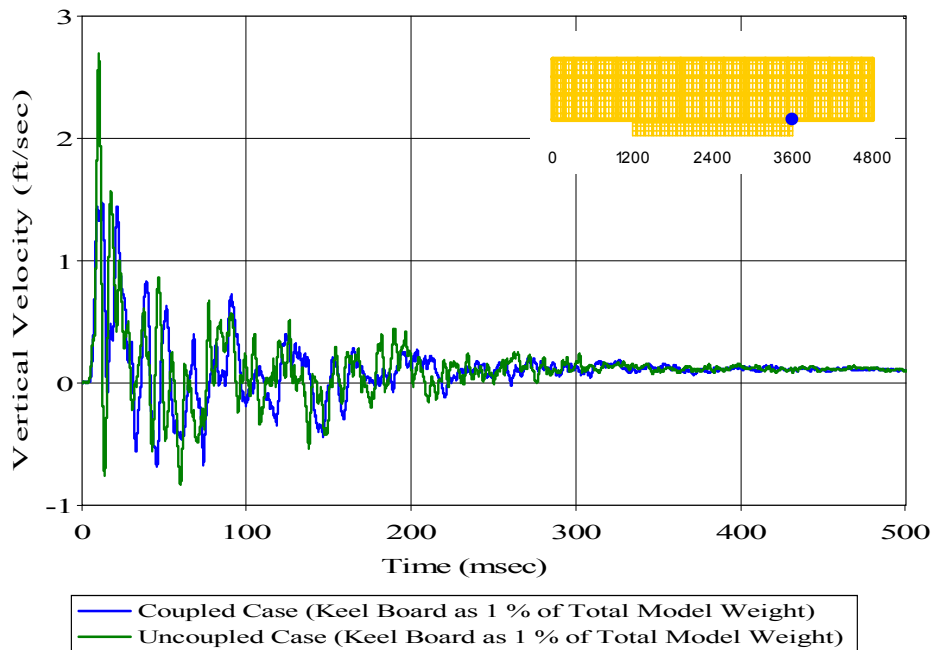
Figure 48.   Node 8170: (RM = 0.0843, RP = 0.3033, RC = 0.2790)
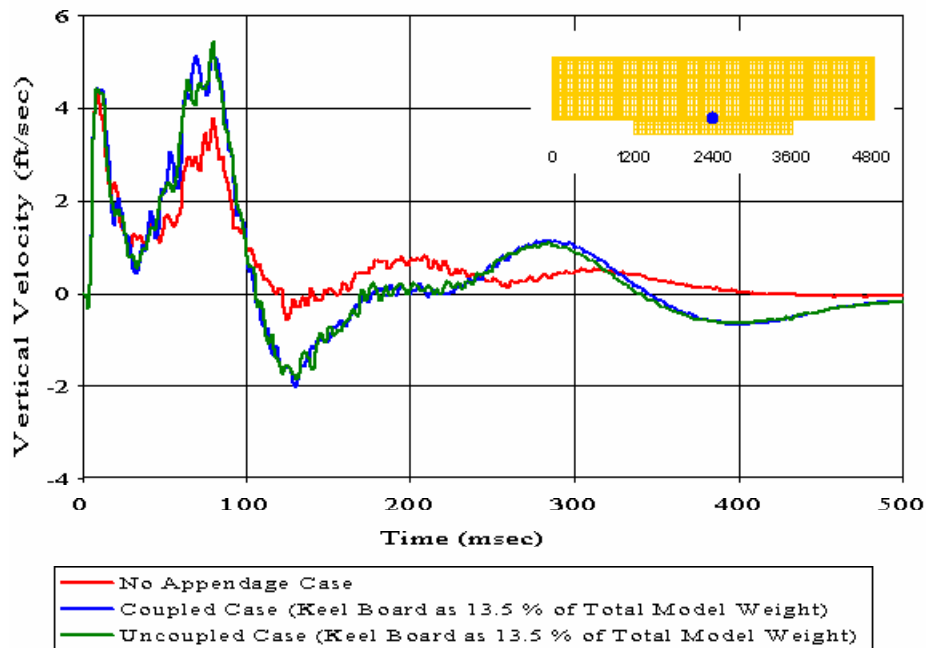
Figure 49.   Keel Node 5308: (RM = -0.0184, RP = 0.0396, RC = 0.0387)

The worst correlation found in the athwartship velocity analysis takes place at node 3883 with a Russell's Comprehensive error factor of 0.3396. In the case of the solid keel board that was modeled as 1 % of the total model weight, this correlation is created. This node is not located at the extremities of the solid keel board but close to them. As seen in Figure 50, the phases do not match along the overall response. This explains that the large phase error found in this correlation drives the Russell's Comprehensive error factor higher. This correlation along with the other bad correlations found at the extremities of the solid keel board affect the overall correlation results in the athwartship direction. Furthermore, Figure 51 with node 148 demonstrates the best correlation at RC = 0.0914 in the athwartship direction with respect to the overall correlations in Table 16. The uncoupled case anticipates the dynamic response of the coupled case, which represents the real case in an UNDEX event, well enough particularly in the early time response. This correlation occurs in the case of the solid keel board modeled as 13.5 % of the total model weight. Since the best correlations occur between the coupled and uncoupled cases when the solid keel board has been modeled as

88

13.5 % of the total model weight, by examining the Russell's error factor comparison and the complete time history plots, it can be concluded that the uncoupled case of the actual weight percentage predicts the coupled case well in both vertical and athwartship directions relative to the other cases in this analysis.
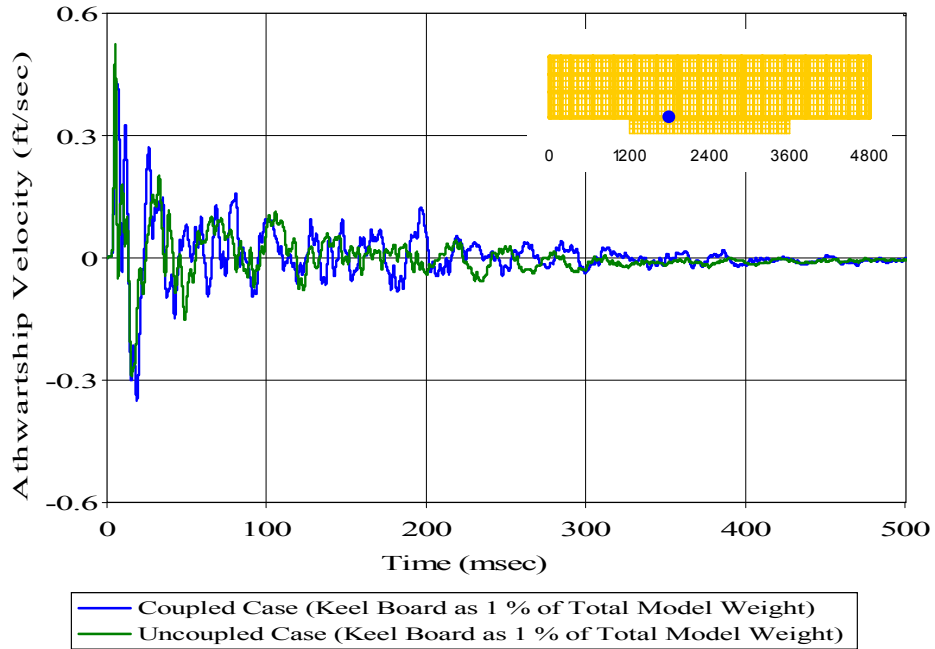
Figure 50.   **Keel Node 3883: (RM = -0.1200, RP = 0.3639, RC = 0.3396)**

Meko-Like Box Model with Solid Keel Board

Node 148 at Bulkhead (x=0 y=-20 z=160)
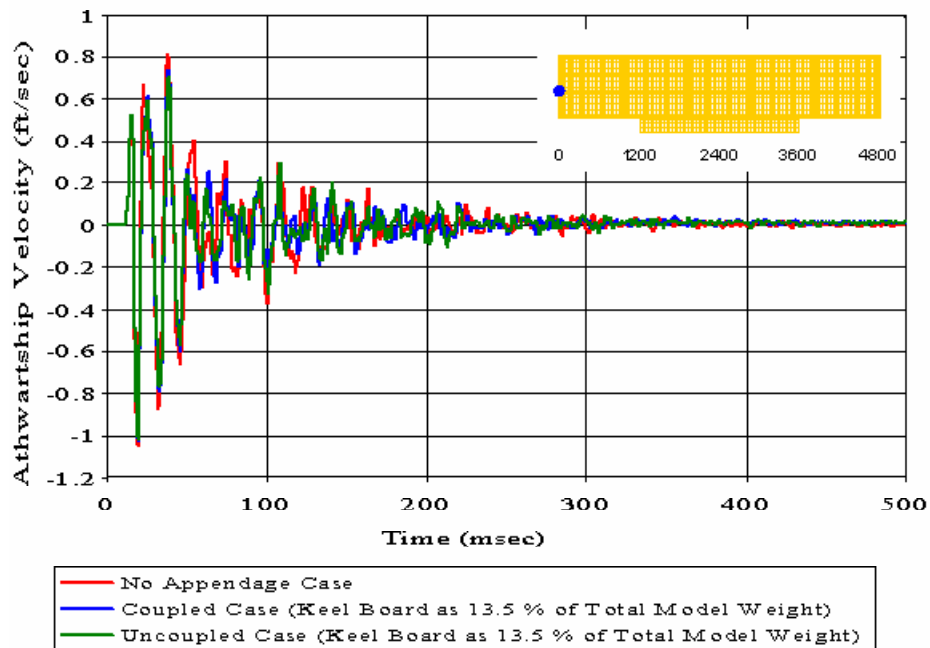
Figure 51.   Bulkhead Node 148: (RM = -0.0143, RP = 0.1022, RC = 0.0914)

Figures 52 and 53 with nodes 5313 and 2454, respectively, represent the worst correlations in the vertical and athwartship directions, respectively, found in the case of the solid keel board modeled as 13.5 % of the total structural weight. Node 5313 produces the Russell's Comprehensive error factor of 0.1590 while node 2454 generates 0.3062.

Meko–Like Box Model with Solid Keel Board
Node 5313 at Keel (x=2400 y=20 z=0)
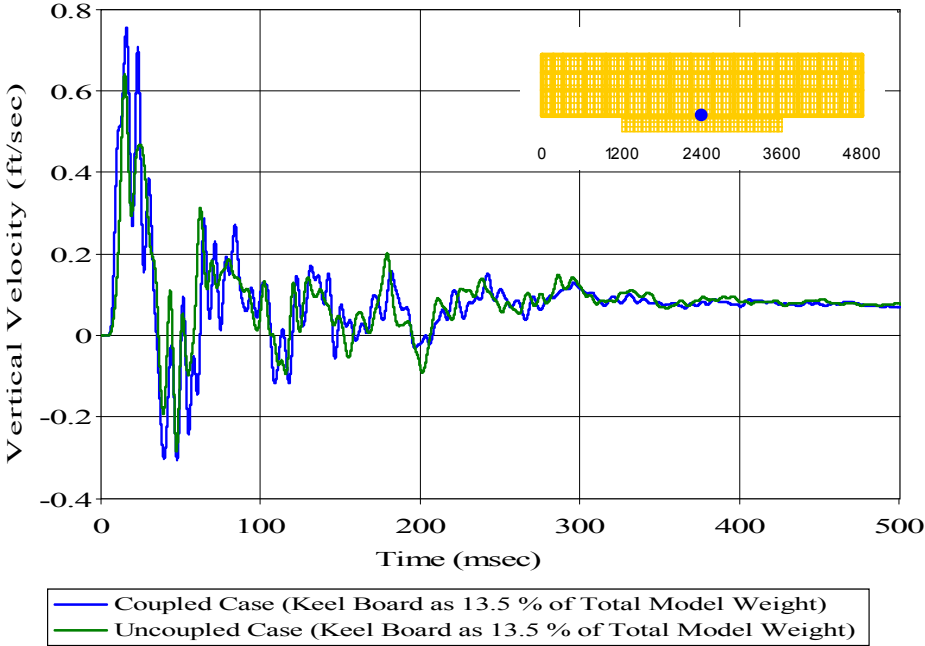
Figure 52. Keel Node 5313: (RM = -0.0900, RP = 0.1552, RC = 0.1590)

Meko–Like Box Model with Solid Keel Board
Node 2454 at Keel (x=1200 y=-20 z=0)
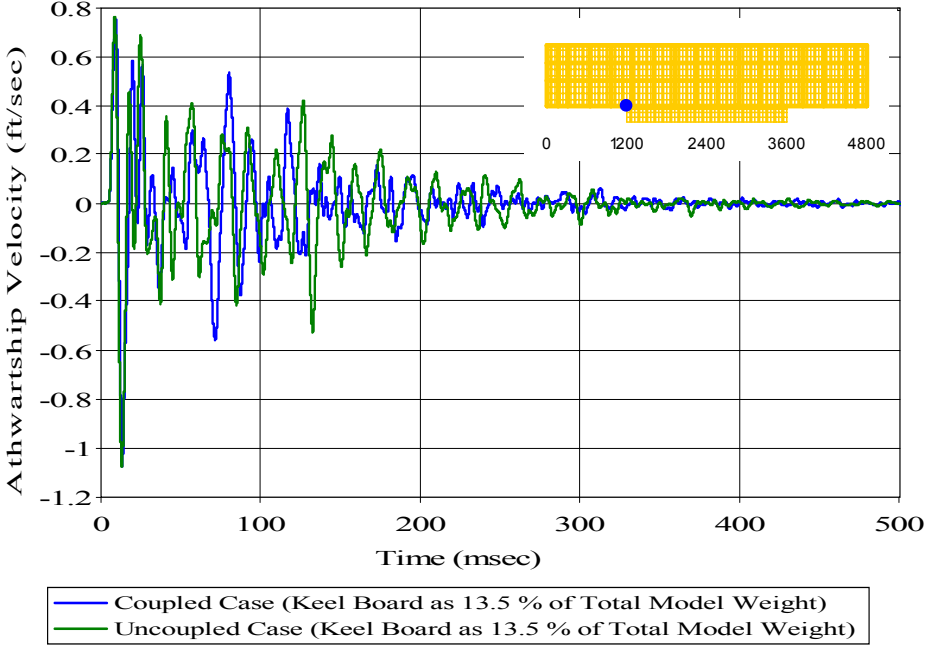
Figure 53. Keel Node 2454: (RM = 0.0477, RP = 0.3422, RC = 0.3062)

d.   *Shock Spectra Plots*

Evaluating the data in the frequency domain allows for a different perspective about the physical behavior of an UNDEX attack in both coupled and uncoupled cases. To look into the differences between coupled and uncoupled cases, shock spectra plots of 10 nodes located throughout the structure will be evaluated in the vertical and athwartship directions in this case. The nodes investigated cover the best and worst correlations based on the Russell's Comprehensive error factors found in the case of the solid keel board having 13.5 % of the total model weight. The case of the actual weight percentage will be examined in this shock spectra analysis only.

Figures 54, 55, 56 and 57 are representative of the shock spectra plots resulting from the vertical and athwartship velocity analyses of the meko-like box model with solid keel board and are provided as samples of the complete set of shock spectra plots found in Appendix E. Figures 54 and 55 with nodes 5313 and 5308 represent the worst and best correlations, respectively, occurring in the vertical direction while Figures 56 and 57 of 2454 and 148, respectively, stand for the worst and best correlations, likewise, in the athwartship direction. The shock spectra plots of the best correlations produce more matched results between the coupled and uncoupled cases than those of the worst correlations in the frequency domain. If all of the shock spectra plots are evaluated in terms of the magnitudes of the vertical and athwartship motions, the majority of all the data presented in both vertical and athwartship shock spectra plots is below 5 ft/sec in magnitude of velocity. However, some peak values obtained from the vertical velocity analysis are between 10 and 12 ft/sec and some of those resulting from the athwartship velocity analysis give up to 20 ft/sec.
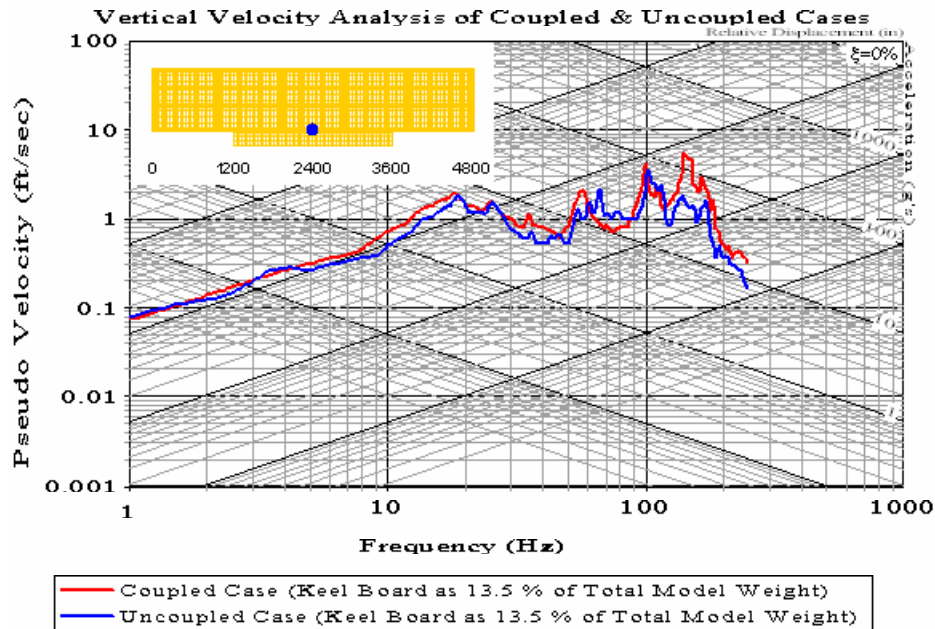
Figure 54. Shock Spectra Plot: Keel Node 5313
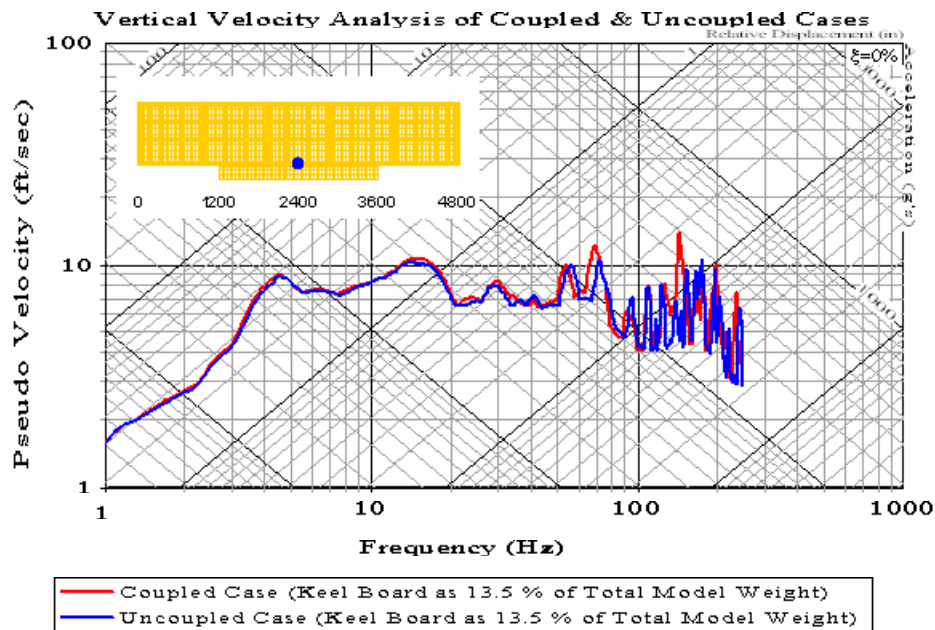
Figure 55. Shock Spectra Plot: Keel Node 5308
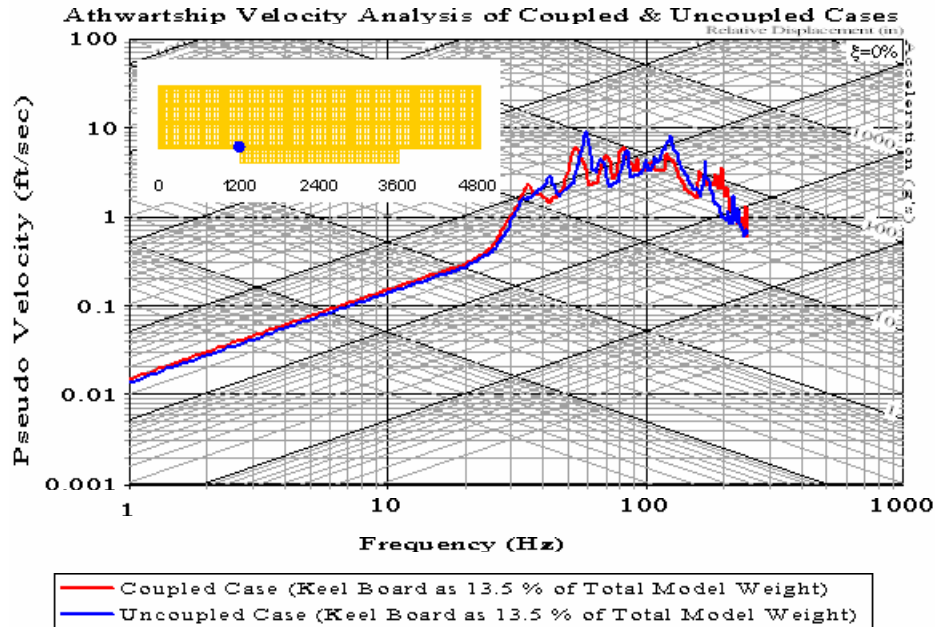
Figure 56.   Shock Spectra Plot: Keel Node 2454
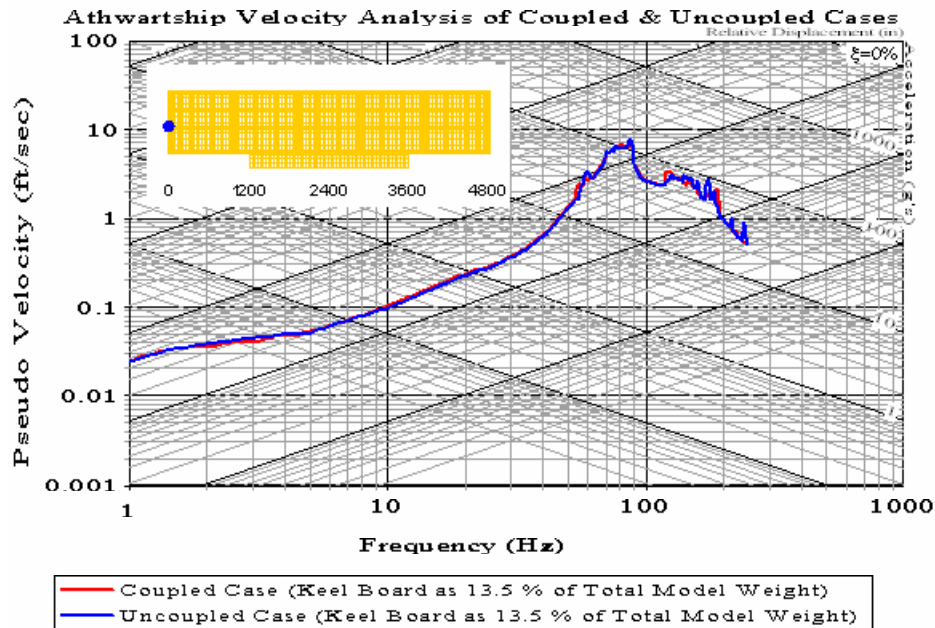
Figure 57.   Shock Spectra Plot: Bulkhead Node 148

The uncoupled case has predicted the response of the coupled case exceptionally well in the 1 to 50 Hz range for both vertical and athwartship velocity analyses; there is almost no difference between the two curves of coupled and uncoupled cases in this range. Furthermore, in the range between 50 and 100 Hz, the predicted results obtained from the uncoupled case also produces very accurate responses in both directions by generating small differences between the two curves. Most of the vertical shock spectra plots display a gradual rise in amplitude up to 20 Hz as the frequency increases while almost all of the athwartship shock spectra plots exhibit a gradual rise with oscillation up to the 70 to 100 Hz range. The peak values occur between 100 and 250 Hz along with relatively more oscillations, and then there is a downward trend in both vertical and athwartship velocity analyses. These peak values tend to be formed from spikes between 100 and 120 Hz. Above 100 Hz, the responses in the vertical and athwartship directions fluctuates much more but the downward trend is prevailing. It can be shown that the uncoupled case slightly under predicts the high frequency responses mainly from 100 Hz upwards. Nevertheless, the two curves still remain very close based on the log-log scale. The upper limit of the frequency for all of these shock spectra plots was set at 250 Hz since the data obtained from the shock simulations was made low-pass filtered. Table 17 summarizes the shock spectra analysis in the case of solid keel board according to the frequency range.

Table 17.   Summary of Shock Spectra Analysis for Meko-Like Box Model with Solid Keel Board

Frequency Range	Trend of Curves	Vertical Velocity Analysis	Ayhwartship Velocity Analysis
1 to 20 Hz	Gradual rise	Uncoupled case closely matches coupled case	Uncoupled case closely matches coupled case
20 to 50 Hz	Oscillation and decrease in vertical direction, gradual rise in athwartship direction	Uncoupled case closely matches coupled case	Uncoupled case closely matches coupled case
50 to 100 Hz	Oscillation near the values of 2 to 10 ft/sec in vertical direction, gradual rise with oscillation up to 10 ft/sec in athwartship direction	Uncoupled case closely matches or barely under predicts coupled case	Uncoupled case closely matches or barely under predicts coupled case
100 to 250 Hz	High degree of oscillation and peak values occur (10 to 12 ft/sec in vertical direction, up to 20 ft/sec in athwartship direction)	Uncoupled case closely matches or slightly under predicts coupled case	Uncoupled case closely matches or slightly under predicts coupled case

2. Meko-Like Box Model with Shell Keel Board

The hull appendage shell keel board was built using shell elements as its construction process was described previously. The shell keel board was modeled as coupled and uncoupled structures with respect to the surrounding fluid as in the case of the solid keel board. A detailed study will be presented on the validity of including shell keel board, the proposed coupling scheme for this shell keel board by utilizing the time history and shock spectra plots of the vertical and athwartship velocity response comparisons and Russell's error factor analysis. Table 18 lists the 22 selected nodes, which were decided upon by selecting them right through the interface between the hull and the shell keel board in addition to the decks above this interface, and their locations on the structural model along with their ID numbers to be evaluated in this series of comparisons and analysis.

**Table 18.   Vertical and Athwartship Velocity Response Node Locations
(Meko-Like Box Model with Shell Keel Board)**

NODE	X (in)	Y (in)	Z (in)	Location
15	0	-20	0	Bulkhead
148	0	-20	160	Bulkhead
268	0	-20	280	Bulkhead
388	0	-20	400	Bulkhead
2454	1200	-20	0	Keel
2648	1200	-20	160	First Deck
2820	1200	-20	280	Second Deck
2970	1200	-20	400	Top Deck
3883	1800	-20	0	Keel
5251	2400	-300	0	Keel
5308	2400	-180	0	Keel
5310	2400	-100	0	Keel
5312	2400	-20	0	Keel
5313	2400	20	0	Keel
5315	2400	100	0	Keel
5317	2400	180	0	Keel
5320	2400	300	0	Keel
6741	3000	-20	0	Keel
8170	3600	-20	0	Keel
8364	3600	-20	160	First Deck
8536	3600	-20	280	Second Deck
8686	3600	-20	400	Top Deck

a.　　　*Error Comparison*

Contrary to the vertical velocity analysis in the case of solid keel board, the data distribution throughout the structure has a relatively less accuracy and precision associated with it. As seen in Figure 58, most of the vertical velocity response values are distributed as a tight group, with the values very close to each other, in the excellent region, while the rest are more scattered through the acceptable and poor regions. There are only four error values out of 22 falling into the poor region at all. At this time, the magnitude error also drives the Russell's Comprehensive error factor higher for the scattered points as much as the phase error. Figure 61 with node 2454, which had the worst correlation at RC = 0.4189, shows the difference of both curves in magnitude as well as in phase. The error in magnitude and phase are, RM = 0.3018, RP = 0.3638, respectively. The best correlation at RC = 0.0936, whose time history will be illustrated in Figure 62 with node 5308, explains how similar the two curves developed from the coupled and uncoupled cases are in magnitude and in phase. In this case, the error in magnitude and phase are, RM = 0.0772, RP = 0.0722, respectively. Table 19 provides a complete description of the error factors for the meko-like box model with shell keel board.
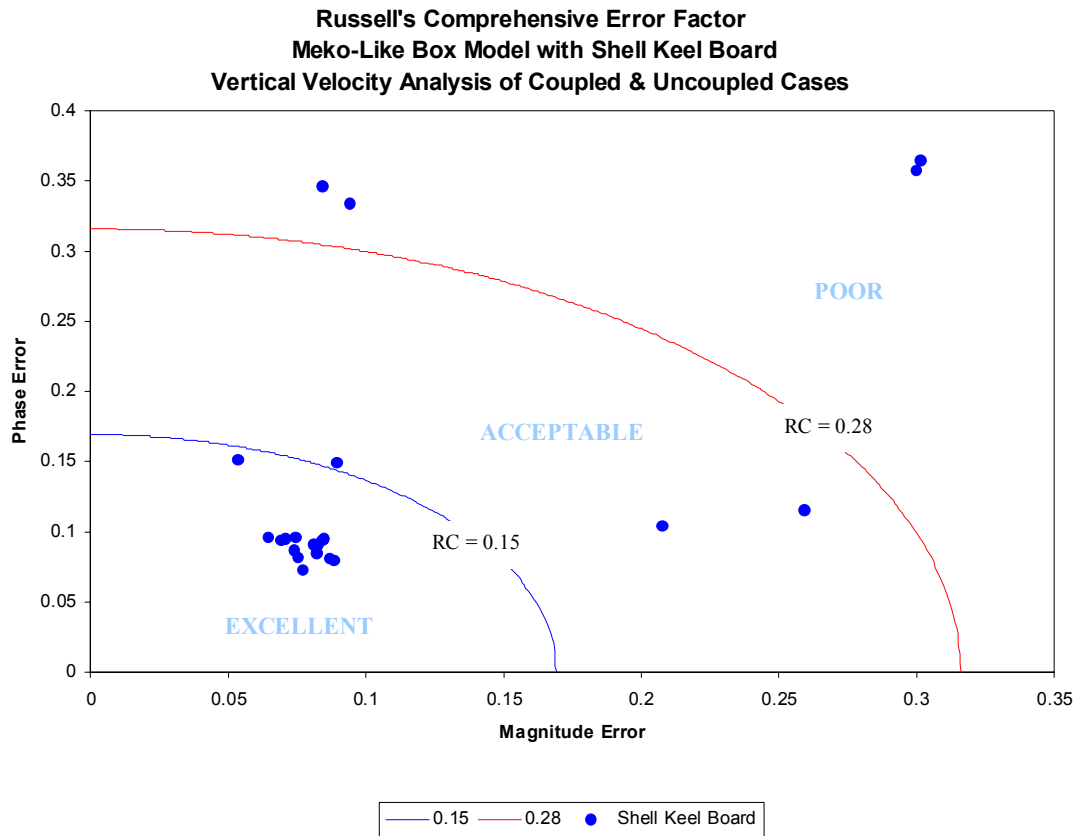
Figure 58. **Russell's Error Factor Comparison for Meko-Like Box Model with Shell Keel Board (Vertical Velocity)**

The Russell's error factor comparison for the athwartship velocity analysis produces an exceptional correlation between the coupled and uncoupled cases. As seen in Figure 59, all of the error values fall into the excellent region. The magnitude error as well as the phase error is consistently low throughout the data set. Therefore, the data set in this athwartship velocity analysis essentially constitutes an extremely desirable correlation. Even the worst correlation at RC = 0.1449, whose time history plot will be seen in Figure 63 with node 5251, is within the excellent range. The overall superior correlation in the athwartship direction indicates that the athwartship velocity response resulting from the uncoupled case produces very accurate results, and predicts the coupled case very well.

Russell's Comprehensive Error Factor
Meko-Like Box Model with Shell Keel Board
Athwartship Velocity Analysis of Coupled & Uncoupled Cases
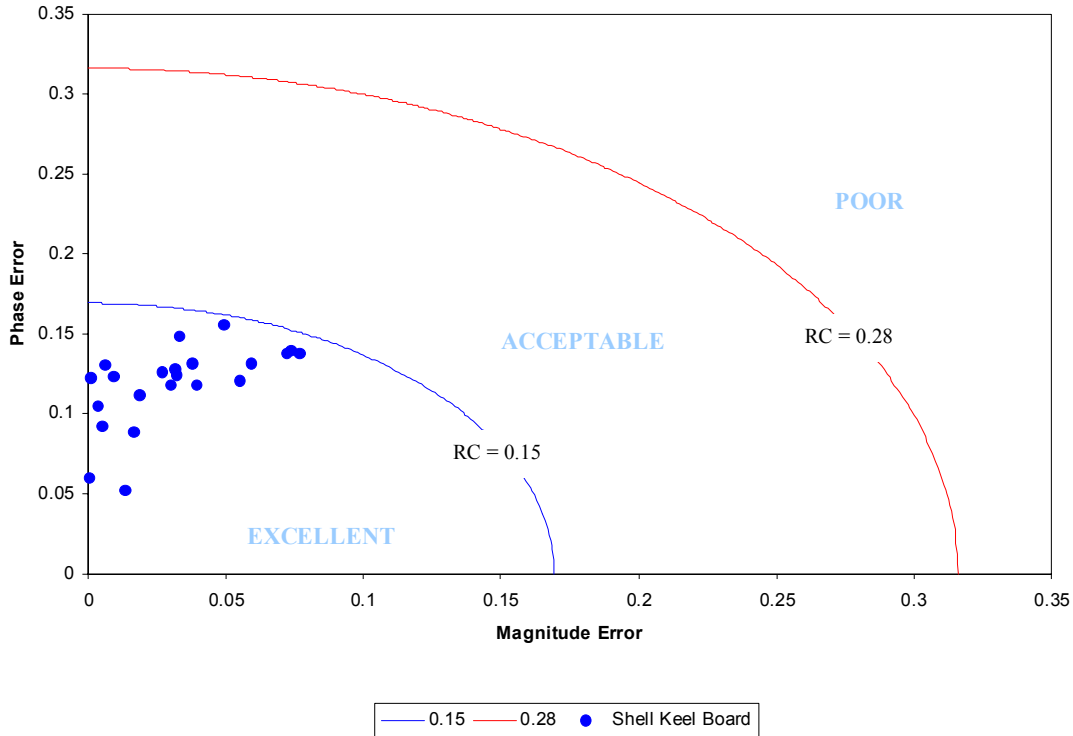
Figure 59.   Russell's Error Factor Comparison for Meko-Like Box Model with Shell Keel Board (Athwartship Velocity)

Table 19.   Russell's Error Factors for Meko-Like Box Model with Shell Keel Board

Simulation runtime = 500 msec					Meko-Like Box Model with Shell Keel Board					
					Vertical Velocity Comparison			Athwartship Velocity Comparison		
NODE	X (in)	Y (in)	Z (in)	Location	COUPLED & UNCOUPLED CASES			COUPLED & UNCOUPLED CASES		
					LS-DYNA/USA DATA (<250HZ)			LS-DYNA/USA DATA (<250HZ)		
					RM	RP	RC	RM	RP	RC
15	0	-20	0	Bulkhead	0.0644	0.0962	0.1026	0.0038	0.1044	0.0926
148	0	-20	160	Bulkhead	0.0756	0.0813	0.0984	0.0165	0.0880	0.0793
268	0	-20	280	Bulkhead	0.0739	0.0865	0.1008	-0.0052	0.0922	0.0819
388	0	-20	400	Bulkhead	0.0709	0.0949	0.1050	-0.0186	0.1118	0.1005
2454	1200	-20	0	Keel	0.3018	0.3638	0.4189	0.0741	0.1392	0.1398
2648	1200	-20	160	First Deck	0.0872	0.0807	0.1053	0.0332	0.1485	0.1349
2820	1200	-20	280	Second Deck	0.0829	0.0908	0.1089	0.0396	0.1182	0.1105
2970	1200	-20	400	Top Deck	0.0814	0.0908	0.1081	0.0008	0.1225	0.1086
3883	1800	-20	0	Keel	0.0942	0.3332	0.3069	0.0723	0.1371	0.1374

99

Simulation runtime = 500 msec					Meko-Like Box Model with Shell Keel Board					
					Vertical Velocity Comparison			Athwartship Velocity Comparison		
NODE	X (in)	Y (in)	Z (in)	Location	COUPLED & UNCOUPLED CASES			COUPLED & UNCOUPLED CASES		
					LS-DYNA/USA DATA (<250HZ)			LS-DYNA/USA DATA (<250HZ)		
					RM	RP	RC	RM	RP	RC
5251	2400	-300	0	Keel	0.0536	0.1511	0.1421	0.0494	0.1558	0.1449
5308	2400	-180	0	Keel	0.0772	0.0722	0.0936	0.0378	0.1310	0.1208
5310	2400	-100	0	Keel	0.0821	0.0846	0.1045	0.0325	0.1243	0.1138
5312	2400	-20	0	Keel	0.0693	0.0939	0.1034	0.0006	0.0601	0.0533
5313	2400	20	0	Keel	0.0744	0.0960	0.1076	0.0134	0.0520	0.0476
5315	2400	100	0	Keel	0.2594	0.1150	0.2515	0.0272	0.1255	0.1138
5317	2400	180	0	Keel	0.2080	0.1038	0.2061	0.0094	0.1230	0.1093
5320	2400	300	0	Keel	0.0894	0.1486	0.1537	0.0065	0.1302	0.1156
6741	3000	-20	0	Keel	0.0844	0.3460	0.3156	0.0594	0.1314	0.1278
8170	3600	-20	0	Keel	0.3000	0.3571	0.4134	0.0770	0.1372	0.1395
8364	3600	-20	160	First Deck	0.0886	0.0797	0.1056	0.0317	0.1279	0.1167
8536	3600	-20	280	Second Deck	0.0846	0.0934	0.1117	0.0553	0.1201	0.1171
8686	3600	-20	400	Top Deck	0.0849	0.0946	0.1126	0.0301	0.1180	0.1079
Russell Error Correlation				Sum(E(X))	2.4882	3.1542	3.6763	0.6468	2.5984	2.4136
> 0.28		Poor		Sum(E(X^2))	0.4052	0.6693	0.8440	0.0345	0.3207	0.2790
< 0.15		Excellent		**Mean**	**0.1131**	**0.1434**	**0.1671**	**0.0294**	**0.1181**	**0.1097**
				Standard Deviation	0.0768	0.1017	0.1046	0.0271	0.0256	0.0260

Table 20 represents the complete statistical data analysis performed for the correlation process in the case of the shell keel board. In general, the results in the athwartship direction were found to be more accurate than those in the vertical direction. In contrast to the case of the solid keel board, this would indicate that the athwartship velocity response resulting from the shock simulation of the uncoupled case indeed more accurately caught the range of the dynamic response of the coupled case. It can be said that the magnitude error in the vertical velocity analysis caused Russell's Comprehensive error factors to be more spread in some cases as well as the contribution of the phase error. The mean correlation in the vertical direction was determined to be RC = 0.1671; well within the RC = 0.28 acceptable limit. In addition, the mean correlation in the athwartship direction was determined to be RC = 0.1097; well within the RC = 0.15 excellent limit. Based on the statistical data analysis of Russell's Comprehensive error factors presented in Table 20, 100% of the nodes have a RC ≤ 0.15 in the athwartship velocity comparison while 82 % of the nodes have a RC ≤ 0.28 in the athwartship velocity comparison. However, the data within one standard deviation was found to be in

82 % of the nodes for both vertical and athwartship velocity comparisons. Based on the mean correlation value and the percentages of the nodes associated with Russell's Comprehensive error factors and the data within one standard deviation, the results throughout the meko-like box model in the vertical direction also seem to be accurately generating an attractive correlation between the coupled and uncoupled cases in so far as those in the athwartship direction are concerned.

Table 20.   Statistical Data for Meko-Like Box Model with Shell Keel Board (Coupled and Uncoupled Cases)

Russell's Comprehensive Error Factor	Vertical Velocity Comparison	Athwartship Velocity Comparison
RC < 0.30	82 %	100 %
RC < 0.28	82 %	100 %
RC < 0.25	77 %	100 %
RC < 0.20	73 %	100 %
RC < 0.18	73 %	100 %
RC < 0.15	68 %	100 %
Mean RC	0.1671	0.1097
Standard Deviation	0.1046	0.0260
Mean + Standard Deviation	0.2717	0.1357
Data within One Standard Deviation	82 %	82 %

The weakest correlations in the vertical and athwartship directions (except node 5251 in the athwartship direction) throughout the structure occur for the two nodes, 8170 and 2454 located at the bow and stern of the interface, respectively, between the hull and shell keel board. These correlations at the extremities of the shell keel board are inline with the results obtained from the vertical and athwartship velocity analyses. This indicates that there is a direct correlation between the longitudinal position of a node within the finite element model and the accuracy of the data of the uncoupled case when compared to the corresponding data of the coupled case. As seen in Figure 60, the bow and stern sides of the shell keel board consistently showed poor correlation between the coupled and uncoupled cases for both vertical and athwartship velocity responses.
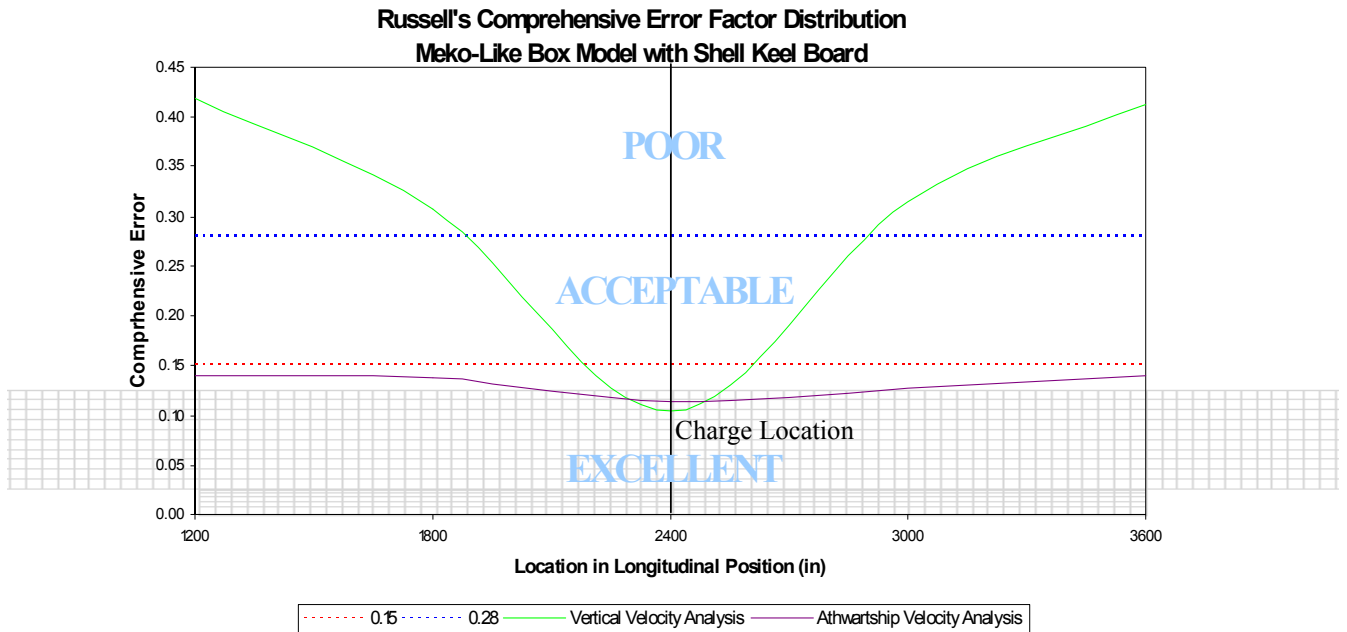
Figure 60. Russell's Comprehensive Error as a Function of Position (Shell Keel Board)

b. *Detailed Velocity Plots*

The following velocity comparison plots were conducted to make the comparison for the shell keel board, which was modeled as coupled and uncoupled structures with respect to the surrounding fluid, and to help visualize Russell's error factor correlations discussed before. In addition, the effects due to the inclusion of the shell keel board were examined herein. The vertical and athwartship velocity time history plots were used for the comparison. The rest of the vertical and athwartship velocity time history plots can be found in Appendices D and E, respectively. Figure 61 with node 2454 shows the time history response of the stern point of the shell keel board on the keel, implying the worst correlation at RC = 0.4189 in the vertical velocity analysis of Russell's error factor comparison. It is obvious that the curves of the coupled and uncoupled cases significantly differ from each other in magnitude and phase.

Meko-Like Box Model with Shell Keel Board
Node 2454 at Keel (x=1200 y=-20 z=0)
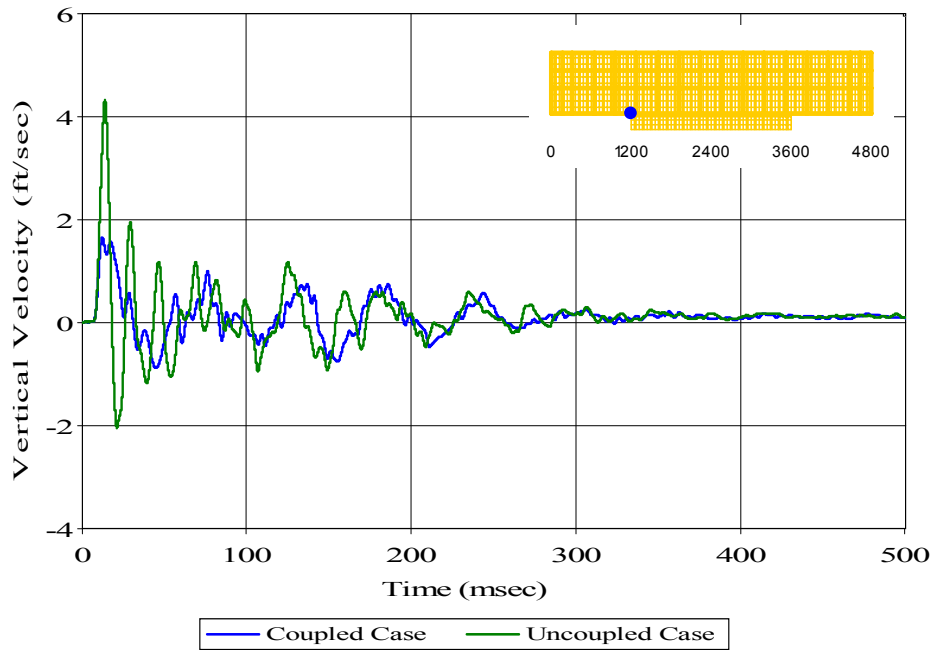
Figure 61.   Keel Node 2454: (RM = 0.3018, RP = 0.3638, RC = 0.4189)

Meko-Like Box Model with Shell Keel Board
Node 5308 at Keel (x=2400 y=-180 z=0)
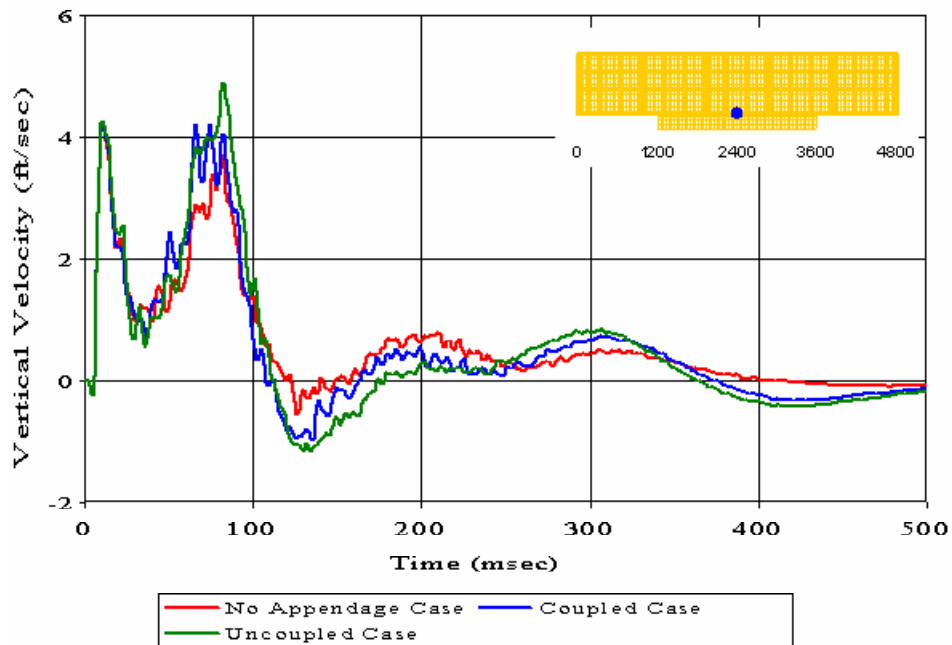
Figure 62.   Keel Node 5308: (RM = 0.0772, RP = 0.0722, RC = 0.0936)

103

As seen in Figure 58, the overall correlation of the vertical velocity analysis is affected by the poor correlations at the extremities of the shell keel board; node 2454 corresponds to one of these nodes. In addition, if the overall results obtained from the other nodes located close to the shell keel board are examined, it can be seen that there are relatively large discrepancies between the no appendage case and the case of the shell keel board. However, Figure 62 with node 5308, which is located at the center to the right side of the structural model on the keel, illustrates how similar the time history response of the coupled and uncoupled cases are generated based on the best correlation at RC = 0.0936. The phases of the coupled and uncoupled cases match almost perfectly while there are relatively large differences in the magnitudes of the vertical velocity response. It can be concluded that the responses of node 5308 produce a very good correlation between the coupled and uncoupled cases because this node is far from the extremities of the shell keel board. In addition, if the curves of the coupled and uncoupled cases are contrasted to the no appendage case, the same kind of relationship takes place based on the similarities and differences of the phase and response values, respectively.

In the athwartship direction, the worst correlation occurs on node 5251 along with Russell's Comprehensive error factor of 0.1449. Even though this node is located away from the end points of the shell keel board, it is the closest node on the structure to the charge location. Therefore, its location on the structure can be considered as one reason for this correlation. However, this correlation falls into the excellent range of Russell's error factor comparison as stated and seen previously. If Figure 63 is examined carefully, notice that, although there are small dissimilarities in the phases, the magnitudes of the responses of the coupled and uncoupled cases are very similar to each other not only in the early time response but also in the late time response. Hence, even in the worst case in the athwartship direction, the uncoupled case predicts the dynamic response of the coupled case sufficiently. Furthermore, Figure 64 demonstrates the best correlation at RC = 0.0476 in the athwartship direction with respect to the overall correlations in Table 20. The uncoupled case anticipates the dynamic response of the coupled case, which represents the real case in an UNDEX event, exceptionally. The early time and late time responses show that the peak responses of the coupled case in

addition to the phases are captured very well. Additionally, the inclusion of the shell keel board does not affect the athwartship velocity responses as much as the vertical velocity responses if the complete time history plots are examined. As stated in the case of the solid keel board, examining the overall response of the structural model, the inclusion of the shell keel board creates differences on the dynamic response of the system due to the relatively large exposed surface area, which is 20.5 % of the underwater surface area of the structural model, especially in the vertical direction.
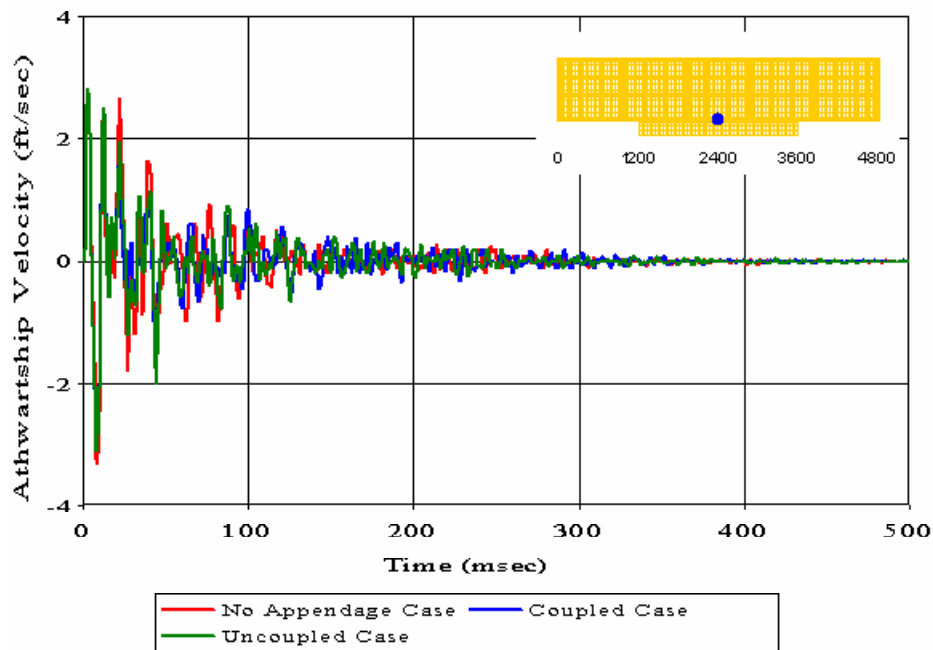
Figure 63.   Keel Node 5251: (RM = 0.0494, RP = 0.1558, RC = 0.1449)

Meko–Like Box Model with Shell Keel Board

Node 5313 at Keel (x=2400 y=20 z=0)
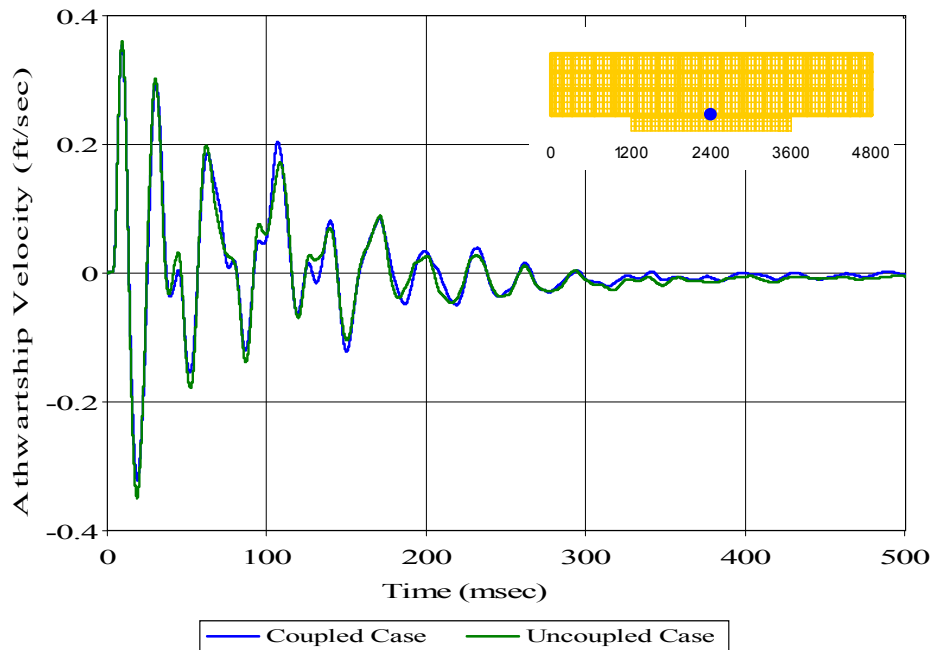
Figure 64. **Keel Node 5313: (RM = 0.0134, RP = 0.0520, RC = 0.0476)**

c. *Shock Spectra Plots*

As previously stated in the case of solid keel board, examining the data in the frequency domain provides a different perspective of the physical behavior of an UNDEX attack in both coupled and uncoupled cases. In this case, to study the differences between coupled and uncoupled cases, shock spectra plots of 11 nodes located throughout the structure will be evaluated in the vertical and athwartship directions. The nodes investigated include the best and worst correlations according to the Russell's Comprehensive error factors found in the case of the shell keel board.

The following figures are representative of the shock spectra plots resulting from the vertical and athwartship velocity analyses of the meko-like box model with shell keel board and are obtained as samples of the entire set of shock spectra plots found in Appendix F. Figures 65 and 66 with nodes 2454 and 5308, respectively, represent the worst and best correlations, respectively, occurring in the vertical direction while Figures 67 and 68 of 5251 and 5313, respectively, stand for the worst and best correlations, respectively, in the athwartship direction.

106
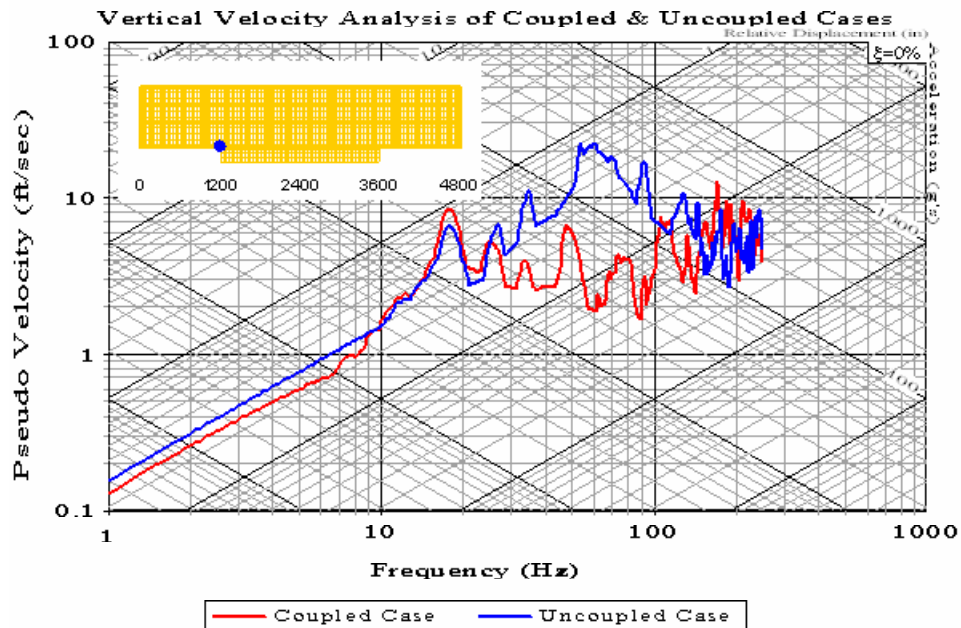
Figure 65. Shock Spectra Plot: Keel Node 2454
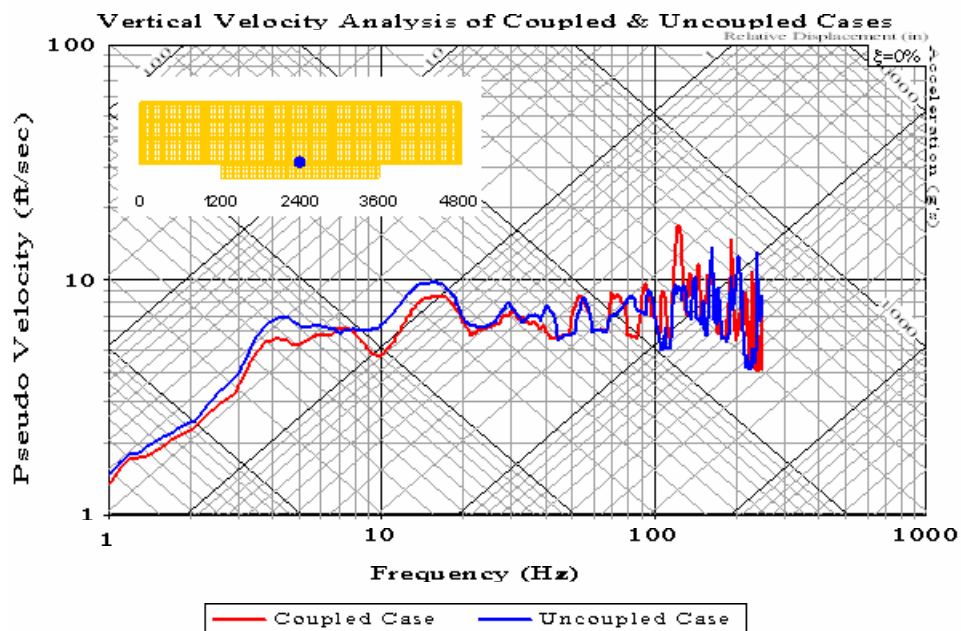
Figure 66. Shock Spectra Plot: Keel Node 5308

107
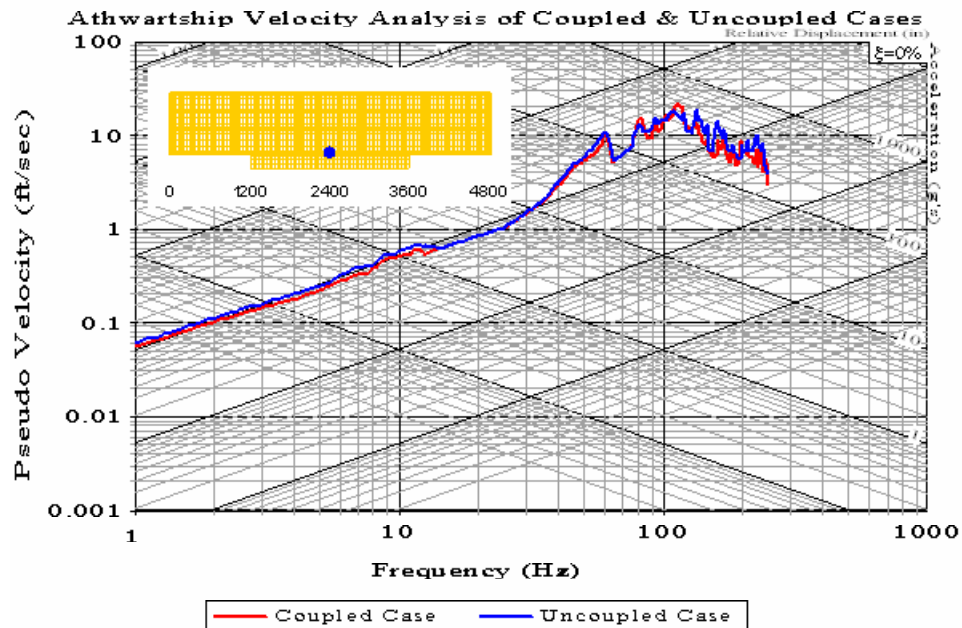
Figure 67. **Shock Spectra Plot: Keel Node 5251**
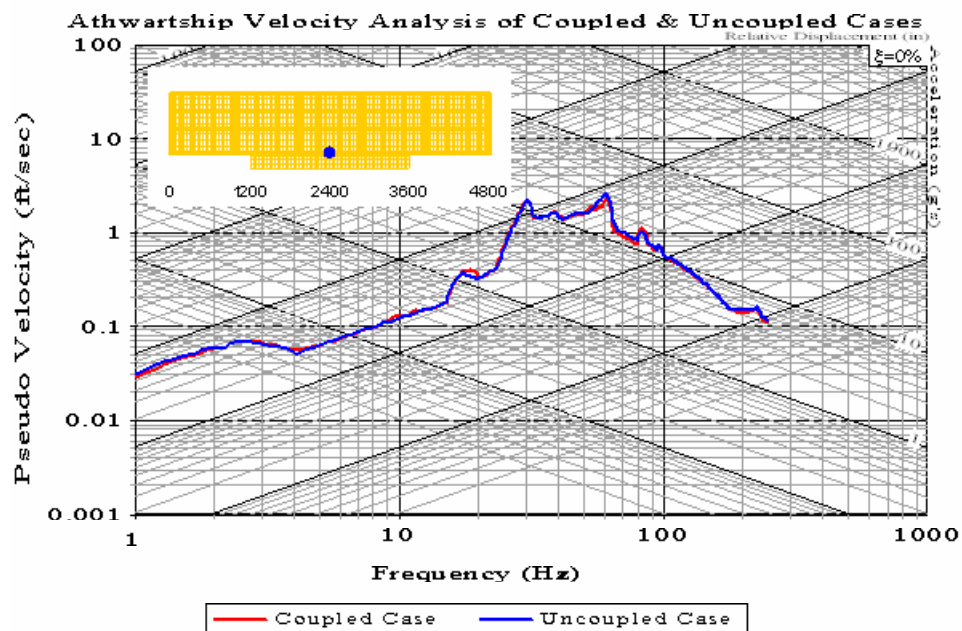
Figure 68. **Shock Spectra Plot: Keel Node 5313**

108

As observed in these figures, the shock spectra plots of the best correlations imply more harmonized results between the coupled and uncoupled cases than those of the worst correlations. Most of the data presented in both vertical and athwartship shock spectra plots is below 6 ft/sec based on all of the shock spectra plots evaluated in terms of the magnitudes of the vertical and athwartship motions. Although, some of the peak values obtained from both analyses turn out to be 20 ft/sec while most of them are slightly below or above 10 ft/sec.

According to all of the shock spectra plots including the plots in Appendix F, the uncoupled case has predicted the response of the coupled case well enough in the 1 to 50 Hz range for both vertical and athwartship velocity analyses; obviously, there are small differences between the two curves of coupled and uncoupled cases in this range. Moreover, the shock spectra plots of the athwartship velocity analysis anticipate an almost perfect correlation between the coupled and uncoupled cases throughout the frequency domain. This situation corresponds to the excellent correlation found in the Russell's error factor comparison discussed earlier. However, in the range between 50 and 100 Hz, the predicted results obtained from the uncoupled case tend to differ from the coupled case in the vertical direction by generating large discrepancies between the two curves. Although this situation improves slightly between 100 and 250 Hz, the curves pursue the same kind of pattern in the vertical velocity analysis.

Most of the vertical shock spectra plots display a gradual rise in amplitude up to almost 18 Hz along with some oscillations through 20 Hz as the frequency increases while almost all of the athwartship shock spectra plots exhibit a gradual rise with oscillation up to the 60 to 70 Hz range. While some peak values occur between 100 and 250 Hz along with relatively more oscillations, some occur between 50 and 100 Hz in both vertical and athwartship velocity analyses. When these peak values take place in these ranges, there is a high degree of oscillation near the peak values or a downward trend through the end of the frequency domain. Above 100 Hz, the responses in the vertical and athwartship directions tend to fluctuate much more. Note that the uncoupled case noticeably over predicts the high frequency responses mainly from 50 Hz upwards in the vertical direction while it barely over predicts the high frequency responses from 100 upwards in the athwartship direction. As usual, the upper limit of the frequency for

all of these shock spectra plots was set at 250 Hz. Table 21 summarizes the shock spectra analysis in the case of shell keel board according to the frequency range.

Table 21. **Summary of Shock Spectra Analysis for Meko-Like Box Model with Shell Keel Board**

Frequency Range	Trend of Curves	Vertical Velocity Analysis	Ayhwartship Velocity Analysis
1 to 20 Hz	Gradual rise up to 18 Hz in the vertical direction	Uncoupled case closely matches or slightly over predicts coupled case	Uncoupled case closely matches coupled case
20 to 50 Hz	Small oscillations in vertical direction, gradual rise in athwartship direction	Uncoupled case closely matches or over predicts coupled case in general	Uncoupled case closely matches coupled case
50 to 100 Hz	Peak values occur with oscillation up to 20 ft/sec in vertical direction, gradual rise up to peak value of 10 ft/sec with very small oscillations or downward trend in athwartship direction	Uncoupled case matches or noticeably over predicts coupled case	Uncoupled case closely matches coupled case
100 to 250 Hz	High degree of oscillation and peak values occur (up to 18 ft/sec in vertical direction, 20 ft/sec in athwartship direction)	Uncoupled case matches or noticeably over predicts coupled case	Uncoupled case closely matches or slightly over predicts coupled case

3. Meko-Like Box Model with Open Keel Board

The open keel board, which is another modification of the meko-like box model, was created using solid elements to simulate the shafts of a meko-class ship. Based on the total surface area of both shafts exposed to the UNDEX, the rectangular cross-section area of the brick element is supposed to simulate the circular cross-section area of an actual shaft. The open keel board, which was modeled as coupled and uncoupled structures in conjunction with the surrounding fluid, can be considered as the solid keel board with a big hole where the material has been removed. The analysis for the open keel board will cover the validity of including open keel board, the planned coupling proposal for this open keel board by using the time history and shock spectra plots of the vertical and athwartship velocity response comparisons as well as Russell's error factor analysis. Table 22 lists the 20 selected nodes, which were determined by selecting them throughout the interface between the hull and the open keel board, and the decks above this interface, and their locations on the structural model along with their ID numbers to be evaluated in this series of comparisons and analysis.

110

Table 22.   **Vertical and Athwartship Velocity Response Node Locations**
(Meko-Like Box Model with Open Keel Board)

NODE	X (in)	Y (in)	Z (in)	Location
15	0	-20	0	Bulkhead
148	0	-20	160	Bulkhead
268	0	-20	280	Bulkhead
388	0	-20	400	Bulkhead
2454	1200	-20	0	Keel
2648	1200	-20	160	First Deck
2820	1200	-20	280	Second Deck
2970	1200	-20	400	Top Deck
3883	1800	-20	0	Keel
5251	2400	-300	0	Keel
5308	2400	-180	0	Keel
5310	2400	-100	0	Keel
5315	2400	100	0	Keel
5317	2400	180	0	Keel
5320	2400	300	0	Keel
6741	3000	-20	0	Keel
8170	3600	-20	0	Keel
8364	3600	-20	160	First Deck
8536	3600	-20	280	Second Deck
8686	3600	-20	400	Top Deck

a. *Error Comparison*

Similar to the vertical velocity analysis in the case of solid keel board, the error correlation throughout the meko-like box model has an excellent accuracy and precision related to it. Figure 69 shows that all of the results are tightly clustered in the excellent range (with the exception of nodes 2454 and 8170). Even though these two exceptions are far from this group, they fall into the acceptable region with Russell's Comprehensive error factors of 0.2741 and 0.2752. Nodes 2454 and 8170 are located at the extremities of the open keel board. The magnitude error in addition to the phase error is consistently low throughout the data set for the error correlations in the excellent region.
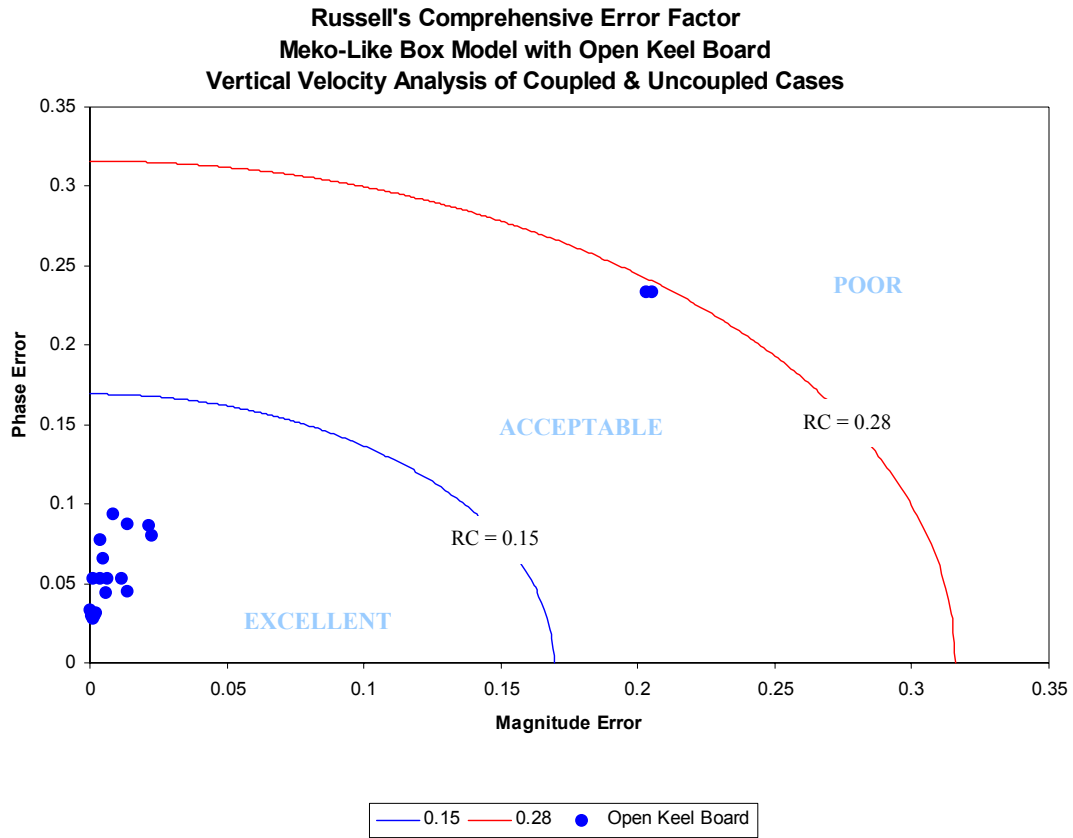
Figure 69.   Russell's Error Factor Comparison for Meko-Like Box Model with Open Keel Board (Vertical Velocity)

The Russell's error factor comparison for the athwartship velocity analysis also produces a very reliable correlation between the coupled and uncoupled cases. As seen in Figure 70, 13 out of 20 error values fall into the excellent region while the rest of them fall into the acceptable region. The phase errors are relatively larger than the magnitude errors, meaning that these phase errors possibly drive Russell's Comprehensive error factors higher in most cases. Even the worst correlation at RC = 0.2173, whose time history plot will be seen in Figure 74 with node 2454, is within the acceptable range. For node 2454, the error in magnitude and phase are, RM = 0.1083, RP = 0.2199, respectively. Table 23 provides a complete description of the error factors for the meko-like box model with open keel board.

Figure 70. **Russell's Error Factor Comparison for Meko-Like Box Model with Open Keel Board (Athwartship Velocity)**

Table 23. **Russell's Error Factors for Meko-like Box Model with Open Keel Board**

Simulation runtime = 500 msec					Meko-Like Box Model with Open Keel Board					
					Vertical Velocity Comparison			Athwartship Velocity Comparison		
NODE	X (in)	Y (in)	Z (in)	Location	COUPLED & UNCOUPLED CASES			COUPLED & UNCOUPLED CASES		
					LS-DYNA/USA DATA (<250HZ)			LS-DYNA/USA DATA (<250HZ)		
					RM	RP	RC	RM	RP	RC
15	0	-20	0	Bulkhead	-0.0036	0.0777	0.0689	0.0122	0.1331	0.1185
148	0	-20	160	Bulkhead	0.0013	0.0528	0.0468	0.0171	0.0987	0.0887
268	0	-20	280	Bulkhead	0.0035	0.0536	0.0476	0.0239	0.1085	0.0985
388	0	-20	400	Bulkhead	0.0049	0.0658	0.0585	0.0235	0.1159	0.1049
2454	1200	-20	0	Keel	-0.2030	0.2333	0.2741	-0.1083	0.2199	0.2173
2648	1200	-20	160	First Deck	0.0006	0.0302	0.0267	0.0013	0.1857	0.1646
2820	1200	-20	280	Second Deck	-0.0016	0.0301	0.0267	0.0331	0.1758	0.1585
2970	1200	-20	400	Top Deck	0.0001	0.0335	0.0297	0.0263	0.1768	0.1584
3883	1800	-20	0	Keel	0.0216	0.0862	0.0788	0.0094	0.1034	0.0920

Simulation runtime = 500 msec					Meko-Like Box Model with Open Keel Board					
					Vertical Velocity Comparison			Athwartship Velocity Comparison		
NODE	X (in)	Y (in)	Z (in)	Location	COUPLED & UNCOUPLED CASES			COUPLED & UNCOUPLED CASES		
					LS-DYNA/USA DATA (<250HZ)			LS-DYNA/USA DATA (<250HZ)		
					RM	RP	RC	RM	RP	RC
5251	2400	-300	0	Keel	-0.0136	0.0871	0.0781	-0.0059	0.1292	0.1146
5308	2400	-180	0	Keel	-0.0060	0.0446	0.0398	-0.0138	0.1130	0.1009
5310	2400	-100	0	Keel	-0.0137	0.0452	0.0418	-0.0163	0.1127	0.1009
5315	2400	100	0	Keel	0.0114	0.0534	0.0484	0.0112	0.1018	0.0908
5317	2400	180	0	Keel	0.0065	0.0535	0.0477	0.0100	0.0935	0.0833
5320	2400	300	0	Keel	0.0083	0.0939	0.0835	0.0077	0.1077	0.0957
6741	3000	-20	0	Keel	0.0223	0.0801	0.0737	0.0179	0.1259	0.1127
8170	3600	-20	0	Keel	-0.2050	0.2333	0.2752	-0.1034	0.2059	0.2042
8364	3600	-20	160	First Deck	-0.0020	0.0319	0.0284	0.0128	0.1788	0.1588
8536	3600	-20	280	Second Deck	-0.0012	0.0282	0.0250	0.0446	0.1767	0.1615
8686	3600	-20	400	Top Deck	-0.0003	0.0315	0.0279	0.0345	0.1565	0.1420
Russell Error Correlation				Sum(E(X))	-0.3695	1.4459	1.4273	0.0378	2.8195	2.5668
> 0.28	Poor			Sum(E(X^2))	0.0849	0.1706	0.2007	0.0303	0.4272	0.3593
< 0.15	Excellent			**Mean**	**-0.0185**	**0.0723**	**0.0714**	**0.0019**	**0.1410**	**0.1283**
				Standard Deviation	0.0641	0.0590	0.0721	0.0399	0.0395	0.0397

Table 24 represents the complete statistical data analysis performed for the correlation process in the case of the open keel board. If two data sets in the vertical and athwartship directions are compared to each other in general, it can be said that the results resulting from both of them are found to be very accurate. Moreover, this would indicate that the vertical and athwartship velocity responses developed from the shock simulation of the uncoupled case really captured the range of the dynamic response of the coupled case very precisely. Investigating the mean correlations that were found to be RC = 0.0714 and RC = 0.1283 in the vertical and athwartship directions, respectively, it is concluded that the results in each direction produce a very satisfactory correlation between the coupled and uncoupled cases. The mean Russell's Comprehensive error factor in the vertical direction is the best mean correlation in the hull appendage analysis of the meko-like box model. Based on the statistical data analysis of Russell's Comprehensive error factors presented in Table 24, 100% of the nodes have a RC ≤ 0.28 in the vertical and athwartship velocity comparisons while 90 % of the nodes have error values within one standard deviation again in both comparisons.

Table 24.   Statistical Data for Meko-Like Box Model with Open Keel Board
(Coupled and Uncoupled Cases)

Russell's Comprehensive Error Factor	Vertical Velocity Comparison	Athwartship Velocity Comparison
RC < 0.30	100 %	100 %
RC < 0.28	100 %	100 %
RC < 0.25	90 %	100 %
RC < 0.20	90 %	90 %
RC < 0.18	90 %	90 %
RC < 0.15	90 %	65 %
Mean RC	0.0714	0.1283
Standard Deviation	0.0721	0.0397
Mean + Standard Deviation	0.1435	0.1680
Data within One Standard Deviation	90 %	90 %

As seen in the case of hell keel board, the weakest correlations in the vertical and athwartship directions all the way through the structure occur on the two nodes, 8170 and 2454 located at the bow and stern of the interface, respectively, between the hull and open keel board. These two correlations at the end points of the open keel board are inline with the results resulting from the vertical and athwartship velocity analyses. This shows that a direct correlation is happening between the longitudinal position of a node within the finite element model and the accuracy of the data of the uncoupled case when compared to the corresponding data of the coupled case. Figure 71 illustrates that the bow and stern areas of the shell keel board consistently produce poorer correlation between the coupled and uncoupled cases for both vertical and athwartship velocity responses.
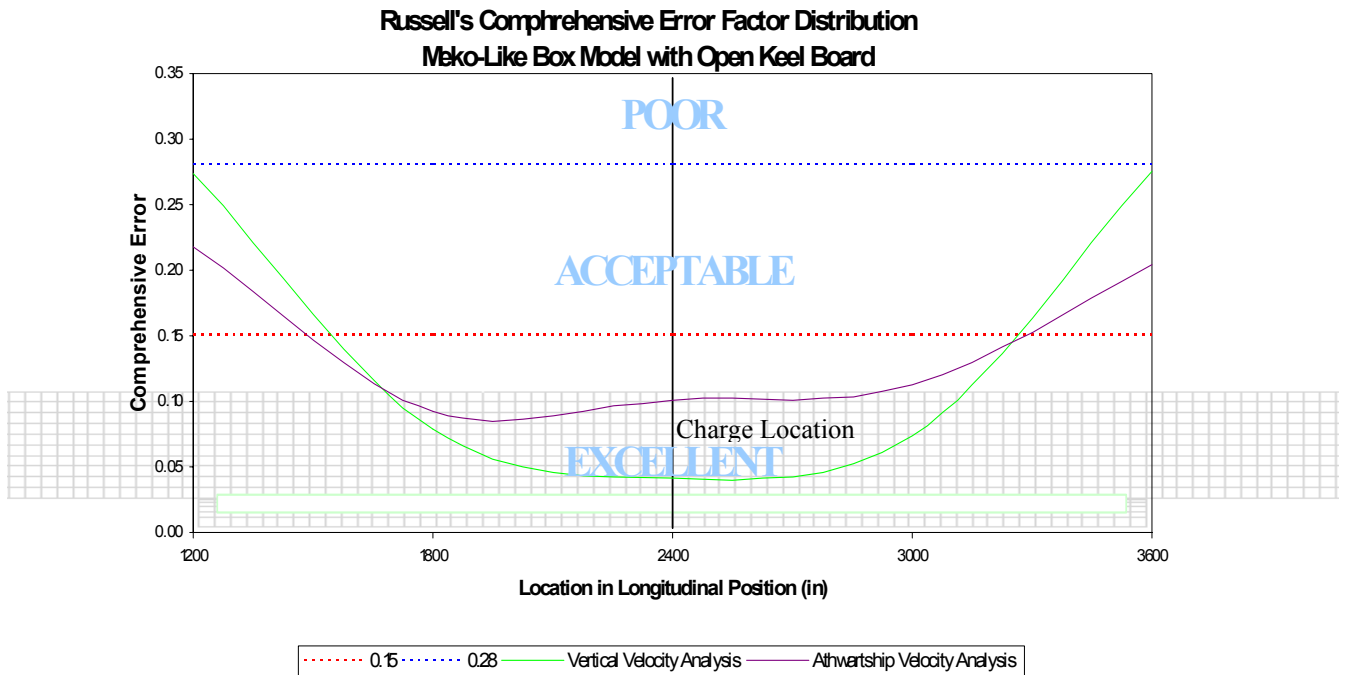
Figure 71. **Russell's Comprehensive Error as a Function of Position (Open Keel Board)**

b. *Detailed Velocity Plots*

The following figures are representative of the results obtained from the vertical and athwartship velocity analyses of the meko-like box model with open keel board and are provided as samples of the complete set of time history plots found in Appendices D and E, respectively. The Russell's Comprehensive error factors in the vertical direction for nodes 8170 and 8536 are RC = 0.2752 and RC = 0.0250, respectively. The time history plot of the vertical velocity response of node 8170 represents the worst correlation between the coupled and uncoupled cases while the vertical velocity plot of node 8536 corresponds to the best correlation based on the Russell's Comprehensive error factors found in Table 23. Node 8170 is located at the bow point of the open keel board on the keel and node 8536 is located on the second deck over node 8170. As illustrated in Figure 71, the correlation worsens as one moves to the extremities of the open keel board; this situation can be confirmed based on the correlations of the end nodes (8170 and 2454) of the open keel board. As has been the case in the shell keel board situation, the Russell's Comprehensive error factors significantly varies through the end points of the open keel board particularly for the

116

vertical velocity response. Depending on the correlation values, the athwartship velocity response produces more uniform error values. Figure 72 shows that the phase between the coupled and uncoupled cases differs more in the early time response than the late time response. Although the phases are different in the early time response, based on the Russell's Comprehensive error factor found in the acceptable region, this correlation between the coupled and uncoupled cases do not affect the overall correlation determined in the vertical direction. The best case found on node 8536 represents the well-matching behavior of all of the responses including the no appendage case.
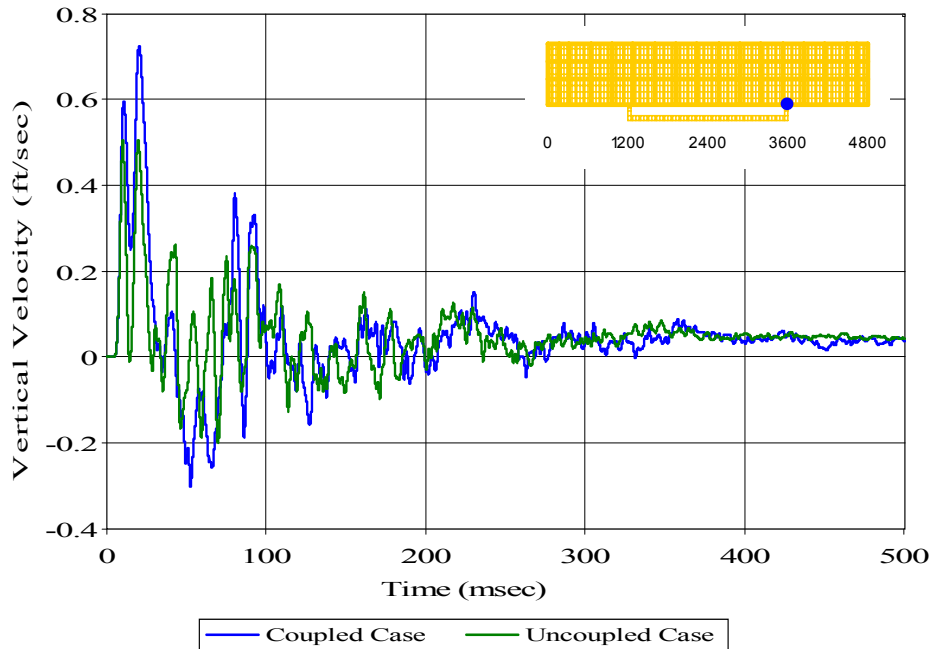
Figure 72.   **Keel Node 8170: (RM = -0.2050, RP = 0.2333, RC = 0.2752)**

Meko-Like Box Model with Open Keel Board

Node 8536 at Second Deck (x=3600 y=-20 z=280)
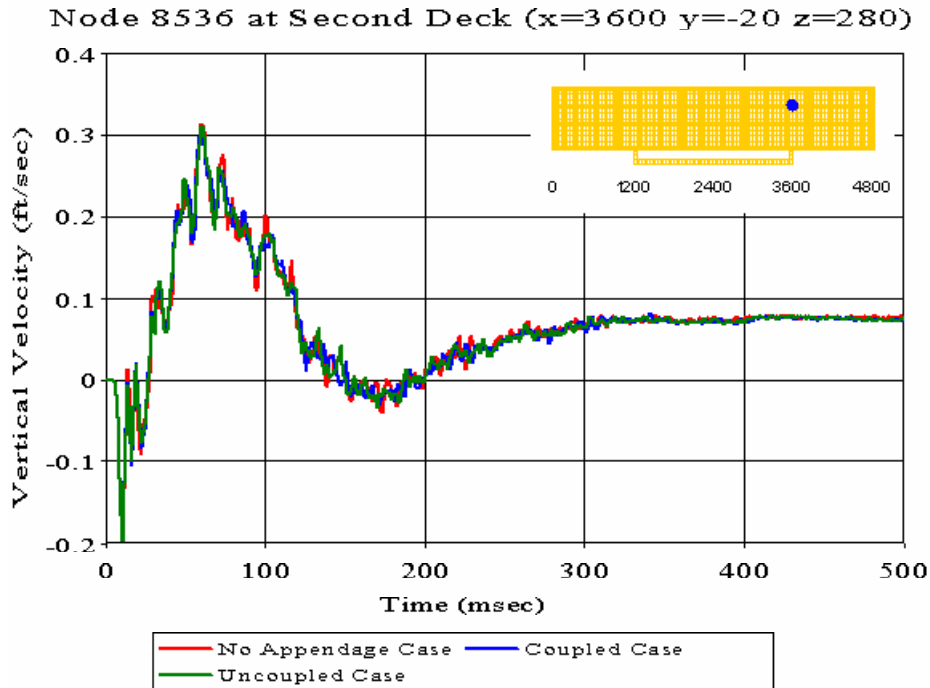
Figure 73.   Second Deck Node 8536: (RM = -0.0012, RP = 0.0282, RC = 0.0250)

For the athwartship velocity analysis, nodes 2454 and 5317 correspond to the worst and best cases, respectively, as seen in Figures 74 and 75. The Russell's Comprehensive error factors are sequentially 0.2173 and 0.0833. The locations of nodes 2454 and 5317 are on the stern point of the open keel board on the keel and on the center to the left side of the meko-like box model, respectively. Like the other cases found in previous analyses, the extreme points on the interface between the hull and open keel board produced the worst correlation while the center node generated the best. Looking at Figure 74, one can see that the phases of the coupled and uncoupled cases match well in the early time response while these phases are not well related to each other immediately after the early time response. Moreover, the peak responses are captured well by the response of the uncoupled case. The response found in the coupled case settles out faster than the predicted response found in the uncoupled case, suggesting that the model of the uncoupled case may be under-damped in this case. However, since the correlation is in the acceptable range, it can be said that the uncoupled case sufficiently predicts the dynamic response of the coupled case in this case. The athwartship velocity response of

118

node 5317 illustrated in Figure 75 shows that, although there are very small differences in the late time response, the overall response corresponds to an excellent correlation based on the perfect match occurred in the early time response.

If the complete set of the time history plots of the case of the open keel board case, since the surface area of the open keel board, which is 9.4 % of the underwater surface area of the structural model, is smaller than that of both solid and shell keel boards, the inclusion of the open keel board does not affect the dynamic response of the whole system as much as the cases of the solid and shell keel boards except for the response of the neighborhood around which the open keel board was built around.
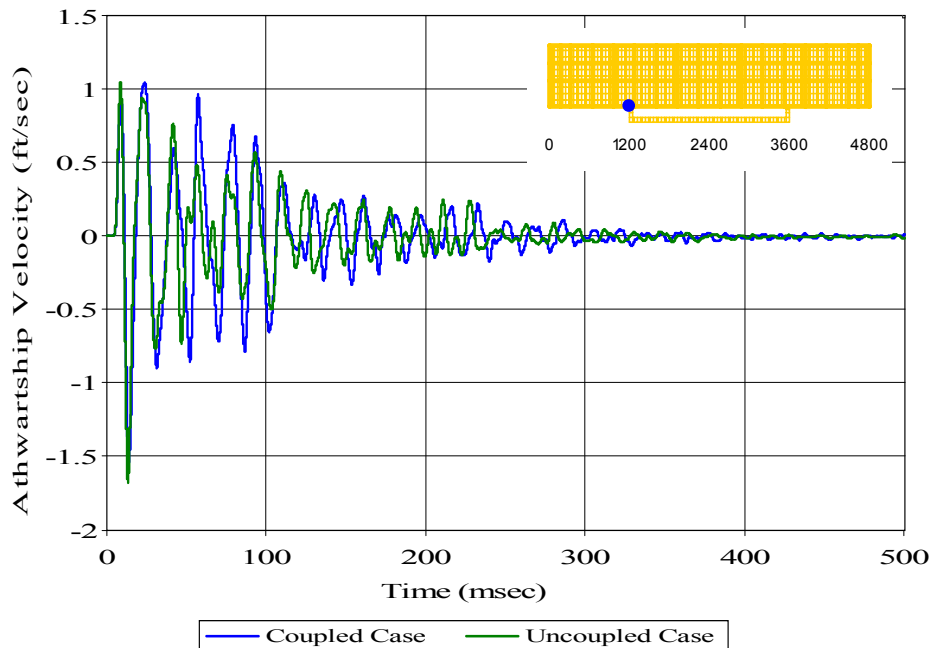
Figure 74.   Keel Node 2454: (RM = -0.1083, RP = 0.2199, RC = 0.2173)

Meko-Like Box Model with Open Keel Board
Node 5317 at Keel (x=2400 y=180 z=0)
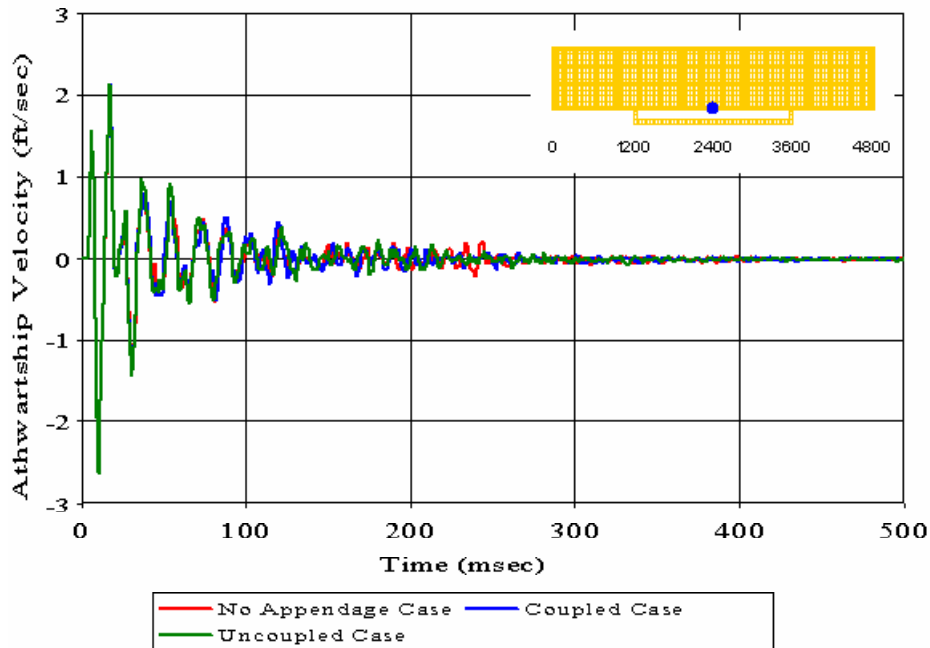
Figure 75.   Keel Node 5317: (RM = 0.0100, RP = 0.0935, RC = 0.0833)

c.   *Shock Spectra Plots*

For the shock spectra analysis, shock spectra plots of eight nodes located right through the meko-like box model will be studied in both vertical and athwartship directions. The nodes, whose figures will be presented below, contain the best and worst correlations in accordance with the Russell's Comprehensive error factors found in the case of the open keel board.

The following figures represent the shock spectra plots resulting from the vertical and athwartship velocity analyses of the meko-like box model with open keel board and are provided as samples of the whole set of shock spectra plots found in Appendix F. As seen in Figures 76 and 77, nodes 8170 and 8536 are referred to as the worst and best correlations, respectively, occurring in the vertical direction. Furthermore, Figures 78 and 79 of 2454 and 5317 represent the worst and best correlations, respectively, in the athwartship direction. It is obvious that the shock spectra plots of the best correlations presented imply more matched results between the coupled and uncoupled cases than those of the worst correlations.
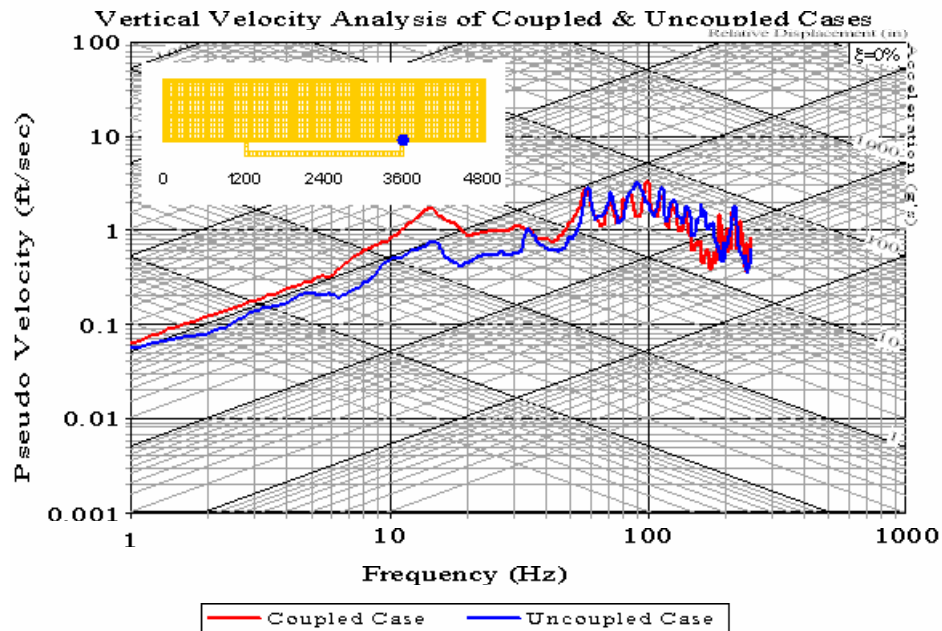
Figure 76. Shock Spectra Plot: Keel Node 8170
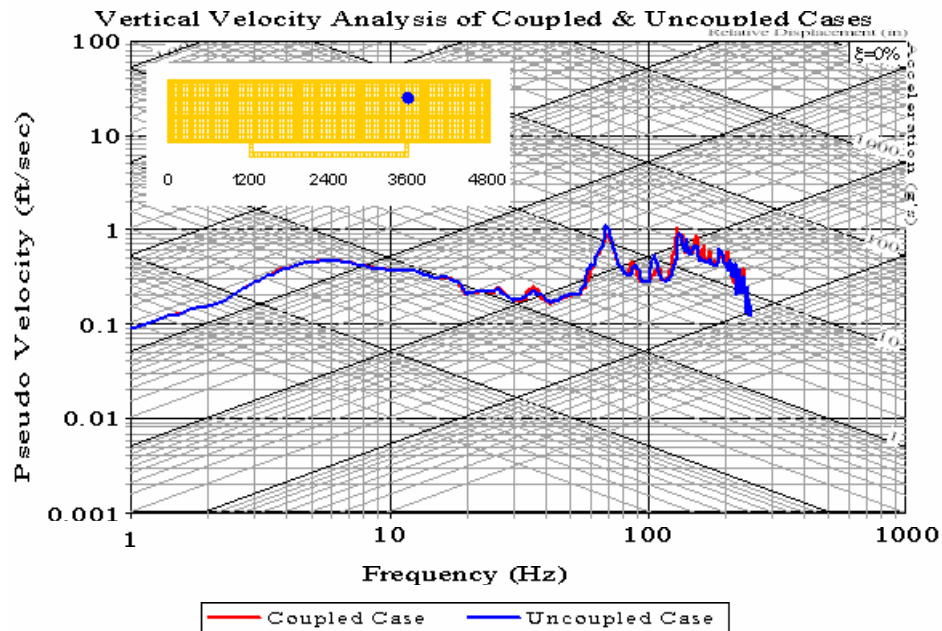
Figure 77. Shock Spectra Plot: Second Deck Node 8536
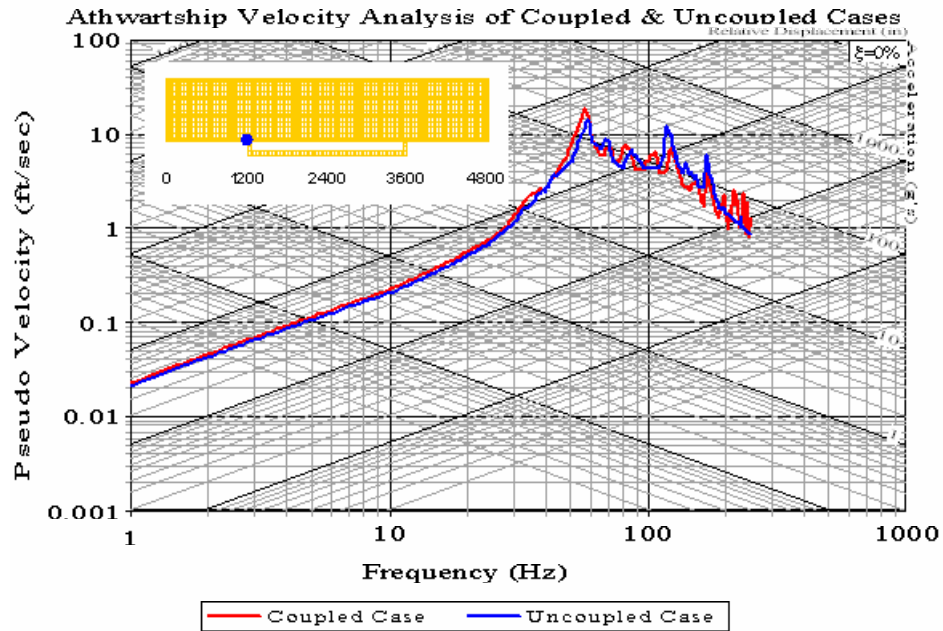
Figure 78.   **Shock Spectra Plot: Keel Node 2454**
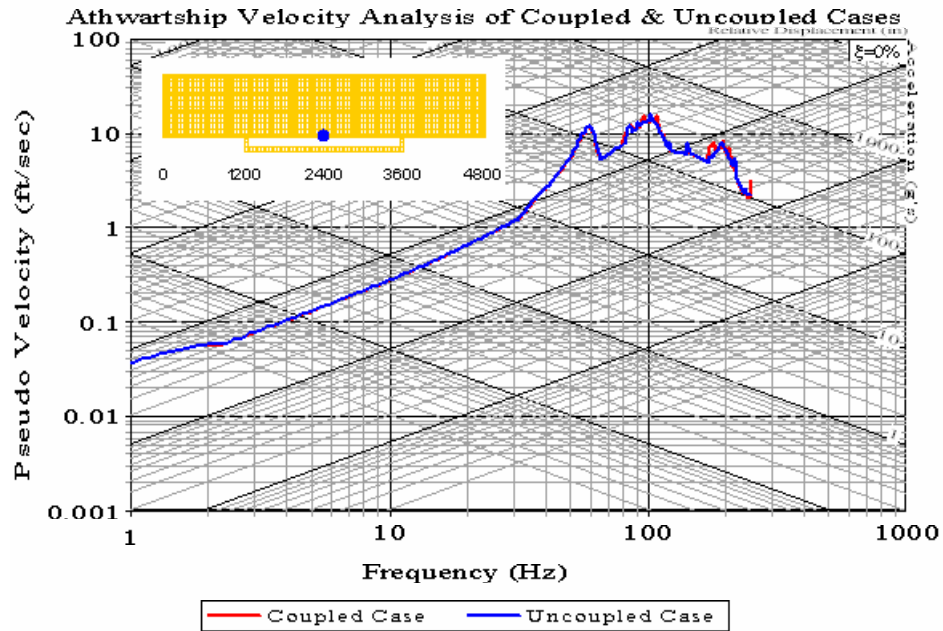
Figure 79.   **Shock Spectra Plot: Keel Node 5317**

122

Most of the data presented in both vertical and athwartship shock spectra plots is below 7 ft/sec based on all of the shock spectra plots investigated. However, the peak values in the vertical direction sometimes reach 10 ft/sec at most while some of those in the athwartship direction reached 20 ft/sec.

If all of the shock spectra plots are evaluated, the uncoupled case has predicted the response of the coupled case very well especially in the 1 to 100 Hz range for both vertical and athwartship velocity analyses. Although there are small variations between the coupled and uncoupled cases, the two responses are very close to each other almost throughout the frequency domain; this verifies the occurrence of very good correlation according to the Russell's error factor comparisons conducted in both vertical and athwartship directions.

Most of the vertical shock spectra plots display a gradual rise in amplitude up to almost 18 Hz along with some oscillations through 20 Hz as the frequency increases while almost all of the athwartship shock spectra plots exhibit a gradual rise with oscillation up to the 60 to 70 Hz range. While some peak values occur between 100 and 250 Hz along with relatively more oscillations, some occur between 50 and 100 Hz in both vertical and athwartship velocity analyses. When these peak values take place in these ranges, there is a high degree of oscillation near the peak values or a downward trend through the end of the frequency domain. Above 100 Hz, the responses in the vertical and athwartship directions tend to fluctuate much more. The uncoupled case in the vertical velocity analysis under predicts the response of the coupled case below 100 Hz while it over predicts the high frequency responses above 100 Hz. Even though the differences between the coupled and uncoupled cases in the athwartship direction seem to be very small, the under and over prediction situation can be observed in the shock spectra plots. Table 25 summarizes the shock spectra analysis in the case of open keel board according to the frequency range.

Table 25.   **Summary of Shock Spectra Analysis for Meko-Like Box Model with Open Keel Board**

Frequency Range	Trend of Curves	Vertical Velocity Analysis	Ayhwartship Velocity Analysis
1 to 20 Hz	Gradual rise up to 18 Hz in the vertical direction	Uncoupled case closely matches or slightly under predicts coupled case	Uncoupled case closely matches or barely under predicts coupled case
20 to 50 Hz	Small oscillations in vertical direction, gradual rise in athwartship direction	Uncoupled case closely matches in general or under predicts coupled case	Uncoupled case closely matches or barely under predicts coupled case
50 to 100 Hz	Peak values occur with oscillation up to 10 ft/sec in vertical direction, gradual rise up to peak value of 20 ft/sec with very small oscillations or downward trend in athwartship direction	Uncoupled case closely matches or under predicts coupled case	Uncoupled case closely matches coupled case with under and over predictions
100 to 250 Hz	High degree of oscillation and peak values occur (up to 10 ft/sec in vertical direction, 20 ft/sec in athwartship direction)	Uncoupled case closely matches or over predicts coupled case	Uncoupled case closely matches or slightly over predicts coupled case

4.   Meko-Like Box Model with Rudders

The last hull appendages rudders to be examined in this analysis was built using shell elements along with varying rudder surface areas, which influence the hull appendage surface area exposed to UNDEX, as their construction process was explained in Chapter III. Like the other three appendages, the rudders were also modeled as coupled and uncoupled structures with respect to the surrounding fluid. This analysis will try to determine the effects on the dynamic response of the meko-like box model obtained from the inclusion and varying rudder surface areas by using the absolute maximum vertical velocity distribution plots and the time history plots of the vertical and athwartship velocity response comparisons. Then, to recognize the predictable coupling scheme for these rudders, an extensive work will be presented based on the time history and shock spectra plots of the vertical and athwartship velocity response comparisons and Russell's error factor analysis. Table 26 lists the 22 preferred nodes, which were decided upon by selecting them during the interface between the hull and the rudders in addition to the decks above this interface, and their locations on the meko-like box model along with their ID numbers to be evaluated in this series of comparisons and analysis.

Table 26. **Vertical and Athwartship Velocity Response Node Locations**
(Meko-Like Box Model with Rudders)

NODE	X (in)	Y (in)	Z (in)	Location
15	0	-20	0	Bulkhead
74	120	-140	0	Keel
81	120	140	0	Keel
148	0	-20	160	Bulkhead
214	120	-140	160	First Deck
221	120	140	160	First Deck
268	0	-20	280	Bulkhead
334	120	-140	280	Second Deck
341	120	140	280	Second Deck
388	0	-20	400	Bulkhead
434	120	-140	400	Top Deck
441	120	140	400	Top Deck
2454	1200	-20	0	Keel
3883	1800	-20	0	Keel
5251	2400	-300	0	Keel
5308	2400	-180	0	Keel
5310	2400	-100	0	Keel
5315	2400	100	0	Keel
5317	2400	180	0	Keel
5320	2400	300	0	Keel
6741	3000	-20	0	Keel
8170	3600	-20	0	Keel

a.   *Velocity Plots*

To be able to examine the consequences of the inclusion and varying surface areas of the rudders on the dynamic response of the meko-like box model, initially, the absolute values of maximum vertical velocity responses of nodes located along the keel and second deck of the meko-like box model will be evaluated for both coupled and uncoupled cases. Based on the construction of the rudders on the hull of the structural model, their surface areas were changed so that their surface areas would set to half and double surface areas besides the actual surface area. Figures 80, 81, 82 and 83 show the differences between the meko-like box model with rudders having different surface areas and the meko-like box model with no appendage. Figures 80 and 82 imply that the maximum vertical velocity response of the meko-like box model excluding rudders is extremely close to that of the meko-like box model including them. In addition, the differences of maximum vertical velocity responses among the structural models including rudders having different surface areas are so small to notice. This study shows

that the addition of the rudders as hull appendages does not considerably affect the dynamic response of the structure as well as different surface areas of the rudders for the keel region. However, in both coupled and uncoupled cases, there are larger differences for the second deck unlike the differences for the keel between the meko-like box model with and without rudders. The similar situation was seen also for the first and top decks of the meko-like box model in coupled and uncoupled cases, and their plots were presented in Appendix D. Yet, one should look into the time history plots to conclude how much both the inclusion and varying surface areas of the rudders affect the dynamic response of the meko-like box model. The comparison of the time history plots will be conducted as a second study. If all the plots of the maximum vertical velocity response comparison counting the figures in Appendix D, as seen in the no appendage case, the meko-like box model with rudders having varying surface areas produces the largest absolute maximum vertical velocity response of 6.93 ft/sec for both coupled and uncoupled cases. Additionally, it can be said that, as one moves to the upper decks, the maximum velocity response values almost gradually decreases with respect to those of the keel for almost all cases.
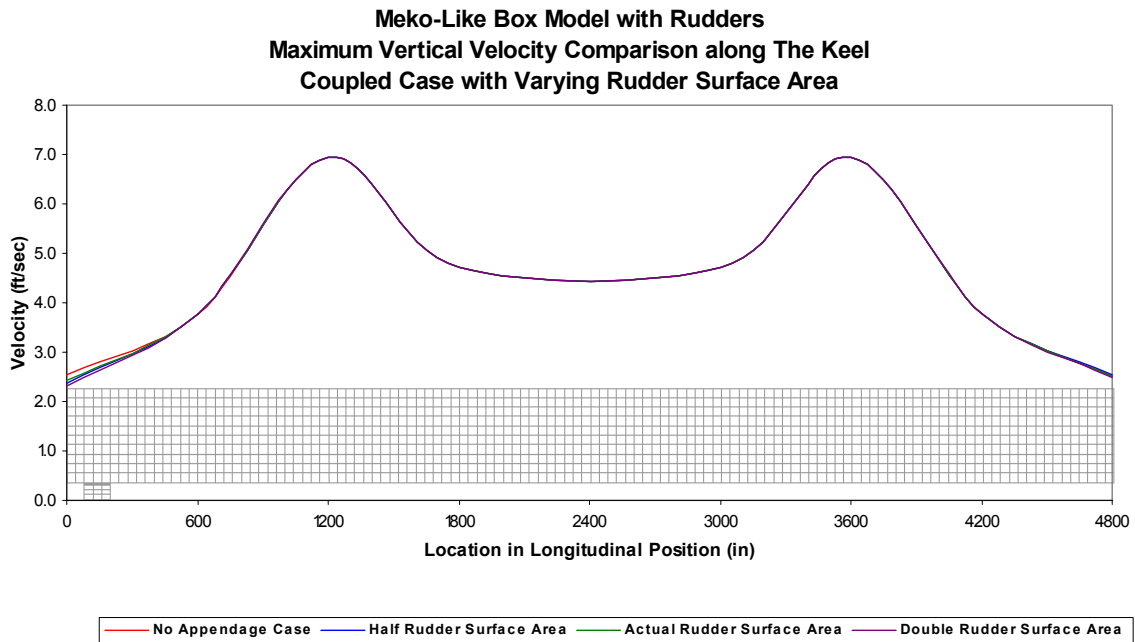
Figure 80. **Absolute Maximum Vertical Velocity as a Function of Position (Keel)**

126
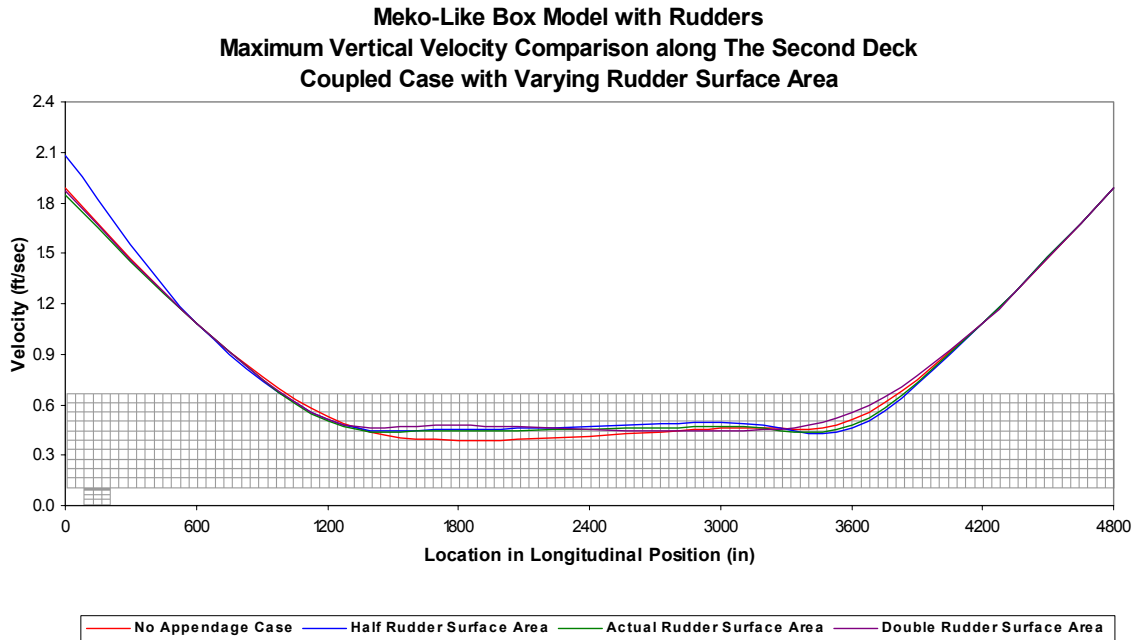
Figure 81. **Absolute Maximum Vertical Velocity as a Function of Position (Second Deck)**
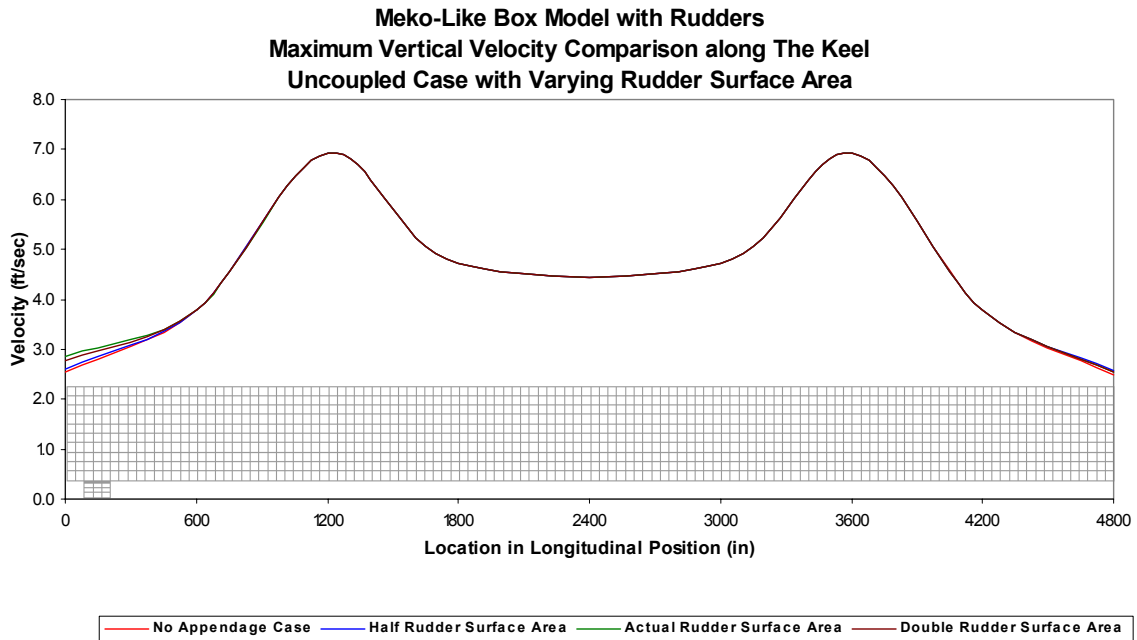
Figure 82. **Absolute Maximum Vertical Velocity as a Function of Position (Keel)**

127
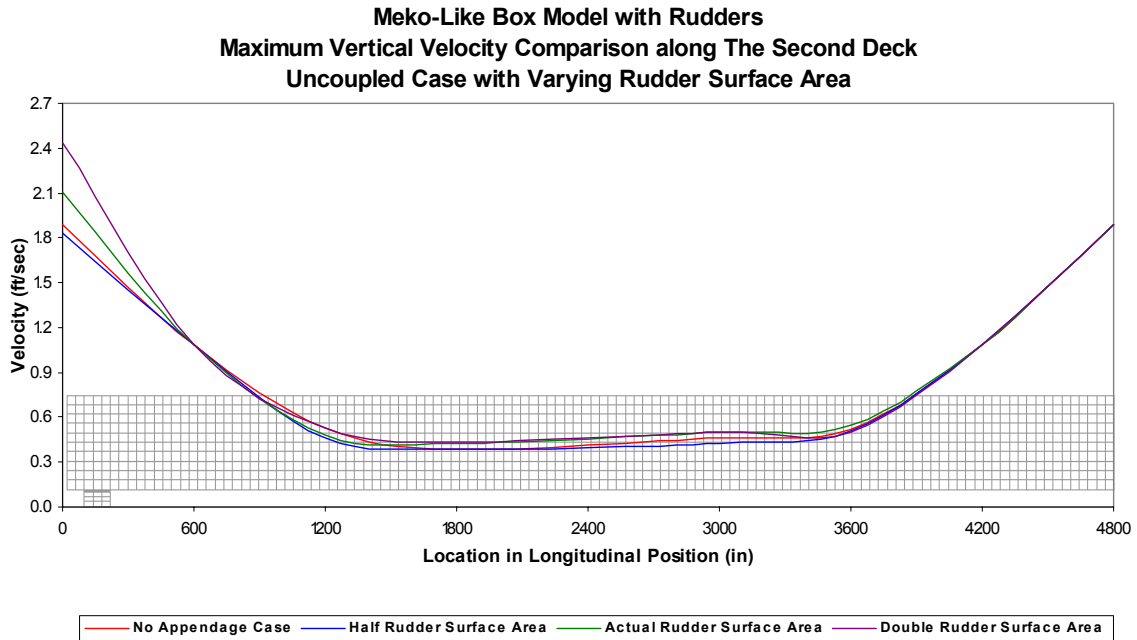
Figure 83.   Absolute Maximum Vertical Velocity as a Function of Position
(Second Deck)
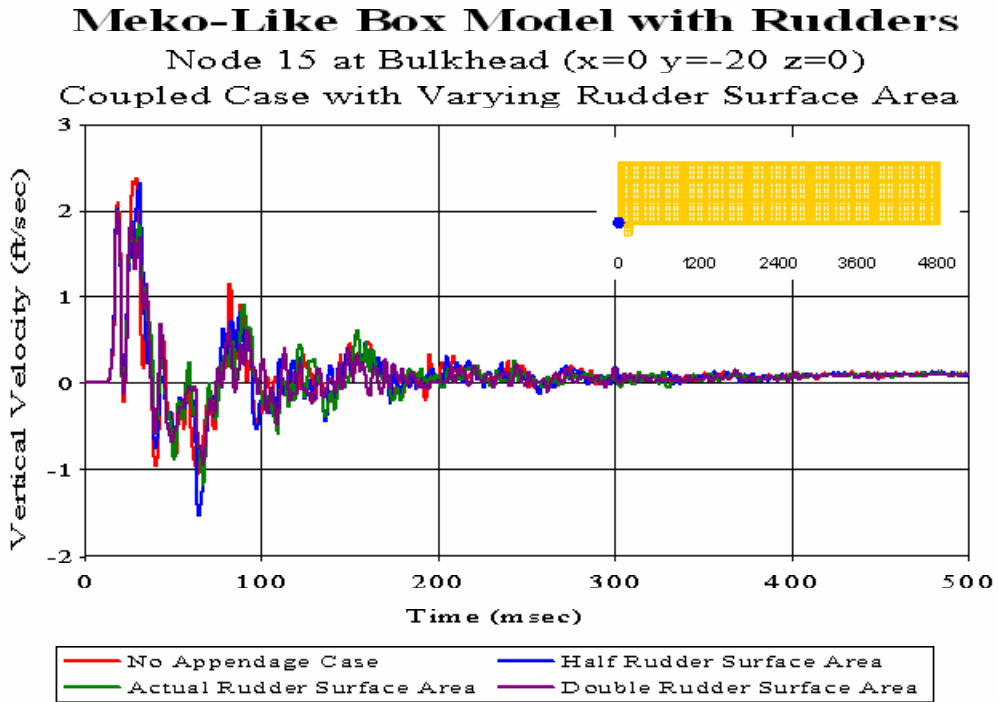
Figure 84.   Coupled Case with Varying Rudder Surface Area: Bulkhead Node 15

To ascertain the effects of the inclusion of rudders along with the varying rudder surface areas, the time history plots will be studied. These figures were resulted from the vertical and athwartsip velocity analyses and were attached as examples of the complete set of time history plots found in Appendices D and E, respectively. These time history plots of both coupled and uncoupled cases were selected regarding the largest and one of smallest differences found between the no appendage case and the rudder case having different exposed surface areas in the absolute maximum vertical velocity distribution plots discussed previously. In this manner, Figure 84 with node 15, where the largest difference occurs, represents that the peak responses of the no appendage case are captured well by the other cases. Although the phases of all of the cases found in this plot do not match perfectly, they tend to be close to each other through the late time response. It can be said that the case of the double rudder surface area differs from the no appendage case the most. The reason is because the surface area exposed to UNDEX is the largest in this case. In addition, since the location of node 15 is very close to the location of the rudders constructed on the structure, the maximum difference occurs between the no appendage case and the rudder case.

Furthermore, as seen in Figure 85 with node 15 in the athwartship velocity response, the discrepancies tend to increase relative to the vertical velocity response. Figure 86 with node 8170 is representative of one of the lowest differences happening between the data sets obtained from all of the cases in the vertical direction. Throughout the response, there is a perfect match among the curves. That the location of this node is very far away from the location of both rudders can be the cause of this perfect match in this situation. Figure 87 is also the time history plot of this node in the athwartship direction.
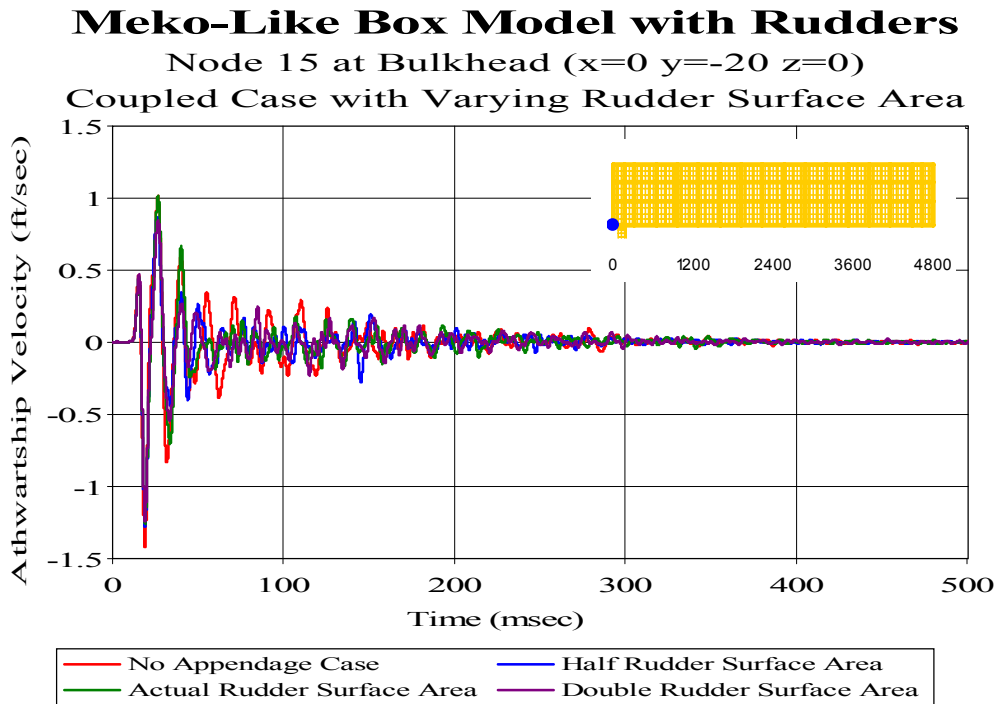
Figure 85.   Coupled Case with Varying Rudder Surface Area: Bulkhead Node 15
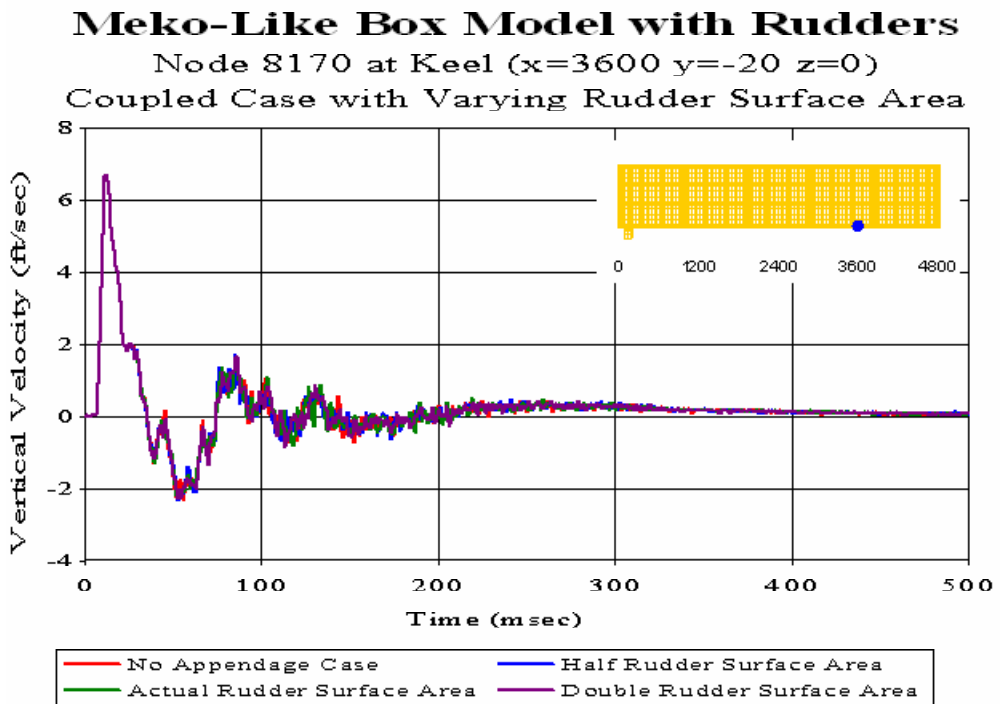
Figure 86.   Coupled Case with Varying Rudder Surface Area: Keel Node 8170

130
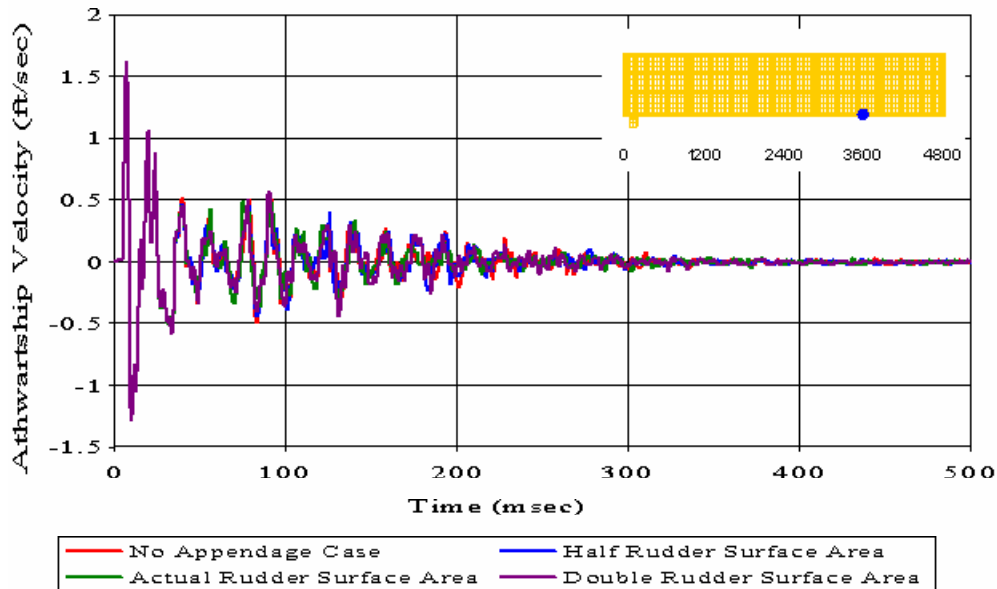
Figure 87. **Coupled Case with Varying Rudder Surface Area: Keel Node 8170**

For the uncoupled case, the vertical and athwartship velocity responses of separate nodes follow the same approach reached in the coupled case. Node 268, which is located very close to the rudders, shows phase differences especially in the vertical direction, while node 3883, which is located through the center of the structure, produces similar results in both vertical and athwartship directions. In particular, the case of the double rudder surface area is inclined to vary from the rest of the other cases investigated herein. Based on the complete set of time history plots throughout the meko-like box model in both coupled and uncoupled cases, as one moves away from the rudders, the differences occurring in the dynamic response among the data sets that denote no appendage case and the rudder case with varying surface areas tend to decrease. As has been the situation in the cases of other hull appendages, these rudders relative to the other positions on the structure affect the dynamic response in the region of rudders more.

131
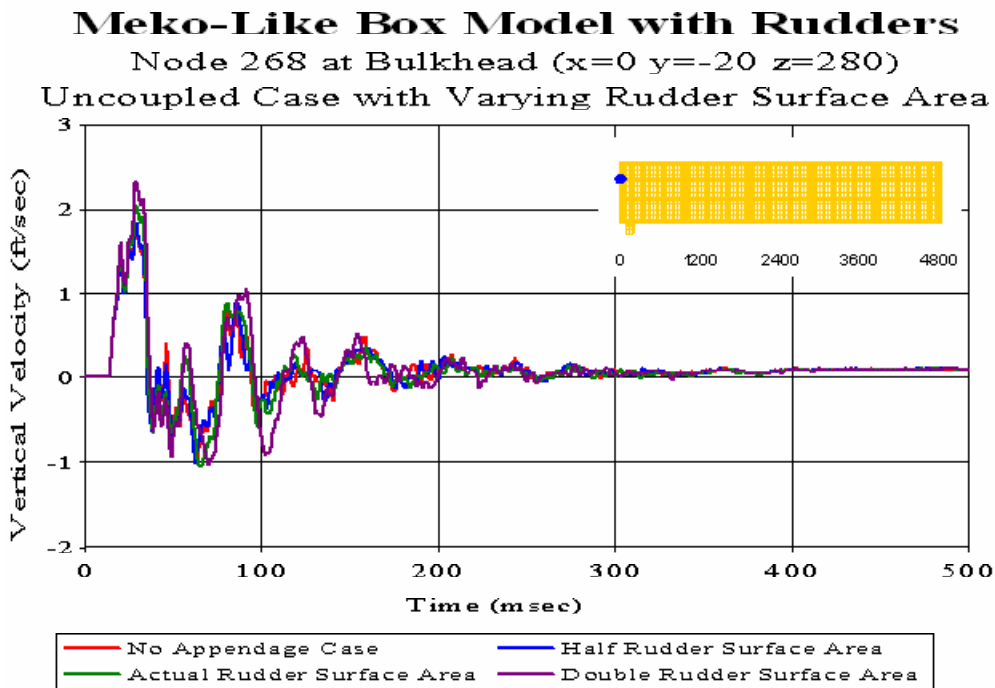
Figure 88. **Uncoupled Case with Varying Rudder Surface Area: Bulkhead Node 268**
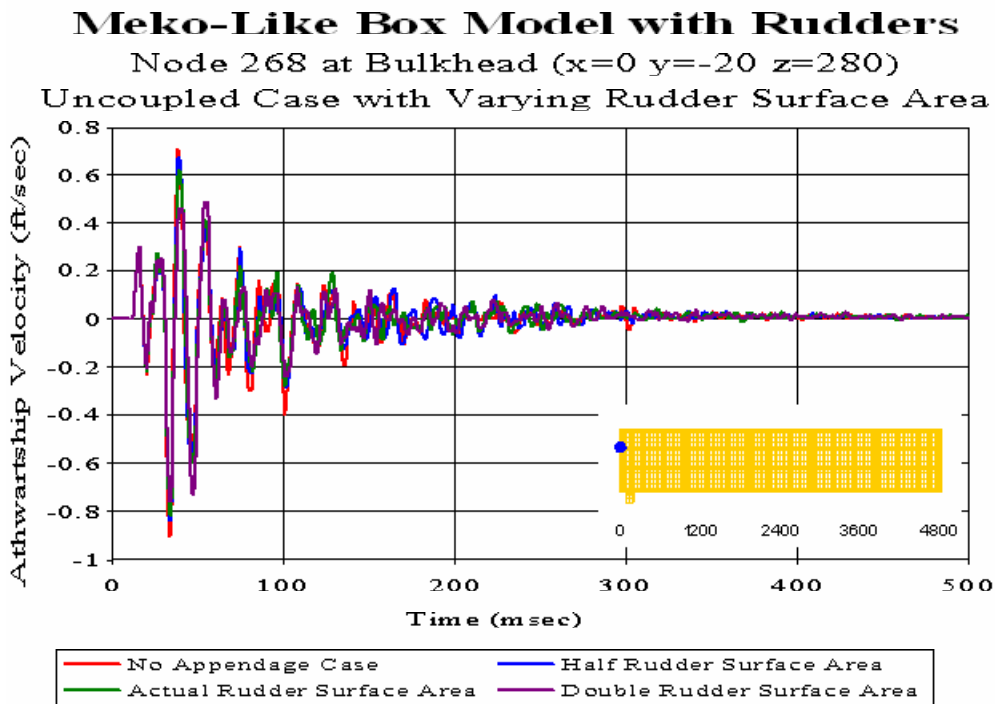
Figure 89. **Uncoupled Case with Varying Rudder Surface Area: Bulkhead Node 268**

132
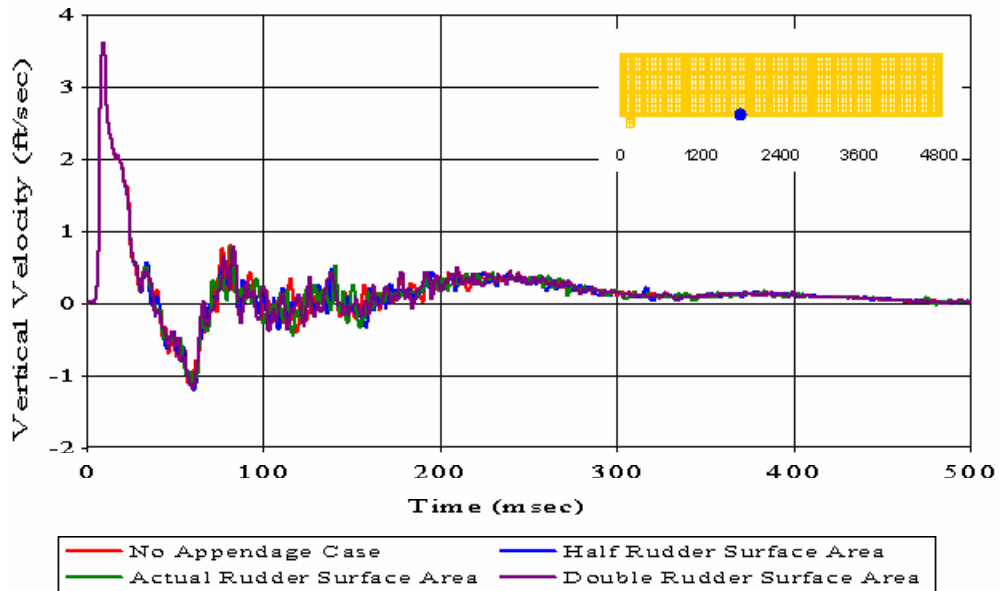
Figure 90. **Uncoupled Case with Varying Rudder Surface Area: Keel Node 3883**
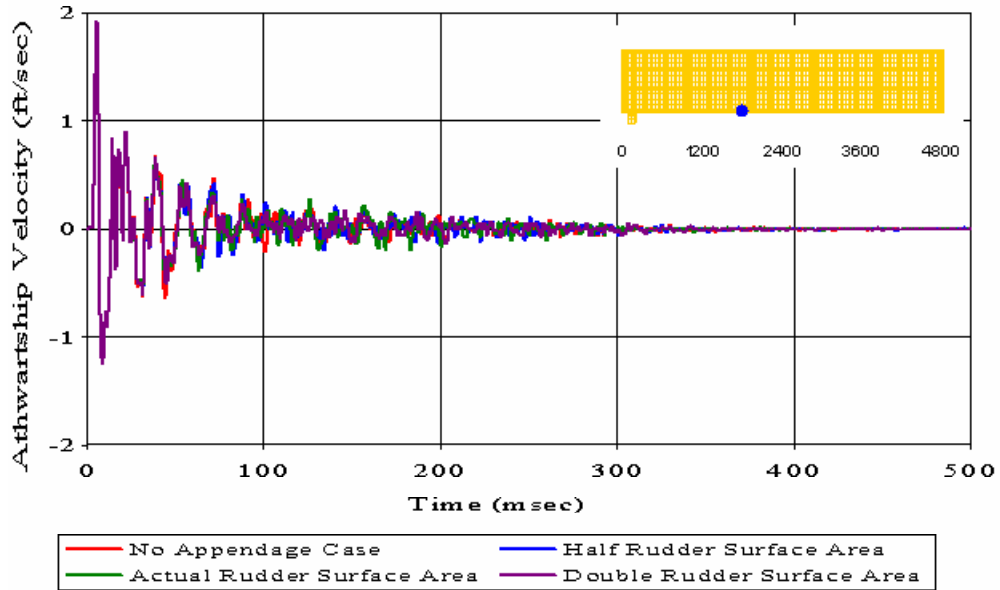
Figure 91. **Uncoupled Case with Varying Rudder Surface Area: Keel Node 3883**

Based on the overall results along the meko-like box model, since the surface areas of the rudders, even the double rudder surface area, are smaller than the solid and shell keel boards, the inclusion of the rudders does not affect the dynamic response of the system as much as the cases of the solid and shell keel boards except the response of the locations in the region of the rudders created as well as seen in the case of the open keel board. It can be stated that the meko-like box model is affected the least in the rudder case if compared to the other three cases investigated previously.

b. *Error Comparison*

The discrepancies developed from the rudders having been modeled as coupled and uncoupled structures according to the surrounding fluid will be investigated subsequently. Based on all of the three different rudder surface areas, vertical and athwartship velocity comparisons between the coupled and uncoupled cases were conducted for this analysis. Figures 92 and 93 illustrate the plots of the comprehensive Russell's error factor comparison composed of all three different rudder surface areas evaluated in the vertical and athwartship velocity directions, respectively. Like the case of the solid keel board, separate plots of Russell's error comparison for each rudder surface area can be found in Appendix G for both vertical and athwartship velocity responses.
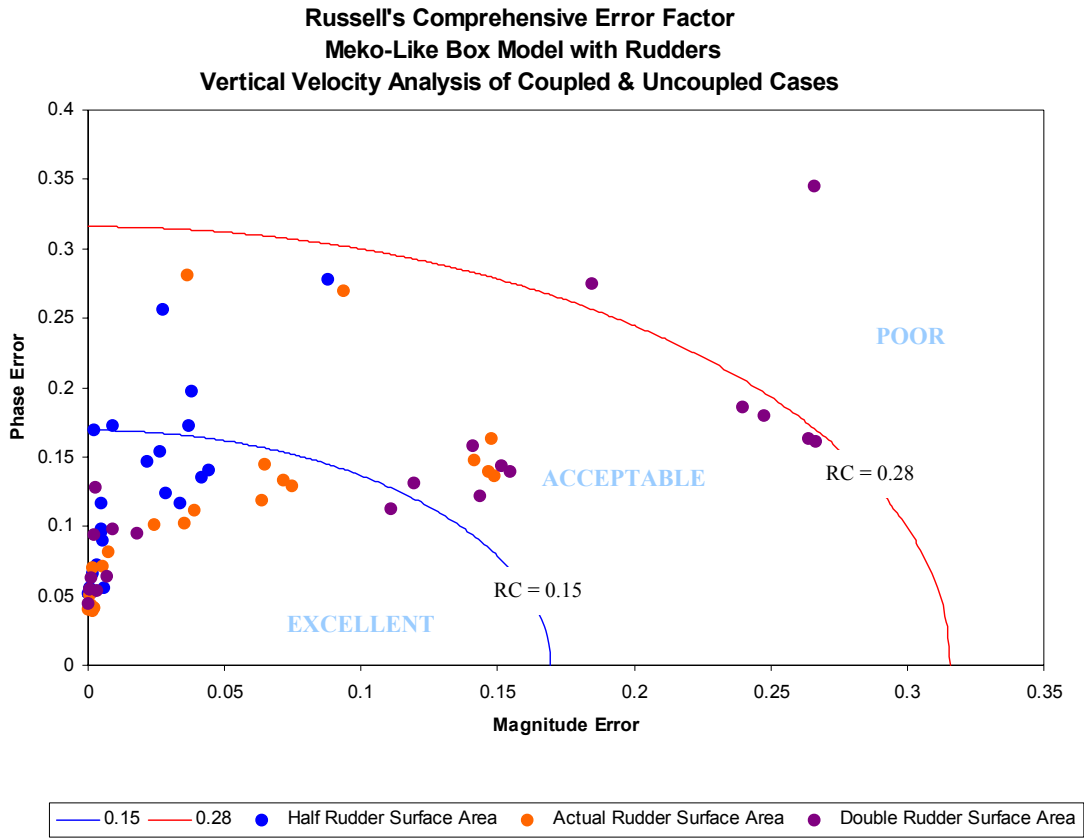
**Figure 92.   Complete Russell's Error Factor Comparison for Meko-Like Box
Model with Rudders (Vertical Velocity)**

As seen in Figure 92, with all but two exceptions, the vertical velocity
response values fall into the excellent and acceptable range. Even one of those two (node
81) falling outside the acceptable region are just barely greater than the 0.28 cut-off
value, and does not necessarily constitute an undesirable correlation. However, the other
point (node 74) is far from the other points with Russell's Comprehensive error factor of
0.3866, and the magnitude and phase errors of 0.2660 and 0.3457, respectively. Those
two errors falling into the poor region represent the two nodes, which are located on the
interface between the rudders and the hull (keel). It can be noticed that node 74 produces
the worst case discussed above because this node lies on the right side of the structure,
which is closer to the charge location detonated in the shock simulations. The magnitude
and phase errors both make Russell's Comprehensive error factors higher in most cases.
As the meko-like box model with solid keel board having the actual weight percentage

13.5 % creates the best correlation in the case of solid keel board according to the mean correlations; the meko-like box model with rudders having actual rudder surface area produces the best correlation in the rudder case.
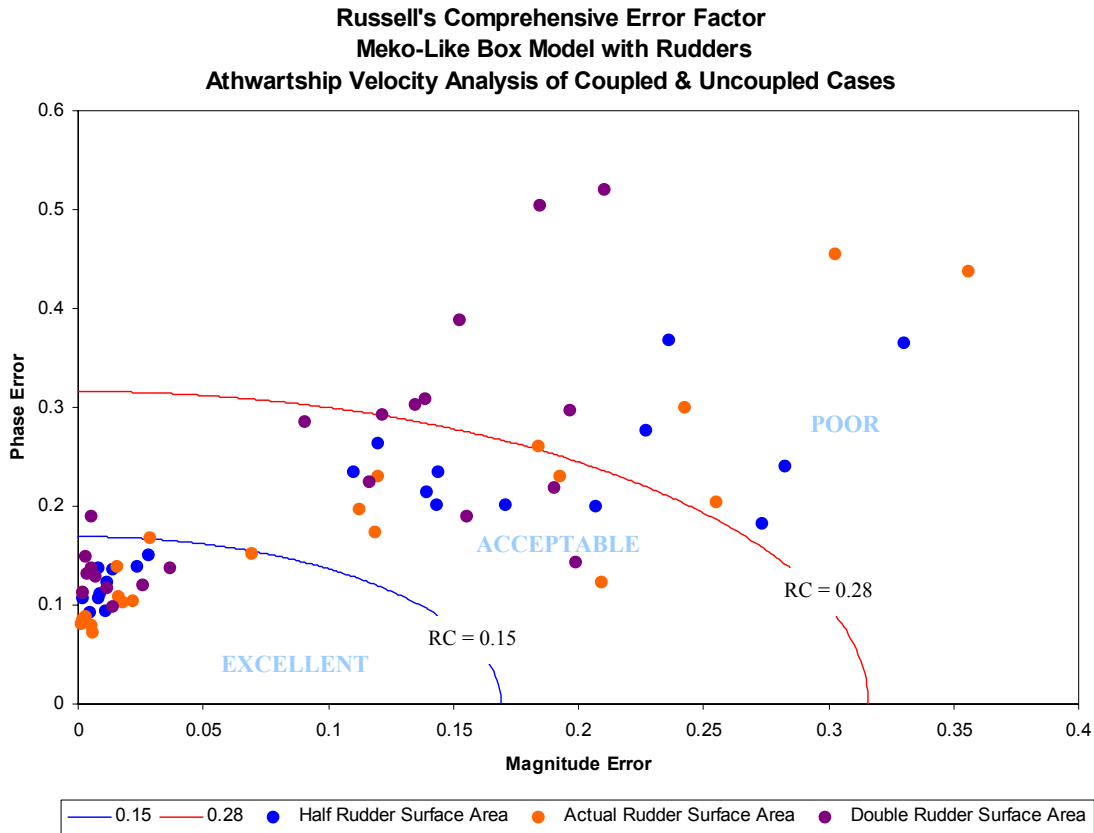
Figure 93.   Complete Russell's Error Factor Comparison for Meko-Like Box Model with Rudders (Athwartship Velocity)

The Russell's error factor comparison in the athwartship direction produces a slightly weak correlation between the coupled and uncoupled cases relative to the comparison in the vertical direction. As seen in Figure 93, most of the error values fall into the excellent and acceptable range, however, 17 points out of 66 are found in the poor region. Most of those falling outside the acceptable region are much greater than the 0.28 cut-off value. Yet, the number of the comparisons in the excellent region is much more than the rest of them, with 65 % of the nodes possessing Russell's Comprehensive error factors less than 0.15 as seen in Table 29. The meko-like box model with rudders

having the actual rudder surface area generates the best correlation between the coupled and uncoupled cases regarding the mean correlations.

The mean Russell's Comprehensive error factors were found to be 0.1129 and 0.1893 for the vertical and athwartship velocity responses, respectively. In comparison, the mean values, in the cases of half and double rudder surface areas, were 0.1155 and 0.1572 in the vertical direction and 0.2045 and 0.2195 in the athwartship direction, respectively. The mean correlations resulting from the vertical velocity analysis predict the improved correlation between the coupled and uncoupled cases if compared to those of the athwartship velocity analysis. Table 27 shows the truly calculated error magnitudes along with the mean and standard deviation values as supporting data when the rudder surface area is modeled as the actual rudder surface area. The other corresponding data tables for each set of Russell's error factor comparison plots can be found in Appendix G. As seen in these tables, overall Russell's error factors decrease as the nodes examined move from the rudder location on the hull. This indicates that the dynamic response of the uncoupled case anticipate the dynamic response of the coupled case more accurately far away from the rudder location on the hull.

Table 27. **Russell's Error Factors for Meko-Like Box Model with Rudders Having Actual Rudder Surface Area**

Simulation runtime = 500 msec					Meko-Like Box Model with Rudders Having Actual Rudder Surface Area					
					Vertical Velocity Comparison			Athwartship Velocity Comparison		
NODE	X (in)	Y (in)	Z (in)	Location	COUPLED & UNCOUPLED CASES			COUPLED & UNCOUPLED CASES		
					LS-DYNA/USA DATA (<250HZ)			LS-DYNA/USA DATA (<250HZ)		
					RM	RP	RC	RM	RP	RC
15	0	-20	0	Bulkhead	0.1477	0.1633	0.1951	0.0289	0.1686	0.1516
74	120	-140	0	Keel	0.0365	0.2814	0.2515	0.1185	0.1745	0.1869
81	120	140	0	Keel	0.0938	0.2693	0.2527	0.0694	0.1515	0.1477
148	0	-20	160	Bulkhead	0.1488	0.1365	0.1790	0.2422	0.2995	0.3413
214	120	-140	160	First Deck	0.0388	0.1113	0.1045	0.1125	0.1965	0.2007
221	120	140	160	First Deck	0.0351	0.1028	0.0963	0.2092	0.1237	0.2154
268	0	-20	280	Bulkhead	0.1466	0.1396	0.1795	0.3558	0.4376	0.4998
334	120	-140	280	Second Deck	0.0745	0.1292	0.1322	0.1926	0.2306	0.2663
341	120	140	280	Second Deck	0.0637	0.1193	0.1198	0.2553	0.2037	0.2895
388	0	-20	400	Bulkhead	0.1412	0.1475	0.1809	0.3025	0.4550	0.4843
434	120	-140	400	Top Deck	0.0645	0.1448	0.1404	0.1841	0.2603	0.2825

Simulation runtime = 500 msec					Meko-Like Box Model with Rudders Having Actual Rudder Surface Area					
					Vertical Velocity Comparison			Athwartship Velocity Comparison		
NODE	X (in)	Y (in)	Z (in)	Location	COUPLED & UNCOUPLED CASES			COUPLED & UNCOUPLED CASES		
					LS-DYNA/USA DATA (<250HZ)			LS-DYNA/USA DATA (<250HZ)		
					RM	RP	RC	RM	RP	RC
441	120	140	400	Top Deck	0.0714	0.1333	0.1340	0.1199	0.2298	0.2297
2454	1200	-20	0	Keel	0.0022	0.0414	0.0368	0.0153	0.1391	0.1240
3883	1800	-20	0	Keel	-0.0018	0.0704	0.0624	0.0160	0.1082	0.0969
5251	2400	-300	0	Keel	0.0242	0.1015	0.0925	-0.0020	0.1125	0.0997
5308	2400	-180	0	Keel	0.0008	0.0436	0.0387	-0.0031	0.0885	0.0785
5310	2400	-100	0	Keel	-0.0014	0.0388	0.0344	-0.0019	0.0848	0.0752
5315	2400	100	0	Keel	-0.0019	0.0417	0.0370	0.0014	0.0818	0.0725
5317	2400	180	0	Keel	-0.0004	0.0505	0.0447	0.0058	0.0725	0.0645
5320	2400	300	0	Keel	0.0074	0.0818	0.0728	0.0052	0.0790	0.0702
6741	3000	-20	0	Keel	0.0050	0.0710	0.0631	-0.0177	0.1026	0.0923
8170	3600	-20	0	Keel	-0.0001	0.0400	0.0355	-0.0216	0.1050	0.0950
Russell Error Correlation			Sum(E(X))		1.0966	2.4590	2.4838	2.1883	3.9053	4.1645
> 0.28	Poor		$Sum(E(X^2))$		0.1178	0.3689	0.3822	0.5048	0.9377	1.1329
< 0.15	Excellent		**Mean**		**0.0498**	**0.1118**	**0.1129**	**0.0995**	**0.1775**	**0.1893**
			Standard Deviation		0.0548	0.0669	0.0696	0.1169	0.1079	0.1281

Furthermore, to predict how well the correlation between the coupled and uncoupled cases was created, statistical data analysis was performed for each Russell's Comprehensive error factor resulting from the three different rudder surface areas. Table 28 shows this statistical study performed for the rudders having actual rudder surface area while the rest of the statistical analyses are in Appendix G. As seen in Table 28, it is obvious that the correlation of the vertical velocity response is much better than that of the athwartship velocity response based on the mean correlations and the percentages of the nodes although 86 % of the nodes produce the data within one standard deviation in both cases.

Table 28.   Statistical Data for Meko-Like Box Model with Rudders Having Actual Rudder Surface Area (Coupled and Uncoupled Cases)

Russell's Comprehensive Error Factor	Vertical Velocity Comparison	Athwartship Velocity Comparison
RC < 0.30	100 %	86 %
RC < 0.28	100 %	77 %
RC < 0.25	91 %	73 %
RC < 0.20	91 %	59 %
RC < 0.18	82 %	55 %
RC < 0.15	73 %	50 %
Mean RC	0.1129	0.1893
Standard Deviation	0.0696	0.1281
Mean + Standard Deviation	0.1825	0.3174
Data within One Standard Deviation	86 %	86 %

Table 29 represents the complete statistical data analysis including all the three different rudder surface areas to recognize the whole picture of the correlation process in case of the rudder. As seen in the case of the solid keel board, in general, the correlation results in the athwartship direction were found to be slightly weak than those in the vertical direction. This situation would specify that the vertical velocity response resulting from the shock simulation of the uncoupled case actually more accurately simulated the range of the motion of the coupled case. The magnitude error as well as the phase error both drives Russell's Comprehensive error factors higher in most cases for both vertical and athwartship velocity analyses. One of the possible contributors to the scattered data through the poor region in both directions is because of the poorer correlations in the neighborhood of the rudders. The mean correlation in the vertical direction was determined to be RC = 0.1286; well within the RC = 0.15 excellent limit. Moreover, the mean correlation in the athwartship direction was determined to be RC = 0.2044; well within the RC = 0.28 acceptable limit. The mean correlation in the athwartship direction represents the second worst case in the hull appendage analysis of the meko-like box model. Even though the data within one standard deviation was found to be in 85 % and 88 % of the nodes for the vertical and athwartship velocity comparisons, respectively, based on the mean correlations and the other percentages of the nodes, the overall results in the vertical direction seem to be better than those in the athwartship direction. However, this does not mean that the athwartship velocity analysis does not constitute a satisfactory correlation between the coupled and uncoupled cases.

Table 29. Complete Statistical Data for Meko-Like Box Model with Rudders (Coupled and Uncoupled Cases)

Russell's Comprehensive Error Factor	Vertical Velocity Comparison	Athwartship Velocity Comparison
RC < 0.30	98 %	82 %
RC < 0.28	97 %	74 %
RC < 0.25	86 %	67 %
RC < 0.20	85 %	50 %
RC < 0.18	77 %	48 %
RC < 0.15	65 %	47 %
Mean RC	0.1286	0.2044
Standard Deviation	0.0798	0.1176
Mean + Standard Deviation	0.2084	0.3220
Data within One Standard Deviation	85 %	88 %

c. Detailed Velocity Plots

Figures 94, 95, 96 and 97 represent the time history plots of the vertical and athwartship velocity responses between the no appendage case (except node 74) and the rudder case, which was modeled as coupled and uncoupled structures with respect to the surrounding fluid. These plots help visualize Russell's error factor correlations discussed previously. The rest of the complete set of the plots can be found in Appendices D and E. Figure 94 with node 74 illustrates the time history response of a node located on the interface between the hull and rudder on the starboard side of the meko-like box model, representing the worst correlation at RC = 0.3866 in the vertical velocity analysis of Russell's error factor comparison. This worst correlation occurs between the coupled and uncoupled cases when the rudder surface area exposed to UNDEX was double. As seen in Figure 92, the overall correlation of the vertical velocity analysis is affected by the relatively poor correlations of the rudders, which correspond to the nodes located on the interface or close to the rudders; node 74 stands for one of these nodes located on the interface. If all of the tables, which show truly calculated error magnitudes, are studied in terms of location, it can be seen that, as the location of the nodes moves from the location of rudders, the Russell's error factors decrease in general relative to the error factors of the nodes close to these rudders. As seen in Figure 94, the response of the uncoupled case in the vertical direction could not capture peak responses of the coupled case at the same phase while the magnitudes of these peak responses also differ from each other. Since the phase between the coupled and uncoupled cases does not match particularly in the early time response, the phase error drives the correlation

140

higher especially in this case. However, node 5310, located far from the location of the rudders, produces the best correlation in the vertical velocity analysis of rudders. The Russell's Comprehensive error is 0.0344 in this case. The model corresponds to the case of the actual rudder surface area. Figure 95 shows how similar the curves developed from the coupled and uncoupled cases in terms of phase and magnitude. That the correlation lies in the excellent region verifies this exceptional relationship occurring between the coupled and uncoupled cases. It can be concluded that the response of node 5310 produces an outstanding correlation between the coupled and uncoupled cases because this node is far from the location of the rudders. Since, in general, the uncoupled case predicts very well based on the Russell's error factor comparison, the complete set of the time history plots of the vertical velocity response represents that the uncoupled case produces sufficiently accurate results, verifying this good correlation found in the vertical velocity analysis. As previously stated, the meko-like box model with rudders having the actual rudder surface area generates the best correlation between the coupled and uncoupled cases regarding the mean correlations, while the case of the double rudder surface area produces the worst. Since it is concluded that the percentage of the surface area is the most driving factor of the differences due to the inclusion of the hull appendage as seen in all of the cases investigated up to this point, the worst correlation occurs in the case of the double surface area, which is 3.3 % of the underwater surface area of the structural model, may be because the responses are affected more by the uncoupled modeling of the rudders due to this surface area.

Meko-Like Box Model with Rudders
Node 74 at Keel (x=120 y=-140 z=0)
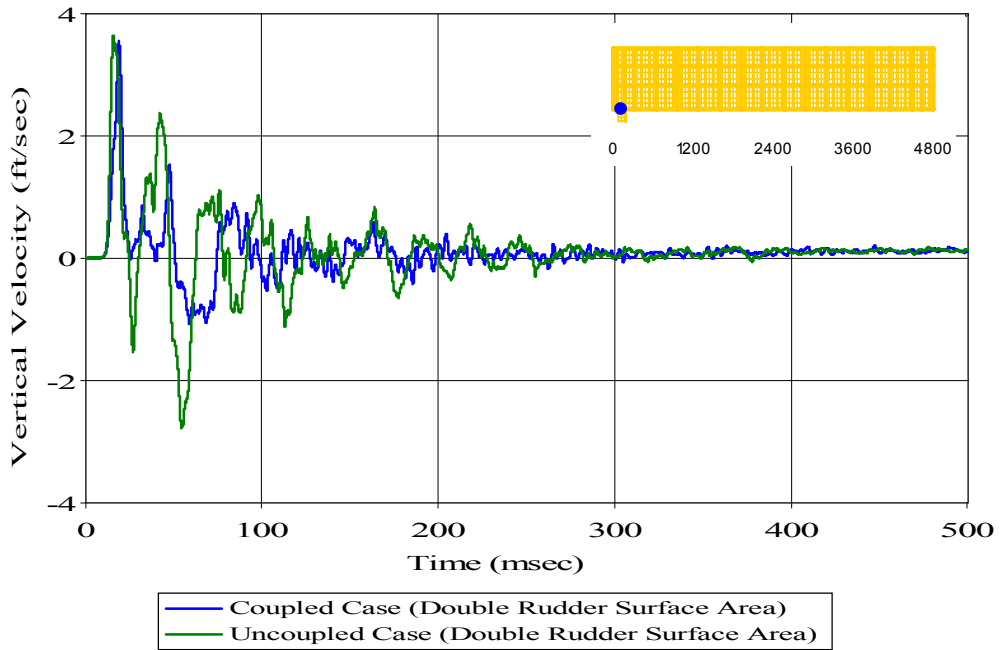
Figure 94.   **Keel Node 74: (RM = 0.2660, RP = 0.3457, RC = 0.3866)**

Meko-Like Box Model with Rudders
Node 5310 at Keel (x=2400 y=-100 z=0)
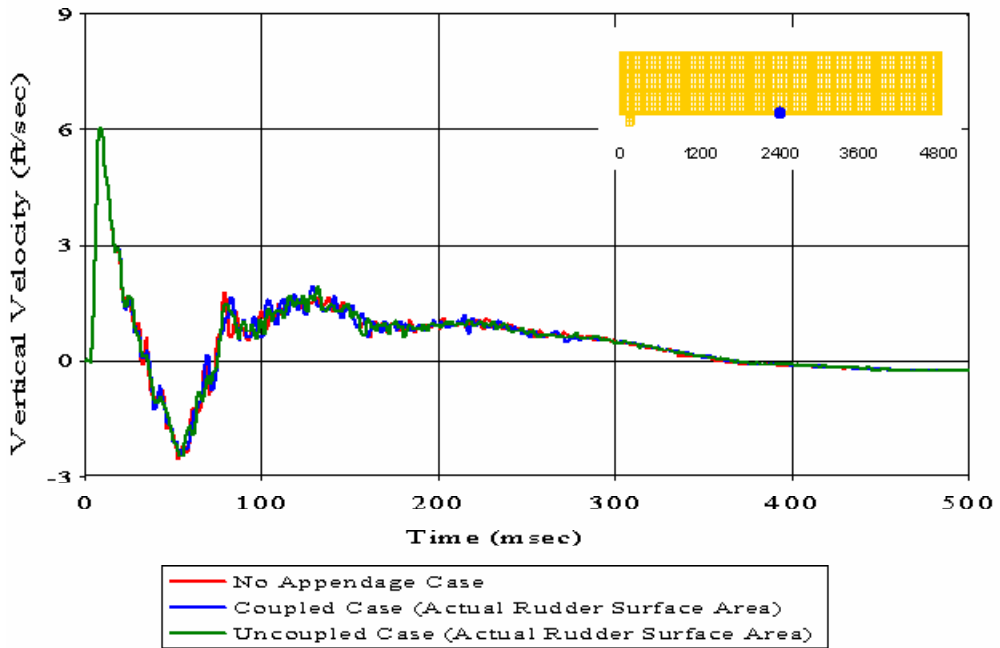
Figure 95.   **Keel Node 5310: (RM = -0.0014, RP = 0.0388, RC = 0.0344)**

142

The worst correlation found in the athwartship velocity analysis takes place on node 268 along with Russell's Comprehensive error factor of 0.4998. In the case of the actual rudder surface area, this very poor correlation is created. As expected, the location of this node is very close to the location of rudders constructed on the hull. As seen in Figure 96, the phases do not match along the overall response as well as the magnitudes of the peak values. This explains that both the phase and magnitude errors found in this correlation drives the Russell's Comprehensive error factor higher. Additionally, it can be said that the uncoupled case generates an over-damped response relative to the response of the coupled case. Again, this correlation along with the other poor correlations found at the vicinity of the rudder affect the overall correlation results in the athwartship direction. Furthermore, Figure 97 with node 5317 demonstrates the best correlation at RC = 0.0645 in the athwartship direction with respect to the overall correlations in Table 29. The uncoupled case corresponding to the case of the actual rudder surface area anticipates the dynamic response of the coupled case, which represents the real case in an UNDEX event, very well throughout the response including the late time response. This node is located far away from the location of the rudders, indicating that the uncoupled case predicts the response of the coupled case much better away from the location of rudders. Since the best correlations occur between the coupled and uncoupled cases when the rudders have been modeled by using the actual rudder surface area, by looking into the Russell's error factor comparison and the complete time history plots, it can be concluded that the uncoupled case of the actual rudder surface area predicts the coupled case well in both vertical and athwartship directions relative to the other cases in this analysis as the similar situation seen in the case of the solid keel board. Again, as expected, the case of double rudder surface area produces the worst correlations according to the mean correlations.
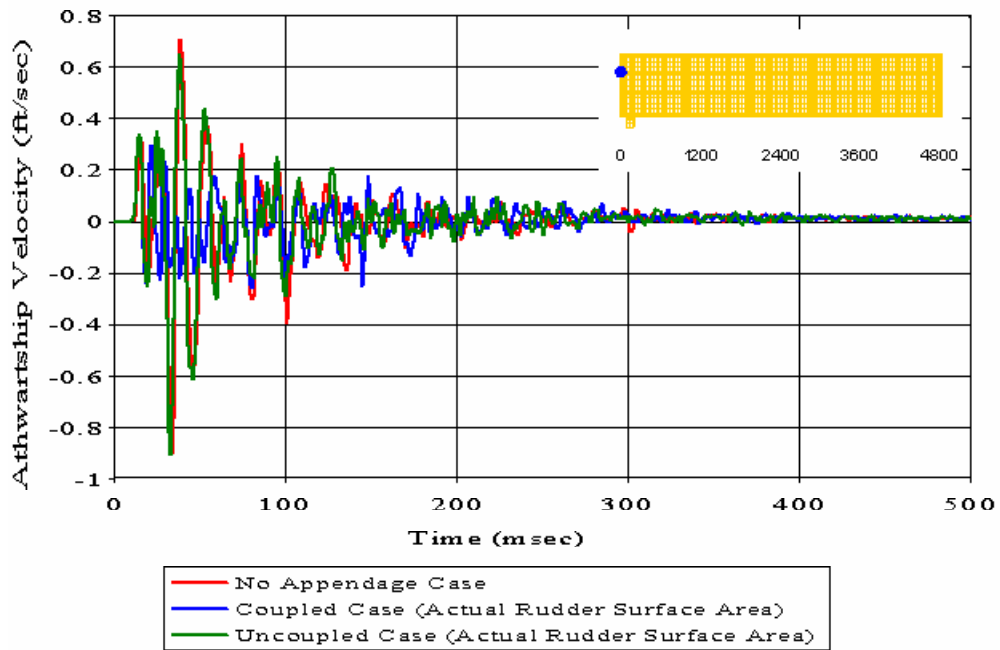
Figure 96. Bulkhead Node 268: (RM = 0.3558, RP = 0.4376, RC = 0.4998)
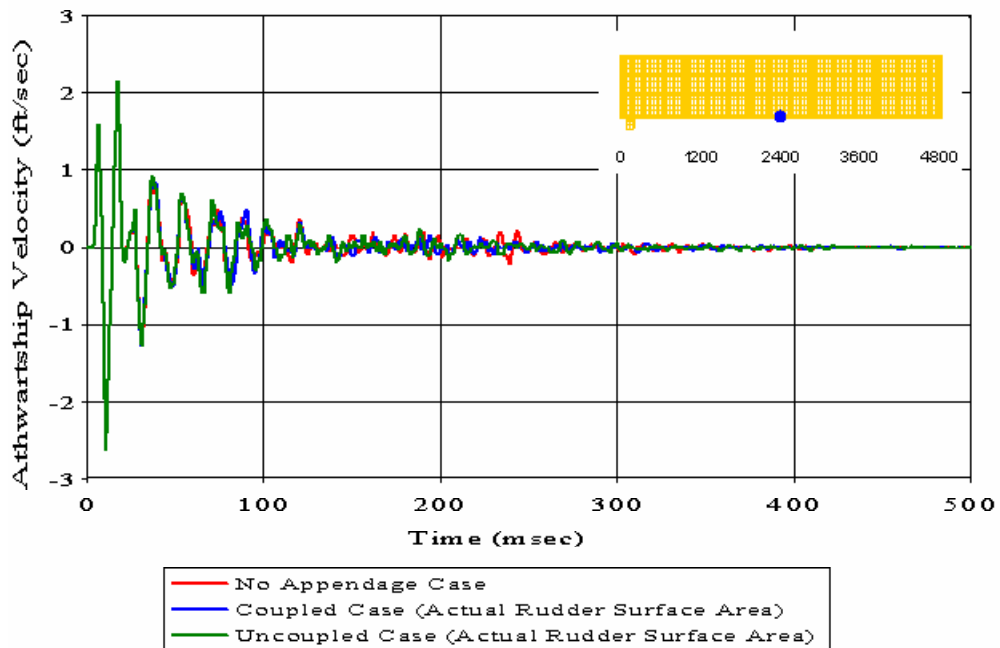
Figure 97. Keel Node 5317: (RM = 0.0058, RP = 0.0725, RC = 0.0645)

One of the nodes located on the interface between the hull and rudder on the port side, 81 produces the worst correlation for the vertical velocity analysis in the case of actual rudder surface area by giving RC = 0.2527. Figure 98 illustrates this worst correlation occurring between the coupled and uncoupled cases.
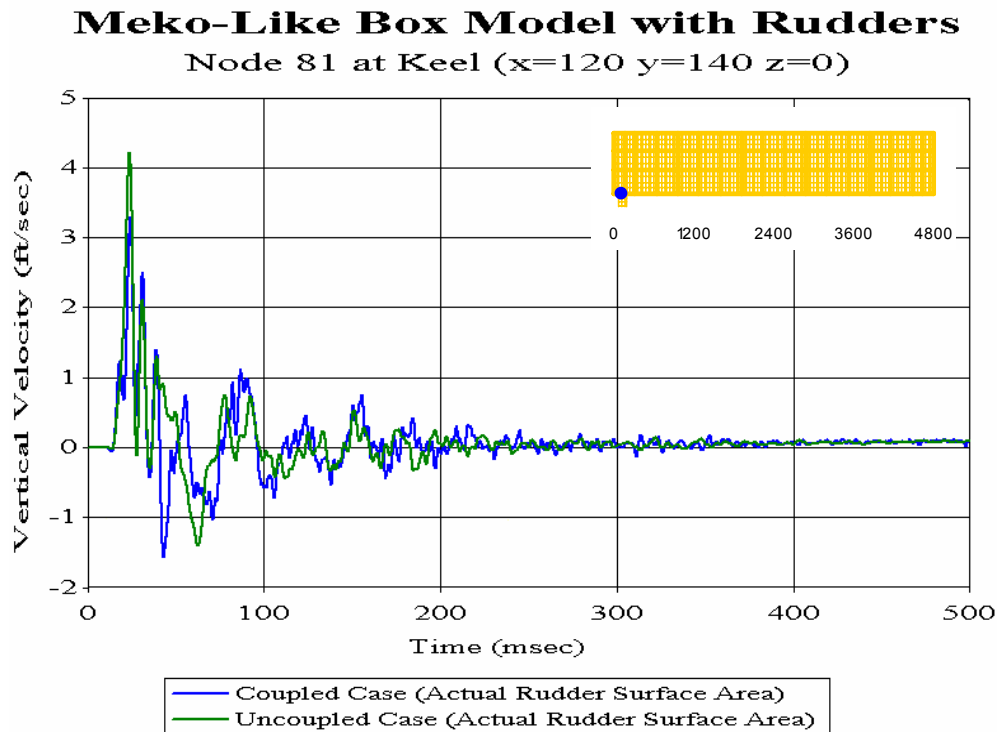
Figure 98. Keel Node 81: (RM = 0.0938, RP = 0.2693, RC = 0.2527)

d. *Shock Spectra Plots*

In the rudder case, shock spectra plots of 10 nodes located during the meko-like box model will be conducted in both vertical and athwartship directions. The figures presented below cover the best and worst correlations according to the Russell's Comprehensive error factors found in the case of the rudder having actual rudder surface area. The case of actual rudder surface area will be investigated in this shock spectra analysis only. The complete set of shock spectra plots can be found in Appendix F.

Figures 99 and 100 with nodes 81 and 5310, respectively, represent the worst and best correlations, respectively, occurring in the vertical direction while Figures 101 and 102 of 268 and 5317, respectively, correspond to the worst and best correlations,

respectively, in the athwartship direction. As seen in previous hull appendage cases, it should be noticed that the shock spectra plots of the best correlations create more matched results between the coupled and uncoupled cases than those of the worst correlations in the frequency domain. If all of the shock spectra plots are evaluated in terms of the magnitudes of the vertical and athwartship motions, the majority of all the data presented in both vertical and athwartship shock spectra plots is below 7 to 8 ft/sec in magnitude of velocity. On the other hand, most of the peak values obtained from the vertical and athwartship velocity analyses lay between 10 and 12 ft/sec while some of them reach 20 ft/sec particularly in the athwartship direction.
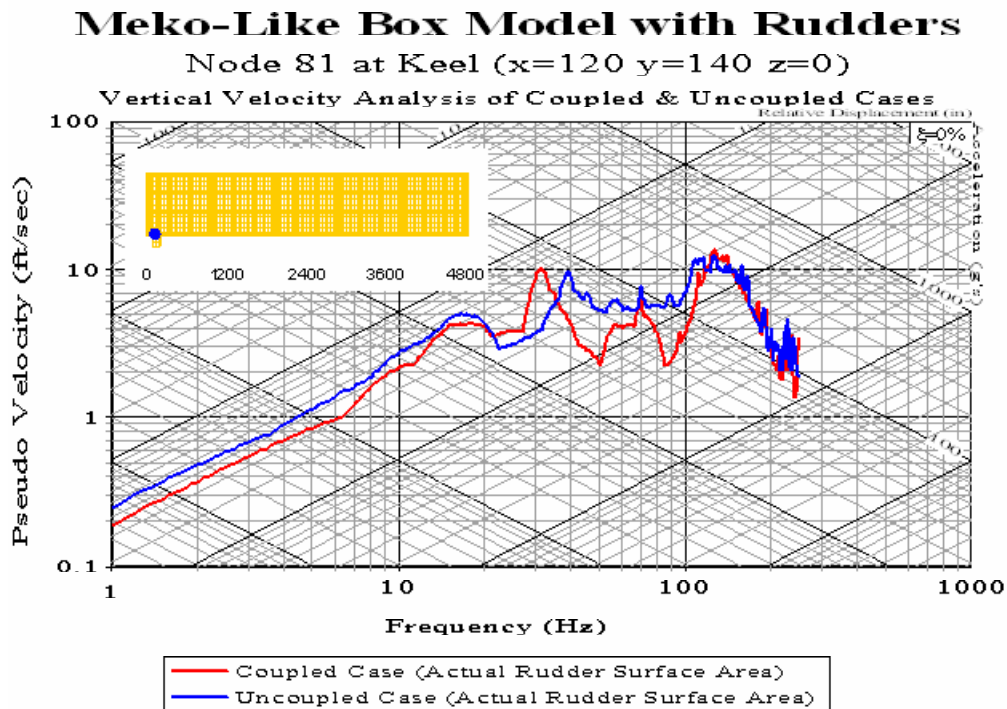
Figure 99.   Shock Spectra Plot: Keel Node 81
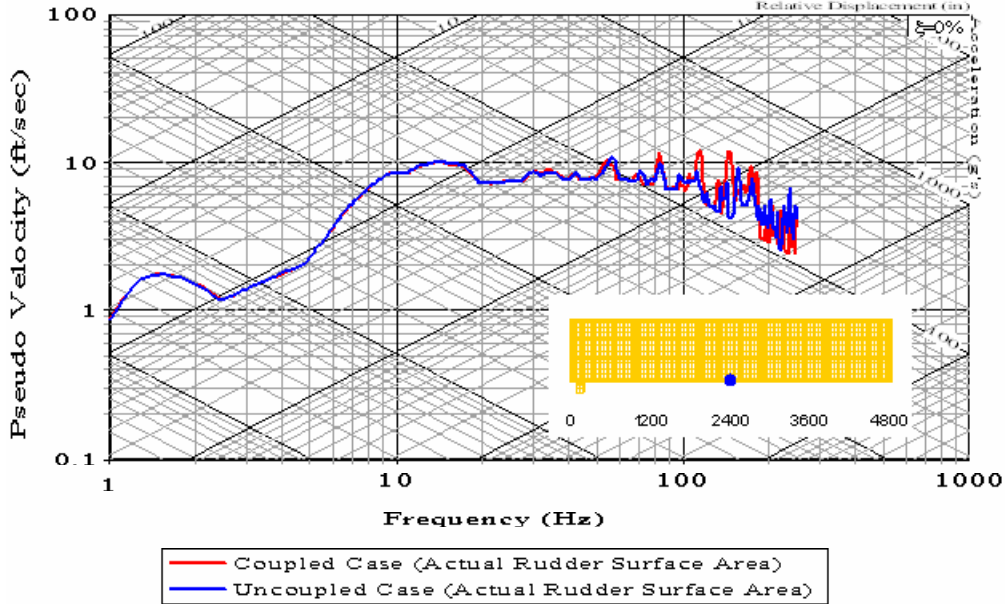
Figure 100.   **Shock Spectra Plot: Keel Node 5310**
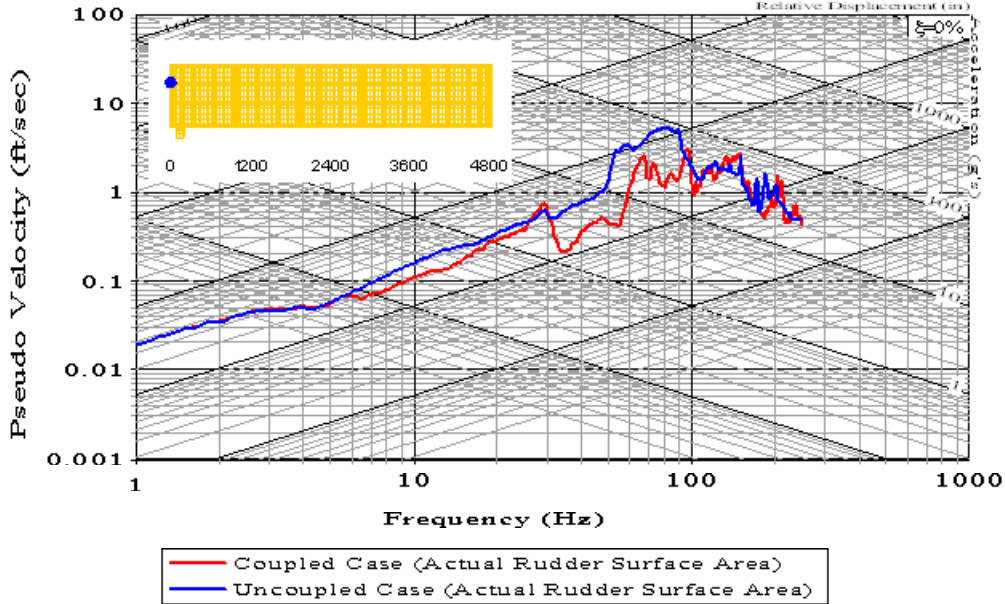
Figure 101.   **Shock Spectra Plot: Bulkhead Node 268**
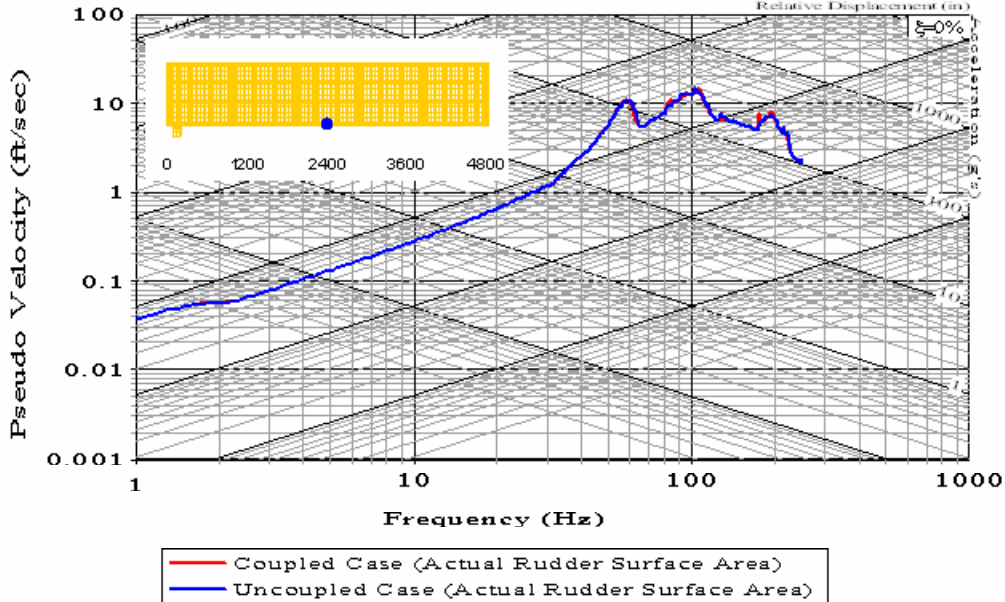
Figure 102.   Shock Spectra Plot: Keel Node 5317

The uncoupled case has predicted the response of the coupled case sufficiently well in the 1 to 50 Hz range for the vertical analyses while the uncoupled case in the athwartship direction generates relatively more matched results with the coupled case in the 1 to 100 Hz in particular. In the rest of the range in both directions, some deviations from the coupled case, which is the actual case in an UNDEX event, occur. The majority of the vertical shock spectra plots display a gradual rise in amplitude up to 18 Hz as the frequency increases while most of the athwartship shock spectra plots exhibit a gradual rise, sometimes with oscillation, up to the 20 to 80 Hz range. All of the peak values in the vertical direction occur between 50 and 100 Hz or between 100 and 250 Hz including oscillations near the peak values, and then a downward trend takes place. It has most of the same characteristics of the peak values in the athwartship direction. Notice that the uncoupled case somewhat over predicts the low and high frequency responses of the coupled case for some cases in both directions. Nevertheless, according to all of the shock spectra plots of both analyses, the two curves found in the

148

figures still remain close enough. Table 30 summarizes the shock spectra analysis in the rudder case along with the frequency range.

Table 30.   Summary of Shock Spectra Analysis for Meko-Like Box Model with Rudders

Frequency Range	Trend of Curves	Vertical Velocity Analysis	Ayhwartship Velocity Analysis
1 to 20 Hz	Gradual rise up to 18 Hz in the vertical direction	Uncoupled case closely matches or slightly over predicts coupled case	Uncoupled case closely matches or barely over predicts coupled case
20 to 50 Hz	Peak values or small oscillations near the peak values occur in vertical direction, gradual rise in athwartship direction	Uncoupled case closely matches or slightly over predicts coupled case	Uncoupled case closely matches or barely over predicts coupled case
50 to 100 Hz	Peak values occur with oscillation up to 12 ft/sec in vertical direction, gradual rise up to peak value of 12 ft/sec with very small oscillations or downward trend in athwartship direction	Uncoupled case closely matches or over predicts coupled case	Uncoupled case closely matches or over predicts coupled case
100 to 250 Hz	High degree of oscillation and peak values occur (up to 12 ft/sec in vertical direction, 20 ft/sec in athwartship direction)	Uncoupled case closely matches or over predicts coupled case	Uncoupled case closely matches or slightly over predicts coupled case

5.   Comparison Results

Table 31 presents the complete statistical data resulting from all of the cases investigated in the hull appendage analysis of the meko-like box model. This table has been included as an overview of the data presented with regard to the vertical and athwartship velocity response analyses conducted between the coupled and uncoupled cases throughout the meko-like box model.

Overall, the correlation results in the athwartship direction were found to be slightly weaker than those in the vertical direction. Using the same 250 Hz low-pass filtering via the UERD Tools built in function, the mean correlation between the coupled and uncoupled cases in the vertical direction was determined to be $RC = 0.1152$; well within the $RC = 0.15$ excellent limit, while the mean correlation in the athwartship direction was found to be $RC = 0.1853$; still well within the $RC = 0.28$ acceptable limit.

Table 31. **Complete Statistical Data for The Hull Appendage Analysis of Meko-Like Box Model (Coupled and Uncoupled Cases)**

Russell's Comprehensive Error Factor	Vertical Velocity Comparison	Athwartship Velocity Comparison
RC < 0.30	97 %	89 %
RC < 0.28	97 %	83 %
RC < 0.25	90 %	75 %
RC < 0.20	89 %	60 %
RC < 0.18	84 %	56 %
RC < 0.15	76 %	48 %
Mean RC	0.1152	0.1853
Standard Deviation	0.0763	0.0926
Mean + Standard Deviation	0.1915	0.2779
Data within One Standard Deviation	86 %	83 %

One of the possible contributors to this slightly less favorable correlation in the athwartship direction is the inherently smaller magnitudes found in the athwartship velocity response as compared to those in the vertical velocity response. However, based on the mean correlations between the coupled and uncoupled cases and the percentages found in the vertical and athwartship directions, there is a high rate of correlation for both vertical and athwartship velocity comparisons examined in the hull appendage analysis of the meko-like box model. The overall results obtained from the vertical and athwartship velocity response data throughout the meko-like box model indicate that the uncoupled case predicts the dynamic response of the coupled case very well and does consistently produce very satisfactory results as compared to the coupled case data.

VII. CONCLUSIONS AND RECOMMENDATIONS

A. RESULTS

Using the data obtained from the shock simulations conducted on meko-like box model, this thesis presented a detailed study of the validity of including hull appendages, the projected coupling scheme for these appendages, and resulting effects on the vertical and athwartship velocity responses by comparing the data resulting from the virtual shock environment analysis based on the modeling and simulation methodology established by the Shock and Vibration Computational Laboratory at NPS. Based on the findings presented in the hull appendage analysis of the meko-like box model, it was determined that the inclusion of hull appendages such as rudders, shafts and keel boards affect the dynamic response of the meko-like box model. The overall comparisons, resulting from the hull appendages having been modeled as coupled and uncoupled structures, obtained from the vertical and athwartship velocity response data throughout the meko-like box model, indicate that the uncoupled case predicts the dynamic response of the coupled case very well and does consistently produce very satisfactory results as compared to the coupled case data. The results produced from this series of parametric studies addresses some of the questions concerning the influence that modeled hull appendages have upon the dynamic response of a multi-degree-of-freedom structural ship model surrounded by a fluid mesh subjected to UNDEX shock simulation.

Looking into the overall results for coupled and uncoupled cases, it can be said that the inclusion of the solid and shell keel boards considerably affects the dynamic response of the structure, especially near the location of the keel boards, while different weight percentages of the solid keel board cause small differences in the dynamic response of the structure. However, the inclusion of the open keel board and rudders on the structure does not have much effect on the dynamic response except the response of the neighborhood around where the open keel board and rudders were constructed. Investigating the surface area percentages of the hull appendages examined herein, these findings imply that any hull appendage, which has a sufficiently large surface area percentage, on the order of 10 % or greater with respect to the underwater surface area of the structural model exposed to UNDEX, noticeably affects the dynamic response of the

whole system. This is particularly true in the immediate region of the location of the hull appendage. Based on this result, it can be concluded that the addition of any hull appendage containing a significant surface area is a more important driving factor affecting the dynamic response than the weight percentages of this hull appendage constructed on the structure. This conclusion is confirmed by the case of the double rudder surface area which is more inclined to have an effect on the dynamic response than the cases of the half and actual rudder areas. Overall, it was discovered that the inclusion of the hull appendage influences the vertical velocity response more than the athwartship velocity response.

It can be said that, in general, the correlation results of the athwartship velocity response between the coupled and uncoupled cases were found to be slightly less desirable than those of the vertical velocity response. One possible contributor to this less favorable correlation in the athwartship direction is the inherently smaller magnitudes found in the athwartship velocity response as compared to those in the vertical velocity response. Nevertheless, based on the overall Russell's Comprehensive error factors, which, in general, fall into the excellent and acceptable regions, exceptionally good mean correlations between the coupled and uncoupled cases, and the overall percentages found in the vertical and athwartship directions, it is evident that there is a high rate of correlation for both vertical and athwartship velocity comparisons examined in the hull appendage analysis of the meko-like box model. Therefore, the results developed from the analysis of the coupled and uncoupled cases proved to be very consistent with the primary and secondary velocity response correlations performed throughout the structure.

B.   FUTURE STUDIES

Possibilities for further courses of study are presented. Based on the derived conclusions, the emphasis should be on the hull appendages located on the keel of the ships in order to simulate the ship shock trials more successfully in the vertical and athwartship directions of the future analyses. In previous ship shock trial simulations, the predicted dynamic of the shock trials in the athwartship direction was less favorable. This could possibly be overcome in future ship shock analyses by including the hull appendages existing on the actual ship which were not previously modeled. Furthermore,

in this analysis, it is suggested that the uncoupled case very sufficiently predicts the dynamic response of the coupled case. Nevertheless, the conclusions attained through the comprehensive analysis of the meko-like box model simulation effort can be further supported by focused study of localized phenomena experienced during an UNDEX event such as whipping. In addition, since the same charge location was used to examine the hull appendage analysis of the meko-like box model, the shock simulations can be conducted by utilizing the other charge locations. The conclusion that the uncoupled case predicts the coupled case very accurately is very significant because the simplicity of the creation of the fluid mesh for the uncoupled case saves tremendous time in the modeling and simulation process, and thus reduces cost. This analysis is solely based on the virtual shock environment, i.e., the comparisons are conducted between the two shock simulation results. Validation of the presented coupling method, that is, using the uncoupled case, is to be verified by comparing the measured ship shock trial data to the shock simulation results in the future.

THIS PAGE INTENTIONALLY LEFT BLANK

APPENDIX A. MATLAB PROGRAM FOR BULK CAVITATION REGION

The following MATLAB program code was written using MATLAB® 6.5 Release 13. This program computes the bulk cavitation region boundaries and provides a visualization of the bulk cavitation region by allowing options for the user to select the charge type, the vertical and horizontal distances of the whole region of interest, the charge weight and the charge depth. This MATLAB program was used to calculate the bulk cavitation region boundaries of the MEKO-LIKE BOX MODEL.

```
clear all; clc;

% Input for type of explosive

TYPE = menu ('TYPE OF EXPLOSIVE', 'TNT','HBX-1','PENTOLITE','CANCEL');
if     TYPE == 1
    %Parameters are for TNT type charge
    K1 = 22505;          %Pmax
    A1 = 1.18;           %Pmax
    K2 = 0.058;          %Decay Constant
    A2 = -0.185;         %Decay Constant
elseif TYPE == 2
    %Parameters are for HBX-1 type charge
    K1 = 22347.6;        %Pmax
    A1 = 1.144;          %Pmax
    K2 = 0.056;          %Decay Constant
    A2 = -0.247;         %Decay Constant
elseif TYPE == 3
    %Parameters are for PENTOLITE type charge
    K1 = 24589;          %Pmax
    A1 = 1.194;          %Pmax
    K2 = 0.052;          %Decay Constant
    A2 = -0.257;         %Decay Constant
elseif TYPE == 4
    return
end

% Input for cavitation space

if TYPE == 1 | TYPE == 2 | TYPE == 3
    DISTANCE = menu ('VERTICAL AND HORIZONTAL DISTANCE','100x1000',...
        '100x2000','100x2500','100x3000','CANCEL');
    if DISTANCE == 1
        VER = 100;
        HOR = 1000;
    elseif DISTANCE == 2
        VER = 100;
        HOR = 2000;
    elseif DISTANCE == 3
```

```matlab
        VER = 100;
        HOR = 2500;
    elseif DISTANCE == 4
        VER = 100;
        HOR = 3000;
    elseif DISTANCE == 5
        return
    end
end

%Input for charge weight and charge depth

if DISTANCE == 1 | DISTANCE == 2 | DISTANCE == 3 | DISTANCE == 4
    PROMPT1 = {'SELECT FIRST CHARGE WEIGHT','SELECT SECOND CHARGE
    WEIGHT','SELECT THIRD CHARGE WEIGHT'};
    DEFAULT1 = {'1000','5000','10000'};
    DATA1 = inputdlg(PROMPT1,'CHARGE WEIGHT INPUT',1,DEFAULT1);
    W1 = str2num(char(DATA1(1)));
    W2 = str2num(char(DATA1(2)));
    W3 = str2num(char(DATA1(3)));
    if isempty(DATA1)==1
        return
    end
    PROMPT2 = {'SELECT FIRST CHARGE DEPTH','SELECT SECOND CHARGE
    DEPTH','SELECT THIRD CHARGE DEPTH'};
    DEFAULT2 = {'164','213','262.5'};
    DATA2 = inputdlg(PROMPT2,'CHARGE DEPTH INPUT',1,DEFAULT2);
    D1 = str2num(char(DATA2(1)));
    D2 = str2num(char(DATA2(2)));
    D3 = str2num(char(DATA2(3)));
    if isempty(DATA2)==1
        return
    end
end

% Atmospheric Constants

P_atm = 14.7;       %Atmpospheric pressure psi
Gamma = 63.989/144; %Weight density of water lb/ft^3
C = 5.078;          %Acoustic velocity of water ft/msec

counter = 0;
for W = [W1,W2,W3]              %Equivalent charge weights
    for D = [D1,D2,D3]          %Charge depths
        counter = counter+1;
        A = zeros(VER,HOR);
        for y = 1:(VER+1)
            for x = 1:(HOR+1)
                R1 = sqrt((D - (y-1))^2 + (x-1)^2);
                R2 = sqrt((D + (y-1))^2 + (x-1)^2);
                theta = K2*(W^(1/3))*(((W^(1/3))/R1)^(A2));
                P =(K1*(W^(1/3)/R1)^(A1))*(exp(-(R2-R1)/(C*theta)))+...
                    P_atm + Gamma*(y-1) - (K1*((W^(1/3)/R2)^(A1)));

                AA = (K1*(W^(1/3)/R1)^(A1))*(exp(-(R2 -R1)/(C*theta)));
                BB = -AA/(C*theta)*(1+(((R2-2*D*((D+(y-1))/R2))/R1)*...
                    ((A2*R2/R1) - A2 - 1)));
```

156

```
                    CC = -(A1*AA/R1^2)*(R2 - 2*D*((D+(y-1))/R2));
                    DD = Gamma*((D+(y-1))/R2) ;
                    EE = (A1/R2)*(AA+P_atm + Gamma*(y-1));
                    G = BB + CC + DD + EE;

                    if P > 0.001
                        if G < 0
                            A(y,x) = 1;
                        end
                    end
                    if G > 0
                        A(y,x) = 1;
                    end
                end
            end

            temp(:,:,counter) = A;
        end

    end

    switch TYPE
        case 1
            type ='TNT';
        case 2
            type ='HBX-1';
        case 3
            type ='PENTOLITE';
    end

    % Plots for different charge weights and charge depths

    figure(1)
    orient landscape
    subplot(3,1,1)
    hold on
    spy(temp(:,:,1))
    title(['Bulk Cavitation Region for Underwater Explosion:',...
    num2str(W1),' lb ',type,' Charge at ',num2str(D1),' ft'])
    xlabel('Radius (ft)')
    ylabel('D (ft)')
    axis([0 HOR 0 VER])
    subplot(3,1,2)
    spy(temp(:,:,2))
    title(['Bulk Cavitation Region for Underwater Explosion:',...
    num2str(W1),' lb ',type,' Charge at ',num2str(D2),' ft'])
    xlabel('Radius (ft)')
    ylabel('D (ft)')
    axis([0 HOR 0 VER])
    subplot(3,1,3)
    spy(temp(:,:,3))
    title(['Bulk Cavitation Region for Underwater Explosion:',...
    num2str(W1),' lb ',type,' Charge at ',num2str(D3),' ft'])
    xlabel('Radius (ft)')
    ylabel('D (ft)')
    axis([0 HOR 0 VER])
    set(gcf,'Units','normalized');
```

157

```
set(gcf,'Position',[0.01,0.04,0.98,0.86]);

figure(2)
orient landscape
hold on
subplot(3,1,1)
spy(temp(:,:,4))
title(['Bulk Cavitation Region for Underwater Explosion:',...
num2str(W2),' lb ',type,' Charge at ',num2str(D1),' ft'])
xlabel('Radius (ft)')
ylabel('D (ft)')
axis([0 HOR 0 VER])
subplot(3,1,2)
spy(temp(:,:,5))
title(['Bulk Cavitation Region for Underwater Explosion:',...
num2str(W2),' lb ',type,' Charge at ',num2str(D2),' ft'])
xlabel('Radius (ft)')
ylabel('D (ft)')
axis([0 HOR 0 VER])
subplot(3,1,3)
spy(temp(:,:,6))
title(['Bulk Cavitation Region for Underwater Explosion:',...
num2str(W2),' lb ',type,' Charge at ',num2str(D3),' ft'])
xlabel('Radius (ft)')
ylabel('D (ft)')
axis([0 HOR 0 VER])
set(gcf,'Units','normalized');
set(gcf,'Position',[0.01,0.04,0.98,0.86]);

figure(3)
orient landscape
hold on
subplot(3,1,1)
spy(temp(:,:,7))
title(['Bulk Cavitation Region for Underwater Explosion:',...
num2str(W3),' lb ',type,' Charge at ',num2str(D1),' ft'])
xlabel('Radius (ft)')
ylabel('D (ft)')
axis([0 HOR 0 VER])
subplot(3,1,2)
spy(temp(:,:,8))
title(['Bulk Cavitation Region for Underwater Explosion:',...
num2str(W3),' lb ',type,' Charge at ',num2str(D2),' ft'])
xlabel('Radius (ft)')
ylabel('D (ft)')
axis([0 HOR 0 VER])
subplot(3,1,3)
spy(temp(:,:,9))
title(['Bulk Cavitation Region for Underwater Explosion:',...
num2str(W3),' lb ',type,' Charge at ',num2str(D3),' ft'])
xlabel('Radius (ft)')
ylabel('D (ft)')
axis([0 HOR 0 VER])
set(gcf,'Units','normalized');
set(gcf,'Position',[0.01,0.04,0.98,0.86]);
```

APPENDIX B.   TRUEGRID MODELING OF MEKO-LIKE BOX MODEL

A.   STRUCTURAL MODELING

The structural modeling portion of this appendix covers the detailed process for generating a structural finite element mesh (meko-like box model), which is a rectangular barge in this case, using the special TrueGrid feature, **BLOCK** command. The fundamentals of utilizing TrueGrid will not be covered here and some familiarity or experience with the code will be assumed. If additional information for using TrueGrid is desired, it can be found in the TrueGrid user manual [Ref. 20].

Basically, the **BLOCK** command is the standard way to generate parts in TrueGrid. When this command is issued, the previous part (if any) is ended as if the **ENDPART** command had been used. The part generating procedure in TrueGrid is as follows, with important commands and menu selections, which are indicated in bold and all capital letters for emphasis:

1.   The **TITLE** command can be used to name the structural or the complete model that the user will create.

2.   The **LSDYMATS** command, which is one of the material commands defined in TrueGrid, is used to characterize the material types of the structural or the complete model including the fluid mesh. This command can be utilized in the TrueGrid code file before each element type such as beam, shell and solid elements has been created. After the **LSDYMATS** has been used to define the material type of the element such as Belytschko-Schiwer beams or Belytschko-Tsay shells, the specifications of the elements such as the cross-section area of the beam elements or the shell thickness of the shell elements can be inputted.

3.   Next, the **PARTS** menu should be selected and the **BLOCK** option must be chosen. Using this option, the user creates a block part. The block or the blocks that have been generated will serve as the "main parts" for the structural mesh. These block parts are created in the same way as a block using the TrueGrid's extrusion feature, the **BLUDE** command which will be described in the part of the fluid modeling. The **BLOCK** command allows the user to create a block part with solid elements or with shell elements. Six lists of numbers follow the **BLOCK** command. The first three lists consist of integers and each list ends with a semi-colon. The second three lists are of real numbers, which indicate the location of the block part to be created and each list is optionally terminated by a semi-colon [Ref. 20]. The first list of integers must start with a 1 or -1. The

integers that follow must be zero or have an absolute value greater than the absolute values of the integers that preceded it in that list. These numbers tell TrueGrid the number of nodes to be created in the first dimension of the computational mesh. A positive integer indicates that there will be a partition at that nodal index in the first dimension of the computational mesh. These partitions are used to break the part into multiple structured blocks. When positive integers are used, solid elements are created. A negative integer in the list also produces a partition in the mesh with a nodal index corresponding to the absolute value of the integer, with shell elements created along that partition in the computational mesh. For the meko-like box model, one block part was created with the shell elements.

4.   The **MATE** command can be used to assign a material number for the block part created. This will be the part number used in the LS-DYNA input deck. The material assignment can be overwritten by other commands (**MT**, **MTI**) for any combination of the regions of the part. The **MT** and **MTI** commands assign a material number to a region, overriding any previous material specifications.

5.   The global beam cross-section definition **BSD** is used to define the specifications of the cross-section of the beam elements to be created. This command overrides the values that have been defined in the **LSDYMATS** command.

6.   To create the beam (stiffness) elements on the structure, the commands **IBMI**, **JBMI** and **KBMI** are utilized. These commands generate an array of beam elements conforming to the geometry and nodes of a solid or shell regions in three different directions. This feature of TrueGrid is useful in generating structural elements embedded within the solid or shell region. Then the **MERGE** command, which will be explained in the fluid modeling part, can be used to combine all the elements created for the structural model.

7.   The **PM** command is used to assign a point mass to the structural mesh generated. This command allows the user to select no mass displacement or no mass rotation in the desired direction.

To demonstrate how the structural finite element mesh was created, the portion of the structural modeling in the TrueGrid code file will be illustrated as follows.

1.   Structural Modeling Part of the TrueGrid Code File

The structural finite element mesh of the meko-like box model was created in the following way as its procedure was described above.

```
title 3d box model
lsdymats 1 1 struct
head belytschko-schiwer beams
beam elfom bs carea 1.7437535 iss 0.01267 itt 5.069 irr
0.049 rho 7.350e-4 e 3.0e7 pr 0.3 ;
lsdymats 2 1 struct
head belytschko-tsay shells
shell elfor bt shth 0.3937008 rho 7.350e-4 e 3.0e7 pr 0.3 ;
block
-1 -5 -9 -17 -25 -33 -41 -49 -57 -65 -73 -81 -89 -97 -105 -113 -117 -
121;
-1 -16;
-1 2 3 4 -5 6 7 -8 9 10 -11;
0 160 320 640 960 1280 1600 1920 2240 2560 2880 3200 3520 3840 4160
4480 4640
4800;
-300 300;
0 40 80 120 160 200 240 280 320 360 400;
mate 2
bsd 1 carea 1.7437535 iss 0.01267 itt 5.069 irr 0.049 ; ;
kbmi 1 18;1 2;1 11;61 2 1 i 1 ;
jbmi 1 18;1 2;1 11;61 2 1 i 1 ;
ibmi 1 18;1 2;1 11;2 11 1 k 1 ;
jbmi 1 18;1 2;1 5;2 2 1 k 1 ;
jbmi 1 18;1 2;5 8;2 2 1 k 1 ;
jbmi 1 18;1 2;8 11;2 2 1 k 1 ;
ibmi 1 18;1 2;1 1;16 1 1 j 1 ;
ibmi 1 18;1 2;5 5;16 1 1 j 1 ;
ibmi 1 18;1 2;8 8;16 1 1 j 1 ;
ibmi 1 18;1 2;11 11;16 1 1 j 1 ;
kbmi 1 1;1 2;1 11;1 16 1 j 1 ;
kbmi 18 18;1 2;1 11;1 16 1 j 1 ;
merge
```

The **PM** command was used to assign point masses to the structural mesh as follows.

```
pm 62 179.424 ;
pm 63 179.424 ;
pm 532 179.424 ;
pm 533 179.424 ;
pm 980 358.848 ;
pm 981 358.848 ;
pm 1702 358.848 ;
pm 1703 358.848 ;
```

B.   FLUID MODELING

This part covers the process for generating a fluid finite element mesh using the TrueGrid's extrusion feature, the **BLUDE** command. Basically, the **BLUDE** command pulls or "extrudes" the structural mesh through a "guide" mesh mated to the structural wetted surface in the form of a block part. The block part is essentially attached to a

surface definition created from a **FACESET** or directly attached to **FACESET** of the wetted elements of the structural mesh. The resulting extruded mesh exactly matches to the structural mesh; this is a prerequisite for successful fluid finite element modeling.

The extrusion procedure in TrueGrid is as follows, with important commands and menu selections, which are indicated in bold and all capital letters for emphasis as in the way of the structural modeling part:

1. As in the generating procedure described previously in the part of the structural modeling above, first, a structural model must be created. For the structural modeling, TrueGrid can be used as has been the case in this thesis, or the **READMESH** command in TrueGrid can be used to input a mesh from another code format, such as LS-DYNA or NASTRAN. It is very important to remember that, when TrueGrid reads in a finite element mesh from an outside code format, it renumbers every element and grid point (node). Therefore, once TrueGrid has finished manipulating the mesh, and it is written as an output file, the grid point (node) and element ID numbers will not match between the original and newly output model from TrueGrid even if the original model has not been modified in TrueGrid.

2. The elements of the structural model that will be in contact with the fluid, i.e., the wetted surface, must be grouped into **FACESETS**. This option can be accessed from the environment window under the **PICK** option by choosing the **SETS** button. The **FACES** button should be selected. Faces which are naturally defined by the geometry of the wet surface are picked. For the meko-like box model, which is considered as a rectangular barge, each face of the structural model was put in a separate **FACESET**, meaning each side, bottom, bow, and stern below the waterline was grouped individually. The reason for this will be clear once the procedure of creating **FACESET** is understood and used. However, for a ship's hull, this face selection would include the port and starboard sides and the stern. In this case, the bow is typically a sharp edge and would not be selected as a **FACESET**. The **HIDE** drawing mode vice **WIREFRAME** should be used for the mesh to ensure that only the visible elements are picked. This will make **FACESET** selection must easier, since it must be done by hand using the lasso tool guided by the mouse. The four-node selection option is the best to use when choosing the **FACESET**. This means that four nodes of an element must be within the selection lasso for the element to be added to the **FACESET**. The selected elements will be highlight in white. If some elements are selected that are not desired in the particular set, they can be easily selected and removed; using the one node selection option is best for this operation. The **REMOVE** button should be pushed also. The set must be named and saved once selected.

3.   The **SURFACE** menu **SD** (surface definition) option can be chosen next. A surface number must be input. The **FACESET** option should be selected from the end of the surface options list and the name of the desired **FACESET** should then be input. This step converts the named **FACESET** into a surface definition. The new surface will be displayed in red in the physical window. However, the procedure of creating fluid finite element mesh can be conducted without converting the **FACESET** into a surface definition. The name of the desired **FACESET** can be directly used in the **BLUDE** command to generate the block parts for the fluid modeling. The fluid finite element mesh for the meko-like box model was created by directly using the names of the desired **FACESET** along with the **BLUDE** command. Although, since the **SURFACE** created should have no holes in it, the **SURFACE** option can be useful in determining the holes which were missed in the **FACESET** selection, the method, which directly uses the **FACESETS** along with the **BLUDE** command, can also be useful in recognizing the holes on the **FACESET** by inspecting the block part created. If the holes exist in the **FACESET** selection, the block part will also have holes in it; this will help the user's troubleshooting the **FACESET.**

4.   Next, the **PARTS** menu should be selected and the **BLUDE** option must be chosen. Using this option, the user creates a block part that will be attached to the created surface or the **FACESET** above. This block will serve as the "guide" for the extrusion of the structural mesh; therefore, the block's mesh must match the structural mesh or be of finer quality in order to obtain a quality extrusion. This block part is created in the same way as a block using the **BLOCK** command. The **BLUDE** command requires two additional inputs, however. First, the face of the block where the extrusion begins must be input. This is simply the face closest to the structure. Next, the name of the **FACESET** to be extruded must input.

5.   If the **SD** was selected in the **SURFACE** menu to create the fluid finite element mesh, the block part created must be attached to the surface created in step 3. It can be attached using any of TrueGrid's available options. The easiest being selection of the face to be attached and then selecting the surface and clicking the **PROJECT** button in the environment window. This will work for simple cases, but a complex surface may require use of other TrueGrid methods. Since the **FACESETS** were directly used with the **BLUDE** command to generate the fluid mesh, this step does not apply the fluid mesh generation in the meko-like box model.

6.   The interface of the extrusion mesh and the structural mesh should be carefully examined. Orthogonality of the fluid and structural mesh is a must (next to the wetted surface) and should be verified; TrueGrid's **DIAGNOSTICS** menu provides the necessary tools. The **ORPT** command in the **DIAGNOSTICS** menu can be used to provide the orthogonality of the fluid and structural mesh. The block mesh can be

modified as needed using various TrueGrid tools to ensure a quality mesh is constructed for the extrusion; two examples of useful tools are the mesh relaxation algorithms and use of a cubic spline to added curvature to the block mesh edges. Material properties can be assigned to the mesh also, just as has been the case in the structural modeling like any other part in TrueGrid. In short, the extrusion mesh should be treated as any other part created in TrueGrid; all of the same options are available.

7. Once the user is satisfied with the extrusion mesh, the **MERGE** command should be used to end the **PARTS** phase and actually perform the extrusion. The **MERGE** command can also be used, as in the case of the meko-like box model, after each block part has been created and finally perform the extrusion. In this way, it can be seen whether the block parts of the fluid have been created as desired. Then, the result will be a fluid mesh, which exactly matches the structural mesh. The mesh will consist of 8-noded solid elements. The **STP** option is used also to ensure that the fluid mesh is merged with the structural mesh and there are no duplicate nodes. When the whole meko-like box model was built in the beginning, because the **STP** command was not used for the fluid mesh's merging with the structural mesh and therefore, duplicate nodes took place between the fluid and structural meshes, the simulation program LS-DYNA could not be run for the analysis. LS-DYNA gave the "access violation" error while it was searching the input or keyword file created in TrueGrid for pre-processing of the simulation procedure. Then, the **STP** command was used to give a lower tolerance value for merging of the fluid and structural meshes; this allowed many duplicate nodes to be deleted in the whole model and to run LS-DYNA without giving the same kind of error.

8. Additional extrusions can be performed, including on any newly extruded mesh surfaces. This must usually be done to form a fluid mesh around the structural model completely.

9. After all the parts created have been merged, since USA is a boundary element code that solves the fluid-structure interaction equations using the Doubly Asymptotic Approximation (DAA), a DAA boundary, which does not include the free surface of the fluid mesh, must be selected. First-order DAA (DAA_1) boundary, which was used for the analyses in this thesis, can be chosen by using the **FACESET** feature of TrueGrid. Since the DAA boundary is truncated to the outer surface of the fluid mesh in LS-DYNA/USA, which is an example of the closely coupled form, each face of the fluid mesh should be put in a one **FACESET**, meaning each side, bottom, back, and front sides of the fluid mesh up to the waterline should be grouped together. TrueGrid's **DIAGNOSTICS** menu can be used to determine the number of segments on the DAA boundary to be able to input it to the USA input decks (FLUMAS and AUGMAT).

10. Postscript images of the model and the mesh can be made using the **POSTSCRIPT** command. The command postscript is given at the

164

command prompt with the desired output filename. The **DRAW** button in the environment window should then be clicked to redraw the image. This creates the postscript file. Additional files will be generated as long as the command is active and the model is manipulated in such a way so that it must be regenerated in the display window. The postscript command can be turned off by typing **POSTSCRIPT OFF**. One additional command that is quite useful in generating quality image files is the **RESO** command. The **RESO** command is entered prior to the **POSTSCRIPT** command. The syntax is the command followed by a number, which is the desired resolution available in TrueGrid.

11. Finally, to write the output file of the whole model together with the structural model, the **OUTPUT** menu is used. In this menu, there are many different kinds of options of simulation programs such as **LS-DYNA**, **NASTRAN**, etc. for the user to select them for the simulation purposes. After the meko-like box model had been completely built by creating the structural and fluid finite element meshes, first, the option **LS-DYNA** keyword format was selected, and then the command **WRITE**, which is also an option in the **OUTPUT** menu, was chosen to write the output file, which is, in fact, the input file for LS-DYNA, of the whole model created in TrueGrid.

The meko-like box model has been used in investigating what happens when any kind of hull appendage is added to the structure, and specifically in the case in which these hull appendages are not only coupled but also uncoupled with the fluid surrounding the structure. The extrusion procedure of the fluid finite element mesh described above can be used to build the fluid model as it is coupled or uncoupled with the hull appendages created. To demonstrate how the fluid finite element mesh was created, some portions of the fluid modeling in the TrueGrid code file will be illustrated as follows.

2. Fluid Modeling Parts of the TrueGrid Code File

The **FACESETS** of the structural mesh were selected for the right side as follows. The same procedure was done for the other sides of the structural mesh. The **BLUDE**, **MATE** and **MERGE** commands were utilized to block mesh to extrude the selected faceset, assign a material number to the block part as in the structural model and to merge the parts created previously, respectively.

```
fset rightsid = ls
c linear shells
 16:19 95:98 114:117 133:136 486:489 565:568 584:587 603:606 956:963
1099:1106
1122:1129 1145:1152 1746:1753 1889:1896 1912:1919 1935:1942 2536:2543
2679:2686
2702:2709 2725:2732 3326:3333 3469:3476 3492:3499 3515:3522 4116:4123
4259:4266
```

```
4282:4289 4305:4312 4906:4913 5049:5056 5072:5079 5095:5102 5696:5703
5839:5846
5862:5869 5885:5892 6486:6493 6629:6636 6652:6659 6675:6682 7276:7283
7419:7426
7442:7449 7465:7472 8066:8073 8209:8216 8232:8239 8255:8262 8856:8863
8999:9006
 9022:9029 9045:9052 9646:9653 9789:9796 9812:9819 9835:9842
10436:10443
10579:10586 10602:10609 10625:10632 11226:11229 11305:11308 11324:11327
11343:11346 11696:11699 11775:11778 11794:11797 11813:11816;;
blude 3 rightsid 1 121;1 3 4 5 6 7 8 10 12;1 5;
0 4800;-300 -314 -330 -350 -374 -404 -440 -520 -620;0 160;
mate 3
merge
```

Additional extrusions were performed, including on any newly extruded mesh surfaces to form a fluid mesh around the structural model completely.

```
fset face3 = lb5
c linear bricks - face #5
 11881:11960 12481:12520 13681:13700 15281:15320 15821:15840
17561:17620
18161:18180 19861:19880;;
blude 1 face3 1 3 4 5 6 7 8 10 12;1 16;1 3 4 5 6 7 8 21;
0 -14 -30 -50 -74 -104 -140 -220 -320;-300 300;
0 -14 -30 -50 -74 -110 -150 -800;
mate 3
merge
```

The DAA boundary was selected by using the **FACESET** feature of TrueGrid.

```
fset daa = lb1
c linear bricks - face #1
 11 22 33 44 55 66 77 88 99 110 121 132 143 154 165 176 187 198 209 220
231 242
253 264 275 286 297 308 319 330 341 352 363 374 385 396 407 418 429 440
451 462
473 484 495 506 517 528 539 550 561 572 583 594 605 616 627 638 649 660
671 682
693 704 715 726 737 748 759 770 781 792 803 814 825 836 847 858 869 880
891 902
913 924 935 946 957 968 979 990 1001 1012 1023 1034 1045 1056 1067 1078
1089
1100
 1111 1122 1133 1144 1155 1166 1177 1188 1199 1210 1221 1232 1243 1254
1265
1276 1287 1298 1309 1320 1331 1342 1353 1364 1375 1386 1397 1408 1419
1430 1441
1452 1463 1474 1485 1496 1507 1518 1529 1540 1551 1562 1573 1584 1595
1606 1617
1628 1639 1650 1661 1672 1683 1694 1705 1716 1727 1738 1749 1760 1771
1782 1793
1804 1815 1826 1837 1848 1859 1870 1881 1892 1903 1914 1925 1936 1947
1958 1969
```

```
1980 1991 2002 2013 2024 2035 2046 2057 2068 2079 2090 2101 2112 2123
2134 2145
2156 2167 2178 2189 2200
```

The **STP** option is used to ensure that the fluid mesh is merged with the structural mesh and there are no duplicate nodes. Giving a lower tolerance value for merging the fluid and structural meshes, it allowed many duplicate nodes to be deleted from the model.

```
c                      MERGED NODES SUMMARY
c        605 nodes merged between parts      1 and      2
c        605 nodes merged between parts      1 and      3
c         80 nodes merged between parts      1 and      4
c         80 nodes merged between parts      1 and      5
c       1936 nodes merged between parts      1 and      6
c        121 nodes merged between parts      1 and      7
c       1331 nodes merged between parts      2 and      7
c       2420 nodes merged between parts      6 and      7
c        121 nodes merged between parts      1 and      8
c       1331 nodes merged between parts      3 and      8
c       2420 nodes merged between parts      6 and      8
c         16 nodes merged between parts      1 and      9
c        176 nodes merged between parts      4 and      9
c        320 nodes merged between parts      6 and      9
c         16 nodes merged between parts      1 and     10
c        176 nodes merged between parts      5 and     10
c        320 nodes merged between parts      6 and     10
c          6 nodes merged between parts      1 and     11
c         66 nodes merged between parts      3 and     11
c         66 nodes merged between parts      4 and     11
c         20 nodes merged between parts      6 and     11
c        220 nodes merged between parts      8 and     11
c        220 nodes merged between parts      9 and     11
c        121 nodes merged between parts     11 and     11
c          6 nodes merged between parts      1 and     12
c         66 nodes merged between parts      2 and     12
c         66 nodes merged between parts      4 and     12
c         20 nodes merged between parts      6 and     12
c        220 nodes merged between parts      7 and     12
c        220 nodes merged between parts      9 and     12
c        121 nodes merged between parts     12 and     12
c          6 nodes merged between parts      1 and     13
c         66 nodes merged between parts      3 and     13
c         66 nodes merged between parts      5 and     13
c         20 nodes merged between parts      6 and     13
c        220 nodes merged between parts      8 and     13
c        220 nodes merged between parts     10 and     13
c        121 nodes merged between parts     13 and     13
c          6 nodes merged between parts      1 and     14
c         66 nodes merged between parts      2 and     14
c         66 nodes merged between parts      5 and     14
c         20 nodes merged between parts      6 and     14
c        220 nodes merged between parts      7 and     14
c        220 nodes merged between parts     10 and     14
```

```
c        121 nodes merged between parts       14 and        14
c      14950 nodes were deleted by tolerancing
stp 0.01
```

The **ORPT** command in the **DIAGNOSTICS** menu was utilized to ensure the orthogonality of the fluid and structural mesh.

```
orpt
-
0
0
0
```

The **LS-DYNA** keyword format option and **WRITE** command in the **OPTION** menu was used to generate an LS-DYNA input deck.

```
lsdyna keyword
c  output file name is trugrdo
c  creating LS-DYNA KEYWORD input deck
write
```

APPENDIX C. LS-DYNA/USA INPUT DECKS

A.   LS-DYNA KEYWORD FILE

The following parts of the keyword file are selected to show how the finite element model is translated to the LS-DYNA keyword format. This includes only the key parts of the LS-DYNA keyword file which were used to simulate the meko-like box model with no appendage.

```
*KEYWORD
$ MEKO-LIKE BOX MODEL WITH NO APPENDAGE
$ dt = 4.0E-6, ts = 0.9
$ 07 APRIL 2005 - model was created by using Truegrid
$ 07 APRIL 2005 - 500 msec run
$
$ BEAM ELEMENTS MASS DENSITY = 7.350E-04 lbf-s^2/in^4.
$ SHELL ELEMENTS MASS DENSITY = 7.350E-04 lbf-s^2/in^4.
$ FLUID DENSITY = 9.345E-05 lbf-s^2/in^4.
$ TOTAL LUMPED MASS = 43061.76 lbf-s^2/in.
$
$ RAYLEIGH DAMPING SET W/ ALPHA = 19.2, BETA = 2.09E-6
$
$ *****************************************************************
*TITLE
Meko-like box model with belytschko-schiwer beams and belytschko-tsay
shells
*CONTROL_TERMINATION
0.5
*CONTROL_TIMESTEP
4.0E-6,0.9,0,0.0,0.0,1,0
*CONTROL_PARALLEL
1,0,1
*DEFINE_CURVE
1
0.,4.0E-6
0.5,4.0E-6
*DATABASE_HISTORY_NODE
$ NODES AT THE BOTTOM
15,1025,2454,3883,5312,6741,8170,9599
$ NODES AT THE SECOND DECK (at 160 inches)
148,1219,2648,4077,5506,6935,8364,9743
$ NODES AT THE THIRD DECK (at 280 inches)
268,1391,2820,4249,5678,7107,8536,9965
$ NODES AT THE TOP DECK (at 400 inches)
388,1541,2970,4399,5828,7257,8686,10115
$ CENTER NODES AT THE BOTTOM (from left to right)
5320,5317,5315,5313,5311,5310,5308,5251
$ CENTER NODES AT THE SECOND DECK (at 160 inches-from left to right)
5514,5511,5509,5507,5505,5504,5502,5428
$ CENTER NODES AT THE THIRD DECK (at 280 inches-from left to right)
5686,5683,5681,5679,5677,5676,5674,5600
$ CENTER NODES AT THE TOP DECK (at 400 inches-from left to right)
5836,5833,5831,5829,5827,5826,5824,5772
```

```
$ CLOSEST FLUID NODE
66233
$
*DATABASE_NODOUT
4.0E-5
*DATABASE_BINARY_D3PLOT
2.0E-3
*DATABASE_BINARY_D3THDT
0.5E-1
*DATABASE_EXTENT_BINARY
0,0,3,1,1,1,1,1
0,0
*BOUNDARY_USA_SURFACE
1,1,0
*INITIAL_DETONATION
-1,2400.0,-3950.0,-1800.0,0.0
663.32,0.00172336,2400.0,-620.0,-800.0,66233
$
$ MATERIAL CARDS
$
$ DEFINITION OF MATERIAL     1
*MAT_ELASTIC
1,7.350E-04,3.000E+07,0.300
*SECTION_BEAM
1,2
1.7437535,0.01267,5.069,0.049
*PART
belytschko-schiwer beams
1,1,1
$
$ DEFINITION OF MATERIAL     2
*MAT_ELASTIC
2,7.350E-04,3.000E+07,0.300
*SECTION_SHELL
2,2
0.3937008,0.3937008,0.3937008,0.3937008
*PART
belytschko-tsay shells
2,2,2
$
$ DEFINITION OF MATERIAL     3
*PART
fluid (acoustic)
3,3,90
*SECTION_SOLID
3,8
*MAT_ACOUSTIC
90,9.345E-05,60945,0.5,1.0,14.7,386.4
0.,0.,160.0,0.,0.,1.0
$
$ NODES
$
*NODE
1,0.0,-300.,0.0,0,0
2,0.0,-300.,40.,0,0
3,0.0,-260.,0.0,0,0
4,0.0,-260.,40.,0,0
```

```
5,0.0,-220.,0.0,0,0
6,0.0,-220.,40.,0,0
7,0.0,-180.,0.0,0,0
8,0.0,-180.,40.,0,0
9,0.0,-140.,0.0,0,0
10,0.0,-140.,40.,0,0

$
$ ELEMENT CARDS FOR SOLID ELEMENTS
$
*ELEMENT_SOLID
1,3,11203,11204,11205,11206,1,2,34,33
2,3,11808,11809,11810,11811,11203,11204,11205,11206
3,3,12413,12414,12415,12416,11808,11809,11810,11811
4,3,13018,13019,13020,13021,12413,12414,12415,12416
5,3,13623,13624,13625,13626,13018,13019,13020,13021
6,3,14228,14229,14230,14231,13623,13624,13625,13626
7,3,14833,14834,14835,14836,14228,14229,14230,14231
8,3,15438,15439,15440,15441,14833,14834,14835,14836
9,3,16043,16044,16045,16046,15438,15439,15440,15441
10,3,16648,16649,16650,16651,16043,16044,16045,16046

$
$ ELEMENT CARDS FOR SHELL ELEMENTS
*ELEMENT_SHELL_THICKNESS
1,2,1,3,4,2
0.3937008,0.3937008,0.3937008,0.3937008
2,2,3,5,6,4
0.3937008,0.3937008,0.3937008,0.3937008
3,2,5,7,8,6
0.3937008,0.3937008,0.3937008,0.3937008
4,2,7,9,10,8
0.3937008,0.3937008,0.3937008,0.3937008
5,2,9,11,12,10
0.3937008,0.3937008,0.3937008,0.3937008
6,2,11,13,14,12
0.3937008,0.3937008,0.3937008,0.3937008
7,2,13,15,16,14
0.3937008,0.3937008,0.3937008,0.3937008
8,2,15,17,18,16
0.3937008,0.3937008,0.3937008,0.3937008
9,2,17,19,20,18
0.3937008,0.3937008,0.3937008,0.3937008
10,2,19,21,22,20
0.3937008,0.3937008,0.3937008,0.3937008

$
$ ELEMENT CARDS FOR BEAM ELEMENTS
*ELEMENT_BEAM_THICKNESS
1,1,1,2,33,0,0,0,0
1.7437535,0.01267,5.069,0.049,1.4531279
2,1,2,101,34,0,0,0,0
1.7437535,0.01267,5.069,0.049,1.4531279
3,1,101,121,117,0,0,0,0
1.7437535,0.01267,5.069,0.049,1.4531279
4,1,121,141,137,0,0,0,0
1.7437535,0.01267,5.069,0.049,1.4531279
```

```
5,1,141,161,157,0,0,0,0
1.7437535,0.01267,5.069,0.049,1.4531279
6,1,161,241,177,0,0,0,0
1.7437535,0.01267,5.069,0.049,1.4531279
7,1,241,261,257,0,0,0,0
1.7437535,0.01267,5.069,0.049,1.4531279
8,1,261,281,277,0,0,0,0
1.7437535,0.01267,5.069,0.049,1.4531279
9,1,281,361,297,0,0,0,0
1.7437535,0.01267,5.069,0.049,1.4531279
10,1,361,381,377,0,0,0,0
1.7437535,0.01267,5.069,0.049,1.4531279

$
$ DISCRETE LUMPED MASSES
$
*ELEMENT_MASS
$ KEEL
1,62,179.424
2,63,179.424
3,532,179.424
4,533,179.424
5,980,358.848

$ FIRST DECK (at 160 inches)
35,202,179.424
36,203,179.424
37,650,179.424
38,651,179.424
39,1174,358.848

$ SECOND DECK (at 280 inches)
69,322,179.424
70,323,179.424
71,750,179.424
72,751,179.424
73,1346,358.848

$ TOP DECK (at 400 inches)
103,422,179.424
104,423,179.424
105,832,179.424
106,833,179.424
107,1496,358.848
108,1497,358.848
109,2218,358.848
110,2219,358.848
111,2940,358.848
112,2941,358.848

$
$ Face set daa
$
*SET_SEGMENT
1,0.0,0.0,0.0,0.0
17256,17255,17254,17253,0.0,0.0,0.0,0.0
17259,17258,17257,17255,0.0,0.0,0.0,0.0
```

172

```
17267,17266,17265,17264,0.0,0.0,0.0,0.0
17283,17282,17281,17280,0.0,0.0,0.0,0.0
17314,17313,17312,17311,0.0,0.0,0.0,0.0
17363,17311,17362,17361,0.0,0.0,0.0,0.0
23908,23909,23910,23911,0.0,0.0,0.0,0.0
23911,23910,23912,23913,0.0,0.0,0.0,0.0
23918,23919,23920,23921,0.0,0.0,0.0,0.0
23934,23935,23936,23937,0.0,0.0,0.0,0.0

$
$ RAYLEIGH DAMPING
$
*DAMPING_GLOBAL
        0     19.2
*DAMPING_PART_STIFFNESS
$ BEAM ELEMENTS
1,2.09E-06
$ SHELL ELEMENTS
2,2.09E-06
*END
```

B.   USA INPUT DECKS

1.   FLUMAS

```
FLUMAS INPUT FILE FOR MEKO-LIKE BOX MODEL
flunam geonam strnam daanam                 $ FLUNAM GEONAM GRDNAM DAANAM
F F F T                                     $ PRTGMT PRTTRN PRTAMF CALCAM
T F F F                                     $ EIGMAF TWODIM HAFMOD QUAMOD
F F T F                                     $ PCHCDS NASTAM STOMAS STOINV
F F F T                                     $ FRWTFL FRWTGE FRWTGR FRESUR
F T F F                                     $ RENUMB STOGMT ROTGEO ROTQUA
F F F F                                     $ PRTCOE STRMAS SPHERE ROTSYM
F F F F                                     $ OCTMOD CAVFLU FRWTFV INTCAV
F F                                         $ BOTREF MASREF
0 137372 0 13842                            $ NSTRC NSTRF NGEN NGENF
0 0 0                                       $ NBRA NCYL NCAV
9.345E-05 60945.0                           $ RHO CEE
2                                           $ NVEC
160. 0. 0. 1.                               $ DEPTH CXFS CYFS CZFS
14.7 386.4                                  $ PATM GRAVAC
0                                           $ NSRADI
0                                           $ NSORDR
```

2.   AUGMAT

```
AUGMAT INPUT FILE FOR MEKO-LIKE BOX MODEL
strnam flunam geonam prenam                 $ STRNAM FLUNAM GEONAM PRENAM
F F F F                                     $ FRWTGE FRWTST FRWTFL LUMPFM
F F F T                                     $ FLUSKY DAAFRM SYMCON DOFTAB
F F F F                                     $ PRTGMT PRTTRN PRTSTF PRTAUG
F F F F                                     $ MODTRN STRLCL INTWAT CFAPRE
11                                          $ NTYPDA
```

```
137372 412116 3 3                              $ NSTR NSFR NFRE NFTR
1                                              $ NSETLC
0 1 13842 1                                    $ NDICOS JSTART JSTOP JINC
```

3.   TIMINT

```
TIMINT INPUT FILE FOR MEKO-LIKE BOX MODEL
prenam posnam                                  $ PRENAM POSNAM
resnam                                         $ RESNAM WRTNAM
F T F F                                        $ REFSEC FLUMEM PWACAV ITERAT
F F F                                          $ INCSTR CENINT BUOYAN
1                                              $ NTINT
0.0 4.0E-6                                      $ STRTIM DELTIM
T F F F                                        $ EXPWAV SPLINE VARLIN PACKET
F T F F                                        $ HYPERB EXPLOS DOUBDC VELINP
F F F F                                        $ BUBPUL SHKBUB
1                                              $ NCHARG
0.                                             $ HYDPRE
2400.0 -3950.0 -1800.0                         $ XC YC ZC
2400.0 -620.0 -800.0                           $ SX SY SZ
201                                            $ JPHIST
1. 0.                                          $ PNORM DETIM
5.1E-5                                         $ DTHIST
2                                              $ CHGTYP
5000.0 339.0 163.33                            $ WEIGHT SLANT CHGDEP
99999 99999                                    $ NSAVER NRESET
0 0 0 0                                        $ LOCBEG LOCRES LOCWRT NSTART
F F F F                                        $ FORWRT STBDA2 ASCWRT
2400.0 -307.0 -7.0                             $ XV YV ZV
F                                              $ DISPLA
```

APPENDIX D. VERTICAL VELOCITY PLOTS

A.   MEKO-LIKE BOX MODEL WITH SOLID KEEL BOARD
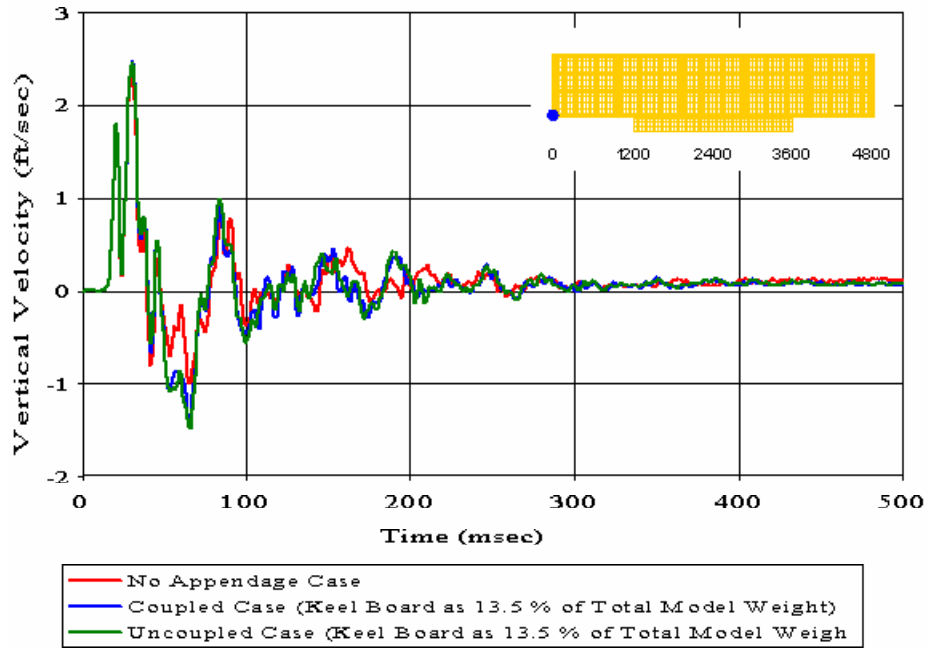
Figure 103.   Bulkhead Node 15: (RM = 0.0253, RP = 0.0705, RC = 0.0664)
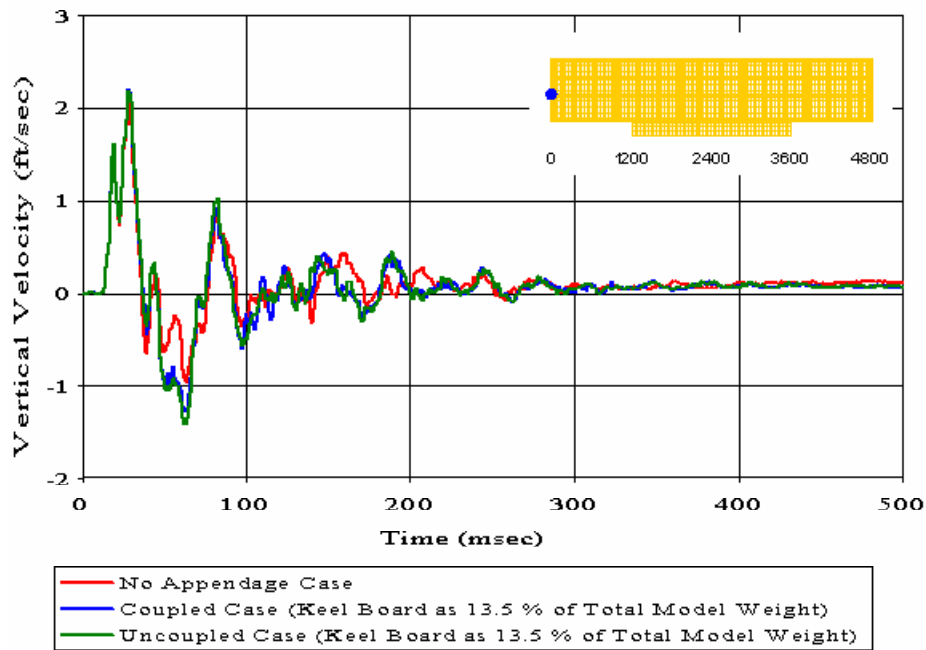
Figure 104.   Bulkhead Node 148: (RM = 0.0326, RP = 0.0477, RC = 0.0512)
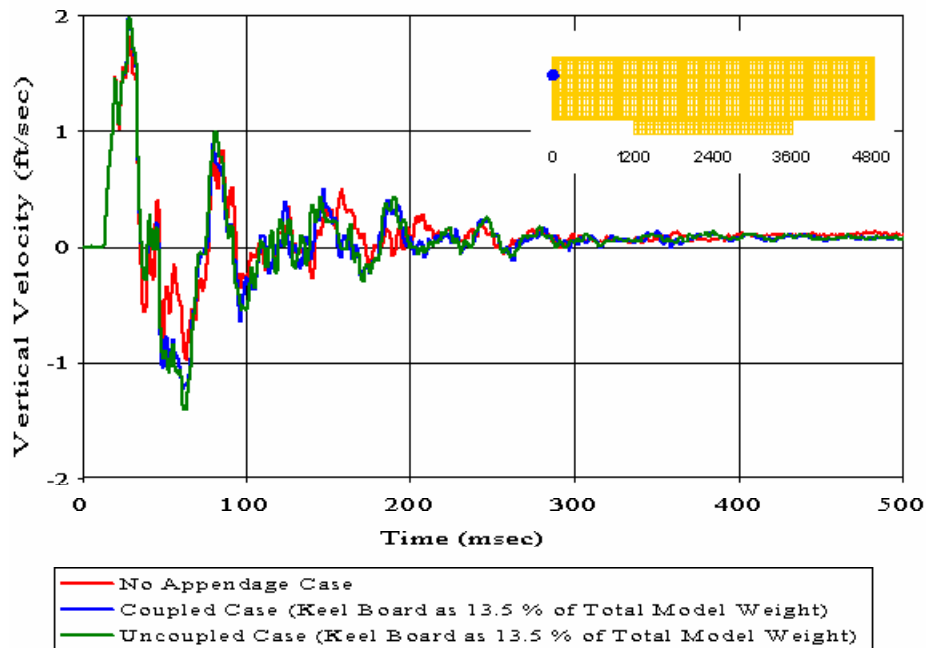
Figure 105.   Bulkhead Node 268: (RM = 0.0333, RP = 0.0625, RC = 0.0628)

176

Meko-Like Box Model with Solid Keel Board

Node 388 at Bulkhead (x=0 y=-20 z=400)
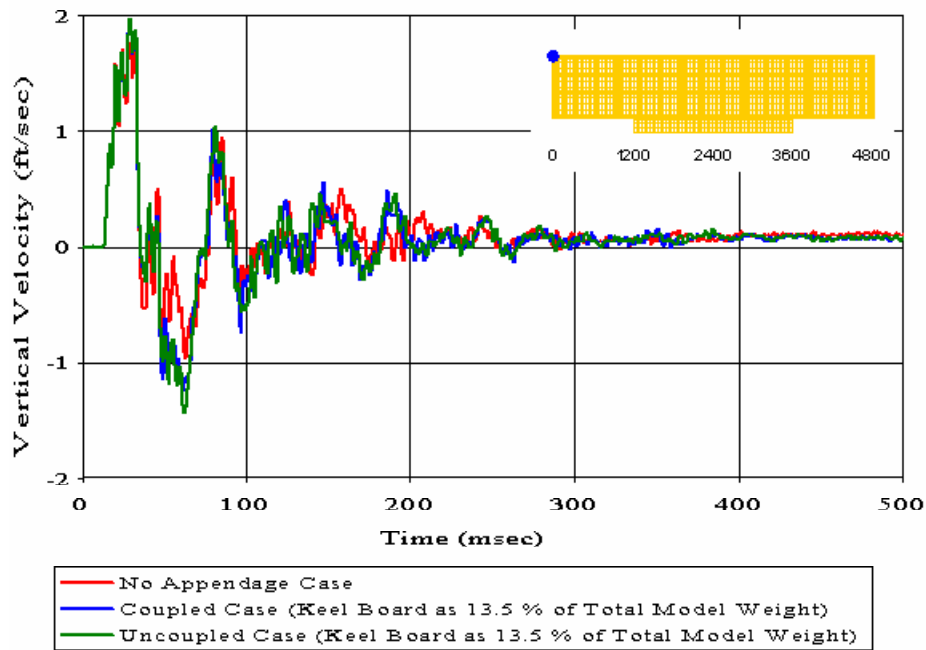
Figure 106.   Bulkhead Node 388: (RM = 0.0314, RP = 0.0786, RC = 0.0750)

Meko–Like Box Model with Solid Keel Board

Node 2454 at Keel (x=1200 y=-20 z=0)
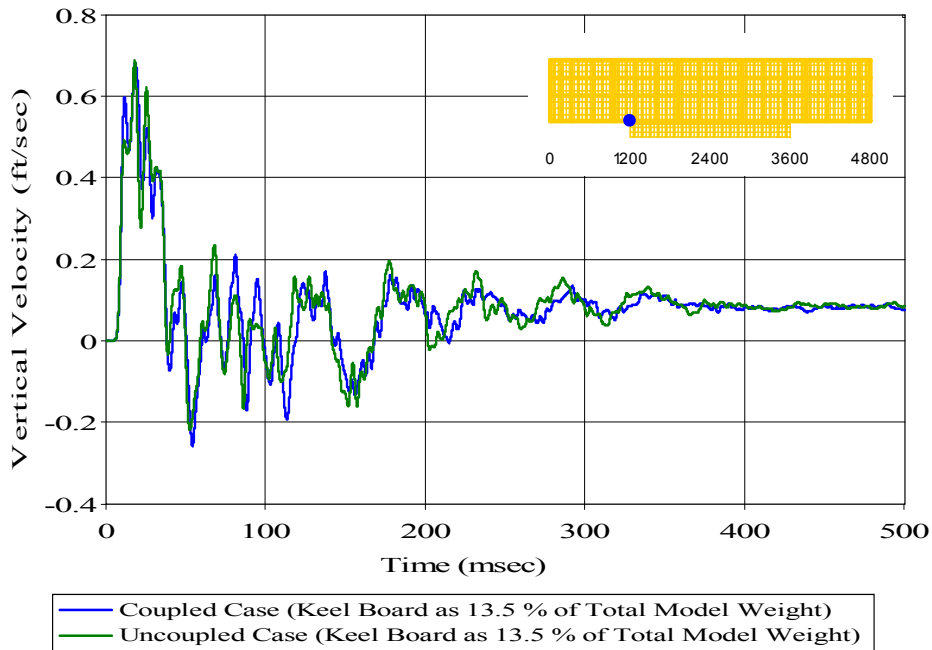
Figure 107.   Keel Node 2454: (RM = 0.0032, RP = 0.0969, RC = 0.0859)
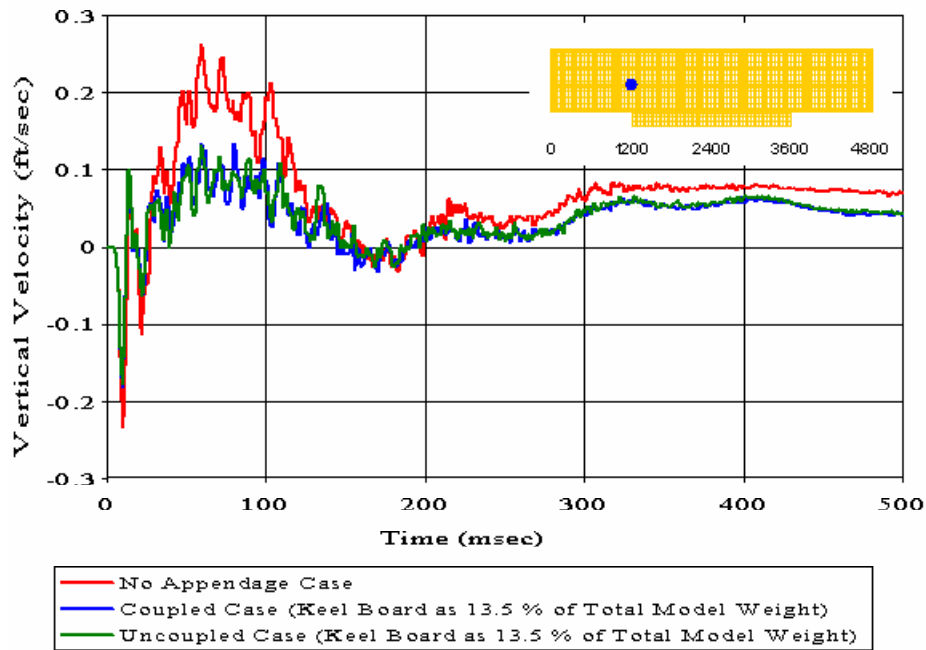
Figure 108.   First Deck Node 2648: (RM = 0.0094, RP = 0.0645, RC = 0.0577)
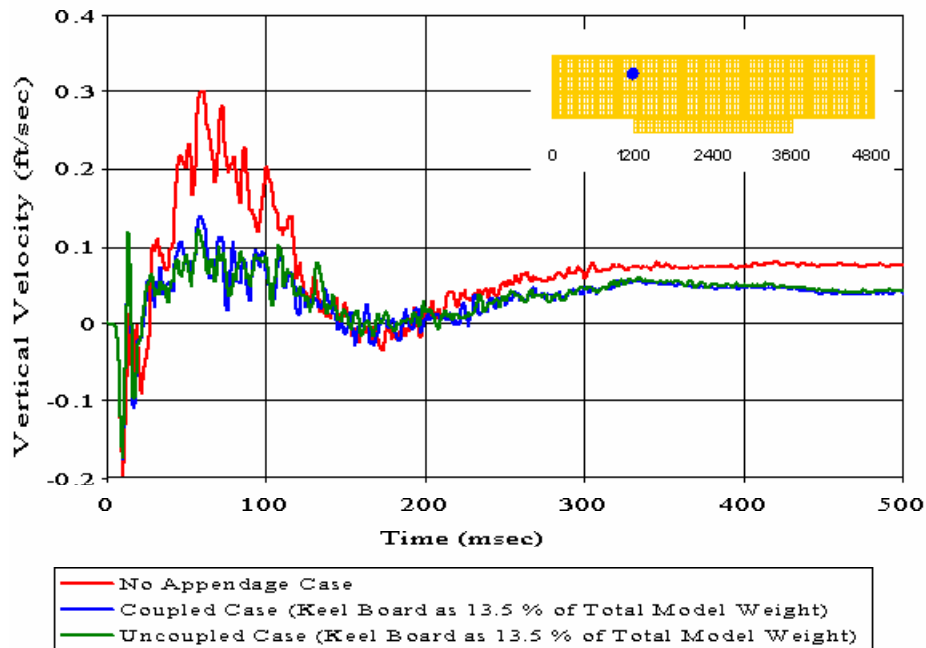
Figure 109.   Second Deck Node 2820: (RM = -0.0038, RP = 0.0754, RC = 0.0669)

Meko–Like Box Model with Solid Keel Board

Node 2970 at Top Deck (x=1200 y=-20 z=400)
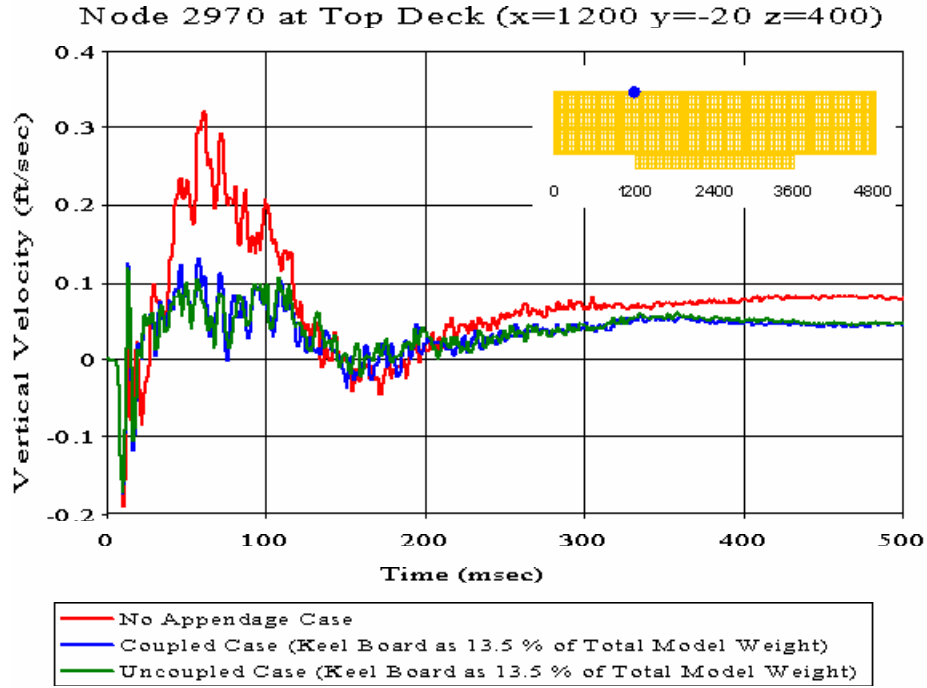
Figure 110.   Top Deck Node 2970: (RM = -0.0003, RP = 0.0783, RC = 0.0694)

Meko–Like Box Model with Solid Keel Board

Node 3883 at Keel (x=1800 y=-20 z=0)
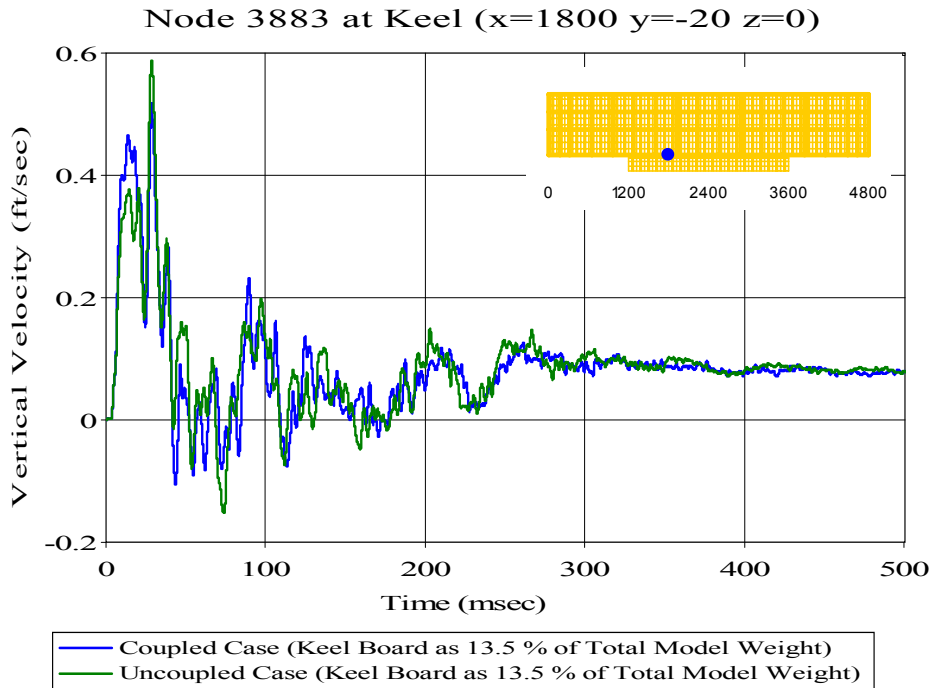
Figure 111.   Keel Node 3883: (RM = 0.0049, RP = 0.1050, RC = 0.0931)

179
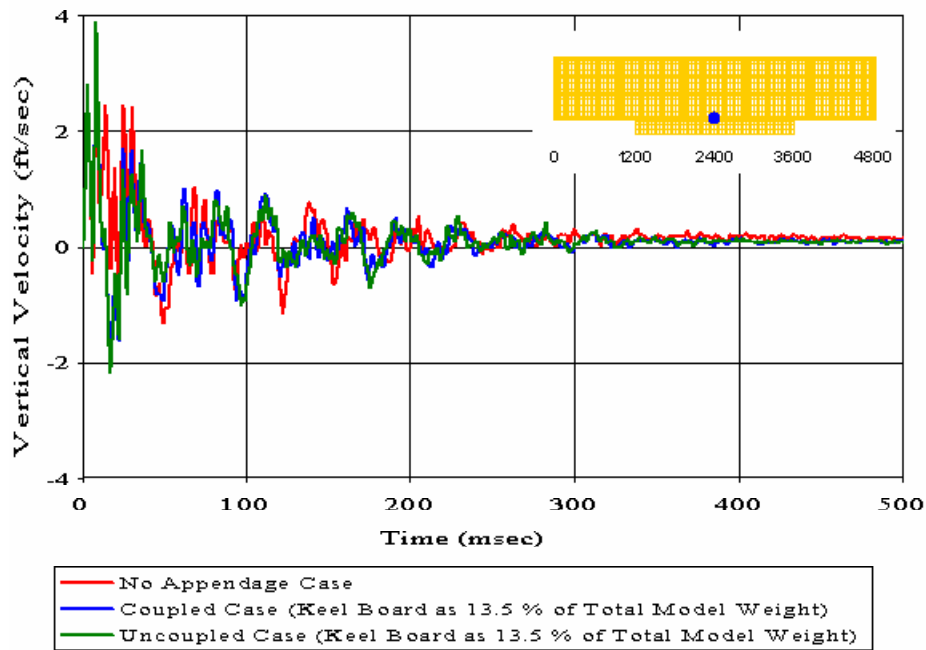
Figure 112. Keel Node 5251: (RM = -0.0237, RP = 0.1149, RC = 0.1040)
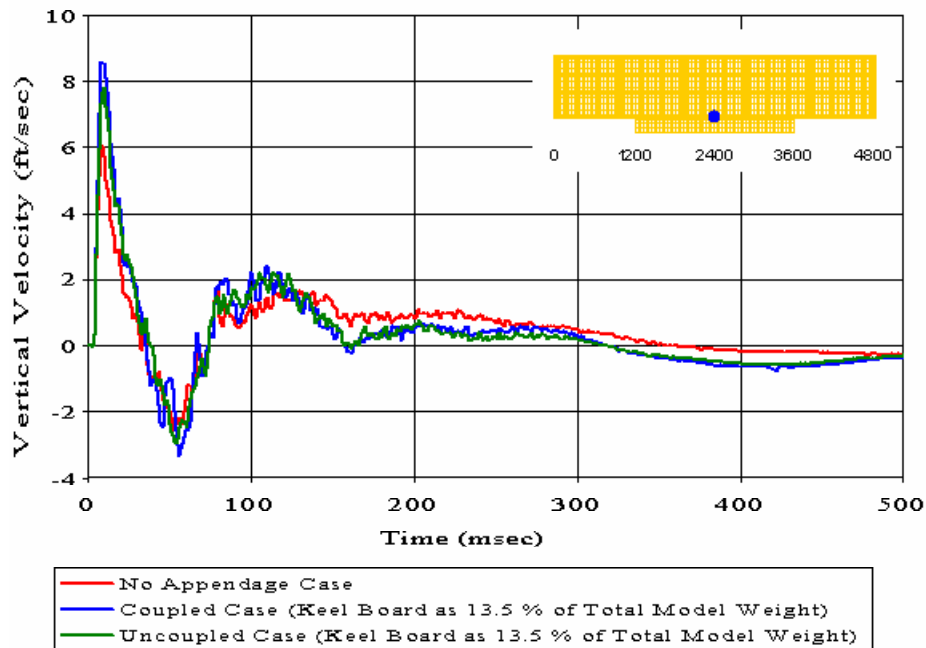
Figure 113. Keel Node 5310: (RM = -0.0634, RP = 0.0688, RC = 0.0829)

Meko–Like Box Model with Solid Keel Board

Node 5312 at Keel (x=2400 y=-20 z=0)
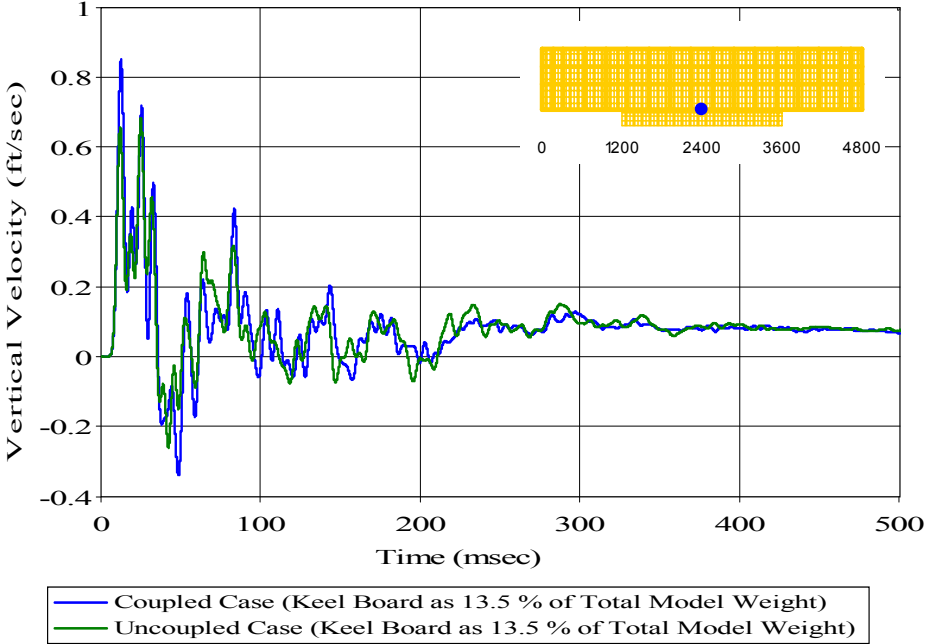
Figure 114. Keel Node 5312: (RM = -0.0517, RP = 0.1220, RC = 0.1174)

Meko–Like Box Model with Solid Keel Board

Node 5315 at Keel (x=2400 y=100 z=0)
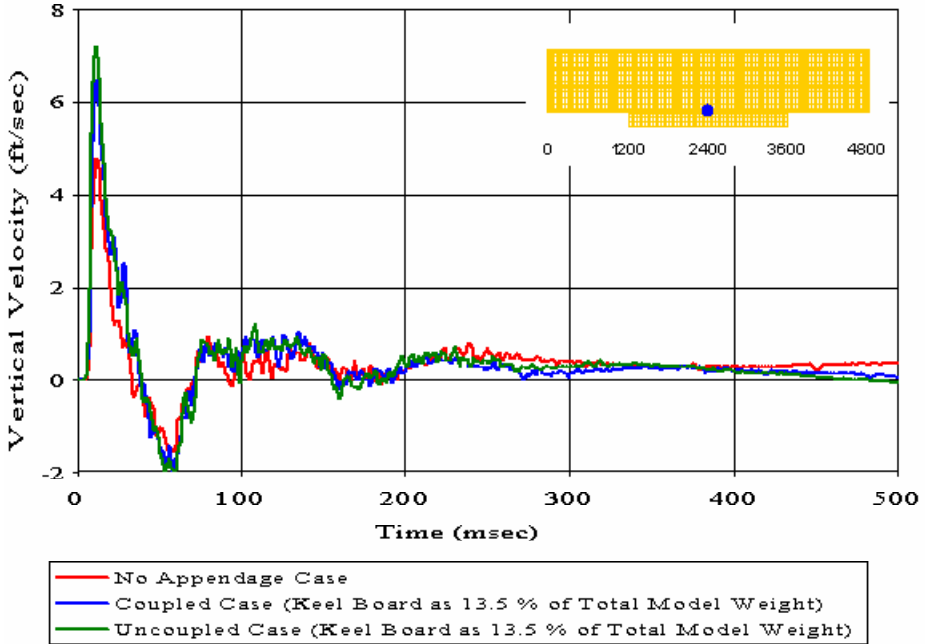
Figure 115. Keel Node 5315: (RM = 0.0790, RP = 0.0584, RC = 0.0871)

181

Meko-Like Box Model with Solid Keel Board

Node 5317 at Keel (x=2400 y=180 z=0)
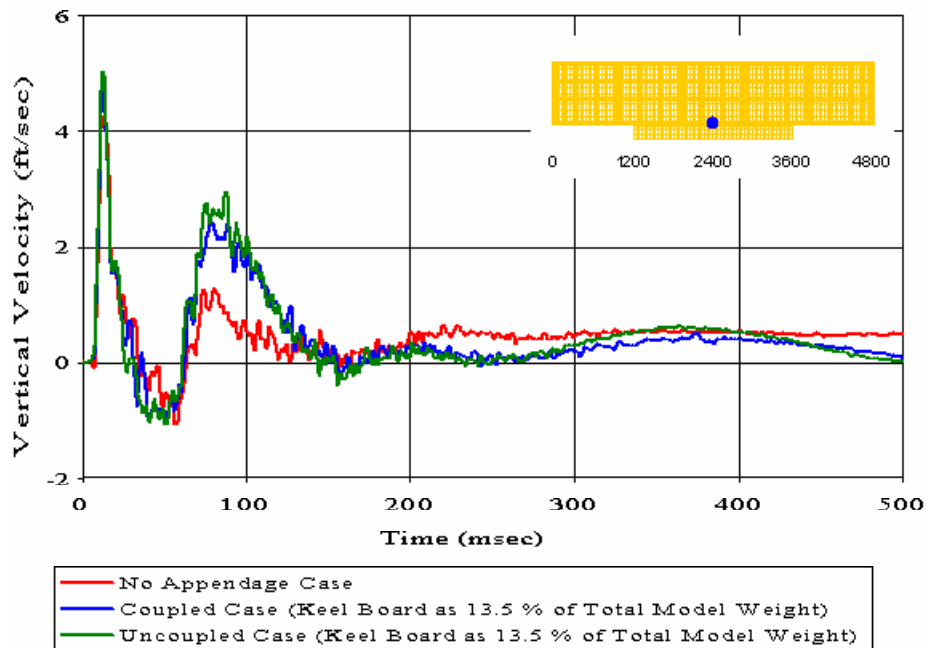
Figure 116. Keel Node 5317: (RM = 0.0834, RP = 0.0631, RC = 0.0927)

Meko-Like Box Model with Solid Keel Board

Node 5320 at Keel (x=2400 y=300 z=0)
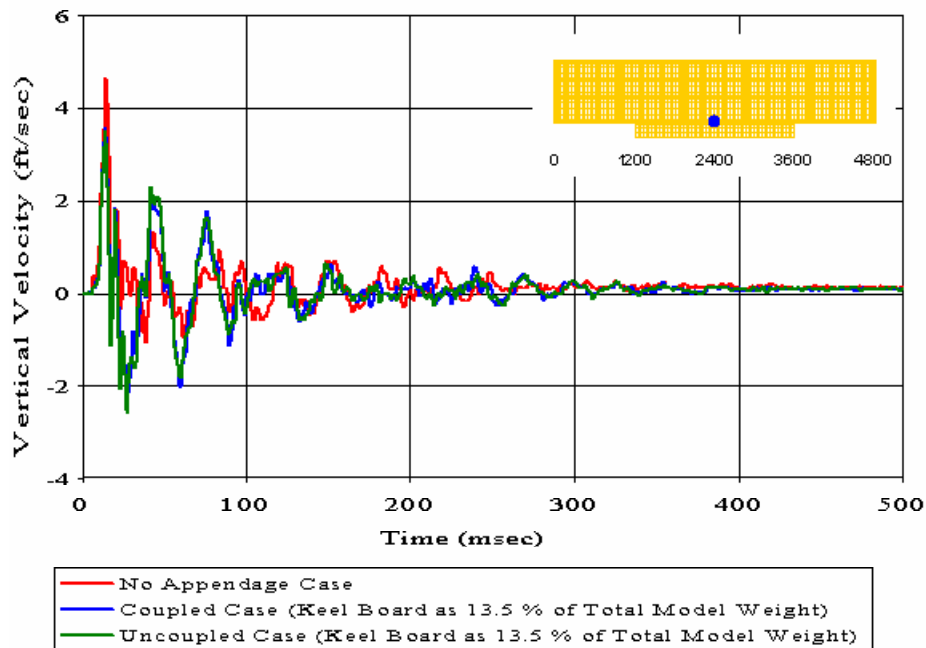
Figure 117. Keel Node 5320: (RM = 0.0324, RP = 0.0854, RC = 0.0809)

182

Meko–Like Box Model with Solid Keel Board

Node 6741 at Keel (x=3000 y=-20 z=0)
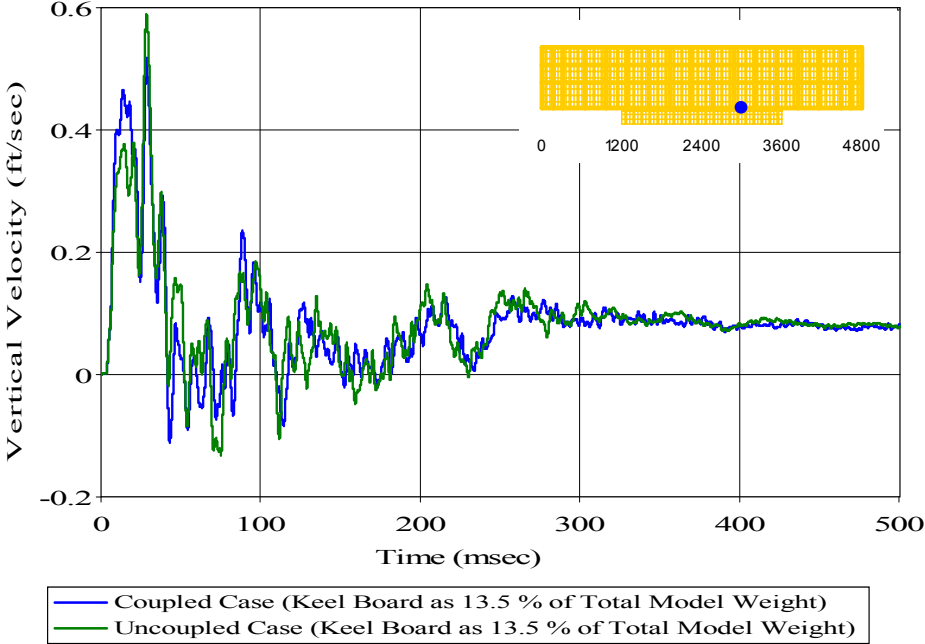
Figure 118.   Keel Node 6741: (RM = 0.0051, RP = 0.1035, RC = 0.0918)

Meko–Like Box Model with Solid Keel Board

Node 8170 at Keel (x=3600 y=-20 z=0)
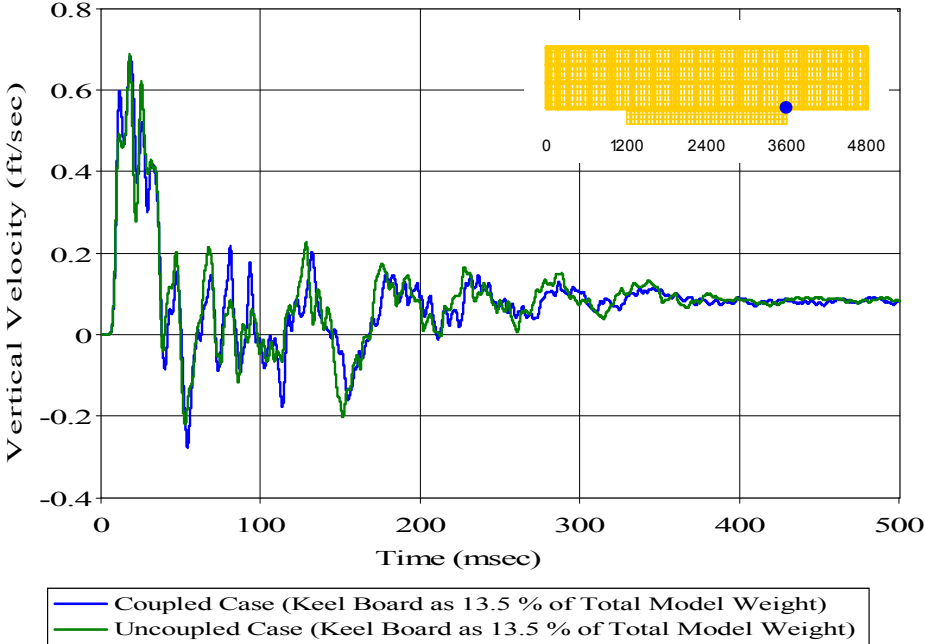
Figure 119.   Keel Node 8170: (RM = 0.0081, RP = 0.0981, RC = 0.0872)
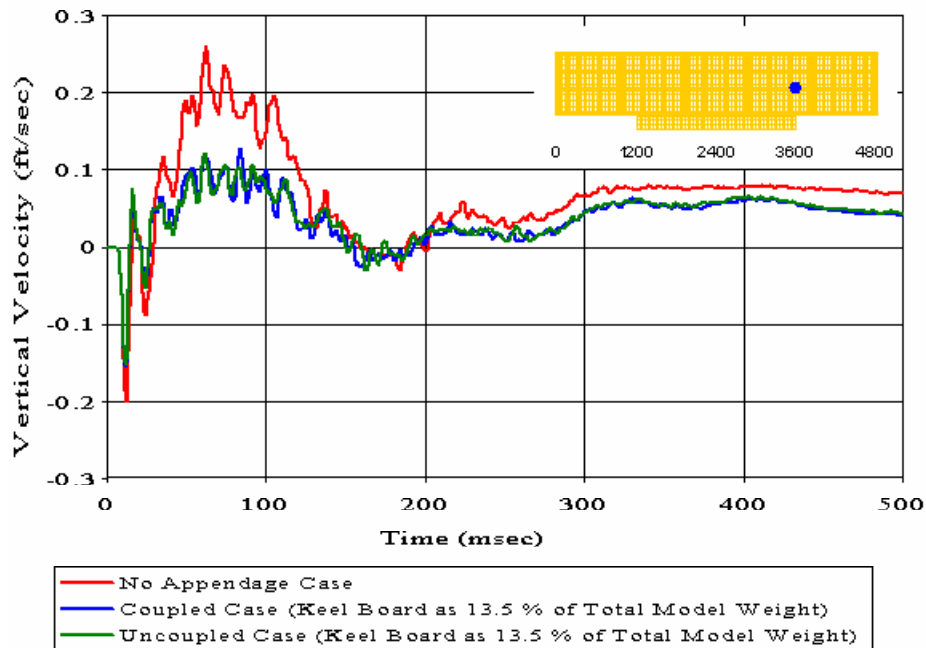
Figure 120.   First Deck Node 8364: (RM = 0.0102, RP = 0.0513, RC = 0.0464)
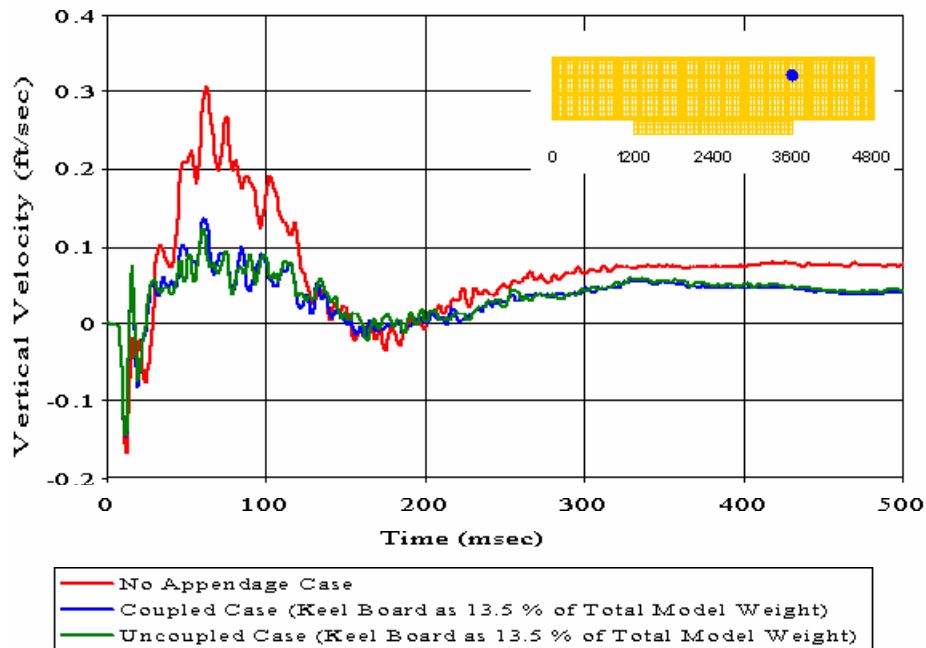
Figure 121.   Second Deck Node 8536: (RM = 0.0016, RP = 0.0585, RC = 0.0519)
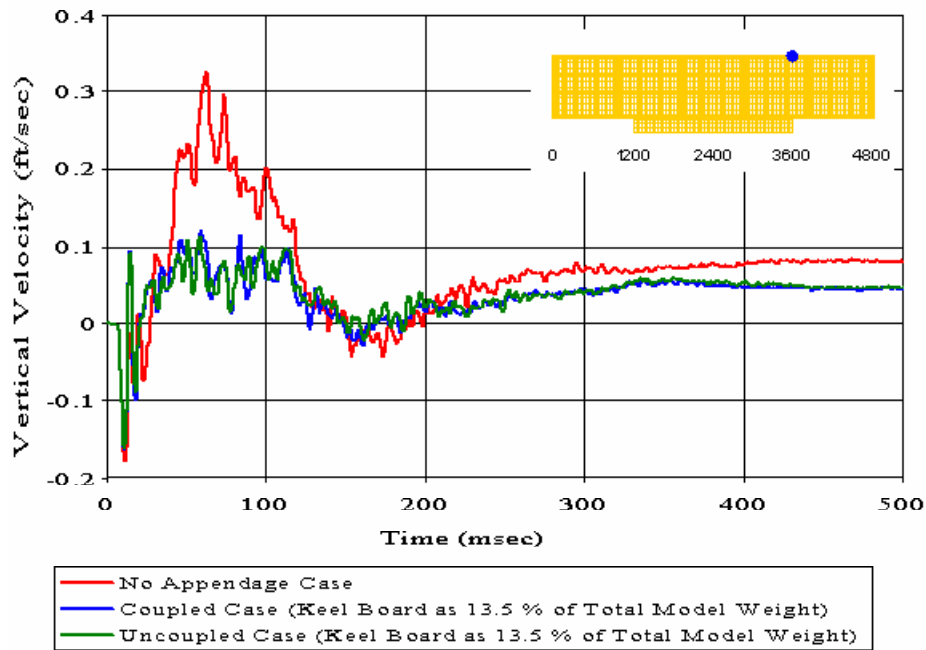
Figure 122. **Top Deck Node 8686: (RM = 0.0054, RP = 0.0675, RC = 0.0600)**
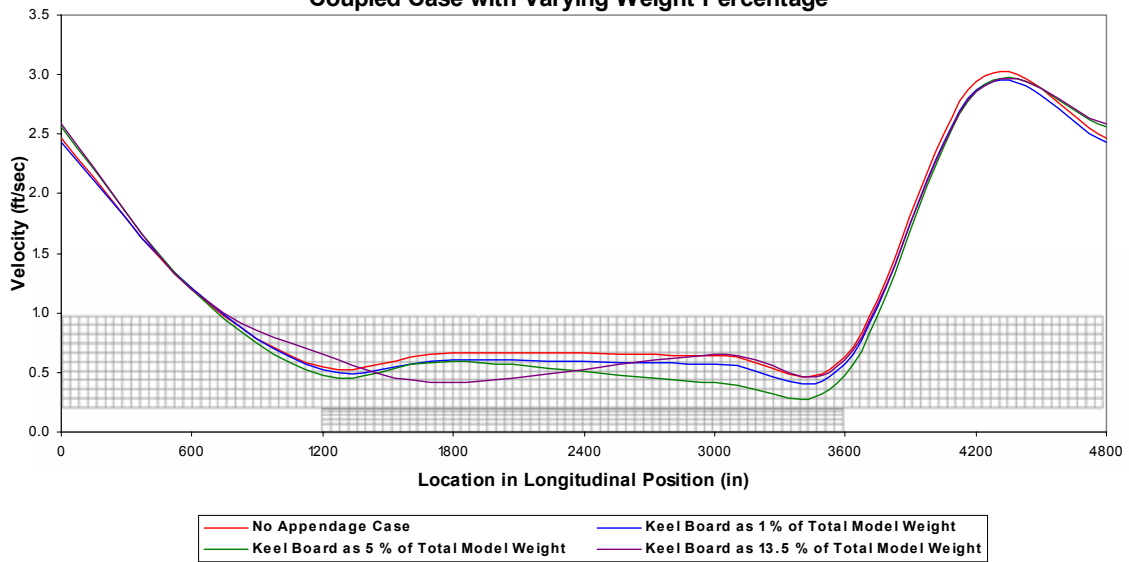
Figure 123. **Absolute Maximum Vertical Velocity as a Function of Position (First Deck)**

185
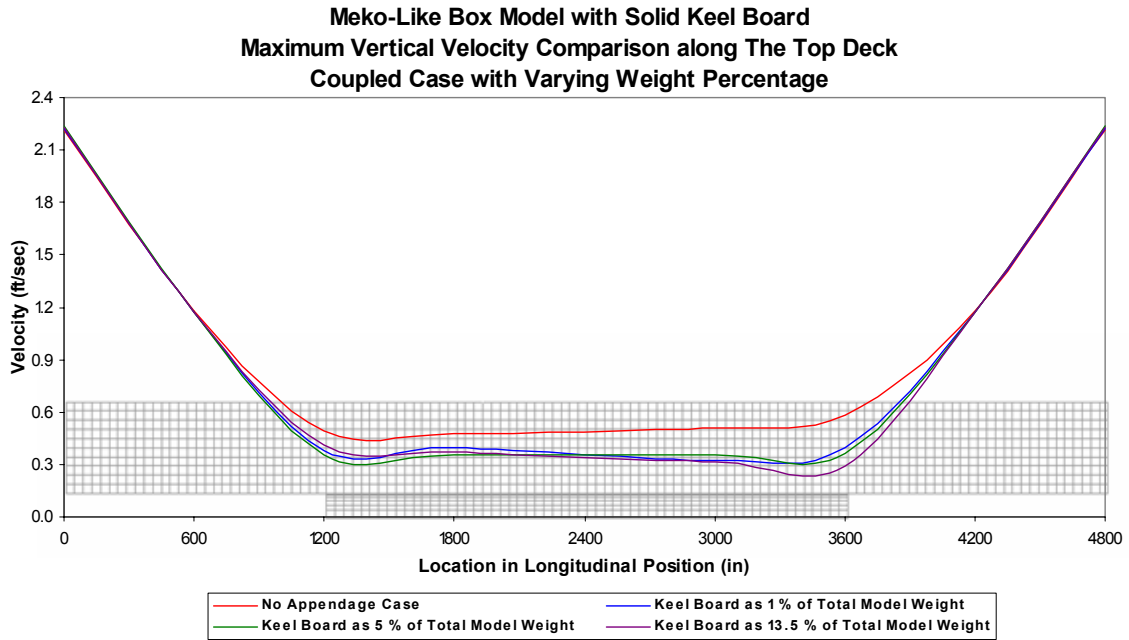
Figure 124. **Absolute Maximum Vertical Velocity as a Function of Position (Top Deck)**
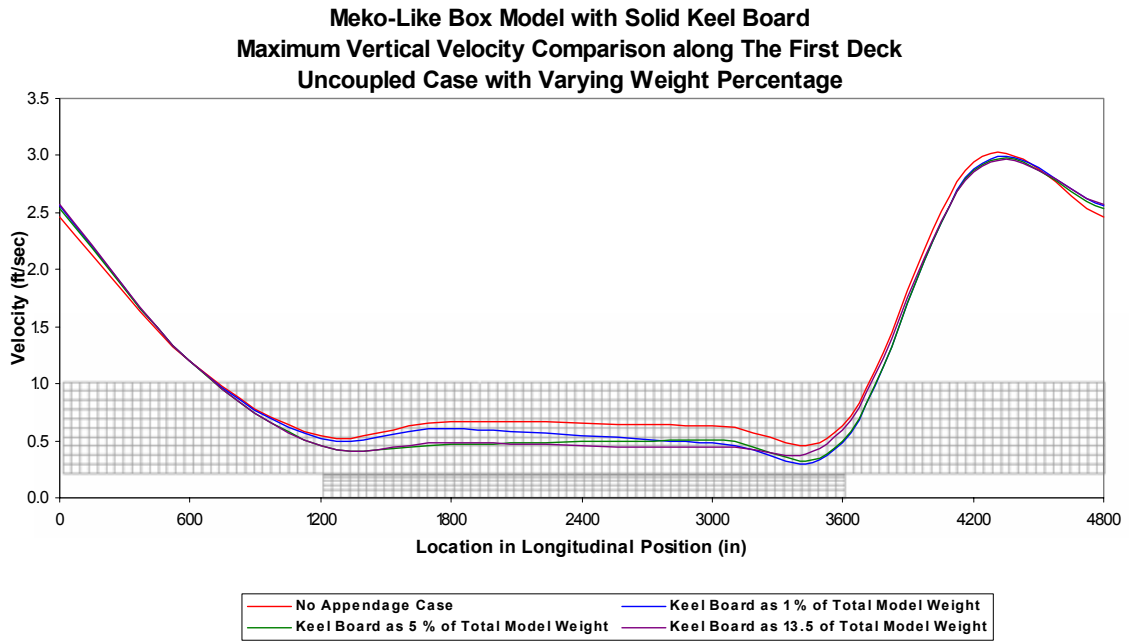
Figure 125. **Absolute Maximum Vertical Velocity as a Function of Position (First Deck)**

Figure 126. **Absolute Maximum Vertical Velocity as a Function of Position (Top Deck)**
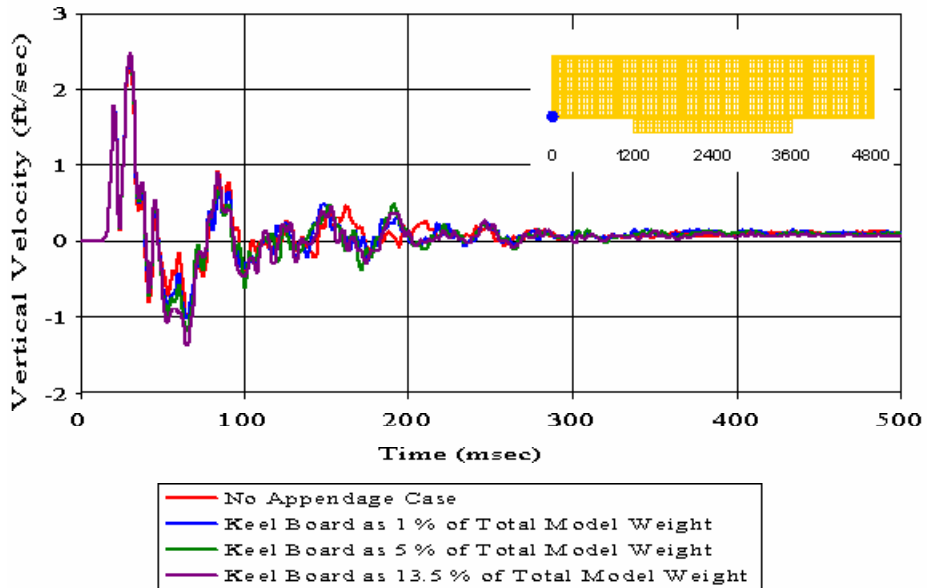
Figure 127. **Coupled Case with Varying Weight Percentage: Bulkhead Node 15**

187

Figure 128.   Coupled Case with Varying Weight Percentage: Bulkhead Node 148

Figure 129.   Coupled Case with Varying Weight Percentage: Bulkhead Node 268

Figure 130. Coupled Case with Varying Weight Percentage: Keel Node 2454

Figure 131. Coupled Case with Varying Weight Percentage: First Deck Node 2648

189

Figure 132. **Coupled Case with Varying Weight Percentage: Second Deck Node 2820**

Figure 133. **Coupled Case with Varying Weight Percentage: Top Deck Node 2970**

190

Figure 134.   Coupled Case with Varying Weight Percentage: Keel Node 3883

Figure 135.   Coupled Case with Varying Weight Percentage: Keel Node 5251

Figure 136.   Coupled Case with Varying Weight Percentage: Keel Node 5308

Figure 137.   Coupled Case with Varying Weight Percentage: Keel Node 5310

192

Figure 138.   Coupled Case with Varying Weight Percentage: Keel Node 5312

Figure 139.   Coupled Case with Varying Weight Percentage: Keel Node 5313

Figure 140.   Coupled Case with Varying Weight Percentage: Keel Node 5315

Figure 141.   Coupled Case with Varying Weight Percentage: Keel Node 5317

Figure 142. **Coupled Case with Varying Weight Percentage: Keel Node 5320**

Figure 143. **Coupled Case with Varying Weight Percentage: Keel Node 6741**

Figure 144.   Coupled Case with Varying Weight Percentage: Keel Node 8170

Figure 145.   Coupled Case with Varying Weight Percentage: First Deck Node 8364

Figure 146. **Coupled Case with Varying Weight Percentage: Second Deck Node 8536**

Figure 147. **Uncoupled Case with Varying Weight Percentage: Bulkhead Node 148**
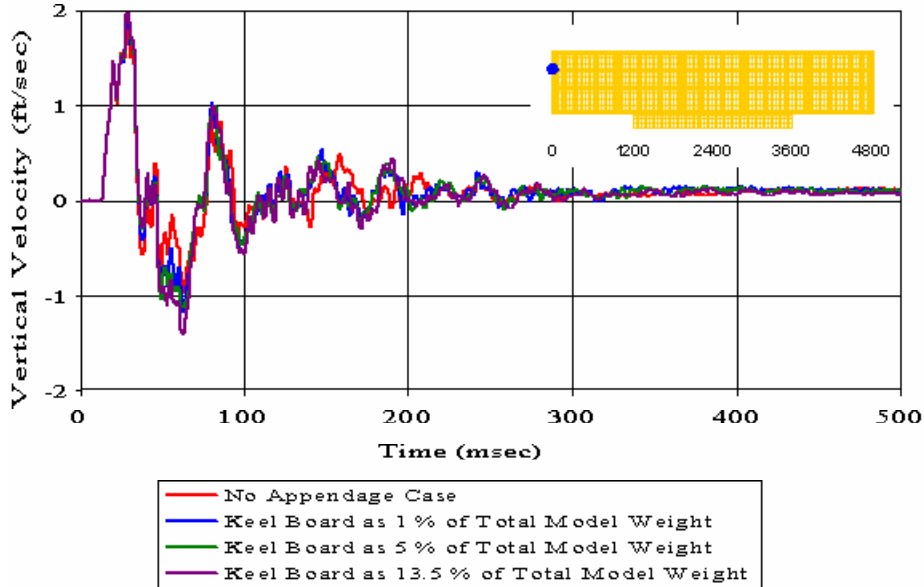
Figure 148. **Uncoupled Case with Varying Weight Percentage: Bulkhead Node 268**

Figure 149. **Uncoupled Case with Varying Weight Percentage: Bulkhead Node 388**

198

Meko-Like Box Model with Solid Keel Board

Node 2454 at Keel (x=1200 y=-20 z=0)

Uncoupled Case with Varying Weight Percentage
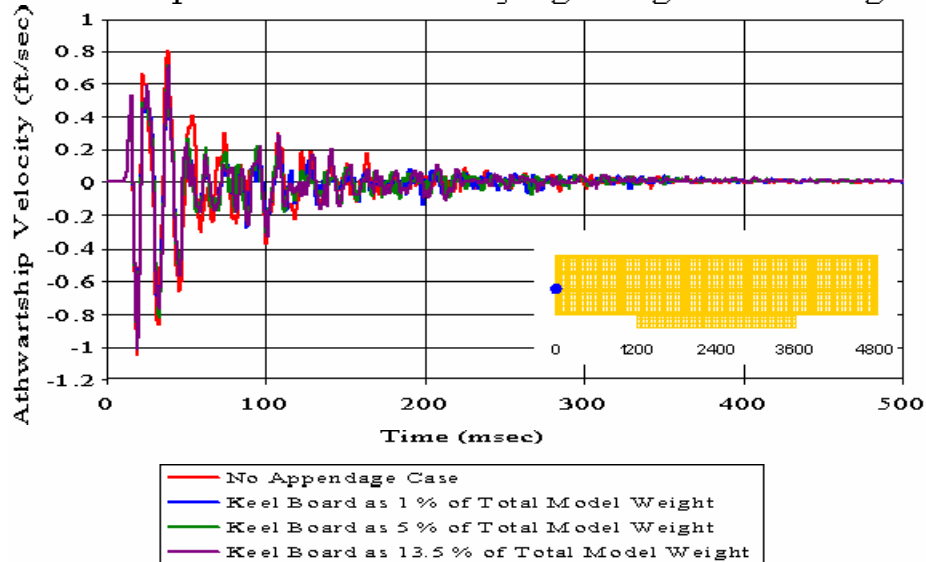

Figure 150.   Uncoupled Case with Varying Weight Percentage: Keel Node 2454

Meko-Like Box Model with Solid Keel Board
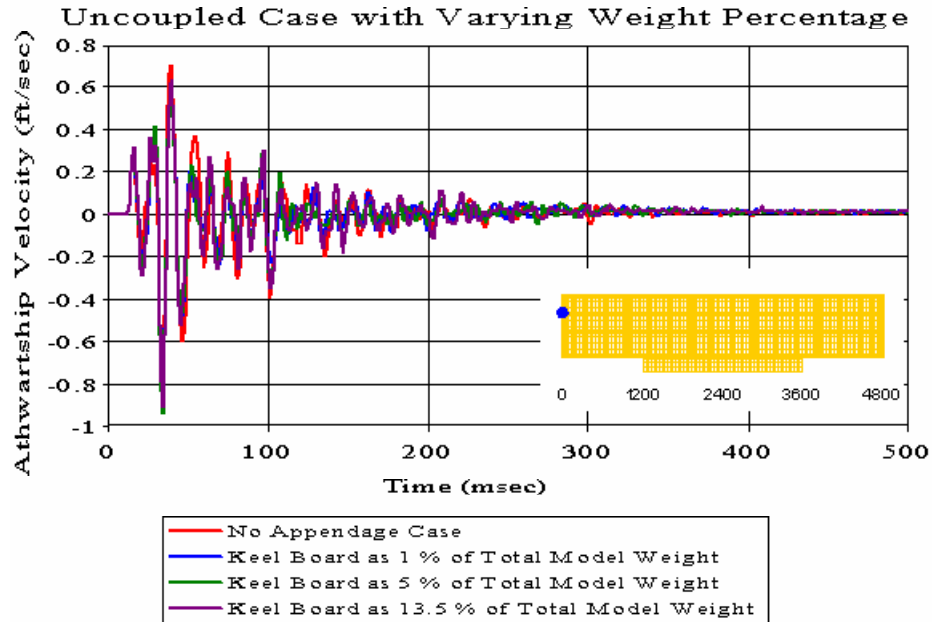
Node 2648 at First Deck (x=1200 y=-20 z=160)

Uncoupled Case with Varying Weight Percentage
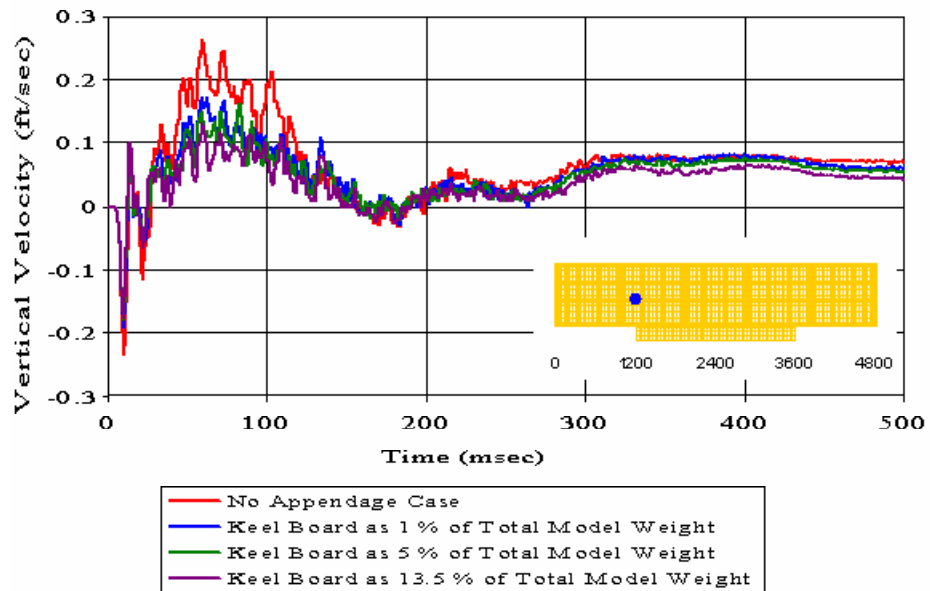
Figure 151.   Uncoupled Case with Varying Weight Percentage: First Deck Node 2648
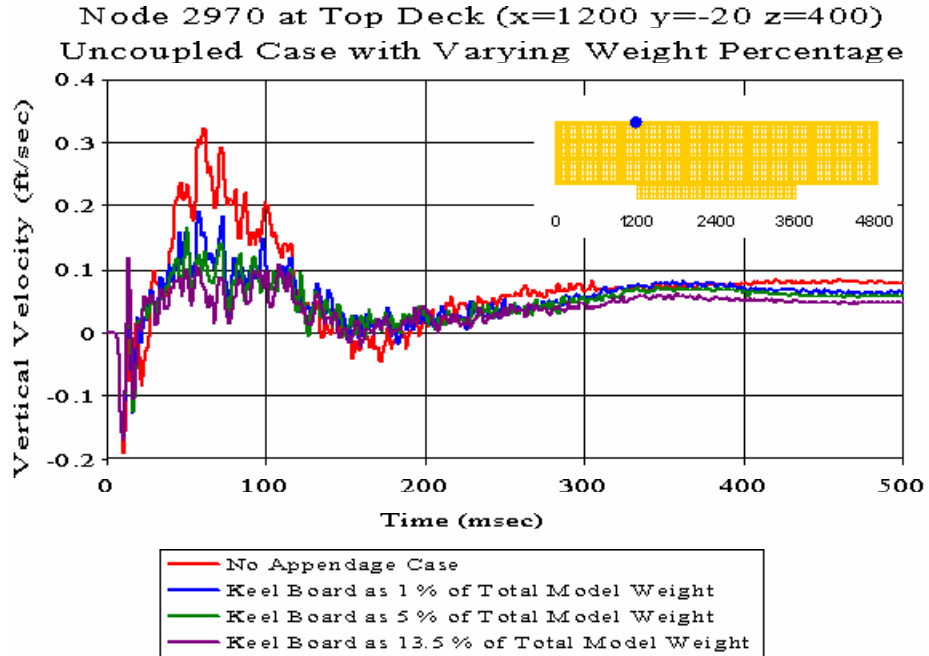
Figure 152.   Uncoupled Case with Varying Weight Percentage: Top Deck Node 2970
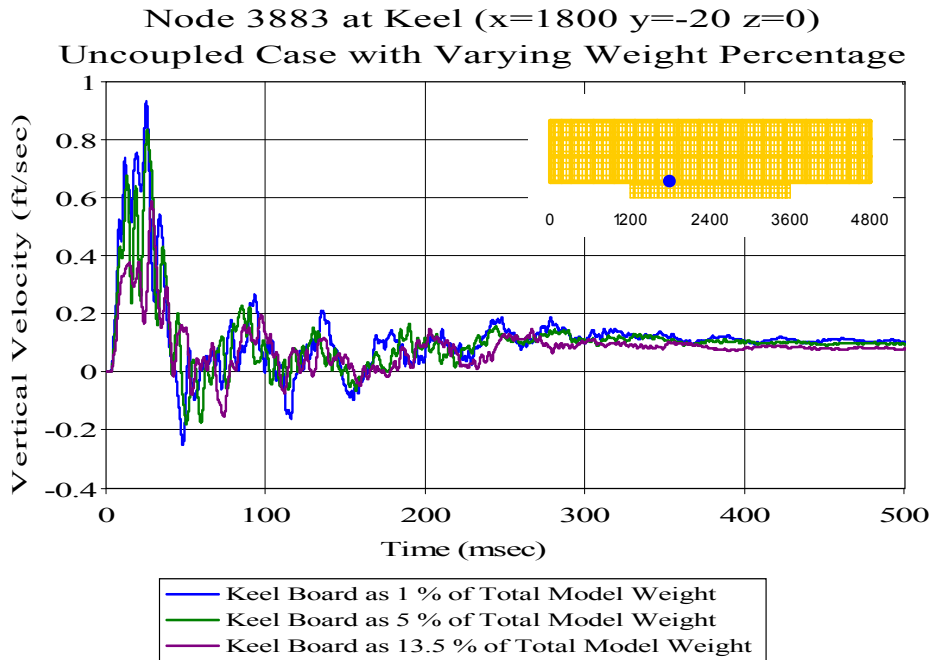
Figure 153.   Uncoupled Case with Varying Weight Percentage: Keel Node 3883

200

Figure 154. Uncoupled Case with Varying Weight Percentage: Keel Node 5251

Figure 155. Uncoupled Case with Varying Weight Percentage: Keel Node 5308

201

Figure 156.   Uncoupled Case with Varying Weight Percentage: Keel Node 5310

Figure 157.   Uncoupled Case with Varying Weight Percentage: Keel Node 5312

Figure 158. Uncoupled Case with Varying Weight Percentage: Keel Node 5313

Figure 159. Uncoupled Case with Varying Weight Percentage: Keel Node 5315

Figure 160. Uncoupled Case with Varying Weight Percentage: Keel Node 5317

Figure 161. Uncoupled Case with Varying Weight Percentage: Keel Node 5320

Figure 162.   Uncoupled Case with Varying Weight Percentage: Keel Node 6741

Figure 163.   Uncoupled Case with Varying Weight Percentage: Keel Node 8170

Figure 164. Uncoupled Case with Varying Weight Percentage: First Deck Node 8364

Figure 165. Uncoupled Case with Varying Weight Percentage: Second Deck Node 8536

206

Figure 166. Uncoupled Case with Varying Weight Percentage: Top Deck Node 8686

B.   MEKO-LIKE BOX MODEL WITH SHELL KEEL BOARD

Figure 167. Bulkhead Node 15: (RM = 0.0644, RP = 0.0962, RC = 0.1026)

Meko-Like Box Model with Shell Keel Board

Node 148 at Bulkhead (x=0 y=-20 z=160)
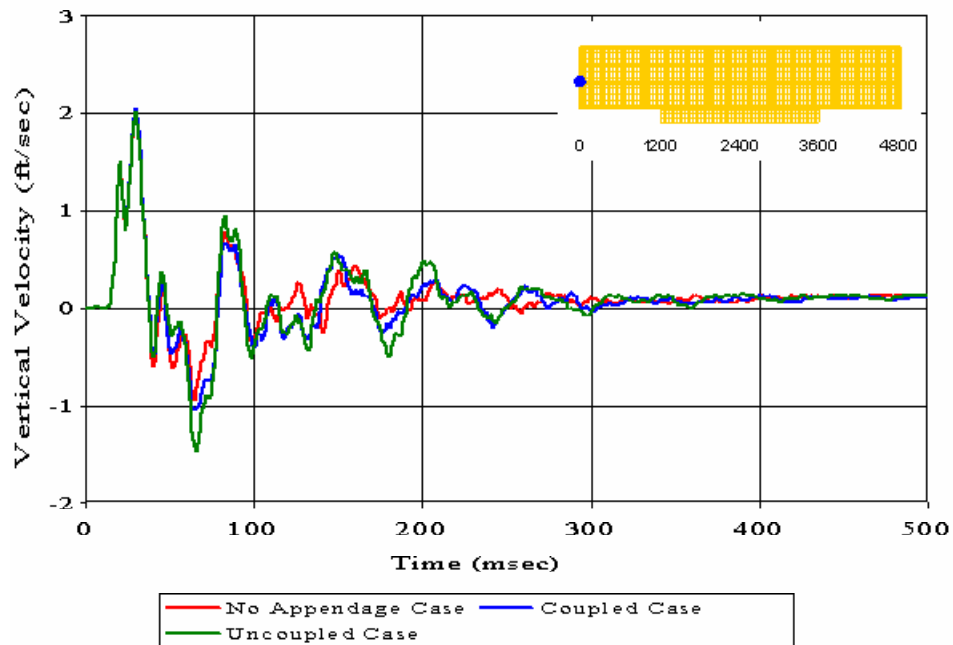
Figure 168. Bulkhead Node 148: (RM = 0.0756, RP = 0.0813, RC = 0.0984)

Meko-Like Box Model with Shell Keel Board

Node 268 at Bulkhead (x=0 y=-20 z=280)
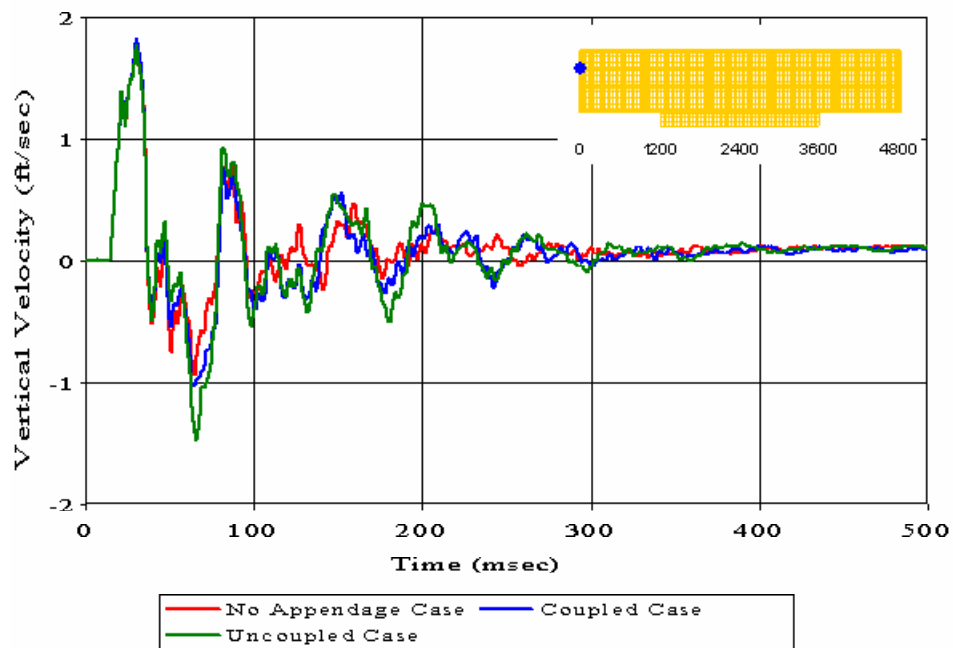
Figure 169. Bulkhead Node 268: (RM = 0.0739, RP = 0.0865, RC = 0.1008)
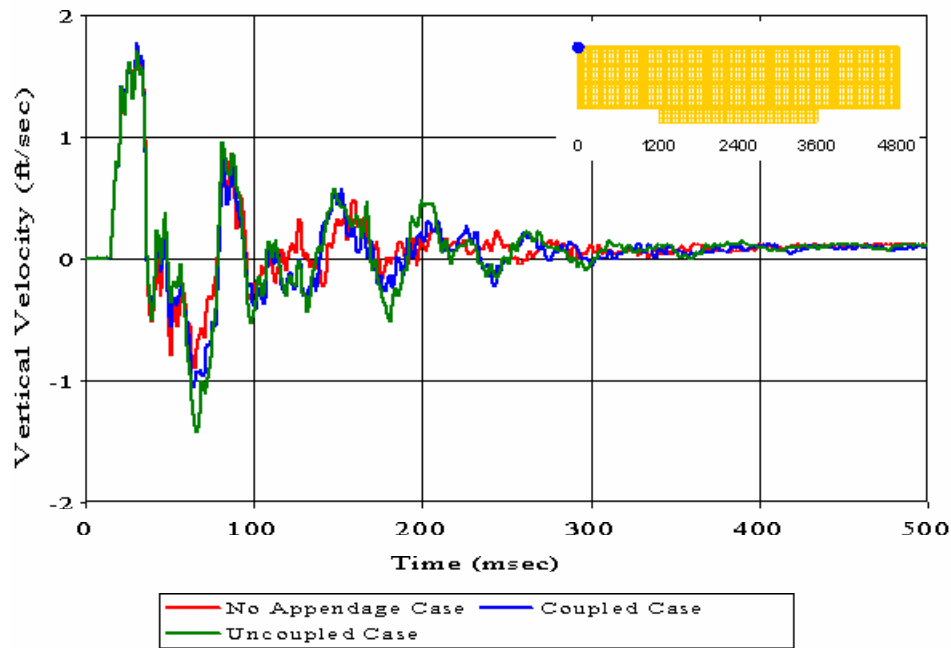
Figure 170.   Bulkhead Node 388: (RM = 0.0709, RP = 0.0949, RC = 0.1050)
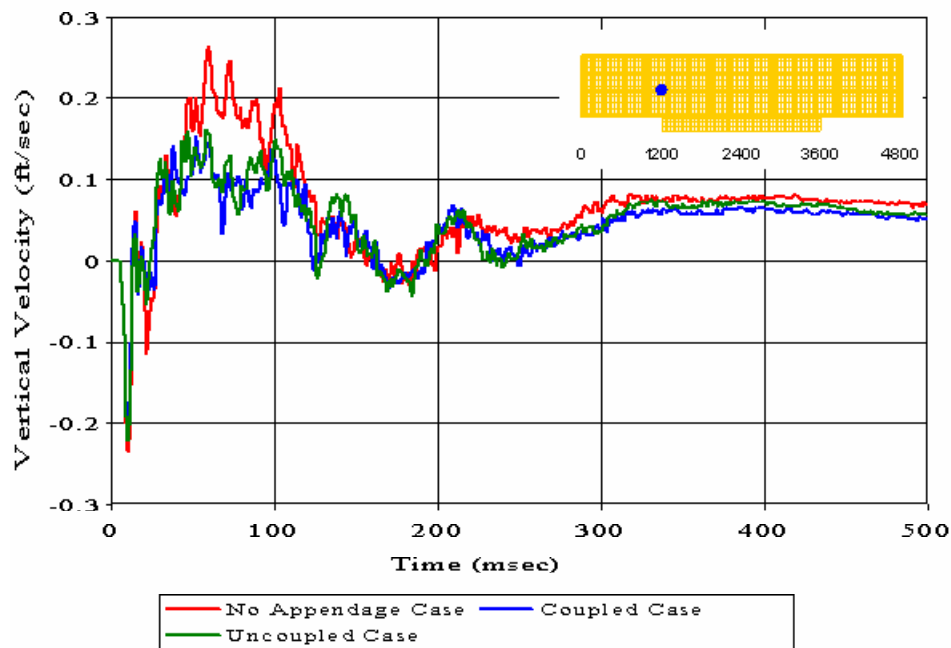
Figure 171.   First Deck Node 2648: (RM = 0.0872, RP = 0.0807, RC = 0.1053)
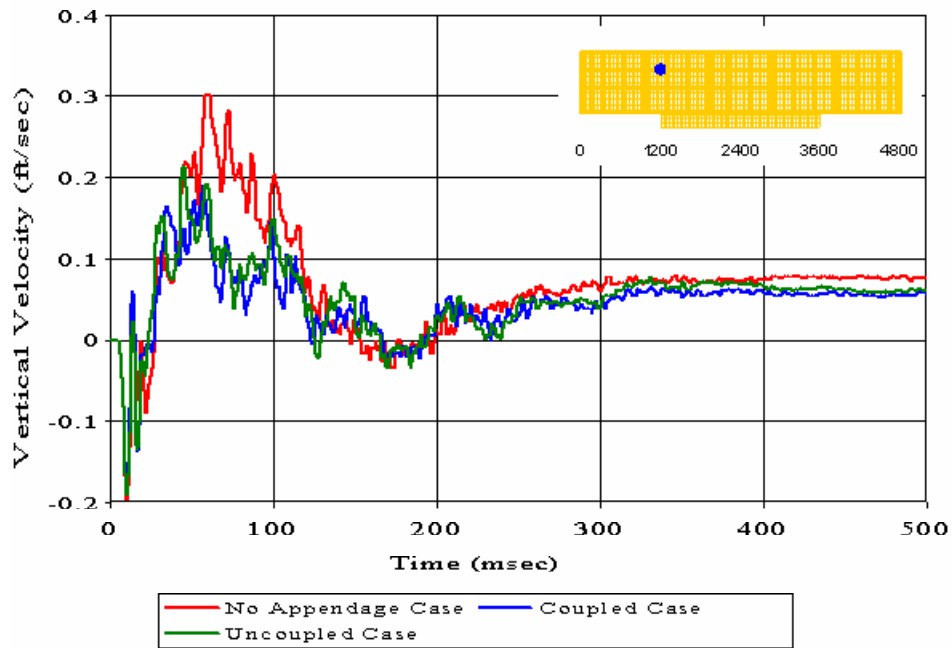
Figure 172.   Second Deck Node 2820: (RM = 0.0829, RP = 0.0908, RC = 0.1089)
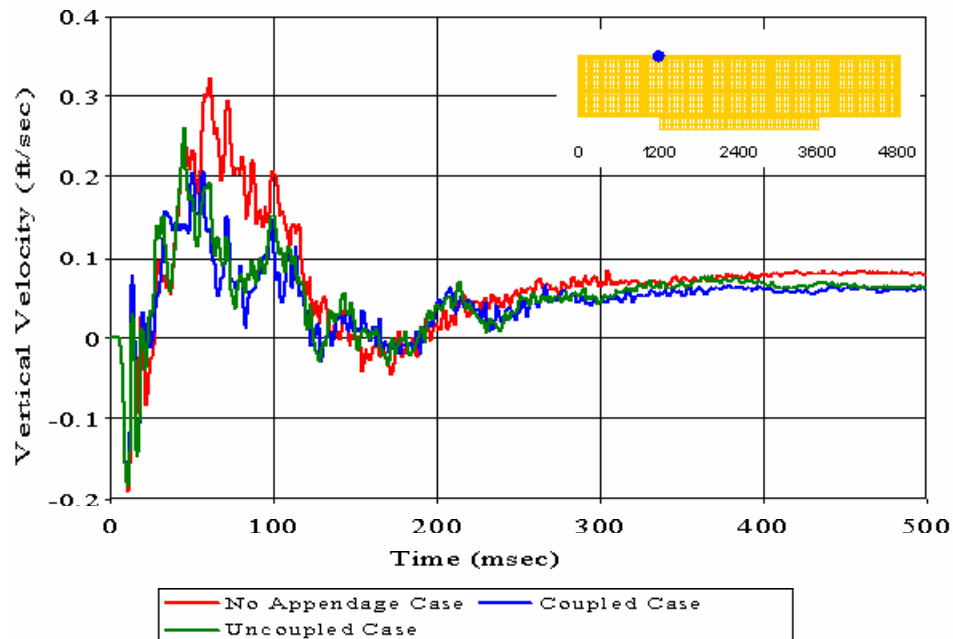
Figure 173.   Top Deck Node 2970: (RM = 0.0814, RP = 0.0908, RC = 0.1081)

Meko-Like Box Model with Shell Keel Board

Node 3883 at Keel (x=1800 y=-20 z=0)
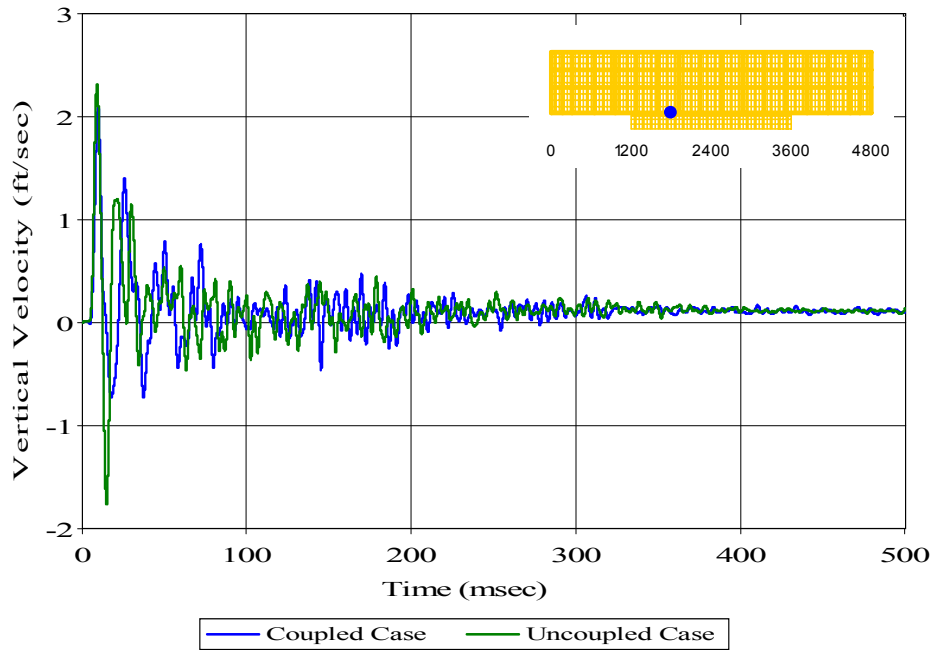
Figure 174.   Keel Node 3883: (RM = 0.0942, RP = 0.3332, RC = 0.3069)

Meko-Like Box Model with Shell Keel Board

Node 5251 at Keel (x=2400 y=-300 z=0)
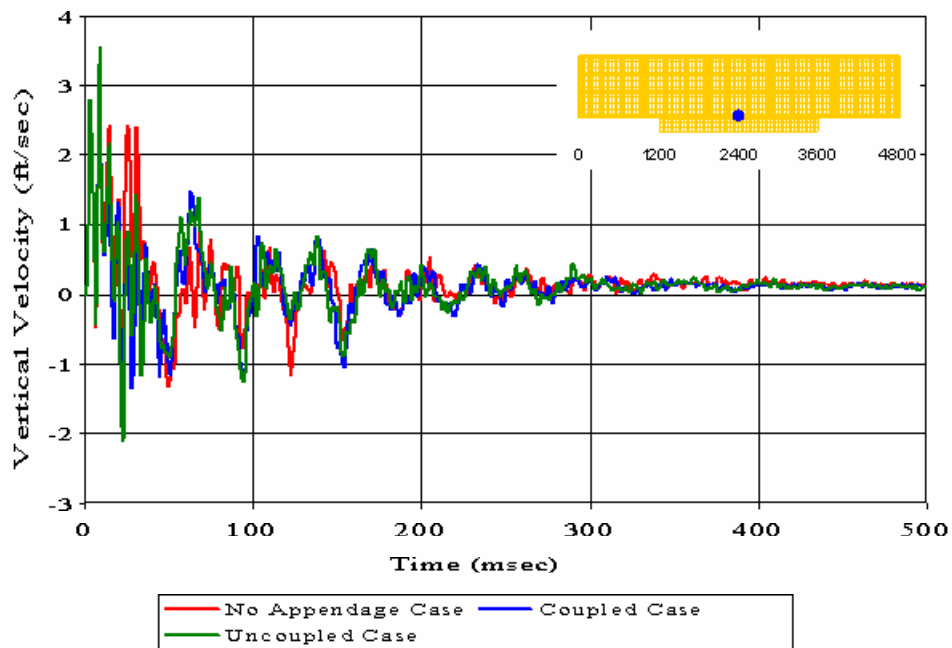
Figure 175.   Keel Node 5251: (RM = 0.0536, RP = 0.1511, RC = 0.1421)
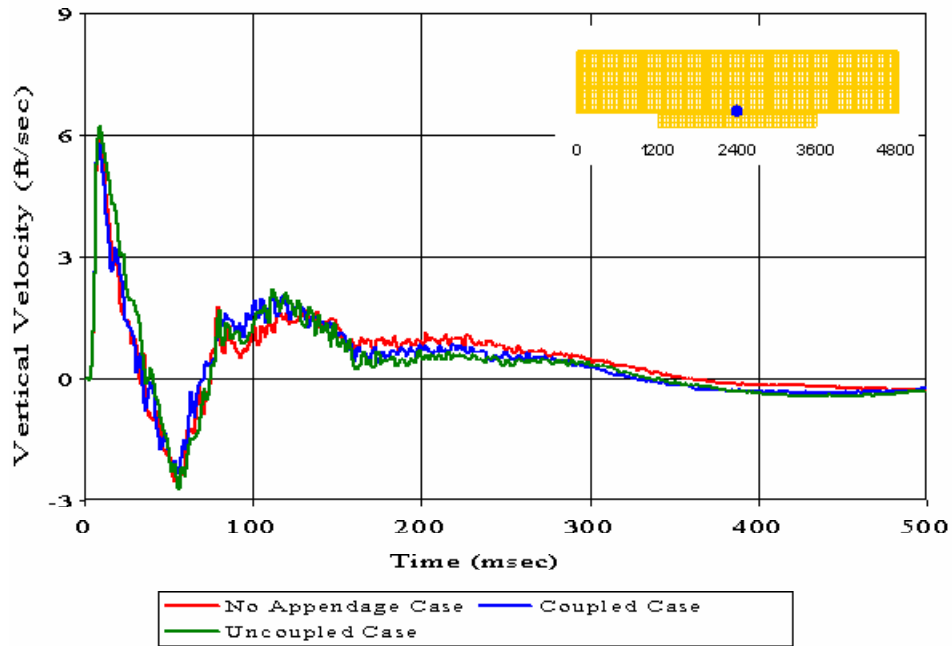
Figure 176. Keel Node 5310: (RM = 0.0821, RP = 0.0846, RC = 0.1045)
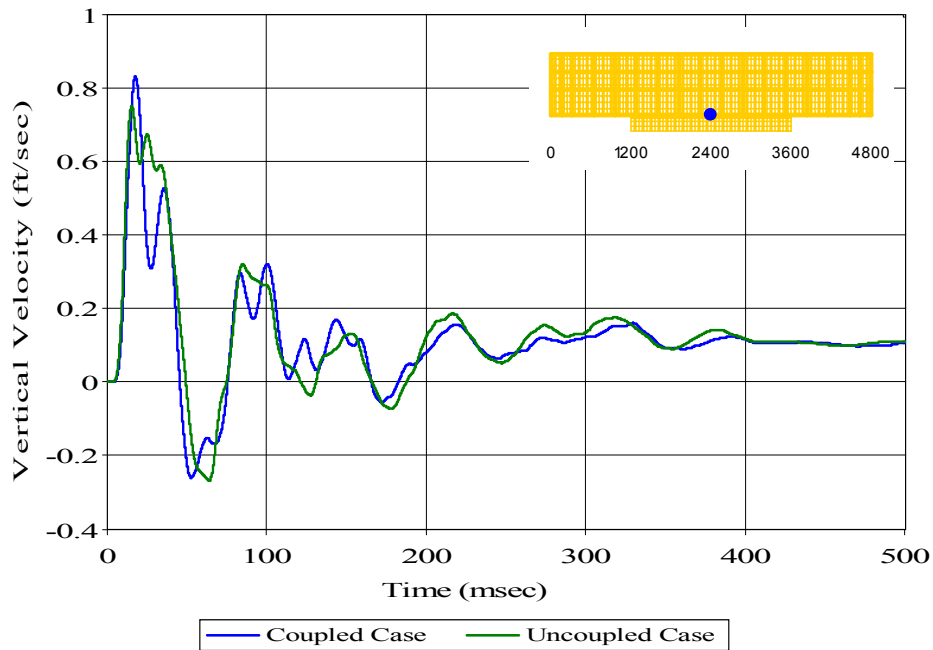
Figure 177. Keel Node 5312: (RM = 0.0693, RP = 0.0939, RC = 0.1034)

212

Meko-Like Box Model with Shell Keel Board
Node 5313 at Keel (x=2400 y=20 z=0)
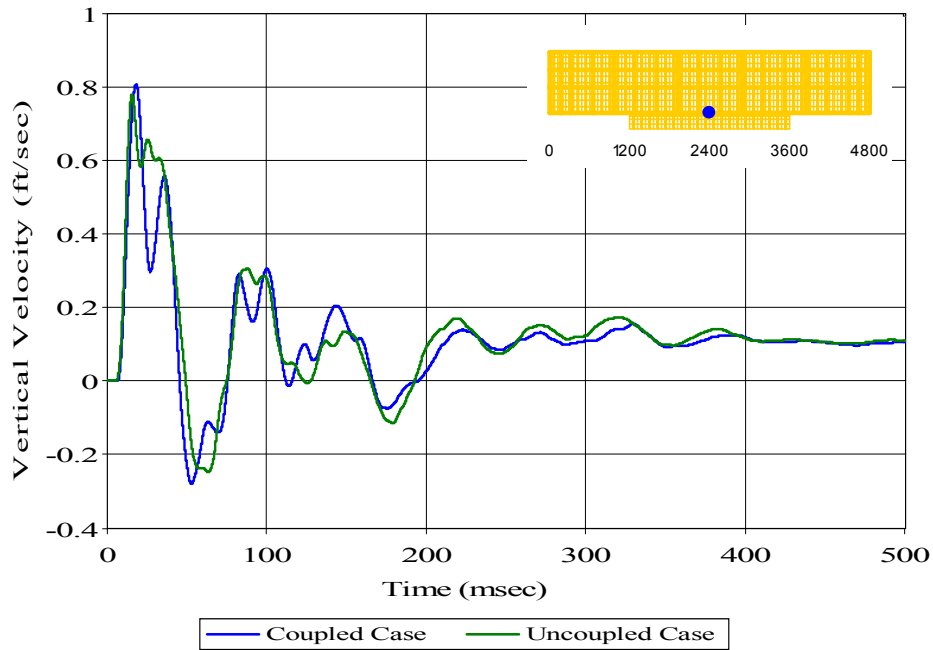
Figure 178.   Keel Node 5313: (RM = 0.0744, RP = 0.0960, RC = 0.1076)

Meko-Like Box Model with Shell Keel Board
Node 5315 at Keel (x=2400 y=100 z=0)
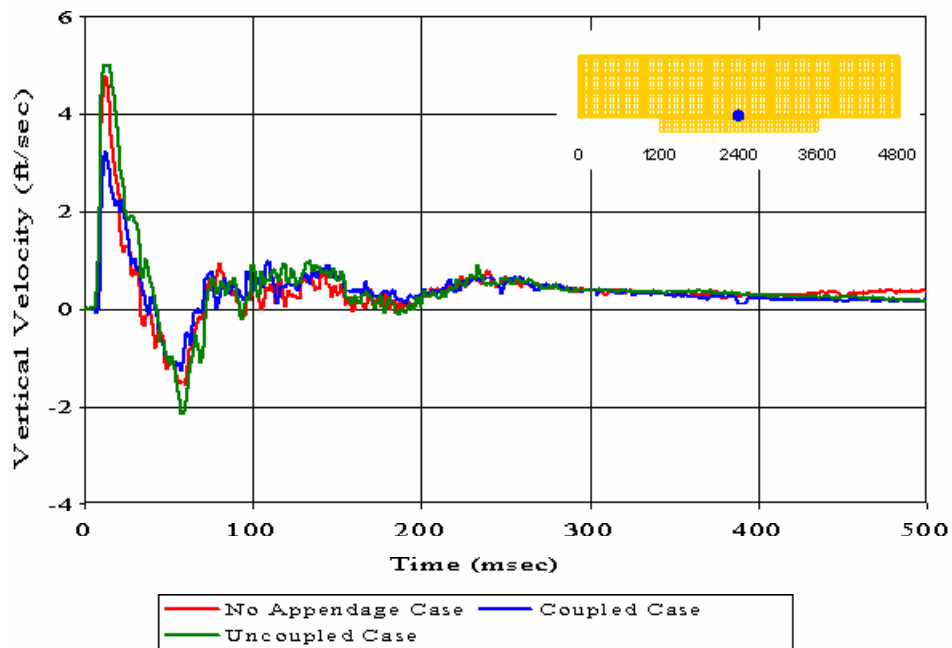
Figure 179.   Keel Node 5315: (RM = 0.2594, RP = 0.1150, RC = 0.2515)

213

Meko-Like Box Model with Shell Keel Board

Node 5317 at Keel (x=2400 y=180 z=0)
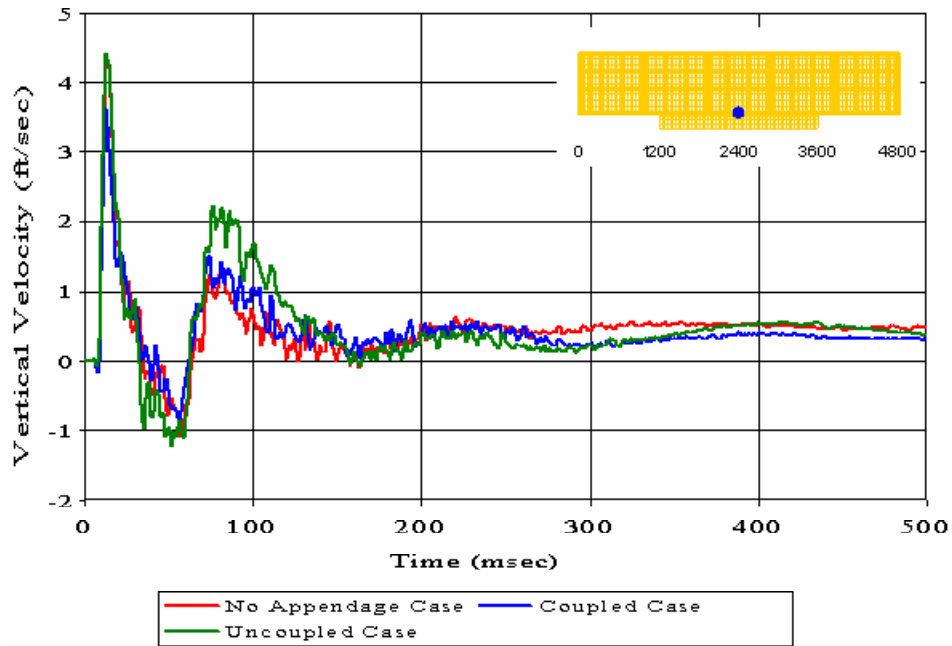
Figure 180. Keel Node 5317: (RM = 0.2080, RP = 0.1038, RC = 0.2061)

Meko-Like Box Model with Shell Keel Board

Node 5320 at Keel (x=2400 y=300 z=0)
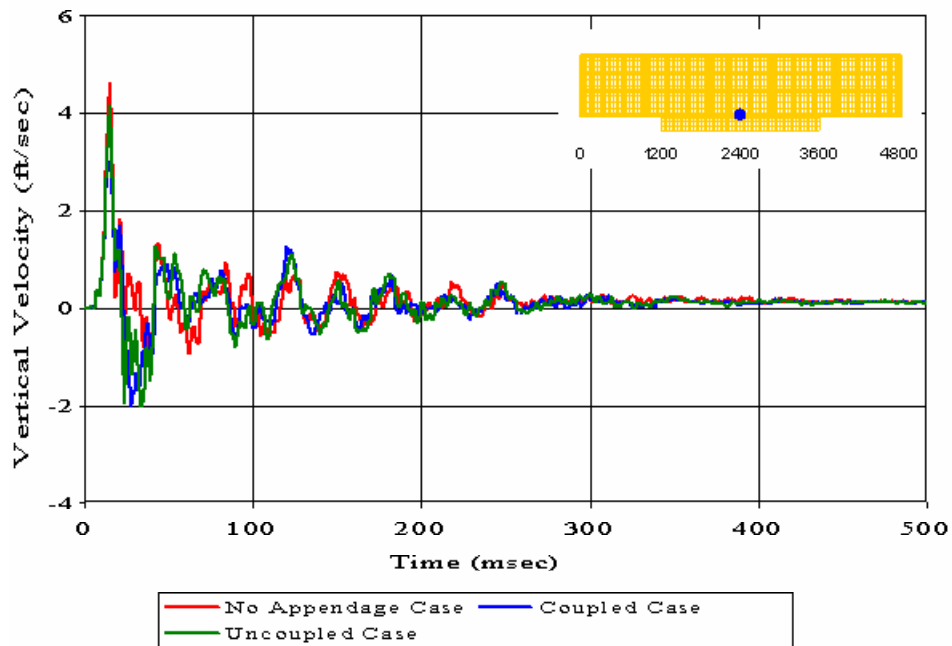
Figure 181. Keel Node 5320: (RM = 0.0894, RP = 0.1486, RC = 0.1537)

Meko–Like Box Model with Shell Keel Board

Node 6741 at Keel (x=3000 y=-20 z=0)
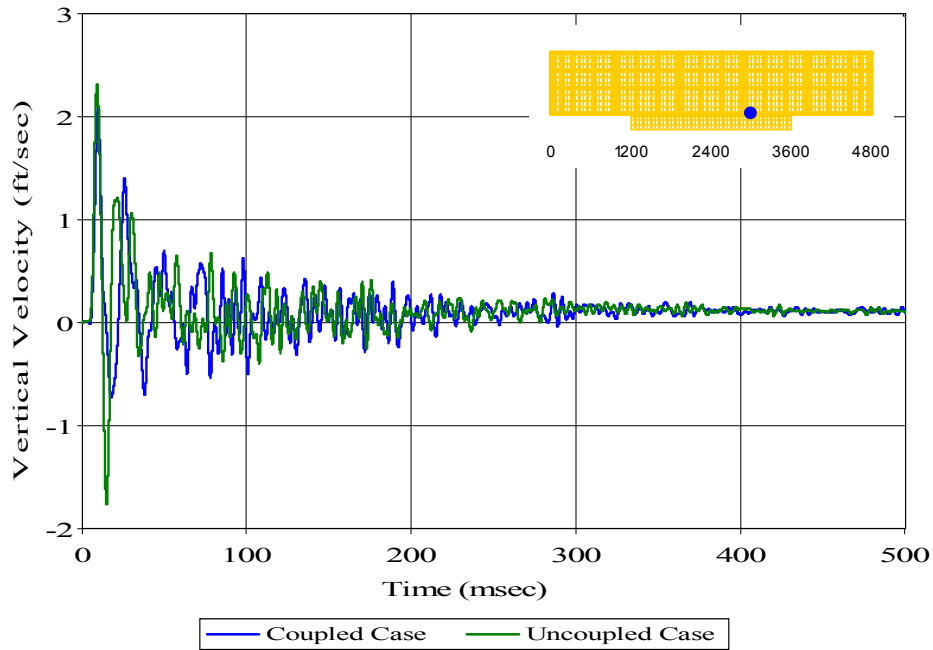
Figure 182. **Keel Node 6741: (RM = 0.0844, RP = 0.3460, RC = 0.3156)**

Meko–Like Box Model with Shell Keel Board

Node 8170 at Keel (x=3600 y=-20 z=0)
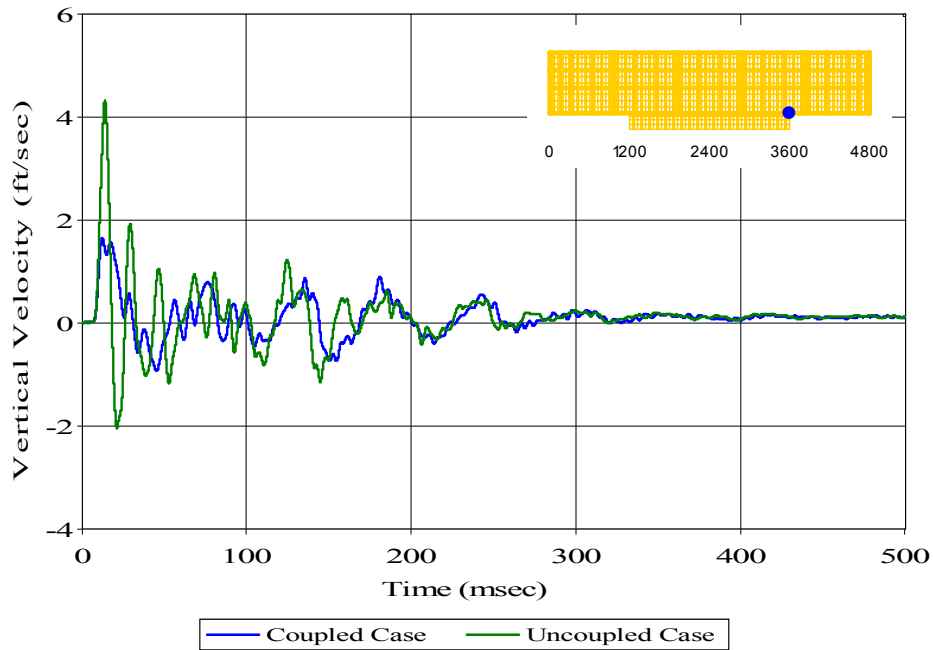
Figure 183. **Keel Node 8170: (RM = 0.3000, RP = 0.3571, RC = 0.4134)**

215

Meko-Like Box Model with Shell Keel Board
Node 8364 at First Deck (x=3600 y=-20 z=160)
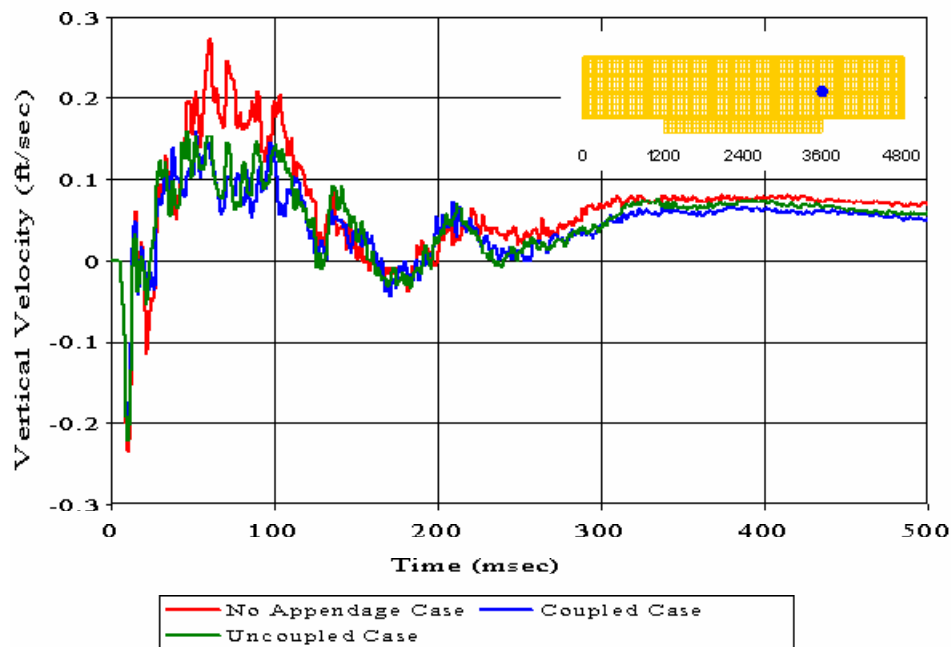
Figure 184.   First Deck Node 8364: (RM = 0.0886, RP = 0.0797, RC = 0.1056)

Meko-Like Box Model with Shell Keel Board
Node 8536 at Second Deck (x=3600 y=-20 z=280)
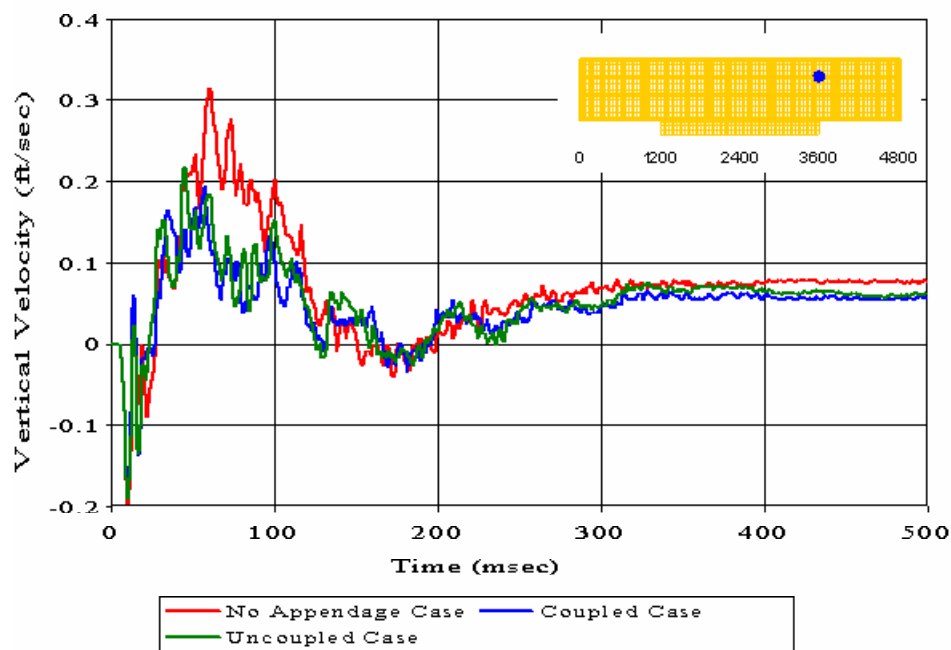
Figure 185.   Second Deck Node 8536: (RM = 0.0846, RP = 0.0934, RC = 0.1117)

216
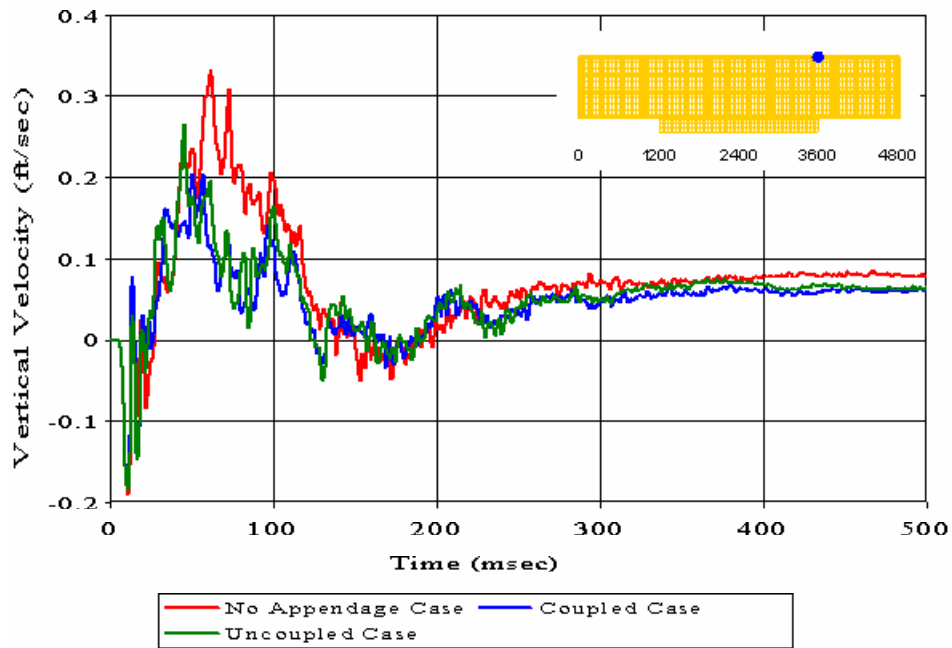
Figure 186.   Top Deck Node 8686: (RM = 0.0849, RP = 0.0946, RC = 0.1126)

C.   MEKO-LIKE BOX MODEL WITH OPEN KEEL BOARD
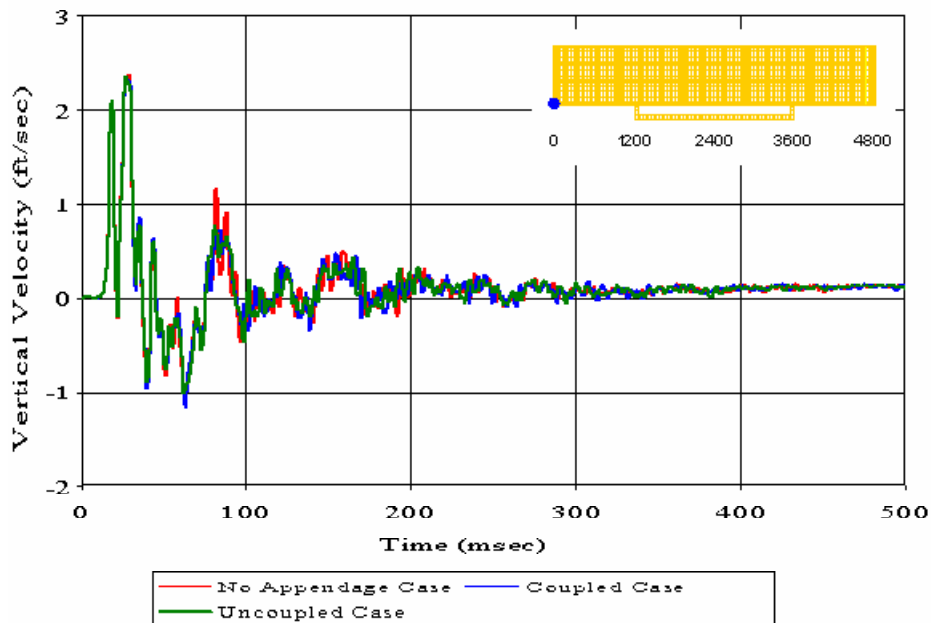
Figure 187.   Bulkhead Node 15: (RM = -0.0036, RP = 0.0777, RC = 0.0689)

Meko-Like Box Model with Open Keel Board

Node 148 at Bulkhead (x=0 y=-20 z=160)
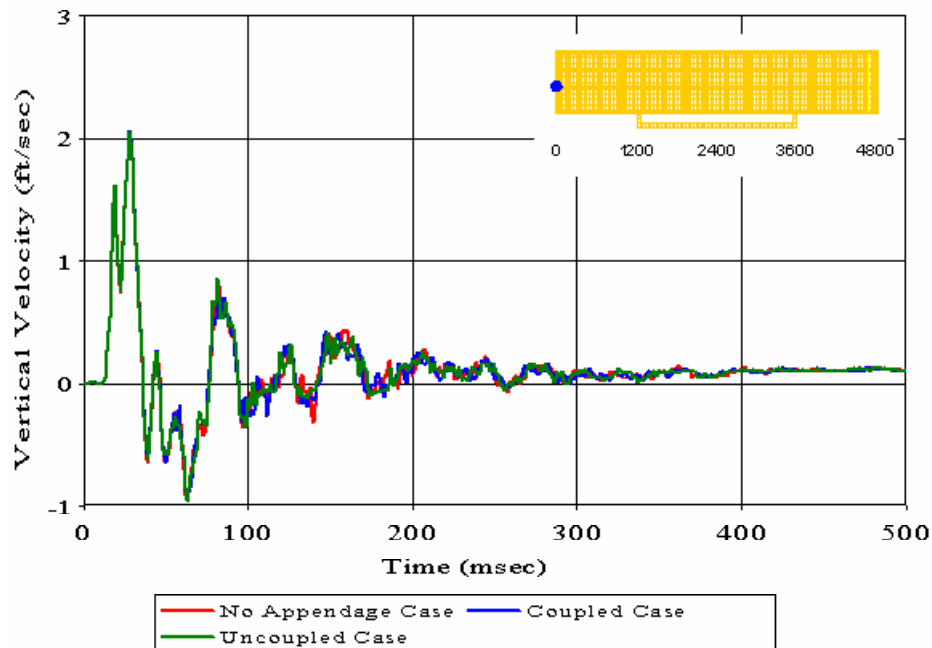
Figure 188. **Bulkhead Node 148: (RM = 0.0013, RP = 0.0528, RC = 0.0468)**

Meko-Like Box Model with Open Keel Board

Node 268 at Bulkhead (x=0 y=-20 z=280)
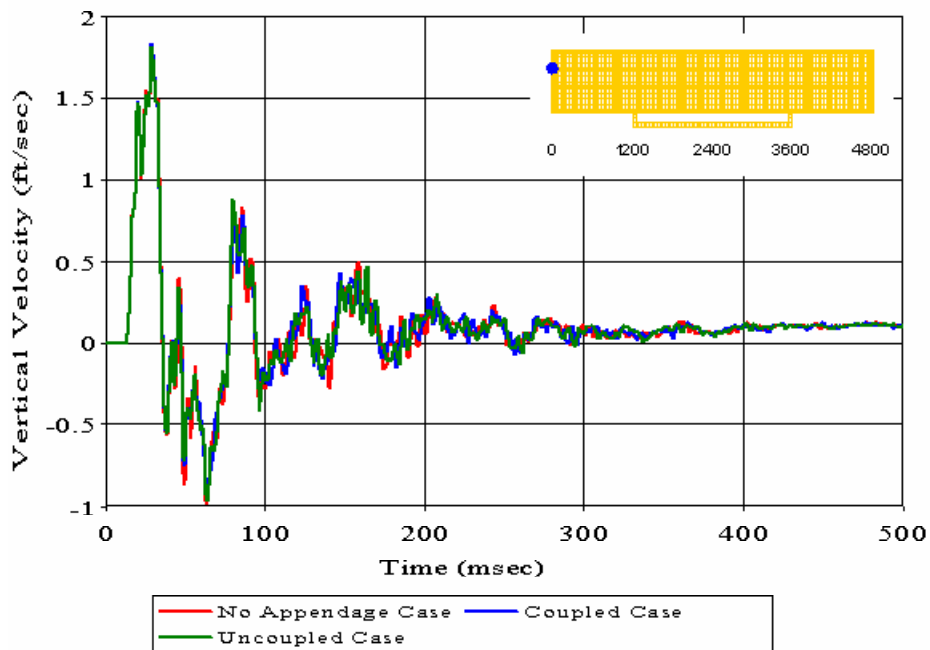
Figure 189. **Bulkhead Node 268: (RM = 0.0035, RP = 0.0536, RC = 0.0476)**

218
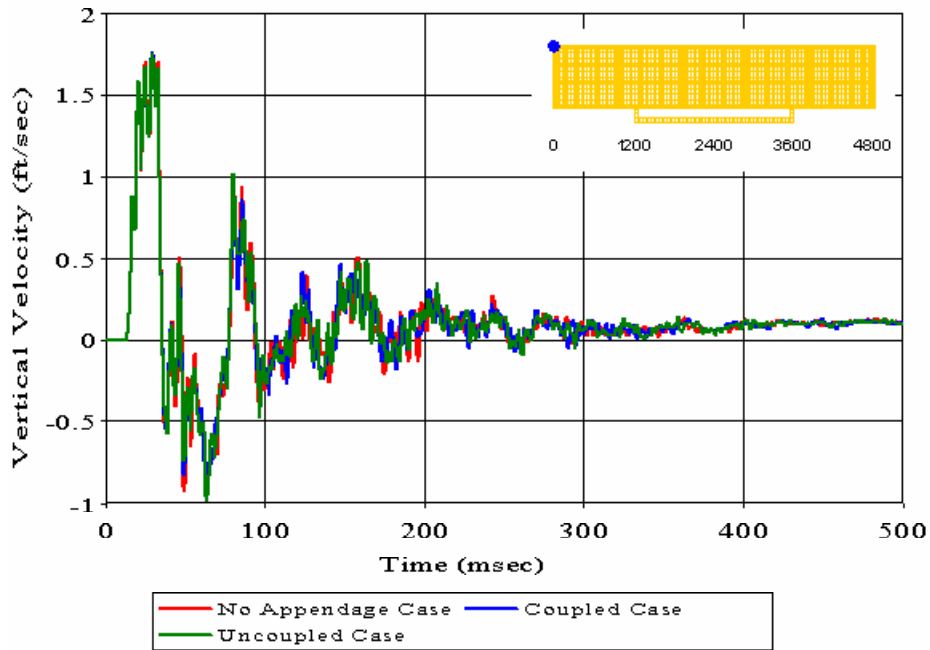
Figure 190.   Bulkhead Node 388: (RM = 0.0049, RP = 0.0658, RC = 0.0585)
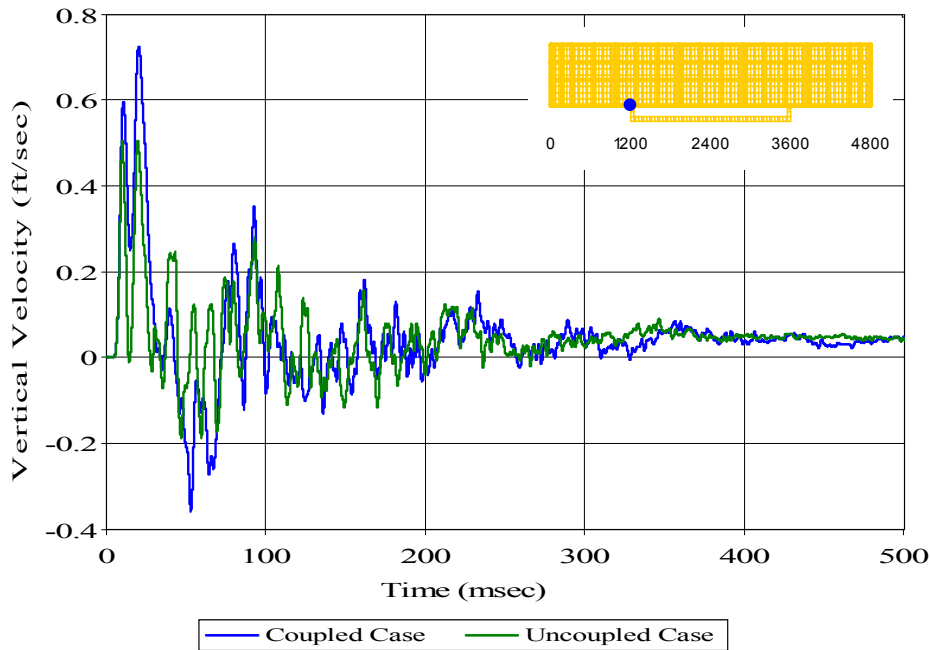
Figure 191.   Keel Node 2454: (RM = -0.2030, RP = 0.2333, RC = 0.2741)
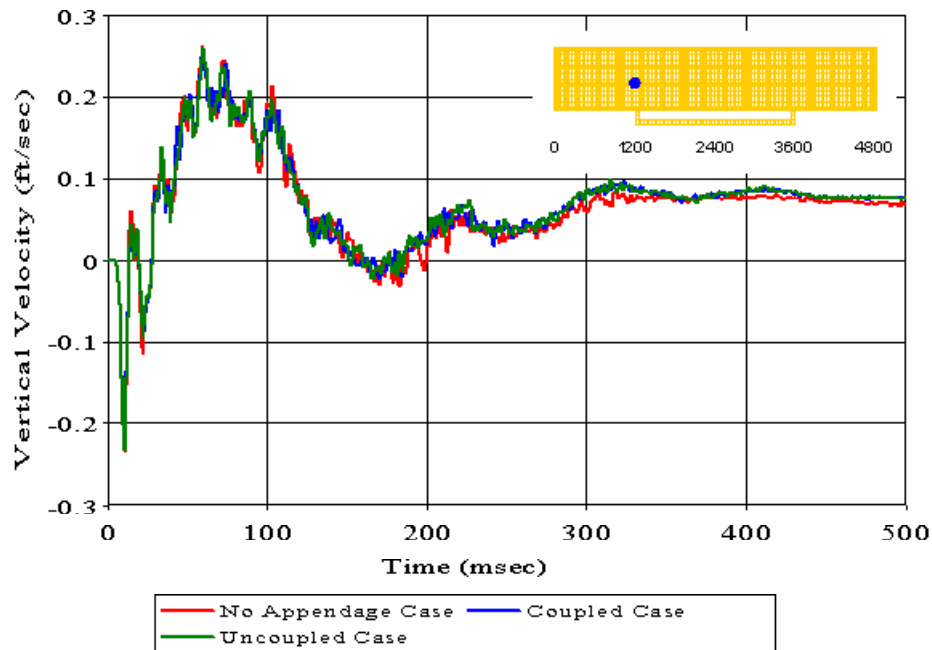
Figure 192.   First Deck Node 2648: (RM = 0.0006, RP = 0.0302, RC = 0.0267)
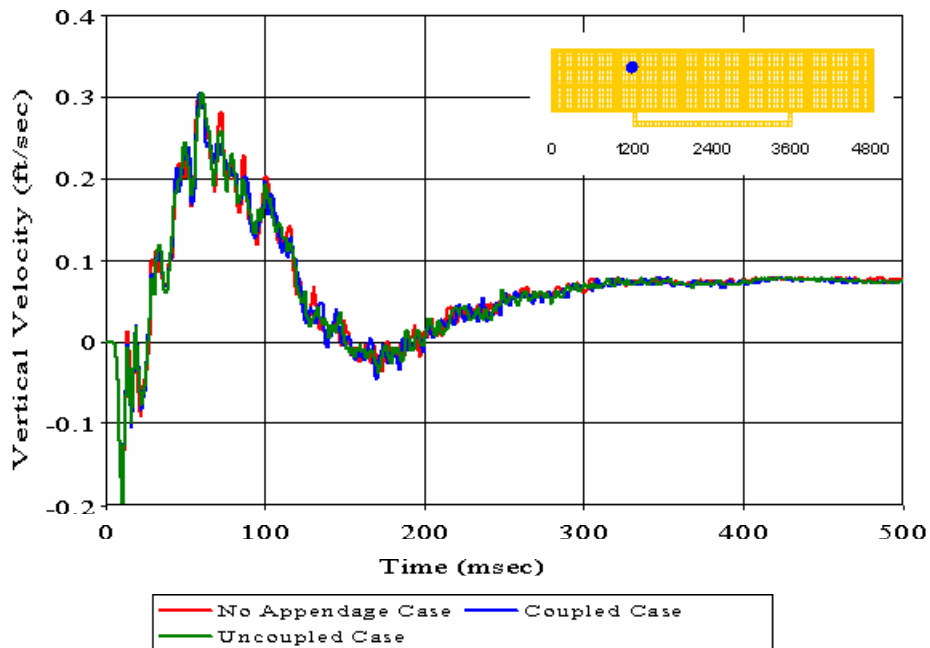
Figure 193.   Second Deck Node 2820: (RM = -0.0016, RP = 0.0301, RC = 0.0267)
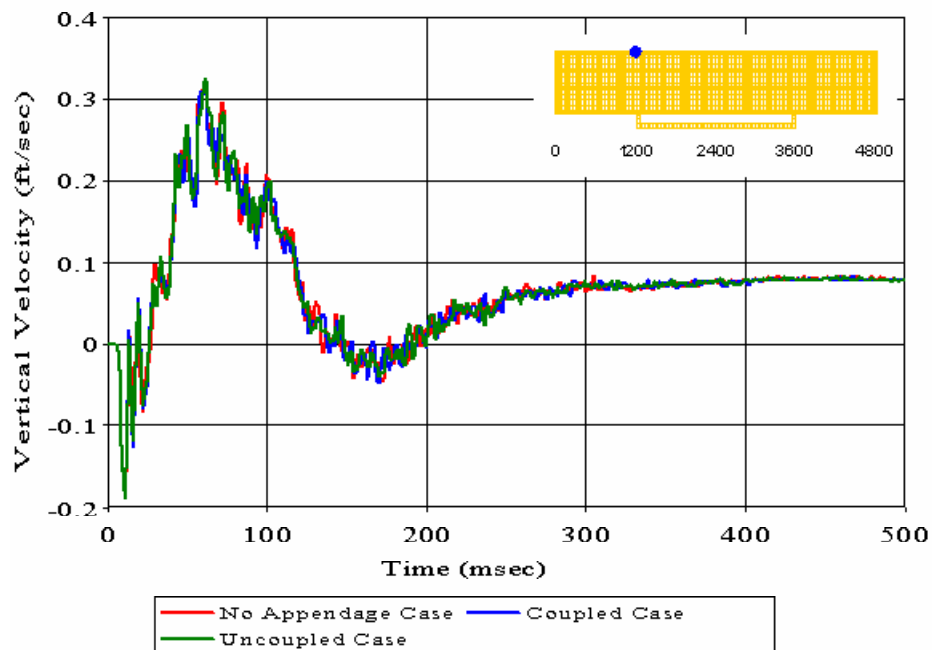
Figure 194. Top Deck Node 2970: (RM = 0.0001, RP = 0.0335, RC = 0.0297)
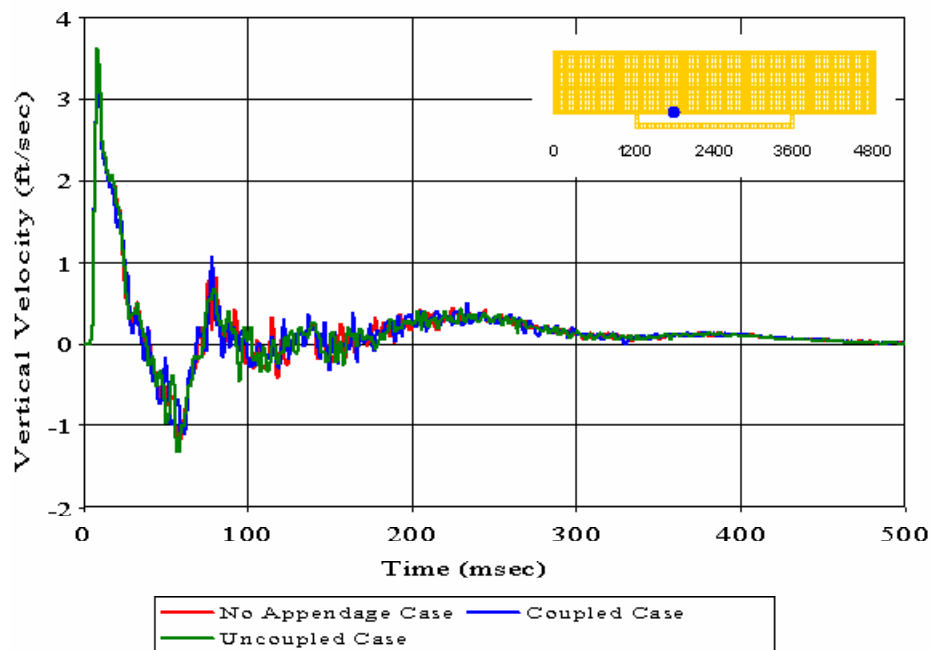
Figure 195. Keel Node 3883: (RM = 0.0216, RP = 0.0862, RC = 0.0788)

221
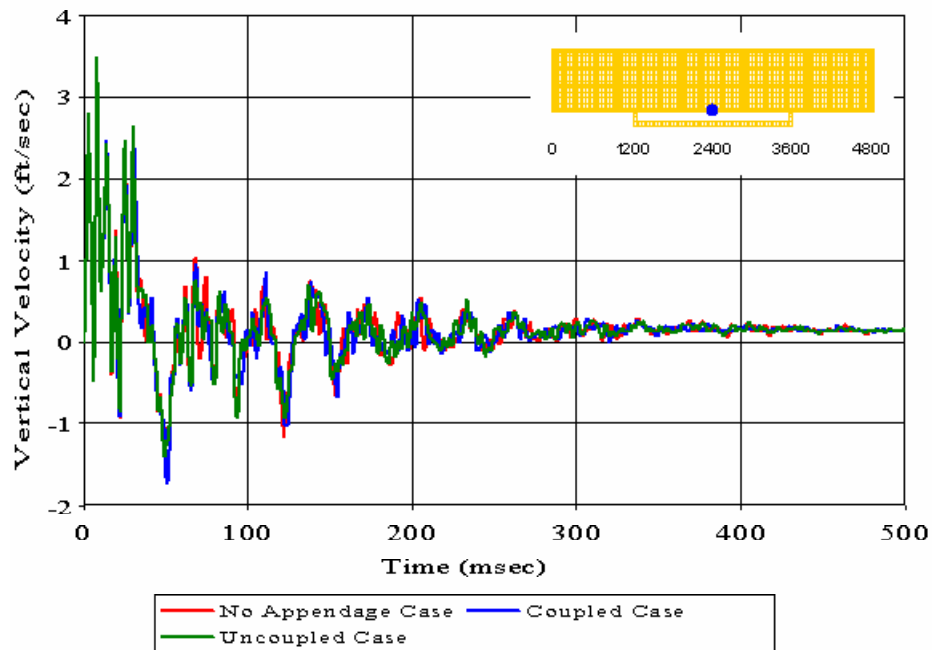
Figure 196. Keel Node 5251: (RM = -0.0136, RP = 0.0871, RC = 0.0781)
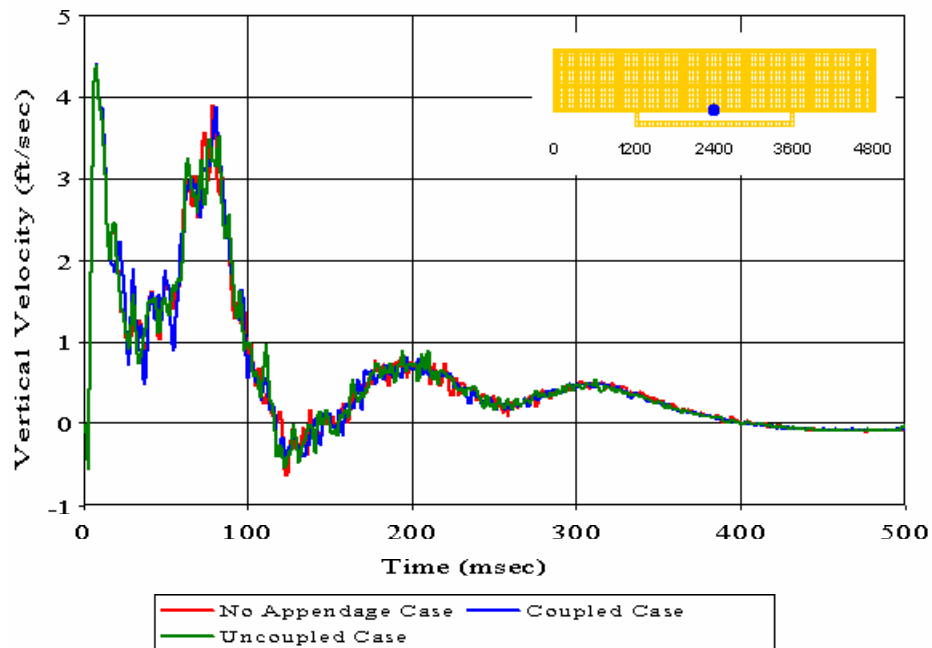
Figure 197. Keel Node 5308: (RM = -0.0060, RP = 0.0446, RC = 0.0398)
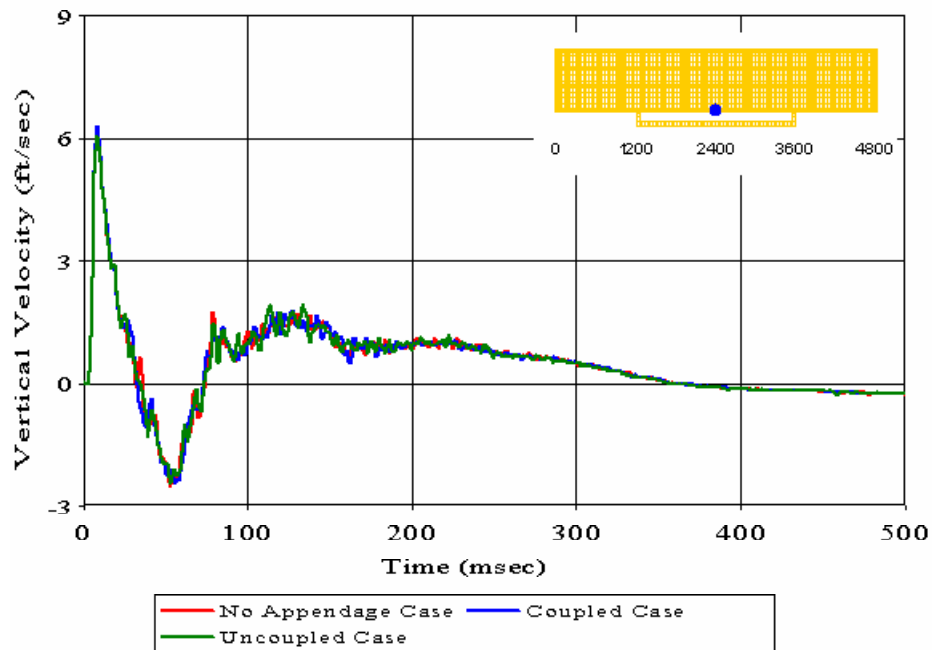
Figure 198. Keel Node 5310: (RM = -0.0137, RP = 0.0452, RC = 0.0418)
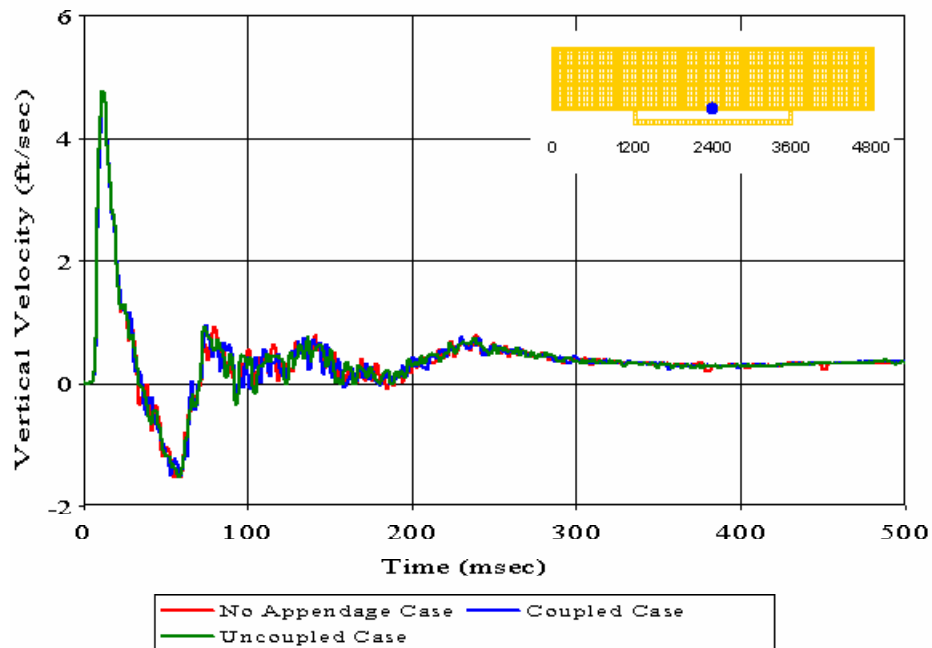
Figure 199. Keel Node 5315: (RM = 0.0114, RP = 0.0534, RC = 0.0484)

223
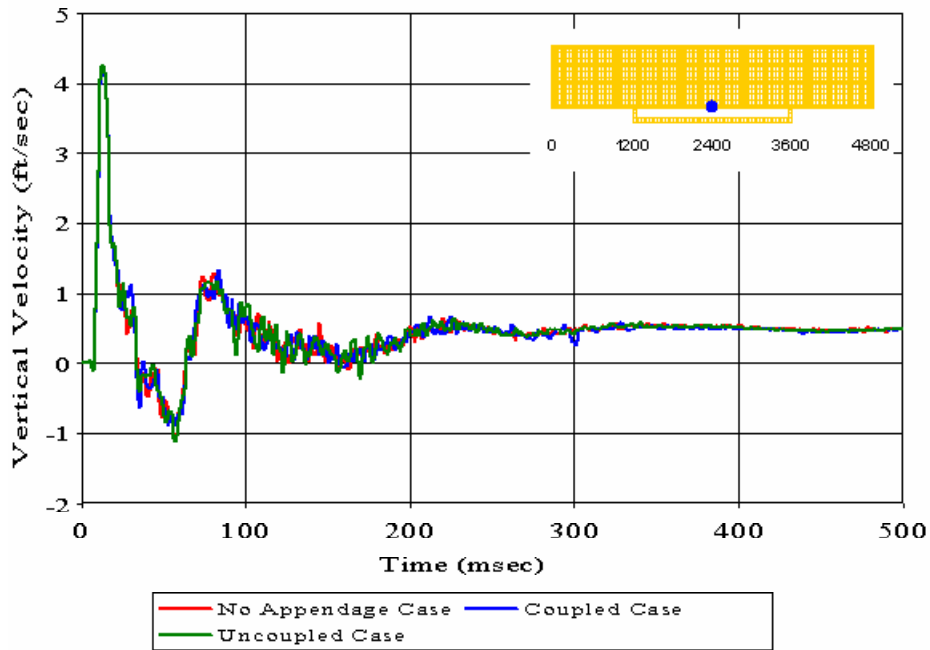
Figure 200. Keel Node 5317: (RM = 0.0065, RP = 0.0535, RC = 0.0477)
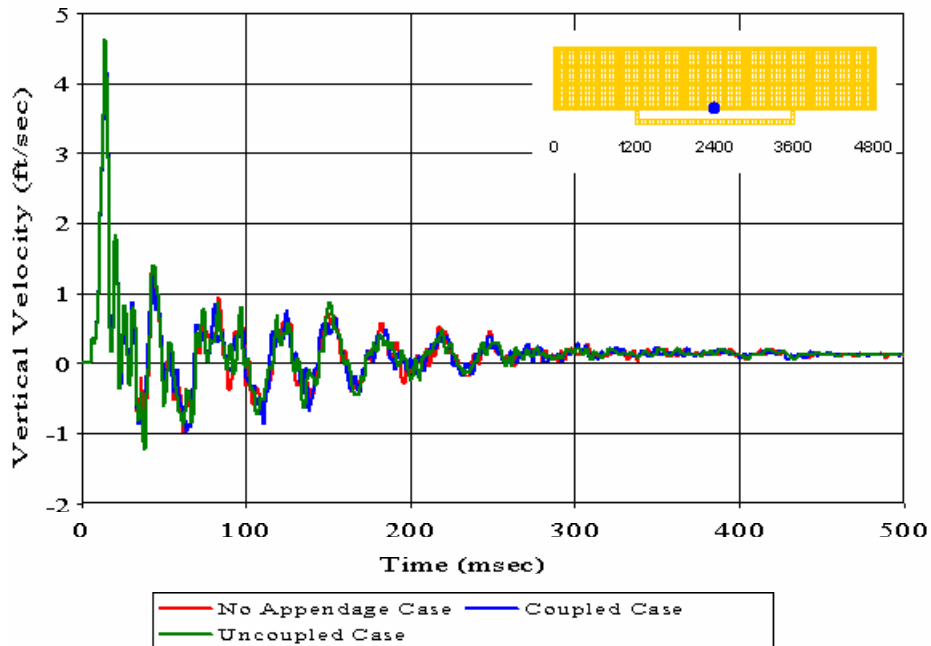
Figure 201. Keel Node 5320: (RM = 0.0083, RP = 0.0939, RC = 0.0835)
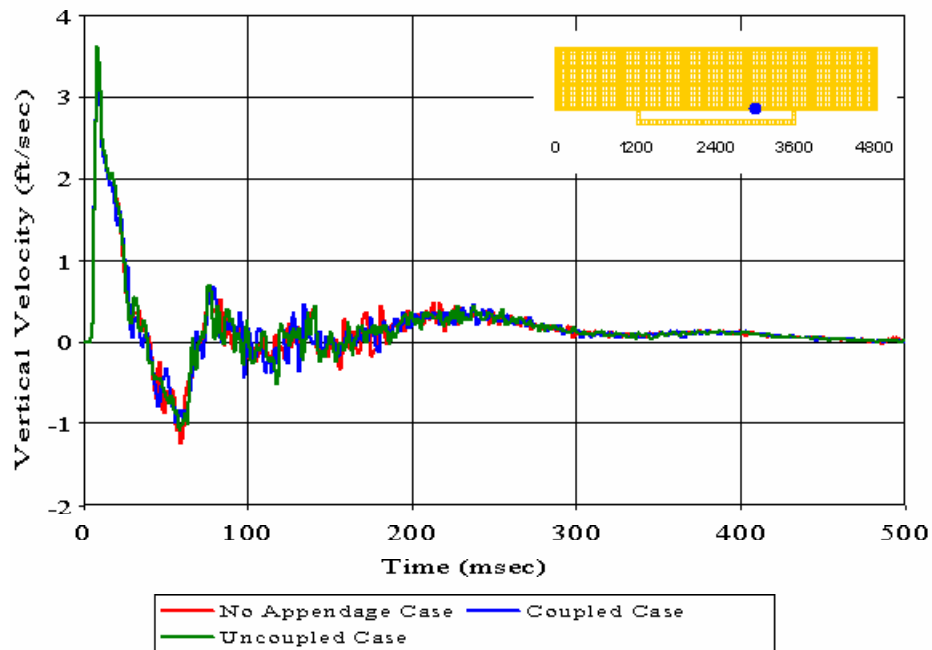
Figure 202.   Keel Node 6741: (RM = 0.0223, RP = 0.0801, RC = 0.0737)
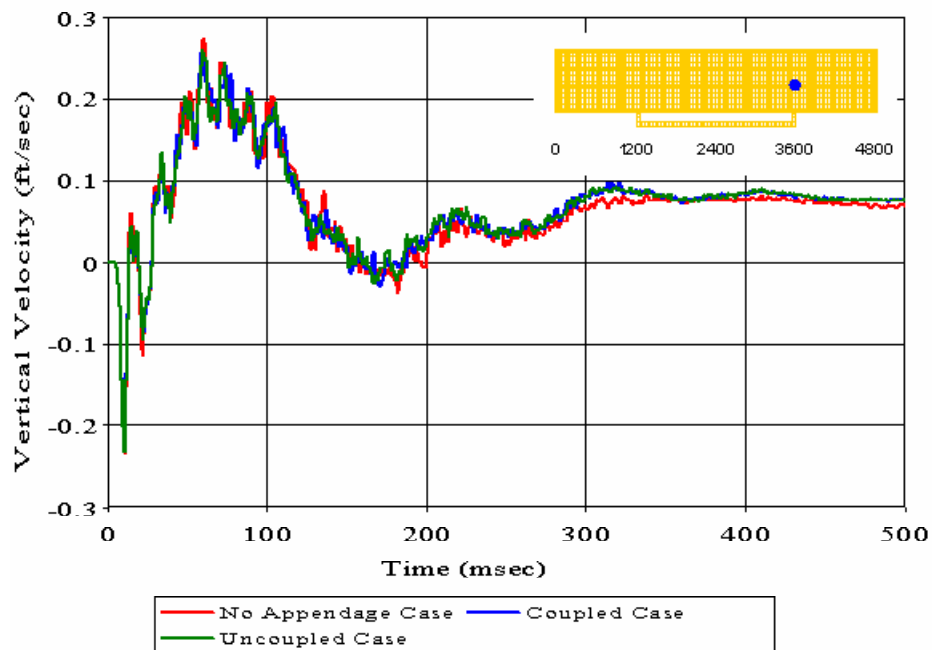
Figure 203.   First Deck Node 8364: (RM = -0.0020, RP = 0.0319, RC = 0.0284)

225
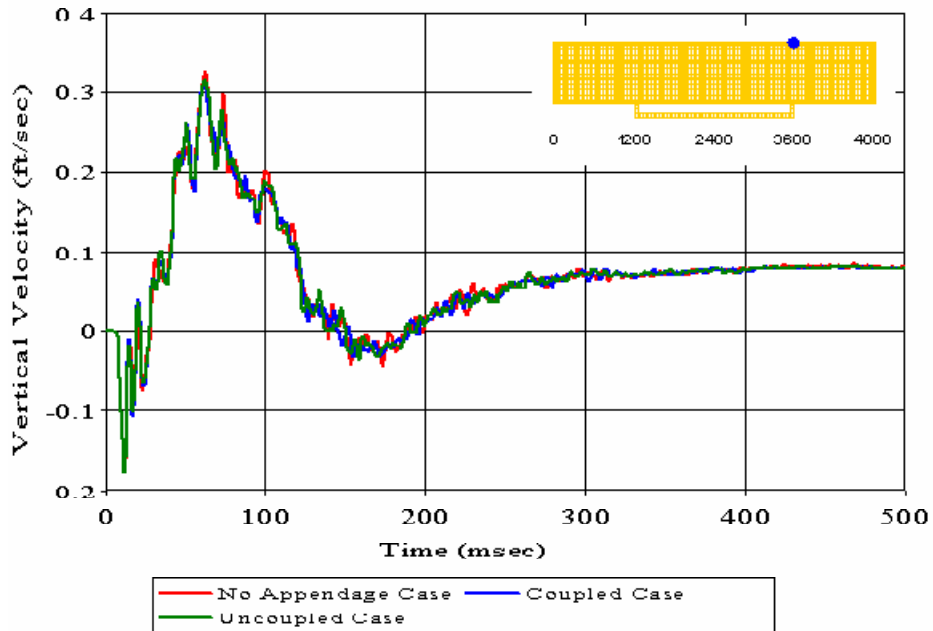
Figure 204.   Top Deck Node 8686: (RM = -0.0003, RP = 0.0315, RC = 0.0279)

D.   MEKO-LIKE BOX MODEL WITH RUDDERS
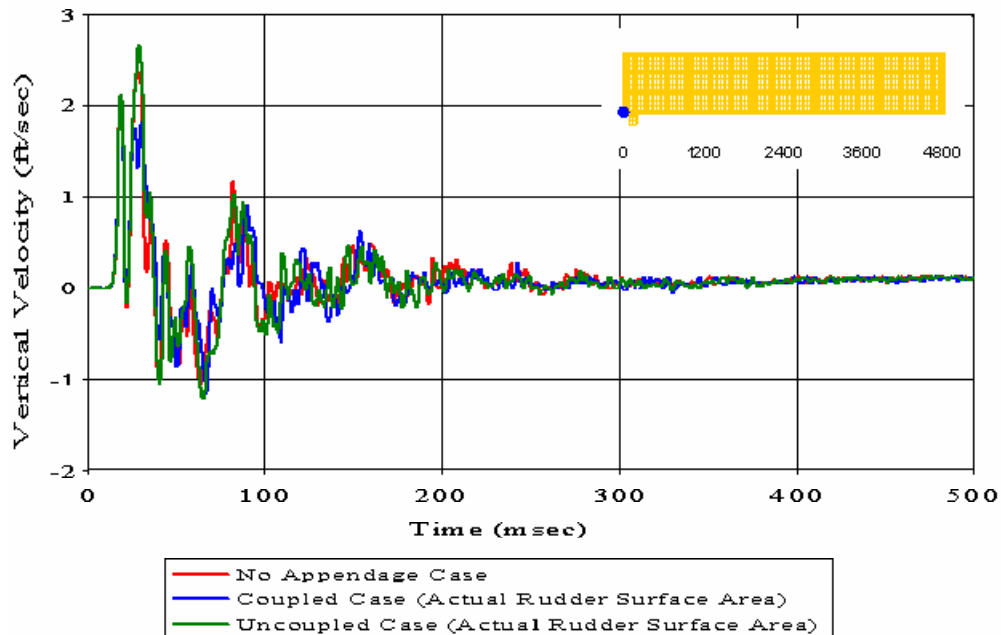
Figure 205.   Bulkhead Node 15: (RM = 0.1477, RP = 0.1633, RC = 0.1951)

226
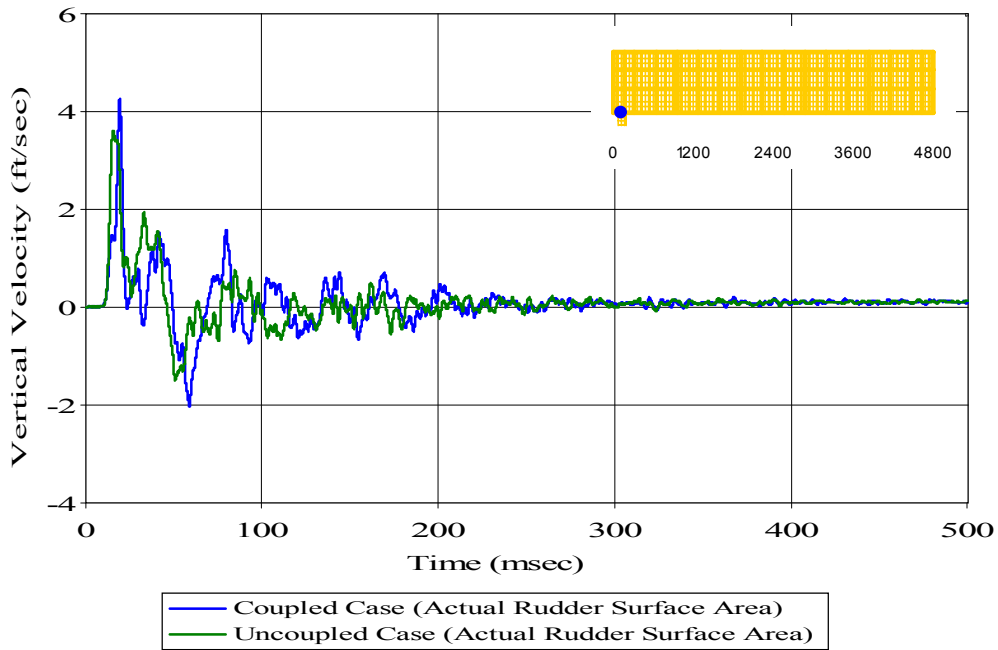
Figure 206. Keel Node 74: (RM = 0.0365, RP = 0.2814, RC = 0.2515)
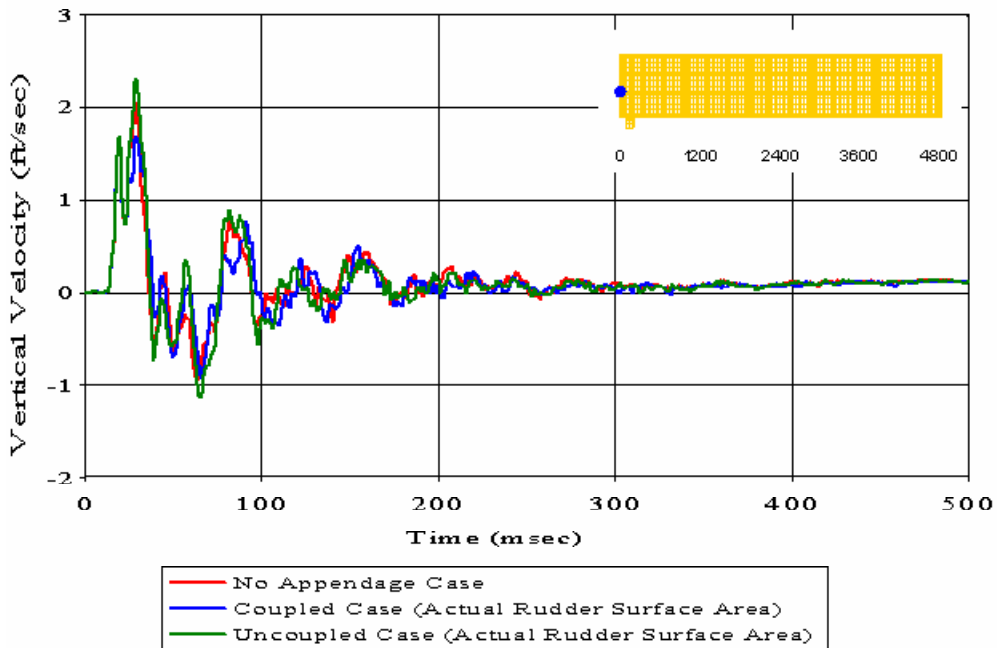
Figure 207. Bulkhead Node 148: (RM = 0.1488, RP = 0.1365, RC = 0.1790)
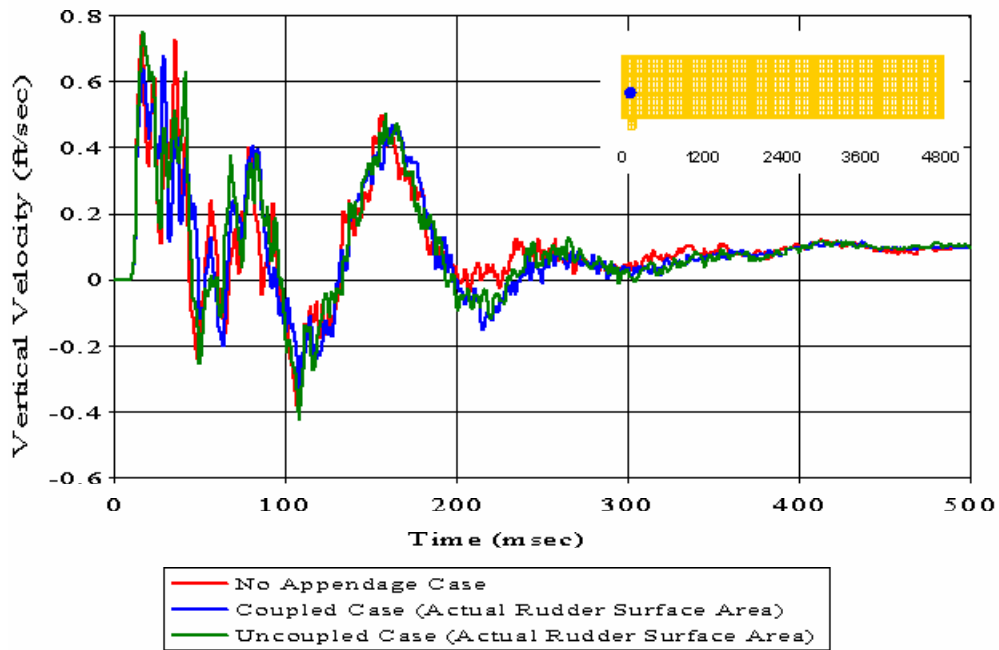
Figure 208.   **First Deck Node 214: (RM = 0.0388, RP = 0.1113, RC = 0.1045)**
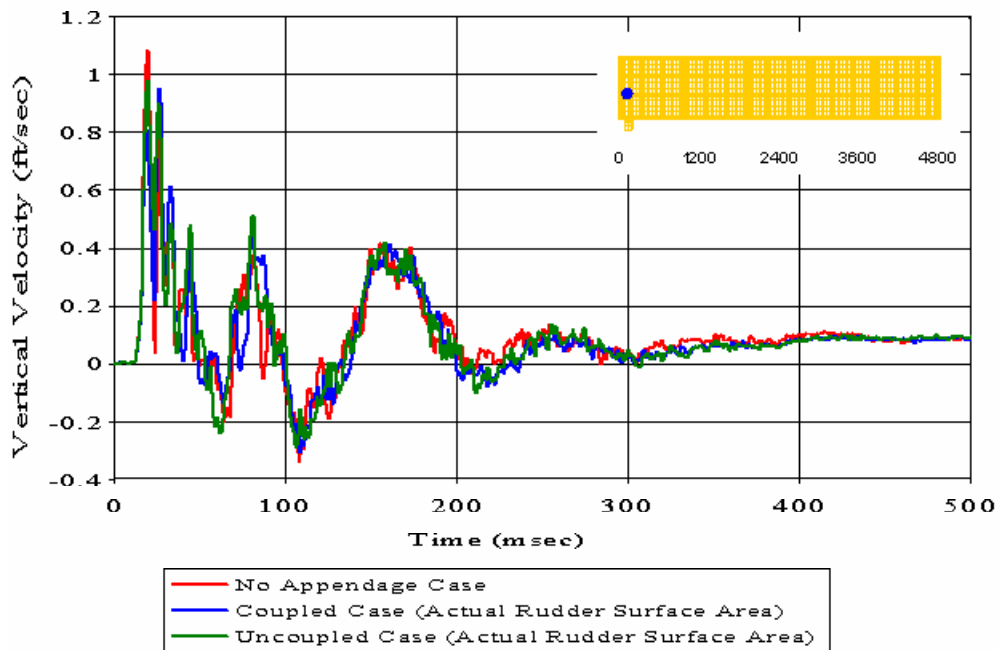
Figure 209.   **First Deck Node 221: (RM = 0.0351, RP = 0.1028, RC = 0.0963)**
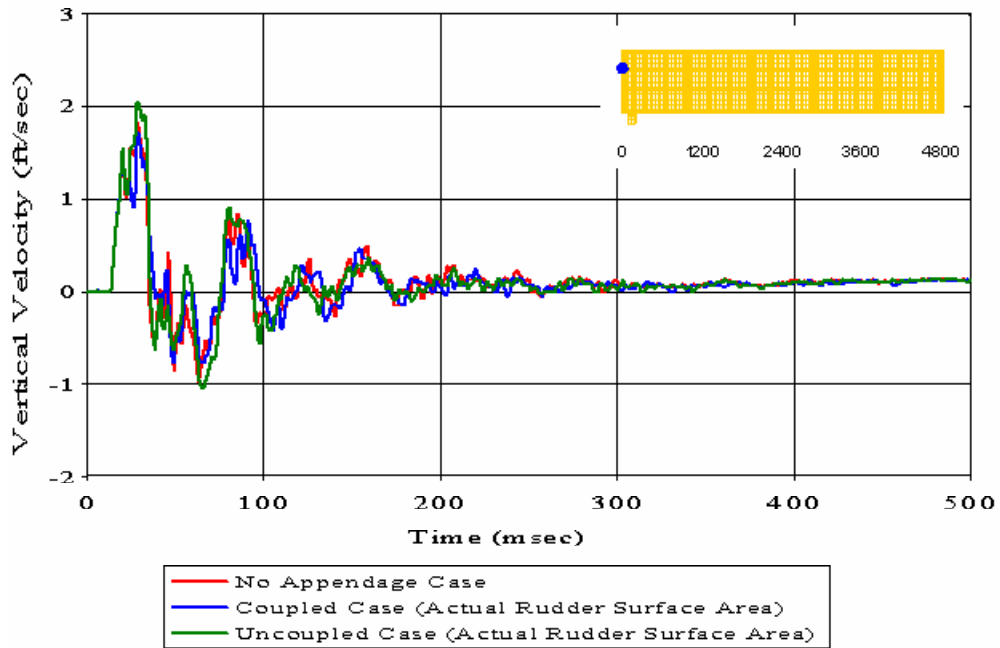
Figure 210.   **Bulkhead Node 268: (RM = 0.1466, RP = 0.1396, RC = 0.1795)**
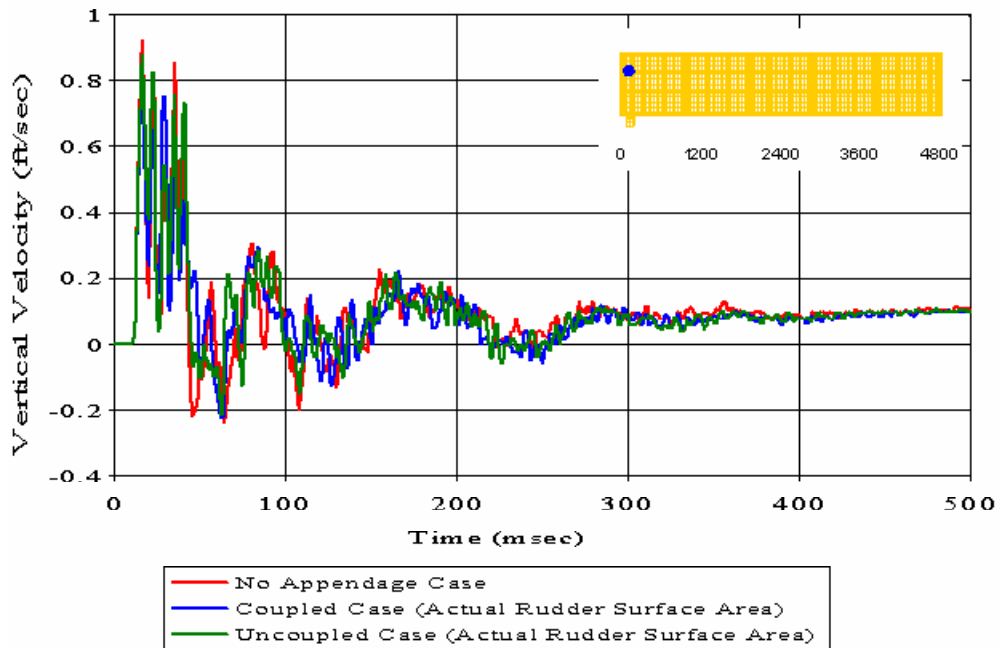
Figure 211.   **Second Deck Node 334: (RM = 0.0745, RP = 0.1292, RC = 0.1322)**
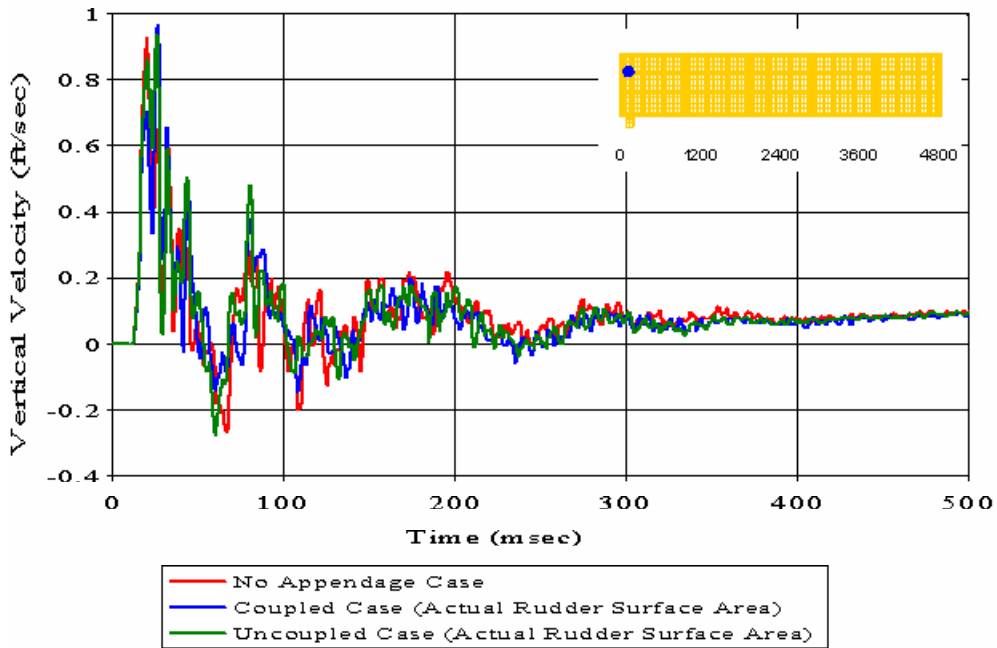
Figure 212. **Second Deck Node 341: (RM = 0.0637, RP = 0.1193, RC = 0.1198)**
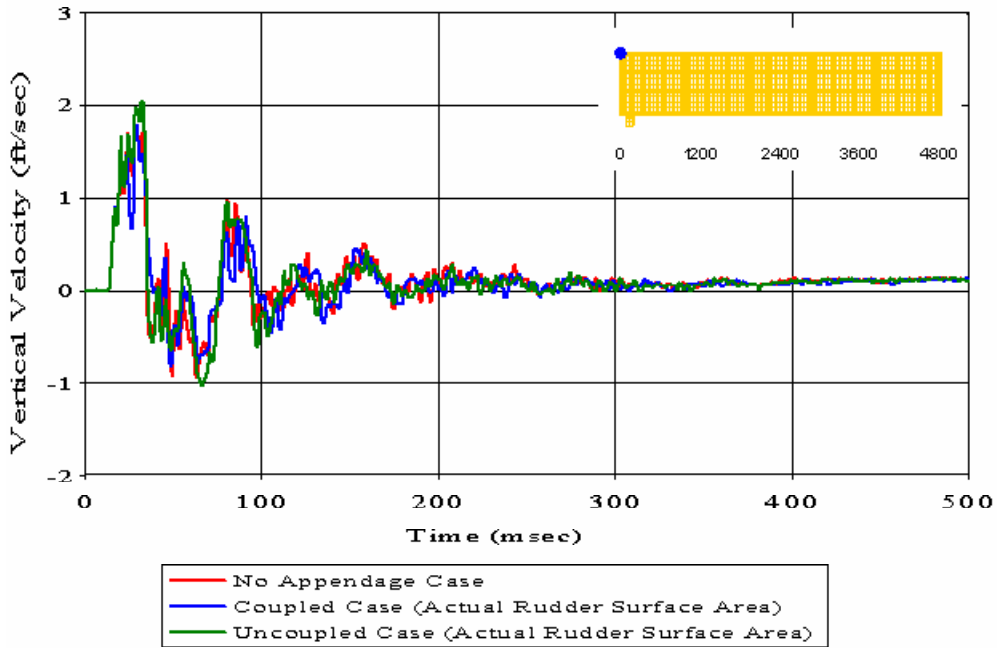
Figure 213. **Bulkhead Node 388: (RM = 0.1412, RP = 0.1475, RC = 0.1809)**
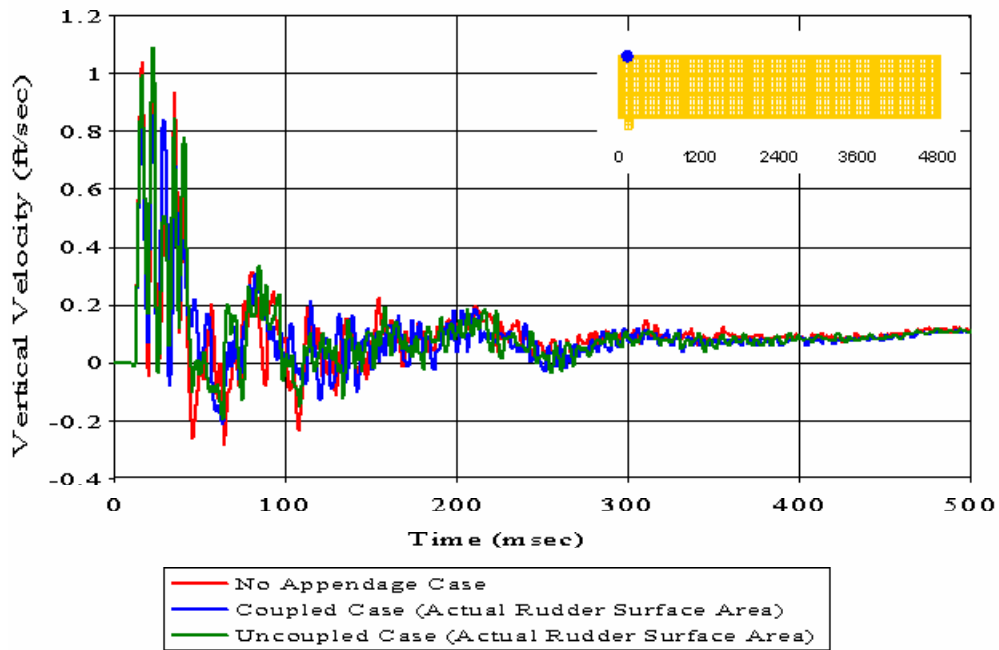
Figure 214. **Top Deck Node 434: (RM = 0.0645, RP = 0.1448, RC = 0.1404)**
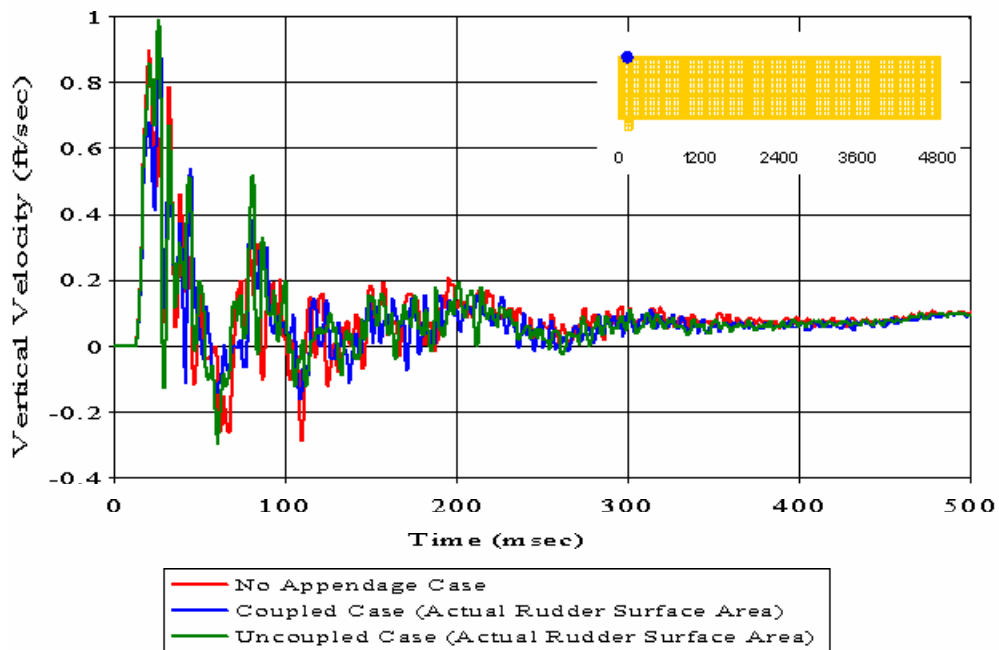
Figure 215. **Top Deck Node 441: (RM = 0.0714, RP = 0.1333, RC = 0.1340)**

231
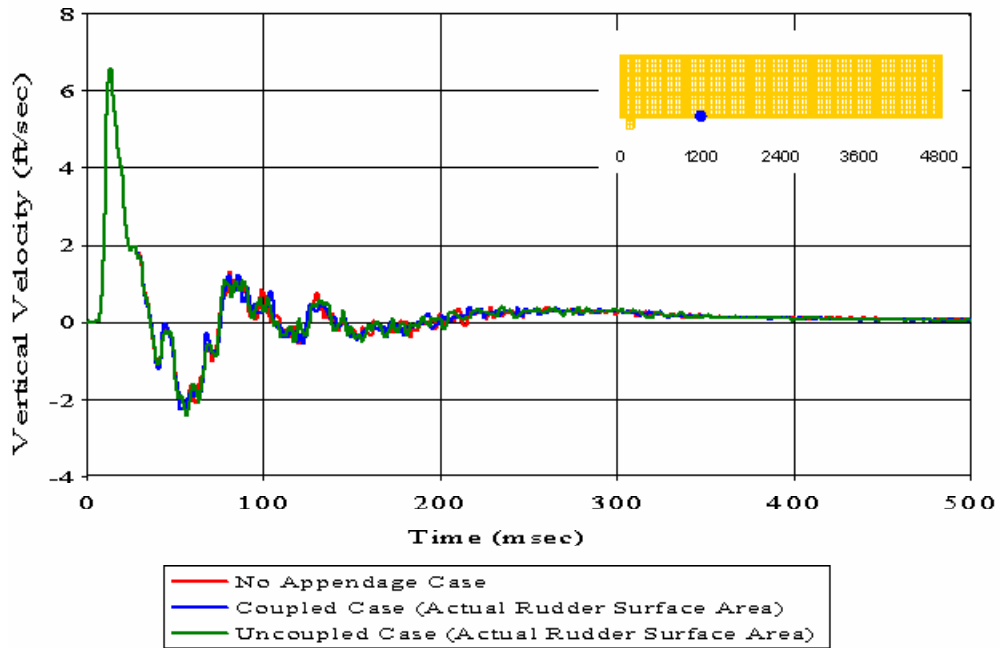
Figure 216. Keel Node 2454: (RM = 0.0022, RP = 0.0414, RC = 0.0368)
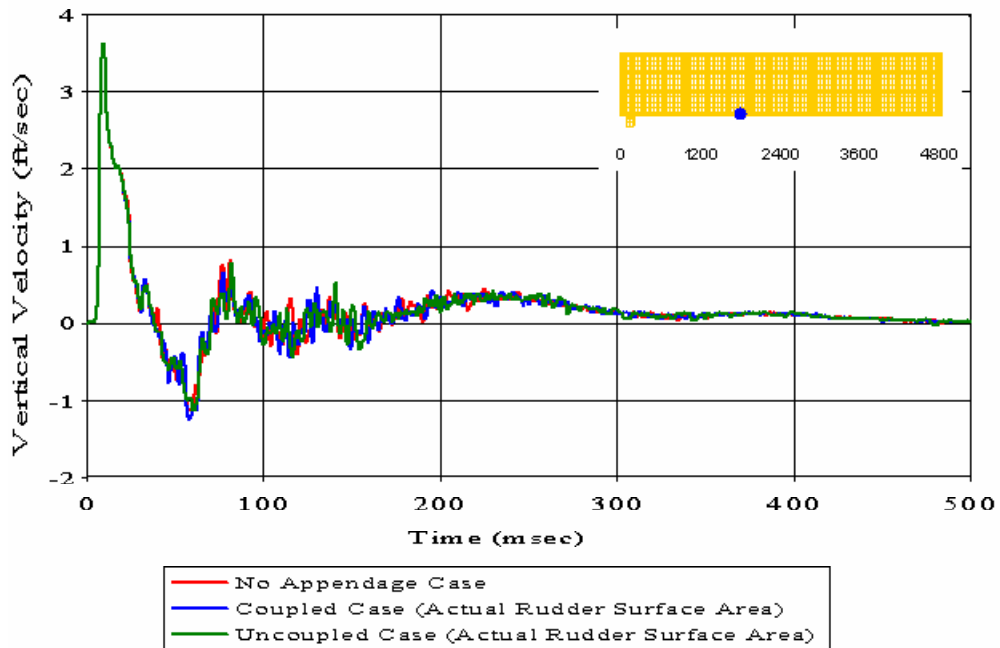
Figure 217. Keel Node 3883: (RM = -0.0018, RP = 0.0704, RC = 0.0624)

232
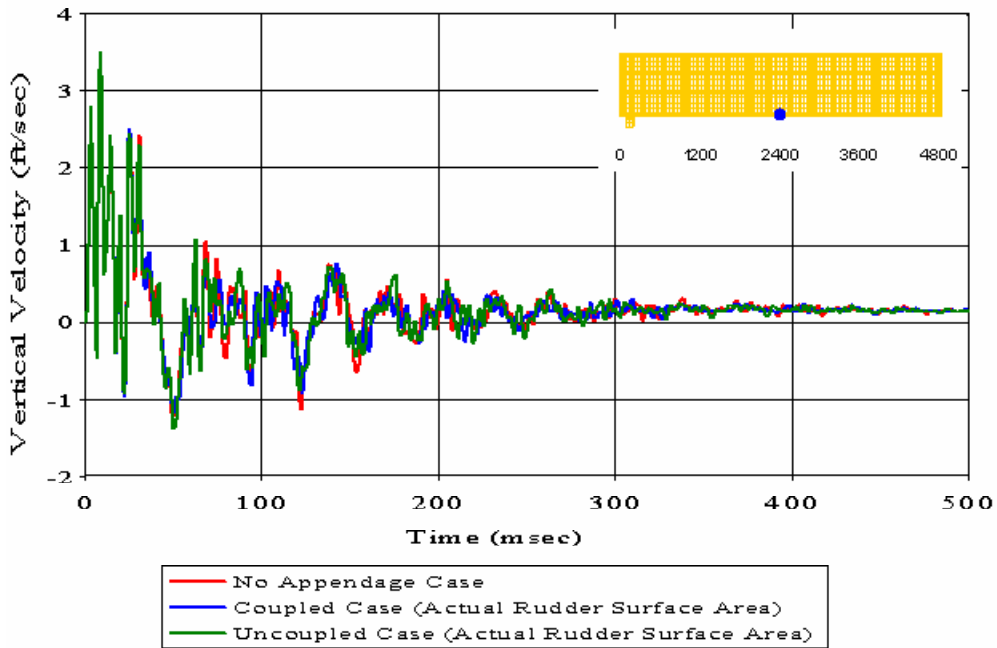
Figure 218.   Keel Node 5251: (RM = 0.0242, RP = 0.1015, RC = 0.0925)
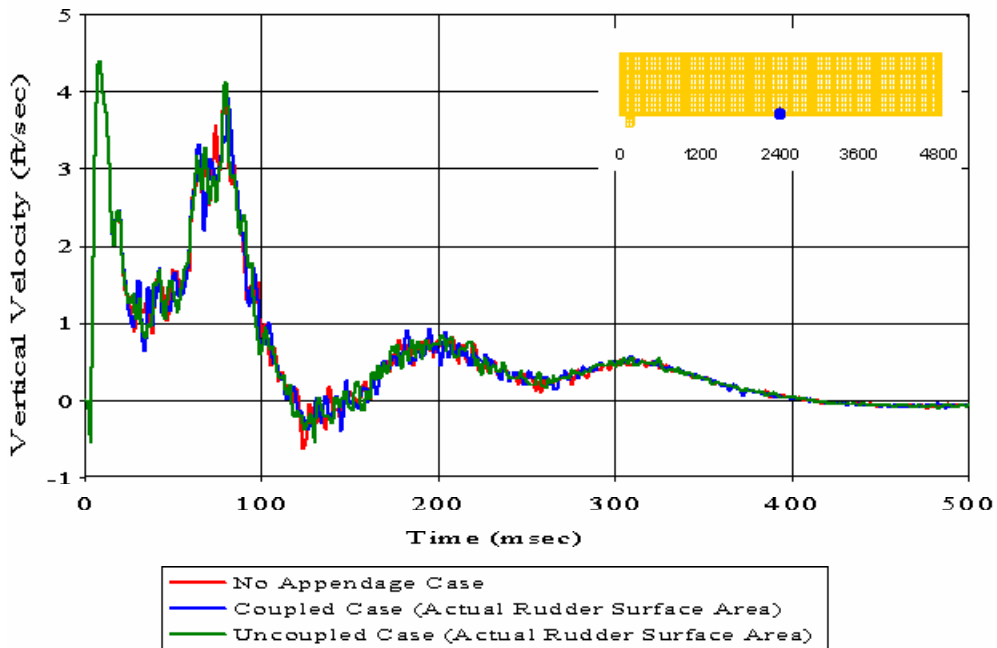
Figure 219.   Keel Node 5308: (RM = 0.0008, RP = 0.0436, RC = 0.0387)
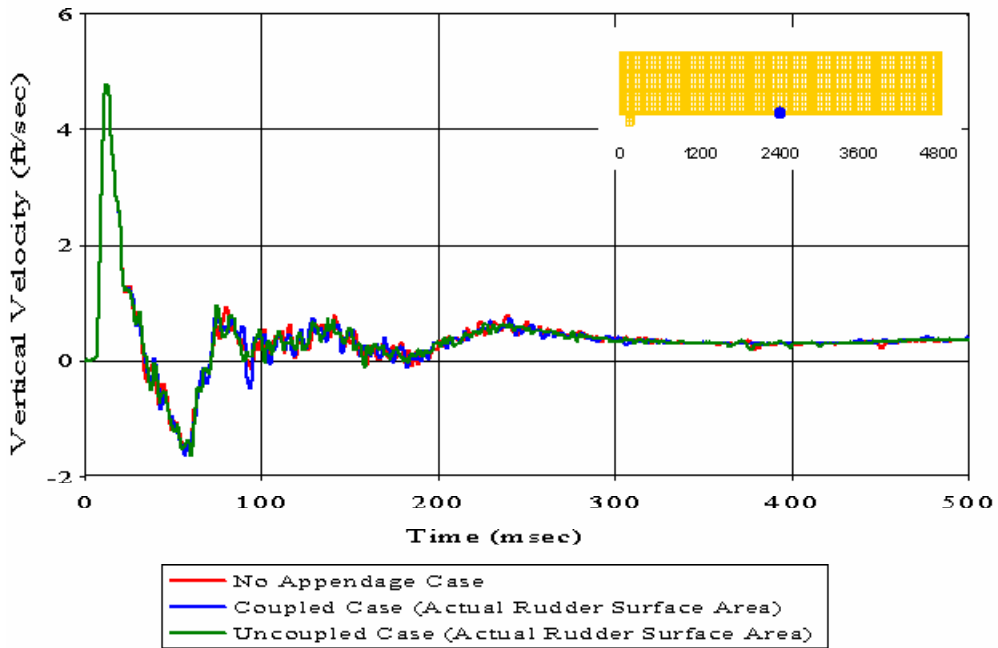
Figure 220.   Keel Node 5315: (RM = -0.0019, RP = 0.0417, RC = 0.0370)
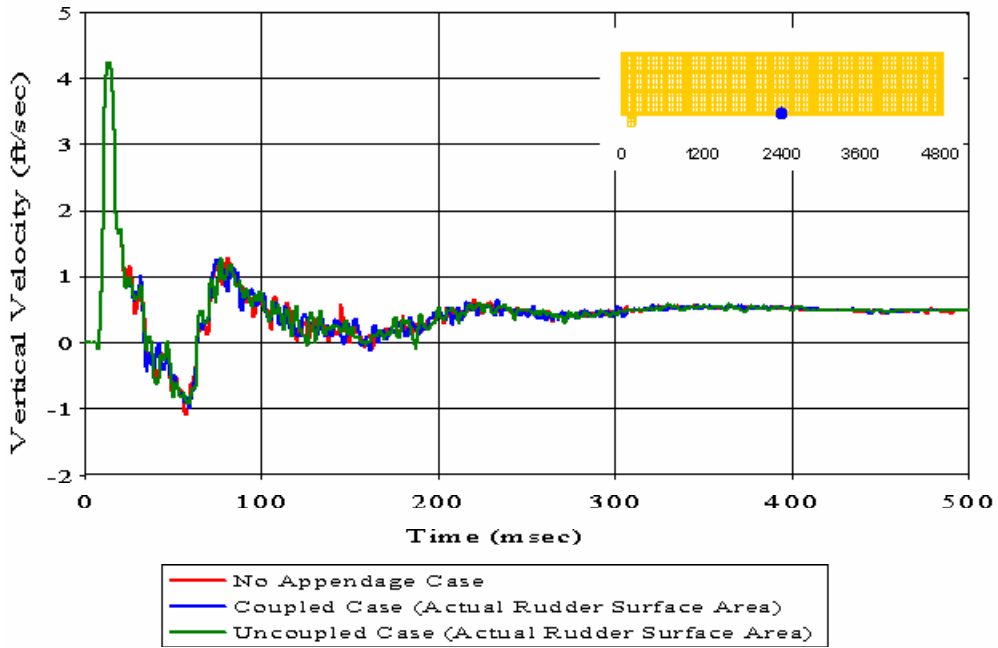
Figure 221.   Keel Node 5317: (RM = -0.0004, RP = 0.0505, RC = 0.0447)
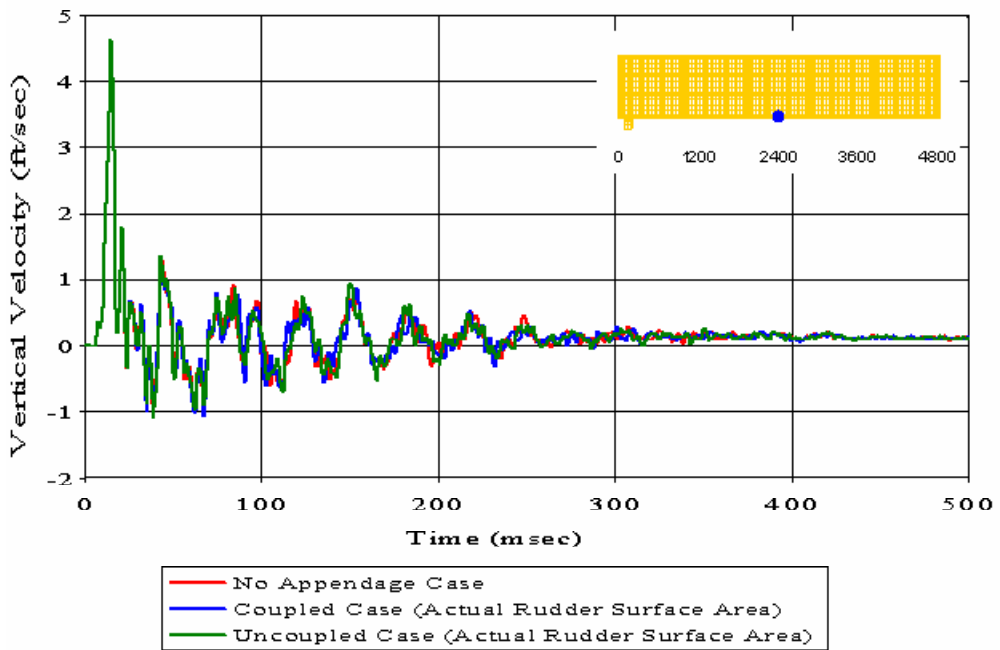
Figure 222. **Keel Node 5320: (RM = 0.0074, RP = 0.0818, RC = 0.0728)**
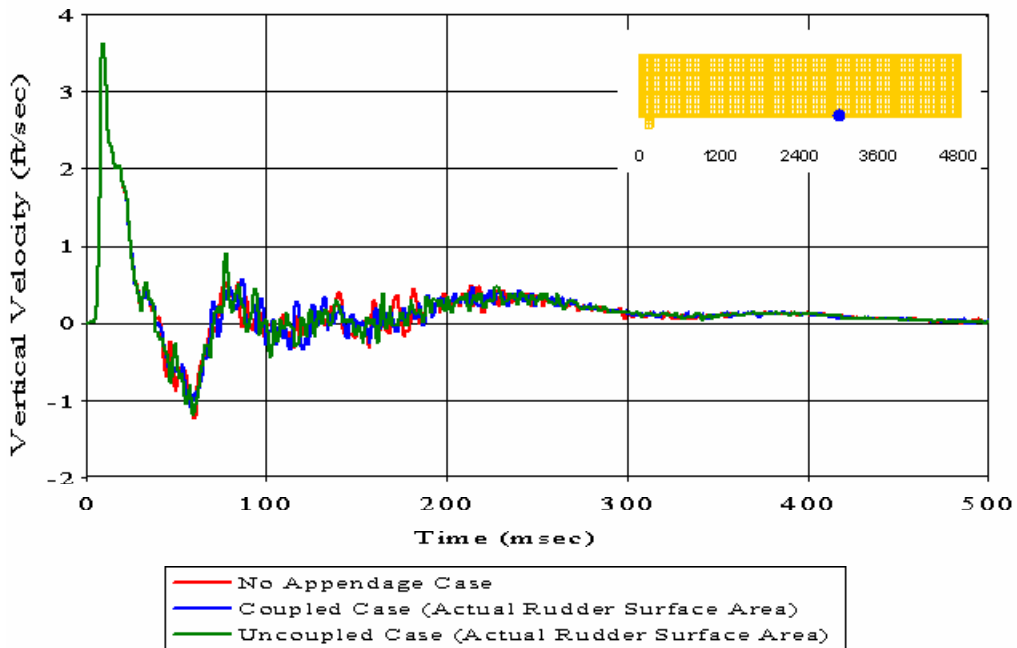
Figure 223. **Keel Node 6741: (RM = 0.0050, RP = 0.0710, RC = 0.0631)**

235
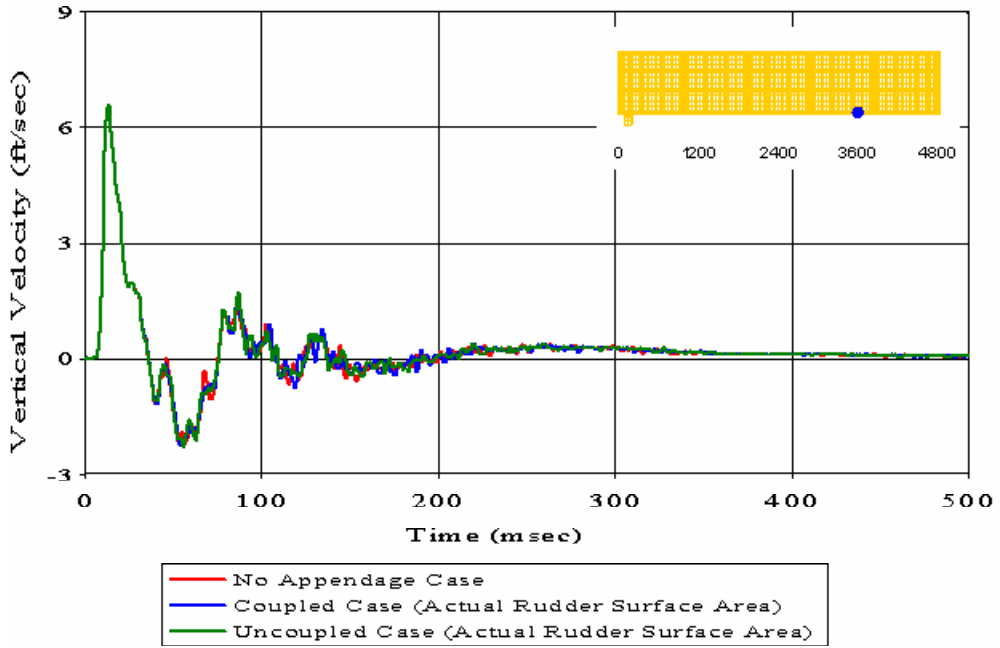
Figure 224. Keel Node 8170: (RM = -0.0001, RP = 0.0400, RC = 0.0355)

Figure 225. Absolute Maximum Vertical Velocity as a Function of Position (First Deck)
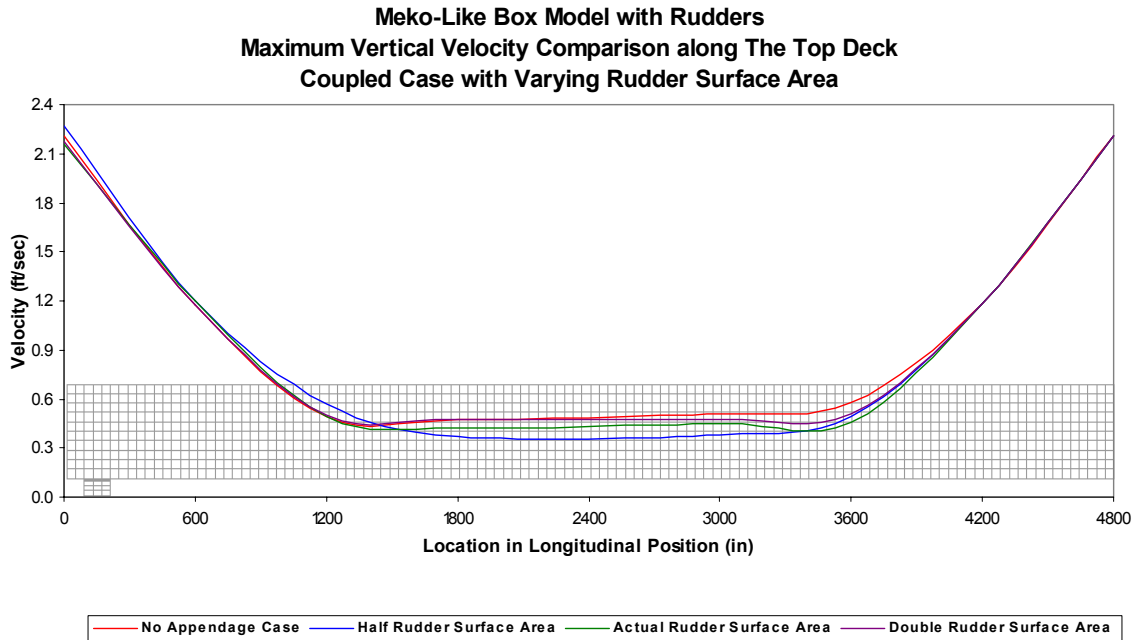
Figure 226.   Absolute Maximum Vertical Velocity as a Function of Position (Top Deck)
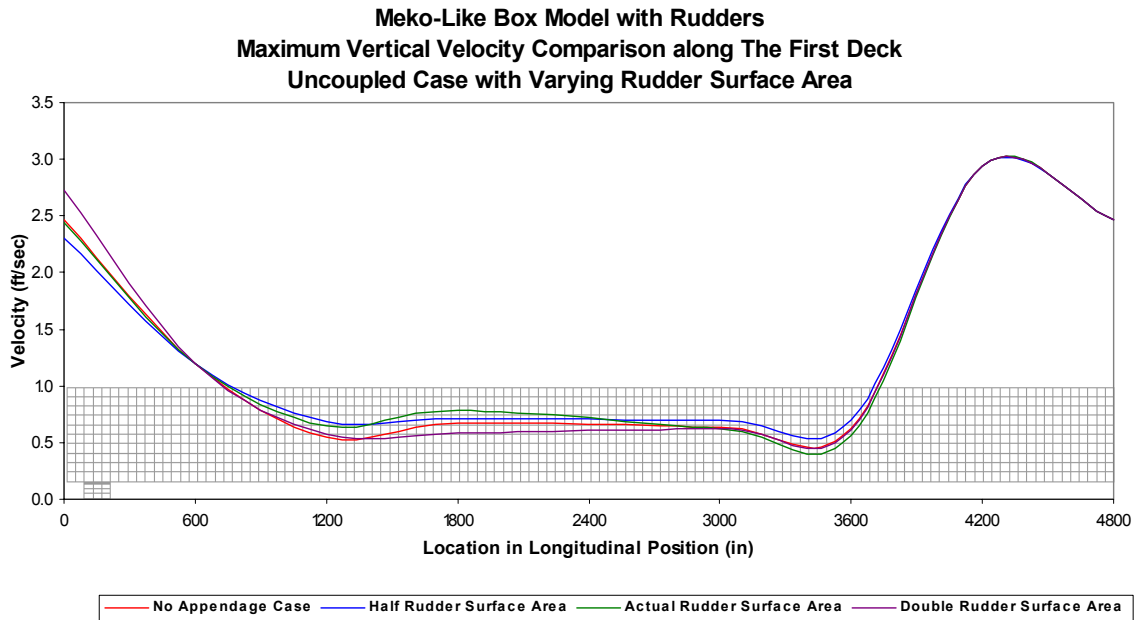
Figure 227.   Absolute Maximum Vertical Velocity as a Function of Position (First Deck)

237

Meko-Like Box Model with Rudders
Maximum Vertical Velocity Comparison along The Top Deck
Uncoupled Case with Varying Rudder Surface Area
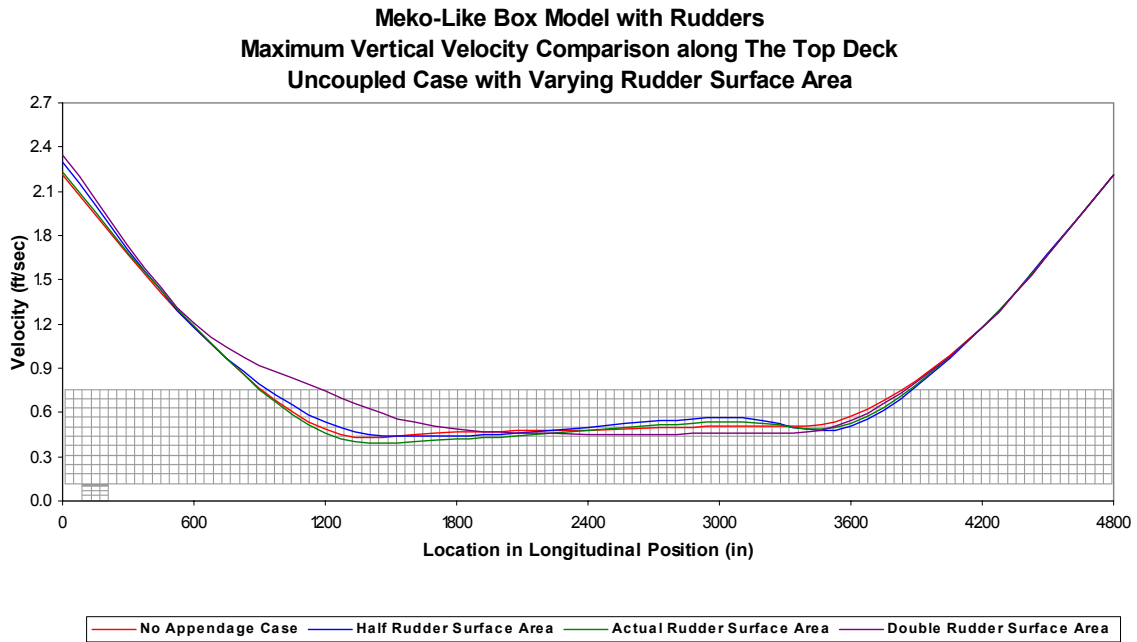
Figure 228.   Absolute Maximum Vertical Velocity as a Function of Position (Top Deck)

Meko–Like Box Model with Rudders
Node 74 at Keel (x=120 y=-140 z=0)
Coupled Case with Varying Rudder Surface Area
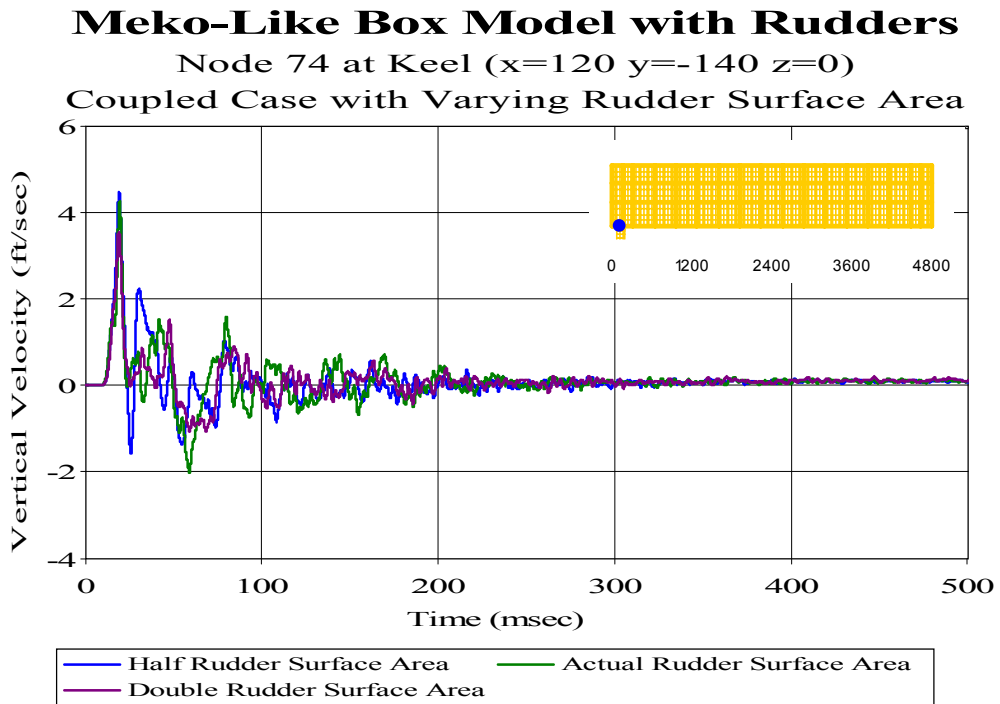
Figure 229.   Coupled Case with Varying Rudder Surface Area: Keel Node 74
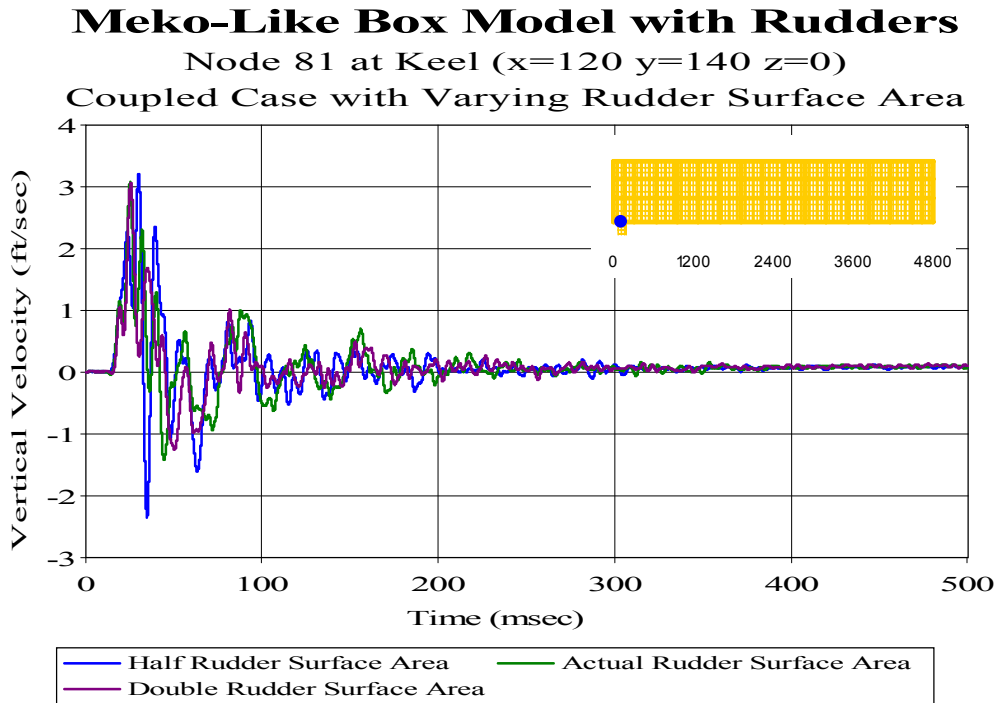
Figure 230.   Coupled Case with Varying Rudder Surface Area: Keel Node 81
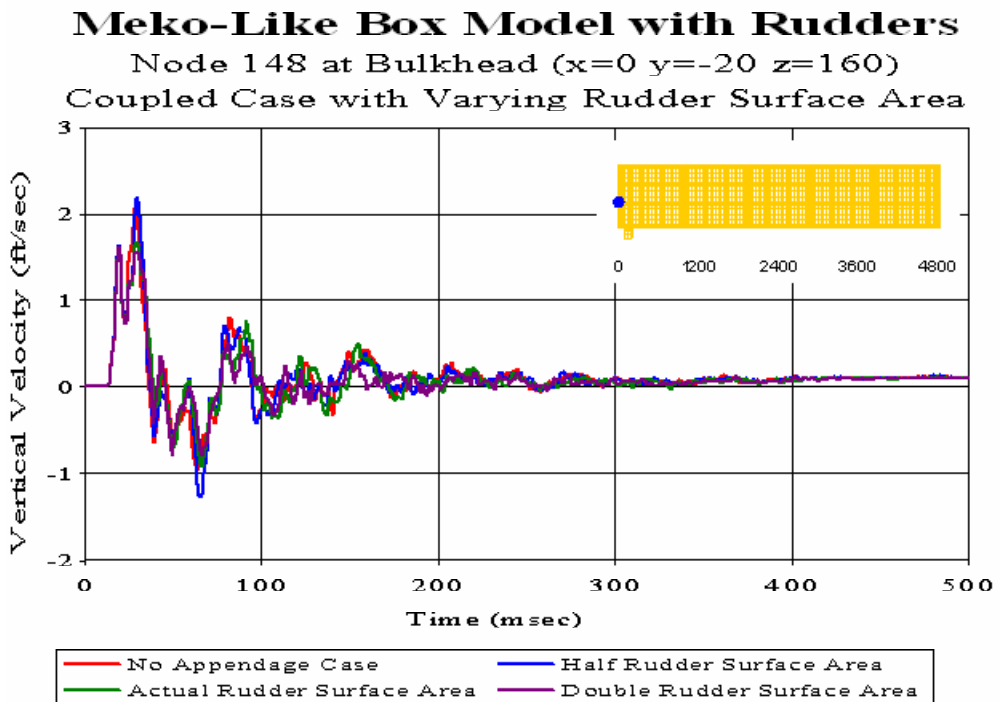
Figure 231.   Coupled Case with Varying Rudder Surface Area: Bulkhead Node 148
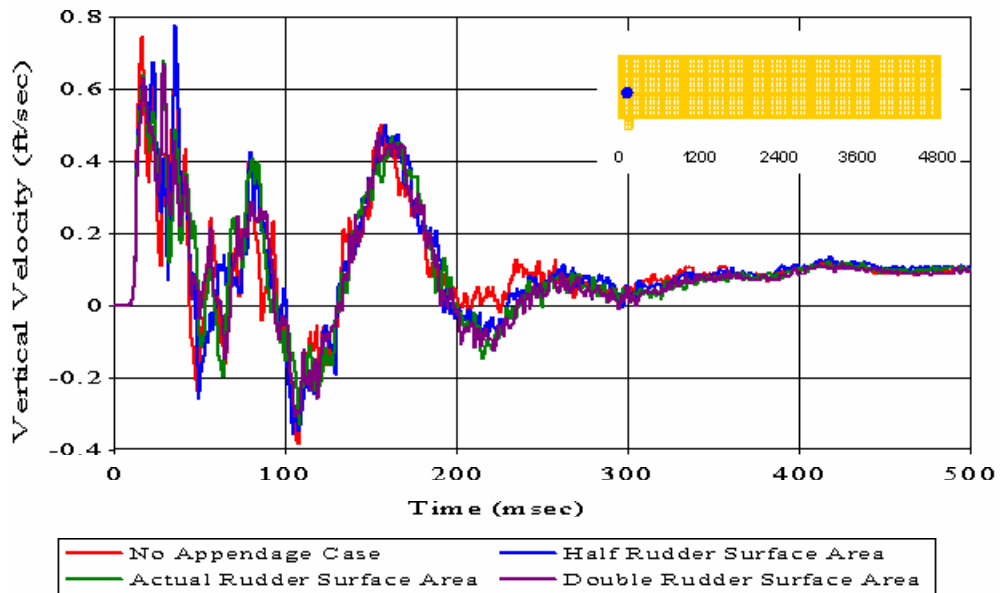
Figure 232. **Coupled Case with Varying Rudder Surface Area: First Deck Node 214**
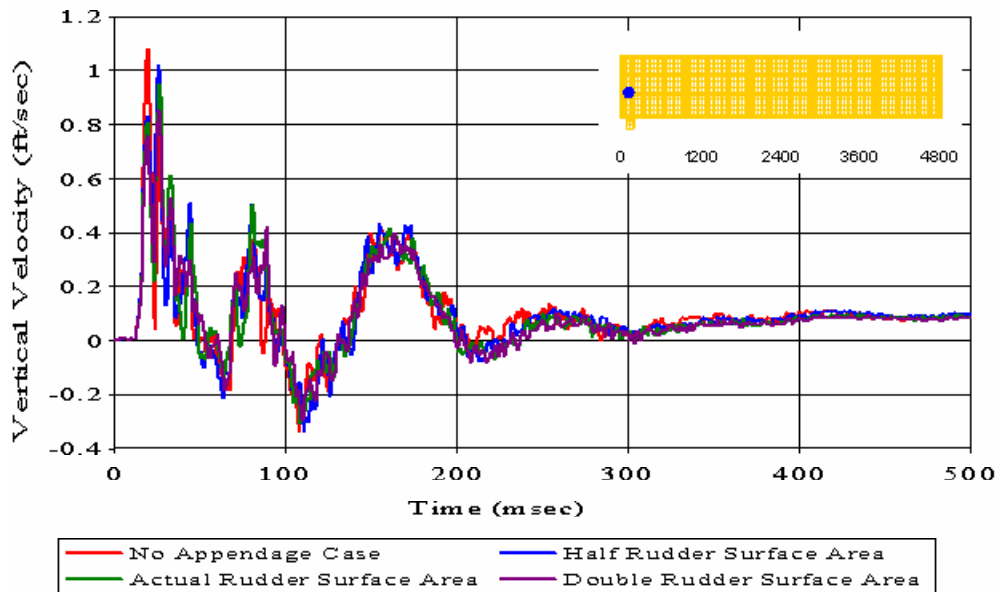
Figure 233. **Coupled Case with Varying Rudder Surface Area: First Deck Node 221**

Figure 234.   Coupled Case with Varying Rudder Surface Area: Bulkhead Node 268

Figure 235.   Coupled Case with Varying Rudder Surface Area: Second Deck Node 334

241

Figure 236. **Coupled Case with Varying Rudder Surface Area: Second Deck Node 341**

Figure 237. **Coupled Case with Varying Rudder Surface Area: Bulkhead Node 388**

242

Figure 238.   Coupled Case with Varying Rudder Surface Area: Top Deck Node 434

Figure 239.   Coupled Case with Varying Rudder Surface Area: Top Deck Node 441

Figure 240. Coupled Case with Varying Rudder Surface Area: Keel Node 2454

Figure 241. Coupled Case with Varying Rudder Surface Area: Keel Node 3883

Figure 242.   Coupled Case with Varying Rudder Surface Area: Keel Node 5251

Figure 243.   Coupled Case with Varying Rudder Surface Area: Keel Node 5308

245

Figure 244.   **Coupled Case with Varying Rudder Surface Area: Keel Node 5310**

Figure 245.   **Coupled Case with Varying Rudder Surface Area: Keel Node 5315**

246

Figure 246.   Coupled Case with Varying Rudder Surface Area: Keel Node 5317

Figure 247.   Coupled Case with Varying Rudder Surface Area: Keel Node 5320

247

Figure 248. Coupled Case with Varying Rudder Surface Area: Keel Node 6741

Figure 249. Uncoupled Case with Varying Rudder Surface Area: Bulkhead Node 15

Figure 250. **Uncoupled Case with Varying Rudder Surface Area: Keel Node 74**

Figure 251. **Uncoupled Case with Varying Rudder Surface Area: Keel Node 81**

249

Figure 252. Uncoupled Case with Varying Rudder Surface Area: Bulkhead Node 148
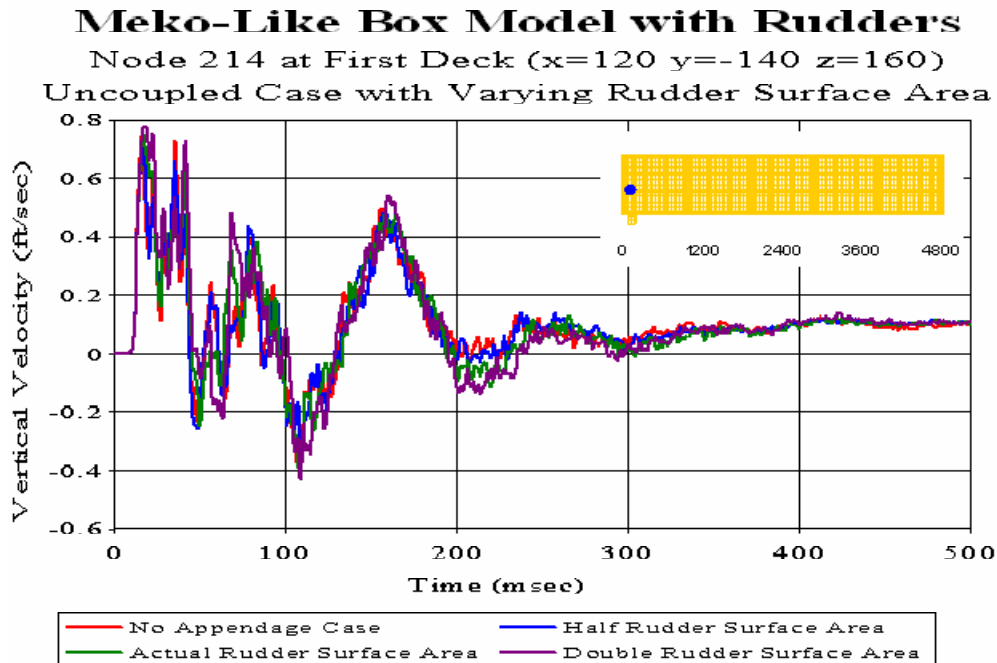
Figure 253. Uncoupled Case with Varying Rudder Surface Area: First Deck Node 214

250

Figure 254. **Uncoupled Case with Varying Rudder Surface Area: First Deck Node 221**

Figure 255. **Uncoupled Case with Varying Rudder Surface Area: Second Deck Node 334**

251

Figure 256.   Uncoupled Case with Varying Rudder Surface Area: Second Deck Node 341

Figure 257.   Uncoupled Case with Varying Rudder Surface Area: Bulkhead Node 388

252

Figure 258. Uncoupled Case with Varying Rudder Surface Area: Top Deck Node 434

Figure 259. Uncoupled Case with Varying Rudder Surface Area: Top Deck Node 441

253

Figure 260. Uncoupled Case with Varying Rudder Surface Area: Keel Node 2454
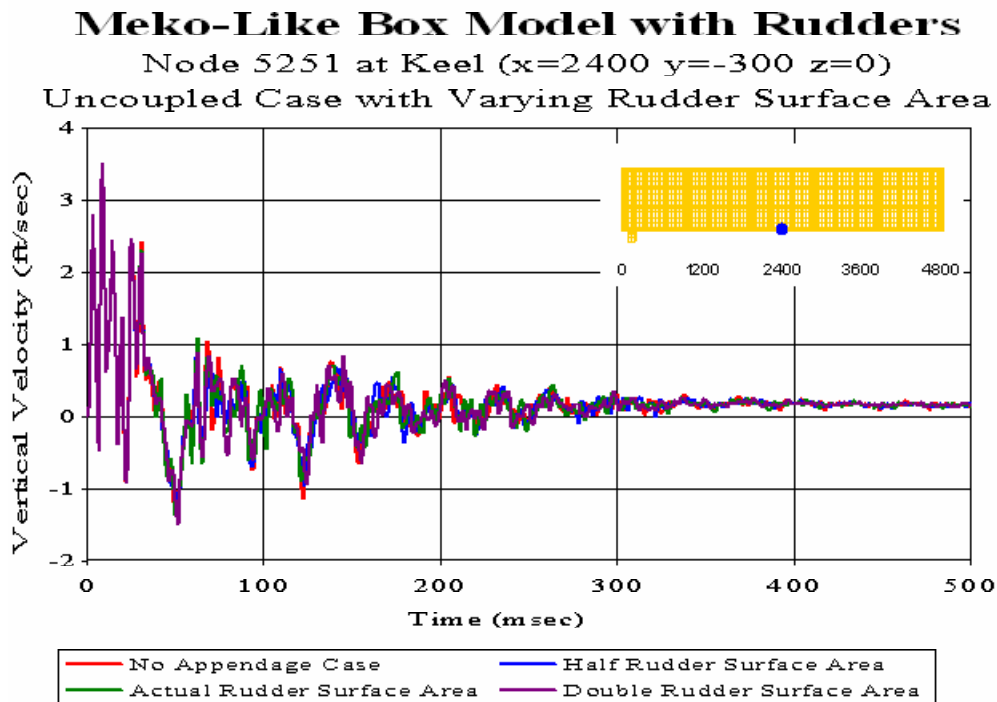
Figure 261. Uncoupled Case with Varying Rudder Surface Area: Keel Node 5251
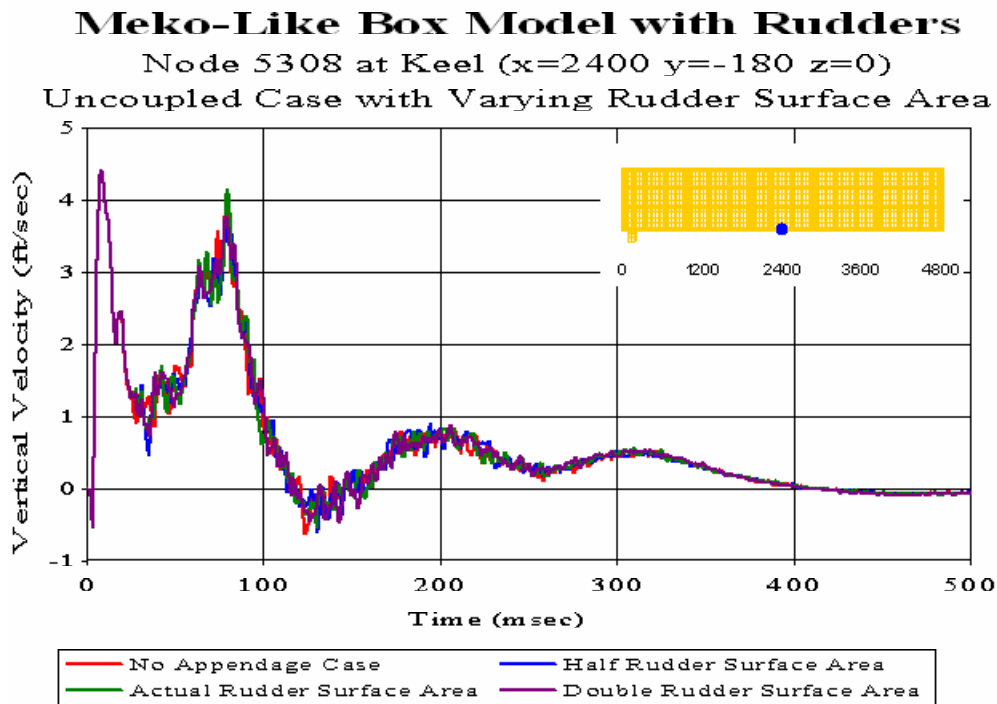
Figure 262. Uncoupled Case with Varying Rudder Surface Area: Keel Node 5308
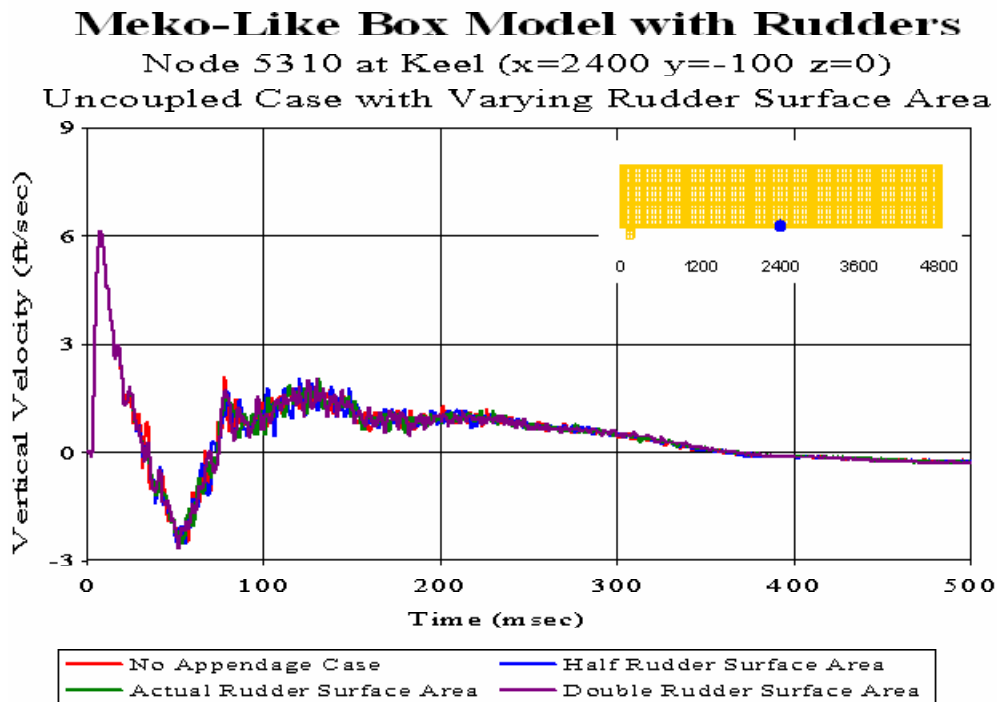
Figure 263. Uncoupled Case with Varying Rudder Surface Area: Keel Node 5310

255
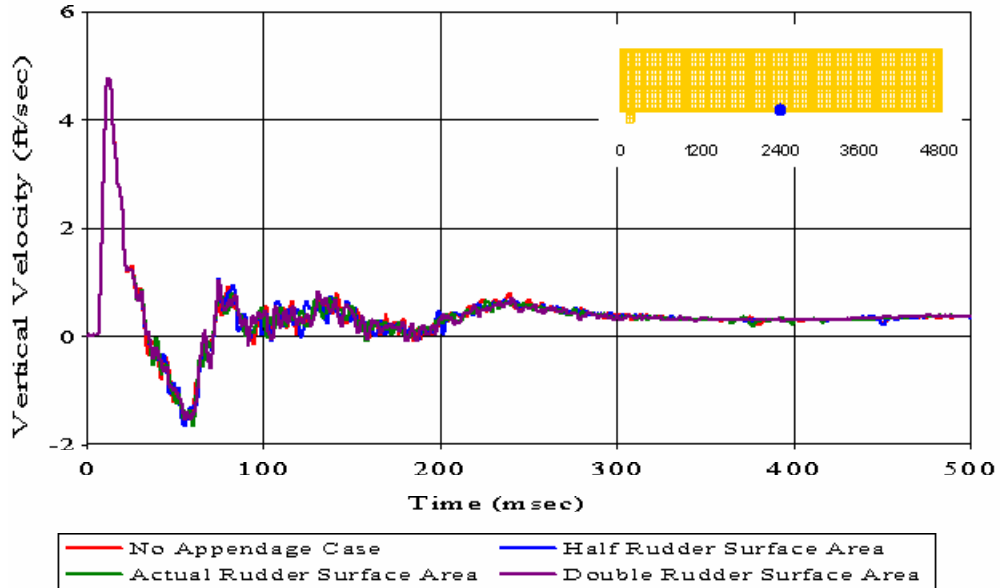
Figure 264. Uncoupled Case with Varying Rudder Surface Area: Keel Node 5315
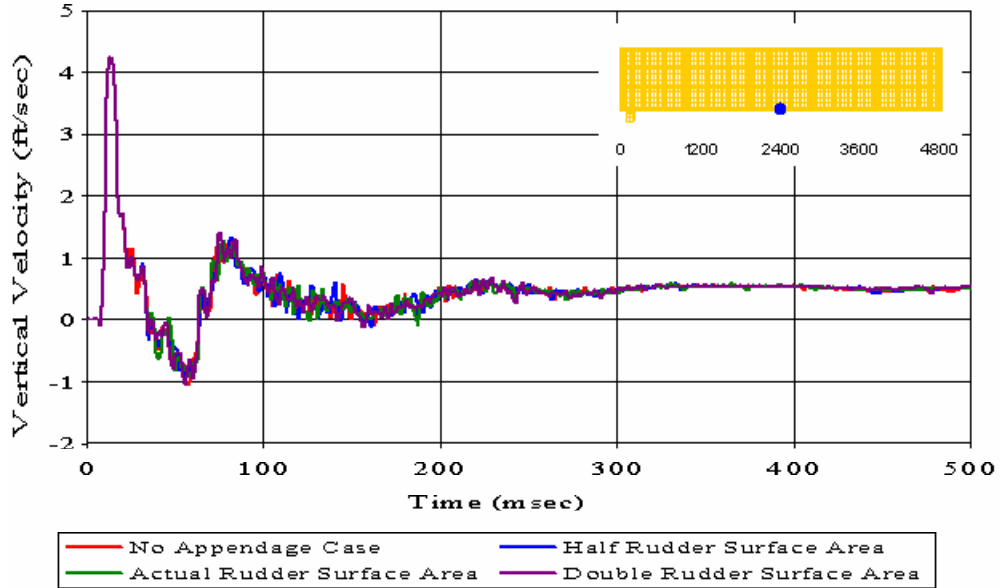
Figure 265. Uncoupled Case with Varying Rudder Surface Area: Keel Node 5317

256
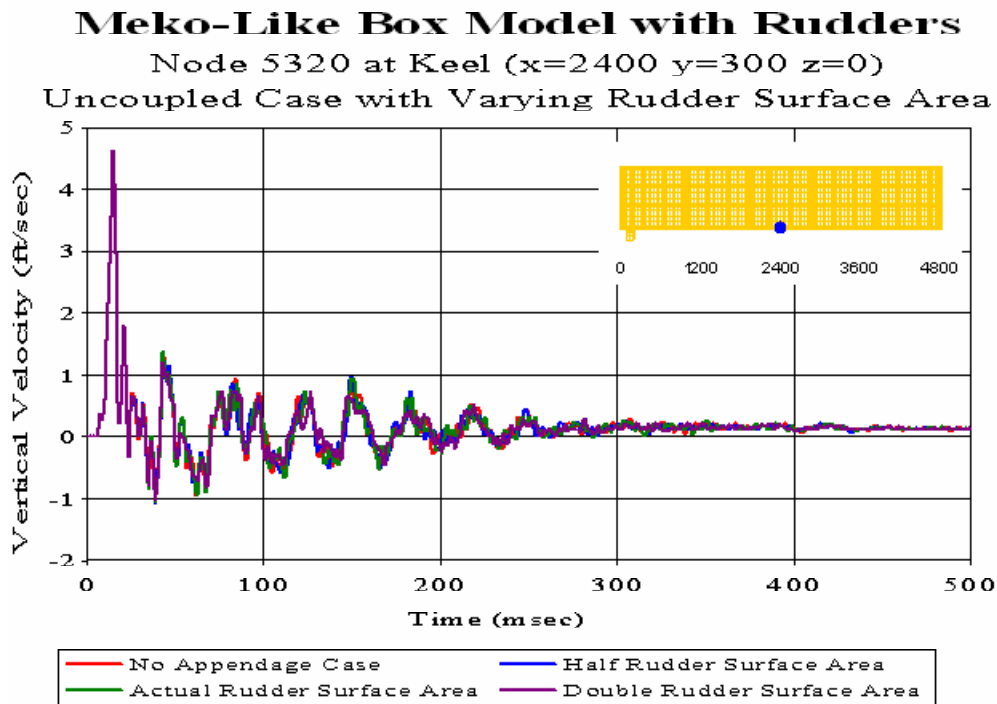
Figure 266.   Uncoupled Case with Varying Rudder Surface Area: Keel Node 5320
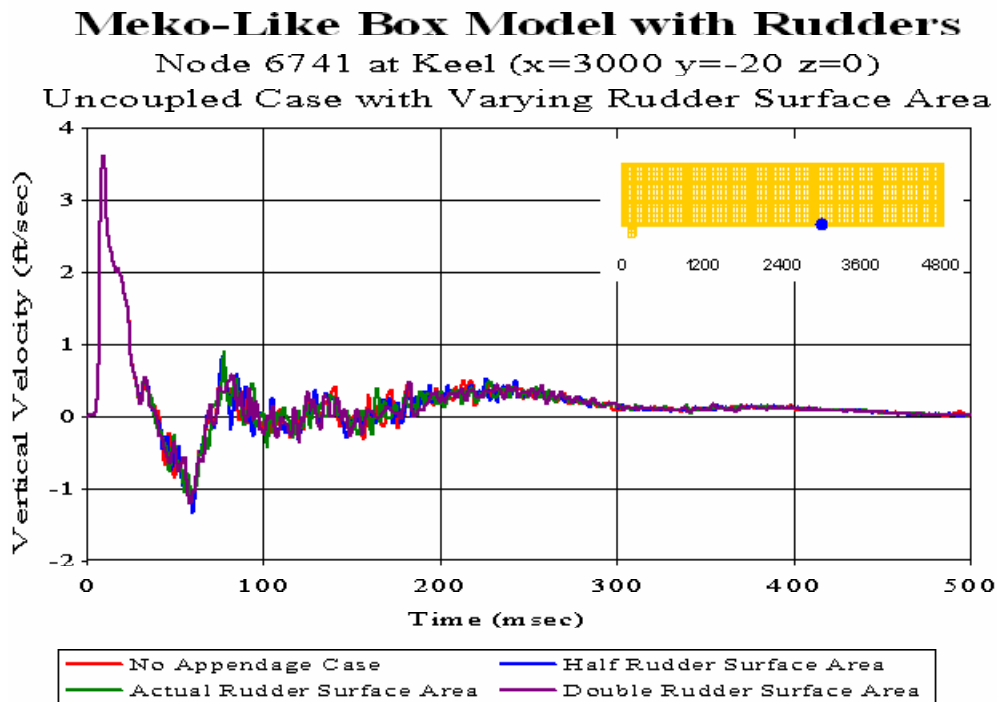
Figure 267.   Uncoupled Case with Varying Rudder Surface Area: Keel Node 6741

257
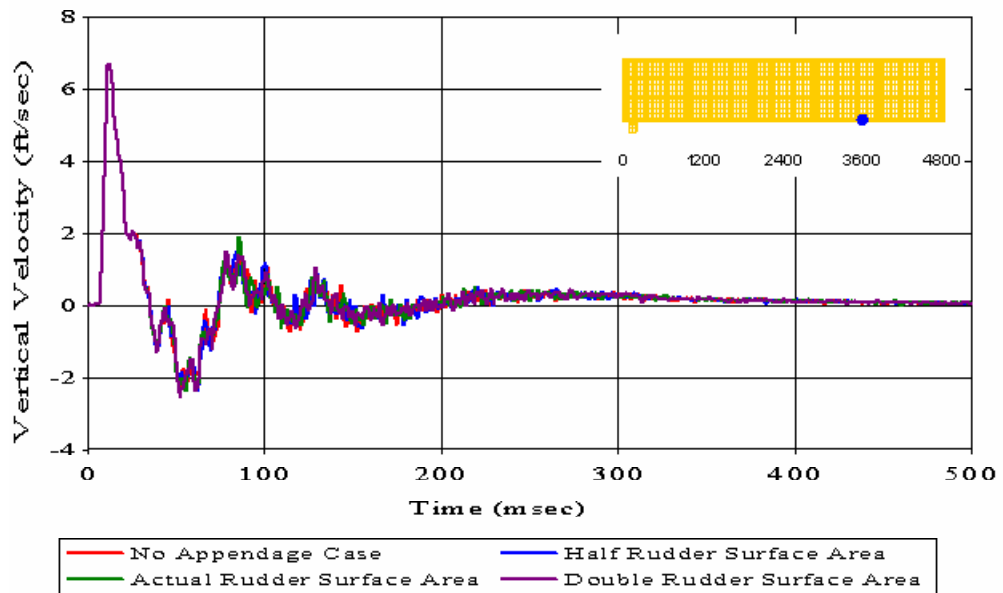
Figure 268. Uncoupled Case with Varying Rudder Surface Area: Keel Node 8170

APPENDIX E. ATHWARTSHIP VELOCITY PLOTS

A.   MEKO-LIKE BOX MODEL WITH SOLID KEEL BOARD
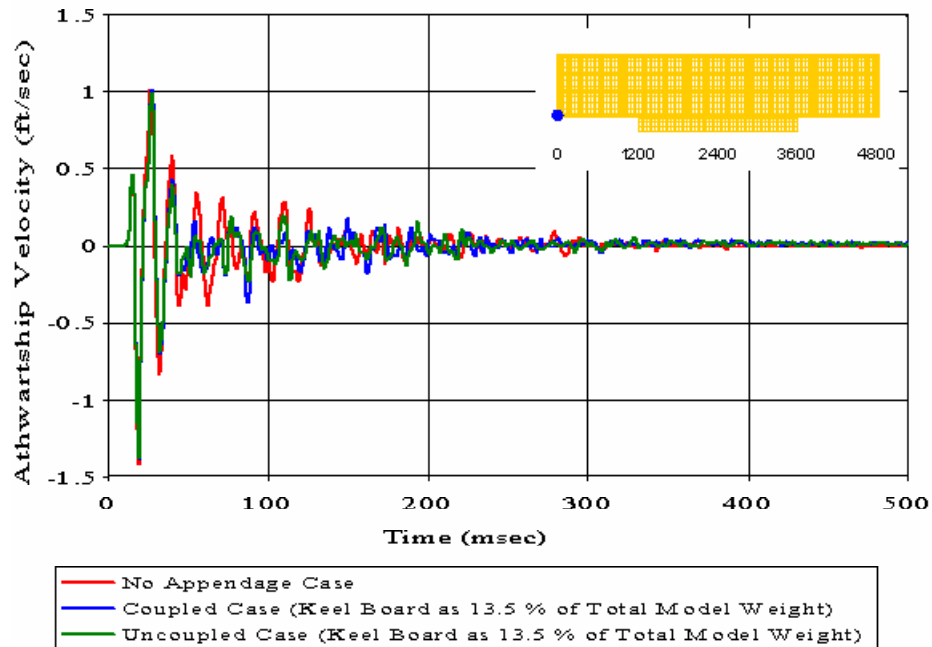
Figure 269.   Bulkhead Node 15: (RM = -0.0221, RP = 0.1100, RC = 0.0994)
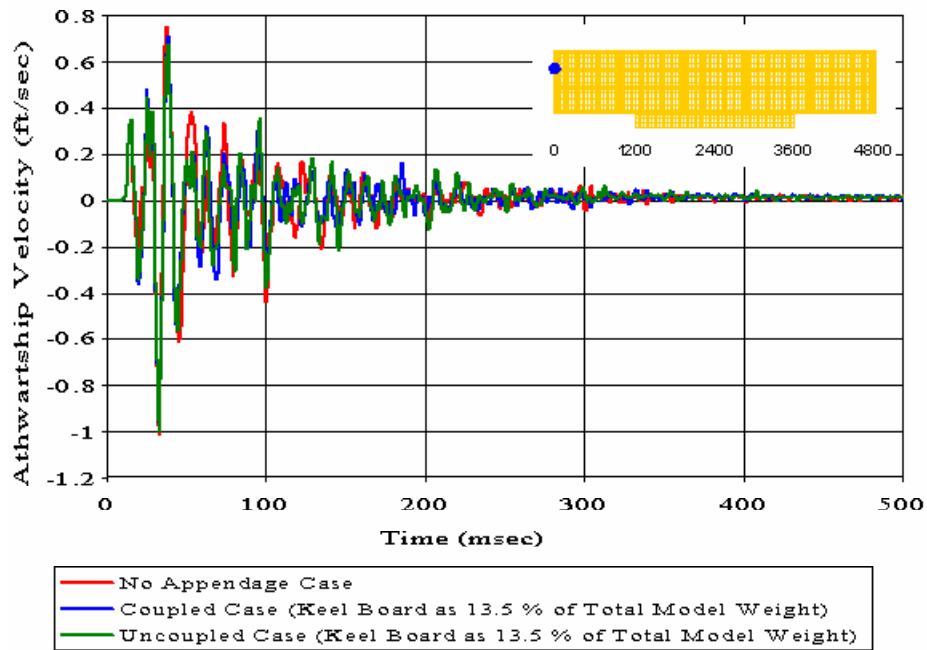
Figure 270. Bulkhead Node 268: (RM = 0.0009, RP = 0.1085, RC = 0.0961)
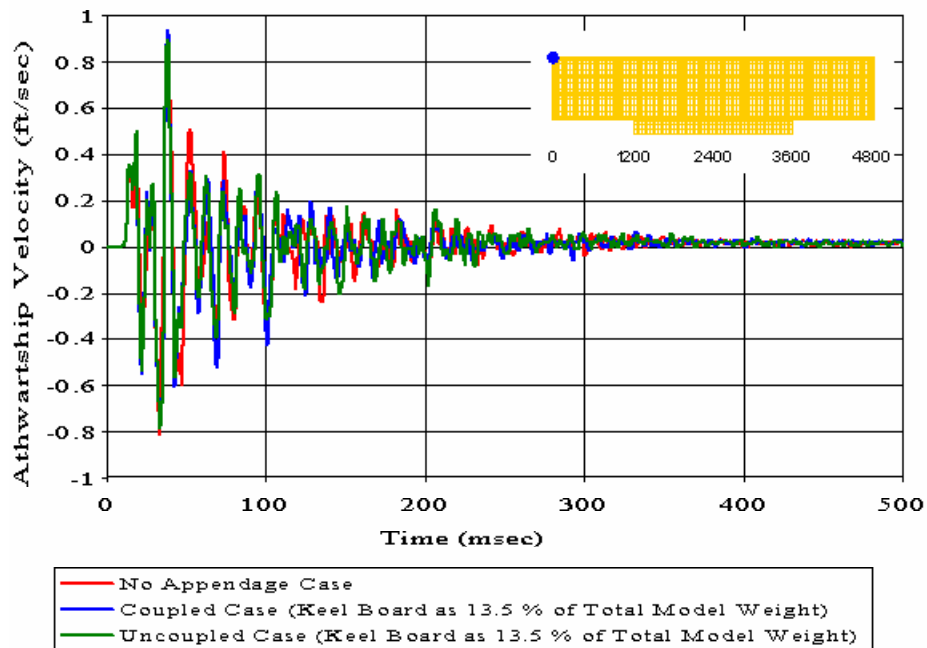
Figure 271. Bulkhead Node 388: (RM = -0.0067, RP = 0.1120, RC = 0.0994)

260
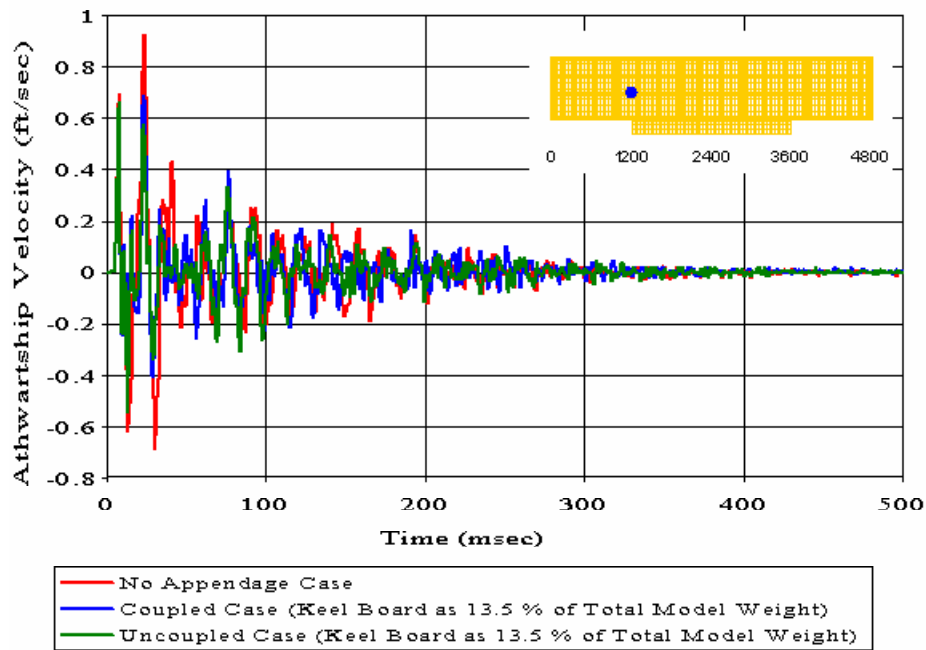
Figure 272. First Deck Node 2648: (RM = -0.0727, RP = 0.2169, RC = 0.2027)
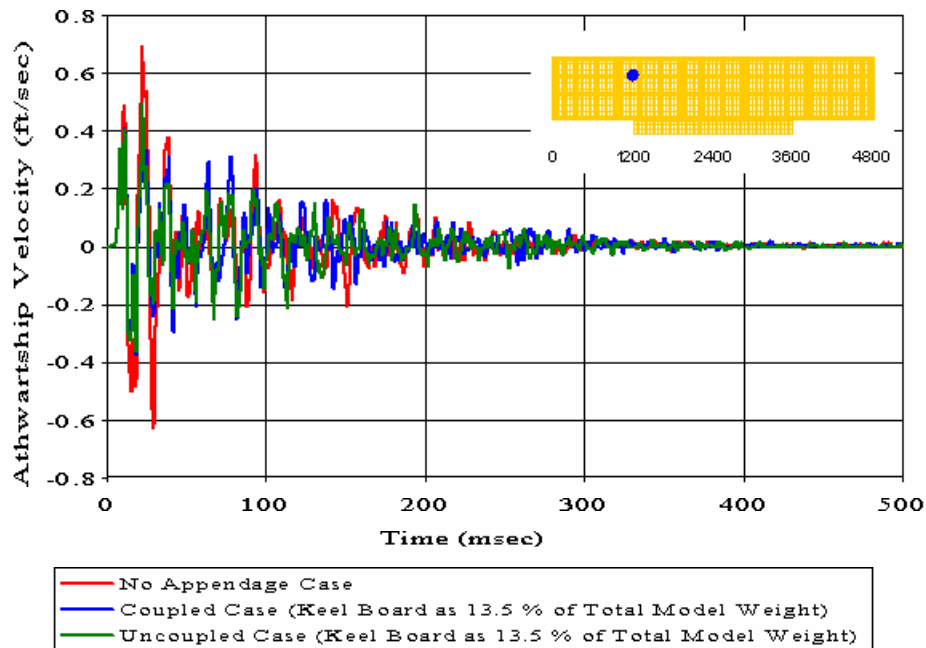
Figure 273. Second Deck Node 2820: (RM = -0.0379, RP = 0.2085, RC = 0.1878)
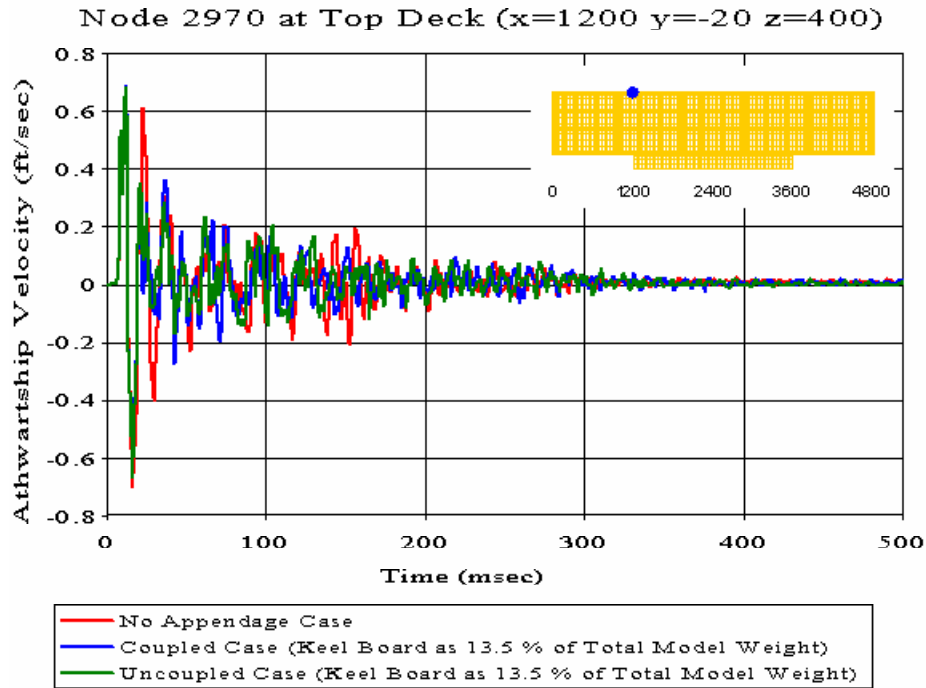
Figure 274. Top Deck Node 2970: (RM = -0.0217, RP = 0.1939, RC = 0.1729)
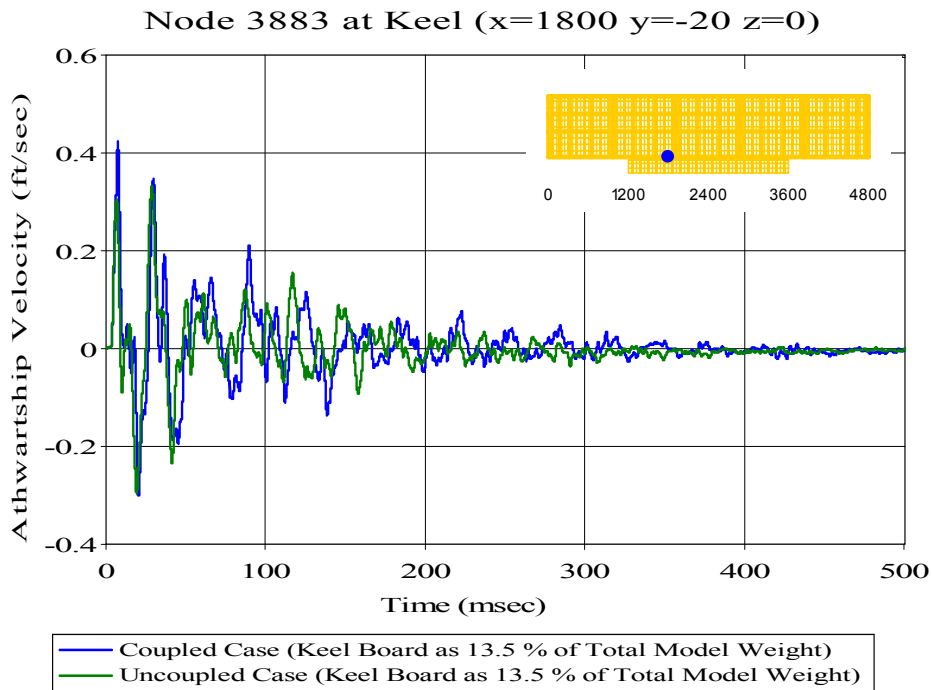
Figure 275. Keel Node 3883: (RM = -0.1031, RP = 0.2857, RC = 0.2691)
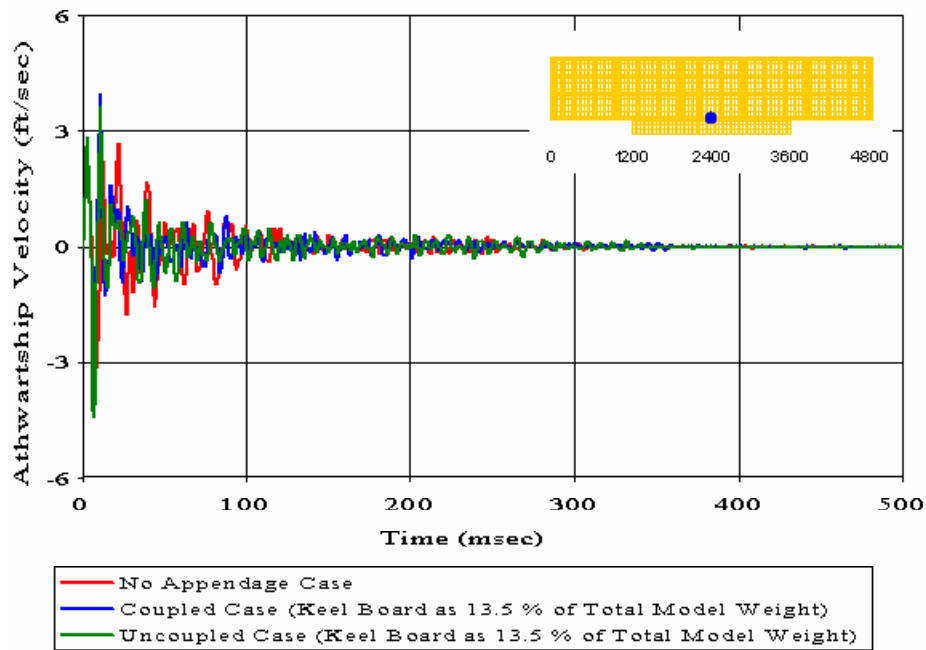
Figure 276. Keel Node 5251: (RM = -0.0258, RP = 0.1715, RC = 0.1537)
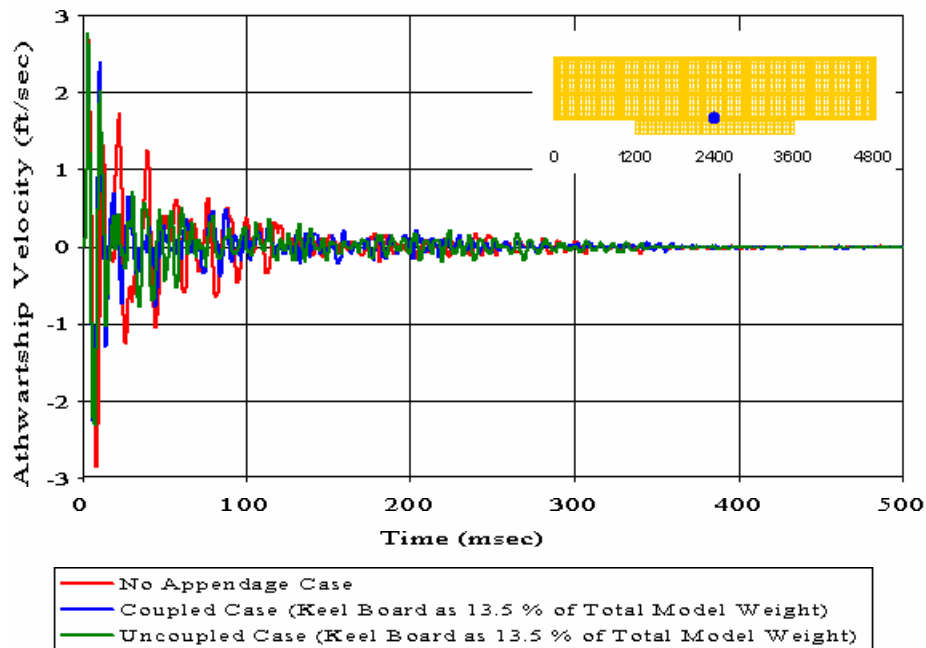
Figure 277. Keel Node 5308: (RM = 0.0036, RP = 0.1647, RC = 0.1460)

263

Meko-Like Box Model with Solid Keel Board

Node 5310 at Keel (x=2400 y=-100 z=0)
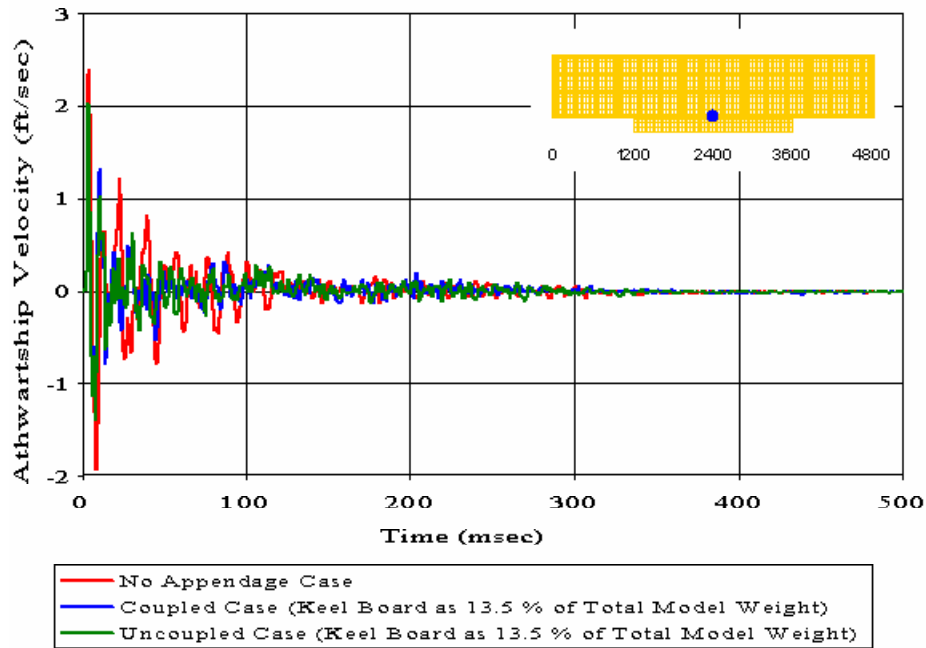
Figure 278. Keel Node 5310: (RM = 0.0069, RP = 0.1588, RC = 0.1409)

Meko–Like Box Model with Solid Keel Board

Node 5312 at Keel (x=2400 y=-20 z=0)
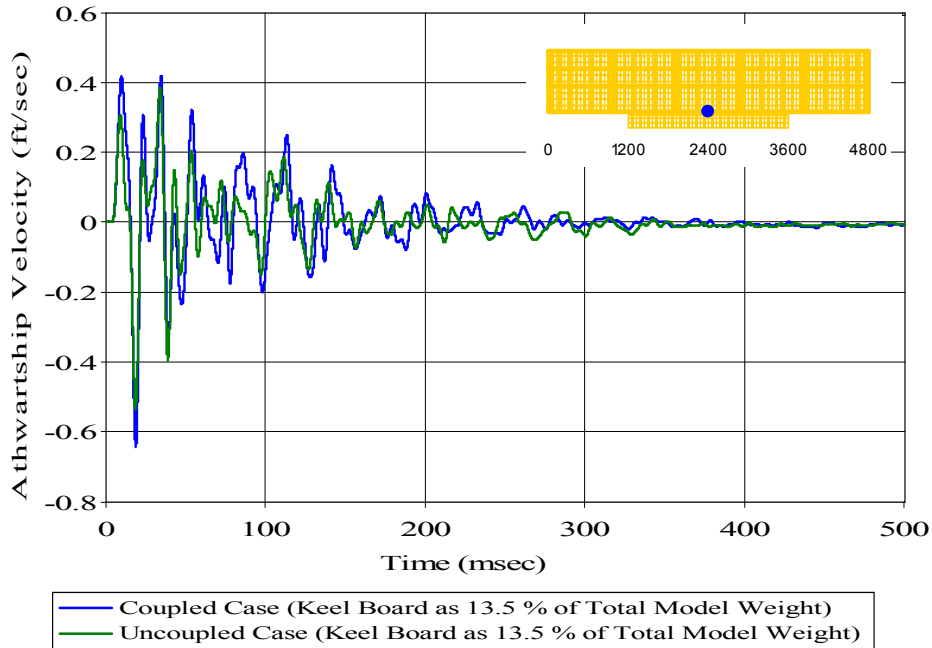
Figure 279. Keel Node 5312: (RM = -0.1650, RP = 0.1960, RC = 0.2271)

264

Meko-Like Box Model with Solid Keel Board

Node 5313 at Keel (x=2400 y=20 z=0)
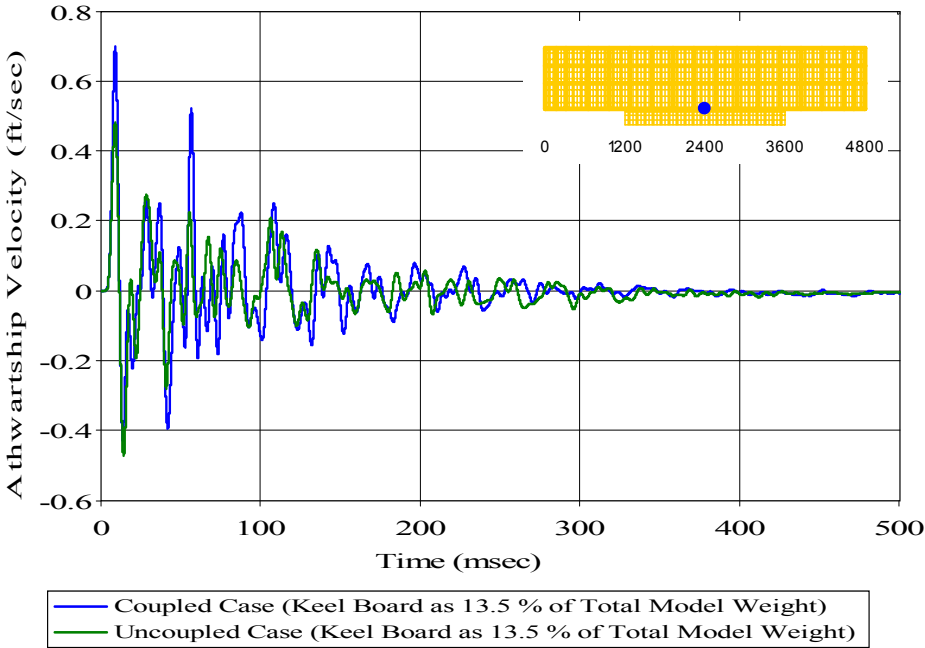
Figure 280.   Keel Node 5313: (RM = -0.1888, RP = 0.2327, RC = 0.2656)

Meko-Like Box Model with Solid Keel Board

Node 5315 at Keel (x=2400 y=100 z=0)
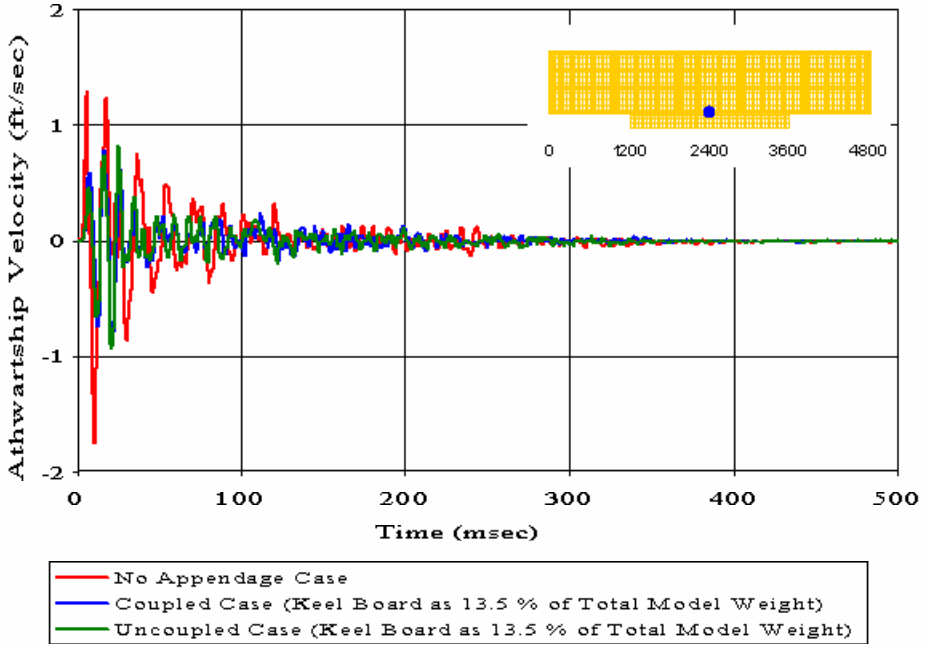
Figure 281.   Keel Node 5315: (RM = 0.0072, RP = 0.1657, RC = 0.1470)

265

Meko-Like Box Model with Solid Keel Board

Node 5317 at Keel (x=2400 y=180 z=0)
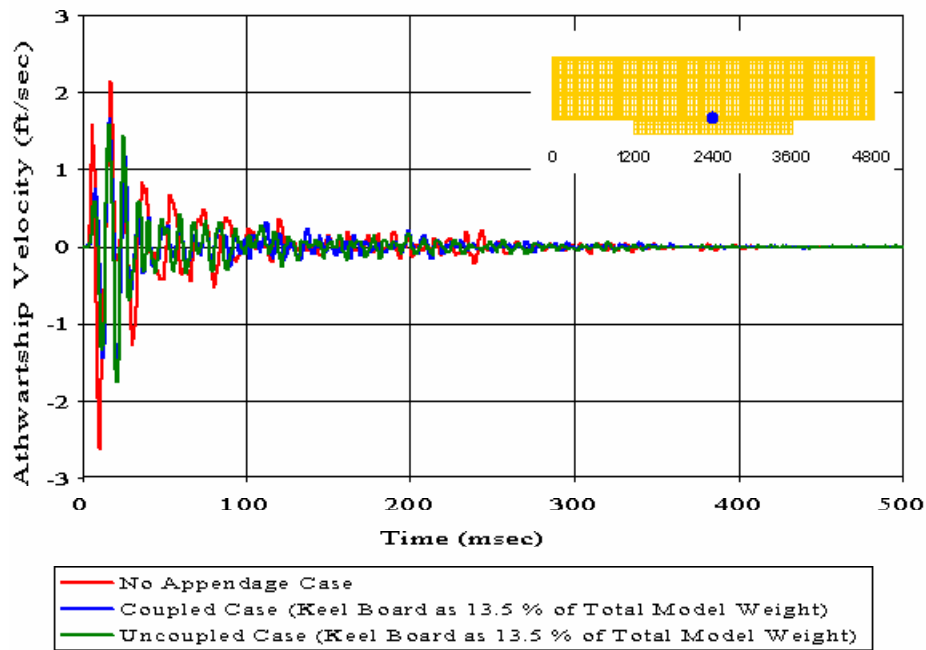
Figure 282.   Keel Node 5317: (RM = 0.0375, RP = 0.1502, RC = 0.1372)

Meko-Like Box Model with Solid Keel Board

Node 5320 at Keel (x=2400 y=300 z=0)
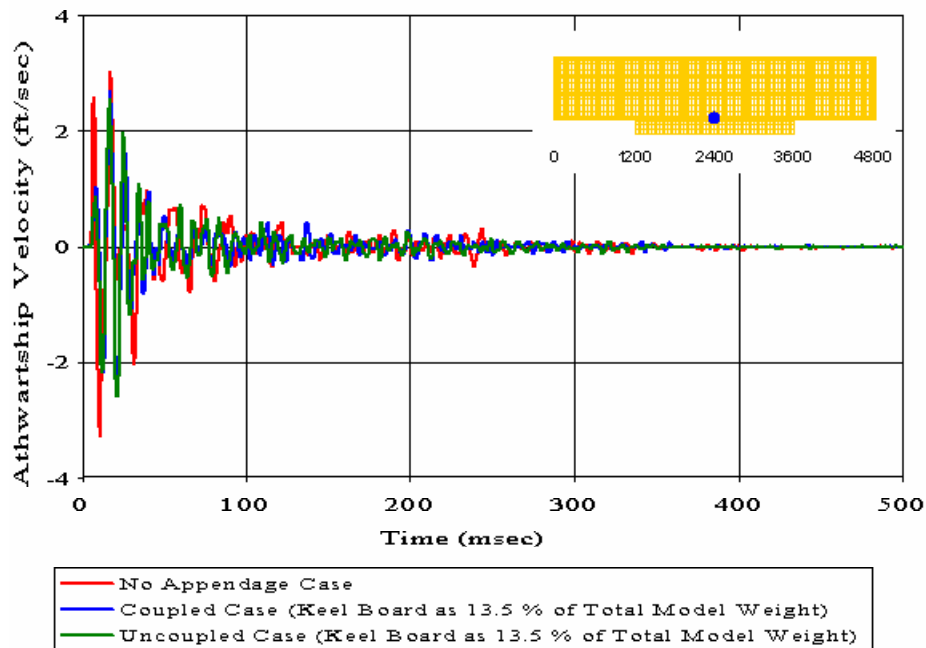
Figure 283.   Keel Node 5320: (RM = 0.0306, RP = 0.1525, RC = 0.1379)

266

Meko–Like Box Model with Solid Keel Board
Node 6741 at Keel (x=3000 y=-20 z=0)
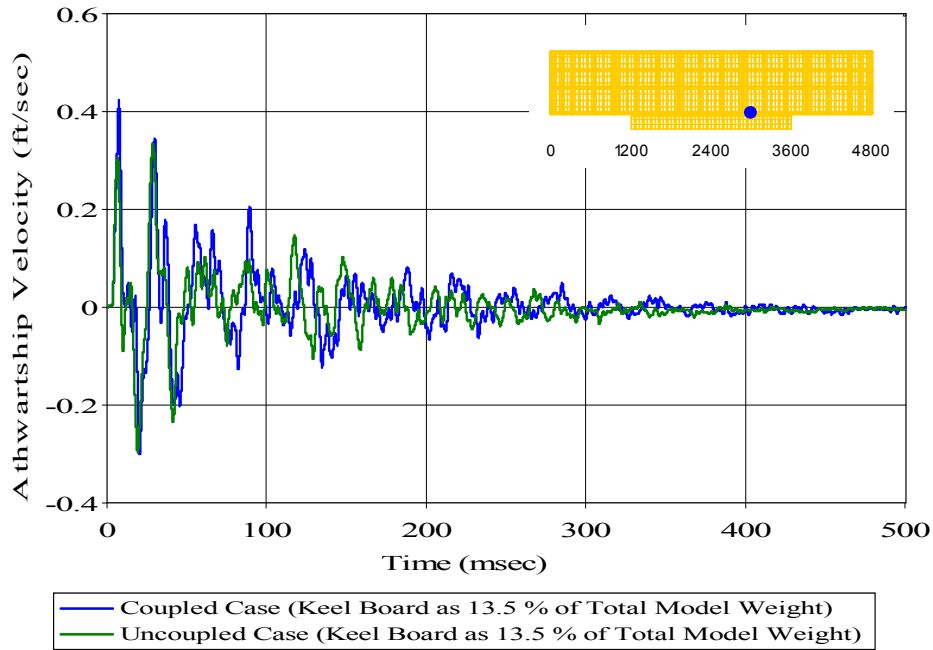
Figure 284. Keel Node 6741: (RM = -0.1053, RP = 0.2881, RC = 0.2719)

Meko–Like Box Model with Solid Keel Board
Node 8170 at Keel (x=3600 y=-20 z=0)
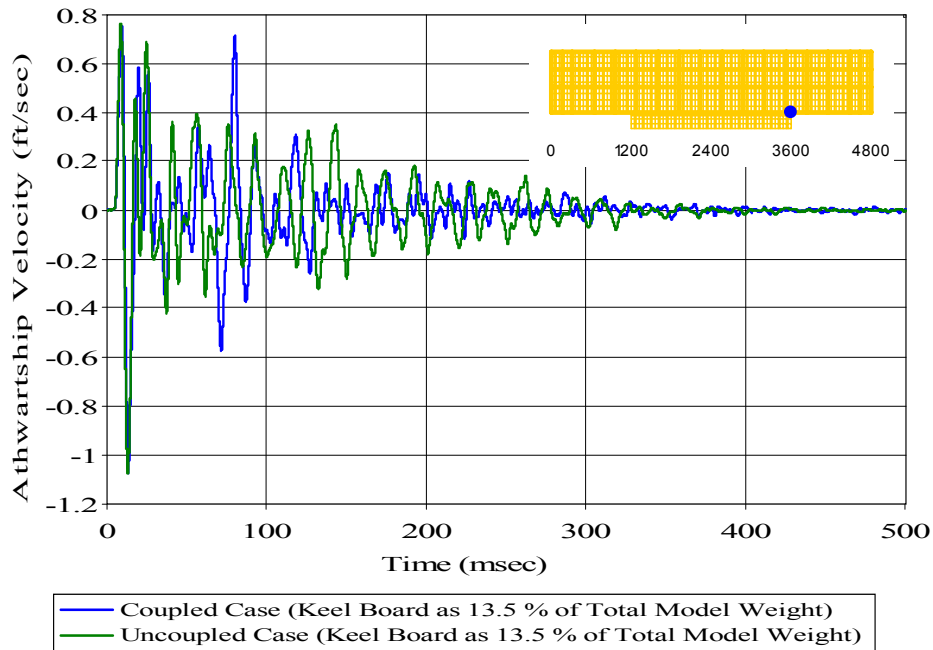
Figure 285. Keel Node 8170: (RM = 0.0441, RP = 0.3348, RC = 0.2993)

267
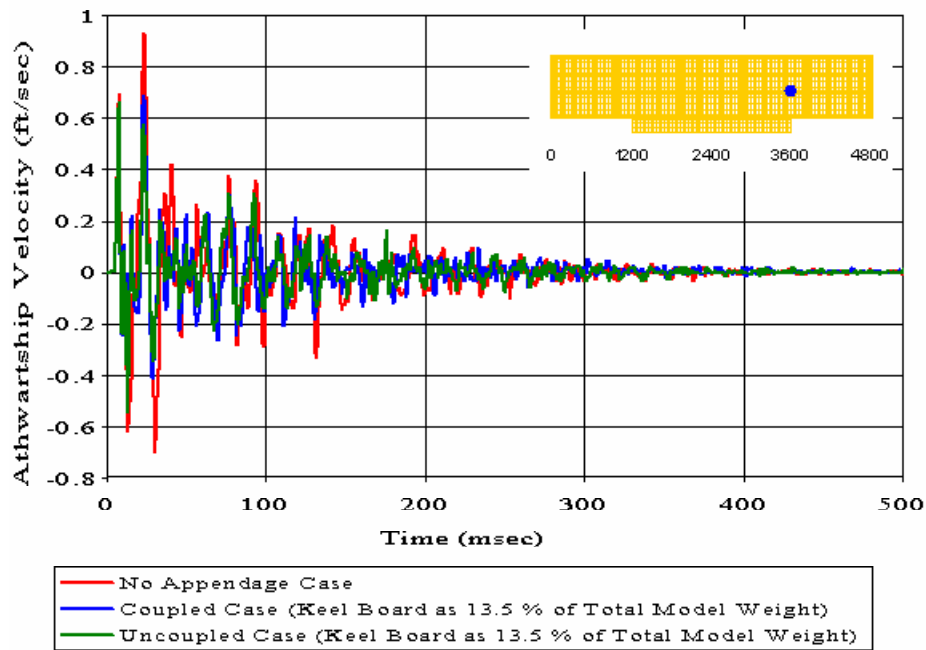
Figure 286.   First Deck Node 8364: (RM = -0.0908, RP = 0.2134, RC = 0.2055)
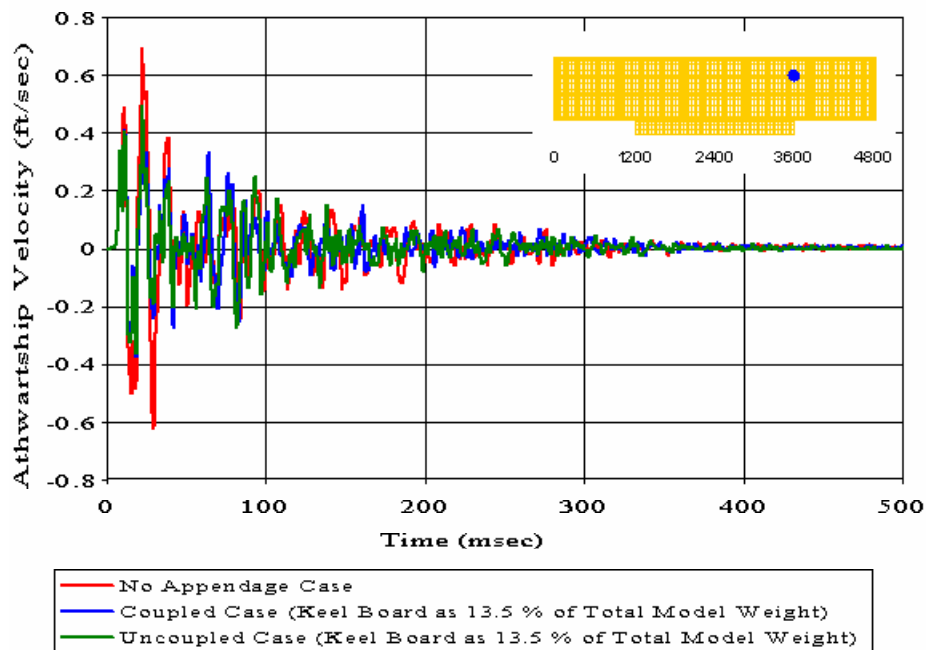
Figure 287.   Second Deck Node 8536: (RM = 0.0038, RP = 0.2001, RC = 0.1774)

268
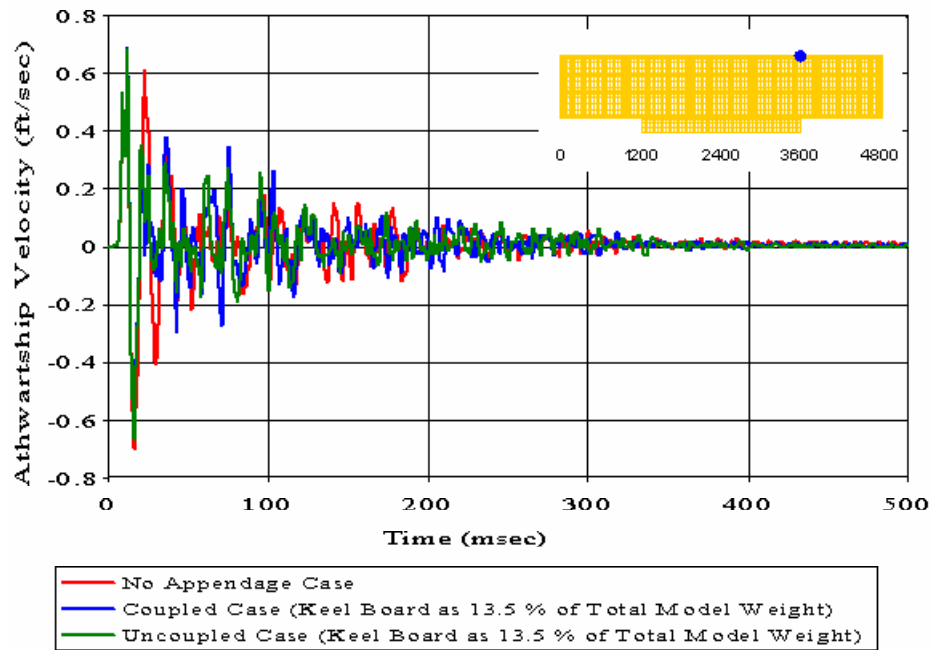
Figure 288. Top Deck Node 8686: (RM = -0.0480, RP = 0.1785, RC = 0.1638)
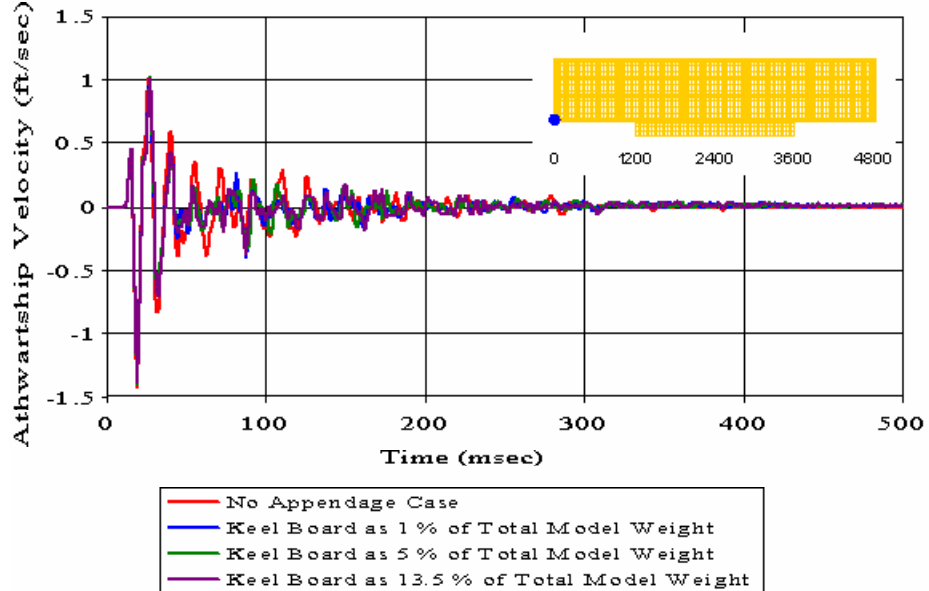
Figure 289. Coupled Case with Varying Weight Percentage: Bulkhead Node 15

269

Figure 290.   Coupled Case with Varying Weight Percentage: Bulkhead Node 148
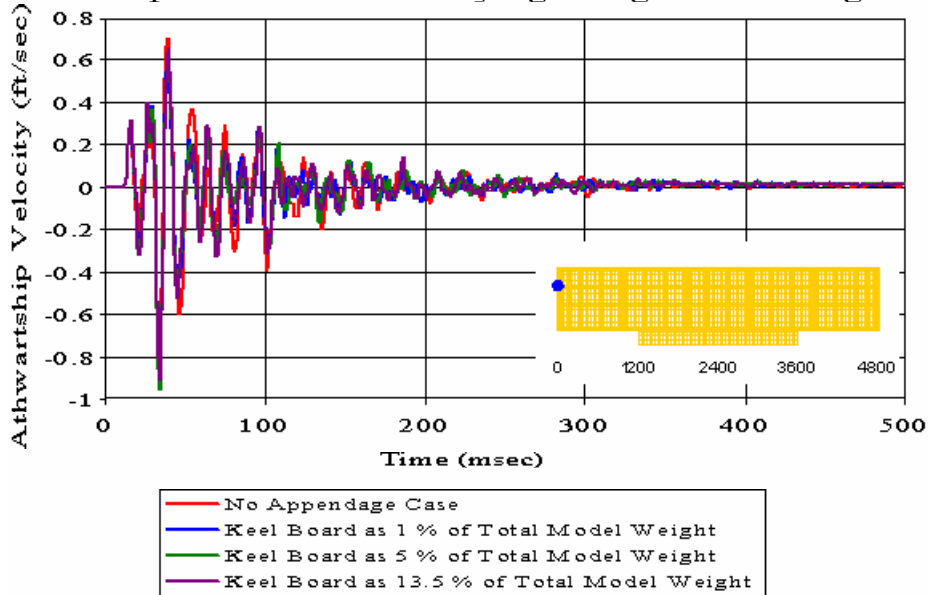
Figure 291.   Coupled Case with Varying Weight Percentage: Bulkhead Node 268

270

Meko-Like Box Model with Solid Keel Board
Node 2454 at Keel (x=1200 y=-20 z=0)
Coupled Case with Varying Weight Percentage

Keel Board as 1 % of Total Model Weight
Keel Board as 5 % of Total Model Weight
Keel Board as 13.5 % of Total Model Weight
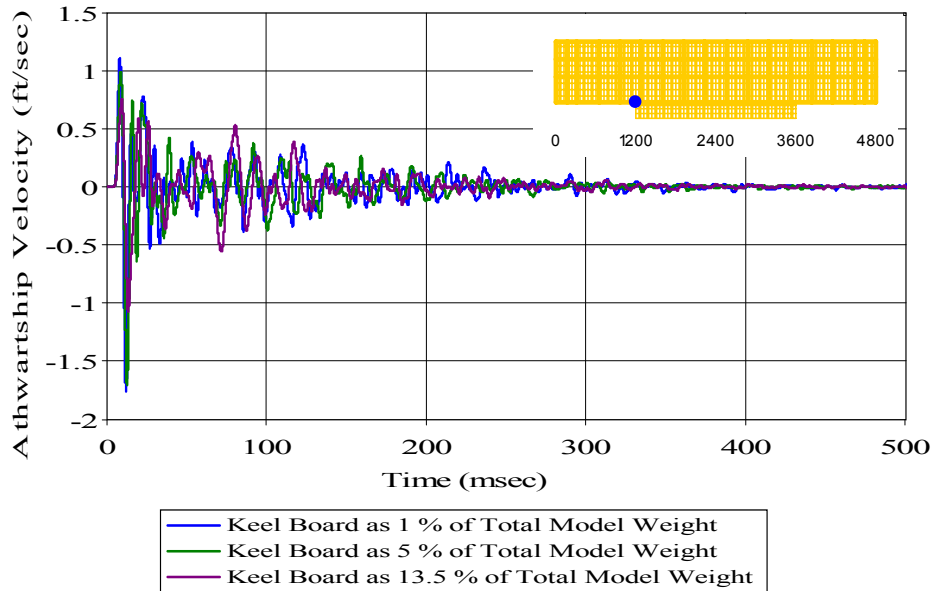
Figure 292.   Coupled Case with Varying Weight Percentage: Keel Node 2454

Meko-Like Box Model with Solid Keel Board
Node 2648 at First Deck (x=1200 y=-20 z=160)
Coupled Case with Varying Weight Percentage

No Appendage Case
Keel Board as 1 % of Total Model Weight
Keel Board as 5 % of Total Model Weight
Keel Board as 13.5 % of Total Model Weight
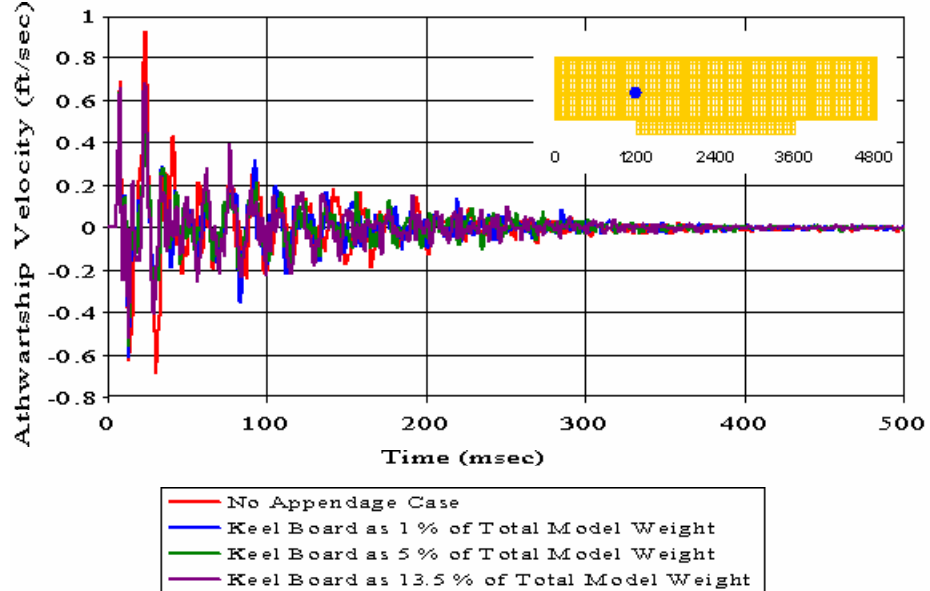
Figure 293.   Coupled Case with Varying Weight Percentage: First Deck Node 2648

271

Figure 294. **Coupled Case with Varying Weight Percentage: Second Deck Node 2820**

Figure 295. **Coupled Case with Varying Weight Percentage: Top Deck Node 2970**
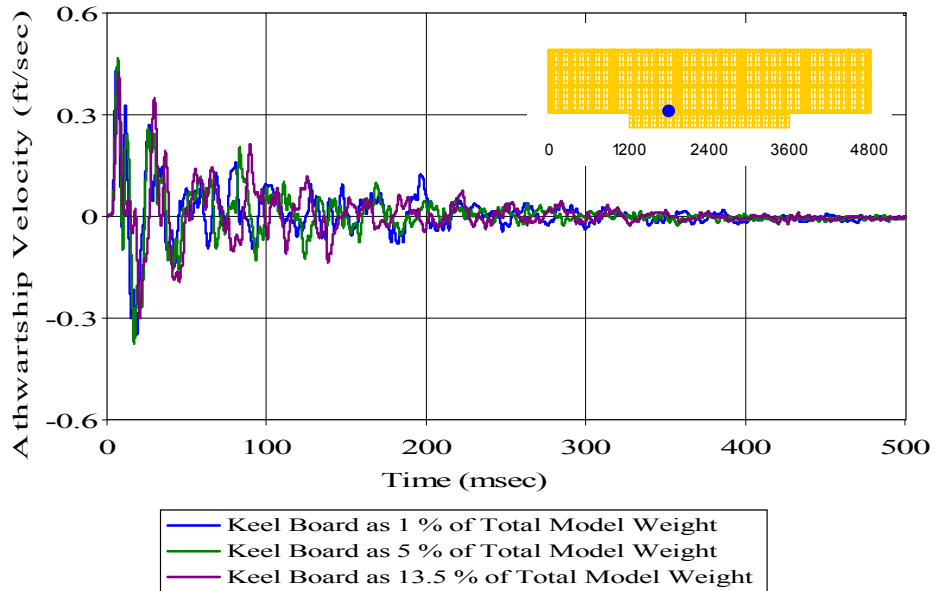
Figure 296.   Coupled Case with Varying Weight Percentage: Keel Node 3883

Figure 297.   Coupled Case with Varying Weight Percentage: Keel Node 5251

273

Figure 298.   **Coupled Case with Varying Weight Percentage: Keel Node 5308**

Figure 299.   **Coupled Case with Varying Weight Percentage: Keel Node 5310**

Meko–Like Box Model with Solid Keel Board

Node 5312 at Keel (x=2400 y=-20 z=0)
Coupled Case with Varying Weight Percentage
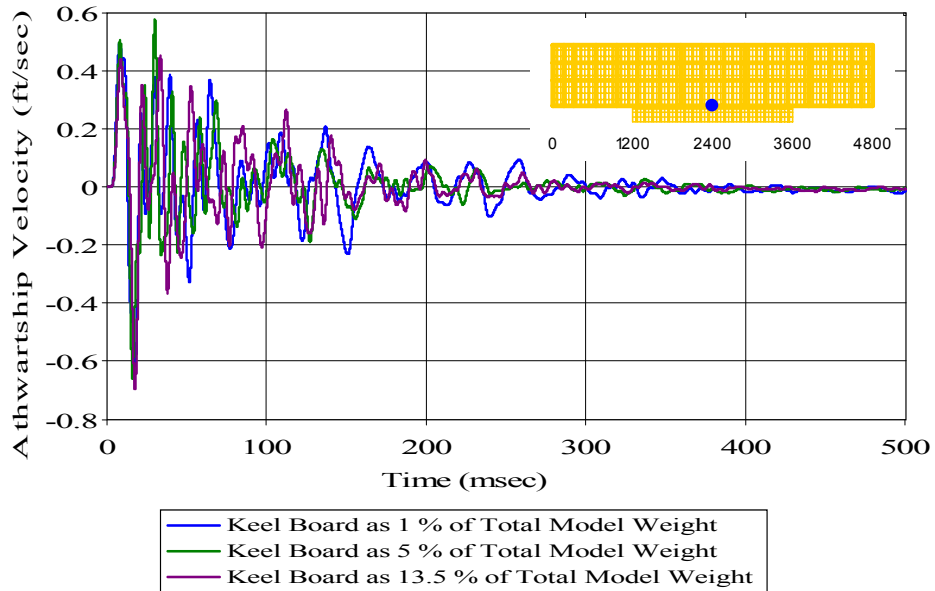
Figure 300.   Coupled Case with Varying Weight Percentage: Keel Node 5312

Meko–Like Box Model with Solid Keel Board

Node 5313 at Keel (x=2400 y=20 z=0)
Coupled Case with Varying Weight Percentage

Figure 301.   Coupled Case with Varying Weight Percentage: Keel Node 5313
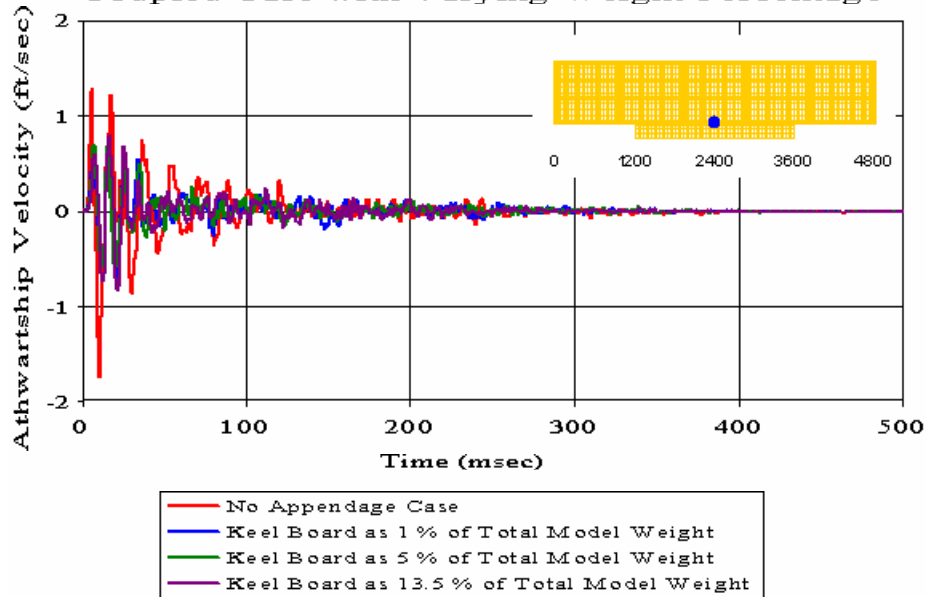
Figure 302. Coupled Case with Varying Weight Percentage: Keel Node 5315
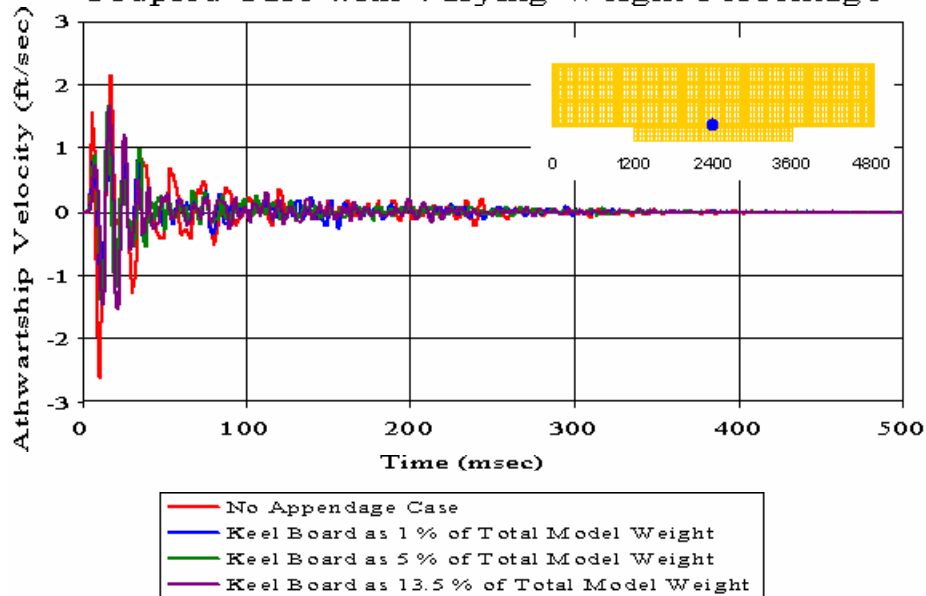
Figure 303. Coupled Case with Varying Weight Percentage: Keel Node 5317
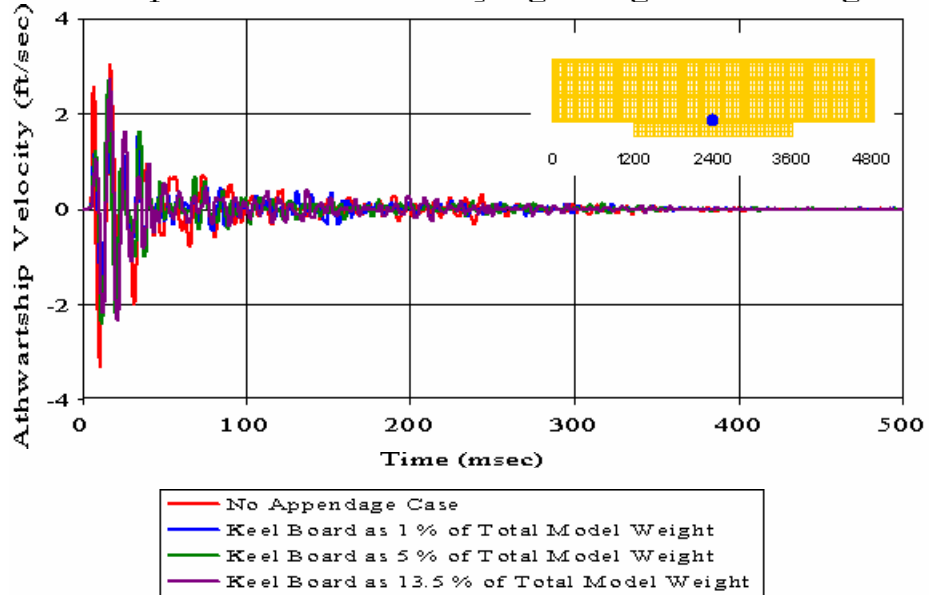
Figure 304.   Coupled Case with Varying Weight Percentage: Keel Node 5320

Figure 305.   Coupled Case with Varying Weight Percentage: Keel Node 6741

277

Figure 306. Coupled Case with Varying Weight Percentage: Keel Node 8170
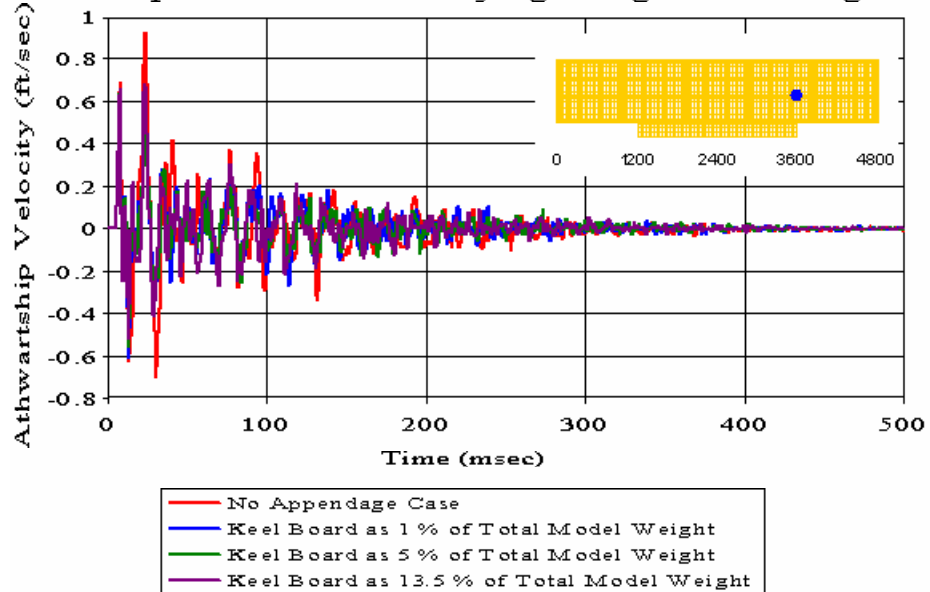
Figure 307. Coupled Case with Varying Weight Percentage: First Deck Node 8364

Figure 308.   Coupled Case with Varying Weight Percentage: Second Deck Node 8536

Figure 309.   Uncoupled Case with Varying Weight Percentage: Bulkhead Node 148

279

Figure 310.   Uncoupled Case with Varying Weight Percentage: Bulkhead Node 268

Figure 311.   Uncoupled Case with Varying Weight Percentage: Bulkhead Node 388

Figure 312. **Uncoupled Case with Varying Weight Percentage: Keel Node 2454**

Figure 313. **Uncoupled Case with Varying Weight Percentage: First Deck Node 2648**

Figure 314.   Uncoupled Case with Varying Weight Percentage: Top Deck Node 2970

Figure 315.   Uncoupled Case with Varying Weight Percentage: Keel Node 3883

Figure 316.   Uncoupled Case with Varying Weight Percentage: Keel Node 5251

Figure 317.   Uncoupled Case with Varying Weight Percentage: Keel Node 5308

Figure 318.   Uncoupled Case with Varying Weight Percentage: Keel Node 5310

Figure 319.   Uncoupled Case with Varying Weight Percentage: Keel Node 5312

Figure 320.   **Uncoupled Case with Varying Weight Percentage: Keel Node 5313**
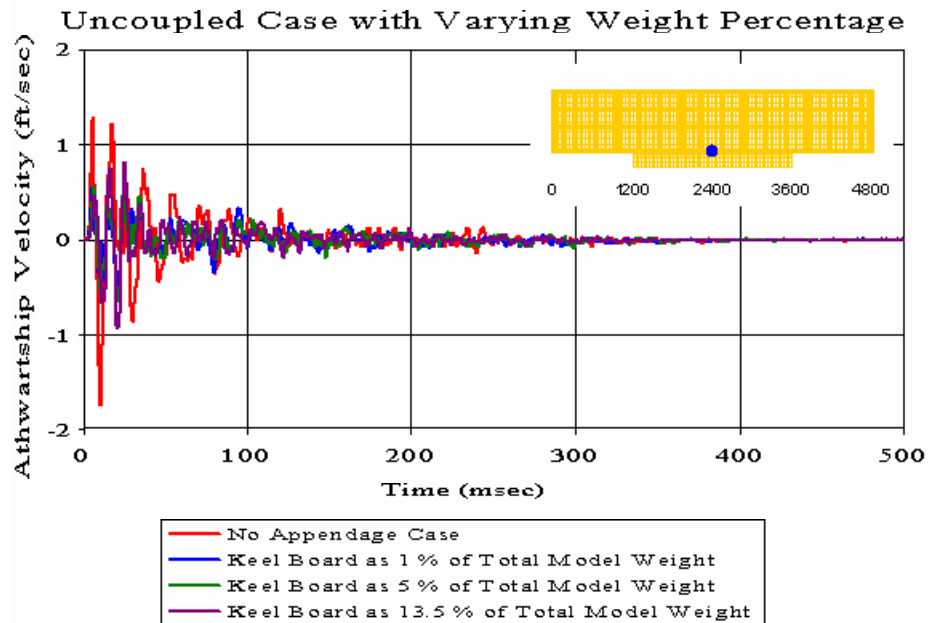
Figure 321.   **Uncoupled Case with Varying Weight Percentage: Keel Node 5315**
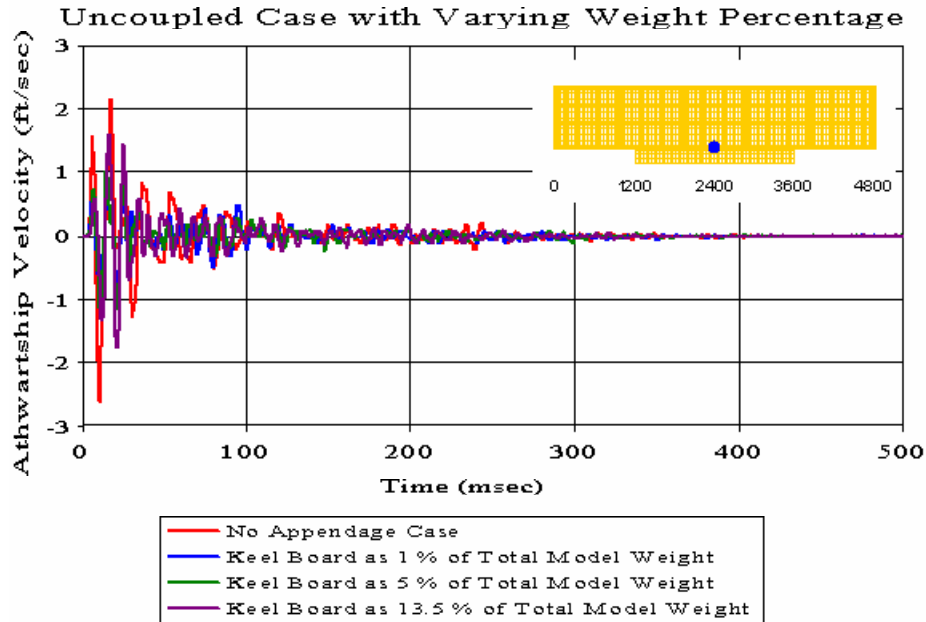
Figure 322. **Uncoupled Case with Varying Weight Percentage: Keel Node 5317**

Figure 323. **Uncoupled Case with Varying Weight Percentage: Keel Node 5320**

Meko–Like Box Model with Solid Keel Board
Node 6741 at Keel (x=3000 y=-20 z=0)
Uncoupled Case with Varying Weight Percentage
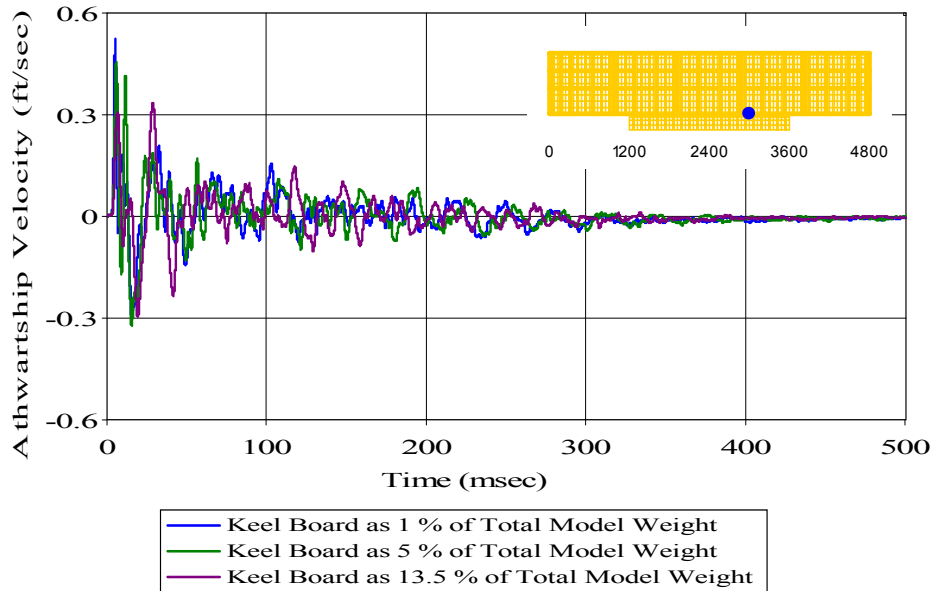
Figure 324.   Uncoupled Case with Varying Weight Percentage: Keel Node 6741

Meko–Like Box Model with Solid Keel Board
Node 8170 at Keel (x=3600 y=-20 z=0)
Uncoupled Case with Varying Weight Percentage
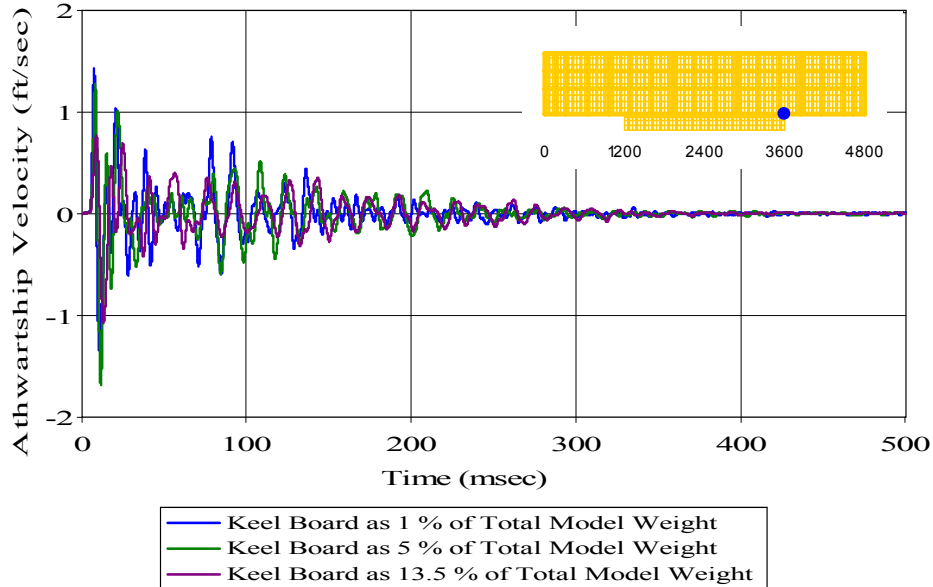
Figure 325.   Uncoupled Case with Varying Weight Percentage: Keel Node 8170
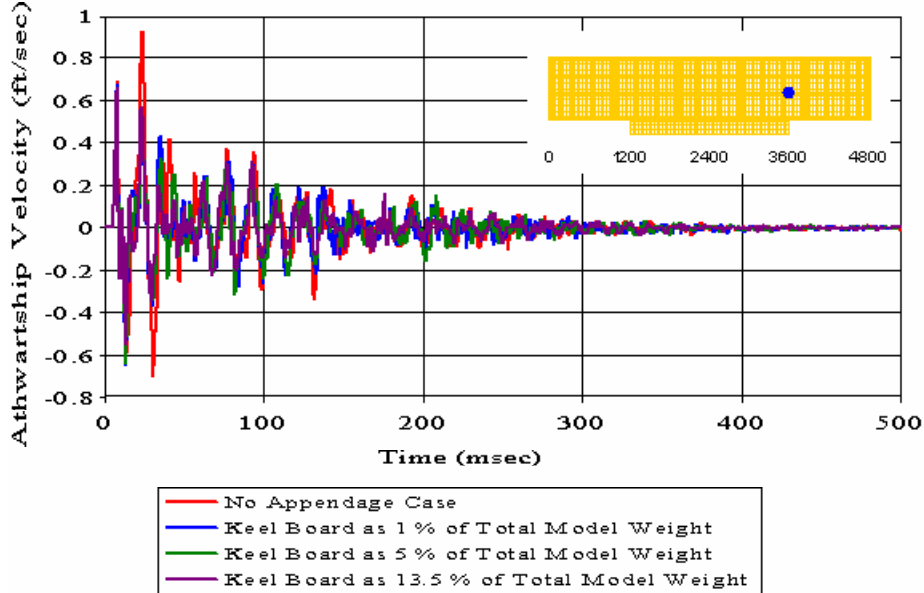
Figure 326. Uncoupled Case with Varying Weight Percentage: First Deck Node 8364
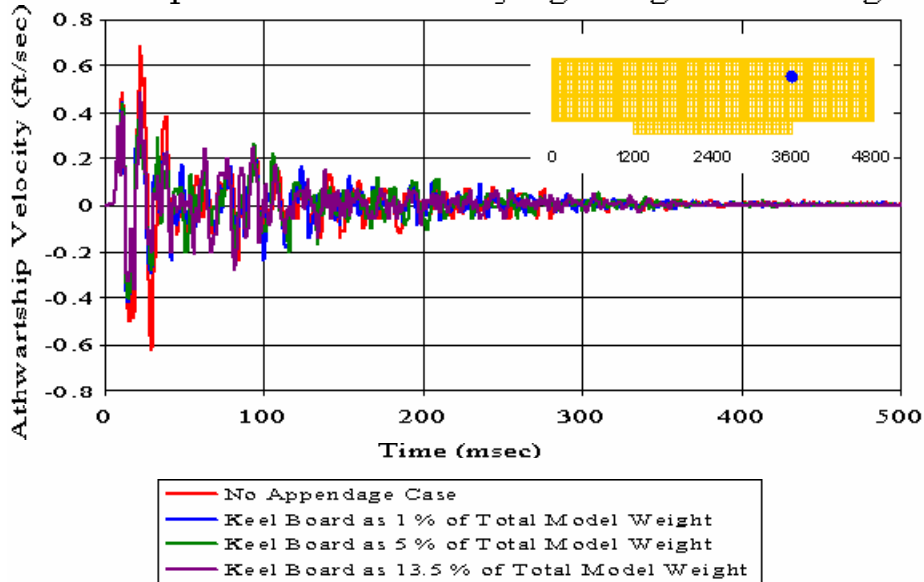
Figure 327. Uncoupled Case with Varying Weight Percentage: Second Deck Node 8536

288
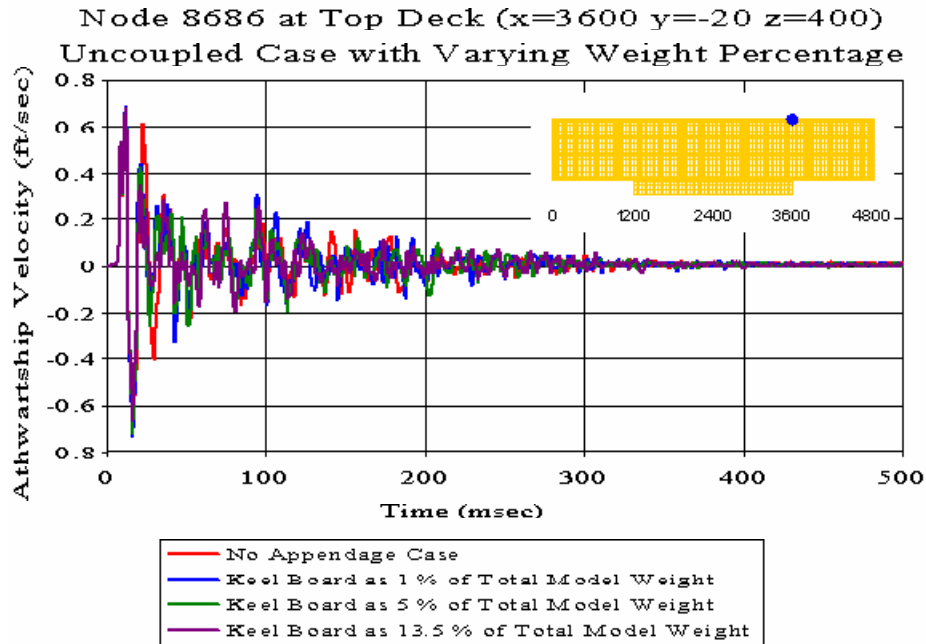
Figure 328. Uncoupled Case with Varying Weight Percentage: Top Deck Node 8686

B.   MEKO-LIKE BOX MODEL WITH SHELL KEEL BOARD
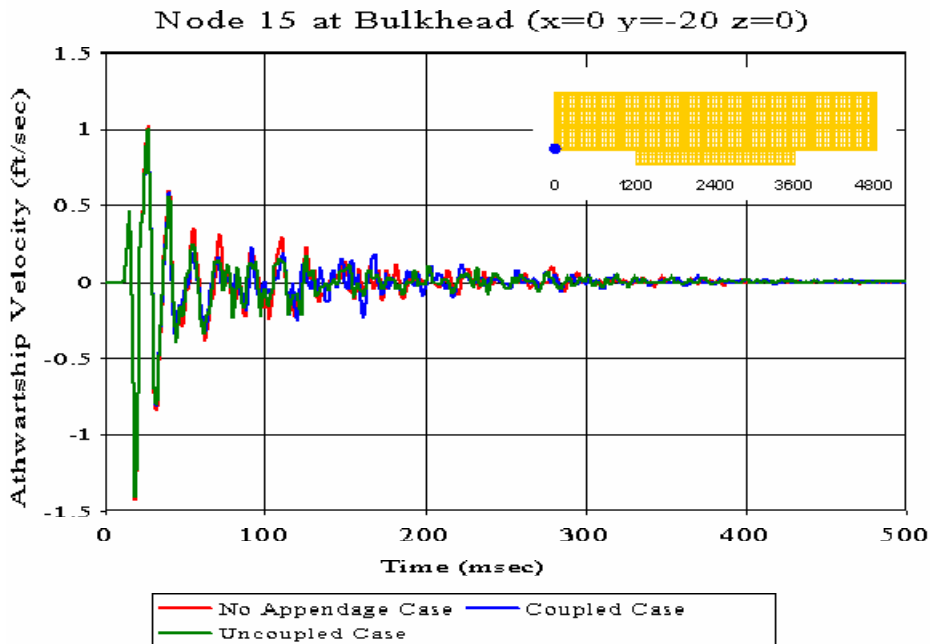
Figure 329. Bulkhead Node 15: (RM = 0.0038, RP = 0.1044, RC = 0.0926)
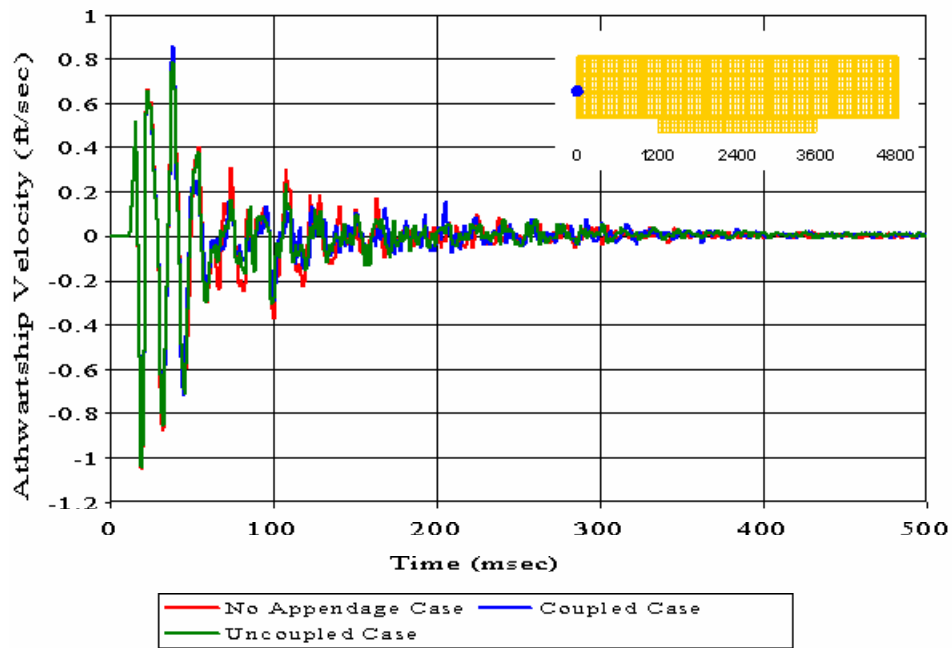
Figure 330.   Bulkhead Node 148: (RM = 0.0165, RP = 0.0880, RC = 0.0793)
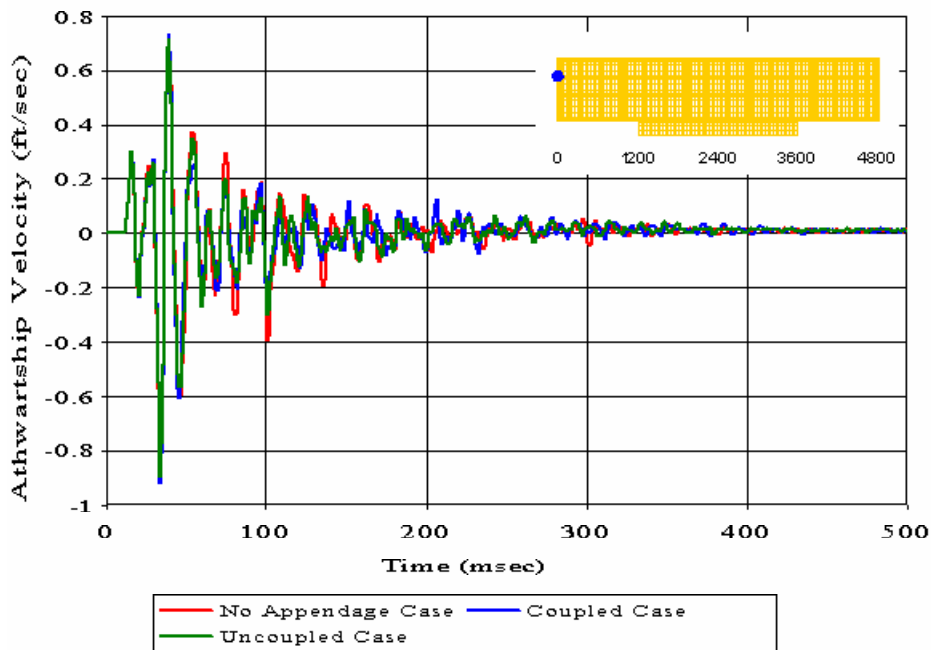
Figure 331.   Bulkhead Node 268: (RM = -0.0052, RP = 0.0922, RC = 0.0819)
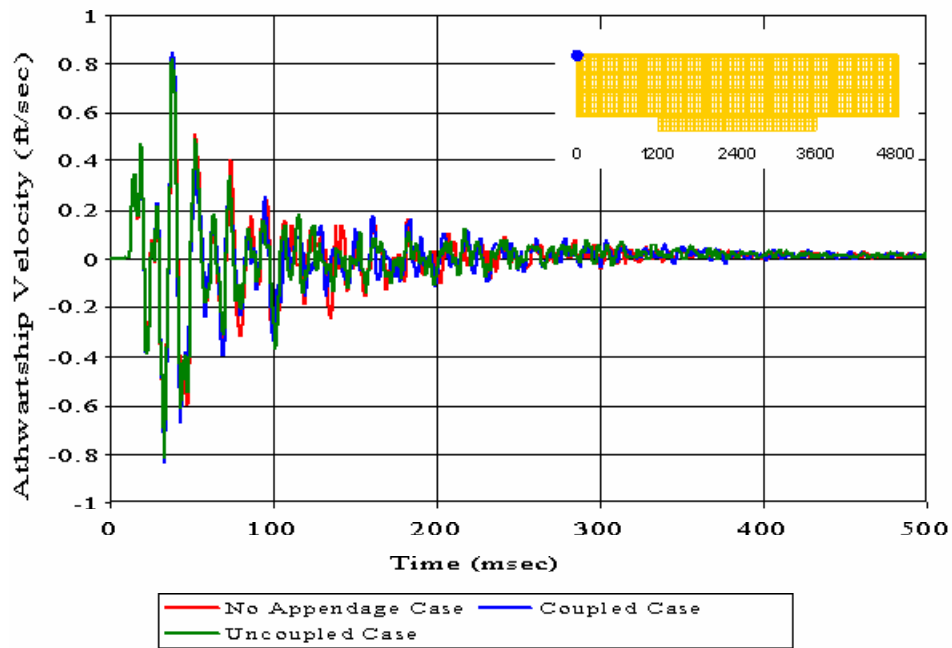
Figure 332. **Bulkhead Node 388: (RM = -0.0186, RP = 0.1118, RC = 0.1005)**

Figure 333. **Keel Node 2454: (RM = 0.0741, RP = 0.1392, RC = 0.1398)**

291
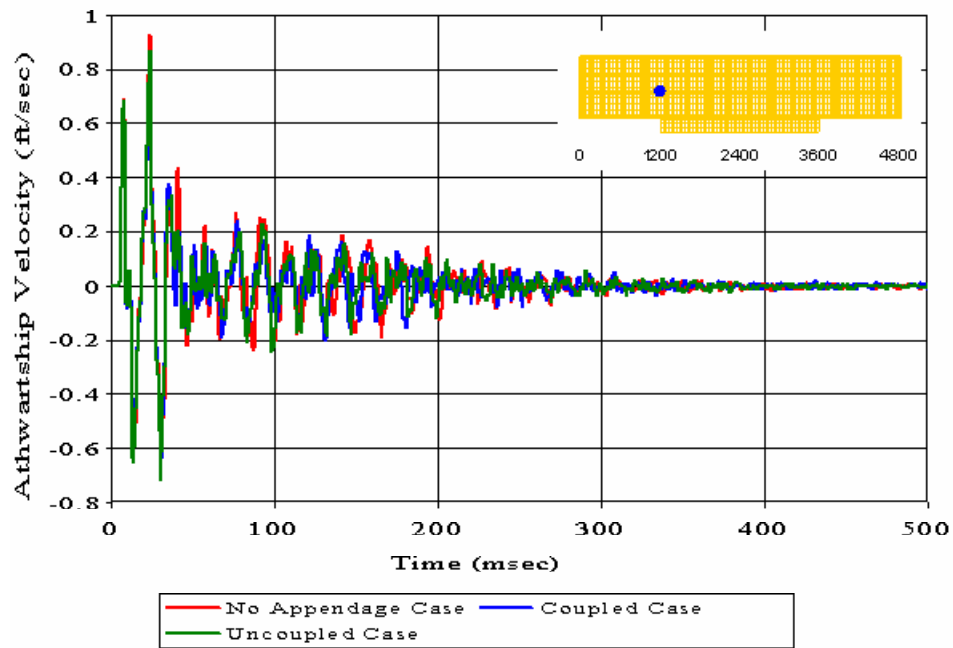
Figure 334. **First Deck Node 2648: (RM = 0.0332, RP = 0.1485, RC = 0.1349)**
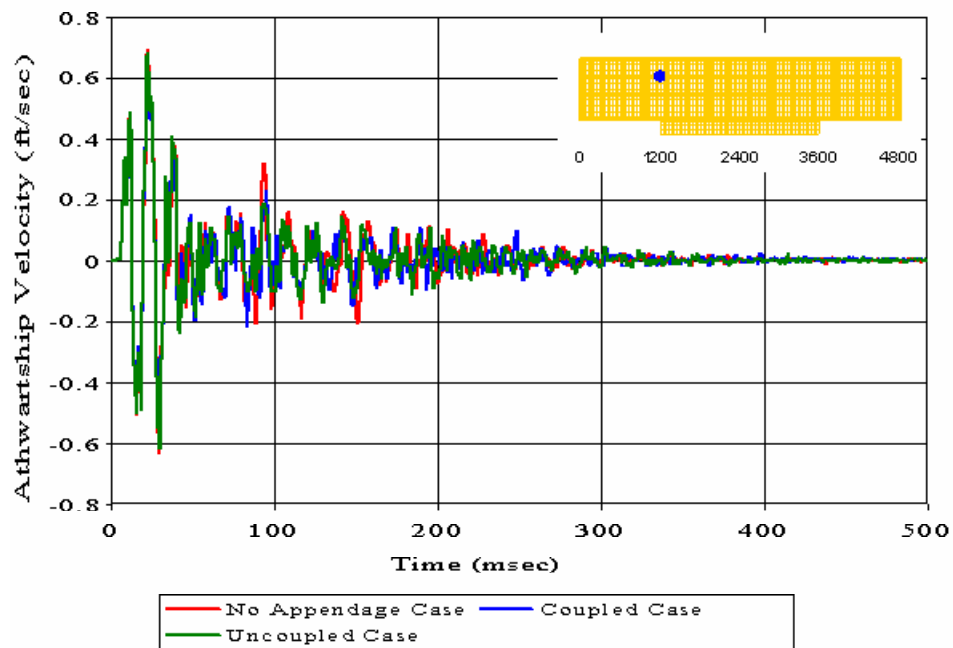
Figure 335. **Second Deck Node 2820: (RM = 0.0396, RP = 0.1182, RC = 0.1105)**

Meko-Like Box Model with Shell Keel Board
Node 2970 at Top Deck (x=1200 y=-20 z=400)
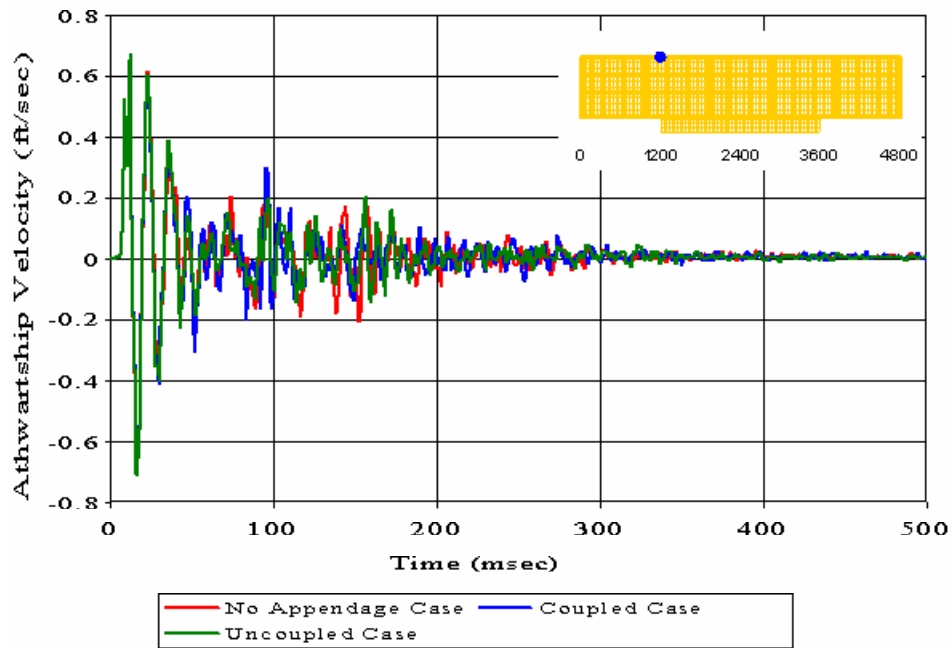
Figure 336.   **Top Deck Node 2970: (RM = 0.0008, RP = 0.1225, RC = 0.1086)**

Meko–Like Box Model with Shell Keel Board
Node 3883 at Keel (x=1800 y=-20 z=0)
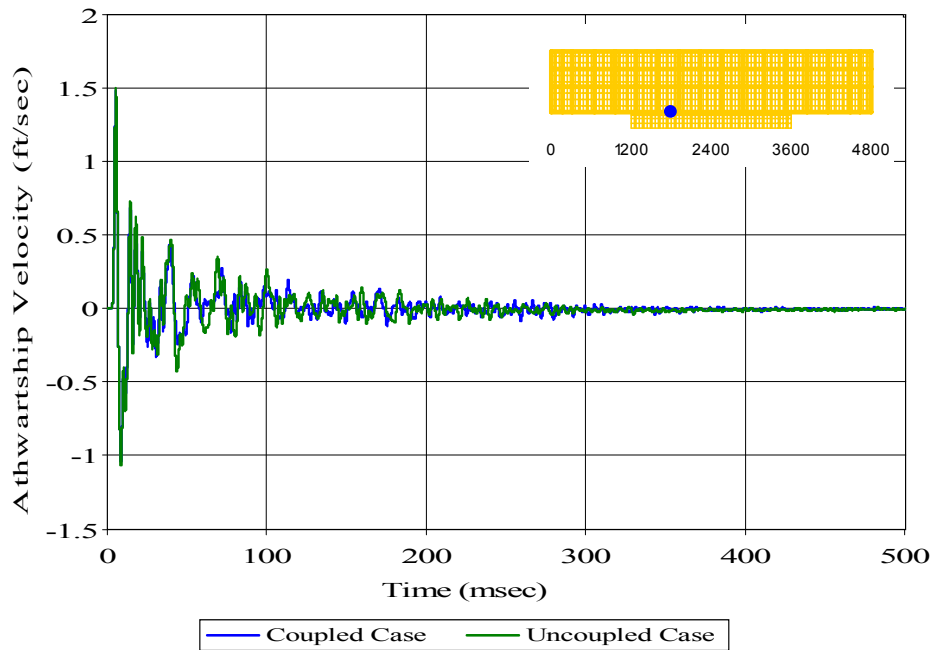
Figure 337.   **Keel Node 3883: (RM = 0.0723, RP = 0.1371, RC = 0.1374)**

293
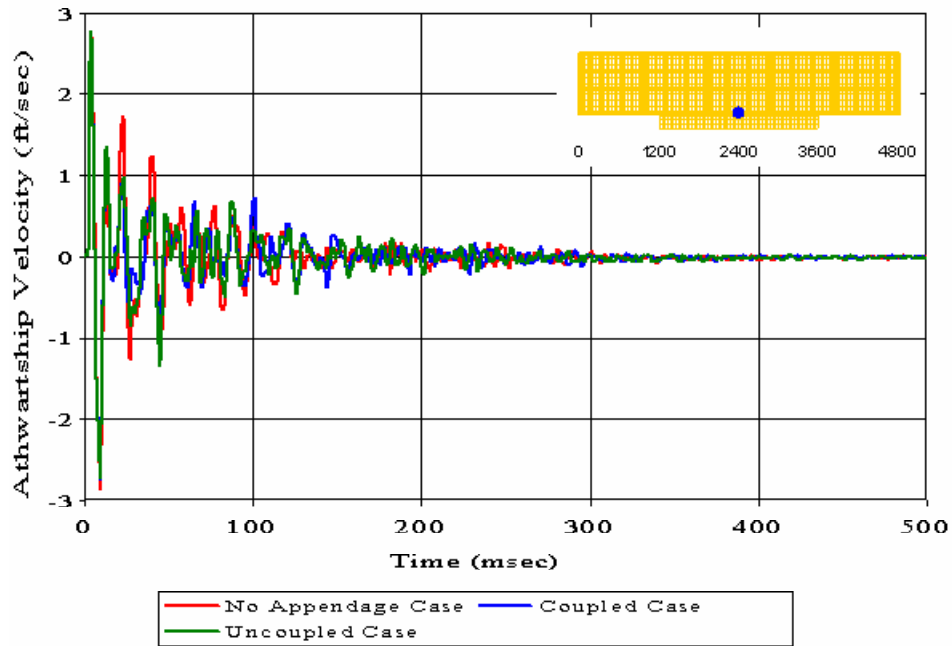
Figure 338.   Keel Node 5308: (RM = 0.0378, RP = 0.1310, RC = 0.1208)
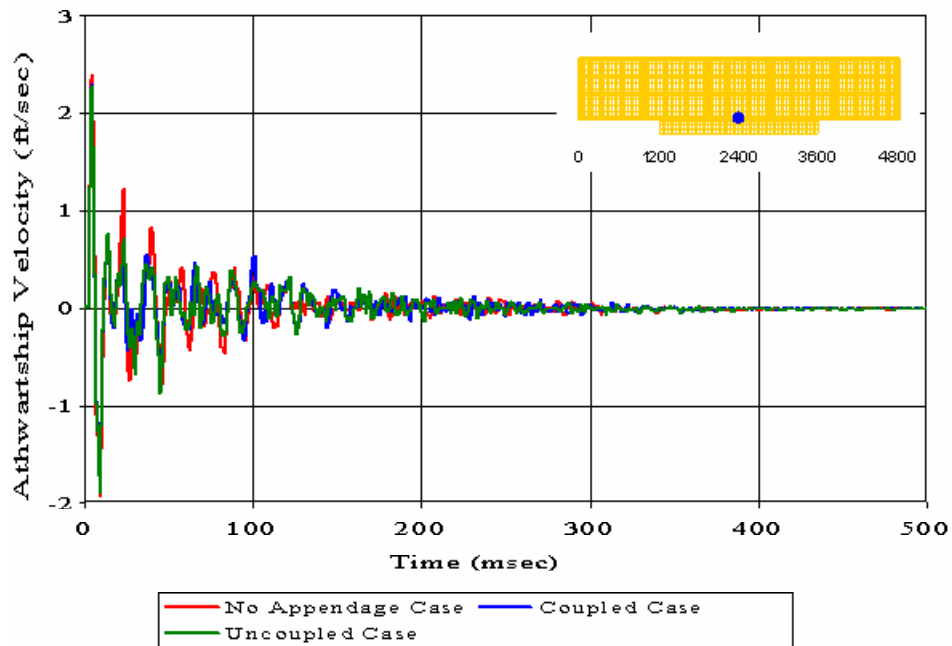
Figure 339.   Keel Node 5310: (RM = 0.0325, RP = 0.1243, RC = 0.1138)

294

Meko–Like Box Model with Shell Keel Board

Node 5312 at Keel (x=2400 y=-20 z=0)
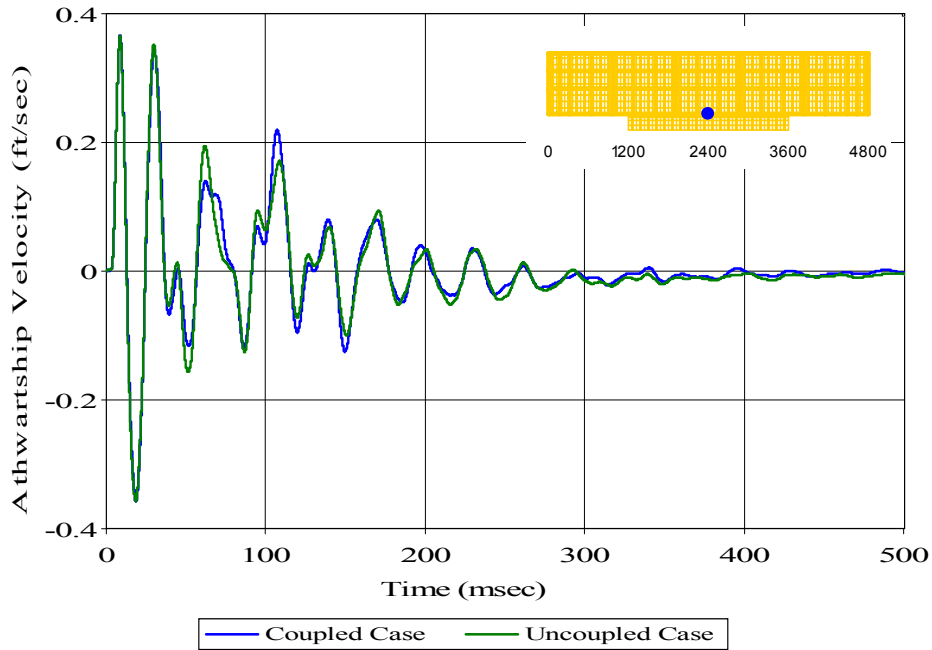
Figure 340.   Keel Node 5312: (RM = 0.0006, RP = 0.0601, RC = 0.0533)

Meko-Like Box Model with Shell Keel Board

Node 5315 at Keel (x=2400 y=100 z=0)
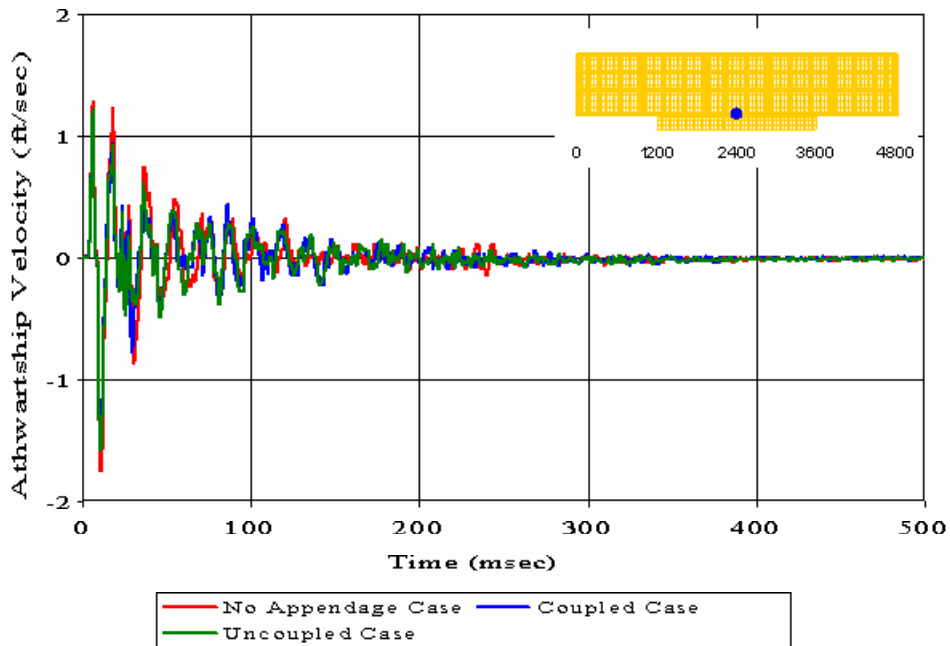
Figure 341.   Keel Node 5315: (RM = 0.0272, RP = 0.1255, RC = 0.1138)
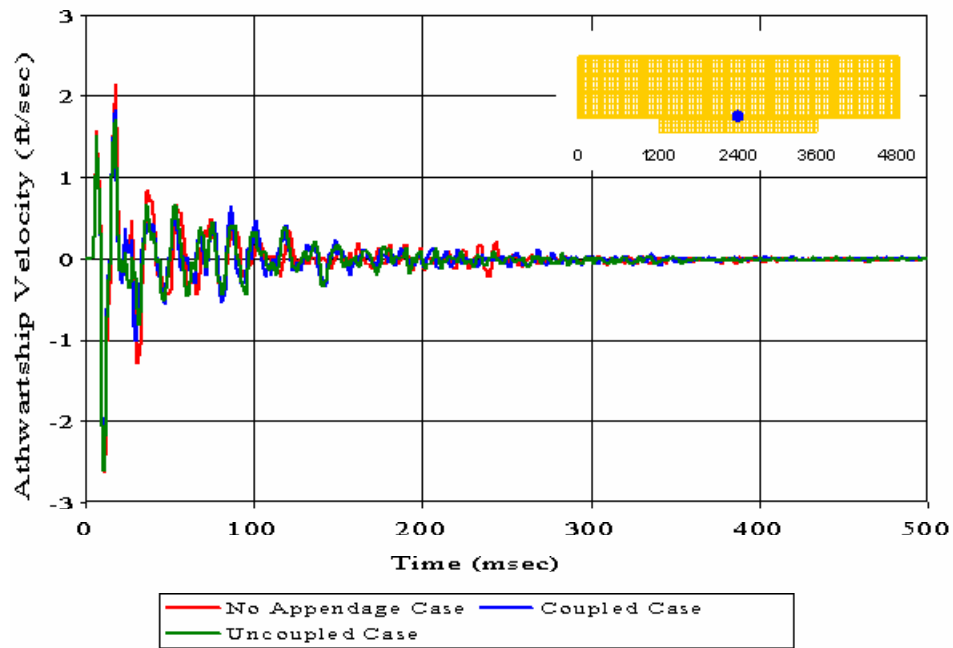
Figure 342. Keel Node 5317: (RM = 0.0094, RP = 0.1230, RC = 0.1093)
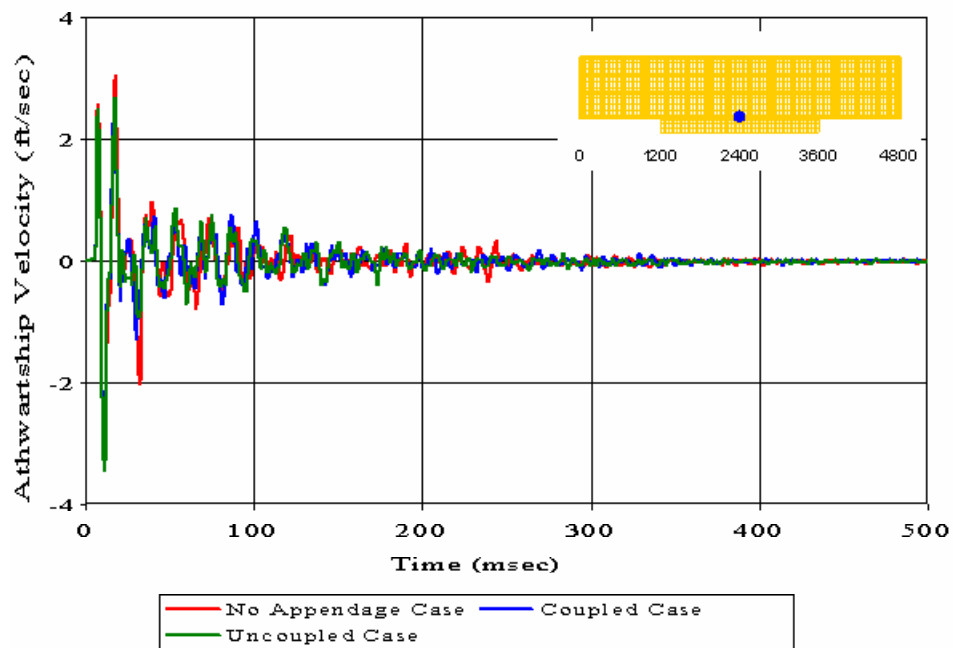
Figure 343. Keel Node 5320: (RM = 0.0065, RP = 0.1302, RC = 0.1156)

Meko–Like Box Model with Shell Keel Board
Node 6741 at Keel (x=3000 y=-20 z=0)
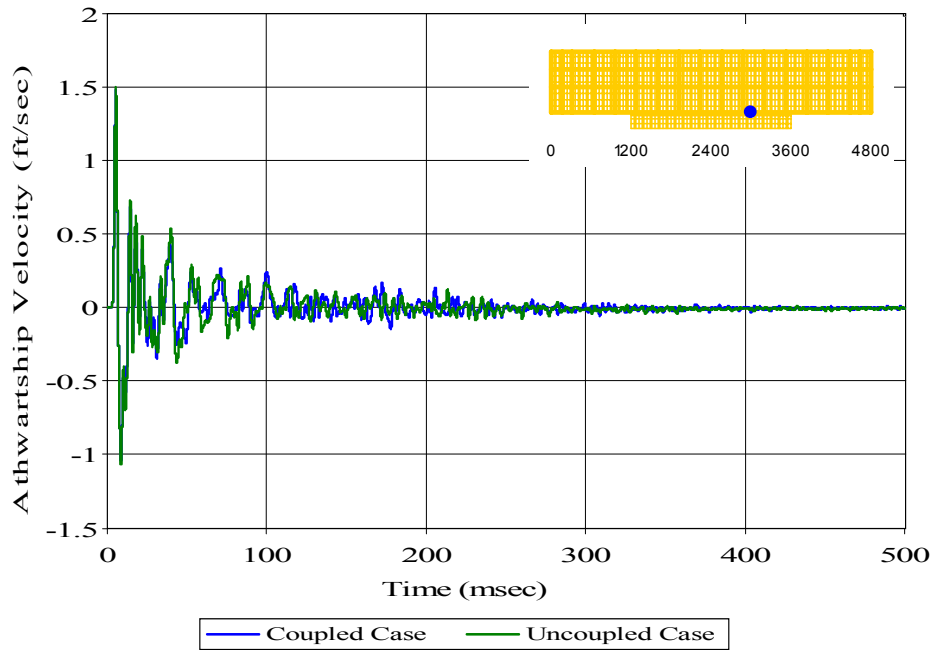
Figure 344.   Keel Node 6741: (RM = 0.0594, RP = 0.1314, RC = 0.1278)

Meko–Like Box Model with Shell Keel Board
Node 8170 at Keel (x=3600 y=-20 z=0)
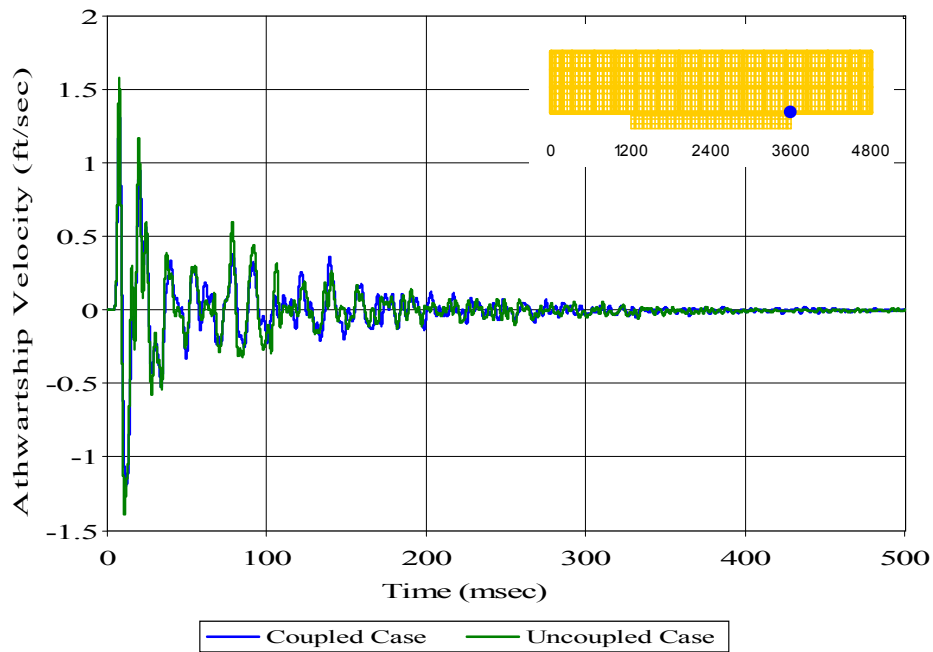
Figure 345.   Keel Node 8170: (RM = 0.0770, RP = 0.1372, RC = 0.1395)

Meko-Like Box Model with Shell Keel Board

Node 8364 at First Deck (x=3600 y=-20 z=160)
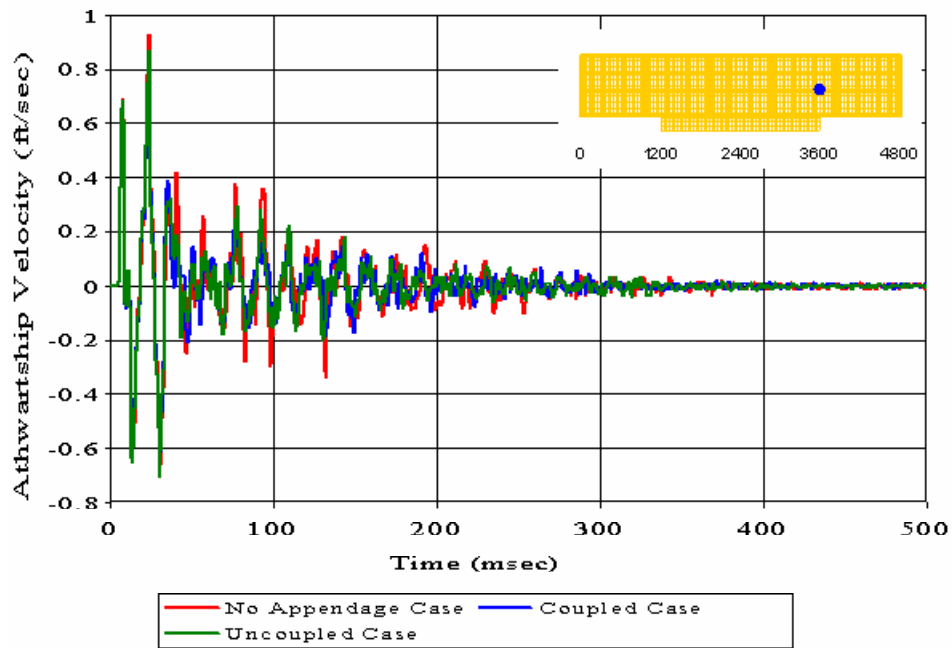
Figure 346. First Deck Node 8364: (RM = 0.0317, RP = 0.1279, RC = 0.1167)

Meko-Like Box Model with Shell Keel Board

Node 8536 at Second Deck (x=3600 y=-20 z=280)
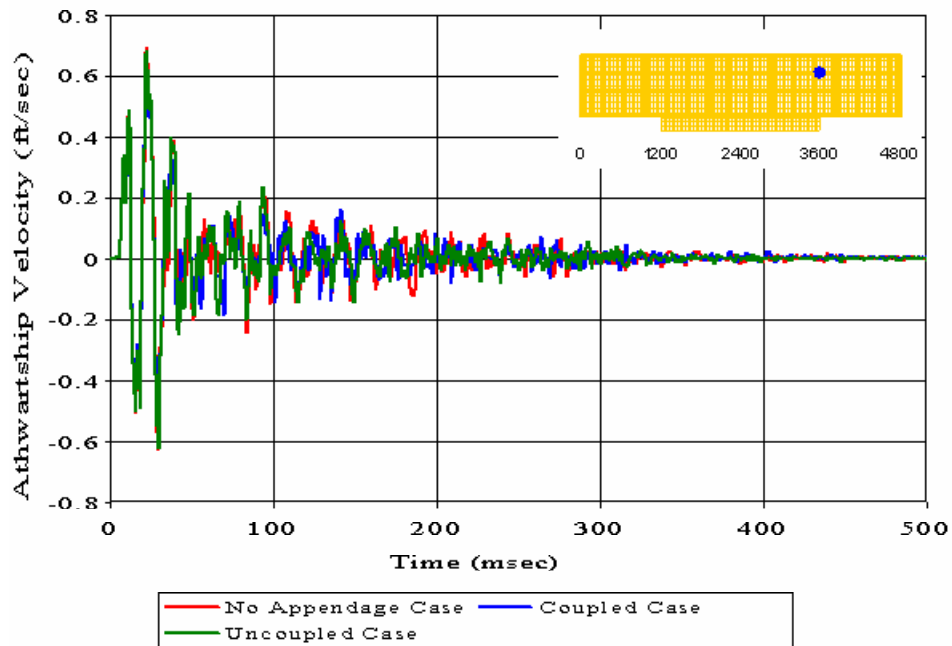
Figure 347. Second Deck Node 8536: (RM = 0.0553, RP = 0.1201, RC = 0.1171)
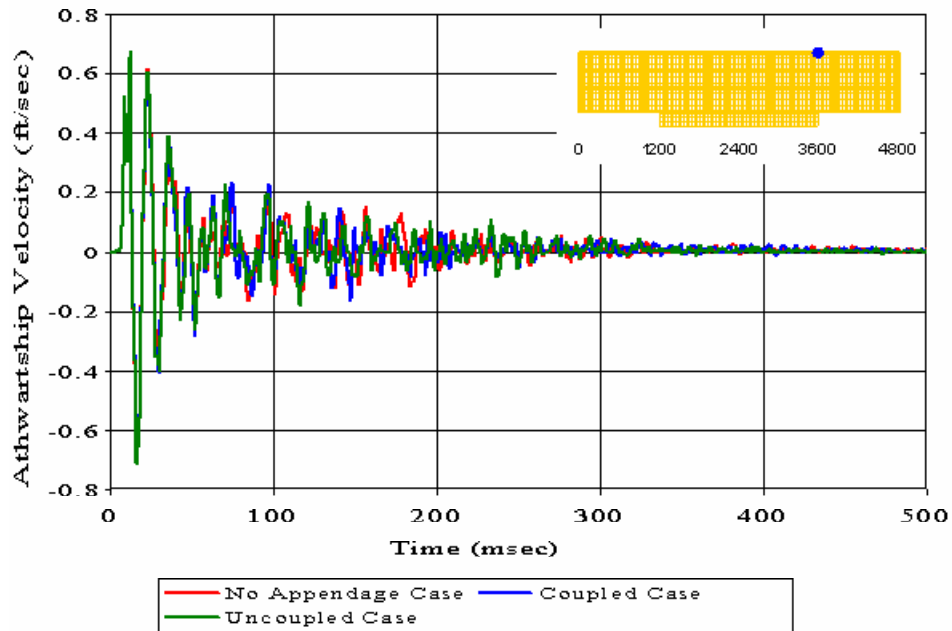
Figure 348. **Top Deck Node 8686: (RM = 0.0301, RP = 0.1180, RC = 0.1079)**

C.   **MEKO-LIKE BOX MODEL WITH OPEN KEEL BOARD**
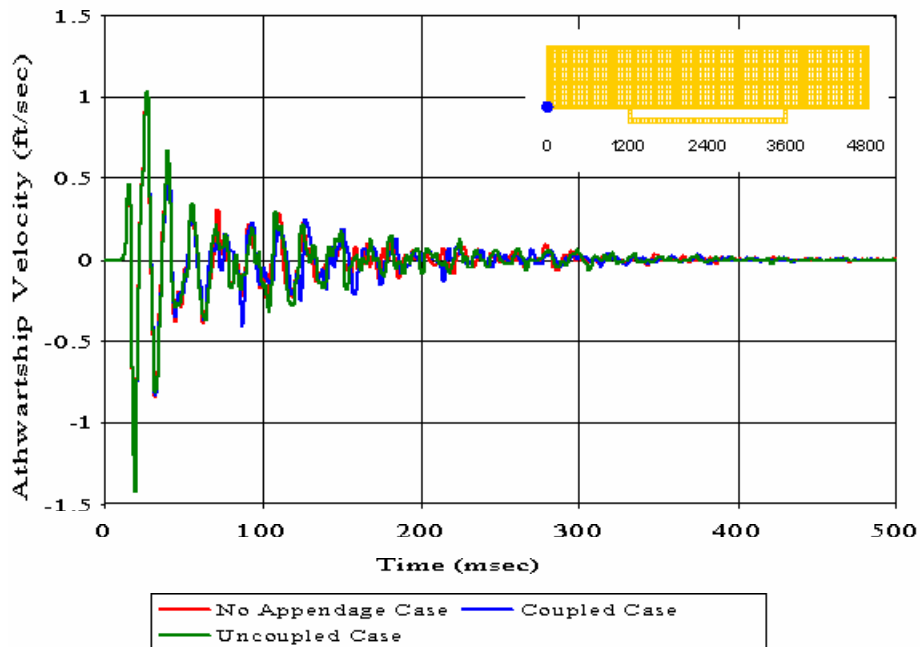
Figure 349. **Bulkhead Node 15: (RM = 0.0122, RP = 0.1331, RC = 0.1185)**

Meko-Like Box Model with Open Keel Board

Node 148 at Bulkhead (x=0 y=-20 z=160)
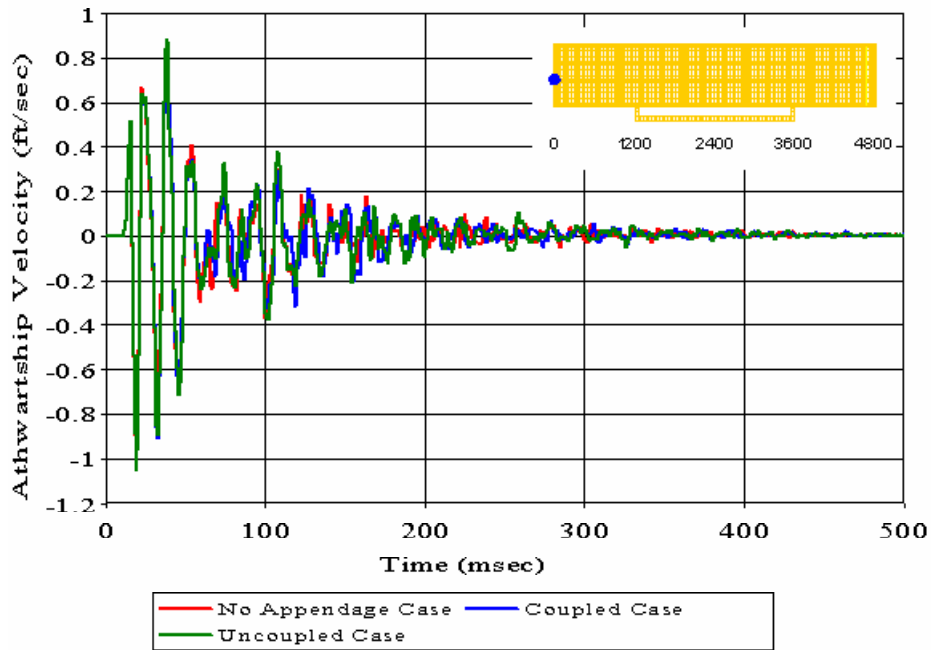
Figure 350.   Bulkhead Node 148: (RM = 0.0171, RP = 0.0987, RC = 0.0887)

Meko-Like Box Model with Open Keel Board

Node 268 at Bulkhead (x=0 y=-20 z=280)
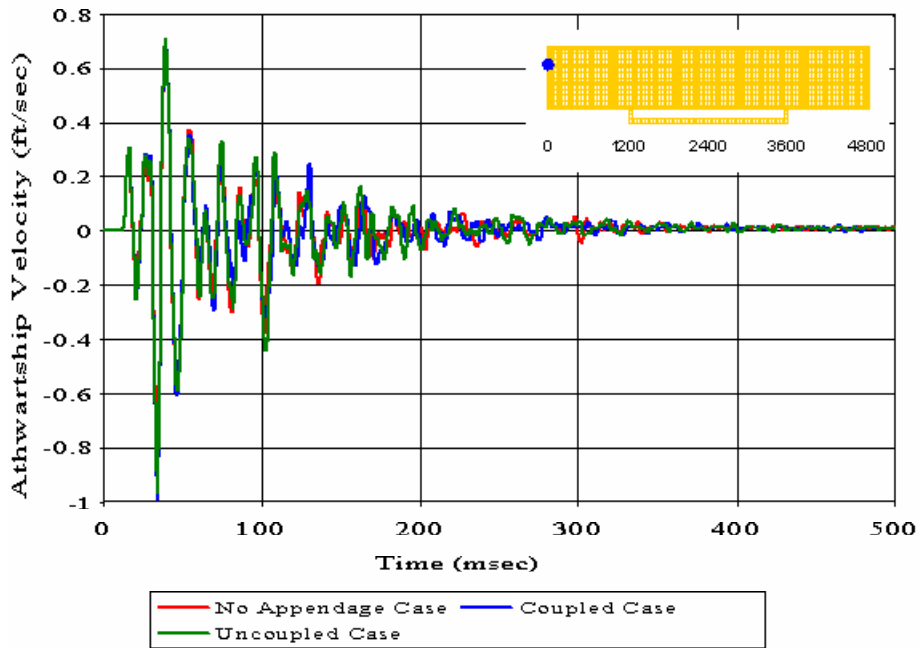
Figure 351.   Bulkhead Node 268: (RM = 0.0239, RP = 0.1085, RC = 0.0985)

300
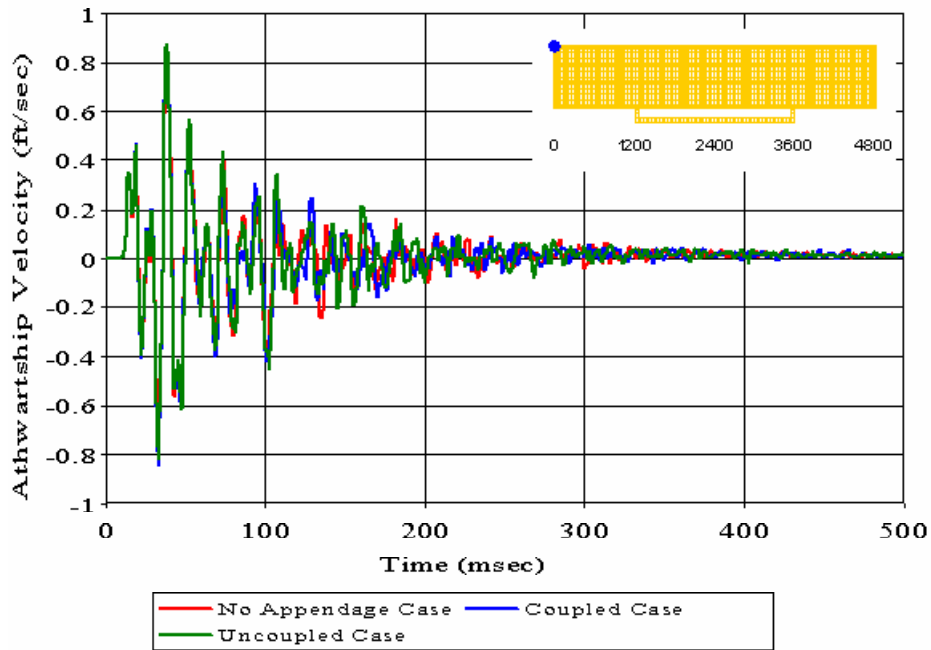
Figure 352.   **Bulkhead Node 388: (RM = 0.0235, RP = 0.1159, RC = 0.1049)**
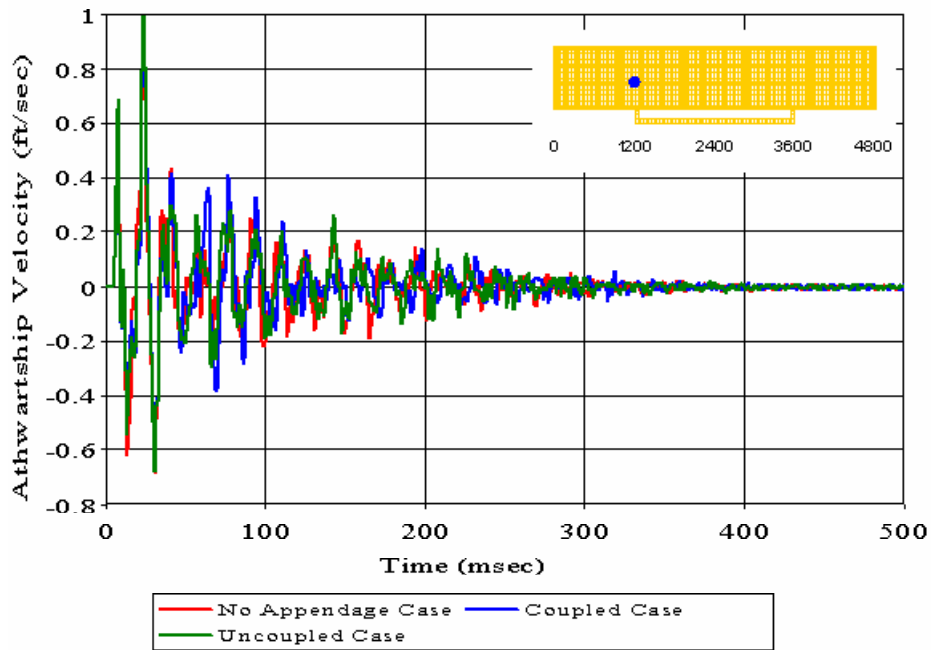
Figure 353.   **First Deck Node 2648: (RM = 0.0013, RP = 0.1857, RC = 0.1646)**
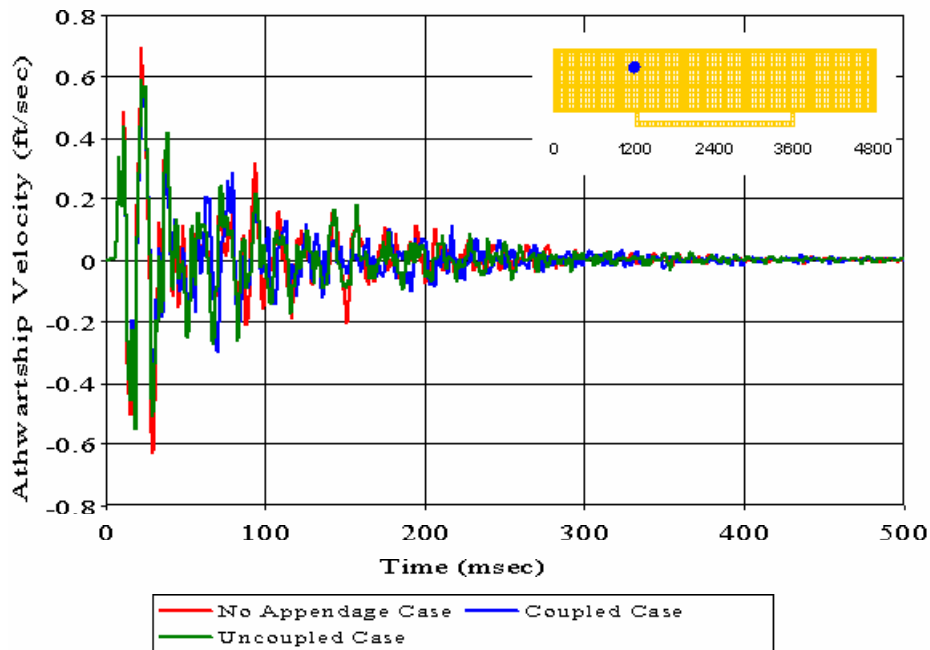
Figure 354.   Second Deck Node 2820: (RM = 0.0331, RP = 0.1758, RC = 0.1585)
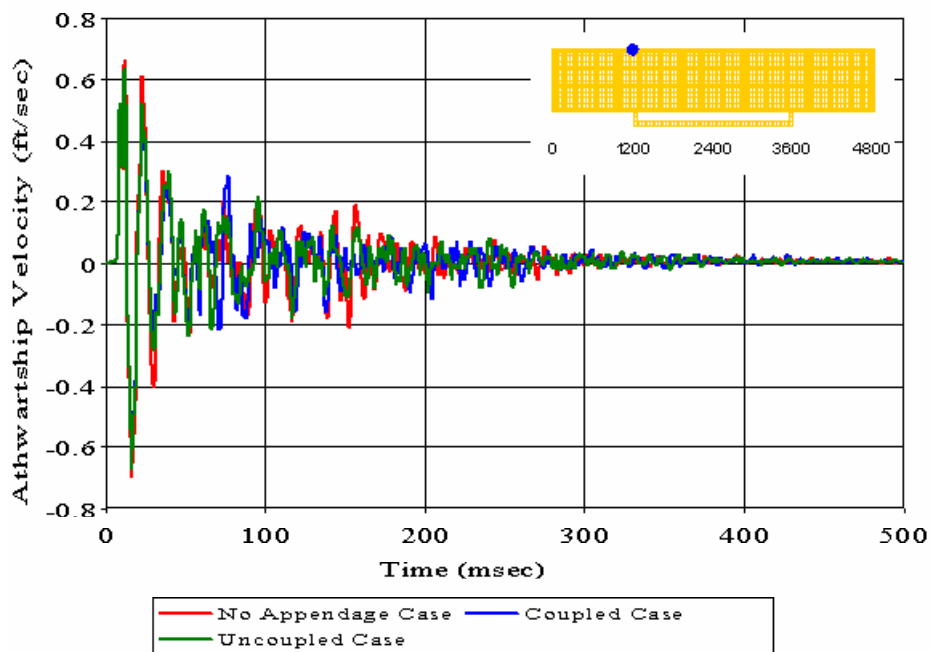
Figure 355.   Top Deck Node 2970: (RM = 0.0263, RP = 0.1768, RC = 0.1584)
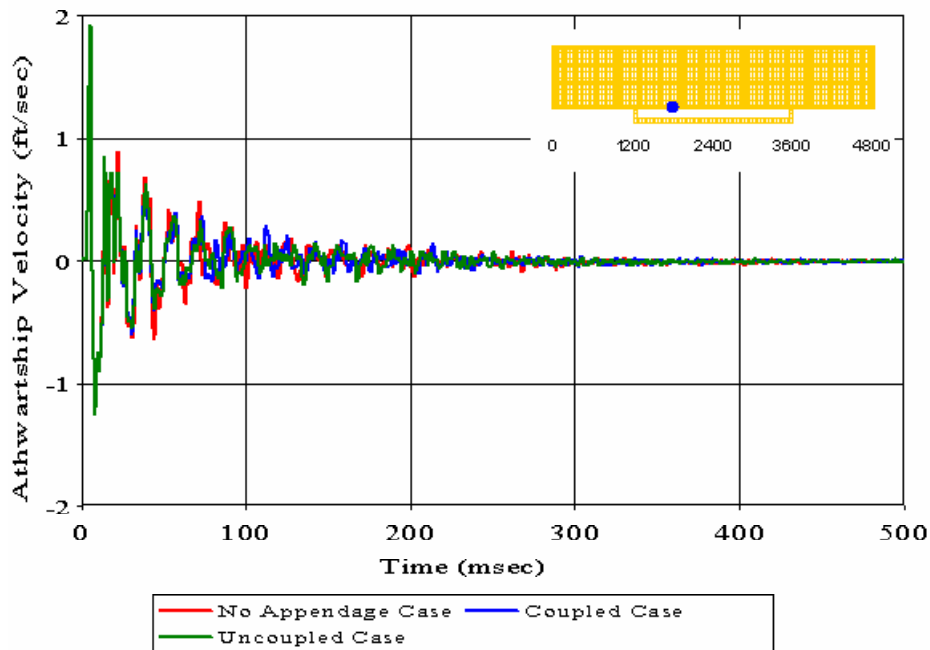
Figure 356. Keel Node 3883: (RM = 0.0094, RP = 0.1034, RC = 0.0920)
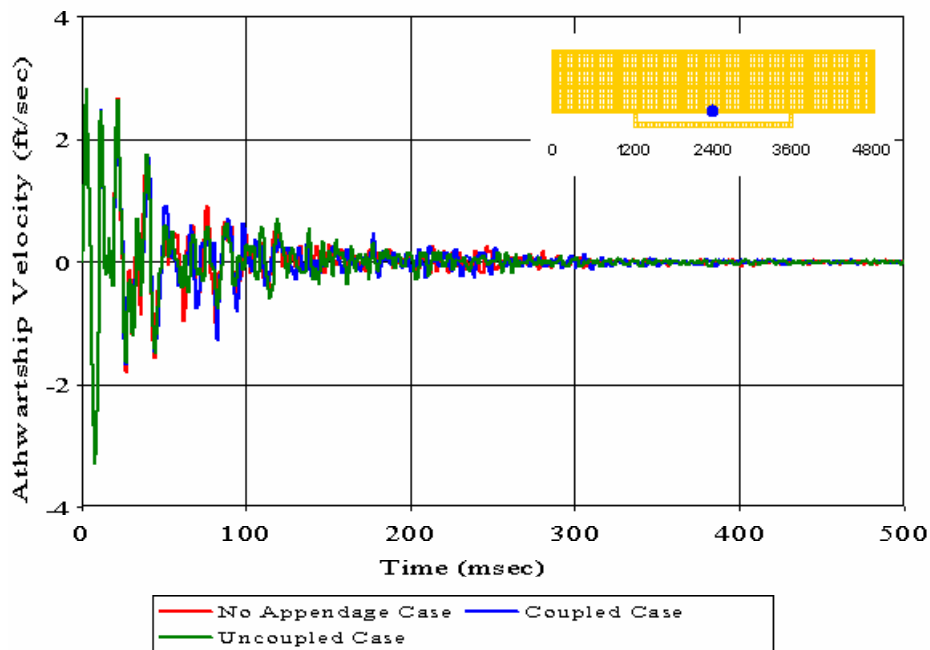
Figure 357. Keel Node 5251: (RM = -0.0059, RP = 0.1292, RC = 0.1146)

303

Meko-Like Box Model with Open Keel Board

Node 5308 at Keel (x=2400 y=-180 z=0)
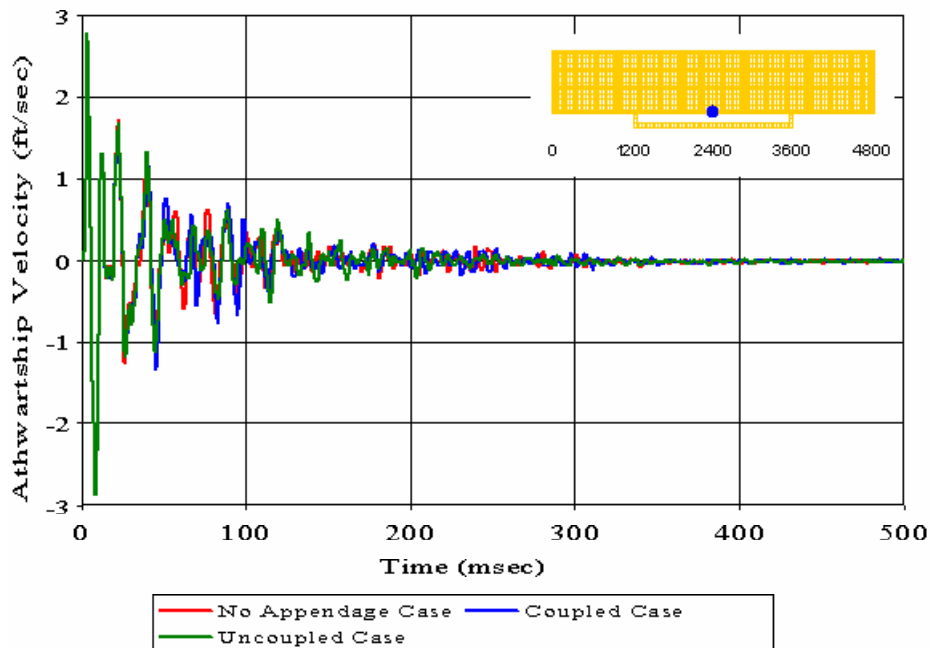
Figure 358. Keel Node 5308: (RM = -0.0138, RP = 0.1130, RC = 0.1009)

Meko-Like Box Model with Open Keel Board

Node 5310 at Keel (x=2400 y=-100 z=0)
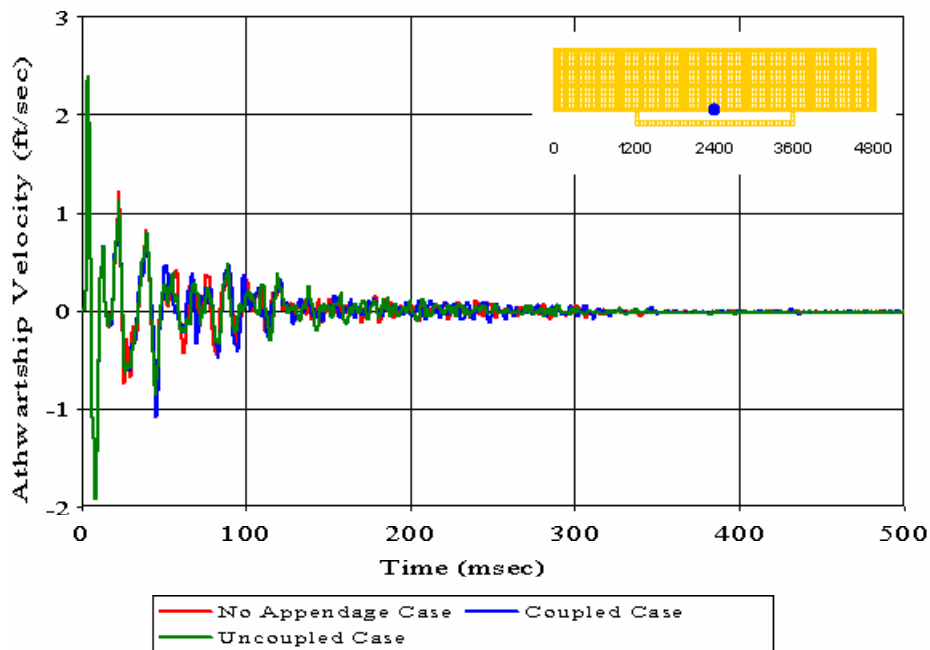
Figure 359. Keel Node 5310: (RM = -0.0163, RP = 0.1127, RC = 0.1009)

304
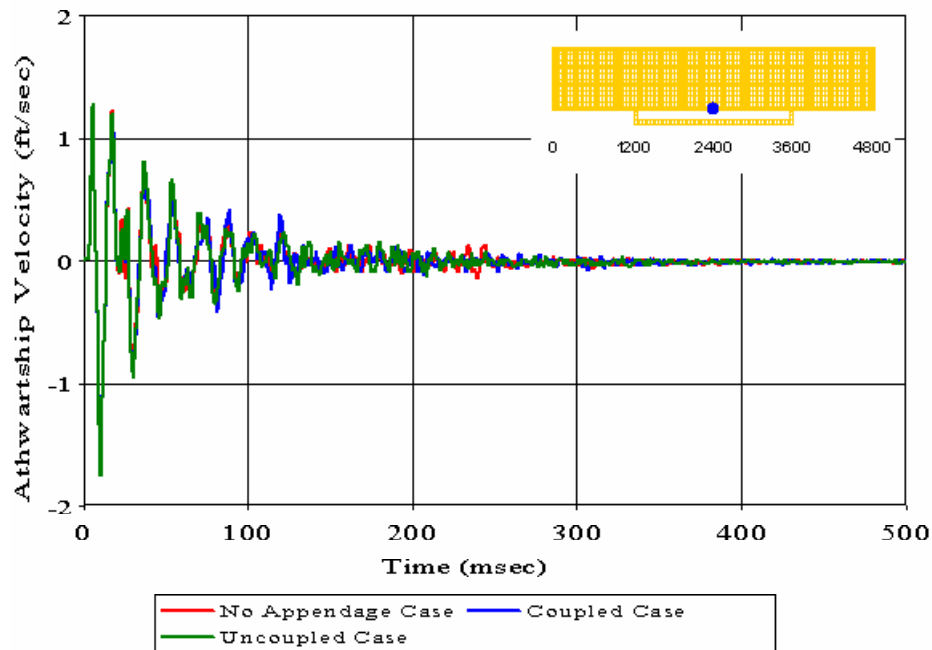
Figure 360. Keel Node 5315: (RM = 0.0112, RP = 0.1018, RC = 0.0908)
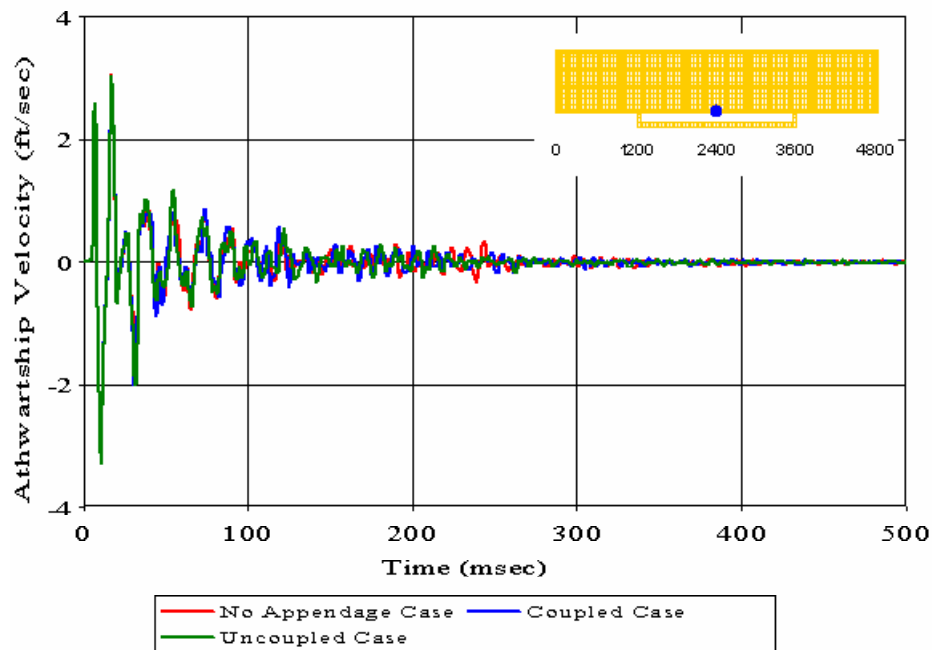
Figure 361. Keel Node 5320: (RM = 0.0077, RP = 0.1077, RC = 0.0957)
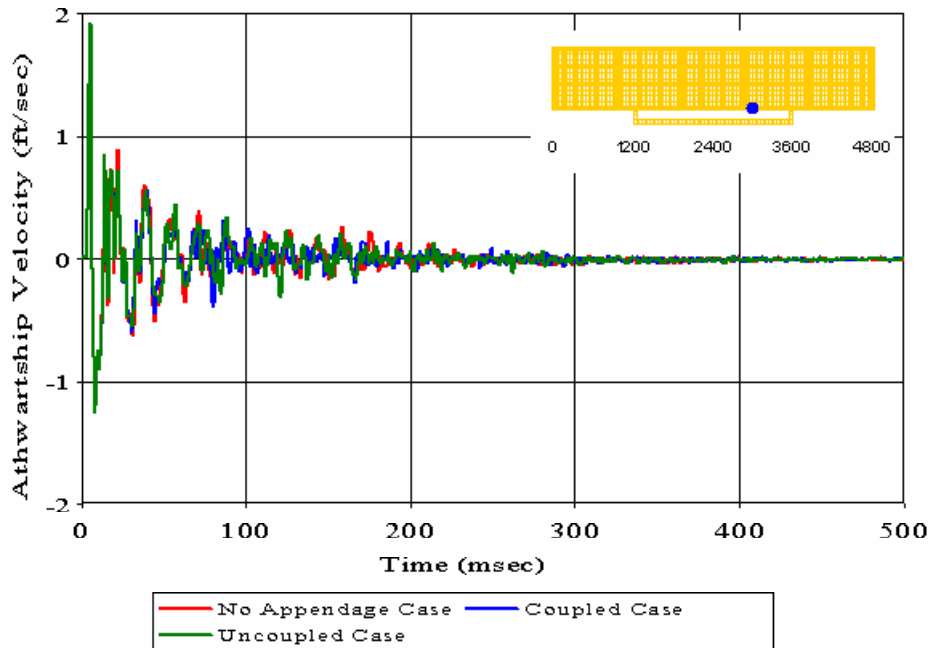
Figure 362.   **Keel Node 6741: (RM = 0.0179, RP = 0.1259, RC = 0.1127)**
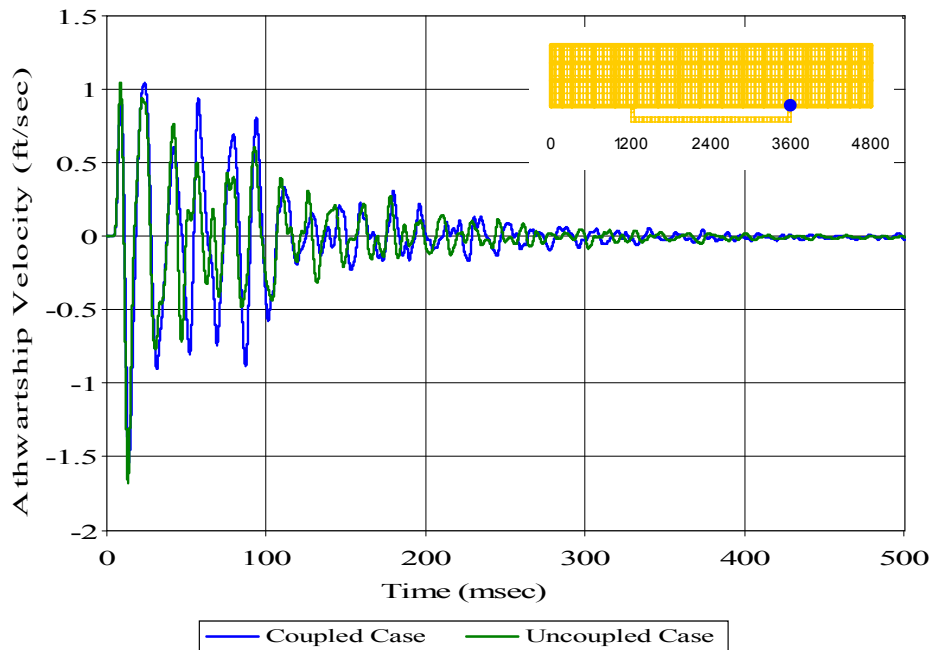
Figure 363.   **Keel Node 8170: (RM = -0.1034, RP = 0.2059, RC = 0.2042)**
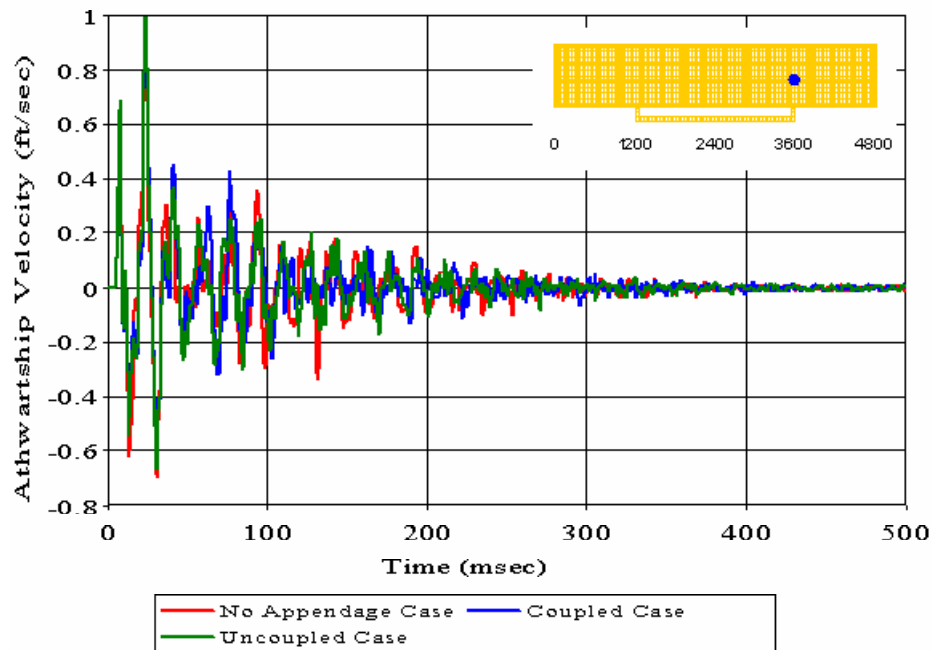
Figure 364.   **First Deck Node 8364: (RM = 0.0128, RP = 0.1788, RC = 0.1588)**
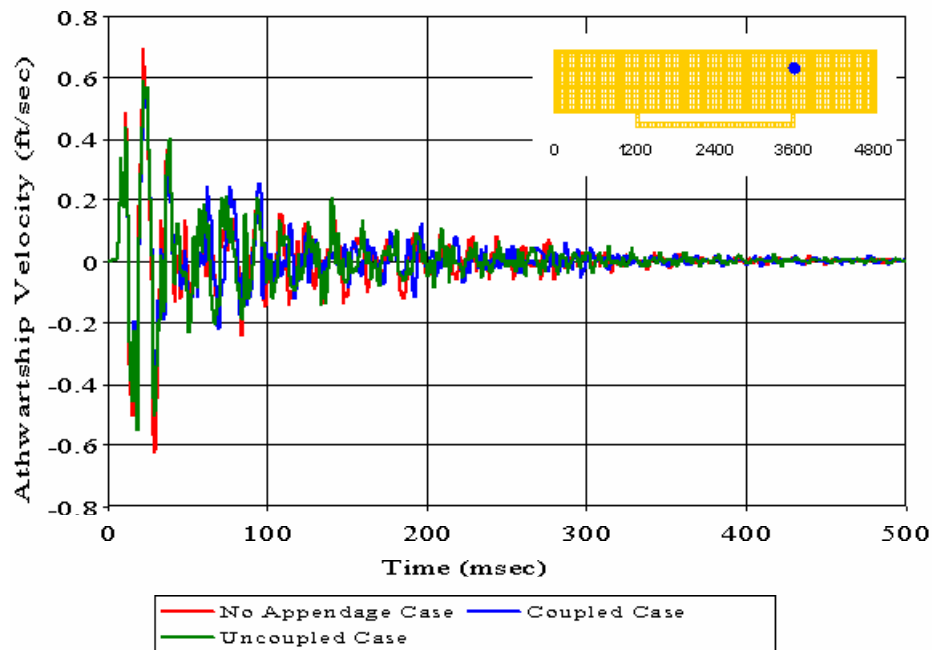
Figure 365.   **Second Deck Node 8536: (RM = 0.0446, RP = 0.1767, RC = 0.1615)**
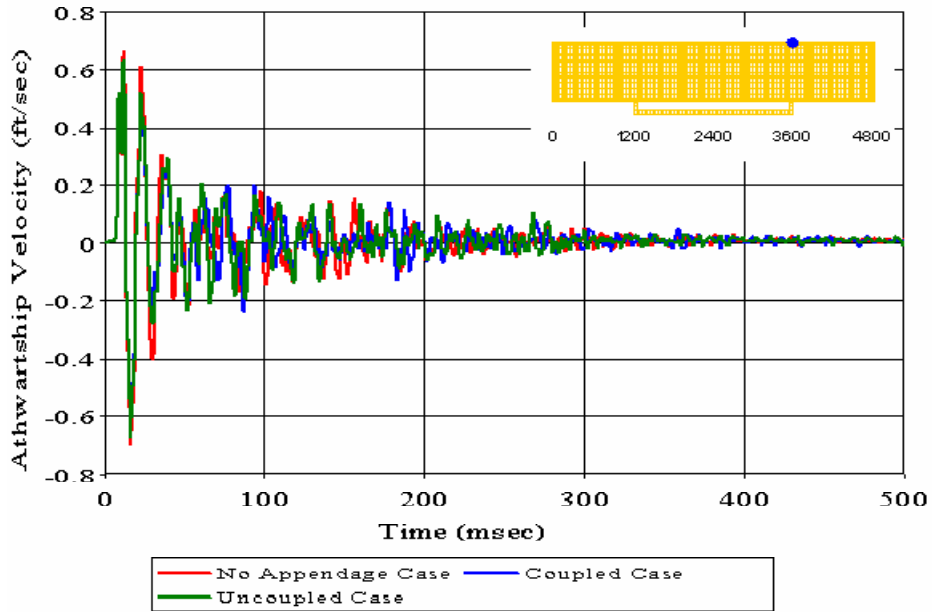
Figure 366.   Top Deck Node 8686: (RM = 0.0345, RP = 0.1565, RC = 0.1420)

D.   MEKO-LIKE BOX MODEL WITH RUDDERS
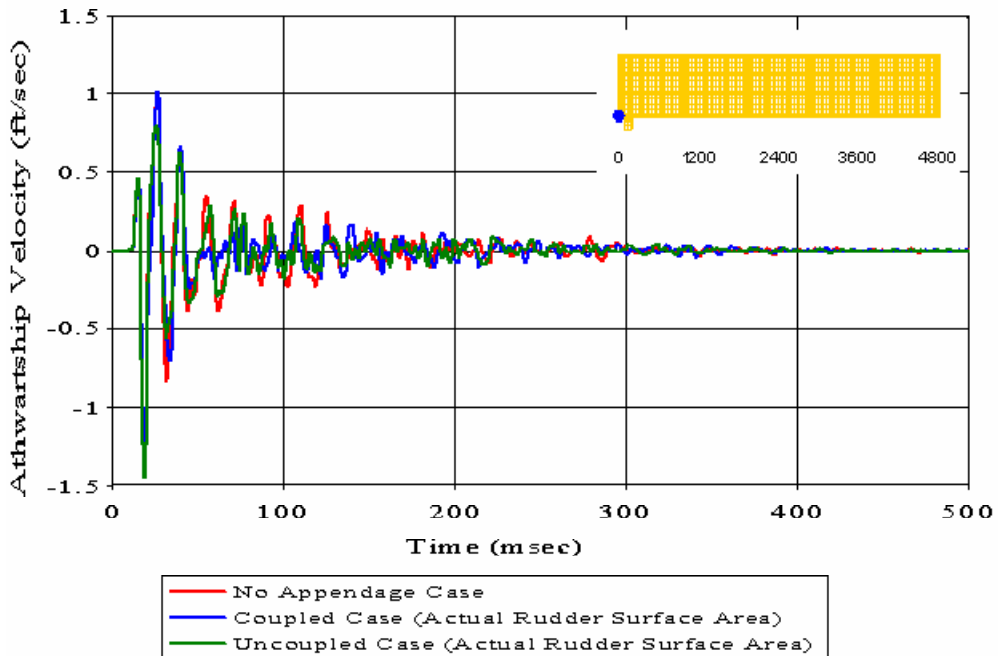
Figure 367.   Bulkhead Node 15: (RM = 0.0289, RP = 0.1686, RC = 0.1516)

308
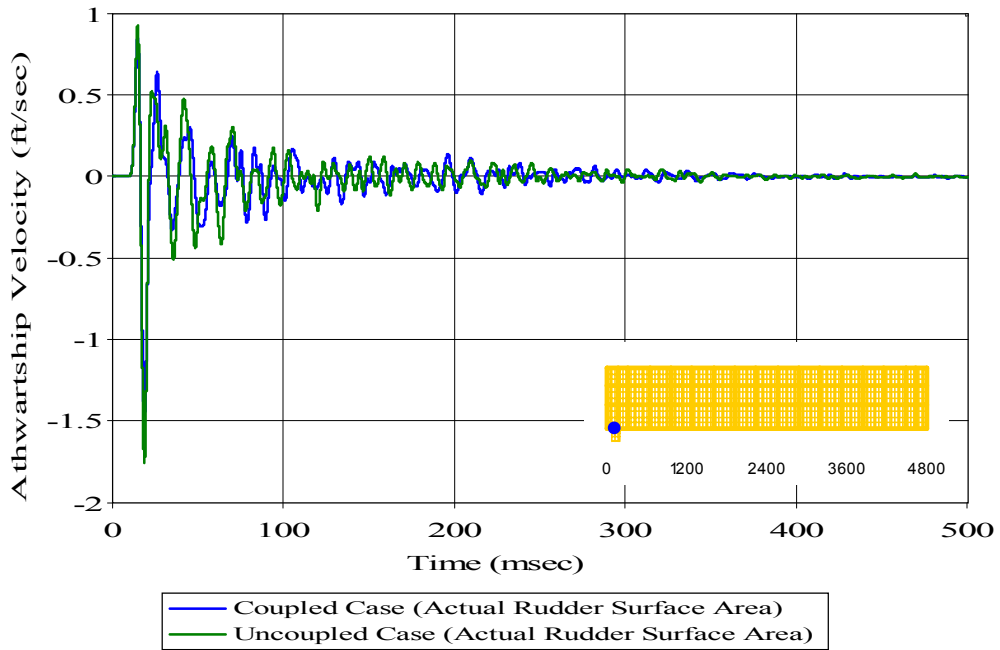
Figure 368. Keel Node 74: (RM = 0.1185, RP = 0.1745, RC = 0.1869)
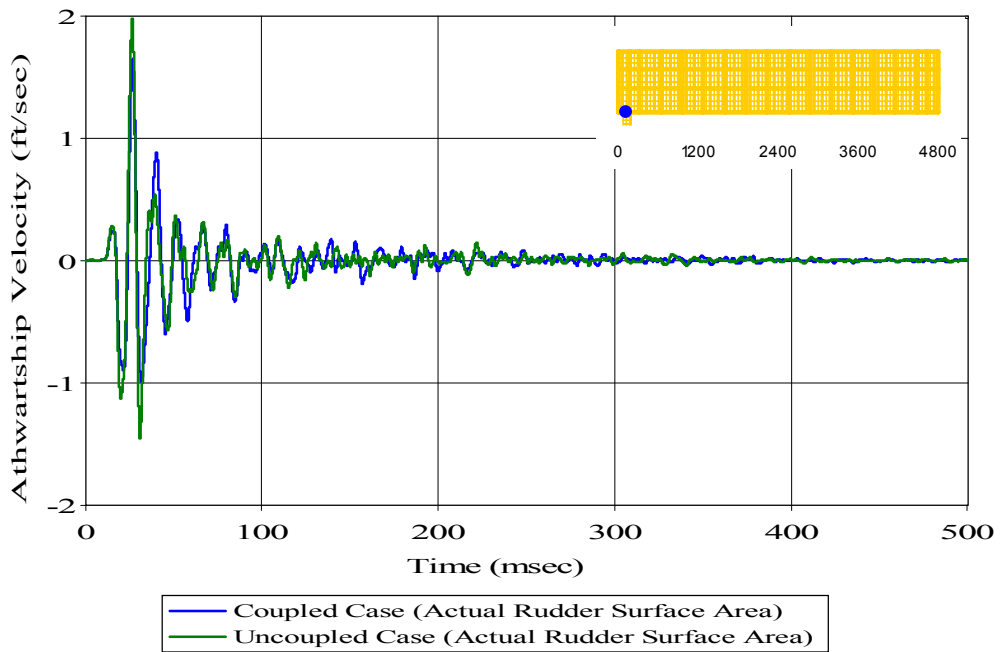
Figure 369. Keel Node 81: (RM = 0.0694, RP = 0.1515, RC = 0.1477)
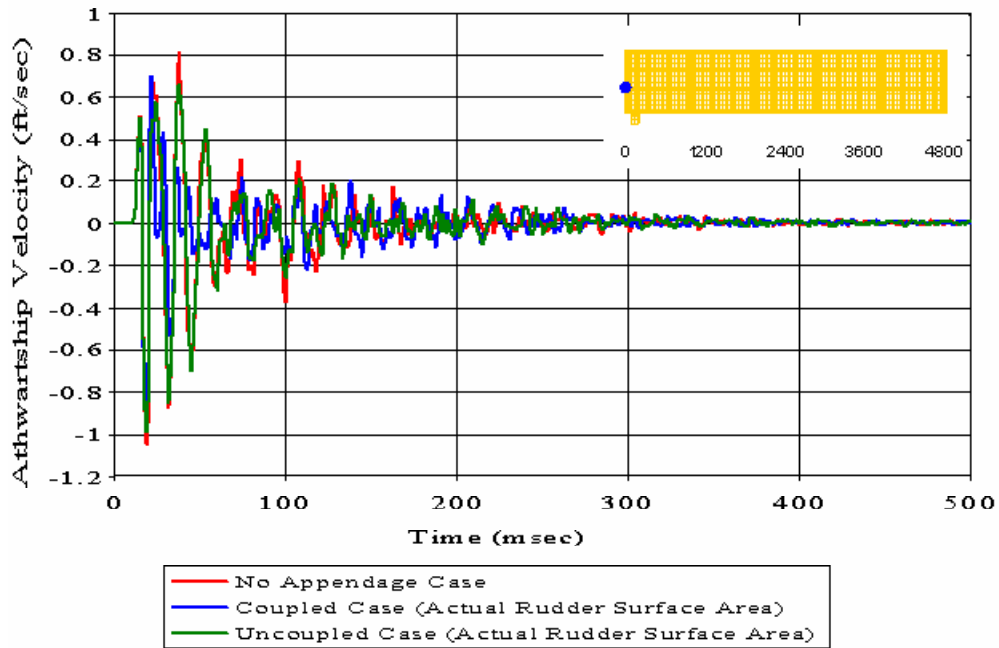
Figure 370.   Bulkhead Node 148: (RM = 0.2422, RP = 0.2995, RC = 0.3413)
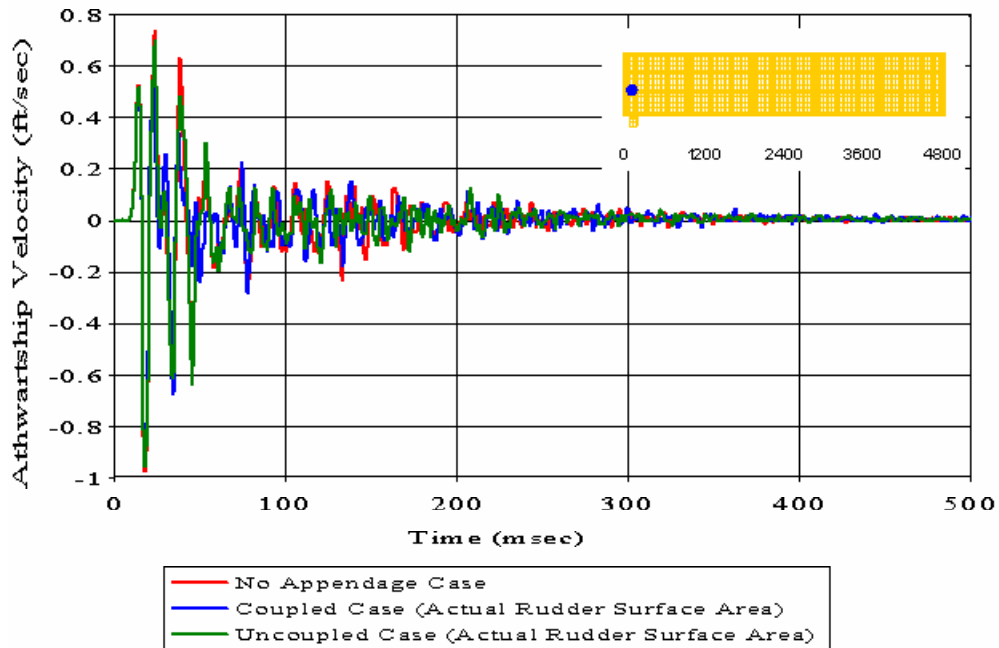
Figure 371.   First Deck Node 214: (RM = 0.1125, RP = 0.1965, RC = 0.2007)

310
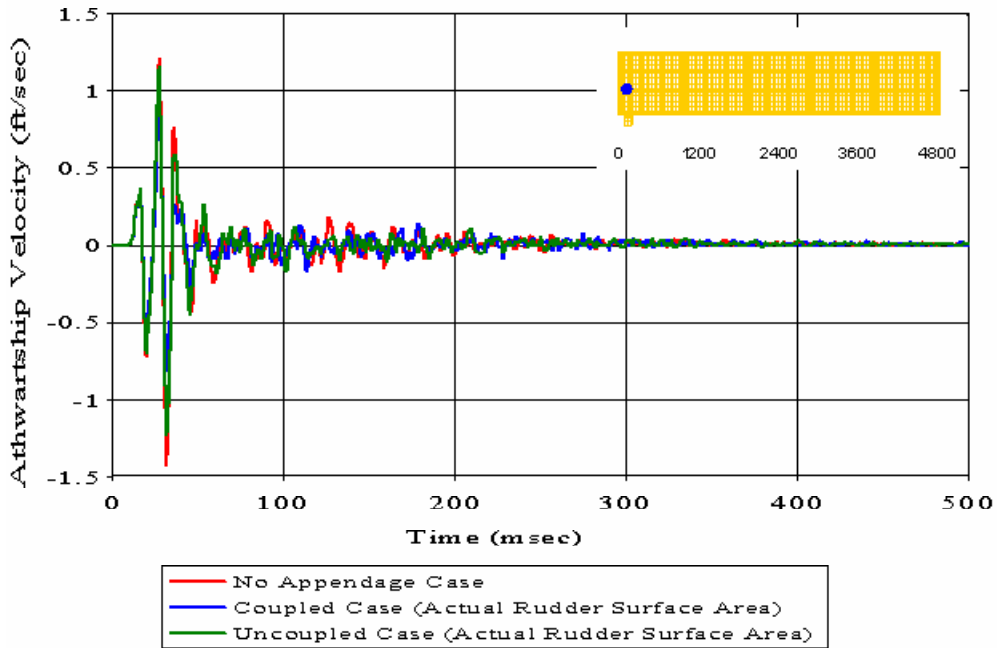
Figure 372.   First Deck Node 221: (RM = 0.2092, RP = 0.1237, RC = 0.2154)
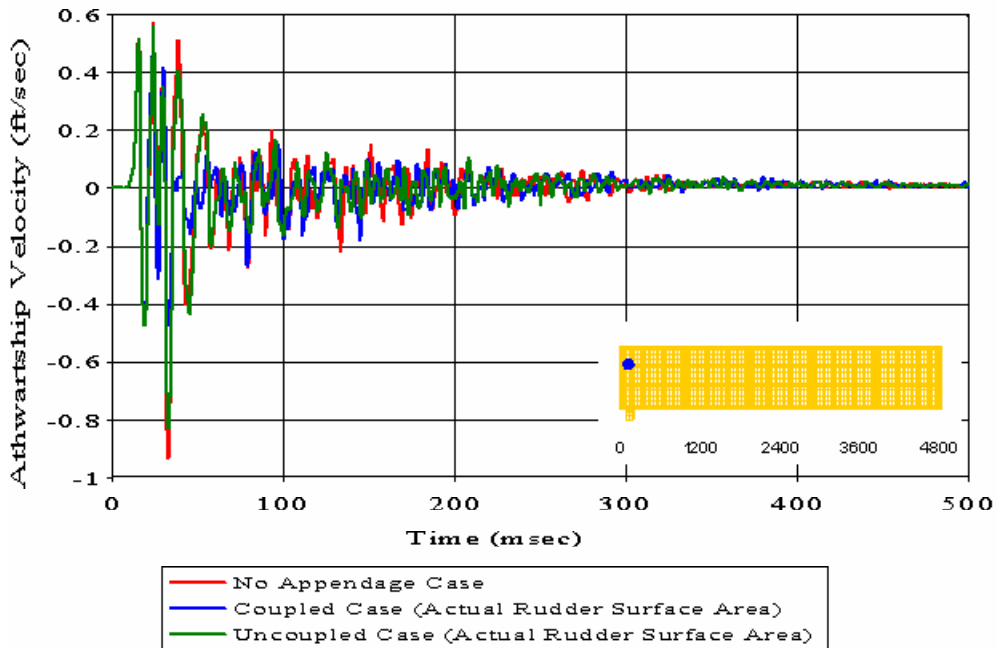
Figure 373.   Second Deck Node 334: (RM = 0.1926, RP = 0.2306, RC = 0.2663)

311
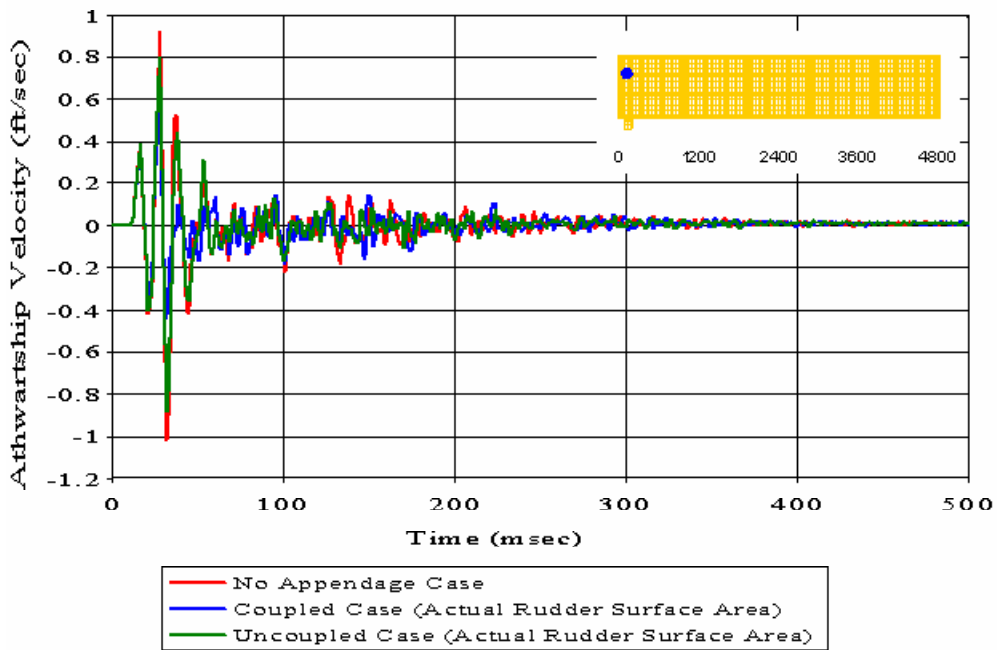
Figure 374. Second Deck Node 341: (RM = 0.2553, RP = 0.2037, RC = 0.2895)
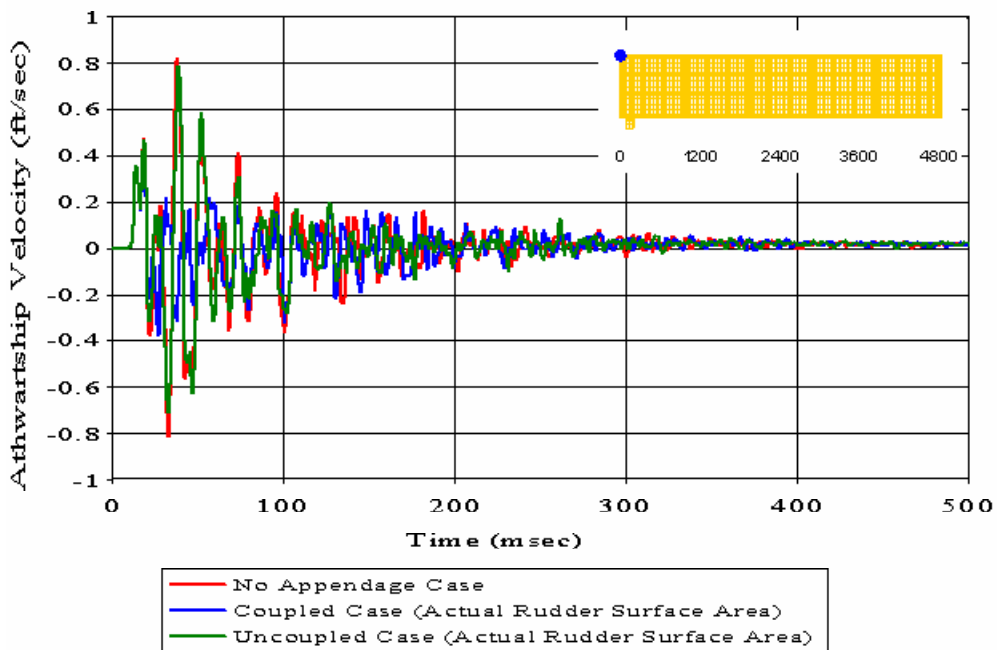
Figure 375. Bulkhead Node 388: (RM = 0.3025, RP = 0.4550, RC = 0.4843)
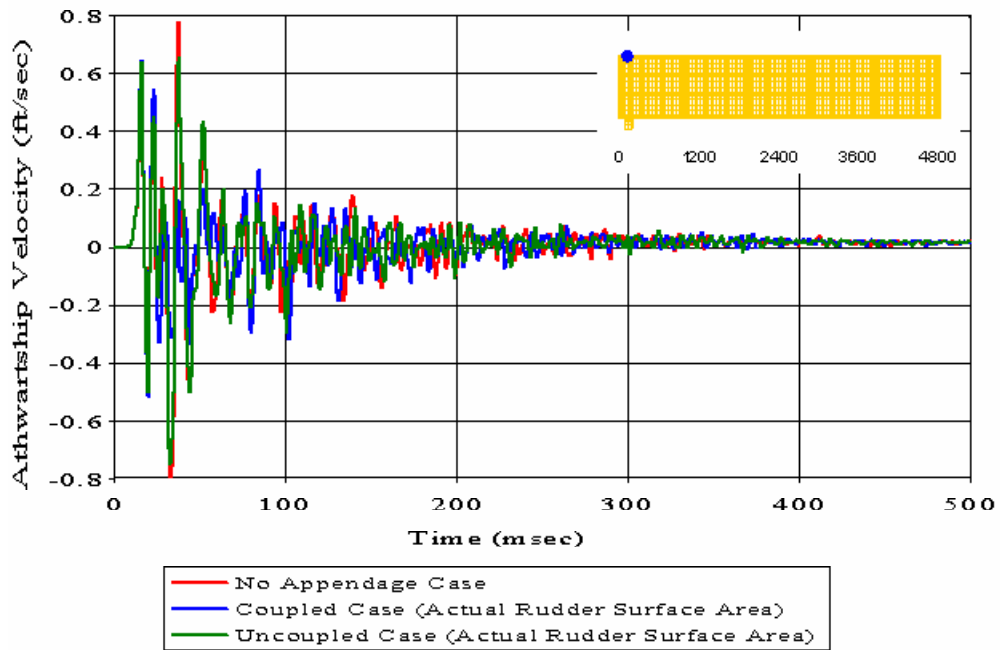
Figure 376. Top Deck Node 434: (RM = 0.1841, RP = 0.2603, RC = 0.2825)
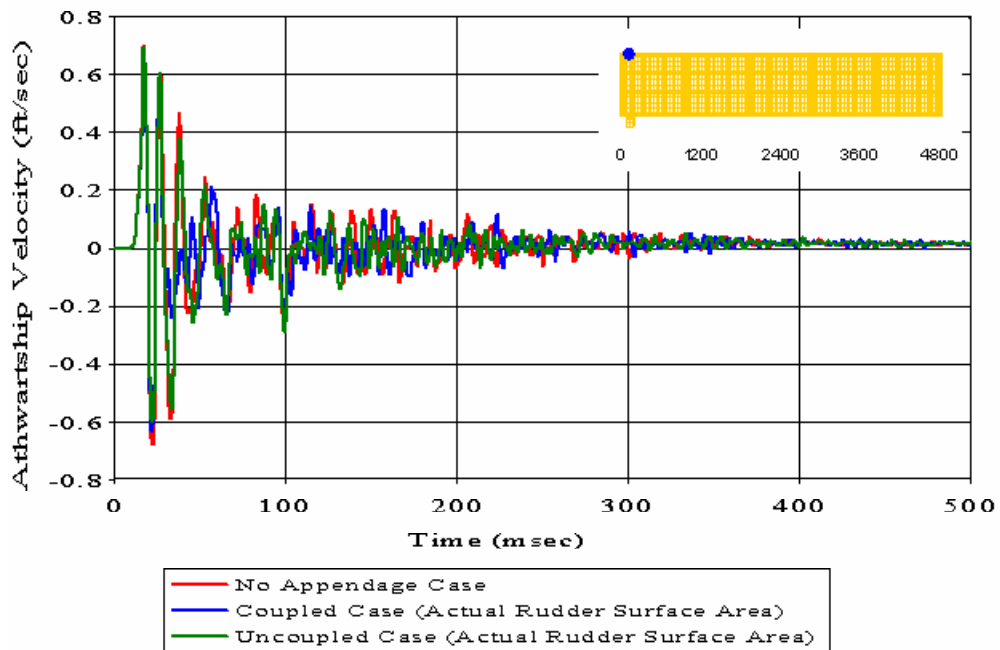
Figure 377. Top Deck Node 441: (RM = 0.1199, RP = 0.2298, RC = 0.2297)
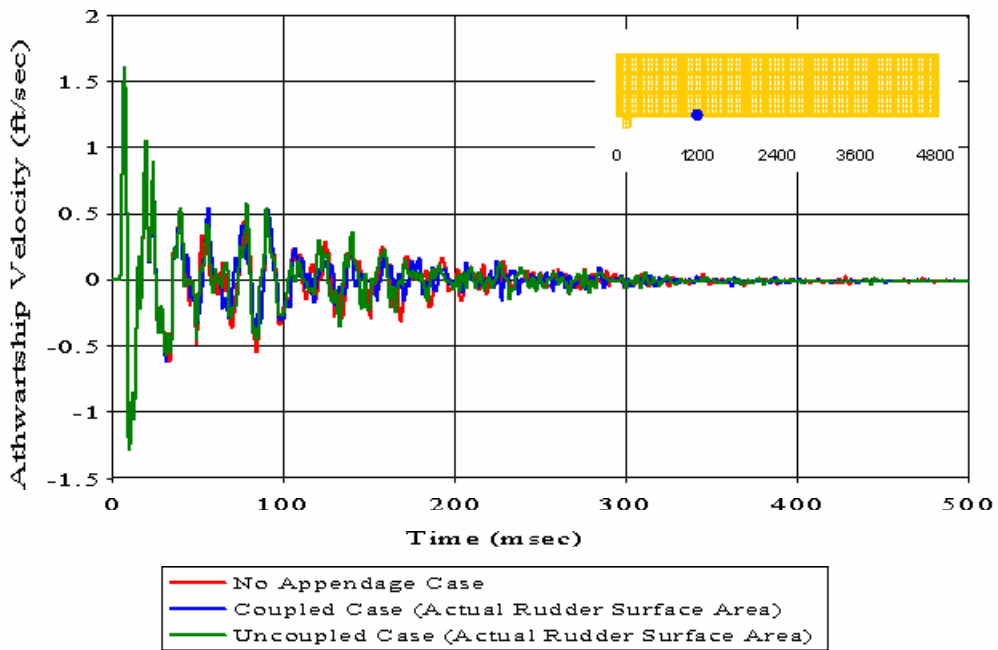
Figure 378. Keel Node 2454: (RM = 0.0153, RP = 0.1391, RC = 0.1240)
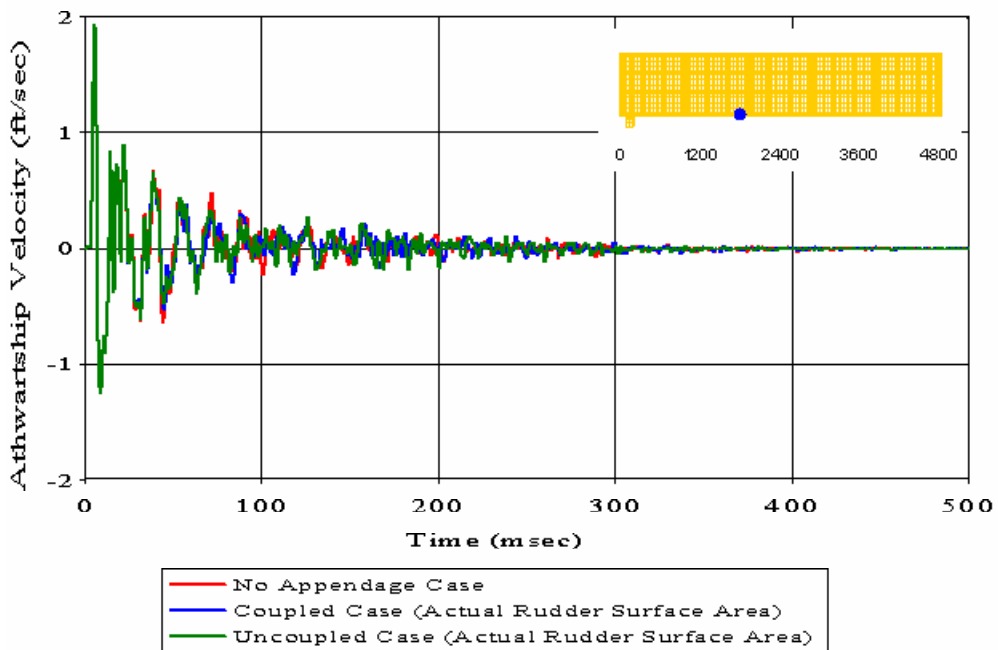
Figure 379. Keel Node 3883: (RM = 0.0160, RP = 0.1082, RC = 0.0969)

314
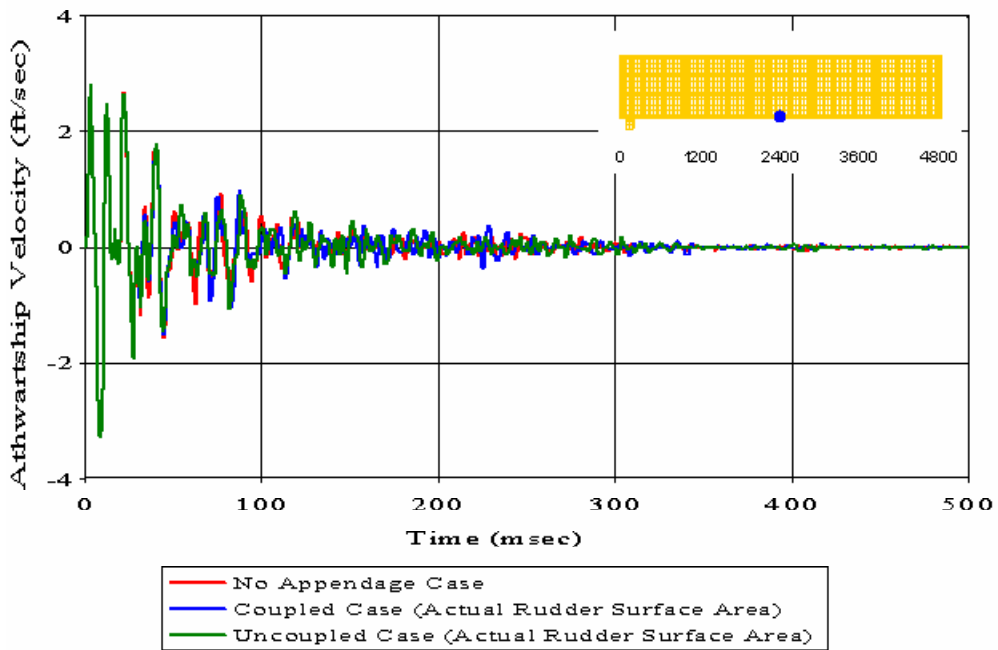
Figure 380. Keel Node 5251: (RM = -0.0020, RP = 0.1125, RC = 0.0997)
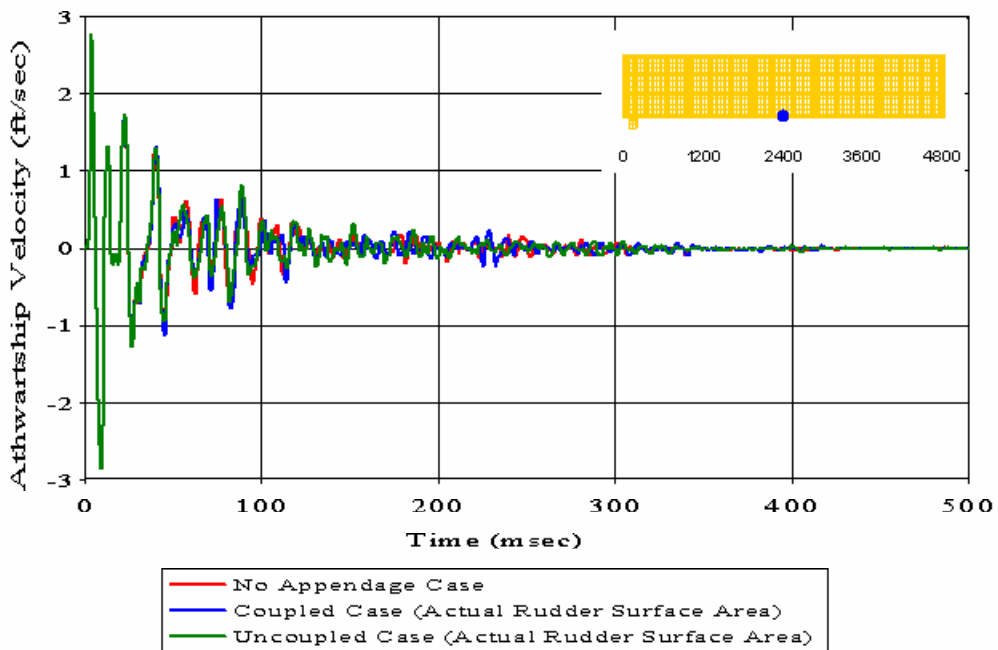
Figure 381. Keel Node 5308: (RM = -0.0031, RP = 0.0885, RC = 0.0785)
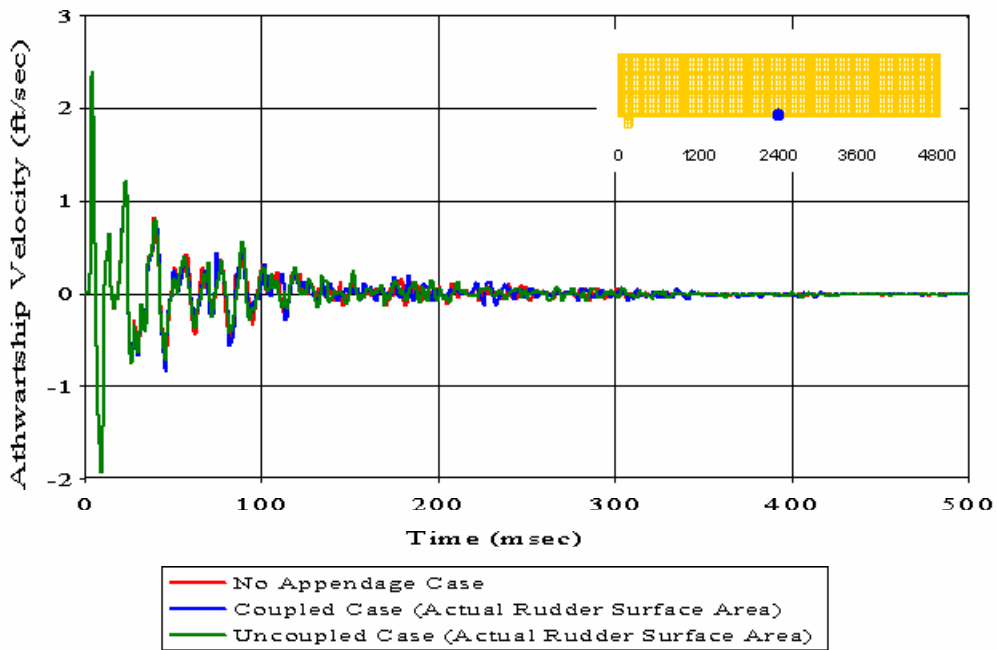
Figure 382. Keel Node 5310: (RM = -0.0019, RP = 0.0848, RC = 0.0752)
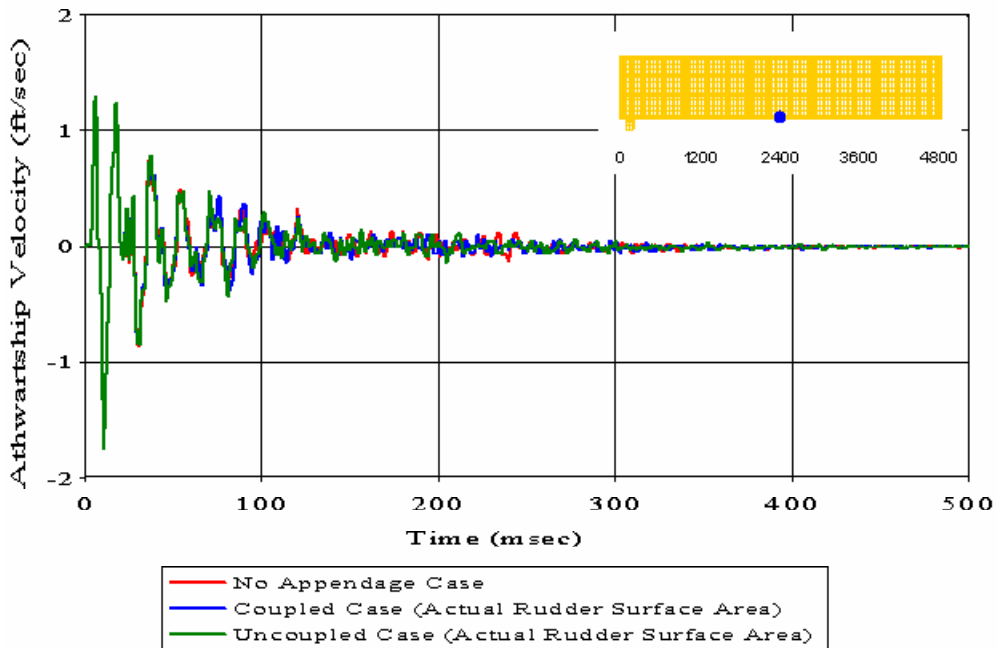
Figure 383. Keel Node 5315: (RM = 0.0014, RP = 0.0818, RC = 0.0725)

316
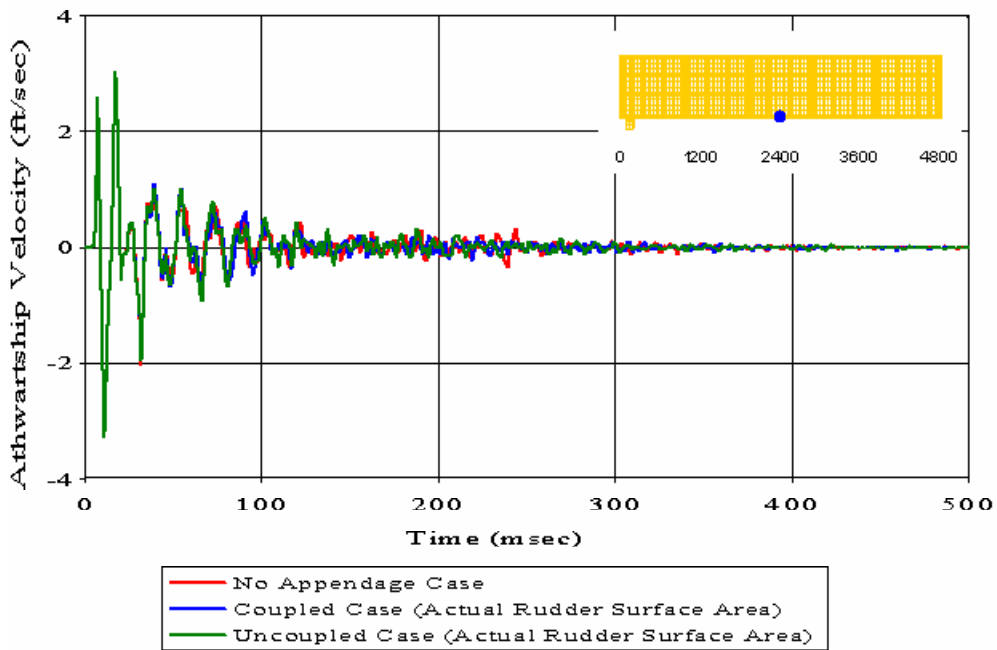
Figure 384.   **Keel Node 5320: (RM = 0.0052, RP = 0.0790, RC = 0.0702)**
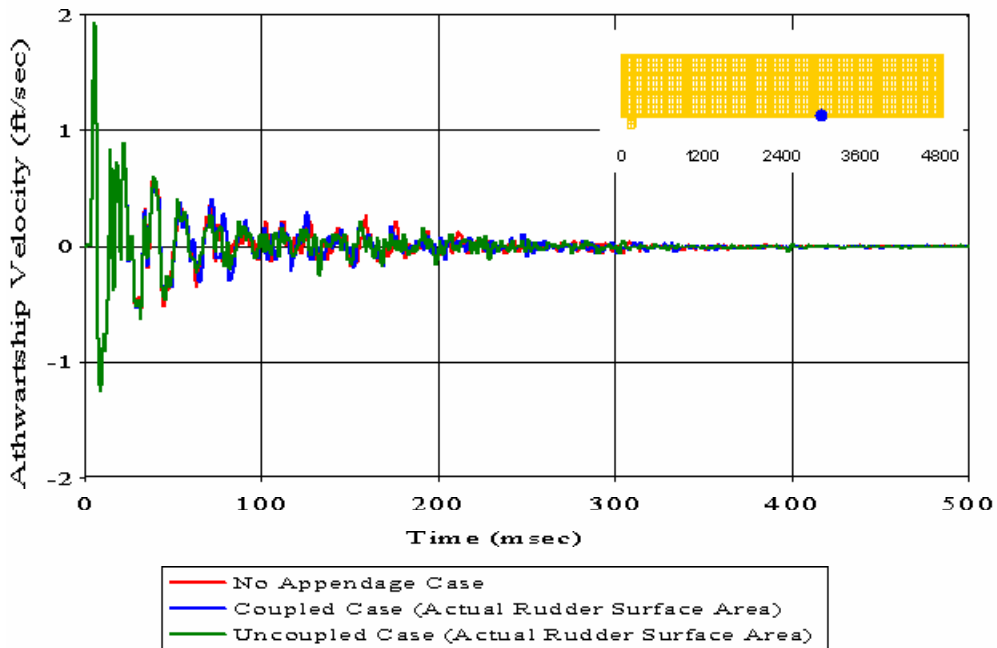
Figure 385.   **Keel Node 6741: (RM = -0.0177, RP = 0.1026, RC = 0.0923)**
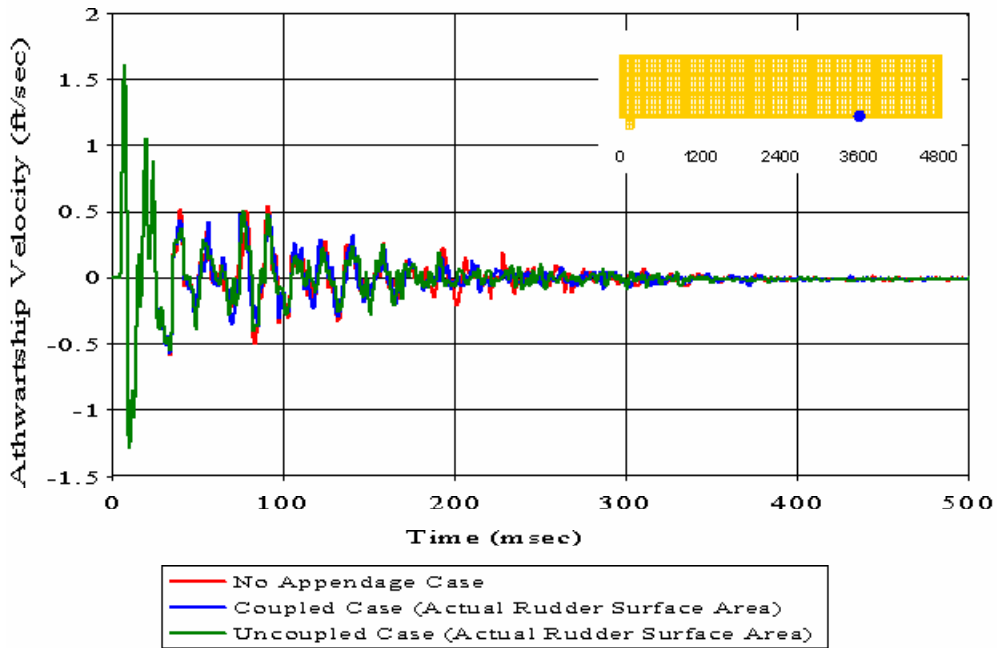
Figure 386.   Keel Node 8170: (RM = -0.0216, RP = 0.1050, RC = 0.0950)
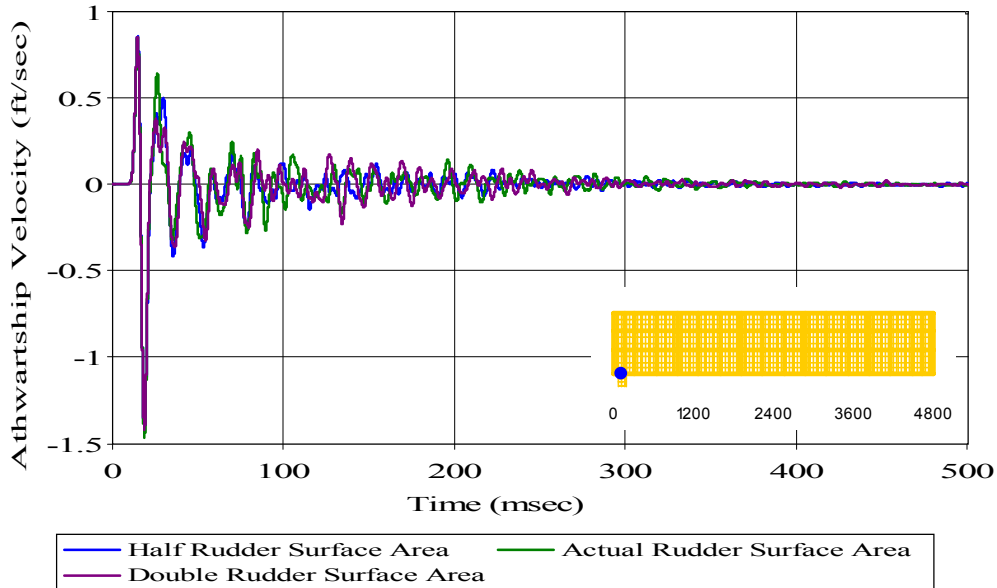
Figure 387.   Coupled Case with Varying Rudder Surface Area: Keel Node 74

318
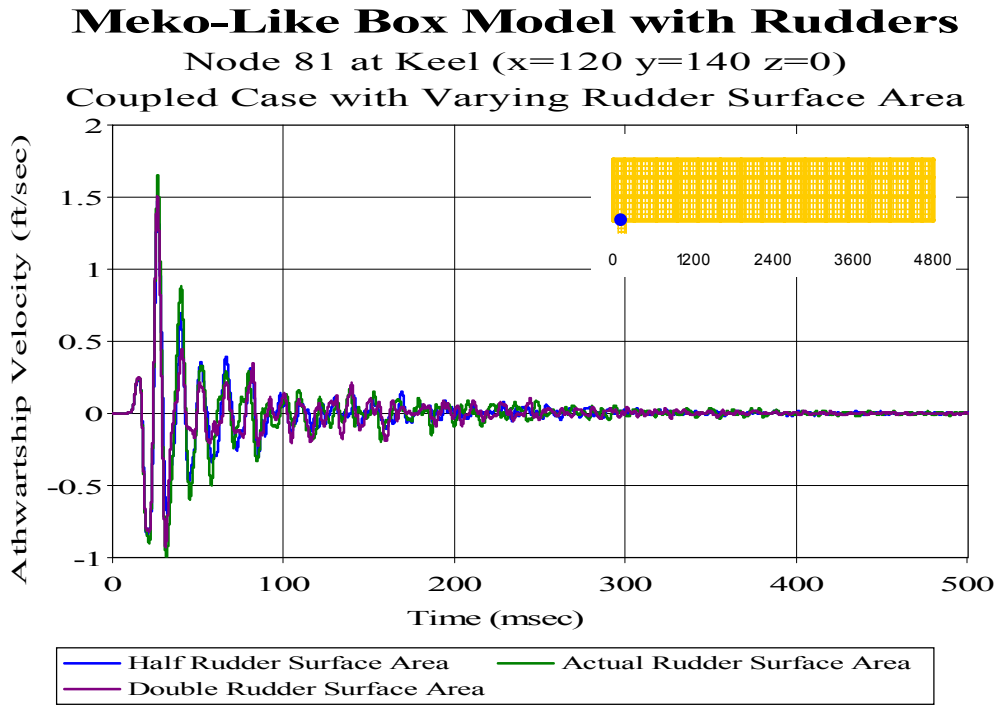
Figure 388.   Coupled Case with Varying Rudder Surface Area: Keel Node 81
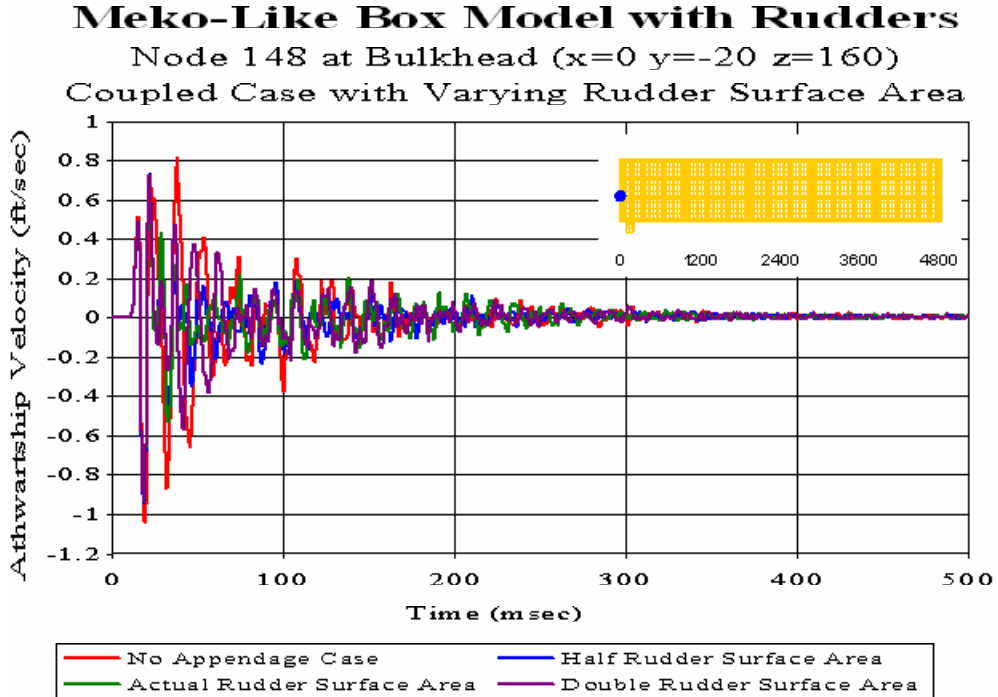
Figure 389.   Coupled Case with Varying Rudder Surface Area: Bulkhead Node 148

319
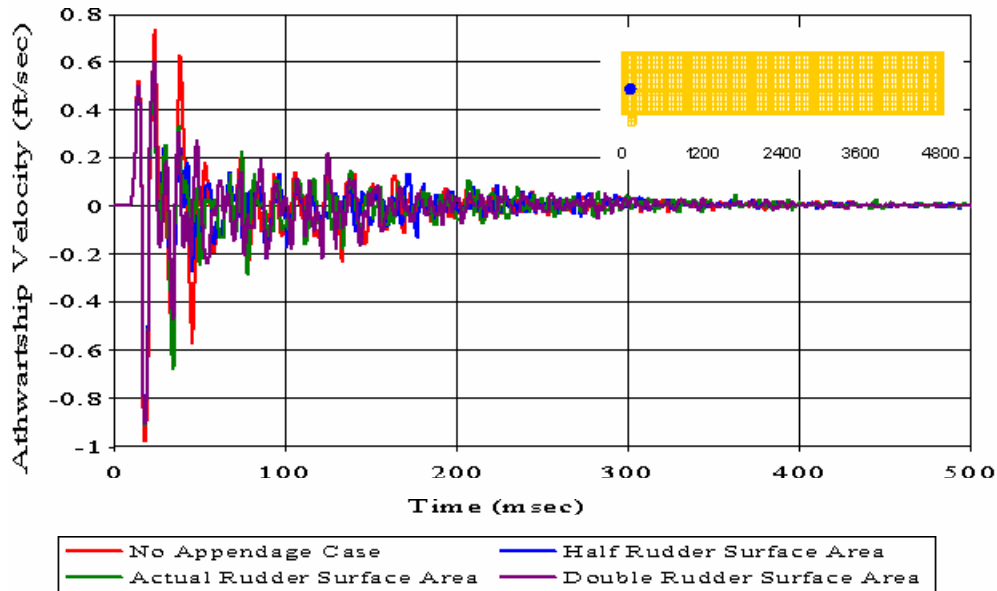
Figure 390.   Coupled Case with Varying Rudder Surface Area: First Deck Node 214
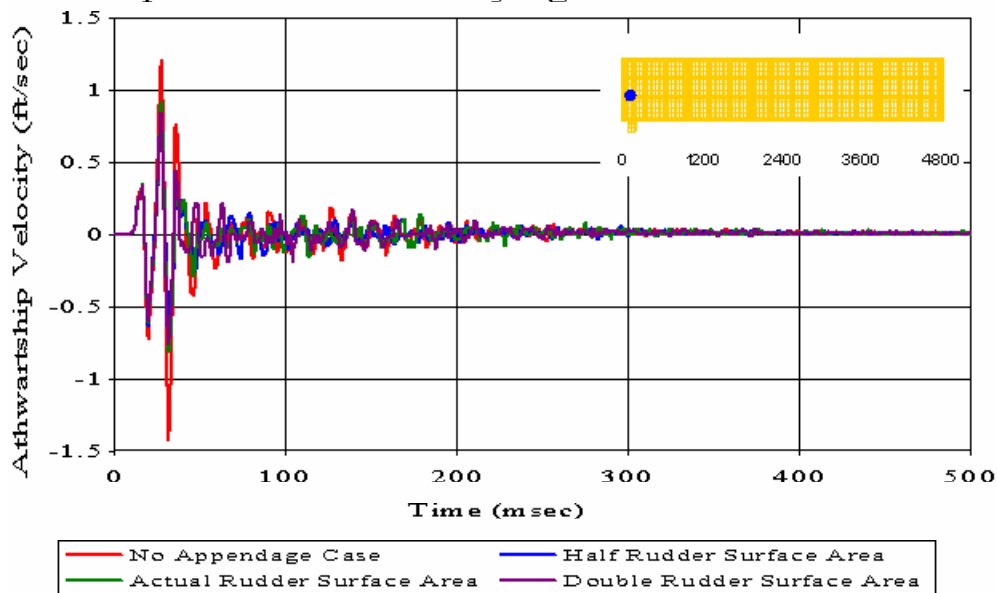
Figure 391.   Coupled Case with Varying Rudder Surface Area: First Deck Node 221

320

Figure 392. **Coupled Case with Varying Rudder Surface Area: Bulkhead Node 268**
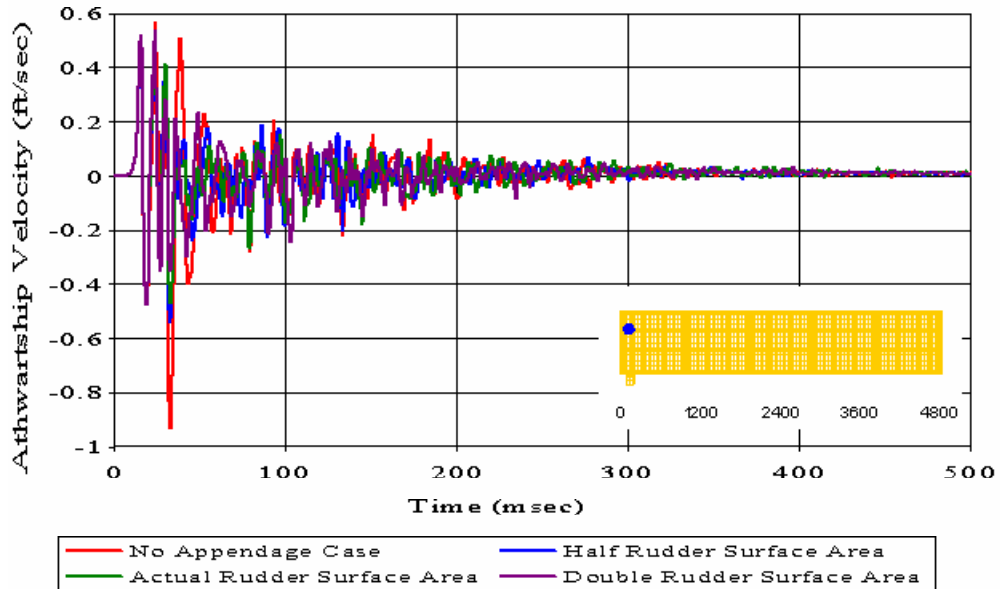
Figure 393. **Coupled Case with Varying Rudder Surface Area: Second Deck Node 334**
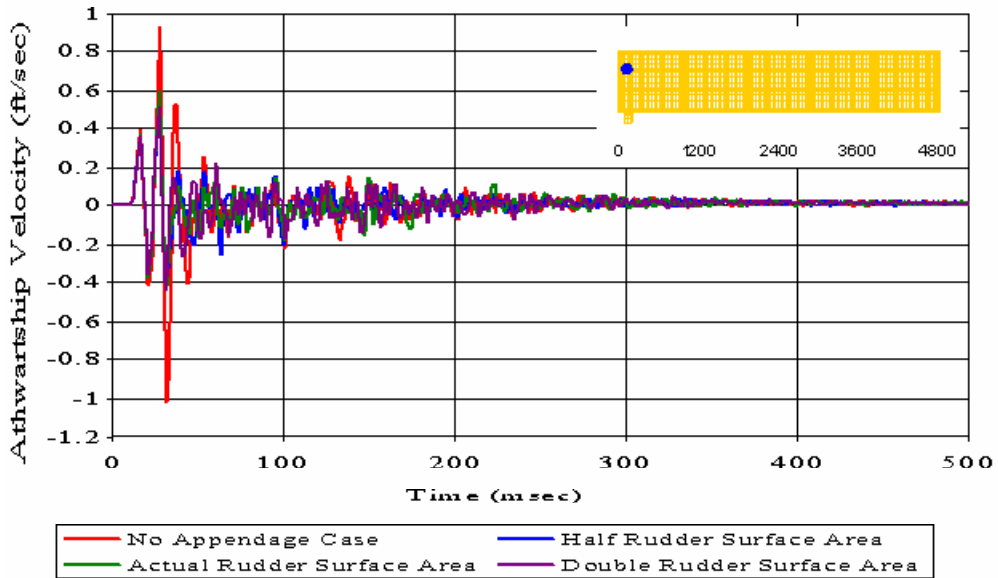
Figure 394. **Coupled Case with Varying Rudder Surface Area: Second Deck Node 341**

Figure 395. **Coupled Case with Varying Rudder Surface Area: Bulkhead Node 388**

322

Figure 396.   Coupled Case with Varying Rudder Surface Area: Top Deck Node 434

Figure 397.   Coupled Case with Varying Rudder Surface Area: Top Deck Node 441

323

Figure 398.   Coupled Case with Varying Rudder Surface Area: Keel Node 2454

Figure 399.   Coupled Case with Varying Rudder Surface Area: Keel Node 3883

Figure 400.   Coupled Case with Varying Rudder Surface Area: Keel Node 5251

Figure 401.   Coupled Case with Varying Rudder Surface Area: Keel Node 5308

Figure 402.   Coupled Case with Varying Rudder Surface Area: Keel Node 5310

Figure 403.   Coupled Case with Varying Rudder Surface Area: Keel Node 5315

326

Figure 404.   Coupled Case with Varying Rudder Surface Area: Keel Node 5317

Figure 405.   Coupled Case with Varying Rudder Surface Area: Keel Node 5320

327

Figure 406. **Coupled Case with Varying Rudder Surface Area: Keel Node 6741**

Figure 407. **Uncoupled Case with Varying Rudder Surface Area: Bulkhead Node 15**

328

Figure 408. **Uncoupled Case with Varying Rudder Surface Area: Keel Node 74**

Figure 409. **Uncoupled Case with Varying Rudder Surface Area: Keel Node 81**
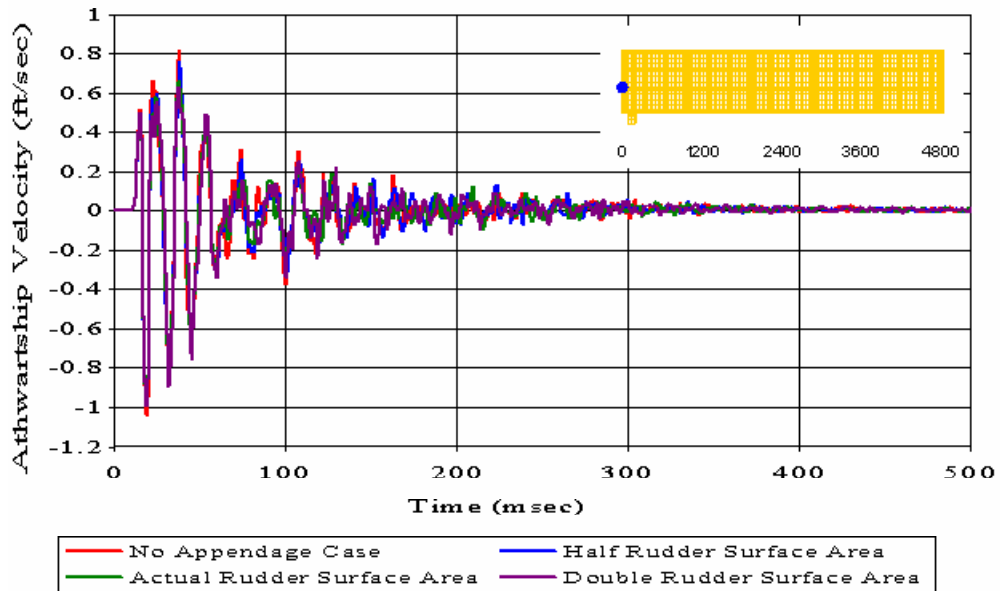
Figure 410.   Uncoupled Case with Varying Rudder Surface Area: Bulkhead Node 148
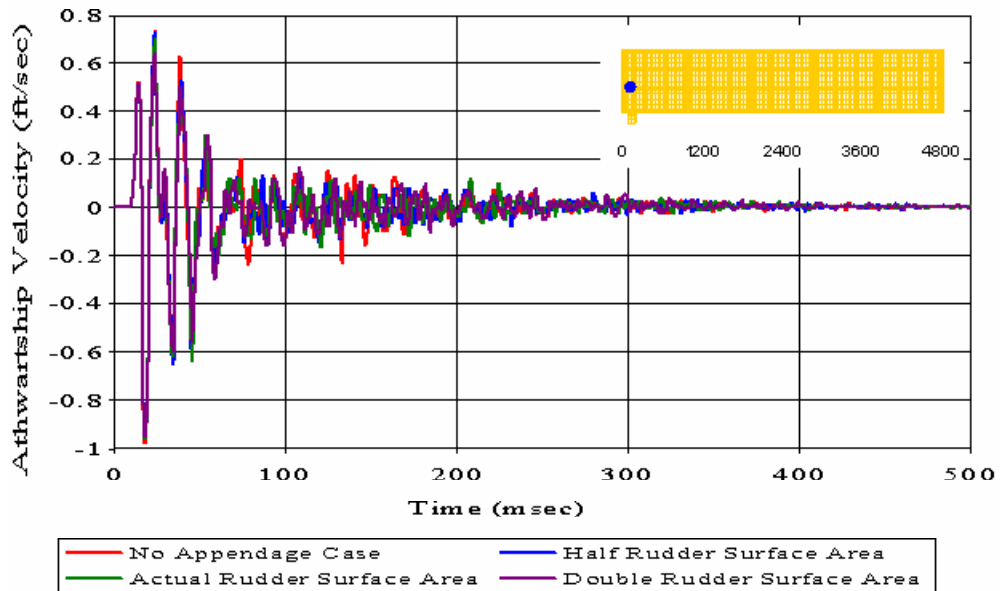
Figure 411.   Uncoupled Case with Varying Rudder Surface Area: First Deck Node 214

330

Figure 412. Uncoupled Case with Varying Rudder Surface Area: First Deck Node 221

Figure 413. Uncoupled Case with Varying Rudder Surface Area: Second Deck Node 334

Figure 414.   **Uncoupled Case with Varying Rudder Surface Area: Second Deck Node 341**

Figure 415.   **Uncoupled Case with Varying Rudder Surface Area: Bulkhead Node 388**

Figure 416. Uncoupled Case with Varying Rudder Surface Area: Top Deck Node 434

Figure 417. Uncoupled Case with Varying Rudder Surface Area: Top Deck Node 441

333

Figure 418. Uncoupled Case with Varying Rudder Surface Area: Keel Node 2454

Figure 419. Uncoupled Case with Varying Rudder Surface Area: Keel Node 5251

Figure 420.   **Uncoupled Case with Varying Rudder Surface Area: Keel Node 5308**

Figure 421.   **Uncoupled Case with Varying Rudder Surface Area: Keel Node 5310**

335

Figure 422. Uncoupled Case with Varying Rudder Surface Area: Keel Node 5315

Figure 423. Uncoupled Case with Varying Rudder Surface Area: Keel Node 5317

Figure 424.   Uncoupled Case with Varying Rudder Surface Area: Keel Node 5320

Figure 425.   Uncoupled Case with Varying Rudder Surface Area: Keel Node 6741
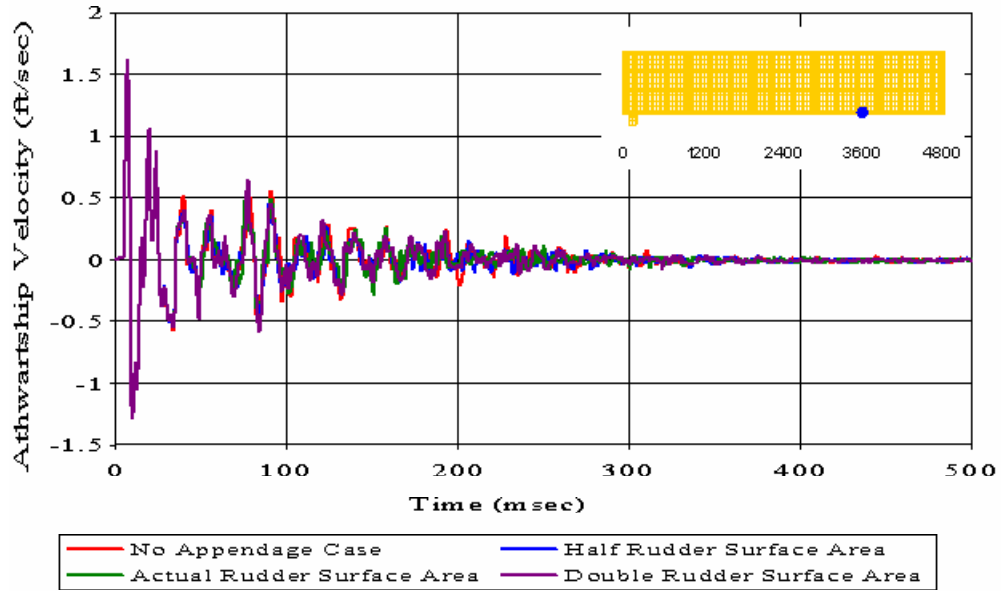
Figure 426.   Uncoupled Case with Varying Rudder Surface Area: Keel Node 8170

APPENDIX F. SHOCK SPECTRA PLOTS

A. MEKO-LIKE BOX MODEL WITH SOLID KEEL BOARD

1. Vertical Velocity Analysis

Figure 427.   Shock Spectra Plot: Bulkhead Node 15

Figure 428. **Shock Spectra Plot: Bulkhead Node 148**

Figure 429. **Shock Spectra Plot: Keel Node 2454**

340

Figure 430.   Shock Spectra Plot: First Deck Node 2648
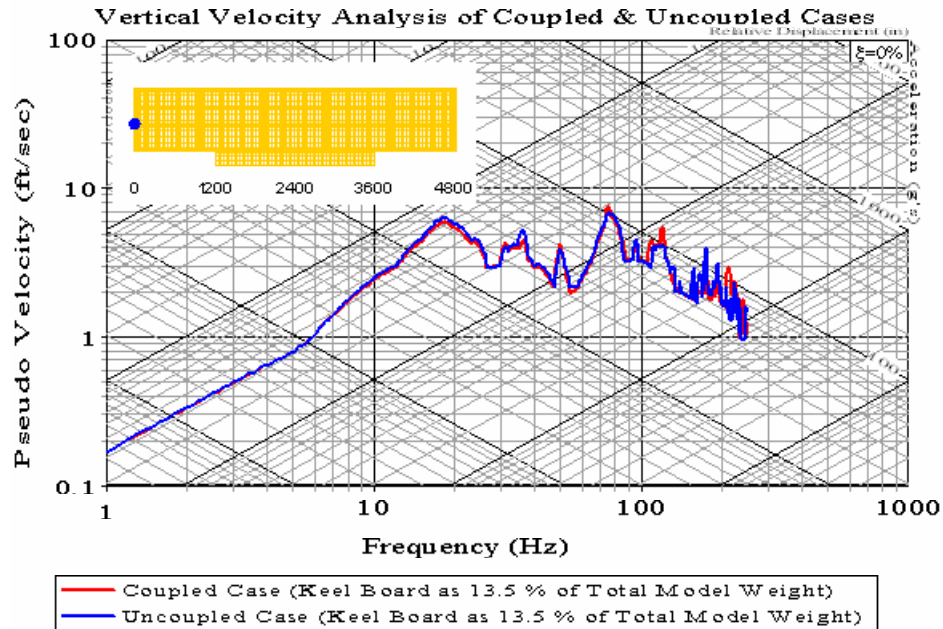

Figure 431.   Shock Spectra Plot: Keel Node 5312

Meko-Like Box Model with Solid Keel Board

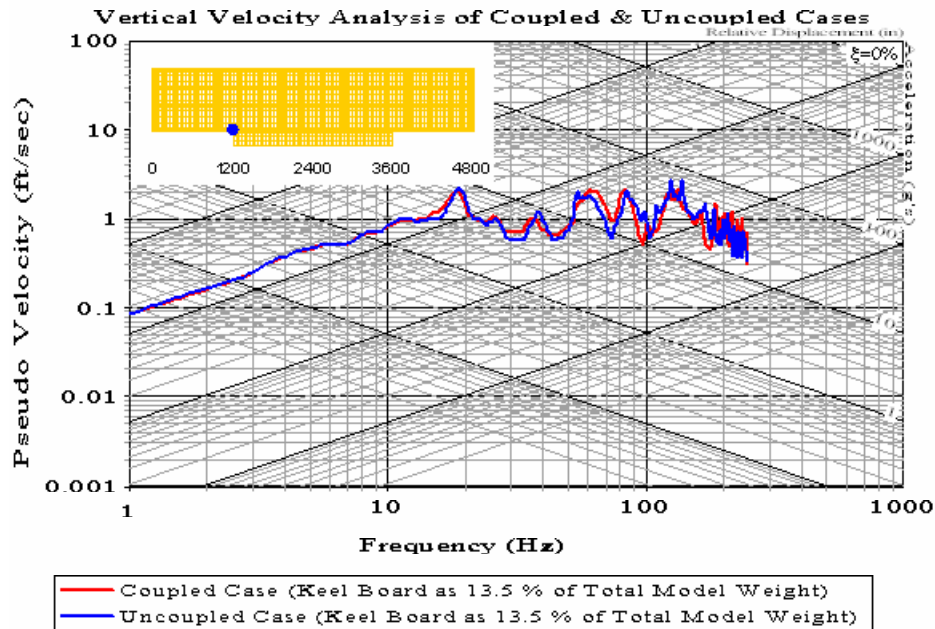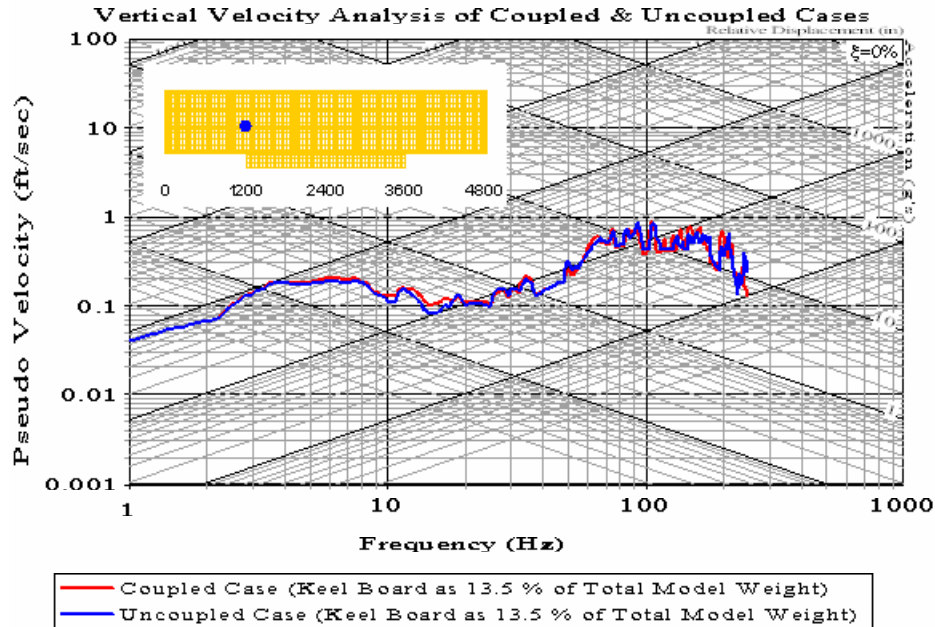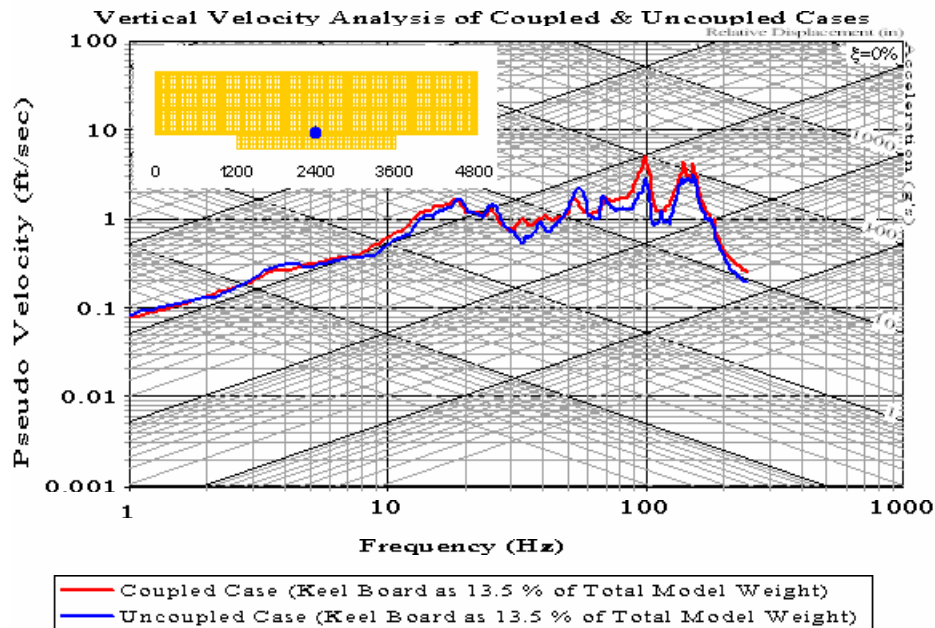Node 5317 at Keel (x=2400 y=180 z=0)
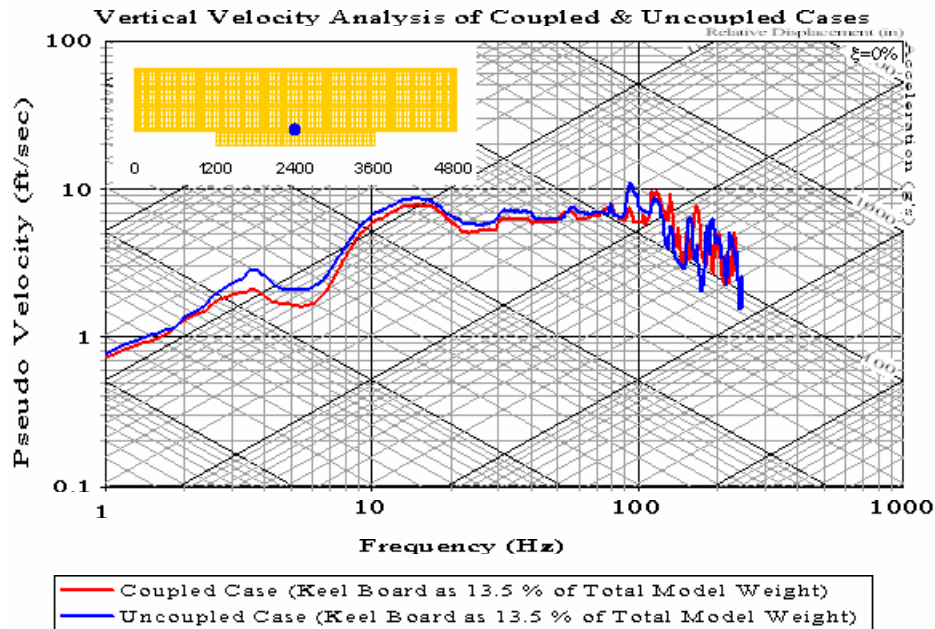
Figure 432.   Shock Spectra Plot: Keel Node 5317

Meko-Like Box Model with Solid Keel Board

Node 8170 at Keel (x=3600 y=-20 z=0)
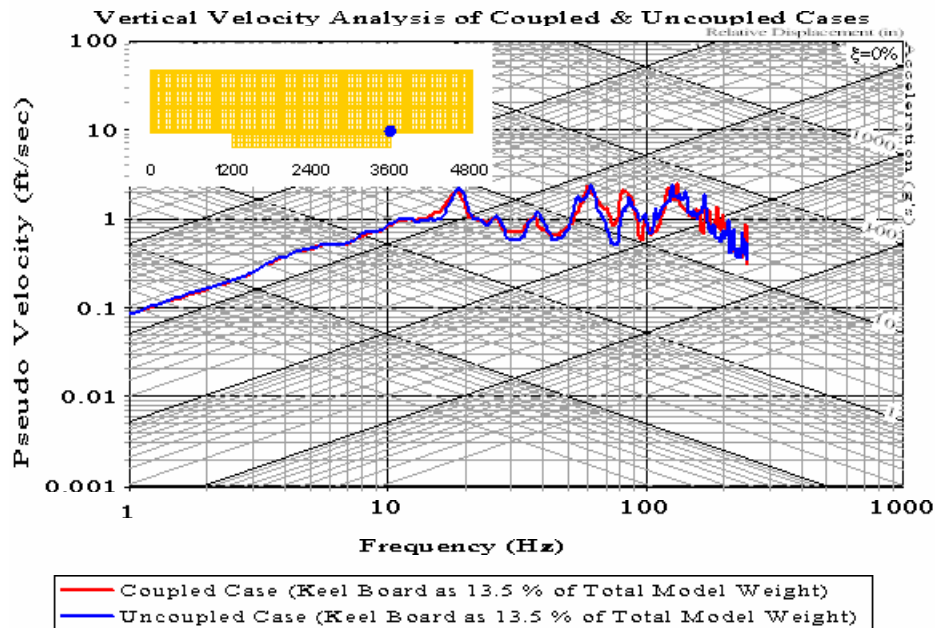
Figure 433.   Shock Spectra Plot: Keel Node 8170

342
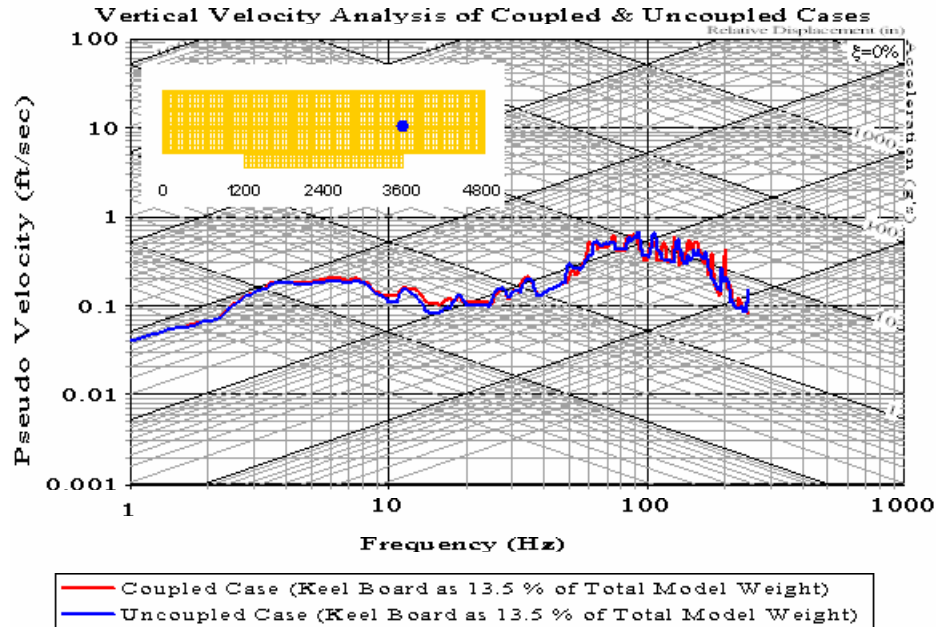
Figure 434.   Shock Spectra Plot: First Deck Node 8364

2.   **Athwartship Velocity Analysis**
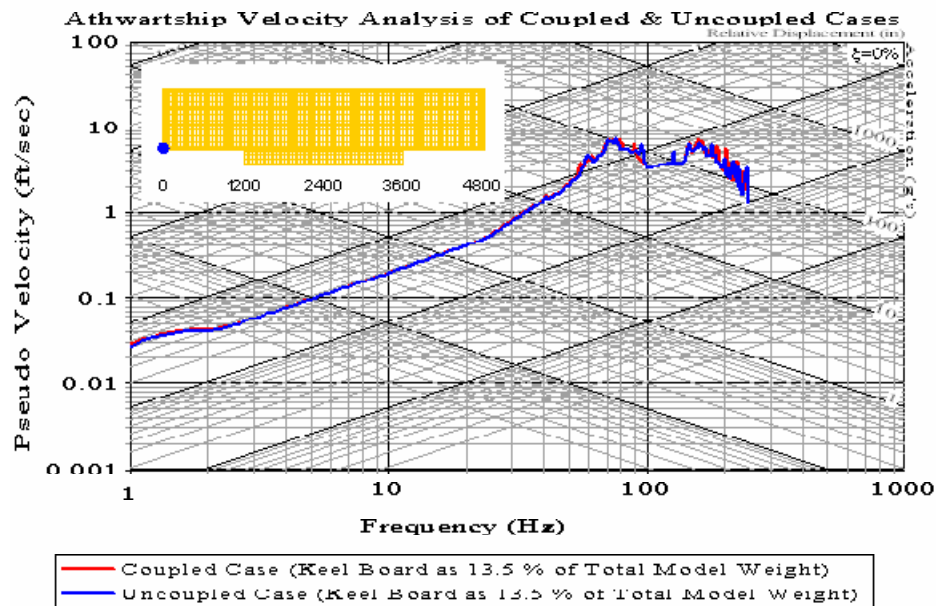
Figure 435.   Shock Spectra Plot: Bulkhead Node 15
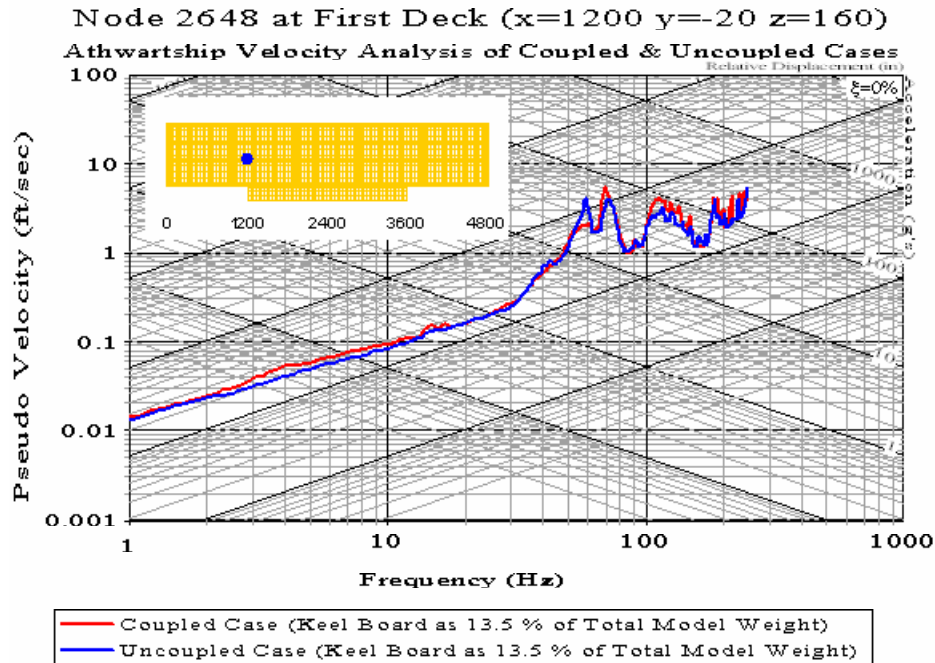
Figure 436.   Shock Spectra Plot: First Deck Node 2648
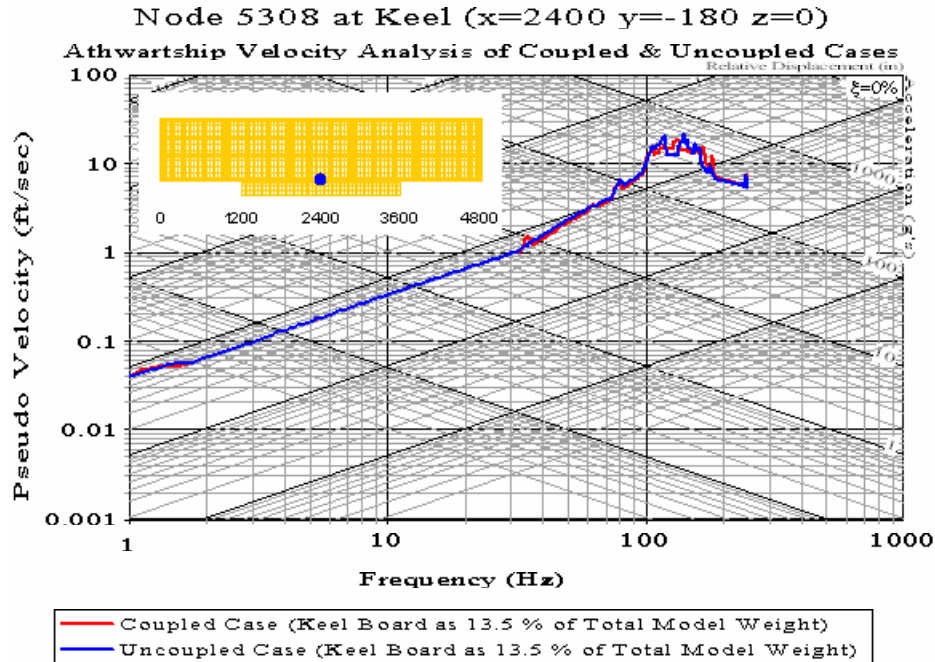
Figure 437.   Shock Spectra Plot: Keel Node 5308

344
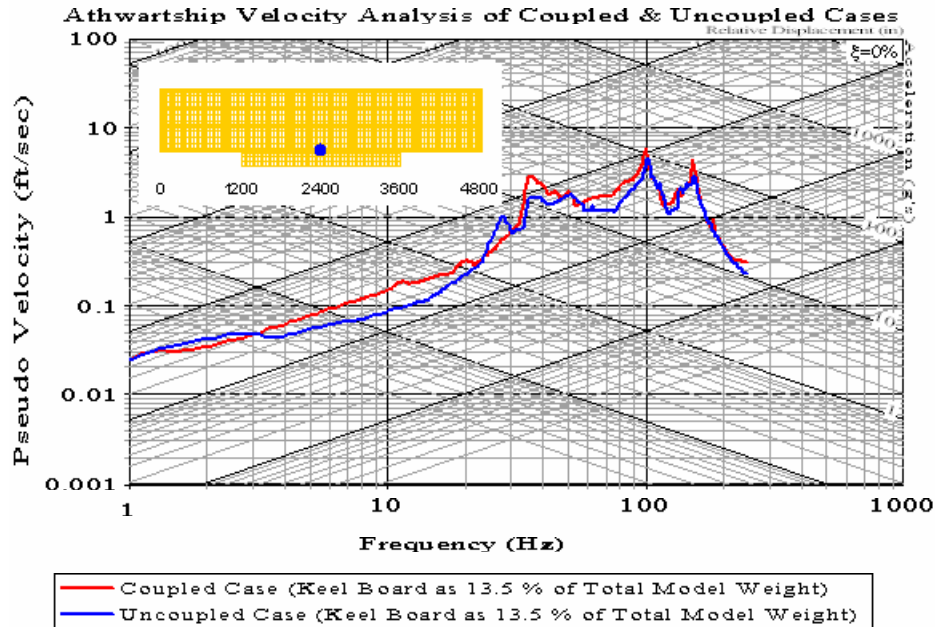
Figure 438. Shock Spectra Plot: Keel Node 5312
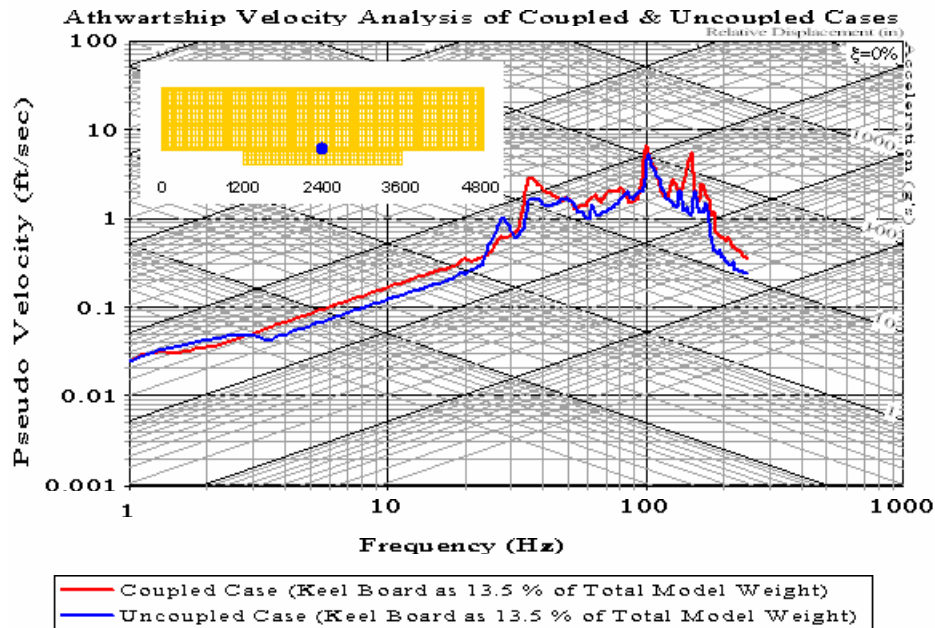
Figure 439. Shock Spectra Plot: Keel Node 5313
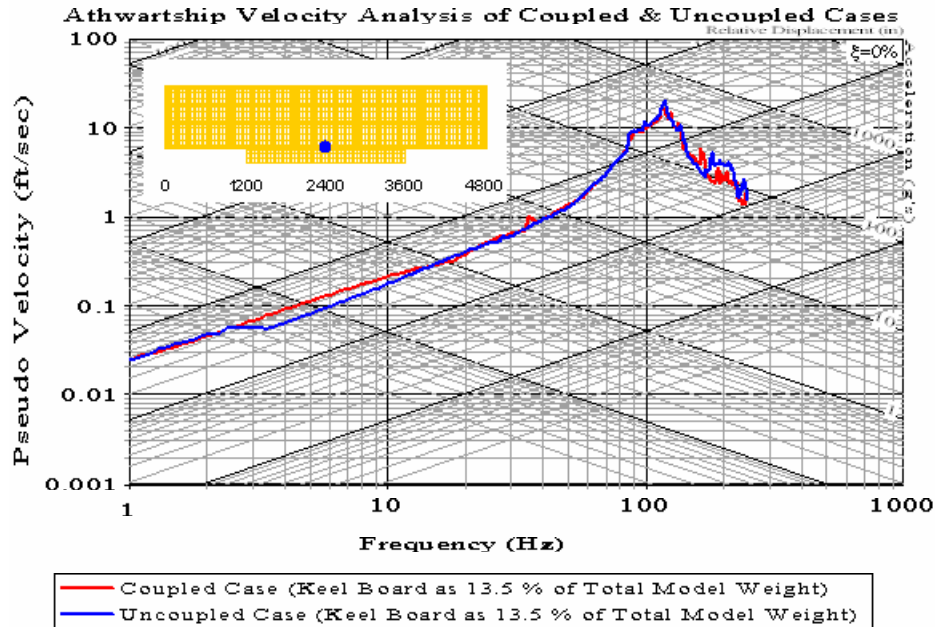
Figure 440. **Shock Spectra Plot: Keel Node 5317**
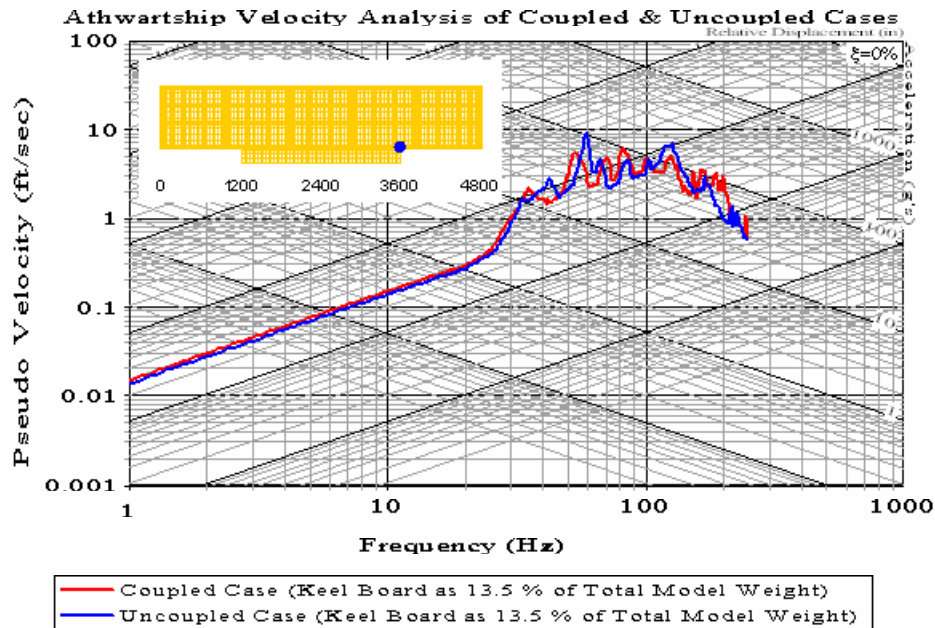
Figure 441. **Shock Spectra Plot: Keel Node 8170**

346
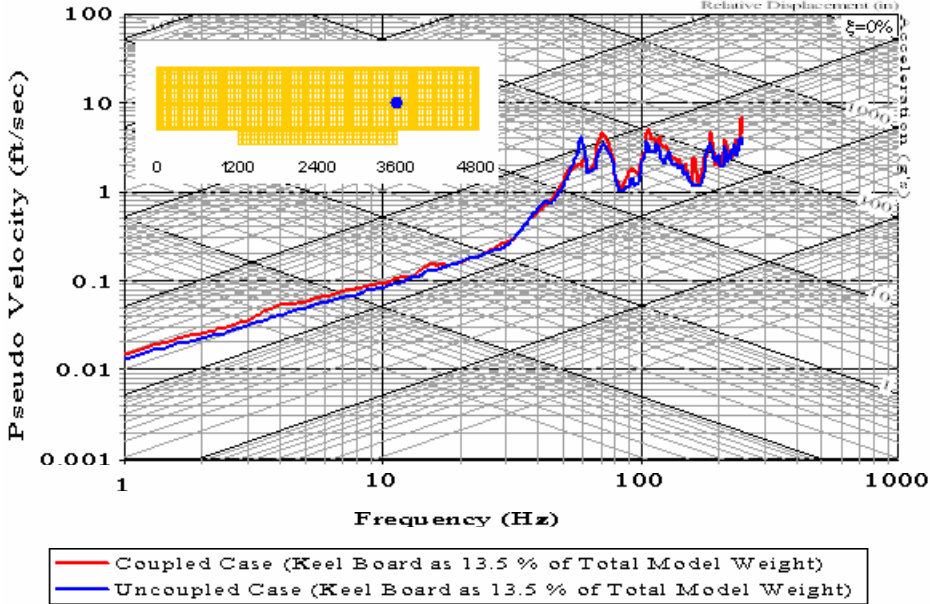
Figure 442.   Shock Spectra Plot: First Deck Node 8364

B. **MEKO-LIKE BOX MODEL WITH SHELL KEEL BOARD**

1. **Vertical Velocity Analysis**

Figure 443. **Shock Spectra Plot: Bulkhead Node 15**

Figure 444.   **Shock Spectra Plot: Bulkhead Node 148**

Figure 445.   **Shock Spectra Plot: First Deck Node 2648**
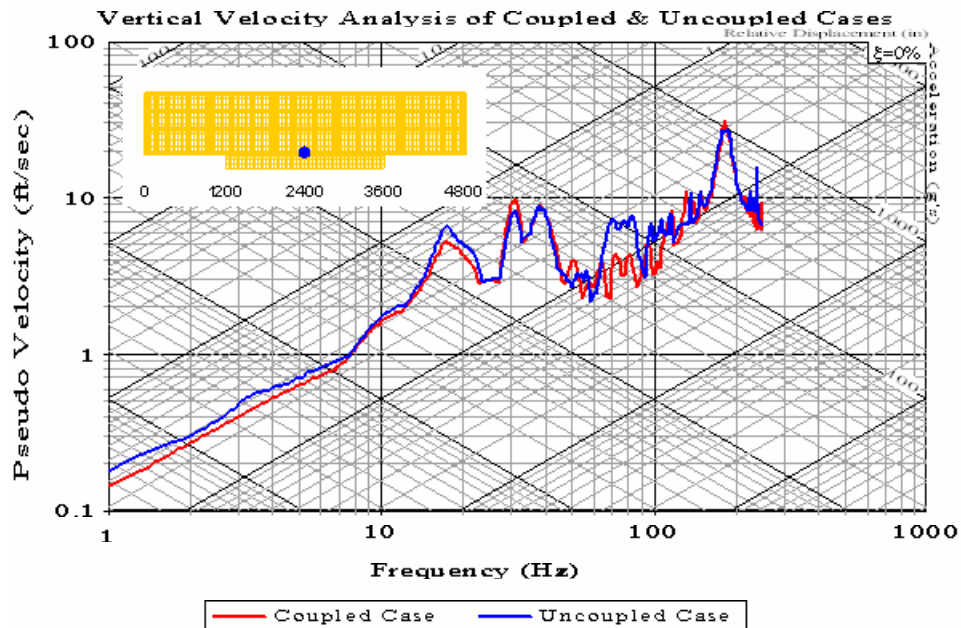
Figure 446.   Shock Spectra Plot: Keel Node 5251

Figure 447.   Shock Spectra Plot: Keel Node 5312

Figure 448. Shock Spectra Plot: Keel Node 5313

Figure 449. Shock Spectra Plot: Keel Node 5317

351

Figure 450.   Shock Spectra Plot: Keel Node 8170
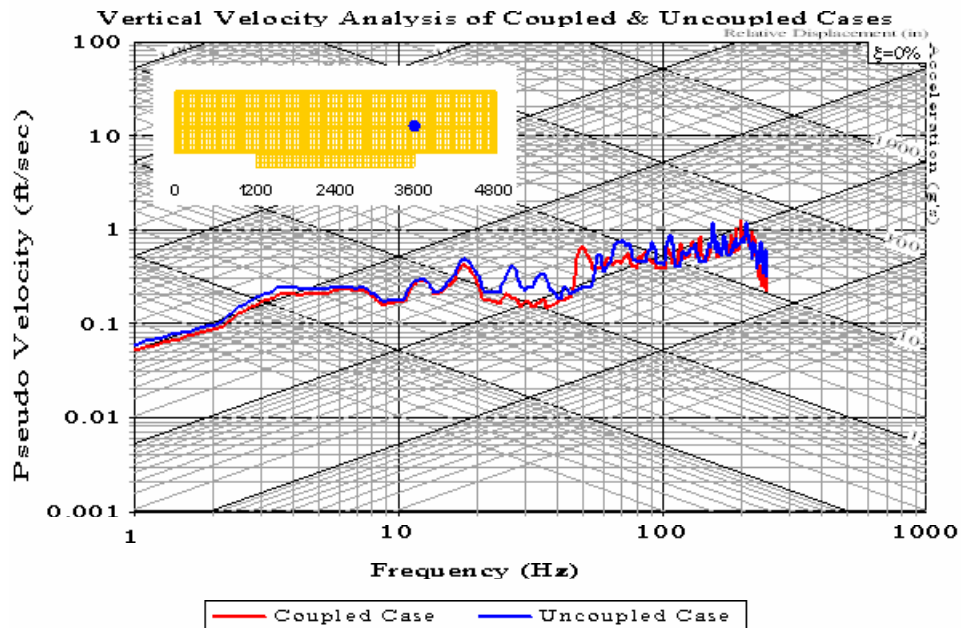
Figure 451.   Shock Spectra Plot: First Deck Node 8364

352

2.   Athwartship Velocity Analysis

Figure 452.   Shock Spectra Plot: Bulkhead Node 15
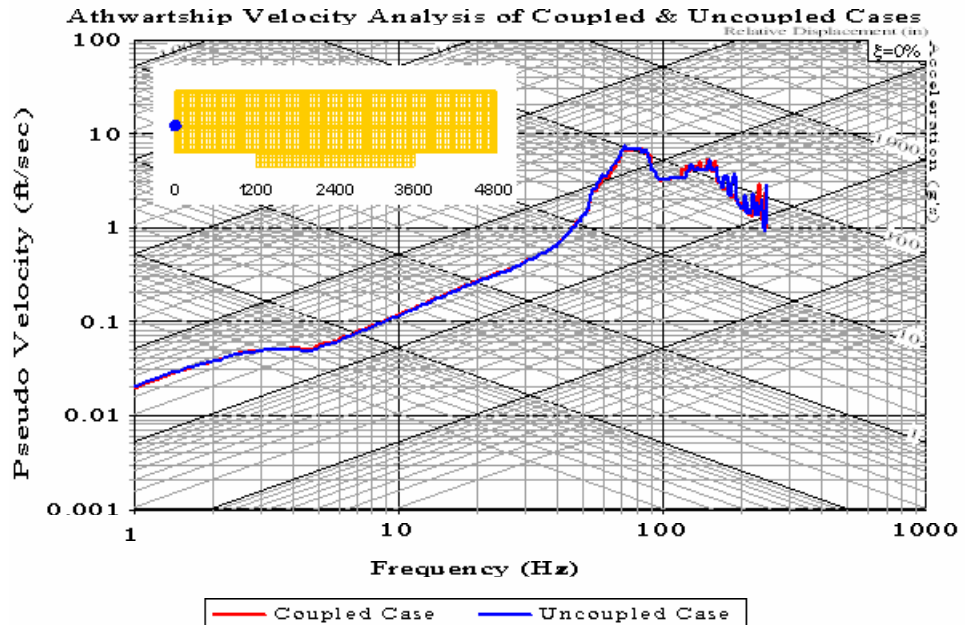
Figure 453.   Shock Spectra Plot: Bulkhead Node 148
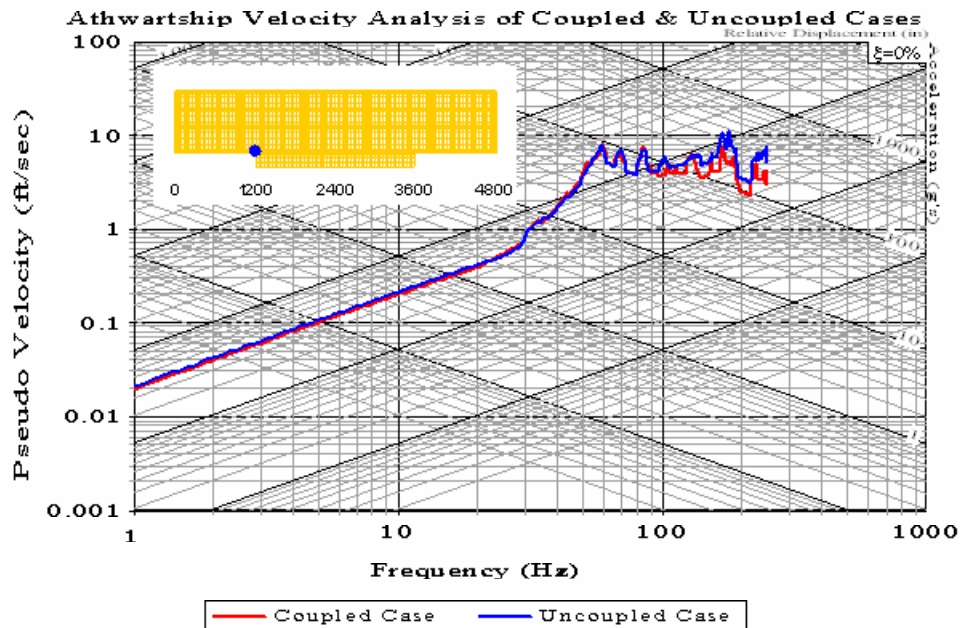
Figure 454. **Shock Spectra Plot: Keel Node 2454**
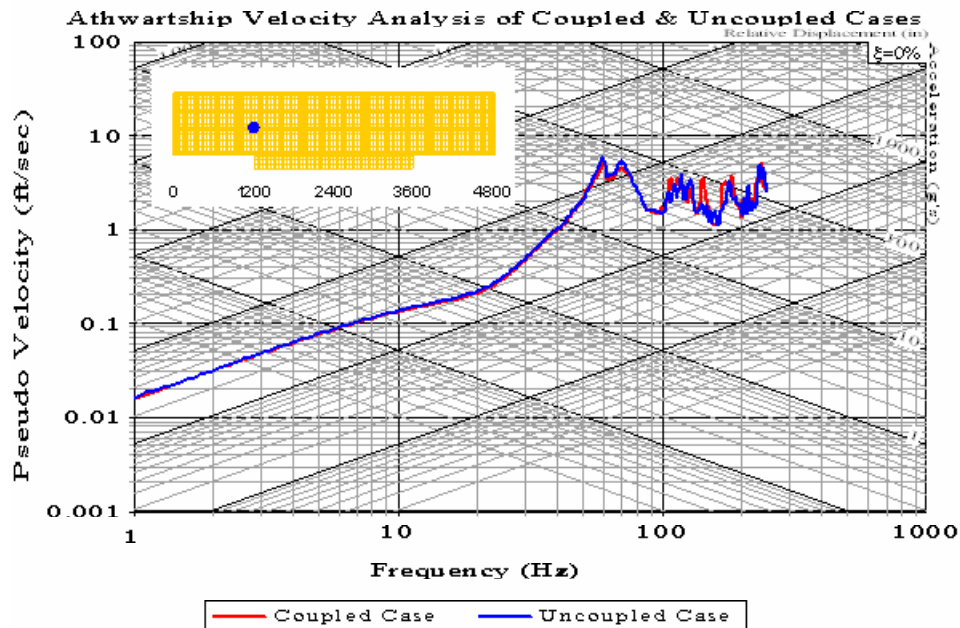
Figure 455. **Shock Spectra Plot: First Deck Node 2648**

354

Figure 456.   **Shock Spectra Plot: Keel Node 5308**
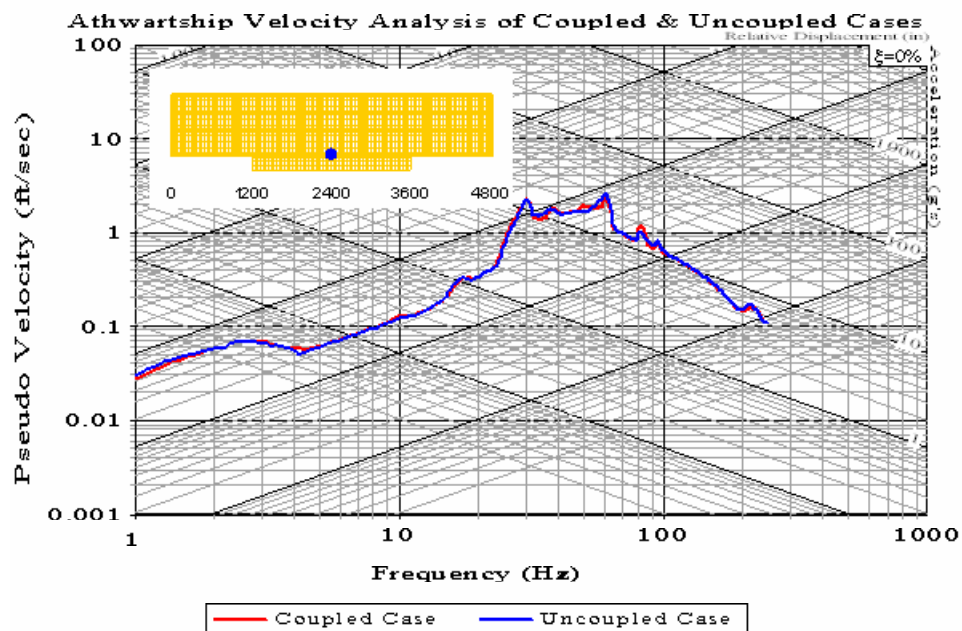
Figure 457.   **Shock Spectra Plot: Keel Node 5312**
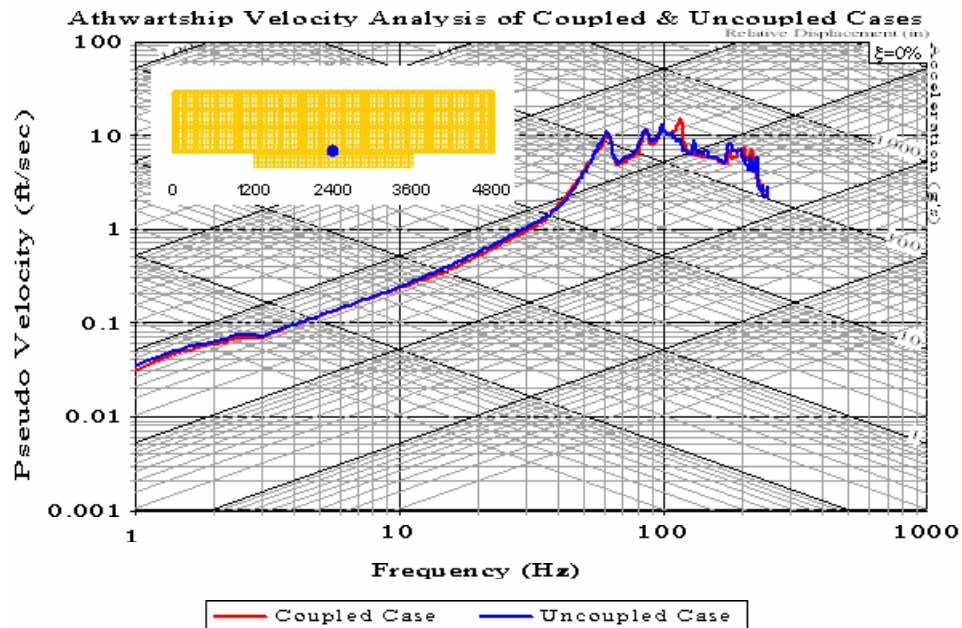
Figure 458.   Shock Spectra Plot: Keel Node 5317

Figure 459.   Shock Spectra Plot: Keel Node 8170

356
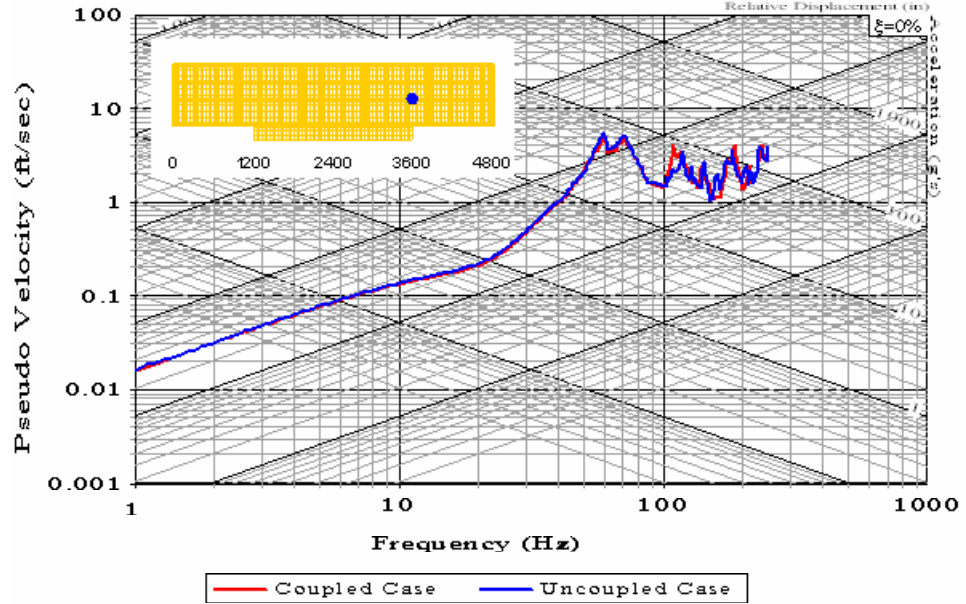
Figure 460.   Shock Spectra Plot: First Deck Node 8364

C.   MEKO-LIKE BOX MODEL WITH OPEN KEEL BOARD

1.   Vertical Velocity Analysis
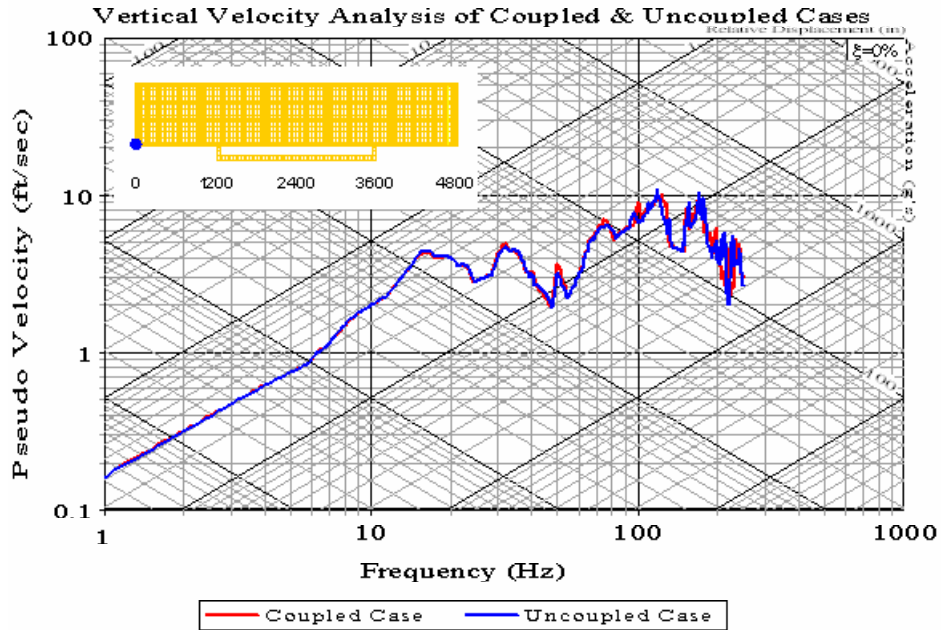
Figure 461.   Shock Spectra Plot: Bulkhead Node 15

Figure 462.   Shock Spectra Plot: Bulkhead Node 268

Figure 463.   Shock Spectra Plot: Keel Node 2454

Figure 464.   Shock Spectra Plot: Second Deck Node 2820

Figure 465.   Shock Spectra Plot: Keel Node 5308

360

Figure 466.   Shock Spectra Plot: Keel Node 5317

2.   Athwartship Velocity Analysis

Figure 467.   Shock Spectra Plot: Bulkhead Node 15

361

Figure 468.   Shock Spectra Plot: Bulkhead Node 268

Figure 469.   Shock Spectra Plot: Second Deck Node 2820

Figure 470.   Shock Spectra Plot: Keel Node 5308

Figure 471.   Shock Spectra Plot: Keel Node 8170

363

Figure 472.   Shock Spectra Plot: Second Deck Node 8536

D.   MEKO-LIKE BOX MODEL WITH RUDDERS

1.   Vertical Velocity Analysis
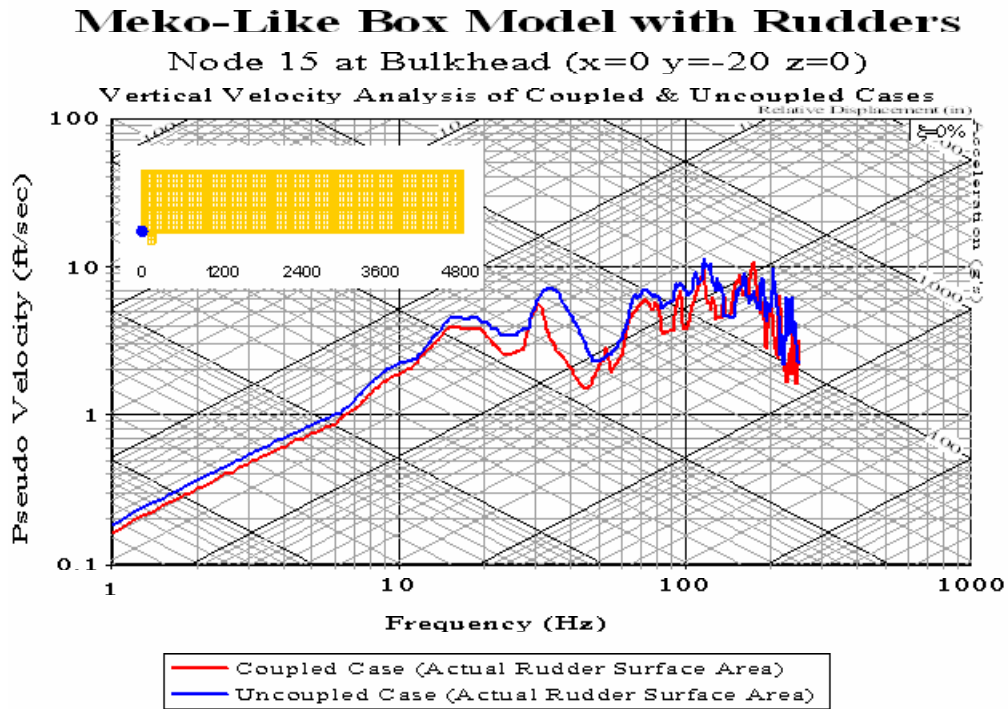
Figure 473.   Shock Spectra Plot: Bulkhead Node 15
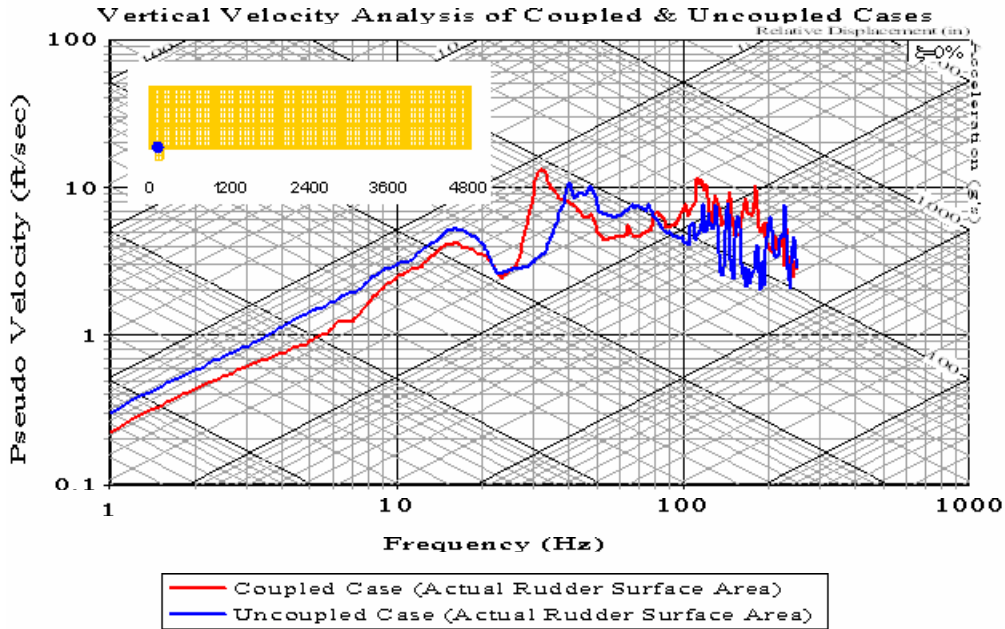
Figure 474.   Shock Spectra Plot: Keel Node 74
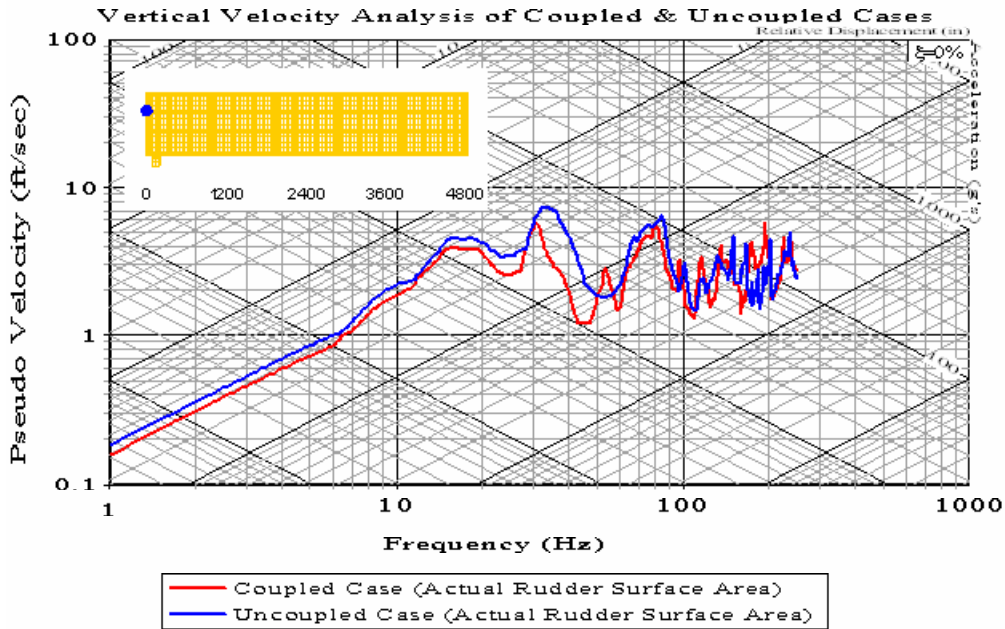
Figure 475.   Shock Spectra Plot: Bulkhead Node 268

366
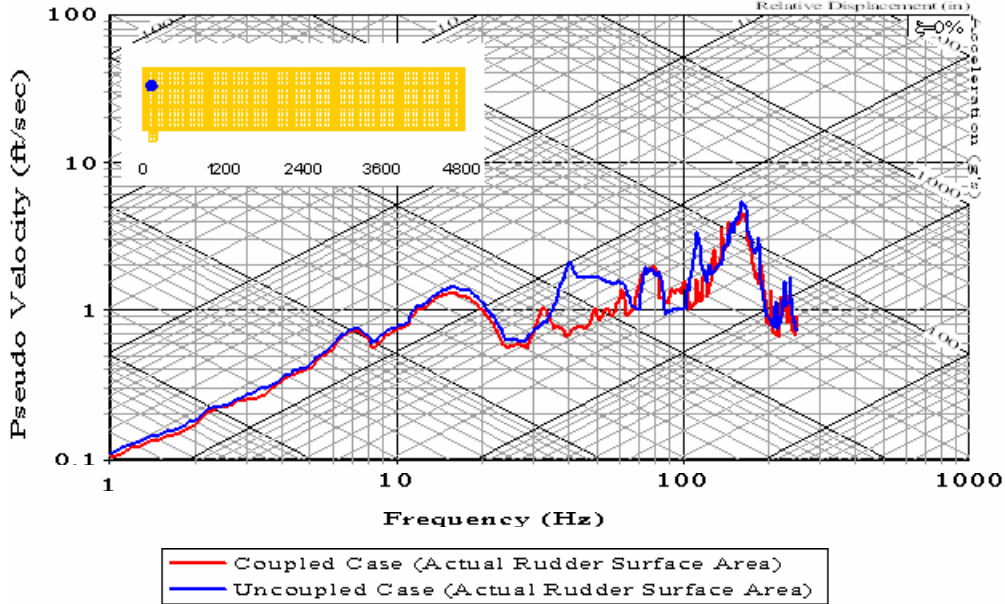
Figure 476.   Shock Spectra Plot: Second Deck Node 334

Figure 477.   Shock Spectra Plot: Second Deck Node 341

367

Figure 478.   Shock Spectra Plot: Keel Node 5308

Figure 479.   Shock Spectra Plot: Keel Node 5315

368

Figure 480.   Shock Spectra Plot: Keel Node 5317

2.   Athwartship Velocity Analysis

Figure 481.   Shock Spectra Plot: Bulkhead Node 15

369

Figure 482.   Shock Spectra Plot: Keel Node 74

Figure 483.   Shock Spectra Plot: Keel Node 81

370

Figure 484. **Shock Spectra Plot: Second Deck Node 334**
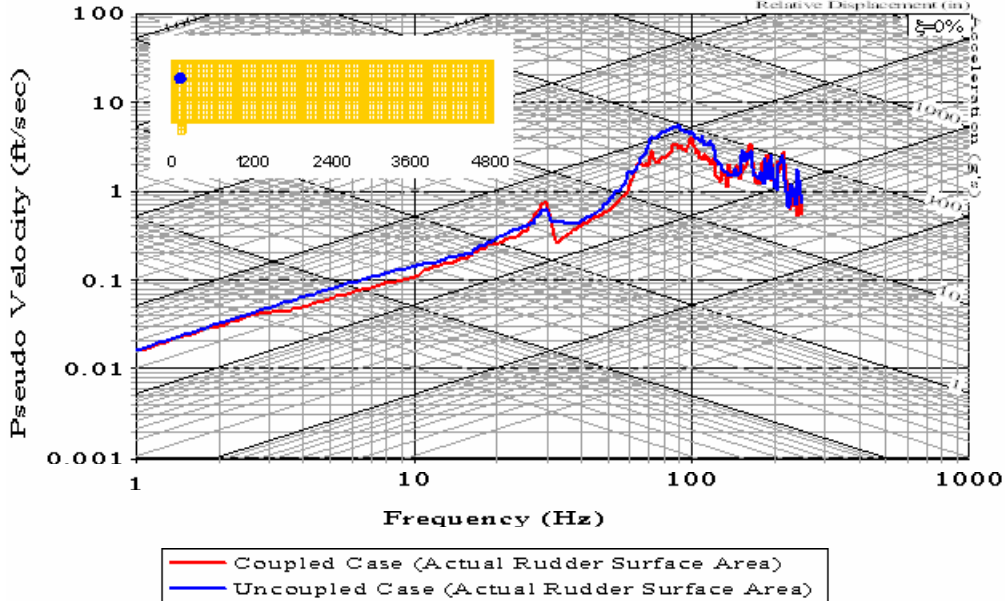
Figure 485. **Shock Spectra Plot: Second Deck Node 341**
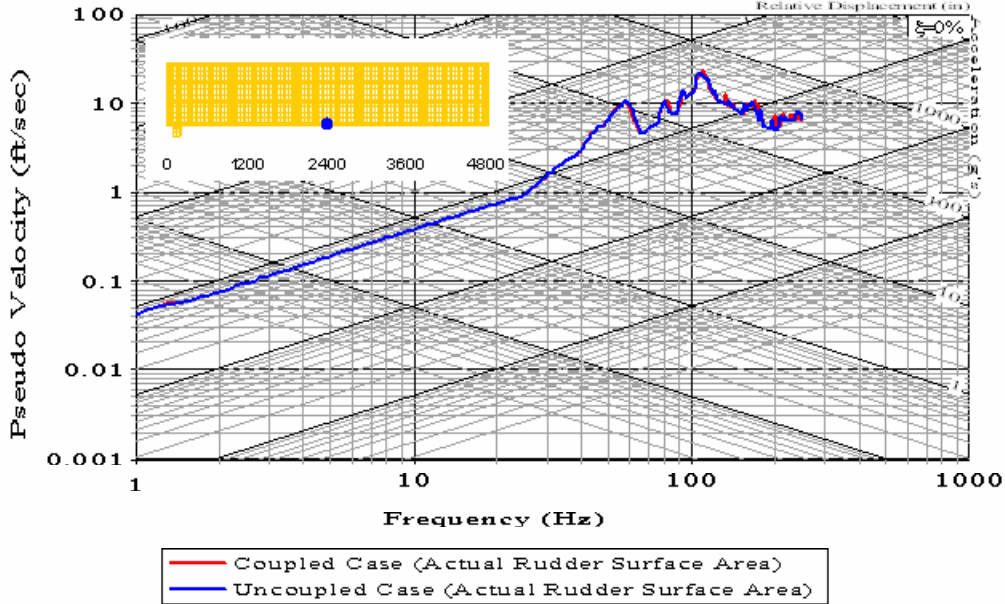
Figure 486.   Shock Spectra Plot: Keel Node 5308

Figure 487.   Shock Spectra Plot: Keel Node 5310

Figure 488.   Shock Spectra Plot: Keel Node 5315

THIS PAGE INTENTIONALLY LEFT BLANK

APPENDIX G. TABLES-GRAPHS OF RUSSELL'S ERROR FACTORS

A.   MEKO-LIKE BOX MODEL WITH SOLID KEEL BOARD

Figure 489.   Russell's Error Factor Comparison for Meko-Like Box Model with Solid Keel Board as 1 % of Total Model Weight (Vertical Velocity)

Figure 490. **Russell's Error Factor Comparison for Meko-Like Box Model with Solid Keel Board as 1 % of Total Model Weight (Athwartship Velocity)**

Table 32. **Statistical Data for Meko-Like Box Model with Solid Keel Board as 1 % of Total Model Weight (Coupled and Uncoupled Cases)**

Russell's Comprehensive Error Factor	Vertical Velocity Comparison	Athwartship Velocity Comparison
RC < 0.30	100 %	86 %
RC < 0.28	100 %	73 %
RC < 0.25	91 %	64 %
RC < 0.20	91 %	45 %
RC < 0.18	91 %	32 %
RC < 0.15	82 %	18 %
Mean RC	0.1122	0.2207
Standard Deviation	0.0606	0.0669
Mean + Standard Deviation	0.1728	0.2876
Data within One Standard Deviation	91 %	82 %

Table 33.   Russell's Error Factors for Meko-Like Box Model with Solid Keel Board as 1 % of Total Model Weight

Simulation runtime = 500 msec					Meko-Like Box Model with Solid Keel Board as 1 % of Total Model Weight					
					Vertical Velocity Comparison			Athwartship Velocity Comparison		
NODE	X (in)	Y (in)	Z (in)	Location	COUPLED & UNCOUPLED CASES			COUPLED & UNCOUPLED CASES		
					LS-DYNA/USA DATA (<250HZ)			LS-DYNA/USA DATA (<250HZ)		
					RM	RP	RC	RM	RP	RC
15	0	-20	0	Bulkhead	0.0298	0.1163	0.1064	-0.0409	0.1530	0.1404
148	0	-20	160	Bulkhead	0.0456	0.0735	0.0767	-0.0309	0.1403	0.1273
268	0	-20	280	Bulkhead	0.0436	0.0759	0.0776	-0.0400	0.1408	0.1297
388	0	-20	400	Bulkhead	0.0428	0.0975	0.0944	-0.0297	0.1561	0.1408
2454	1200	-20	0	Keel	0.0613	0.3040	0.2748	0.0480	0.3418	0.3059
2648	1200	-20	160	First Deck	0.0347	0.0816	0.0786	0.0259	0.2389	0.2130
2820	1200	-20	280	Second Deck	0.0234	0.0769	0.0712	0.0104	0.2300	0.2041
2970	1200	-20	400	Top Deck	0.0220	0.0803	0.0738	0.0133	0.2195	0.1949
3883	1800	-20	0	Keel	-0.0206	0.1370	0.1228	-0.1200	0.3639	0.3396
5251	2400	-300	0	Keel	-0.0493	0.1455	0.1361	0.0955	0.1879	0.1868
5308	2400	-180	0	Keel	0.0031	0.0522	0.0463	0.0988	0.1678	0.1726
5310	2400	-100	0	Keel	-0.0248	0.0714	0.0670	0.0453	0.1728	0.1583
5312	2400	-20	0	Keel	-0.0569	0.1612	0.1515	-0.1328	0.2692	0.2660
5313	2400	20	0	Keel	-0.0677	0.1648	0.1579	-0.1145	0.2237	0.2227
5315	2400	100	0	Keel	0.0855	0.0827	0.1054	-0.0567	0.3038	0.2739
5317	2400	180	0	Keel	0.0813	0.0735	0.0972	-0.1559	0.2810	0.2848
5320	2400	300	0	Keel	0.0357	0.1205	0.1114	-0.1614	0.2911	0.2950
6741	3000	-20	0	Keel	-0.0181	0.1369	0.1224	-0.1040	0.3579	0.3303
8170	3600	-20	0	Keel	0.0843	0.3033	0.2790	0.0479	0.3184	0.2853
8364	3600	-20	160	First Deck	0.0328	0.0831	0.0792	0.0452	0.2497	0.2249
8536	3600	-20	280	Second Deck	0.0198	0.0752	0.0689	0.0189	0.2138	0.1903
8686	3600	-20	400	Top Deck	0.0163	0.0771	0.0698	0.0521	0.1839	0.1694
Russell Error Correlation			Sum(E(X))		0.4246	2.5904	2.4684	-0.4855	5.2053	4.8560
> 0.28	Poor		$\text{Sum}(E(X^2))$		0.0484	0.4025	0.3541	0.1462	1.3379	1.1657
< 0.15	Excellent		**Mean**		**0.0193**	**0.1177**	**0.1122**	**-0.0221**	**0.2366**	**0.2207**
			Standard Deviation		0.0437	0.0681	0.0606	0.0803	0.0711	0.0669
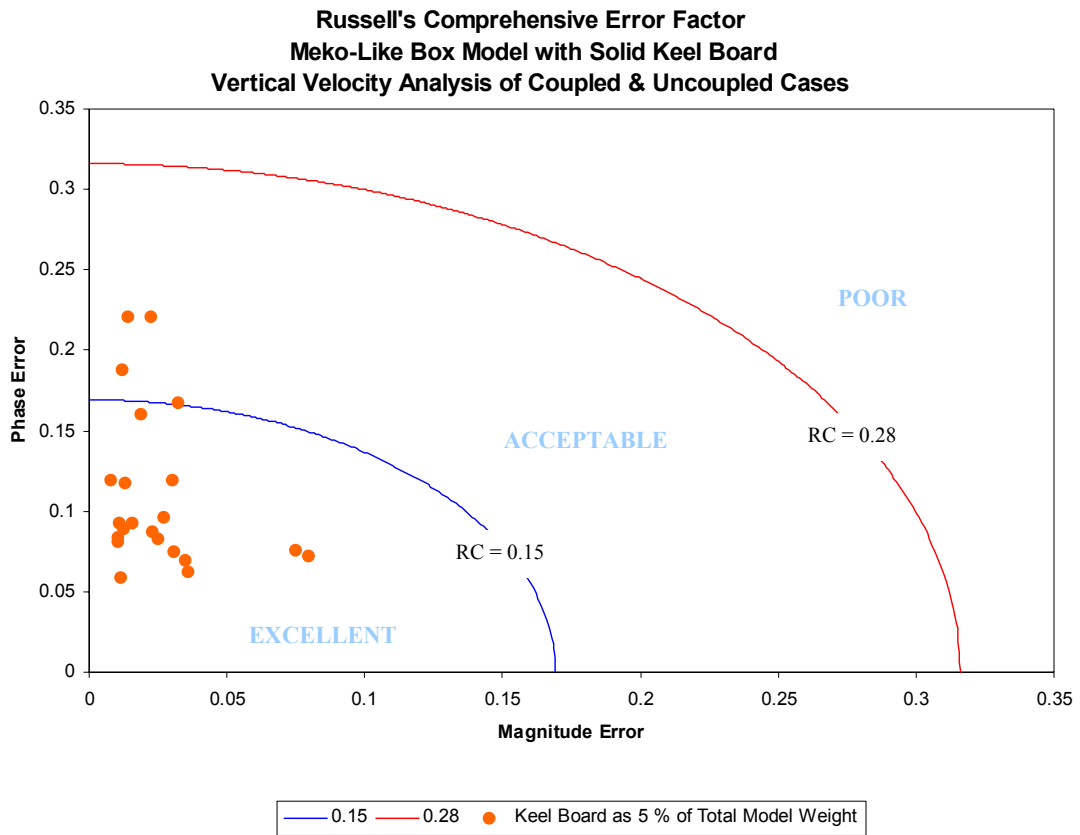
Figure 491.   Russell's Error Factor Comparison for Meko-Like Box Model with Solid Keel Board as 5 % of Total Model Weight (Vertical Velocity)
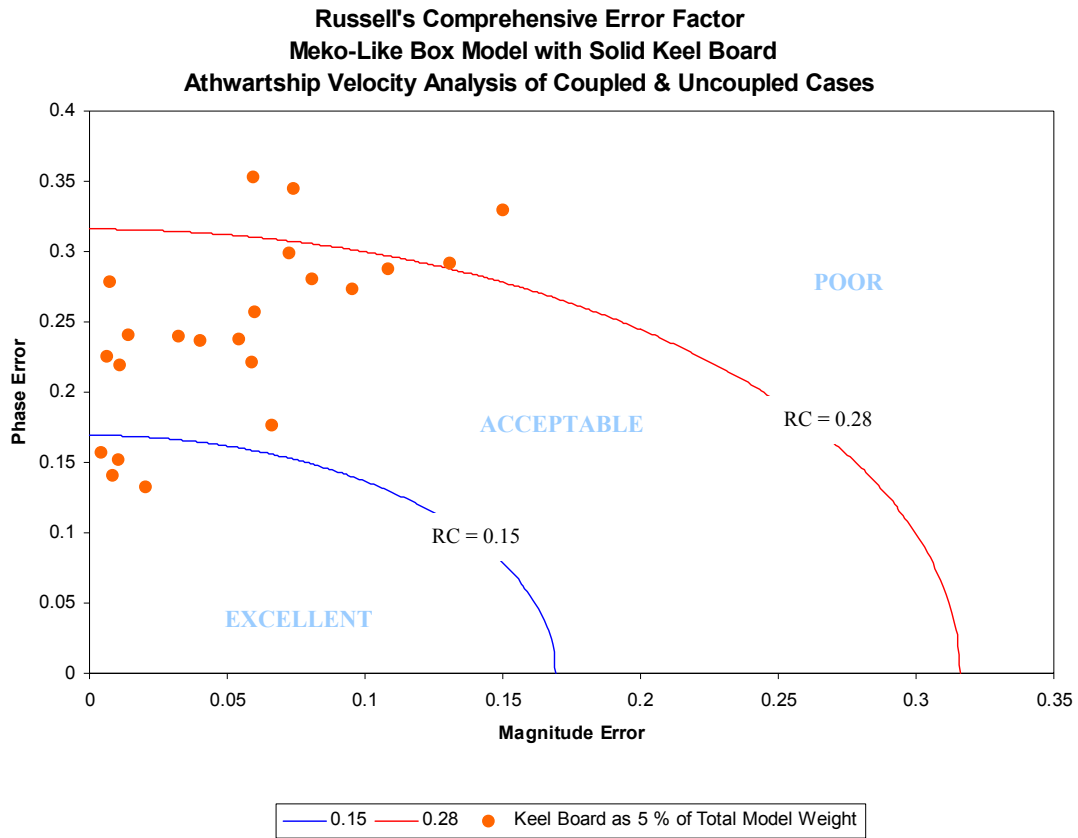
Figure 492. Russell's Error Factor Comparison for Meko-Like Box Model with Solid Keel Board as 5 % of Total Model Weight (Athwartship Velocity)

Table 34. Statistical Data for Meko-Like Box Model with Solid Keel Board as 5 % of Total Model Weight (Coupled and Uncoupled Cases)

Russell's Comprehensive Error Factor	Vertical Velocity Comparison	Athwartship Velocity Comparison
RC < 0.30	100 %	86 %
RC < 0.28	100 %	82 %
RC < 0.25	100 %	64 %
RC < 0.20	100 %	32 %
RC < 0.18	91 %	23 %
RC < 0.15	82 %	18 %
Mean RC	0.1027	0.2234
Standard Deviation	0.0416	0.0611
Mean + Standard Deviation	0.1773	0.2845
Data within One Standard Deviation	91 %	86 %

Table 35.   Russell's Error Factors for Meko-Like Box Model with Solid Keel Board as 5 % of Total Model Weight

Simulation runtime = 500 msec					Meko-Like Box Model with Solid Keel Board as 5 % of Total Model Weight					
					Vertical Velocity Comparison			Athwartship Velocity Comparison		
NODE	X (in)	Y (in)	Z (in)	Location	COUPLED & UNCOUPLED CASES			COUPLED & UNCOUPLED CASES		
					LS-DYNA/USA DATA (<250HZ)			LS-DYNA/USA DATA (<250HZ)		
					RM	RP	RC	RM	RP	RC
15	0	-20	0	Bulkhead	0.0156	0.0930	0.0835	0.0044	0.1576	0.1398
148	0	-20	160	Bulkhead	0.0347	0.0692	0.0686	-0.0201	0.1322	0.1185
268	0	-20	280	Bulkhead	0.0308	0.0750	0.0719	-0.0081	0.1406	0.1248
388	0	-20	400	Bulkhead	0.0268	0.0965	0.0887	-0.0105	0.1525	0.1355
2454	1200	-20	0	Keel	0.0222	0.2212	0.1971	0.0955	0.2731	0.2564
2648	1200	-20	160	First Deck	0.0227	0.0870	0.0797	0.0401	0.2365	0.2126
2820	1200	-20	280	Second Deck	0.0104	0.0837	0.0748	0.0139	0.2412	0.2142
2970	1200	-20	400	Top Deck	0.0111	0.0925	0.0826	0.0061	0.2252	0.1997
3883	1800	-20	0	Keel	-0.0080	0.1195	0.1061	-0.0596	0.3530	0.3173
5251	2400	-300	0	Keel	-0.0186	0.1601	0.1428	0.0073	0.2784	0.2469
5308	2400	-180	0	Keel	-0.0117	0.0585	0.0529	0.0586	0.2218	0.2033
5310	2400	-100	0	Keel	-0.0360	0.0627	0.0640	0.0659	0.1764	0.1669
5312	2400	-20	0	Keel	-0.0122	0.1876	0.1666	-0.0723	0.2990	0.2726
5313	2400	20	0	Keel	-0.0320	0.1677	0.1513	-0.0321	0.2394	0.2141
5315	2400	100	0	Keel	0.0748	0.0754	0.0941	-0.1084	0.2874	0.2722
5317	2400	180	0	Keel	0.0798	0.0717	0.0950	-0.1308	0.2914	0.2831
5320	2400	300	0	Keel	0.0304	0.1191	0.1089	-0.1498	0.3296	0.3209
6741	3000	-20	0	Keel	-0.0130	0.1179	0.1051	-0.0737	0.3450	0.3127
8170	3600	-20	0	Keel	0.0141	0.2211	0.1964	0.0806	0.2806	0.2588
8364	3600	-20	160	First Deck	0.0249	0.0830	0.0767	0.0601	0.2574	0.2342
8536	3600	-20	280	Second Deck	0.0106	0.0811	0.0724	0.0541	0.2378	0.2161
8686	3600	-20	400	Top Deck	0.0124	0.0890	0.0796	-0.0109	0.2193	0.1946
Russell Error Correlation				Sum(E(X))	0.2898	2.4325	2.2588	-0.1897	5.3754	4.9152
> 0.28	Poor			Sum(E(X^2))	0.0215	0.3202	0.2683	0.0991	1.3987	1.1766
< 0.15	Excellent			**Mean**	**0.0132**	**0.1106**	**0.1027**	**-0.0086**	**0.2443**	**0.2234**
				Standard Deviation	0.0290	0.0494	0.0416	0.0681	0.0637	0.0611
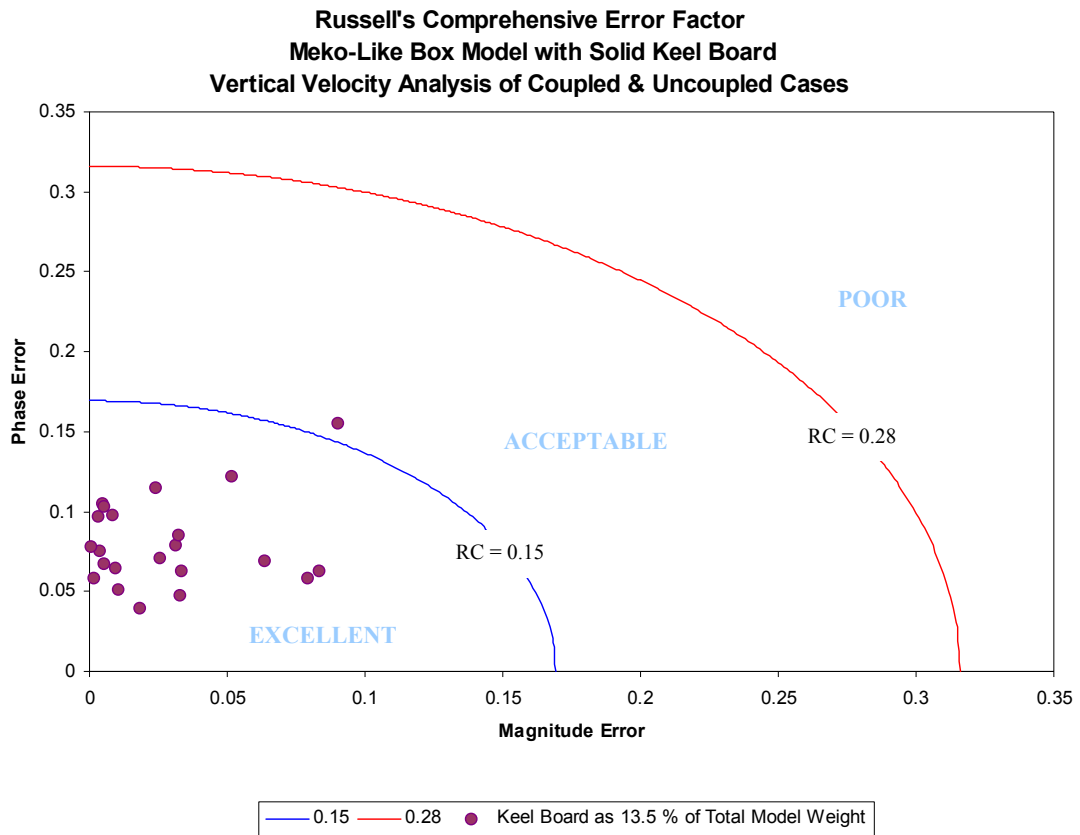
Figure 493. **Russell's Error Factor Comparison for Meko-Like Box Model with Solid Keel Board as 13.5 % of Total Model Weight (Vertical Velocity)**
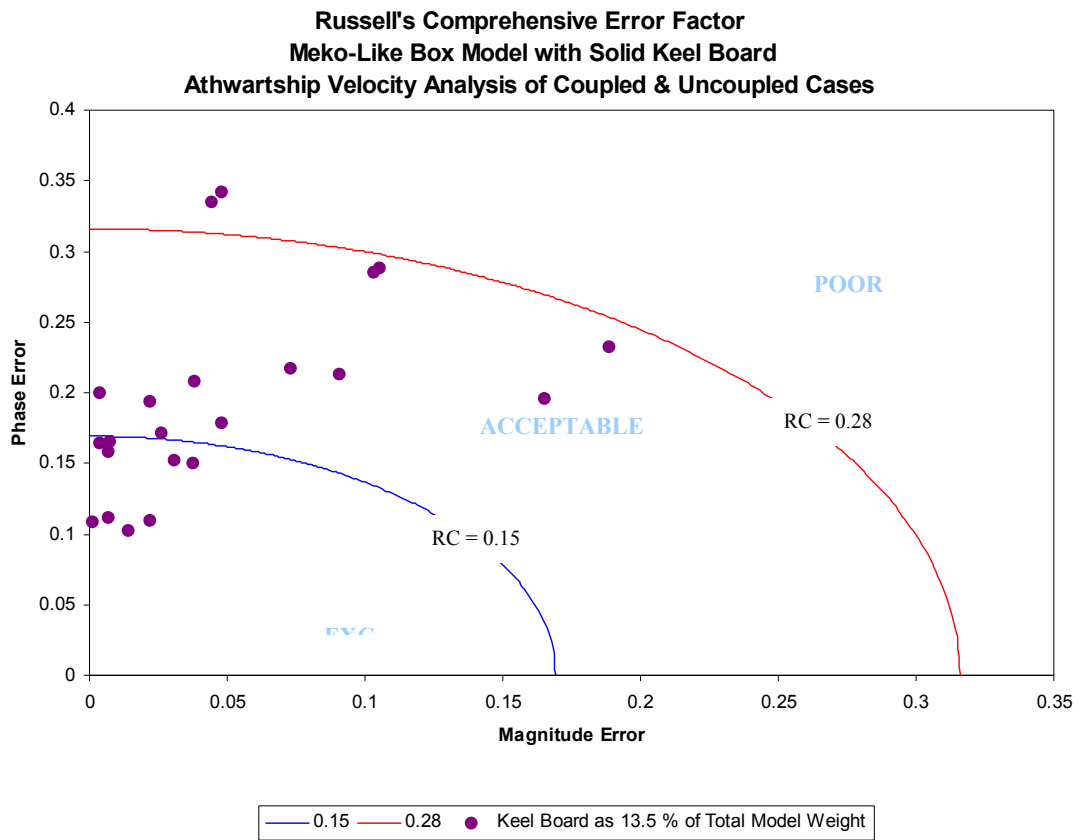
Figure 494.   Russell's Error Factor Comparison for Meko-Like Box Model with Solid Keel Board as 13.5 % of Total Model Weight (Athwartship Velocity)
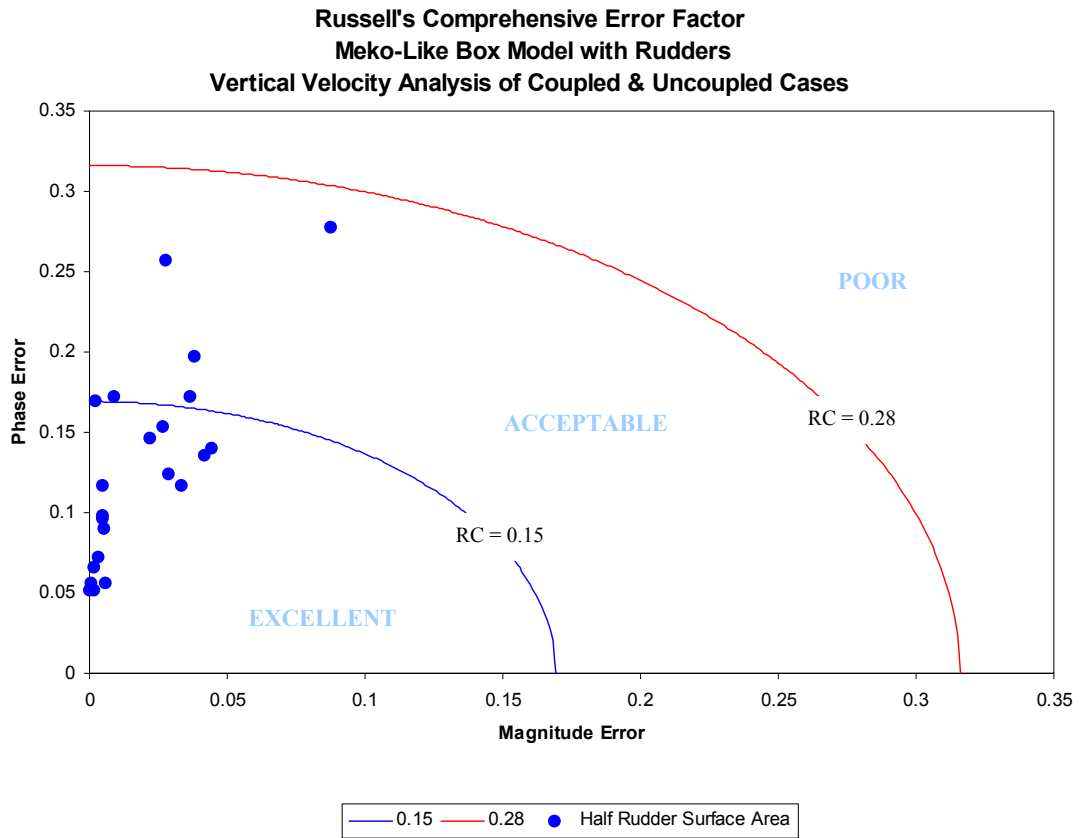
Figure 495.   Russell's Error Factor Comparison for Meko-Like Box Model with Rudders Having Half Rudder Surface Area (Vertical Velocity)

**Russell's Comprehensive Error Factor
Meko-Like Box Model with Rudders
Athwartship Velocity Analysis of Coupled & Uncoupled Cases**

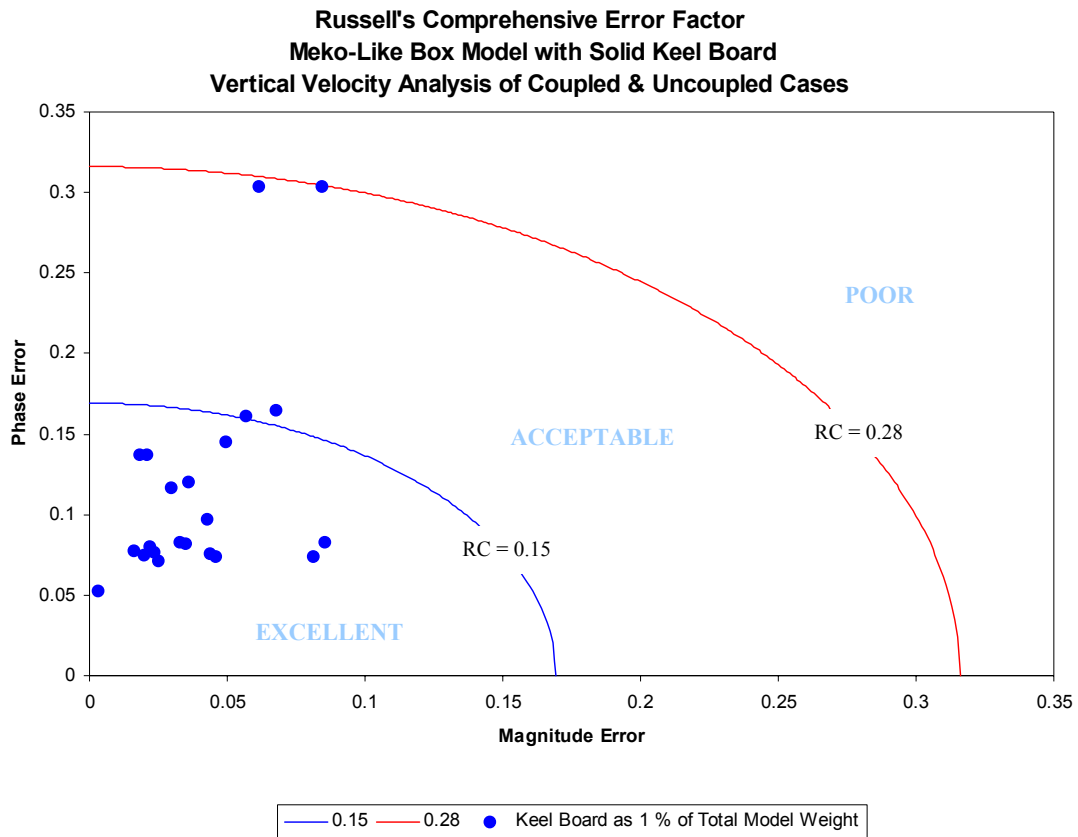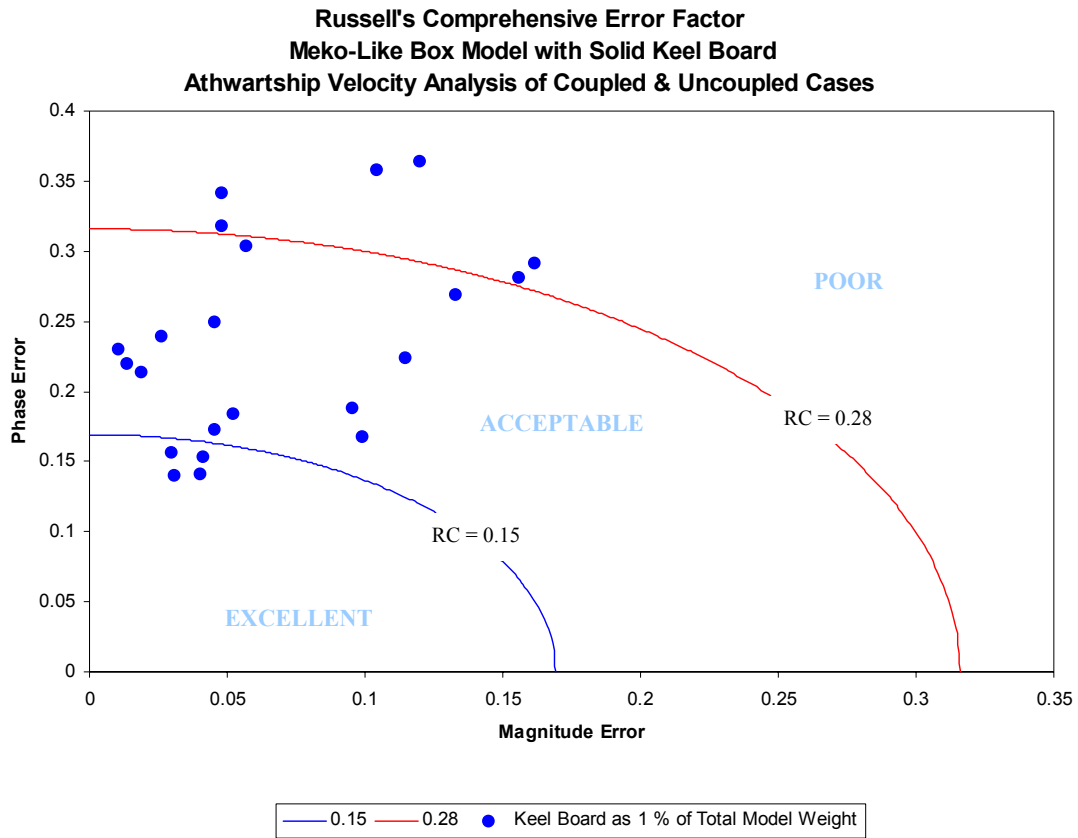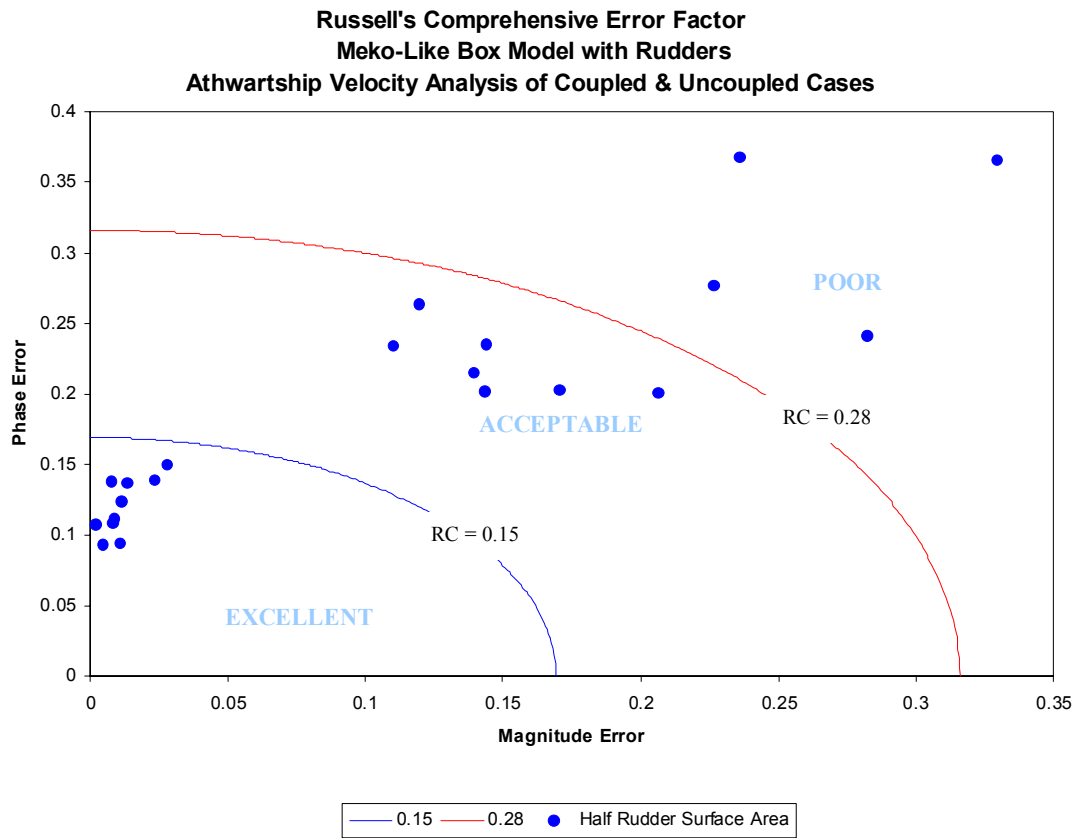**Figure 496.   Russell's Error Factor Comparison for Meko-Like Box Model with Rudders Having Half Rudder Surface Area (Athwartship Velocity)**

Table 36.   Statistical Data for Meko-Like Box Model with Rudders Having Half Rudder Surface Area (Coupled and Uncoupled Cases)

Russell's Comprehensive Error Factor	Vertical Velocity Comparison	Athwartship Velocity Comparison
RC < 0.30	100 %	82 %
RC < 0.28	100 %	77 %
RC < 0.25	95 %	68 %
RC < 0.20	91 %	45 %
RC < 0.18	91 %	45 %
RC < 0.15	73 %	45 %
Mean RC	0.1155	0.2045
Standard Deviation	0.0576	0.1046
Mean + Standard Deviation	0.1731	0.3091
Data within One Standard Deviation	86 %	82 %

Table 37.   Russell's Error Factors for Meko-Like Box Model with Rudders Having Half Rudder Surface Area

Simulation runtime = 500 msec					Meko-Like Box Model with Rudders Having Half Rudder Surface Area					
					Vertical Velocity Comparison			Athwartship Velocity Comparison		
NODE	X (in)	Y (in)	Z (in)	Location	COUPLED & UNCOUPLED CASES			COUPLED & UNCOUPLED CASES		
					LS-DYNA/USA DATA (<250HZ)			LS-DYNA/USA DATA (<250HZ)		
					RM	RP	RC	RM	RP	RC
15	0	-20	0	Bulkhead	-0.0023	0.1693	0.1501	0.1393	0.2151	0.2271
74	120	-140	0	Keel	0.0275	0.2568	0.2289	0.1706	0.2021	0.2344
81	120	140	0	Keel	-0.0877	0.2776	0.2580	0.2066	0.2004	0.2550
148	0	-20	160	Bulkhead	-0.0334	0.1168	0.1076	0.2268	0.2768	0.3171
214	120	-140	160	First Deck	-0.0443	0.1405	0.1306	0.1433	0.2016	0.2192
221	120	140	160	First Deck	-0.0417	0.1354	0.1256	0.2733	0.1831	0.2915
268	0	-20	280	Bulkhead	-0.0285	0.1239	0.1127	0.3299	0.3651	0.4361
334	120	-140	280	Second Deck	0.0265	0.1540	0.1385	0.1440	0.2353	0.2445
341	120	140	280	Second Deck	-0.0366	0.1721	0.1559	0.2826	0.2409	0.3291
388	0	-20	400	Bulkhead	-0.0217	0.1467	0.1315	0.2363	0.3679	0.3875
434	120	-140	400	Top Deck	0.0088	0.1726	0.1532	0.1196	0.2637	0.2566
441	120	140	400	Top Deck	-0.0380	0.1976	0.1783	0.1101	0.2341	0.2293
2454	1200	-20	0	Keel	-0.0059	0.0560	0.0499	-0.0234	0.1392	0.1251
3883	1800	-20	0	Keel	-0.0051	0.0902	0.0800	0.0078	0.1377	0.1222
5251	2400	-300	0	Keel	-0.0046	0.1168	0.1036	0.0114	0.1236	0.1100
5308	2400	-180	0	Keel	-0.0018	0.0522	0.0463	0.0108	0.0945	0.0843
5310	2400	-100	0	Keel	-0.0005	0.0562	0.0498	0.0087	0.1117	0.0993
5315	2400	100	0	Keel	-0.0031	0.0726	0.0644	0.0081	0.1079	0.0959
5317	2400	180	0	Keel	-0.0018	0.0657	0.0583	0.0048	0.0928	0.0823
5320	2400	300	0	Keel	0.0045	0.0962	0.0853	0.0019	0.1073	0.0951
6741	3000	-20	0	Keel	0.0045	0.0983	0.0872	-0.0135	0.1363	0.1213
8170	3600	-20	0	Keel	0.0001	0.0520	0.0461	-0.0282	0.1502	0.1354
Russell Error Correlation			Sum(E(X))		-0.2851	2.8195	2.5418	2.3708	4.1873	4.4983
> 0.28	Poor		Sum(E(X^2))		0.0183	0.4444	0.3634	0.5316	0.9324	1.1497
< 0.15	Excellent		**Mean**		**-0.0130**	**0.1282**	**0.1155**	**0.1078**	**0.1903**	**0.2045**
			Standard Deviation		0.0263	0.0629	0.0576	0.1147	0.0803	0.1046
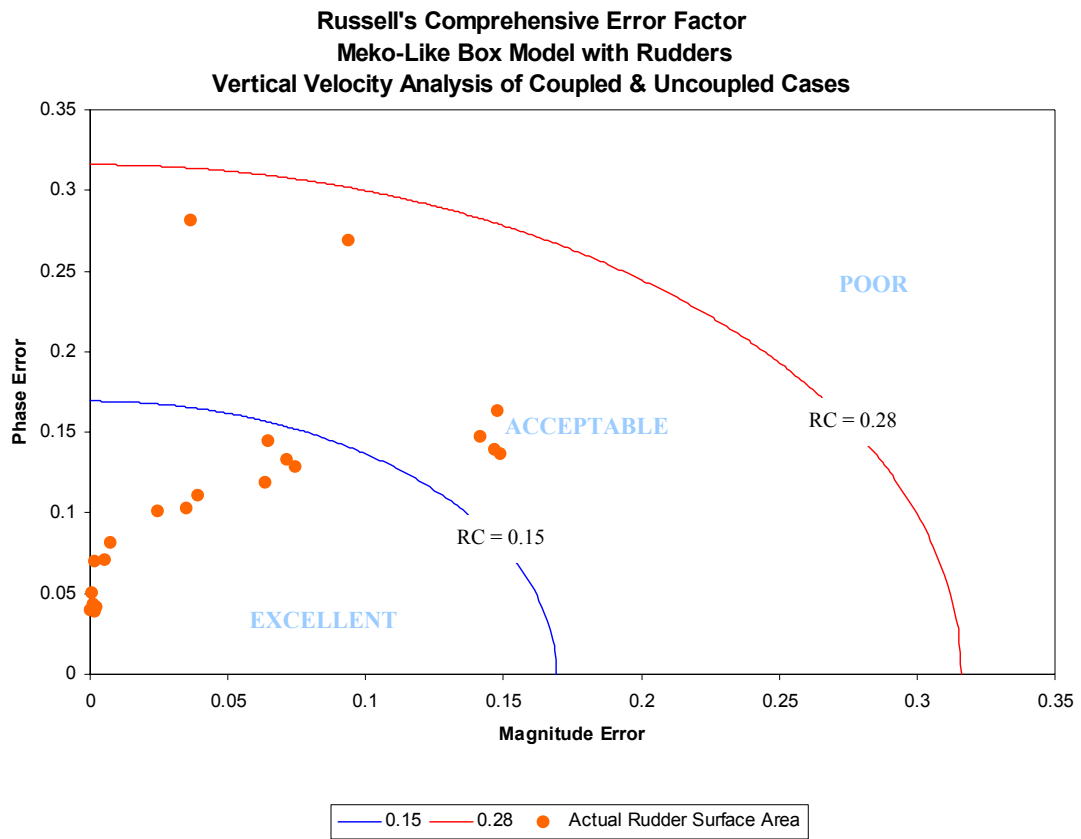
Figure 497.   Russell's Error Factor Comparison for Meko-Like Box Model with Rudders Having Actual Rudder Surface Area (Vertical Velocity)
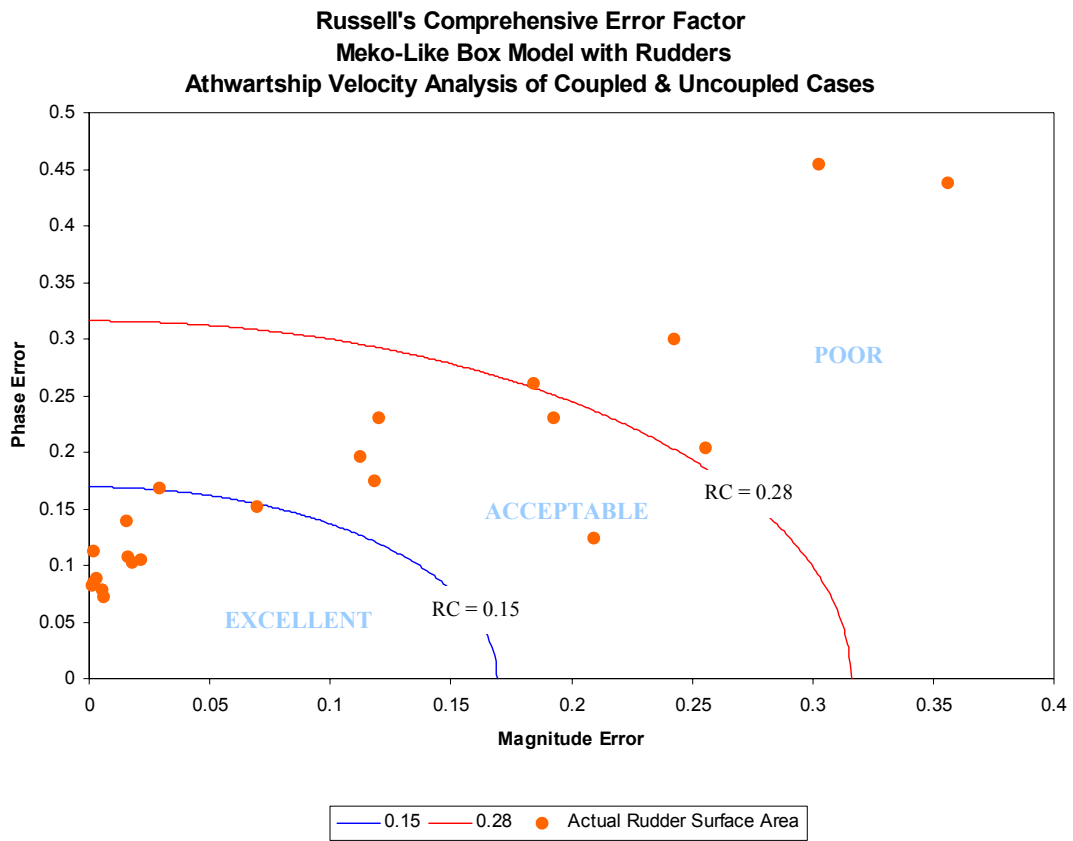
Figure 498. **Russell's Error Factor Comparison for Meko-Like Box Model with Rudders Having Actual Rudder Surface Area (Athwartship Velocity)**
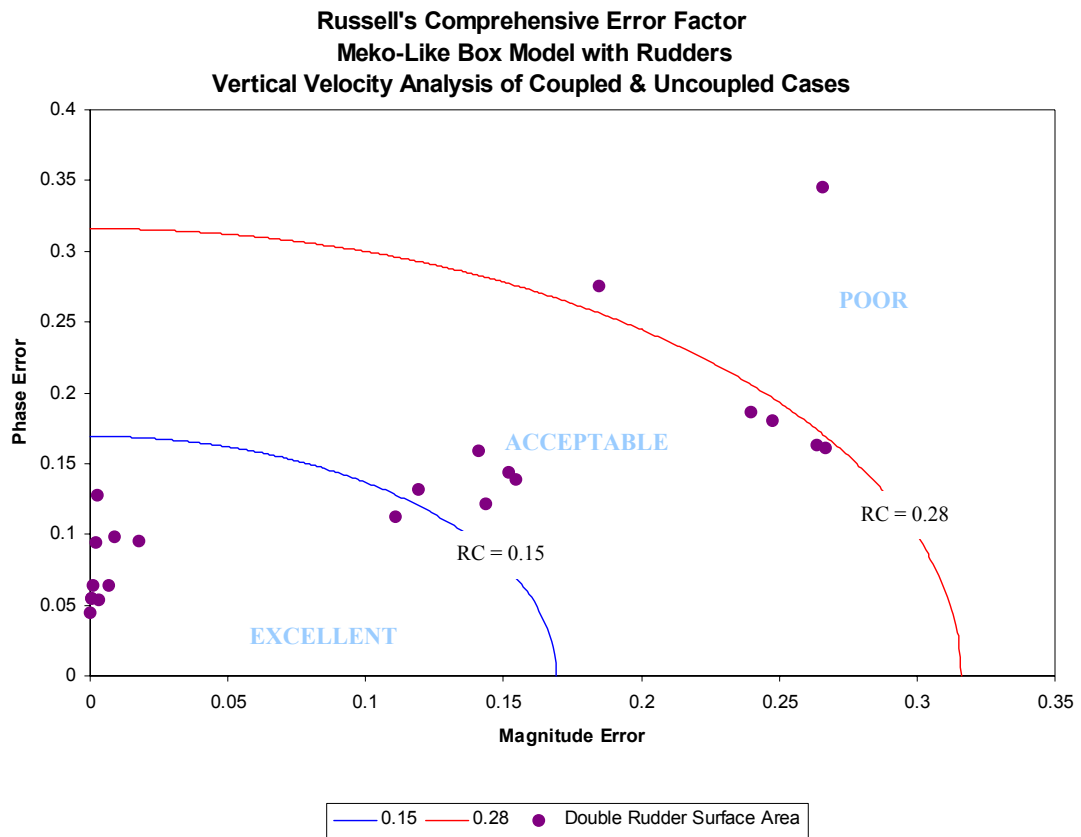
Figure 499.   Russell's Error Factor Comparison for Meko-Like Box Model with Rudders Having Double Rudder Surface Area (Vertical Velocity)
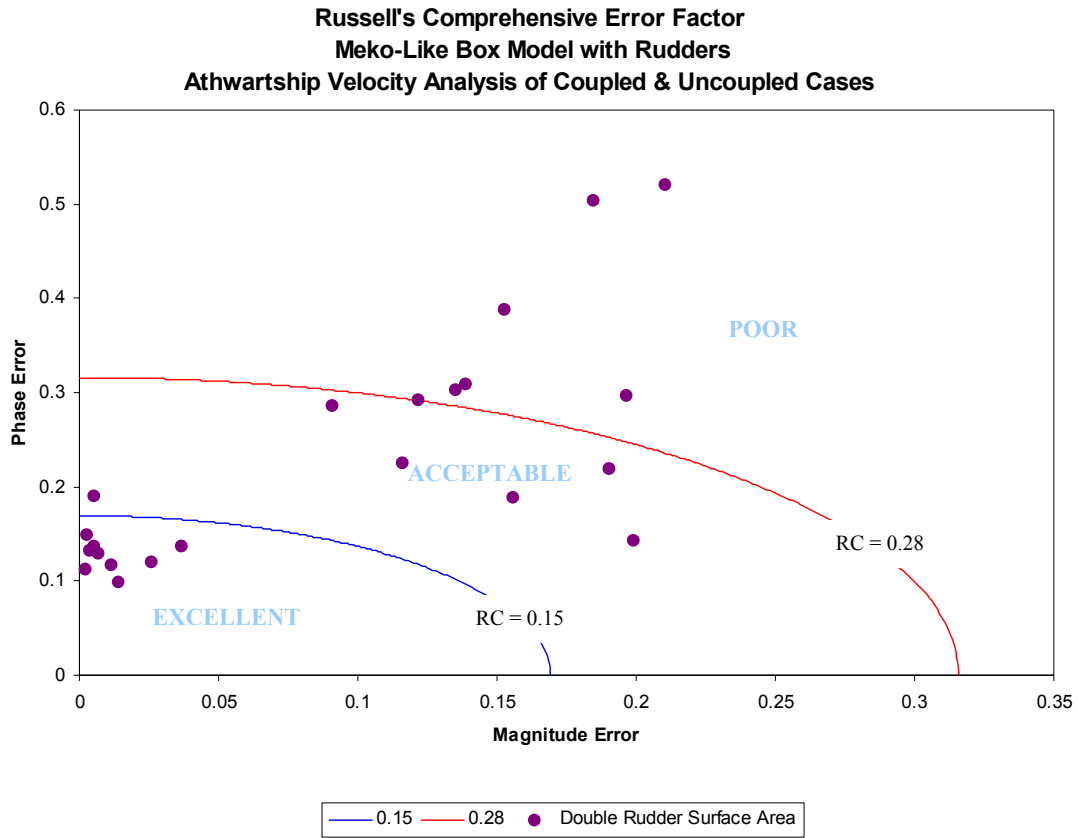
Figure 500.   Russell's Error Factor Comparison for Meko-Like Box Model with Rudders Having Double Rudder Surface Area (Athwartship Velocity)

Table 38.   Statistical Data for Meko-Like Box Model with Rudders Having Double Rudder Surface Area (Coupled and Uncoupled Cases)

Russell's Comprehensive Error Factor	Vertical Velocity Comparison	Athwartship Velocity Comparison
RC < 0.30	95 %	77 %
RC < 0.28	91 %	68 %
RC < 0.25	73 %	59 %
RC < 0.20	73 %	45 %
RC < 0.18	59 %	45 %
RC < 0.15	50 %	45 %
Mean RC	0.1572	0.2195
Standard Deviation	0.1011	0.1223
Mean + Standard Deviation	0.2583	0.3418
Data within One Standard Deviation	73 %	86 %

Table 39. Russell's Error Factors for Meko-Like Box Model with Rudders Having Double Rudder Surface Area

Simulation runtime = 500 msec					Meko-Like Box Model with Rudders Having Double Rudder Surface Area					
					Vertical Velocity Comparison			Athwartship Velocity Comparison		
NODE	X (in)	Y (in)	Z (in)	Location	COUPLED & UNCOUPLED CASES			COUPLED & UNCOUPLED CASES		
					LS-DYNA/USA DATA (<250HZ)			LS-DYNA/USA DATA (<250HZ)		
					RM	RP	RC	RM	RP	RC
15	0	-20	0	Bulkhead	0.2398	0.1860	0.2690	0.1162	0.2253	0.2247
74	120	-140	0	Keel	0.2660	0.3457	0.3866	0.1555	0.1893	0.2171
81	120	140	0	Keel	0.1844	0.2751	0.2935	0.1991	0.1435	0.2175
148	0	-20	160	Bulkhead	0.2667	0.1608	0.2760	0.1524	0.3889	0.3701
214	120	-140	160	First Deck	0.1191	0.1316	0.1573	0.0908	0.2861	0.2660
221	120	140	160	First Deck	0.1107	0.1127	0.1400	0.1900	0.2186	0.2567
268	0	-20	280	Bulkhead	0.2637	0.1634	0.2749	0.2102	0.5207	0.4976
334	120	-140	280	Second Deck	0.1516	0.1438	0.1852	0.1387	0.3093	0.3004
341	120	140	280	Second Deck	0.1434	0.1215	0.1666	0.1964	0.2969	0.3155
388	0	-20	400	Bulkhead	0.2475	0.1798	0.2711	0.1846	0.5048	0.4763
434	120	-140	400	Top Deck	0.1410	0.1586	0.1880	0.1216	0.2928	0.2810
441	120	140	400	Top Deck	0.1546	0.1391	0.1843	0.1348	0.3035	0.2943
2454	1200	-20	0	Keel	0.0003	0.0547	0.0485	-0.0364	0.1375	0.1261
3883	1800	-20	0	Keel	0.0087	0.0978	0.0870	0.0036	0.1322	0.1172
5251	2400	-300	0	Keel	-0.0028	0.1279	0.1134	0.0259	0.1205	0.1092
5308	2400	-180	0	Keel	0.0029	0.0541	0.0480	0.0137	0.0985	0.0881
5310	2400	-100	0	Keel	-0.0001	0.0444	0.0394	0.0113	0.1169	0.1041
5315	2400	100	0	Keel	-0.0010	0.0635	0.0563	-0.0066	0.1293	0.1147
5317	2400	180	0	Keel	-0.0069	0.0636	0.0567	-0.0052	0.1904	0.0970
5320	2400	300	0	Keel	-0.0179	0.0947	0.0854	0.0019	0.1132	0.1003
6741	3000	-20	0	Keel	-0.0021	0.0941	0.0834	0.0049	0.1374	0.1218
8170	3600	-20	0	Keel	0.0004	0.0543	0.0481	-0.0026	0.1493	0.1323
Russell Error Correlation			Sum(E(X))		2.2700	2.8672	3.4587	1.9008	5.0049	4.8280
> 0.28	Poor		Sum(E(X^2))		0.4784	0.4873	0.7585	0.3164	1.4569	1.3735
< 0.15	Excellent		**Mean**		**0.1032**	**0.1303**	**0.1572**	**0.0864**	**0.2275**	**0.2195**
			Standard Deviation		0.1078	0.0736	0.1011	0.0851	0.1231	0.1223

LIST OF REFERENCES

1.   NSWCCD/UERD, www.dt.navy.mil/sur-str-mat/sur-wea-eff/his, April 2005.

2.   NSWCCD/UERD, www.dt.navy.mil/sites/uerd/history.html, April 2005.

3.   OPNAV Instruction 9072.2, "Shock Hardening of Surface Ships," 12 January 1987.

4.   NAVSEA 0908-LP-000-3010A, Shock Design Criteria for Surface Ships, October 1994.

5.   Military Specification, MIL-S-901D, Shock Tests, High Impact Shipboard Machinery, Equipment and Systems, Requirements for, March 1989.

6.   DOT&E FY97 Annual Report, www.globalsecurity.org/military/library/budget/fy1997/dot-e/navy/97ddg51.html, May 2005.

7.   Shin, Y. S. and Park, S. Y., "Ship Shock Trial Simulation of USS John Paul Jones (DDG 53) Using LS-DYNA/USA: Three Dimensional Analysis," 70th Shock and Vibration Symposium Proceedings, Vol. I, November 1999.

8.   Schneider, N. A., "Prediction of Surface Ship Response to Severe Underwater Explosions Using a Virtual Underwater Shock Environment," Master's Thesis, Naval Postgraduate School, Monterey, California, 2003.

9.   Shin, Y. S., "Naval Ship Shock and Design Analysis," Course Notes for Underwater Shock Analysis, Naval Postgraduate School, Monterey, California, 1996.

10.   Cole, R. H., *Underwater Explosions*, pp. 1-15, Princeton University Press, 1948.

11.   DeRuntz, Jr., J. A., *The Underwater Shock Analysis (USA) Manual*, Unique Software Applications, Colorado Springs, Colorado, May 1996.

12.   Arons, A. B., et al., "Long Range Shock Propagation in Underwater Explosion Phenomena II", Underwater Explosion Compendium, Vol. 1, October 1949.

13.   Shin, Y. S., "LS-DYNA Training Guide: Nonlinear Dynamic Analysis of Structures in 3-D Code Coupled with Underwater Shock Analysis Code for Ship Shock Modeling and Simulation," Naval Postgraduate School, July 2002.

14.   DeRuntz, Jr., J. A. "The Underwater Shock Analysis Code and Its Applications," 60th Shock and Vibration Symposium, Vol. I, pp. 89-107, November 1989.

15.   Shin, Y. S., "Ship-Shock Modeling and Simulation with Applications Using LS-DYNA/USA Code, and Review of DDAM," Naval Postgraduate School, Monterey, California, July 2002.

16.   Geers, T. L., "Doubly Asymptotic Approximations for Transient Motions of Submerged Structures," Journal of the Acoustical Society of America, Vol. 64, pp 1500-1508, 1978.

17.   DeRuntz, Jr. J. A. and Rankin, C. C., "Applications of the USA-STAGS-CFA Code to Nonlinear Fluid-Structure Interaction Problems in Underwater Shock of Submerged Structures," Proceedings of the 60th Shock and Vibration Symposium, 1989.

18.   Geers, T.L., "Residual Potential and Approximate Methods for Three-Dimensional Fluid-Structure Interaction Problems," The Journal of the Acoustical Society of America, Vol. 49, pp. 1505-1510, 1971.

19.   Shin, Y. S. and Santiago, L. D., "Surface Ship Modeling and Simulation," The ASME PVP, Vol. 351, pp. 29-34, 1997 ASME PVP Conference, July 1997.

20.   XYZ Scientific Applications, Inc., *TrueGrid Manual*, Livermore, California, 1997.

21.   Turkish Navy Command, www.dzkk.tsk.mil.tr/English/AnaSayfa.asp, April 2005.

22.   Livermore Software Technology Corporation, *LS-DYNA Keyword User's Manual, Version 940*, Livermore, California, 1997.

23.   Riedel, J. S., DDG 51 Shipbuilding Program (PMS 400D), "USS WINSTON S. CHURCHILL (DDG 81) Shock Trial Overview," Presentation at Naval Postgraduate School, Monterey, California, February 2002.

24.   Hart, D. T., "Ship Shock Trial Simulation of USS Winston S. Churchill (DDG-81): Surrounding Fluid Effect," Master's Thesis, Naval Postgraduate School, Monterey, California, 2003.

25.   DeRuntz, Jr., J. A. "Application of the USA Code to Underwater Shock Problems," 72nd Shock and Vibration Symposium, November 2001.

26.   DeRuntz, Jr., J. A. and Shin, Y. S., "USA/LS-DYNA3D Software Training Course", Naval Postgraduate School, Monterey, California, June 1996.

27.   Geer, T. L., "An objective Error Measure for the Comparison of Calculated and Measured Transient Response Histories," The Shock and Vibration Bulletin, SAVIAC, NRL, Washington, DC, June, 1984.

28.   Ceetron ASA, "GLview Pro Installation Guide and Tutorial: GLview Pro 6.3," Trondheim, Norway, 2001.

29.	Didoszak, Jarema M., "Parametric Studies of DDG-81 Ship Shock Trial Simulations," Master's Thesis, Naval Postgraduate School, Monterey, California, 2004.

30.	Russell, D. D., "Error Measures for Comparing Transient Data: Part I: Development of a Comprehensive Error Measure," 68th Shock and Vibration Symposium Proceedings, Vol. I, November 1997.

31.	Russell, D. D., "Error Measures for Comparing Transient Data: Part II: Error Measure Case Study," 68th Shock and Vibration Symposium Proceedings, Vol. I, November 1997.

32.	Russell, D. D., "DDG53 Shock Trial Simulation Acceptance Criteria," 69th Shock and Vibration Symposium, October 1998.

33.	Rutgerson, S. E., NSWCCD/UERD Code 661, "Review of DDG 81 Modeling and Simulation Results," Presentation at Naval Postgraduate School, Monterey, California, July 2003.

34.	Shin, Y. S. and Ham, I., "Damping Modeling Strategy for Naval Ship System," Tech. Report NPS-ME-03-003, Naval Postgraduate School, Monterey, California, September 2003.

THIS PAGE INTENTIONALLY LEFT BLANK

INITIAL DISTRIBUTION LIST

1.   Defense Technical Information Center
      Ft. Belvoir, Virginia

2.   Dudley Knox Library
      Naval Postgraduate School
      Monterey, California

3.   Mechanical Engineering Department Chairman, Code ME
      Naval Postgraduate School
      Monterey, California

4.   Naval/Mechanical Engineering Curriculum Code 74
      Naval Postgraduate School
      Monterey, California

5.   Prof. Young S. Shin, Code ME/Sg
      Department of Mechanical and Astronautical Engineering
      Naval Postgraduate School
      Monterey, California

6.   Research Assistant Prof. Jarema M. Didoszak, ME/Di
      Department of Mechanical and Astronautical Engineering
      Naval Postgraduate School
      Monterey, California

7.   Michael J. Harrington
      Gibbs and Cox, Inc.
      Arlington, Virginia

8.   Constintine Constant
      Naval Sea Systems Command
      Washington, District of Columbia

9.   Frederick A. Costanzo
      Underwater Explosion Research Department (UERD)
      Naval Surface Warfare Center – Carderock Division
      West Bethesda, Maryland

10.   Steven E. Rutgerson
      Underwater Explosion Research Department (UERD)
      Naval Surface Warfare Center – Carderock Division
      West Bethesda, Maryland

11.   Hans U. Mair
        Institute for Defense Analysis
        Alexandria, Virginia